

KATHOLIEKE UNIVERSITEIT LEUVEN
FACULTEIT TOEGEPASTE WETENSCHAPPEN
DEPARTEMENT ELEKTROTECHNIEK
Kasteelpark Arenberg 10, 3001 Leuven (Heverlee)

ADVANCED EQUALIZATION TECHNIQUES FOR DMT-BASED SYSTEMS

Jury:
Prof. dr. ir. G. De Roeck, voorzitter
Prof. dr. ir. M. Moonen, promotor
Prof. dr. ir. A. Bultheel
Prof. dr. ir. M. Engels
Prof. dr. ir. M. Moeneclaey (U. Gent)
Prof. dr. ir. L. Vandendorpe (U.C.L.)
Prof. dr. ir. L. Van der Perre (U.A. en IMEC)
Prof. dr. ir. J. Vandewalle

Proefschrift voorgedragen tot
het behalen van het doctoraat
in de toegepaste wetenschappen

door

Koen VANBLEU

UDC 681.3*C26 Oktober 2004

© Katholieke Universiteit Leuven – Faculteit Toegepaste Wetenschappen
Arenbergkasteel, B-3001 Heverlee (Belgium)

Alle rechten voorbehouden. Niets uit deze uitgave mag vermenigvuldigd en/of openbaar gemaakt worden door middel van druk, fotocopie, microfilm, elektronisch of op welke andere wijze ook zonder voorafgaande schriftelijke toestemming van de uitgever.

All rights reserved. No part of the publication may be reproduced in any form by print, photoprint, microfilm or any other means without written permission from the publisher.

D/2004/7515/90

ISBN 90-5682-552-6

Voorwoord

In oktober 1999 vertrok ik op reis, met eindbestemming 'doctoraat'. Nu, 61 maanden later, ben ik op die bestemming aangekomen. De reis was zeker niet eenvoudig, maar vele mensen wezen me onderweg de juiste richting aan. Ik wil dan ook allen danken die me hielpen het einddoel te bereiken.

Vooreerst ben ik mijn promotor Prof. Marc Moonen zeer dankbaar. Vijf jaar geleden schetste hij mij een heel realistisch beeld van een doctoraat: een periode van grote vrijheid, maar waarin je geregeld dient bij te sturen en — als in elk ander beroep — verantwoordelijkheid dient op te nemen om de taak tot een goed einde te brengen. Marc, ik waardeer de vrijheid en richting die je me onderweg gaf, je vertrouwen in de goede afloop en je appreciatie voor de behaalde resultaten.

Vervolgens wens ik de leden van mijn begeleidingscommissie, Prof. Adhemar Bultheel, Prof. Marc Engels, Prof. Marc Moeneclaey en Prof. Joos Vandewalle, te bedanken voor het nalezen van het proefschrift en de waardevolle suggesties en aanvullingen. Ik dank ook Prof. Luc Vandendorpe en Prof. Liesbet Van der Perre voor hun onmiddellijke bereidheid om deel uit te maken van de examencommissie. Verder dank ik Prof. Guido De Roeck voor het aanvaarden van het voorzitterschap van de jury.

Bijzonder interessant gedurende de afgelopen jaren was de nauwe samenwerking met Alcatel, Antwerpen. Deze zorgde voor de nodige voeling met de 'buitenwereld' en betekende dan ook een belangrijke verrijking van mijn werk. Ik dank dan ook alle mensen binnen Alcatel waarmee ik mocht samenwerken.

I am grateful to Prof. C. Richard Johnson, Jr., who invited Geert Ysebaert and me for a visit to his research group at Cornell University in Ithaca, USA. The discussions, lunches, dinners, coffee breaks and beer drinks with him, his team mates (Rick, Andy and John), Prof. Brian Evans (University of Texas at Austin, USA) and Ming made it an unforgettable experience.

Een speciaal woordje van dank richt ik aan de DSL-Geerten: dank je, Geert Ysebaert en Geert Leus, voor de nuttige discussies en het samen geleverde werk.

Ik ben het F.W.O.-Vlaanderen erkentelijk voor de financiële ondersteuning gedurende de eerste vier jaren van mijn doctoraat.

Bij deze gelegenheid wil ik ook alle (ex-)collega's van de DSP-kliek danken voor de toffe sfeer in ESAT en daarbuiten: op een rustig Leuvens terrasje, aan Hilaires met wijn overgoten tafel, tijdens een verjaardags- of ander feestje, op het carting-circuit in Herselt, ... Dank je, Geert L, Geert R, Geert VM, Geert Y, Gert, Hilde, Imad, Jan S, Jan V, Katleen, Koen E, Narendra, Olivier, Paschalis, Raphael, Ruben, Simon, Thomas en Toon.

Aan familie en vrienden, bedankt voor jullie interesse, vriendschap en het gezellige samenzijn! Moatjes, wuk zoekik zin zoender hidder ...

Mama, Papa en Zus, dank voor de warme thuis en de kansen die jullie me steeds geboden hebben.

Aurel en Magda, dank voor alle steun, warmte en goede zorgen.

Tenslotte, maar niet in het minst: dank voor alles, Ann, keppe va mie!

Koen Vanbleu
Oktober 2004

Abstract

Digital subscriber line (DSL) technology is one of the fastest growing broadband internet access media. Whereas asymmetric DSL (ADSL) already offers data rates of a few megabits per second, next-generation ADSL2+ and VDSL promise even higher bit rates to support so-called triple play (high-quality video, voice and high-speed data).

The use of a large bandwidth over the phone line (up to 12 MHz for VDSL) induces impairments, such as severe channel distortion, echo, narrow-band radio-frequency interference (RFI) and crosstalk from other DSL systems. DSL communication makes use of so-called discrete multitone (DMT) modulation, supplemented with advanced digital signal processing algorithms, to tackle these impairments and serve a maximum number of customers. In this thesis, we focus on channel equalization and RFI mitigation algorithms that outperform existing algorithms in terms of bit rate.

DMT equalization is typically done by means of a channel-shortening time-domain equalizer (TEQ) and a one-tap frequency-domain equalizer per used tone. We first derive a TEQ design criterion that corresponds to true bit rate maximization, an unsolved problem so far. The *bit rate maximizing TEQ* (BM-TEQ) can also be posted as the solution to an iteratively-reweighted separable non-linear least-squares (LS) problem. This alternative formulation gives rise to an LS-based framework for DMT equalization. It also leads to an *adaptive* optimization algorithm that allows to track changing channel conditions and, as such, integrates well with the so-called seamless rate adaptation functionality of ADSL2/ADSL2+.

A complete range of adaptive bit rate maximizing equalizers then opens up, offering a flexible trade-off between computational and memory cost while keeping bit rate performance at the same level. The memory-efficient adaptive BM-TEQ and the computationally efficient so-called adaptive per-tone equalizer (PTEQ) form extreme cases of the set of bit rate maximizing per-group equalizers, which equalize groups of tones in parallel. A tone-grouping solution with as few as 4 equally-sized tone groups gives close-to-PTEQ performance in

harsh, RFI-dominated scenarios.

To further enhance the RFI mitigation capabilities, *receiver windowing* offers a cheap and effective solution. We extend the BM-TEQ design criterion and optimization algorithm to incorporate an optimal receiver window and perform joint equalization and RFI mitigation. Several important special cases are also discussed, such as the bit rate maximizing windowing-only case, the per-group and per-tone combined equalizer and windowing case and the BM-TEQ design in combination with a fixed window.

Finally, we provide low-cost *linear and decision-feedback BM-TEQ and PTEQ extensions* that exploit so-called frequency-domain transmit redundancy from pilot, unused and/or feedback tones. These extensions accommodate infinite impulse response channels as well as a reduced DMT cyclic prefix length.

Korte inhoud

De ‘digital subscriber line’ (DSL)-technologie is één van de zich snelst verspreidende media voor breedband-internettoegang. Asymmetrische DSL (ADSL) realiseert reeds bitsnelheden van verscheidene megabits per seconde. Toekomstige DSL-systemen, zoals ADSL2+ en VDSL, beloven nog hogere bitsnelheden die zogenaamde ‘triple-play’ (video en spraak van hoge kwaliteit alsook datacommunicatie tegen een hoge snelheid) zullen mogelijk maken.

Het gebruik van een grote bandbreedte (tot 12 MHz voor VDSL) gaat gepaard met ruis t.g.v. het kanaal, echo, smalbandige radio-frequente interferentie (RFI) en overspraak van andere DSL-systemen. DSL-communicatie maakt gebruik van zogenaamde ‘discrete multitone modulation’ (DMT), in combinatie met geavanceerde digitale signaalverwerkingsalgoritmen, om deze ruisbronnen aan te pakken en een maximaal aantal klanten te bedienen. In deze thesis focusseren we ons op algoritmes voor kanaalegalisatie en RFI-onderdrukking die een hogere bitsnelheid bieden dan bestaande algoritmes.

DMT-egalisatie is meestal gebaseerd op een kanaalverkortend tijdsdomein egalisatiefilter (‘time-domain equalizer’, TEQ), gecombineerd met een 1-tap frequentiedomein egalisator. Eerst leiden we een TEQ-ontwerpcriterium af dat aanleiding geeft tot een exacte optimalisatie van de bitsnelheid. Dit probleem bleef tot nu toe onopgelost. De bitsnelheid-maximaliserende TEQ (‘bitrate maximizing TEQ’, BM-TEQ) kan ook gevonden worden als de oplossing van een iteratief herwogen, scheidbaar, niet-lineair, kleinste-kwadraten (‘least-squares’, LS) probleem. Deze alternatieve formulering levert een LS-gebaseerd kader voor DMT-egalisatie. Bovendien leidt ze tot een adaptief optimalisatie-algoritme dat toelaat om veranderende kanaalcondities te volgen en dat daardoor zeer geschikt is voor integratie met de ‘seamless rate adaptation’-functionaliteit zoals aangeboden door ADSL2/ADSL2+.

Op deze manier ontstaat een volledig gamma van adaptieve bitsnelheid-maximaliserende egalisatoren met grosso modo gelijke bitsnelheid, hetgeen een flexibele afweging van geheugen- en berekeningskost toelaat. De geheugen-efficiënte adaptieve BM-TEQ en de berekeningsefficiënte zogenaamde per-toon egalisator

('per-tone equalizer', PTEQ) vormen twee extreme gevallen van de klasse van bitsnelheid-maximaliserende per-groep egalisatoren, die in parallel een aantal toongroepen egaliseren. Zelfs in moeilijke scenarios met dominante RFI blijkt een oplossing met slechts 4 even grote toongroepen quasi even goed te presteren als de PTEQ.

De RFI-onderdrukking kan op goedkope en effectieve wijze verder verbeterd worden m.b.v. een vensterfunctie aan de ontvanger. We breiden het BM-TEQ-ontwerpcriterium en optimalisatie-algoritme uit met een optimale vensterfunctie, wat toelaat om tegelijk aan egalisatie en RFI-onderdrukking te doen. We bespreken ook interessante, speciale gevallen, b.v. de bitsnelheid-maximaliserende vensterfunctie (zonder egalisator), het gecombineerd ontwerp van egalisator en vensterfunctie per toon of per toongroep en het BM-TEQ-ontwerp in combinatie met een vaste vensterfunctie.

Tenslotte stellen we goedkope uitbreidingen van de BM-TEQ en PTEQ voor (zowel lineaire als niet-lineaire uitbreidingen met terugkoppeling van de beslissingen). Deze uitbreidingen buiten zogenaamde frequentiedomein redundantie vanwege piloottonen, ongebruikte tonen en/of teruggekoppelde tonen uit. Ze bieden een oplossing voor kanalen met een oneindige impulsresponsie en een korte DMT cyclische prefix.

Glossary

List of symbols

$\mathbf{0}_{i\times j}$	$i \times j$ all-zero matrix
$\mathbf{1}_{i\times j}$	$i \times j$ all-one matrix
$\mathbf{a}$	IIR channel model denominator
$\mathbf{b}$	(1) target impulse response (TIR) (Chapter 3 and 4) or (2) IIR channel model numerator (Chapter 7)
b	number of bits per DMT symbol
B	channel bandwidth
b_n	number of bits per DMT symbol for tone n
$\mathbf{c} = \mathbf{h} \star \mathbf{w}$	effective channel impulse response = shortened impulse response (SIR)
C	channel capacity
$\tilde{d}_n$	FEQ for tone n
$\mathbf{e}_j$	canonical vector with element one in the j-th position
f	frequency (Hz)
$\mathcal{F}_a$	$N_a \times N$ submatrix of $\mathcal{F}_N$ with the N_a rows of the tone set $\mathcal{S}_a$
$\mathcal{F}_n$	n-th row of $\mathcal{F}_N$
$\mathcal{F}_{n,i:j}$	elements i to j of $\mathcal{F}_{n,i:j}$
$\mathcal{F}_N$	$N \times N$ DFT matrix
$\mathcal{F}_p$	$N_p \times N$ submatrix of $\mathcal{F}_N$ with the N_p rows of the tone set $\mathcal{S}_p$
f_s	DMT symbol rate (in Hz)
f'_s	DMT sampling rate (in Hz); $f'_s = (N + \nu)f_s$
$\mathbf{h}$	channel impulse response (CIR)
$\mathbf{I}_m$	$m \times m$ identity matrix
$\mathbf{J}_m$	$m \times m$ exchange matrix (i.e., with ones on the antidiagonal)
k	DMT (block) symbol index
K	number of data symbols in least-squares criterion

l	sample index
L	channel delay spread (in samples) = FIR channel order
L_a	IIR channel denominator order
L_b	IIR channel numerator order
n	(1) tone index or (2) noise
M	constellation size
N	(I)DFT size
N_a	number of active tones in $\mathcal{S}_a$
N_f	number of feedback tones in $\mathcal{S}_f$
N_g	number of tone groups
N_p	number of pilot tones in $\mathcal{S}_p$
N_u	number of unused tones in $\mathcal{S}_u$
R	bit rate
$\mathbf{S}$	inverse transpose of a Cholesky factor
$\mathcal{S}_a$	set of N_a active tones
$\mathcal{S}_f$	set of N_f feedback tones
$\mathcal{S}_p$	set of N_p pilot tones
$\mathcal{S}_u$	set of N_u unused tones
T	number of TEQ taps, PTEQ taps per tone or PGEQ taps per group
T_g	guard period (in seconds)
T_h	channel delay spread (in seconds)
T_s	DMT symbol time (in seconds); $T_s = \frac{1}{f_s}$
T_s'	DMT sample time (in seconds); $T_s' = \frac{1}{f_s'}$
$\mathbf{u}$	window taper
$\mathbf{U}$	Cholesky factor
$\mathbf{v}_n$	per-tone equalizer (PTEQ)
$\mathbf{w}$	time-domain equalizer (TEQ)
$\mathbf{w}_g$	per-group equalizer (PGEQ)
$\mathbf{w}_n$	per-tone equalizer (PTEQ)
x	transmitter related signals, symbols and samples
y	receiver related signals, symbols and samples
$\tilde{\mathbf{y}}_{k,n}$	$1 \times T$ sliding DFT output vector on tone n, time k
$\mathbf{z}_{k,n}$	$= \begin{bmatrix} \Delta\mathbf{y}_k^T & \tilde{y}_{k,n} \end{bmatrix}$; $1 \times T$ PTEQ input vector on tone n
δ	decision delay parameter
δ_0	propagation delay
Δ	synchronization delay parameter
Γ_n	SNR gap for tone n
λ	(1) (generalized) eigenvalue or (2) Lagrange multiplier
μ	window taper length
ρ^2	squared, normalized correlation
σ_a^2	variance/power of a
$\boldsymbol{\sigma}_{a\mathbf{b}}$	crosscorrelation vector of a and $\mathbf{b}$
$\boldsymbol{\Sigma}_{\mathbf{ab}}$	crosscorrelation matrix of $\mathbf{a}$ and $\mathbf{b}$

$\mathbf{\Sigma}_{\mathbf{a}}^2$	autocorrelation matrix of $\mathbf{a}$
$\boldsymbol{\theta}$	$= \left[\begin{array}{cc} \mathbf{w}^H & \tilde{\mathbf{d}}^H \end{array} \right]^H$; joint parameter vector in $\mathbf{w}$ and $\tilde{\mathbf{d}}$
ν	cyclic prefix length

Mathematical notation

a	scalar a
$\lfloor a \rfloor$	largest integer smaller than or equal to a
$\lvert a \rvert$	absolute value of a
$a \ll b$	a is much smaller than b
$a \gg b$	a is much larger than b
$\mathbf{a}$	vector $\mathbf{a}$
$\mathbf{a}[l]$	the l-th element of $\mathbf{a}$ (index starts from 0)
$\mathbf{a}_{i:j}$	elements i to j of $\mathbf{a}$
$\bar{\mathbf{a}}$	the vector $\mathbf{a}$ with elements in reverse order
$\lVert \mathbf{a} \rVert$	two-norm of $\mathbf{a}$
$\mathrm{diag}(\mathbf{a})$	diagonal matrix with $\mathbf{a}$ along the diagonal
$\mathbf{a} \star \mathbf{b}$	linear convolution of $\mathbf{a}$ and $\mathbf{b}$
$\mathbf{a} \odot \mathbf{b}$	element-wise multiplication of $\mathbf{a}$ and $\mathbf{b}$
$\mathbf{A} \otimes \mathbf{B}$	Kronecker product of $\mathbf{A}$ and $\mathbf{B}$
$\tilde{\mathbf{a}}_N$	$N \times 1$ frequency-domain vector, where N is the DFT size
$\tilde{\mathbf{a}}$	frequency-domain vector, typically of size $N_a \times 1$ with entries corresponding to the active tone set $\mathcal{S}_a$
$\tilde{a}_n$	frequency-domain entry of $\tilde{\mathbf{a}}$ or $\tilde{\mathbf{a}}_N$ on tone n; $\tilde{a}_n = \tilde{\mathbf{a}}_N[n]$
$\hat{\tilde{a}}, \hat{\tilde{\mathbf{a}}}$	estimate of $\tilde{a}$ or $\tilde{\mathbf{a}}$
$\mathbf{A}$	matrix $\mathbf{A}$
$\mathbf{A}^*$	complex conjugate of $\mathbf{A}$
$\mathbf{A}^T$	transpose of $\mathbf{A}$
$\mathbf{A}^H$	Hermitian of $\mathbf{A}$
$\mathbf{A}^{-1}$	inverse of $\mathbf{A}$
$\Re\{\cdot\}$	real operator
$\Im\{\cdot\}$	imaginary operator
$\mathcal{E}\{\cdot\}$	statistical expectation operator
$\nabla_a J$	gradient of J with respect to a

Acronyms and abbreviations

ADC	Analog-to-Digital Converter
ADSL	Asymmetric Digital Subscriber Line
AM	Amplitude Modulation
ANSI	American National Standards Institute

AWGN	Additive White Gaussian Noise
BER	Bit Error Rate
bMMSE	biased Minimum Mean-Square-Error
BM	Bit rate Maximizing
(BM-)FWinTEQ	(Bit rate Maximizing) TEQ design with Fixed Windowing
BM-TEQ	Bit rate Maximizing Time-Domain Equalizer
(BM-)PGEQ	(Bit rate Maximizing) Per-Group Equalizer
(BM-)PGWinEQ	(Bit rate Maximizing) Per-Group combined Window and Equalizer
(BM-)WinTEQ	(Bit rate Maximizing) combined Window and Time-Domain Equalizer
bps	bits per second
CDMA	Code-Division Multiple Access
CIR	Channel Impulse Response
CLLS	Constrained Linear Least-Squares
CO	Central Office
CP	Cyclic Prefix
CSA	Carrier Serving Area
CSI	Channel-State Information
DAC	Digital-to-Analog Converter
dB	decibel
DF	Decision-Feedback
DFE	Decision-Feedback Equalizer
DFT	Discrete Fourier Transform
DMT	Discrete Multitone
DSL	Digital Subscriber Line
DSM	Dynamic Spectrum Management
DSP	Digital Signal Processing
ETSI	European Telecommunications Standards Institute
EV	Eigenvalue
EVD	Eigenvalue Decomposition
FD	Frequency-Domain
FDD	Frequency-Division Duplexing
FEQ	Frequency-Domain Equalizer
FEXT	Far-End Crosstalk
FFT	Fast Fourier Transform
FIR	Finite Impulse Response
FMT	Filtered Multitone
FTTH	Fiber-To-The-Home
FTTN	Fiber-To-The-Neighbourhood
GEV	Generalized Eigenvalue
GN	Gauss-Newton
GSNR	Geometric Signal-to-Noise Ratio
HDSL	High bit rate DSL

HIPERLAN	High Performance Radio LAN
ICI	Intercarrier Interference
IDFT	Inverse Discrete Fourier Transform
IEEE	Institute of Electrical and Electronics Engineers
IFFT	Inverse Fast Fourier Transform
IIR	Infinite Impulse Response
INR	ISI/ICI-to-Noise Ratio
IP	Internet Protocol
IR-SNLLS	Iteratively Reweighted Separable Non-Linear Least-Squares
ISDN	Integrated Services Digital Network
ISI	Intersymbol Interference
ITU	International Telecommunication Union
kbps	kilobits per second
LAN	Local-Area Network
LM	Levenberg-Marquardt
L-MMSE	Linear Minimum Mean-Square-Error
LMS	Least-Mean-Square
LS	Least-Squares
L-ZF	Linear Zero-Forcing
Mbps	Megabits per second
MC	Multicarrier
MCH	Multichannel
MERRY	Multicarrier Equalization by Restoration of RedundancY
MIMO	Multiple-Input Multiple-Output
ML	Maximum Likelihood
MMSE	Minimum Mean-Square-Error
MSE	Mean-Square-Error
MSSNR	Maximum Shortening Signal-to-Noise Ratio
NBI	Narrow-Band Interference
NEXT	Near-End Crosstalk
OFDM	Orthogonal Frequency-Division Multiplexing
OLT	Optical Line Terminal
ONU	Optical Network Unit
PC	Personal Computer
POTS	Plain Old Telephone Service
PSD	Power Spectral Density
PTEQ	Per-Tone Equalizer
QAM	Quadrature Amplitude Modulation
RFI	Radio Frequency Interference/Interferer
RLM	Recursive Levenberg-Marquardt
RLS	Recursive Least-Squares
rmps	real multiplications per second
RX	Receive(r)

SAM	Sum-squared Autocorrelation Minimization
SIR	Shortened Impulse Response
SISO	Single-Input Single-Output
SNLLS	Separable Non-Linear Least-Squares
SNR	Signal-to-Noise Ratio
SOS	Second-Order Statistics
SR	Square-Root
SVD	Singular Value Decomposition
TD	Time-Domain
TEQ	Time-Domain Equalizer
TIR	Target Impulse Response
TX	Transmit(ter)
UDSL	Uni-Digital Subscriber Line
UEC	Unit-Energy Constraint
uMMSE	unbiased Minimum Mean-Square-Error
UNC	Unit-Norm Constraint
UTC	Unit-Tap Constraint
VC	Vector Coding
VDSL	Very high bit rate Digital Subscriber Line
WLAN	Wireless Local-Area Network
WMAN	Wireless Metropolitan-Area Network
ZF	Zero-Forcing

Contents

Abstract **iii**

Korte inhoud **v**

Glossary **vii**

Contents **xiii**

Nederlandse samenvatting **xix**

1 Introduction **1**

1.1 Internet access: driver application for digital subscriber lines (DSL) 1

1.2 History and future of DSL 3

1.3 DSL environment 6

1.3.1 Impairments 6

1.3.2 Multicarrier modulation 10

1.4 Thesis outline and contributions 12

1.4.1 Research motivation 12

1.4.2 Chapter-by-chapter overview 13

1.5 Conclusions 16

2 Basic concepts and data model **19**

2.1 Multicarrier modulation and vector coding 20

2.1.1 Multichannel modulation concept 20

2.1.2 Multicarrier modulation concept 20

2.1.3 Channel capacity 22

2.1.4 Water-filling principle and bit loading 23

2.1.5 Vector coding 26

2.2 Discrete multitone transmission 29

2.2.1 Cyclic prefix 30

2.2.2 DMT transmitter 32

2.2.3 DMT receiver 33

2.2.4 Time-domain equalization 36

2.2.5 Windowing 39

2.3 Data model 40

2.3.1 Data model based on an FIR channel model 40

2.3.2 Data model based on an IIR channel model 43

2.4 Conclusions 44

3 Equalization for discrete multitone-based systems **45**

3.1 Common framework 46

3.2 MMSE-TEQ and MSSNR-TEQ design 48

3.2.1 MMSE-TEQ design 49

3.2.2 MSSNR-TEQ design 53

3.3 TEQ design aimed at bit rate maximization 56

3.3.1 Al-Dhahir's TEQ design 57

3.3.2 Henkel's TEQ design 59

3.3.3 Arslan's TEQ design 59

3.3.4 Milosevic's TEQ design 60
3.4 Per-tone equalizer design 61
3.4.1 PTEQ concept 61
3.4.2 Efficient, adaptive PTEQ design algorithm 65
3.5 Conclusions 67

4 Bit rate maximizing time-domain equalizer design 69
4.1 Channel-based SNR model 70
4.2 Bit rate maximizing TEQ design 76
4.2.1 SNR model at the FEQ output 77
4.2.2 Unbiased versus biased FEQs 78
4.2.3 SNR model revisited 79
4.2.4 BM-TEQ design criterion 80
4.2.5 Optimizing the BM-TEQ design criterion 83
4.3 Least-squares-based time-domain and frequency-domain MMSE-TEQ designs 84
4.3.1 CLLS-based TD-MMSE-TEQ design 85
4.3.2 CLLS-based FD-MMSE-TEQ design 86
4.3.3 SNLLS-based FD-MMSE-TEQ design 91
4.3.4 IR-SNLLS-based BM-TEQ design 92
4.3.5 Iterative Gauss-Newton-based BM-TEQ design algorithm 96
4.3.6 Relation between FD-MMSE-TEQ and PTEQ designs . 100
4.3.7 Relation between the GEV problem formulations 102
4.4 Simulations 102
4.5 Conclusions 108
4.A Appendix 111

5 Adaptive bit rate maximizing time-domain and per-group equalizer design 115

5.1 Bit rate maximizing per-group equalizer design 118

5.2 Recursive Levenberg-Marquardt-based BM-TEQ and BM-PGEQ 120

5.2.1 Basic RLM algorithm 122

5.2.2 Reducing the SOS memory cost 126

5.2.3 Further refinements to the RLM algorithm 127

5.2.3.1 Exponential weighting factor λ 127

5.2.3.2 Equalizer input power normalization 128

5.2.3.3 Adaptive regularization 129

5.2.4 Summary of the adaptive BM-TEQ and BM-PGEQ algorithm 130

5.3 Memory and computational cost of the adaptive BM equalizers 133

5.4 Simulations 137

5.5 Conclusions 144

6 Bit rate maximizing window and time-domain equalizer design 147

6.1 Data model 150

6.2 Bit rate maximizing combined window and TEQ design 152

6.2.1 First BM-WinTEQ design criterion 152

6.2.2 IR-SNLLS-based BM-WinTEQ design criterion 154

6.3 Special cases 155

6.3.1 Bit rate maximizing per-group combined window and equalizer design (BM-PGWinEQ) 155

6.3.2 Per-tone combined window and equalizer design (PTEQ) 156

6.3.3 Bit rate maximizing window-only design (BM-Win) . . 157

6.3.4 Bit rate maximizing TEQ design with fixed window (BM-FWinTEQ) 160

6.4 Memory and computational cost 160
6.5 Guidelines for optimizing the BM-WinTEQ design criterion . . 162
6.6 Simulations 166
6.7 Conclusions 172

7 Equalization of DMT-based systems over IIR channels 177
7.1 Notation and DMT data model 180
7.1.1 Notation 180
7.1.2 Data model 180
7.1.3 Outline of this chapter 184
7.2 DMT equalization of an IIR channel with $L_b \leq \nu$ 184
7.2.1 Optimum L-ZF block equalization 185
7.2.2 Discussion and interpretation 186
7.3 DMT equalization of an IIR channel with $L_b > \nu$ 188
7.3.1 Optimum L-ZF block equalization 188
7.3.2 Discussion and interpretation 190
7.4 Low-complexity extensions of the L-MMSE PTEQ 191
7.4.1 The L-PTEQ extension 192
7.4.2 The DF-PTEQ extension 194
7.4.3 RFI suppression capability 196
7.5 Low-complexity extensions of the BM-TEQ 197
7.5.1 Linear and decision-feedback BM-TEQ extensions . . . 198
7.5.2 Guidelines for optimizing the linear BM-TEQ extension 200
7.6 Simulations 202
7.7 Conclusions 210
7.A Appendix 211

8 Conclusions and further research 215

8.1 Conclusions 215
8.2 Further research 219

Bibliography **223**

List of publications **237**

Curriculum vitae **241**

Geavanceerde egalisatietechnieken voor DMT-gebaseerde systemen

Nederlandse samenvatting

Hoofdstuk 1: Inleiding

Breedband-internettoegang: drijfveer voor 'digital subscriber line' (DSL)-technologie

Internet heeft vandaag de dag wereldwijd naar schatting 800 miljoen gebruikers. In België zijn dat er om en bij de 4 miljoen. Het aantal toepassingen en diensten via het wereldwijde computernetwerk (b.v. e-mail, surfen op het web, online winkelen, streaming media, virtuele privénetwerken, enz.) is groot en neemt nog toe. Deze toepassingen en diensten gaan gepaard met intensief dataverkeer, wat leidt tot een continu aanhoudende en toenemende vraag naar breedband-internettoegang.

Sinds het einde van de jaren negentig heeft breedband-internettoegang zijn weg naar het grote publiek gevonden. Op het einde van 2003 waren er wereldwijd meer dan 100 miljoen breedbandlijnen. In België zijn 1,4 miljoen van de 2 miljoen internetverbindingen breedbandig, wat resulteert in de derde grootste penetratie ter wereld.

Breedbandcommunicatie kan over verschillende media verlopen. De getwiste koperen telefoonlijn, de coaxiale TV-kabel, het elektriciteitsnet en optische vezel zijn zogenaamde bedrade media; draadloze communicatie vormt een vijfde optie. De zogenaamde DSL- en de kabelmodemtechnologie zijn het wijdst verspreid: in België zijn er ongeveer 1 miljoen DSL-verbindingen, tegenover 400000 kabelmodemgebruikers.

Geschiedenis en toekomst van DSL

In deze thesis focusseren we ons op DSL-breedband-internettoegang. De geschiedenis van de datacommunicatie over de telefoonlijn begint in de 19e eeuw met de uitvinding van de elektrische telegraaf en de telefoon. Het duurde tot het einde van de jaren tachtig alvorens de mogelijkheid van breedbandcommunicatie over de telefoonlijn werd onderkend; voorheen vond datacommunicatie plaats in de spraakband. Breedbandtechnologieën zoals 'high bit rate DSL' (HDSL) en 'symmetric single-pair DSL' (SDSL) bleken te duur voor residentiële gebruikers. Asymmetrische DSL (ADSL) daarentegen was het antwoord van de telefoonoperatoren op het overvloedige aanbod aan TV-kanalen door kabelmaatschappijen: met bitsnelheden tot 8 Mbps liet ADSL toe om video van hoge kwaliteit aan te bieden. Video-op-aanvraag brak echter nooit door. In de plaats daarvan bleek ADSL dé oplossing voor PC gebruikers die een hogesnelheidstoegang tot het internet of het bedrijfsnetwerk wensten.

Zoals reeds aangehaald heeft ADSL verschillende concurrenten. Door aanpassing van het TV-distributienetwerk zijn kabelmaatschappijen eveneens in staat breedband-internettoegang aan te bieden. Hiertoe is de coaxkabel bovendien een gemakkelijker medium. Het belangrijkste nadeel van kabeltoegang wordt gevormd door het feit dat de bandbreedte over meerdere gebruikers verdeeld wordt. Communicatie over het elektriciteitsnetwerk en optischevezelnetwerken zijn in opkomst. Vermoedelijk zal draadloze breedband-toegang reeds sneller een belangrijke concurrent vormen: 'wireless local area network' (WLAN)-technologie wordt fel gesmaakt door het grote publiek; de recente IEEE-standaard 802.16 zal een stuwende kracht vormen voor de ontwikkeling van zogenaamde 'wireless metropolitan area networks' (WMAN). Binnenkort zal ook UMTS op grote schaal gelanceerd worden, wat mobiele breedbandtoegang verzekert.

Om aan de concurrentie het hoofd te bieden gaat de DSL-wereld in de tegenaanval. Toekomstige DSL-systemen, zoals ADSL2+ en 'very high bit rate DSL' (VDSL), beloven nog hogere bitsnelheden die zogenaamde 'triple-play' (video en spraak van hoge kwaliteit alsook datacommunicatie tegen een hoge snelheid) zullen mogelijk maken. Een overzicht van de nieuwste DSL systemen wordt gegeven in **Tabel 1.1**. Dergelijke bitsnelheden zijn slechts mogelijk door de lijnlengte te reduceren en de bandbreedte te vergroten. Zoals weergegeven in **Figuur 1.1** kan de lijn verkort worden door optische vezel verder in het netwerk te laten doordringen, b.v. tot aan een optische netwerkeenheid ('optical network unit', ONU) op de hoek van de straat. De zogenaamde laatste kilometer tot bij de klant wordt dan overbrugd met ADSL2+- of VDSL-technologie.

De DSL-omgeving

Het gebruik van een grote bandbreedte voor datacommunicatie over een telefoonlijn (tot 12 MHz voor VDSL i.p.v. 4 kHz voor spraak) is niet evident. Er moet rekening gehouden worden met verschillende vormen van interferentie en

ruis. Een schematisch overzicht van deze stoorbronnen wordt weergegeven in **Figuur 1.2**. Zoals in elk communicatiesysteem veroorzaakt het transmissiekanaal signaaldistortie en -verzwakking. O.w.v. de grote bandbreedte zijn deze frequentie-afhankelijk. Bovendien worden signaalreflecties veroorzaakt door de aanwezigheid van vertakkingen ('bridged taps') en het combineren van verschillende draaddiameters ('wire gauges'). Het grote dynamische bereik van de kanaalfrequentieresponsie en het effect van de lijnlengte worden geïllustreerd in **Figuur 1.3**. Om kanaaldistortie tegen te gaan wordt gebruik gemaakt van een *egalisator*. In tegenstelling tot de draadloze communicatie-omgeving is het bedrade kanaal traag tijdsvariërend. Vandaar dat het ontwerp van trainingsgebaseerde adaptieve egalisatoren het voornaamste onderwerp van deze thesis vormt.

Andere externe ruisbronnen worden gevormd door echo, smalbandige radiofrequente interferentie (RFI) en overspraak van naburige DSL-systemen. Echo- en overspraakonderdrukking komen niet aan bod in deze thesis. Wel stellen we gecombineerde oplossingen voor RFI-onderdrukking en egalisatie voor. Er zijn twee belangrijke vormen van RFI. VDSL heeft vooral te lijden onder interferentie vanwege radio-amateurs. Deze RFI-vorm kan zeer schadelijk zijn aangezien ze regelmatig aan- en afschakelt en de dragerfrequentie vaak wijzigt. ADSL en ADSL2+ hebben eerder te maken met RFI vanwege AM-radiozenders; die zijn meer stationair aangezien zij continu uitzenden.

DSL-communicatie maakt gebruik van zogenaamde 'discrete multitone modulation' (DMT), in combinatie met geavanceerde digitale signaalverwerkingsalgoritmen, om deze ruisbronnen aan te pakken en een maximaal aantal klanten te bedienen. DMT-modulatie is een volledig digitale implementatie van zogenaamde 'multicarrier' (MC)-modulatie. MC-modulatie is een vorm van 'multichannel' (MCH)-modulatie, waarbij de bandbreedte van het communicatiekanaal verdeeld wordt over een aantal parallelle en orthogonale frequentiebanden (tonen). Dit laat toe om b.v. egalisatie en RFI-onderdrukking als een aantal parallelle, onafhankelijke en kleinere problemen op te lossen. Een illustratie van het MC-concept zoals toegepast in ADSL wordt geboden in **Figuur 1.4**. In deze thesis focusseren we ons op algoritmes voor kanaalegalisatie en RFI-onderdrukking die een hogere bitsnelheid bieden dan bestaande algoritmes.

Onderzoeksmotivatie

De keuze voor MC-modulatie in DSL is deels gebaseerd op de theoretisch aantrekkelijke eigenschappen van het transmissieschema: in het ideale geval van een groot aantal, perfect gescheiden tonen zijn egalisatie en RFI-onderdrukking in een MC-systeem zeer eenvoudig en kan optimale performantie (d.i. een bitsnelheid gelijk aan de kanaalcapaciteit) behaald worden. Echter, om tot een haalbare implementatie van MC-modulatie te komen zijn verscheidene benaderingen nodig: o.w.v. complexiteitsbeperkingen is het maximum aantal tonen begrensd en dient een zekere spectrale overlap toegelaten te worden. Toegepast

in een reële DSL-omgeving haalt het resulterende DMT-transmissieschema in zijn basisvorm dan ook slechts een heel beperkte performantie. Hierdoor worden potentiële klanten, die te ver van de centrale wonen of onder slechte lijncondities lijden, uitgesloten. Meer geavanceerde egalisatie- en RFI-onderdrukkingsstrategieën zijn dan ook nodig om DMT-modulatie geschikt te maken voor DSL.

De huidige ADSL- en VDSL-modems bevatten een digitale signaalverwerkingseenheid om aan egalisatie en RFI-onderdrukking te doen. De behaalde performantie blijft echter vaak ver beneden de optimale performantie. Bovendien neemt het belang van digitale signaalverwerkingsalgoritmes ('digital signal processing', DSP) nog toe o.w.v. de grotere bandbreedte van ADSL2+ en VDSL.

De egalisatie- en RFI-onderdrukkingsalgoritmes, ontwikkeld in deze thesis, hebben de volgende voordelen.

- Hun voordeel in termen van bitsnelheid kan omgezet worden in een uitbreiding van de dekking of een toename van de marge, wat een maat is voor de systeemrobuustheid.
- Hun geheugen- en berekeningskost valt binnen de limieten van de huidige, beschikbare hardware.
- De algoritmes voegen adaptiviteit toe aan de DMT-ontvanger zodat veranderende lijncondities kunnen gevolgd worden.
- Aangezien de algoritmes de optimale performantie binnen het beschouwde DMT-modulatiekader benaderen, kan hun performantie dienen als maatstaf voor andere ontwerpen.

Hoofdstuk 2: Basisconcepten en datamodel

'Multicarrier'-modulatie en vectorcodering

In dit hoofdstuk introduceren we de theoretische basisconcepten van MCH-, MC- en DMT-modulatie, evenals de basisprincipes van kanaalegalisatie en RFI-onderdrukking, zoals toegepast in DSL-communicatie.

MC-modulatie is een specifieke vorm van MCH-modulatie waarbij het beschikbare spectrum in een aantal parallelle, orthogonale frequentiebanden wordt onderverdeeld. De basisstructuur voor MC-modulatie is weergegeven in **Figuur 2.1**. De bitstroom wordt gesplitst in opeenvolgende blokken van 'quadrature amplitude modulation' (QAM)-symbolen die elk een drager moduleren. Het verstuurde signaal is dan een superpositie van QAM-signalen die elk een afzonderlijke frequentieband gebruiken. De maximum haalbare QAM-constellaties worden bepaald door de kanaalcapaciteit. De kanaalcapaciteit

is een maat voor de optimaal haalbare performantie, gegeven de signaal-opruisverhouding ('signal-to-noise ratio', SNR) van het transmissiekanaal. MC-modulatie is in het ideale geval in staat de kanaalcapaciteit te bereiken door een eenvoudige egalisatie en de toepassing van het 'water-filling'-principe (zie **Figuur 2.2**). Echter, verschillende benaderingen zijn nodig om MC-modulatie praktisch toepasbaar te maken: het gebruik van symbolen uit een eindig alfabet, een geheel aantal bits per symbool, modulatorfuncties van eindige lengte en een eindig aantal tonen zorgen ervoor dat er een zekere SNR-kloof moet toegestaan worden tussen de werkelijk haalbare bitsnelheid en de kanaalcapaciteit.

Tot in de jaren '70 werd de praktische implementatie van MC-modulatie gehinderd door de beperkingen van analoge signaalverwerkingstechnieken. De omschakeling naar DSP-technieken en de introductie van de 'discrete Fourier transform' (DFT) zorgden voor een hernieuwde interesse voor MC-modulatie. Het gebruik van digitale i.p.v. analoge filters maakt het gemakkelijker om tonen voldoende te scheiden, zij het dat dit tot een complex egalisatieprobleem leidt. Een alternatief schema met goedkope egalisatie wordt gevormd door de combinatie van zogenaamde vectorcodering (waarbij de modulator- en demodulatorfuncties aan het kanaal worden aangepast) met een wachtperiode/stilte van ν monsters ('guard period') tussen opeenvolgende blokken van symbolen. Indien de lengte ν van de wachtperiode groter dan of gelijk aan de orde van de kanaalimpulsresponsie L is, wordt intersymboolinterferentie (ISI) vermeden (zie **Figuur 2.3**).

DMT-modulatie

De belangrijkste tekortkoming van vectorcodering is de kanaalafhankelijkheid van de modulator/demodulatorfuncties. Een eenvoudig middeltje, met een kleine impact op de performantie, bestaat erin de wachtperiode tussen opeenvolgende blokken van symbolen te vervangen door een zogenaamde cyclische prefix (CP). Dit middeltje resulteert in de kanaalonafhankelijke DMT-(de)modulatie op basis van een N-punts inverse DFT-operatie aan de zender en een N-punts DFT-operatie aan de ontvanger (geïmplementeerd m.b.v. een '(inverse) fast Fourier transform', (I)FFT).

De DMT-zender en DMT-ontvanger zijn weergegeven in respectievelijk **Figuur 2.4** en **Figuur 2.5**. Aan de zendzijde wordt de inkomende bitstroom eerst gecodeerd, geïnterleaved en gesplitst in parallelle bitstromen. Elke bitstroom wordt verdeeld in bitwoorden die omgezet worden in QAM-symbolen. Elke IDFT-ingang of toon wordt gemoduleerd door een stroom QAM-symbolen. Door complex-toegevoegde symmetrie op te leggen aan de IDFT-ingangen wordt een blok van N reële tijdsdomein monsters aan de DFT-uitgang verkregen. Na toevoeging van de CP worden deze monsters op de lijn gezet. De DMT-ontvanger voert de duale (demodulatie-)operaties uit: na de verwijdering van de CP worden blokken van ontvangen monsters aan een DFT aangeboden

om zo de QAM-symbolen te recupereren. De ontvanger doet ook aan egalisatie: ondanks de overlappende sinc-vormige toonspectra kan de egalisatie eenvoudigweg gebeuren m.b.v. een 1-tap frequentiedomein egalisator ('frequency-domain equalizer', FEQ) per toon. Dit is een belangrijk voordeel van DMT-modulatie.

Het gebruik van een 1-tap FEQ per toon volstaat enkel als de CP-lengte ν plus 1 groter is dan of gelijk is aan de lengte van de kanaalimpulsresponsie L. Indien dit niet het geval is, ontstaat er ISI en 'intercarrier'-interferentie (ICI) die de SNR op elke toon vermindert. Het vergroten van de CP-lengte ν (in vergelijking met de blokgrootte N) levert geen oplossing aangezien dit leidt tot een belangrijke vermindering in efficiëntie. ADSL-kanaalimpulsresponsies zijn typisch zeer lang. Extra egalisatie is dan nodig om DMT-modulatie geschikt te maken voor ADSL-communicatie. Er wordt meestal gebruik gemaakt van een kanaalverkortend tijdsdomein egalisatiefilter ('time-domain equalizer', TEQ), dat ingevoegd wordt vóór de DFT. Om een maximum aantal klanten te kunnen bedienen mikt DSL-systeemontwerp op het maximaliseren van de bitsnelheid, rekening houdend met het gewijzigde SNR-model aan de DFT-uitgang dat afhangt van de TEQ en zijn impact op de ISI en de ICI. Het TEQ-ontwerp is dan ook cruciaal en tegelijk niet triviaal: de TEQ heeft, door zijn positie vóór de DFT, een impact op de ISI/ICI op alle tonen. De beperkte spectrale selectiviteit van de sinc-vormige tonen bemoeilijkt het TEQ-ontwerp verder. Bijgevolg hebben reeds vele onderzoekers DMT-egalisatie bestudeerd.

Tot nu toe werd TEQ-ontwerp vooral in de DSL-context bestudeerd, hoewel er recent ook een toenemende interesse ontstaat voor TEQ-ontwerp in de context van draadloze systemen, b.v. met meerdere zend- en ontvangstantennes ('multiple input multiple output', MIMO). Wij focusseren ons op de DSL-context. In DMT-gebaseerde DSL-systemen wordt gemikt op maximalisatie van de bitsnelheid in een traag variërende 'single input single output' (SISO)-omgeving. Echter, maximalisatie van de bitsnelheid van het DMT-bloktransmissieschema m.b.v. een TEQ-filter leidt tot een sterk niet-lineair optimalisatieprobleem. Aangezien de TEQ zich voor de DFT bevindt, worden alle tonen gezamenlijk behandeld. Bovendien zorgt de beperkte spectrale selectiviteit van de DFT voor een moeilijke interferentiestructuur die kan leiden tot ruisversterking en het lekken van ruis vanuit een naburige frequentieband.

Een overzicht van de belangrijkste, bestaande TEQ-ontwerpen wordt gegeven in Hoofdstuk 3. Hoofdstuk 3 beschrijft ook de per-toon egalisator ('per-tone equalizer', PTEQ) die ontwikkeld werd als een aantrekkelijk alternatief voor DMT-gebaseerde systemen. In Hoofdstuk 4 leiden we een TEQ-ontwerpcriterium af dat aanleiding geeft tot een exacte optimalisatie van de bitsnelheid en dat bijgevolg bestaande TEQ-ontwerpen in performantie overtreft, vandaar de term 'bit rate maximizing TEQ' (BM-TEQ). In Hoofdstuk 5 wordt aangetoond dat de BM-TEQ en de PTEQ uiterste gevallen zijn van de klasse van zogenaamde bitsnelheid-maximaliserende (BM) per-groep egalisatoren ('bit rate maximizing per-group equalizer', BM-PGEQ).

Door de grote bandbreedte overlappen DSL-systemen met andere communicatiesystemen, zoals radiozenders. Dit resulteert in smalbandige radio-frequente interferentie (RFI). De overlappende sinc-vormige tonen maken dat DMT niet zo robuust is tegen RFI: een RFI verstoort niet alleen de toon waarmee hij samenvalt, maar hij lekt ook naar vele naburige tonen. Toepassing van een tijdsdomein vensterfunctie (b.v. een 'raised' cosinusvenster) aan de ontvanger, vóór de DFT (zie **Figuur 2.6**), levert een goedkope en efficiënte oplossing voor RFI. De vensterfunctie verbetert de spectrale selectiviteit van de demodulerende DFT door het reduceren van de sinc-zijlobben, zonder daarbij de orthogonaliteit te verstoren. Het effect van een vensterfunctie wordt bepaald door de lengte van het venster-'taper' μ: een grotere lengte leidt tot betere performantie. Echter, het venster-'taper' wordt beperkt door de CP-lengte: $\mu \leq \nu$. Bijgevolg is de impact van een vaste vensterfunctie in ADSL beperkt. In Hoofdstuk 5 bestuderen we de performantie van de BM-TEQ en BM-PGEQ in de aanwezigheid van RFI. Hoofdstuk 6 stelt een BM gecombineerd ontwerp van een TEQ en een vensterfunctie voor. In Hoofdstuk 7 tenslotte wordt RFI-onderdrukking door exploitatie van ongebruikte tonen besproken.

Datamodel

Twee datamodellen worden voorgesteld. Het eerste datamodel, op basis van een kanaalimpulsreponsie van eindige lengte ('finite impulse response', FIR), zal gebruikt worden in Hoofdstuk 3 tot 6 en beschrijft de modellering van de TEQ en de vensterfunctie. Het tweede datamodel is gebaseerd op een kanaalmodel van oneindige lengte ('infinite impulse response', IIR), d.i. een model met nullen en polen, wat een beknopte voorstellingswijze van het kanaal toelaat. M.b.v. dit IIR-model wordt in Hoofdstuk 7 DMT-egalisatie opnieuw bekeken voor willekeurige IIR-modelordes en een willekeurige CP-lengte.

Hoofdstuk 3: Egalisatie van DMT-gebaseerde systemen

Algemeen kader

Dit hoofdstuk voorziet in een algemeen kader en een uniforme notatie voor DMT-egalisatorontwerpen, op basis van een product van M veralgemeende Rayleigh-quotiënten. Voor elk van de egalisatorontwerpen in de volgende secties zal aangetoond worden hoe de kostfunctie binnen het algemeen kader past. Door de introductie van dit algemeen kader is het gemakkelijk in te zien dat de meeste TEQ-ontwerpen gelijkaardige oplossingsmethoden vergen en hoe TEQ-ontwerpen verschillen in het aantal factoren M en de bepalende matrices $\mathbf{A}_n$ en $\mathbf{B}_n$. Voor het algemene geval $M \neq 1$ is het kostcriterium niet-convex en zijn er bijgevolg lokale optima die niet noodzakelijk globaal optimaal zijn. Voor $M = 1$ kan het veralgemeende Rayleigh-quotiënt herleid worden tot een veralgemeend eigenwaardenprobleem.

MMSE-TEQ- en MSSNR-TEQ-ontwerp

O.w.v. het ingewikkelde karakter van optimaal TEQ-ontwerp wordt vaak een toevlucht genomen tot vereenvoudigde procedures op basis van het concept van kanaalverkorting. Twee van de meest populaire en oudste kanaalverkortende TEQ-ontwerpen zijn de 'minimum mean-square-error' (MMSE)-TEQ en de 'maximum shortening-SNR' (MSSNR)-TEQ.

De MMSE-TEQ werd oorspronkelijk geïntroduceerd in de jaren '70 om de impulsresponsie van het communicatiekanaal te verkorten en zo een exponentiële vermindering van de kost van een 'maximum likelihood'-ontvanger te verkrijgen. Begin van de jaren '90 werd het idee overgenomen om de kanaalimpulsresponsie in DMT-gebaseerde systemen te verkorten tot een 'target' impulsresponsie (TIR), zie **Figuur 3.2**, op basis van een foutenergie die de som is van een zekere tijdsdomein signaal- en ruisenergie. Om de triviale nuloplossing te vermijden dient een beperking op de TEQ-taps en/of de TIR-taps opgelegd te worden.

Het MMSE-TEQ-ontwerpcriterium is erg populair: aangezien het kwadratisch is, heeft het een unieke oplossing dat kan verkregen worden m.b.v. goed gekende matrixmanipulaties, zoals een matrixinverse en een eigenwaardenontbinding. Recente verbeteringen laten toe om de berekeningscomplexiteit verder terug te dringen, b.v. door een symmetrische TIR op te leggen. Echter, aangezien het MMSE-TEQ-criterium een tijdsdomein foutenergie minimaliseert, wordt er geen rekening gehouden met de DFT en zijn beperkte spectrale selectiviteit. Bijgevolg is het moeilijk te voorspellen welke beperking tot de beste performantie leidt. Een ander gevolg is de grote gevoeligheid van de behaalde bitsnelheid aan de synchronisatieparameter Δ. In Hoofdstuk 4 worden op basis van dit tijdsdomein (TD) MMSE-TEQ-ontwerp twee frequentiedomein (FD) MMSE-TEQ-ontwerpen afgeleid. Deze nieuwe ontwerpen leveren een nuttige TEQ-oplossing met een performantie tussen de TD-MMSE-TEQ en de BM-TEQ.

De MSSNR-TEQ houdt enkel rekening met de kanaalimpulsresponsie en negeert de ruis: dit TEQ-ontwerp minimaliseert de energie in de verkorte kanaalimpulsresponsie buiten een venster van $\nu + 1$ monsters onder de beperking dat de energie binnen dit venster gelijk is aan 1, zie **Figuur 3.3**.

Verschillende veralgemeningen voor de MSSNR-TEQ werden voorgesteld. De MSSNR-TEQ van oneindige lengte blijkt steeds symmetrisch of 'skew'-symmetrisch te zijn en bijgevolg presteert een symmetrische MSSNR-TEQ quasi even goed bij een gevoelig kleinere berekeningskost. De 'minimum ISI'-TEQ probeert de residuele ISI spectraal te vormen zodat de ISI op de tonen met de laagste SNR geplaatst wordt. De zogenaamde MERRY- en SAM-algoritmes zijn blinde, adaptieve TEQ-ontwerpprocedures, gerelateerd aan het MSSNR-TEQ-ontwerp.

TEQ-ontwerpen die maximalisatie van de bitsnelheid claimen

In de loop der jaren werden verscheidene TEQ-ontwerpen voorgesteld die de bitsnelheid claimen te maximaliseren, maar die dit in werkelijkheid niet doen. De suboptimaliteit volgt steeds uit benaderingen en veronderstellingen die leiden tot een foutieve modellering van één of meerdere termen in het SNR-model aan de DFT-uitgang. Als gevolg hiervan lijden deze TEQ-ontwerpen vaak aan een onvoorspelbare performantie in functie van de synchronisatieparameter Δ.

Sectie 3.3 geeft in chronologische volgorde een overzicht van de TEQ-ontwerpen voorgesteld door Al-Dhahir, Henkel, Arslan en Milosevic. We verklaren de gemaakte benaderingen en de steeds meer rigoureuze SNR-modellen. Deze SNR-modellen moeten vergeleken worden met het exacte SNR-model zoals afgeleid in Sectie 4.1.

Al-Dhahir's TEQ-ontwerp verwaarloost onder andere de ISI, de ICI en de spectrale lek van signaal en ruis wegens de DFT. Henkel houdt wel rekening met ISI en de spectrale lek van ruis, maar verwaarloost de ICI. Bovendien wordt verondersteld dat alle tonen actief zijn en een gelijk zendvermogen hebben. Arslan's TEQ-ontwerp is gebaseerd op verbeteringen van Al-Dhahir's SNR-model. Echter, het SNR-model vertelt niet het volledige verhaal over ISI, ICI en gewenst signaal en het effect van de spectrale lek op ISI en ruis wordt verwaarloosd. Milosevic's SNR-model verbetert Arslan's SNR-model, maar is ook suboptimaal door de veronderstelling dat de TEQ-uitgang het resultaat is van een cyclische convolutie van het verkorte kanaal met het verstuurde signaal.

Per-toon egalisatie

Een aantrekkelijke, alternatieve egalisatorstructuur die (als eerste) maximalisatie van de bitsnelheid garandeert, is de PTEQ. De PTEQ bestaat uit een complexe egalisator voor elke toon afzonderlijk die het effect van een TEQ en FEQ combineert, zie **Figuur 3.4**. Hierdoor presteert de PTEQ-gebaseerd DMT-ontvanger op zijn minst even goed als, en meestal beter dan, een TEQ-gebaseerde DMT-ontvanger. Een TEQ met T reële taps en een PTEQ met T complexe taps per toon hebben een gelijkaardige berekeningscomplexiteit. Het nadeel van de PTEQ is zijn grotere geheugenkost.

De PTEQ is gebaseerd op twee sleutelobservaties die later, o.a. bij de afleiding van het BM-TEQ-kostcriterium, meermaals zullen toegepast worden. De eerste sleutelobservatie bestaat uit het feit dat de geëgaliseerde DFT-uitgang ook kan verkregen worden als een lineaire combinatie (m.b.v. de TEQ-coëfficiënten) van de T uitgangen van een 'sliding' DFT, toegepast op het niet-geëgaliseerde ontvangen signaal. De tweede sleutelobservatie zegt dat de T 'sliding' DFT-uitgangen voor toon n goedkoper kunnen verkregen worden aan de hand van 1 DFT-uitgang die op intelligente wijze gecombineerd wordt met $T-1$ zogenaamde verschiltermen.

Aangezien het oplossen van een MMSE-probleem per toon een te grote berekeningskost vraagt, wordt de PTEQ bij voorkeur adaptief ontworpen m.b.v. een trainingssignaal. M.b.v. een 'square-root recursive least-squares' (RLS)-gebaseerde adaptieve algoritme wordt een efficiënte PTEQ-ontwerpprocedure verkrege, die een groot deel van de RLS-berekeningen voor alle tonen gemeenschappelijk uitvoert. Een verdere vereenvoudiging is mogelijk door gebruik te maken van een hybriede RLS/LMS-algoritme. Deze adaptieve algoritmes kunnen ook gebruikt worden om veranderingen in kanaal en ruis te volgen. Bovendien zullen de algoritmes nauw gerelateerd blijken aan het adaptieve BM-TEQ-algoritme, dat ontwikkeld wordt in Hoofdstuk 5.

Hoofdstuk 4: Bitsnelheid-maximaliserend TEQ-ontwerp

Kanaalgebaseerd SNR-model

In Sectie 4.1 wordt een exact SNR-model afgeleid op basis van het FIR-datamodel. Voor de helderheid wordt hierbij gebruik gemaakt van een eenvoudig voorbeeld op basis van een kort kanaal, een kleine DFT-grootte en een korte CP. Door vergelijking van dit SNR-model met de SNR-modellen uit Sectie 3.3 kan de nauwkeurigheid van deze laatste nagegaan worden. Het exacte SNR-model blijkt op een niet-triviale manier af te hangen van de tweede-orde statistieken ('second-order statistics', SOS) van signaal en ruis, het kanaalmodel en de TEQ.

BM-TEQ-ontwerp

Een TEQ-ontwerp dat zonder benadering de bitsnelheid van een DMT-gebaseerd DSL-systeem maximaliseert, bleef tot nu toe onbeschikbaar. In dit hoofdstuk worden twee BM-TEQ-kostcriteria afgeleid en besproken. In Sectie 4.2 stellen we een eerste BM-TEQ-ontwerp voor. Daartoe wordt een alternatief, compact en elegant SNR-model afgeleid dat equivalent is met het SNR-model uit Sectie 4.1, maar dat beschreven wordt in termen van SOS aan zender en ontvanger, i.p.v. het kanaal en SOS van signaal en ruis. De sleutel in de afleiding van het nieuwe SNR-model wordt gevormd door de observatie dat de SNR-afhankelijkheid van de TEQ-coëfficiënten gemakkelijk in rekening te brengen is door de SNR aan de uitgang van de FEQs te beschouwen. Vroegere TEQ-ontwerpen waren eerder gebaseerd op een (benaderend) SNR-model aan de ingang van de FEQs, d.i. de DFT-uitgang. De SNR voor en achter de FEQ is gelijk aangezien de FEQs zowel de teller (de gewenste energie) als de noemer (de foutenergie) van de SNR schalen. In eerste instantie komen in het nieuwe SNR-model ook de FEQs voor, maar die kunnen geëlimineerd worden doordat de FEQs in functie van de TEQ-taps kunnen geschreven worden.

Dit nieuwe SNR-model leidt dan tot het BM-TEQ-ontwerpcriterium (4.32) dat past in het algemeen kader van Sectie 3.1. Zowel de SNR als het BM-TEQ-

criterium worden uitgedrukt in termen van de TEQ **w** en de SOS aan de zender en de ontvanger.

Figuur 4.2 toont een hoogtelijnendiagram van de BM-TEQ-kostfunctie voor een specifiek ADSL-scenario en $T = 3$ TEQ-coëfficiënten. Er is een duidelijk zichtbaar maximum en minimum. Bijgevolg is de kostfunctie niet-convex. Hoewel er geen lokale maxima zichtbaar zijn, hebben simulaties aangeduid dat deze wel degelijk bestaan voor andere scenario's.

De BM-TEQ-kostfunctie kan opgelost worden m.b.v. klassieke niet-lineaire optimalisatieroutines, zoals iteratieve, (quasi-)Newton- en simplex-algoritmes, die leiden tot een lokaal optimum. De SOS die nodig zijn voor het berekenen van de kostfunctie kunnen verkregen worden op basis van een schatting van het transmissiekanaal en de ruis of, recursief, aan de hand van een trainingssignaal, verstuurd tijdens het opzetten van de verbinding.

Kleinste-kwadraten ('least-squares', LS)-gebaseerd TD- en FD-MMSE-TEQ-ontwerp

Het eerste BM-TEQ-criterium is een niet-lineaire kostfunctie in de TEQ-taps **w** die de specifieke TEQ-FEQ-ontvangerstructuur verbergt. In Sectie 4.3 wordt een alternatief, zogenaamd iteratief herwogen, scheidbaar, niet-lineair LS ('iteratively-reweighted separable non-linear least-squares', IR-SNLLS) BM-TEQ-criterium voorgesteld: de kostfunctie is een iteratief herwogen som van kwadratische frequentiedomein fouten tussen de symboolschattingen aan de FEQ-uitgangen en de echte verstuurde symbolen. Dit alternatieve criterium toont veel beter het frequentiedomein DMT-bloktransmissiekarakter.

Het IR-SNLLS-gebaseerde BM-TEQ-criterium biedt dan ook verscheidene voordelen. De kostfunctie kan geoptimaliseerd worden m.b.v. een elegant, iteratief, snel convergerend Gauss-Newton (GN)-gebaseerd optimalisatie-algoritme, dat gestuurd wordt door de fouten aan de FEQ-uitgangen en dat de eigenschap van scheidbaarheid in het ontwerpcriterium uitbuit. Alternatief kan gebruik gemaakt worden van een nauw gerelateerd recursief Levenberg-Marquardt (RLM)-algoritme, voorgesteld in Hoofdstuk 5.

Bovendien wordt een gemeenschappelijk LS-gebaseerd kader voor DMT-egalisatie uitgewerkt. Dit laat toe om een nauw verband te leggen tussen de LS-gebaseerde formulering van de BM-TEQ enerzijds en LS-gebaseerde versies van de TD-MMSE-TEQ en de PTEQ anderzijds d.m.v. twee zogenaamde FD-MMSE-TEQ-ontwerpen. Op het eerste zicht zijn deze egalisatorontwerpen nochtans erg verschillend. De MMSE-TEQ is de oplossing van een beperkt, lineair tijdsdomein MMSE-criterium dat afhangt van de TEQ- en TIR-coëfficiënten. De PTEQ is eerder afgeleid van een onbeperkt, lineair MMSE-criterium dat enkel van de PTEQ-coëfficiënten afhangt. De BM-TEQ tenslotte werd in de vorige sectie voorgesteld als een niet-lineair criterium in de

TEQ-coëfficiënten. Het nauw verband tussen de LS-formuleringen wordt verder geëxpliciteerd door de omzetting naar een veralgemeend eigenwaardenprobleem.

Simulaties

De simulaties maken gebruik van een set van typische ADSL-kanalen, met inbegrip van de 'front-end' filters. Het zijn vooral deze filters die aanleiding geven tot een aanzienlijke hoeveelheid ISI/ICI en een noemenswaardig performantieverschil tussen verschillende TEQ-ontwerpen, zie **Figuur 4.3**.

De simulaties tonen aan dat een BM-TEQ van T taps alle vroeger voorgestelde TEQ-ontwerpen verslaat en de performantie van de PTEQ (met T taps per toon) zeer dicht benadert (zie **Figuur 4.4** tot **Figuur 4.7**). Zowel de BM-TEQ als de PTEQ hebben geen problemen met een wispelturige performantie in functie van de synchronisatieparameter Δ (zie **Figuur 4.5** en **Figuur 4.6**). Bovendien leveren enkel de BM-TEQ en PTEQ een consistent betere performantie voor een toenemend aantal taps (zie **Figuur 4.4**). Ondanks de niet-convexe BM-TEQ-kostfunctie bereikt het iteratieve GN-algoritme lokaal optimale TEQs die amper 6 kbps in bitsnelheid verschillen. In Hoofdstuk 5 leveren moeilijkere scenario's met RFI lokale optima met een iets groter verschil van 100 kbps.

Ook de performantie van de twee FD-MMSE-TEQ-ontwerpen en de snelle convergentie van het iteratief GN-gebaseerd optimalisatie-algoritme worden geïllustreerd, zie **Figuur 4.8** en **Figuur 4.9**.

Hoofdstuk 5: Adaptief bitsnelheid-maximaliserend en per-groep egalisatorontwerp

BM per-groep egalisatorontwerp

De berekeningskost van de PTEQ kan verminderd worden door het toepassen van toongroepering, d.i. door de actieve tonen in een aantal toongroepen te verdelen en enkel de PTEQ van de middelste toon in de groep te optimaliseren. De andere tonen in de groep krijgen dan een getransformeerde versie van de PTEQ voor de middelste toon toegewezen. Het nadeel van deze PTEQ met toongroepering is dat de garantie dat een PTEQ een betere performantie levert dan een TEQ, verloren gaat.

In Sectie 5.1 wordt aangetoond hoe het BM-TEQ-ontwerp kan uitgebreid worden naar een BM per-groep egalisatorontwerp ('bit rate maximizing per-group equalizer', BM-PGEQ). Opnieuw worden de actieve tonen verdeeld in een klein aantal groepen. Echter, deze keer wordt voor elke groep de oplossing van het (gereduceerde) BM-TEQ-ontwerpcriterium bepaald, wat resulteert in een BM-

PGEQ voor die groep. Bijgevolg ligt de performantie van een BM-PGEQ boven die van het oorspronkelijke toongroeperingsschema en tussen die van de BM-TEQ en de PTEQ. Het BM-PGEQ-ontwerp laat dus toe om geheugenkost en performantie tegen elkaar af te wegen, terwijl de berekeningskost tijdens datatransmissie grosso modo onveranderd blijft.

Noteer dat de BM-PGEQ op twee manieren kan geïmplementeerd worden, hetzij met minimale geheugenkost, hetzij met minimale berekeningskost.

RLM-gebaseerd BM-TEQ- en BM-PGEQ-ontwerp

Kanaal- en ruiskarakteristieken in een communicatie-omgeving variëren typisch in de tijd. Zo veroorzaken veranderende weerscondities, temperatuur, overspraak en/of RFI trage tijdsvariaties in een DSL-omgeving. De DMT-ontvanger is dan ook bij voorkeur adaptief zodat de veranderingen in de omgeving, b.v. het wegvallen van een RFI, kunnen gevolgd worden en de performantie op het hoogst mogelijke peil gehouden wordt. Dergelijke adaptiviteit kan ook uitgebuit worden om op efficiënte wijze en m.b.v. een trainingssignaal een egalisator te ontwerpen: de egalisatorcoëfficiënten worden geüpdatet telkens nieuwe trainingsdata binnenkomt, zodat niet alle beschikbare data dient opgeslagen te worden.

In de huidige ADSL-modems wordt de TEQ typisch offline ontworpen: de TEQ wordt berekend bij het opzetten van de verbinding en vervolgens constant gehouden gedurende de datatransmissie. De nieuwste ADSL2- en ADSL2+-standaards ondersteunen zogenaamde 'seamless rate adaptation', waarbij de ADSL-lijnconditie voortdurend geobserveerd wordt en de bitsnelheid en bitallocatie eraan aangepast worden. Bijgevolg is een *adaptief* BM egalisatorontwerp zeer wenselijk. Deze adaptieve procedure kan ook gebruikt worden voor het BM-TEQ-ontwerp tijdens het opzetten van de verbinding: in ADSL/ADSL2+ is een lang trainingssignaal van 16000 tot 32000 trainingssymbolen beschikbaar. Tot nu toe werden slechts een beperkt aantal adaptieve DMT-egalisatoren voorgesteld, o.a. de eerder vermelde adaptieve PTEQ.

In Sectie 5.2 tonen we aan hoe de BM-TEQ en de BM-PGEQ adaptief kunnen ontworpen worden, ondanks hun niet-lineair kostcriterium. Dit adaptatieschema is afgeleid van de IR-SNLLS-gebaseerde BM-TEQ-kostfunctie en het overeenkomstige, iteratieve, GN-gebaseerde optimalisatie-algoritme. Door benaderingen en wijzigingen aan het iteratief GN-gebaseerde algoritme wordt een stabiel en efficiënt RLM-algoritme bekomen dat de gezamenlijke TEQ-FEQ-parametervector op elk tijdstip updatet. Dit adaptief BM-TEQ-algoritme maakt gebruik van exact dezelfde SOS aan de ontvanger als de RLS-gebaseerde adaptieve PTEQ, nl. op basis van de autocorrelatiematrices van de 'sliding'-DFT van het ontvangen signaal. Net zoals bij de RLS- en RLS/LMS-gebaseerde adaptieve PTEQ kan de geheugenkost van de SOS verder gereduceerd worden door de 'sliding'-DFT-structuur uit te buiten. Het RLM-algoritme maakt ge-

bruik van een regularisatieparameter om stabiliteit te garanderen. Deze parameter wordt op efficiënte wijze geadapteerd om de veranderende conditie van de Hessiaan in rekening te brengen. Het adaptieve BM-TEQ-algoritme wordt samengevat in **Tabel 5.1**. Een adaptieve BM-PGEQ wordt verkregen door een aantal gereduceerde adaptieve BM-TEQ-problemen in parallel op te lossen.

Berekenings- en geheugenkost van de adaptieve BM egalisatoren

Op deze manier ontstaat een volledig gamma van adaptieve BM egalisatoren met grosso modo gelijke bitsnelheid, wat een flexibele afweging van geheugen- en berekeningskost toelaat. **Tabel 5.3** geeft een overzicht van de berekeningskost van een BM-TEQ-update. **Tabel 5.2** en **Tabel 5.4** tonen de berekenings- en geheugenkost van elk van de adaptieve algoritmes waarbij een onderscheid gemaakt wordt tussen de kost van de egalisatorupdate en de egalisatie-operatie zelf.

De berekeningskost van de egalisatie zelf is ruwweg gelijk voor alle voorgestelde adaptieve BM egalisatoren, nl. 1 DFT plus $\mathcal{O}(N_a T)$ vermenigvuldigingen. De berekeningskost van de BM-TEQ- en BM-PGEQ-update is ruwweg gelijk, maar ongeveer 8 tot 16 maal complexer dan de PTEQ-update. De geheugenkost voor de egalisatorcoëfficiënten varieert van $N_a T$ complexe coëfficiënten voor een PTEQ (met N_a het aantal actieve tonen) over $N_g T$ reële of complexe PGEQ-coëfficiënten plus N_a FEQs (met $N_g \ll N_a$) tot slechts T reële coëfficiënten plus N_a FEQs voor een BM-TEQ. De geheugenkost voor de SOS, nodig voor de egalisatorupdate, is gelijk voor alle algoritmes.

Onder realistische veronderstellingen blijkt de berekeningscomplexiteit van de PTEQ $3,4 \times 10^6$ tot $10,7 \times 10^6$ vermenigvuldigingen per seconde te vergen, terwijl de BM-TEQ een haalbare $28,5 \times 10^6$ tot 168×10^6 vermenigvuldigingen per seconde vereist.

Simulaties

De simulaties tonen aan dat de BM-PGEQ een nuttige tussenoplossing biedt tussen de BM-TEQ en de PTEQ: de PTEQ-performantie wordt dicht benaderd door een BM-PGEQ-oplossing met slechts 4 toongroepen, zelfs in het geval van een moeilijk ADSL-scenario met RFI en overspraak, zie **Figuur 5.2**. Bovendien is de BM-PGEQ in dergelijke RFI-scenario's minder gevoelig aan lokale optima dan de BM-TEQ, zie **Figuur 5.3**. Net zoals de PTEQ blijken de BM-TEQ en BM-PGEQ impliciet een vensterfunctie te bevatten: de performantie in de aanwezigheid van RFI neemt in belangrijke mate toe door het aantal taps te verhogen.

D.m.v. uitgebreide simulaties met verschillende ADSL-scenario's (met en zonder RFI) en parameterinstellingen wordt aangetoond dat de adaptieve BM-TEQ en BM-PGEQ een snelle convergentiesnelheid hebben, vergelijkbaar met de PTEQ-convergentiesnelheid, zie **Figuur 5.4, Figuur 5.5**, **Figuur 5.6**, **Ta-**

bel 5.5 en **Tabel 5.6**. Bovendien illustreren we in **Figuur 5.7** dat adaptieve BM egalisatoren het mogelijk maken om wijzigingen in kanaal- en ruiskarakteristieken te volgen, wat hen een uitstekende kandidaat maakt voor integratie met de 'seamless rate adaptation'-functionaliteit van ADSL2- en ADSL2+-modems.

Hoofdstuk 6: Gecombineerd bitsnelheid-maximaliserend ontwerp van een vensterfunctie en een TEQ

Gecombineerd BM ontwerp van een vensterfunctie en een TEQ

Tot nu toe hebben we ons vooral gefocusseerd op het DMT-egalisatieprobleem. In dit hoofdstuk beschouwen we het meer algemene geval van gecombineerd egalisator- en vensterfunctie-ontwerp om kanaaldistortie en smalbandige RFI gezamenlijk aan te pakken. Wegens de overlappende sinc-vormige toonspectra met hoge zijlobben is DMT-modulatie niet zo robuust tegen RFI: als gevolg van de spectrale lek kan een voldoende sterke RFI-stoorbron een DMT-gebaseerd systeem zelfs volledig doen falen.

In de literatuur kunnen twee benaderingen voor RFI-onderdrukking onderscheiden worden. Ofwel worden het egalisator- en vensterfunctie-ontwerp volledig onafhankelijk aangepakt. De vensterfunctie (met een 'taper' van μ taps) wordt constant gehouden of adaptief bepaald. In dit geval moet de egalisator het kanaal voldoende verkorten (tot $\nu - \mu + 1$ monsters) zodat de vensterfunctie de orthogonaliteit van de tonen bewaart. Het resultaat is suboptimaal aangezien de voorgestelde vensterfuncties de bitsnelheid niet maximaliseren. Ofwel worden egalisator- en vensterfunctie-ontwerp gecombineerd, zoals in het geval van het gecombineerd PTEQ- en vensterfunctie-ontwerp per toon. Deze vensterfunctie kan zowel vast als adaptief zijn. In het laatste geval betekent dit dat de PTEQ uitgebreid wordt van T naar $T + \mu$ taps per toon, wat leidt tot een aanzienlijke meerkost in geheugen en berekeningen.

Deze kost wordt beperkt door het BM-TEQ-ontwerp uit te breiden met een optimaal tijdsdomein vensterfunctie, zoals voorgesteld in dit hoofdstuk. Zowel de originele BM-TEQ-kostfunctie als de IR-SNLLS-gebaseerde BM-TEQ kunnen uitgebreid worden, zie Sectie 6.2. Het resultaat is een zogenaamd 'bit rate maximizing combined window and time-domain equalizer'-ontwerp (BM-WinTEQ). Aangezien de egalisator en de vensterfunctie nu gezamenlijk ontworpen worden is er geen beperking meer op de lengte van de verkorte kanaalimpulsresponsie. Het SNR-model aan de FEQ-uitgang wordt nu uitgebreid met SOS-termen die niet enkel afhangen van de SOS aan zender en ontvanger, maar ook van het venster-'taper'.

Speciale gevallen

Verschillende speciale gevallen kunnen onderscheiden worden.

Het gecombineerd ontwerp van egalisator en vensterfunctie per toongroep is een natuurlijke uitbreiding van het BM-PGEQ-ontwerp in Hoofdstuk 5. Een speciaal geval wordt bekomen door 1 toon per groep te beschouwen: dan wordt inderdaad een PTEQ met $T + \mu$ i.p.v. T taps per toon bekomen.

De BM vensterfunctie (zonder egalisator) is van nut indien het kanaal voldoende kort is en er bijgevolg geen egalisatie nodig is, b.v. in VDSL. Interessant hier is dat de FEQs onafhankelijk van het venster-'taper' blijken te zijn, zodat de resulterende kostfunctie een iteratief herwogen, *lineair*, LS-gebaseerd criterium in de venstercoëfficiënten wordt. De kostfunctie is dus convex in elke iteratie en bijgevolg convergeert een iteratief optimalisatie-algoritme naar een globaal optimaal venster.

Tenslotte kan ook een egalisator ontworpen worden in de aanwezigheid van een vaste vensterfunctie, zoals een 'raised' cosinusvenster. Het BM-WinTEQ-criterium dient dan geoptimaliseerd te worden voor een vaste, specifieke vensterfunctie. Hoewel vaste vensterfuncties geen maximale bitsnelheid garanderen, zijn ze zeker van belang, aangezien ze de DMT-ontvanger robuuster maken tegen interferentie vanwege niet-stationaire radio-amateurs: een optimale vensterfunctie kan toch aanleiding geven tot een belangrijk performantieverlies indien een RFI opduikt na het vensterontwerp.

Berekenings- en geheugenkost

Tabel 6.1, **Tabel 6.2** en **Tabel 6.3** geven een overzicht van de geheugen- en berekeningskost van de hierboven beschreven gecombineerde egalisator- en vensterfunctie-ontwerpen. Aangezien de lengte van het venster-'taper' μ typisch veel kleiner is dan de DFT-grootte N, is de extra kost door het toevoegen van een tijdsdomein venster verwaarloosbaar. De kost van een PTEQ, zeker in combinatie met een venster per toon, is veel hoger dan de kost van een TEQ in combinatie met een tijdsdomein venster. De berekeningskost van een gecombineerde egalisator en vensterfunctie per toongroep is hoger dan die van een PTEQ.

Richtlijnen voor optimalisatie van het BM-WinTEQ-criterium

O.w.v. de sterke gelijkenissen met het oorspronkelijke IR-SNLLS-gebaseerde BM-TEQ-criterium kan de BM-WinTEQ ook bepaald worden m.b.v. een iteratief GN-gebaseerd of een adaptief RLM-gebaseerd optimalisatie-algoritme. Beide algoritmes bepalen dan tegelijk de TEQ-, venster- en FEQ-coëfficiënten. Het adaptief algoritme maakt gebruik van exact dezelfde SOS als de PTEQ met $T + \mu$ taps per toon. Voor het bepalen van een egalisator in combinatie met een vast venster blijven dezelfde SOS nodig, maar de berekeningskost is lager in vergelijking met de adaptieve BM-WinTEQ.

Simulaties

Traditioneel wordt de TEQ gebruikt om te egaliseren (b.v. in ADSL) en wordt de vensterfunctie voorgesteld als een oplossing voor RFI-onderdrukking (b.v. in VDSL), zie **Figuur 6.3**, **Figuur 6.4** en **Figuur 6.5**. In de simulaties wordt echter aangetoond dat de capaciteit van een vensterfunctie om de DFT-zijlobben te verminderen ook helpt om de ICI te reduceren. Bijgevolg vereenvoudigt een vensterfunctie de egalisatie in ADSL in de afwezigheid van RFI, zie **Figuur 6.6**. Omgekeerd kan een DMT-ontvanger verbeterd worden door het toevoegen van een TEQ-filter om RFI m.b.v. nullen te onderdrukken. Daarom suggereren we om steeds een TEQ te gebruiken met het grootst haalbare aantal taps en dit te combineren met een venster, wat verwaarloosbare complexiteit toevoegt, zie **Figuur 6.7**, **Figuur 6.8**, **Figuur 6.9** en **Figuur 6.10**. Aangezien de robuustheid ten kost gaat van de extra performantie vanwege een BM-WinTEQ, zeker in het geval een RFI opduikt na het vensterontwerp (zie **Figuur 6.11**), raden we ook aan om gebruik te maken van een vast venster indien het aantal egalisatorcoëfficiënten groot is en de aanwezige RFI niet-stationair is.

Hoofdstuk 7: Egalisatie van DMT-gebaseerde systemen over IIR-kanalen

Notatie en datamodel

Tot nu toe hebben we oplossingen voor de DMT-ontvanger beschouwd zonder de DMT-zender te wijzigen. Bijgevolg voldoen de voorgestelde oplossingen aan de ADSL-standaards. In dit hoofdstuk laten we een willekeurige CP-lengte toe: de gestandaardiseerde keuze van 32 monsters blijkt conservatief en het gebruik van een aangepaste egalisatiestructuur laat toe de CP-lengte te herleiden tot b.v. 16 monsters. Dit resulteert in een kleinere 'latency' en efficiëntiereductie zonder de berekenings- en geheugenkost te doen toenemen.

Voor de ontwikkeling van een gepaste DMT-egalisator voor een willekeurige CP-lengte beschouwen we een IIR-kanaalmodel. De ADSL-kanaalimpulsresponsie heeft typisch een lange staart. Daarom werd reeds vroeger in de literatuur een IIR- of pool-nulpunt-kanaalmodel gesuggereerd. Het overeenkomstige IIR-gebaseerde datamodel is opvallend, aangezien het een relatie met de PTEQ suggereert: zowel het datamodel als de PTEQ blijken gebruik te maken van verschiltermen van ontvangen monsters. Op basis van dit datamodel worden twee gevallen beschouwd: het geval waarbij de orde van de teller kleiner is dan of gelijk aan de CP-lengte en het geval waarbij de orde van de teller groter is dan de CP-lengte.

DMT-egalisatie van een IIR-kanaal

Voor beide gevallen worden eerst nodige en voldoende voorwaarden voor het bestaan van een lineaire 'zero-forcing' (ZF)-egalisator afgeleid. Deze voorwaar-

den leggen beperkingen op aan de orde van het IIR-model en de vereiste hoeveelheid zendredundantie per DMT-symbool. Vervolgens leiden we optimale lineaire ZF-egalisatoren af. In beide gevallen blijken die per toon ontkoppeld te kunnen worden met als eindresultaat een lineaire ZF-PTEQ.

Goedkope uitbreidingen van de PTEQ en de BM-TEQ

De optimale lineaire MMSE egalisatoren blijken niet ontkoppeld per toon. Echter, op basis van de optimale lineaire ZF-egalisatoren stellen we goedkope uitbreidingen van de originele MMSE-PTEQ voor die een goede performantie leveren en bijgevolg geschikt zijn voor een willekeurige CP-lengte en orde van het IIR-kanaal. De zogenaamde lineaire PTEQ-uitbreiding (L-PTEQ) maakt gebruik van frequentiedomein zendredundantie die in DMT geboden wordt door ongebruikte tonen en piloottonen, zie **Figuur 7.2**: door de DFT-uitgangen van een aantal ongebruikte tonen en piloottonen (samen met de pilootsymbolen) met voldoende ISI/ICI toe te voegen aan de gemeenschappelijke PTEQ-ingangen kan de egalisatie van de actieve tonen gevoelig verbeterd worden.

De zogenaamde PTEQ-uitbreiding met terugkoppeling van de beslissingen ('decision-feedback PTEQ', DF-PTEQ, zie **Figuur 7.3**) is gebaseerd op de observatie dat elke beslissing op een datasymbool op dezelfde manier kan behandeld worden als de kennis van een pilootsymbool: de ISI/ICI aan de DFT-uitgang van de beschouwde actieve toon kan uitgebuit worden om de egalisatie van de nog te egaliseren actieve tonen te verbeteren. De DF-PTEQ-uitbreiding koppelt een aantal symboolbeslissingen binnen het huidige DMT-symbool terug en gebruikt deze, samen met de overeenkomstige DFT-uitgangen, als extra gemeenschappelijke PTEQ-ingangen voor de resterende tonen.

Door een specifieke keuze van CP-lengte, aantal verschiltermen en aantal piloottonen, ongebruikte tonen en teruggekoppelde tonen wordt impliciet een bepaald IIR-kanaalmodel gekozen. De RLS- en RLS/LMS-gebaseerde adaptieve PTEQ-algoritmes kunnen meteen uitgebreid worden om de nieuwe, gemeenschappelijke ingangen in rekening te brengen. Ook geven we richtlijnen voor de keuze van de gebruikte frequentiedomein redundantie. Daarnaast bespreken we de mogelijkheid om aan RFI-onderdrukking te doen door het uitbuiten van specifieke ongebruikte tonen.

De afleidingen in dit hoofdstuk focusseren vooral op PTEQ-uitbreidingen. Echter, door het nauwe verband tussen de BM-TEQ en de PTEQ, zoals uitvoerig besproken in deze thesis, is het duidelijk dat ook een L-BM-TEQ- en DF-BM-TEQ-uitbreiding voor de hand liggen: een deel van de egalisatie gebeurt dan m.b.v. een TEQ in het tijdsdomein vóór de DFT, terwijl het tweede deel van de egalisatie gebeurt d.m.v. een meertaps-FEQ na de DFT met ongebruikte tonen, piloottonen en pilootsymbolen als extra ingangen. Opnieuw kunnen het iteratieve GN-gebaseerde en het adaptieve RLM-gebaseerde algoritme uitgebreid worden om de egalisatorcoëfficiënten van de BM-TEQ-uitbreidingen te berekenen.

Simulaties

Simulaties voor verschillende ADSL-scenario's, hoeveelheden uitgebuite frequentiedomein zendredundantie, CP-lengtes en aantal taps tonen aan dat de voorgestelde L-PTEQ- en DF-PTEQ-uitbreiding flexibiliteit aan een DMT-gebaseerd systeem toevoegen: de CP-redundantie kan gereduceerd worden tot b.v. 16 monsters; de CP wordt dan ingewisseld voor frequentiedomein redundantie. Zo wordt dezelfde bitsnelheid tegen een lagere berekenings- en geheugenkost verkregen of kan alternatief een hogere bitsnelheid zonder belangrijke toename van de kost bereikt worden (zie **Figuur 7.4** en **Figuur 7.5** voor de L-PTEQ-uitbreiding en **Figuur 7.6**, **Figuur 7.7** en **Figuur 7.8** voor de DF-PTEQ-uitbreiding; zie **Tabel 7.1** voor een vergelijking van de berekenings- en geheugenkost). Bovendien kunnen het aantal verschiltermen en de frequentiedomein redundantie tegen elkaar afgewogen worden om de robuustheid in de aanwezigheid van RFI te verhogen, zie **Figuur 7.9** en **Figuur 7.10**.

Hoofdstuk 8: Besluiten en verder onderzoek

Adaptieve BM-TEQ en BM-WinTEQ

Zoals uitgelegd in Hoofdstuk 5 en Hoofdstuk 6 vereisen de adaptieve BM-TEQ en BM-WinTEQ dezelfde SOS als de adaptieve PTEQ, zij het dat de berekeningskost groter is. In de literatuur zijn allerlei adaptieve algoritmes beschikbaar voor niet-lineaire optimalisatie, b.v. voor training van neurale netwerken. Sommige algoritmes hebben een berekeningskost en convergentiesnelheid die tussen die van de (snelle maar complexe) recursieve GN- en LM-algoritmes en (trage maar goedkope) stochastische-gradiënt-algoritmes ligt (b.v. het 'conjugate gradient'-algoritme). Verder onderzoek is nodig om de toepasbaarheid ervan op het niet-lineaire BM-TEQ- en BM-WinTEQ-ontwerpcriterium na te gaan.

Zoals aangetoond in Hoofdstuk 6 veroorzaakt een RFI die verschijnt na het BM-WinTEQ-ontwerp een significant performantieverlies. Vooral in VDSL waar radio-amateurs niet-stationaire RFI veroorzaken moet dit probleem aangepakt worden.

Egalisatie voor MIMO-DSL

In deze thesis hebben we ons toegelegd op DSL-communicatie in een SISO-context: één DMT-zender communiceert met één DMT-ontvanger. Overspraak, de elektromagnetische koppeling tussen koperlijnen in een bundel, wordt beschouwd als een stoorbron die additieve ruis veroorzaakt. Recent is er een toenemende interesse voor zogenaamde MIMO-DSL: aanzienlijk betere performantie wordt verkregen door de bundel telefoonlijnen als een MIMO-systeem te beschouwen en de zogenaamde 'far-end crosstalk' (FEXT), afkomstig van signalen die zich in dezelfde richting voortplanten, uit te buiten. FEXT is vooral

belangrijk in ADSL2+ en VDSL, omdat deze systemen een grotere bandbreedte gebruiken.

Verschillende vormen van MIMO-DSL worden onderzocht, afhankelijk van de hoeveelheid coördinatie en samenwerking tussen de modems. Echter, voor elk van deze vormen van MIMO-DSL werd tot nu toe in de literatuur verondersteld dat alle kanalen (zowel directe kanalen als overspraakkanalen) gesynchroniseerd en perfect verkort zijn zodat coördinatie en samenwerking per toon afzonderlijk kan gebeuren. In ADSL2+ zijn deze veronderstellingen meestal niet voldaan: de impulsresponsie van het transmissie- en overspraakkanaal zijn typisch veel langer dan de CP. Daarom moet MIMO-ADSL gecombineerd worden met de gepaste egalisatie. Verder onderzoek dient na te gaan hoe groot de impact van onvolledige kanaalverkorting op DSM is en hoe MIMO-egalisatie in MIMO-DSL geïntegreerd kan worden.

Egalisatie van draadloze communicatie

In deze thesis lag de focus op bedrade DSL-communicatie. Echter, MC-modulatie werd ook geselecteerd onder de naam 'orthogonal frequency-division multiplexing' (OFDM) voor verscheidene draadloze toepassingen, b.v. WLANs. Bepaalde tendensen en specifieke aspecten in draadloze communicatie leiden dan ook tot interessante onderwerpen voor verder onderzoek.

Aanvankelijk werd meestal verondersteld dat een TEQ niet nodig is voor OFDM, aangezien de lengte van draadloze kanalen typisch korter is dan de CP-lengte. Echter, de 'front-end' filters in elk draadloos communicatiesysteem maken de kanaalimpulsresponsie langer. Daarom is er recent een toegenomen interesse voor egalisatorontwerp in een draadloze context. Het verdient dan ook aanbeveling de onderstaande aspecten m.b.t. de toepasbaarheid en mogelijke uitbreiding van de voorgestelde TEQ-ontwerpprocedures in een draadloze context te onderzoeken.

De snelle tijdsvariaties van het draadloze communicatiekanaal vormen één van de cruciale verschillen met bedrade systemen. Bijgevolg dienen egalisatoren in draadloze systemen tijdsvariërend en adaptief te zijn zodat tijdsvariaties kunnen gevolgd worden. Hiertoe zijn twee aanpakken mogelijk die gecombineerd kunnen worden: (semi)blinde algoritmes voorkomen efficiëntieverlies tengevolge van trainingssequenties; een zogenaamd 'basis-expansion'-model laat toe om snel variërende kanalen voor te stellen als een gewogen som van basisfuncties, waarbij de gewichten traag tijdsvariërend zijn.

Maximalisatie van de bitsnelheid bij een vaste bitfoutkans is het eigenlijke ontwerpcriterium voor een DSL-ontvanger. De TEQ-ontwerpprocedures die momenteel voor draadloze OFDM-systemen beschouwd worden, houden geen verband met het eigenlijke ontwerpobjectief. Tot nu toe werd er meestal aangenomen dat er geen kanaalinformatie beschikbaar is aan de zender. Bijgevolg

wordt er meestal van uit gegaan dat een zelfde constellatie over alle tonen gebruikt wordt. Het ontwerpobjectief is dan ook vaak het minimaliseren van de bitfoutkans. Recent werden ook OFDM-systemen met gedeeltelijke of volledige kanaalinformatie aan de zender beschouwd. Dit laat het gebruik van adaptieve modulatie toe, en dus ook de maximalisatie van de bitsnelheid (voor een gegeven bitfoutkans) of de minimalisatie van de bitfoutkans (voor een gegeven bitsnelheid).

In draadloze communicatiesystemen wordt tegenwoordig veel aandacht besteed aan MIMO-systemen met meerdere zend- en/of ontvangstantennes, b.v. in combinatie met 'space-time'-codering, adaptieve modulatie en/of 'smart antenna'-technologie. Deze systemen beloven een hogere capaciteit en/of kwaliteit en moeten toelaten om dezelfde bitsnelheden, zoals verkrgen met bedrade systemen, te halen. Bijgevolg is ook hier de uitbreiding naar MIMO-egalisatie vereist.

Tenslotte worden voor draadloze systemen ook andere transmissieschema's beschouwd. Zogenaamde 'single-carrier'-modulatie met CP heeft een aantal interessante voordelen t.o.v. OFDM-modulatie. 'Code-division multiple access' (CDMA) laat toe dat meerdere gebruikers het spectrum delen door aan elke gebruiker een specifieke code toe te kennen. Ook CDMA-modulatie kan gebruik maken van een CP. Voor beide modulatieschema's zijn specifieke kanaalverkortingsalgoritmes nodig om een lange kanaalimpulsresponsie te verkorten.

Chapter 1

Introduction

BROADBAND Internet access is one of the fastest growing technologies in history. Worldwide, there are over 100 million established broadband connections nowadays. One of the techniques that enables this growth is the digital subscriber line (DSL) technology. DSL allows to provide high-speed data communication over the twisted pair telephone network. In order to make broadband access over the twisted pair possible, current asymmetric DSL (ADSL) modems make use of advanced digital signal processing (DSP) solutions. Next-generation DSL systems will deliver even higher bit rates, together with new services. Therefore, a continuing research on enhanced DSP solutions is required.

In Section 1.1, an overview of the expansion of the internet and DSL is given. The history and future of DSL and competing broadband access techniques is discussed in Section 1.2. Broadband communication over the twisted pair telephone network is non-trivial: an overview of the encountered impairments as well as an introduction to the adopted multicarrier modulation scheme are given in Section 1.3. Section 1.4 motivates the need for further DSL research and gives a chapter-by-chapter outline of the thesis. Section 1.5 concludes this chapter.

1.1 Internet access: driver application for digital subscriber lines (DSL)

With an estimate of 800 million users and a 100 % growth over the last 4 years (June 2004), the internet is continuing its worldwide spread [116]. In Belgium, over 4 million people frequently use the internet; 80 % of the personal

computers (PC) in Belgium are connected to the internet (June 2004). The worldwide computer network offers a large and increasing number of applications and services for residential as well as business use, such as e-mail and web browsing, on-line shopping, education, travel planning, banking, interactive gaming, on-line chat, access to streaming media, including video-on-demand and conversational services (e.g., voice over IP), peer-to-peer filesharing, virtual private networks, etc. Large data transfers are involved in many of these applications, hence there is a continuously increasing demand for high-speed broadband internet access.

Broadband internet access has found its way to the consumer and corporate market since the late 90's. At the end of 2003, there were over 100 million broadband lines worldwide. Broadband is growing much faster than mobile phone usage — so far at least. It took mobile phones about 5.5 years to grow from 10 million to 100 million; broadband internet access has achieved the same growth in only 3.5 years [116]. This means that broadband internet access is clearly established as one of the fastest growing new technologies in history. In Belgium, 1.4 million of the almost 2 million internet connections (residential as well as business) are broadband (March 2004) [13]. This results in the third largest residential broadband penetration in the world, after South-Korea and Canada: 1 out of 4 Belgian families has a broadband internet connection.

Broadband communication can take place over several media: the subscriber telephone loop (a twisted pair of copper wires), the coaxial television cable, the powerline and the optical fiber are so called wireline media; wireless communication constitutes a fifth option. So-called digital subscriber line (DSL) technology over the telephone line and cable modem technology have the largest deployment. According to the DSL Forum, a consortium of DSL-related companies, some 73.4 million computers around the world are now connected to the internet via DSL [46]. The DSL Forum's global target is 200 million DSL subscribers or 20 per cent of all phone lines worldwide by the end of 2005. In Belgium, there are around 1 million DSL broadband connections and around 400000 cable modem users (December 2003). With 16.7 DSL connections per 100 phone lines, Belgium ranks third in the world's DSL penetration chart. A possible explanation for this is the large competition among broadband providers, which results in an appealing value for money ratio: the customer gets a downstream speed (i.e., from the operator towards the customer) of 3 to 4 Mbps, at a monthly fee of around 40 EUR.

Price erosion for basic internet access service drives the operators to identify approaches to generate new revenue streams. The introduction of new services over the internet, such as multiple streams of live or on-demand video broadcast, video conferencing, high-definition TV and ultra-fast broadband access, can increase the average revenue per user and enlarge the addressable market [17, 31]. These new services, in turn, could pave the way for next-generation broadband systems.

1.2 History and future of DSL

In this thesis, we focus on *DSL broadband access*. A glimpse on the history and the future of DSL communications is offered in this section.

DSL's history

The history of data communication over the telephone line starts in the 19th century with the invention of the electric telegraph by Samuel Morse and the telephone by Alexander Graham Bell. For more than a century, data communication over telephone lines takes place in the same frequency band as used for the plain old telephone service (POTS), i.e., the voiceband between 300 Hz and 3.4 kHz [94]. The feasibility of sending broadband signals over telephone lines was only demonstrated by Joseph Lechleider, of Bellcore, in the late 1980s.

The first conceived DSL technology with a bandwidth that extended beyond the voiceband, was basic-rate *Integrated Services Digital Network* (ISDN). ISDN provides an aggregate bit rate of 160 kbps using a bandwidth of 80 kHz over a single copper wire pair. In 1992, *High bit rate DSL* (HDSL) [29] was standardized, providing a symmetric bit rate (i.e., with the same upstream and downstream bit rate) of 1.544 Mbps over 2 wire pairs with 200 kHz bandwidth (USA) or 2.048 Mbps over 2 or 3 wire pairs (Europe). *Symmetric or single-pair DSL* (SDSL) realized the same bit rates over a single wire pair.

HDSL and SDSL appeared too expensive for residential users [31]. With the cable companies promising an abundance of TV channels, the telephone companies believed *Asymmetric DSL* (ADSL) was the technology that would allow them to compete. With a downstream bit rate up to 8 Mbps (the upstream bit rate is limited to 1 Mbps, hence the 'asymmetry'), ADSL allowed them to offer high-quality streaming video. ADSL was standardized in 1995 by the American National Standards Institute (ANSI). It uses a bandwidth of 1.1 MHz, shorter loop lengths than ISDN and advanced signal processing [14, 15, 61, 120]. However, video-on-demand never became popular. Instead, the market for DSL has emerged much differently than expected: PC users need high-speed access to the internet and to corporate networks from residences and remote offices. The asymmetry between upstream and downstream bit rate, as offered by ADSL, then proved ideal for residential users because typical applications like web browsing and media streaming demand much higher data rates downstream than upstream [31].

DSL's competitors

The PC user market has captured the attention of both cable TV providers and telephone companies [41]. Cable companies have upgraded their networks, which were originally designed for unidirectional TV distribution, to allow for bidirectional signaling. *Cable modem technology* then allows for broadband

services over the coax cabling. Compared to the twisted pair, the coax cable is an easier medium to deal with as it has a larger useful bandwidth. Current cable modem technology allows downstream speeds up to 40 Mbps using a 6 MHz (USA) or 8MHz (Europe) wide passband in a frequency range between 65 MHz and 850 MHz. Next-generation cable modems will allow 100 to 400 Mbps. Nowadays, broadband over cable has 60 % market share in the USA and 35 % worldwide. The main issues with cable are the limited coverage of cable and the fact that the medium and data rate are to be shared by multiple users, which can limit the final performance and cause security issues [31].

Other broadband access media are emerging in the meantime. *Communication over electric powerlines*, which can be found in essentially all buildings and residences, naturally exhibits potential as a convenient and cheap communication alternative [35]. *Fiber optics* allow to transfer tremendously high bit rates over long distances. Although already considered since the 70's, the large deployment cost of fiber-to-the-home (FTTH) has prevented it from replacing today's DSL and cable technology. Widespread deployment of FTTH will take another 10 to 30 years [31].

It is likely that *wireless broadband access* is a more important competitor for ADSL and cable in the near future. During the past few years, wireless access technology has entered the consumer market and allows the deployment of in-home or in-office *wireless local-area networks* (WLAN) with data rates up to 54 Mbps. Access points to these networks are becoming common in cities and towns worldwide as well as in public areas like airports, hotels and convention centers or anywhere people gather. The breakthrough of WLAN technology was partially due to its standardization by the Institute of Electrical and Electronics Engineers (IEEE) in the standard series IEEE 802.11. It is expected that the newest standard IEEE 802.16 will drive the development of a next generation of wireless systems, namely *Wireless Metropolitan-Area Networks* (WMAN) [26]. This wireless access technology will allow for large wireless networks, which are capable of serving villages and rural areas. As such, they could compete with the current wireline systems that are not able to offer broadband services to remote areas. Suffice it to say that, apart from these wireless low-mobility solutions, the Universal Mobile Telecommunication System (UMTS) will soon be launched onto the mass-market offering *third-generation mobile* broadband wireless access.

DSL's future

Telephone operators have two major concerns: the popularity of wireless phones means many people are substituting their traditional wireline phone service; moreover, other broadband providers, such as cable operators, are adding telephony to their broadband services, in this way offering so-called *triple-play* video, voice and high-speed data services. Moreover, there is an increasing evolution to peer-to-peer services and demand for flexible allocation of upstream

Table 1.1: Overview of the latest DSL technologies.

Type	Bandwidth	Max. bit rate	Max. reach	Standardized in
ADSL	1.1 MHz	8 Mbps down, 1 Mbps up	3.7 km	1995 by ANSI, 1999 by ITU
ADSL2	1.1 MHz	8 Mbps down, 1 Mbps up	3.9 km	2002 by ITU
ADSL2+	2.2 MHz	15 Mbps down, 1.5 Mbps up	1.8 km	2003 by ITU
VDSL	17.6 MHz	52 Mbps down, 2.3 Mbps up	1.2 km	2004 by ITU
VDSL2	17.6 MHz	100 Mbps down or up	?	2005?

and downstream. It is obvious that the DSL world tries to counter these evolutions and enable new services to extract more revenue from the existing copper base [31].

ADSL2 (second generation ADSL) and ADSL2+ (second generation ADSL with extended bandwidth) have been standardized in 2002 and 2003, respectively [60, 63, 64]. After a debate for many years between two competing groups of companies, a decision on the standard technology for ADSL's successor, *Very high bit rate DSL* (VDSL), was finally made in June 2003 on the occasion of the so-called VDSL Olympics [15, 121]. VDSL offers downstream rates up to 52 Mbps over the shortest loops. Second generation VDSL (VDSL2) is expected to be ratified in 2005 [31]. In June 2004, Texas Instruments presented the concept of Uni-DSL (UDSL), which aims at offering one universal DSL service, including ADSL and VDSL, and with an aggregate rate up to 200 Mbps over the shortest loops (or a maximum of 100 Mbps in both upstream and downstream) [31]; other companies expressed similar future visions. An overview of some of the latest DSL technologies, with maximum bit rates, bandwidths and loop lengths, is given in **Table 1.1**.

These high bit rates can only be offered by reducing the twisted pair loop length in combination with a bandwidth extension. As depicted in **Figure 1.1**, the loop length reduction is made possible by extending the optical fiber into the network: modems at the central office (CO) are replaced by so-called optical line terminals (OLT), which are connected with a fiber to an optical network unit (ONU) installed in a remote terminal or cabinet that is closer to the customer, hence the term fiber-to-the-neighbourhood (FTTN). The so-called last mile towards the customer is then bridged using DSL technology (ADSL2+/VDSL) over the twisted pair.

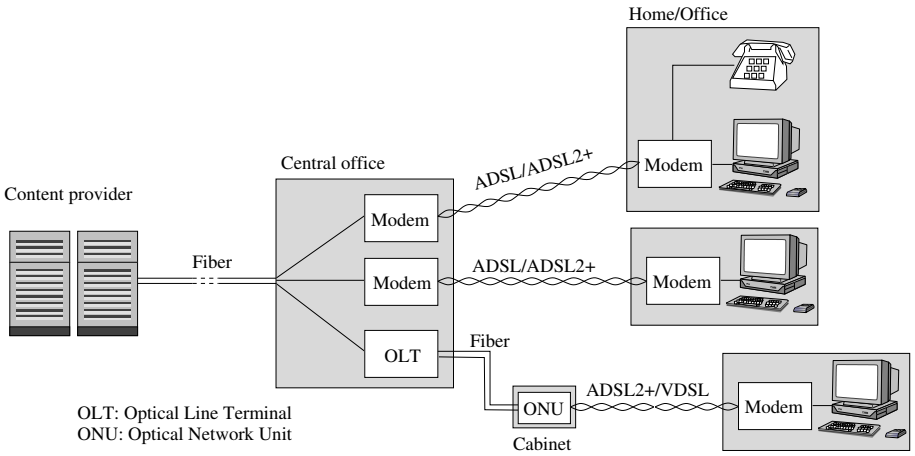


Figure 1.1: DSL network between telephone operator and customer.

1.3 DSL environment

More than 100 years ago, the unshielded twisted pair was found to provide sufficient intelligibility for voice transmission over the telephone system. However, using the same twisted pairs for broadband data transmission instead of 4 kHz wide voice signals appears a nontrivial task. In Section 1.3.1, we give an overview of the major impairments that a DSL system has to deal with. Section 1.3.2 explains why so-called multicarrier modulation is considered an attractive transmission scheme to tackle these impairments.

1.3.1 Impairments

A schematic overview of all impairments is shown in **Figure 1.2**. Below, each of the impairments is discussed in detail.

Transmission channel

Each communication system has to deal with distortion that is caused by the transmission channel. This *channel dispersion*, which is typically represented with a channel impulse response, makes that adjacent transmit symbols overlap at the receiver. In addition, there is always *channel attenuation*, which results in a reduced signal strength at the receiver. The channel attenuation of a twisted pair line is frequency-dependent, with the highest frequencies experiencing the largest attenuation. The attenuation also grows with the loop length, hence customers that are further away from the CO receive a weaker signal.

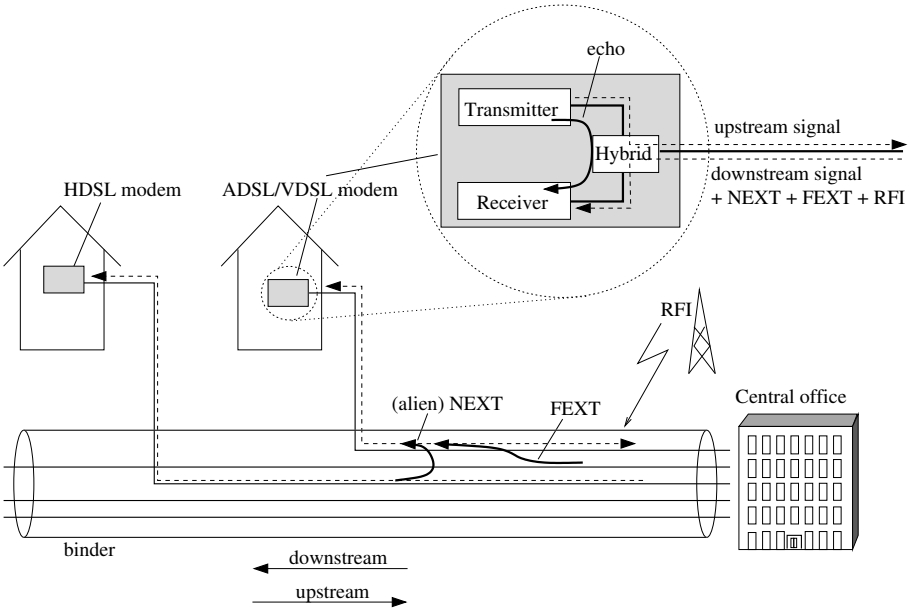


Figure 1.2: Overview of the impairments in a DSL environment.

There are two other sources of channel dispersion and attenuation in the twisted pair telephone network, which are caused by signal reflections. The feeder cable, which leaves the CO, has several branches (distribution cables) that terminate at physically separated locations. A new user is assigned the closest available distribution cable. There are always unused and unterminated distribution cables, referred to as *bridged taps*, causing signal reflections. These signal reflections can interfere destructively with the desired signal. Another source of signal reflections are the application of several *wire gauges* along the line. The selected wire gauge depends on the loop length and should avoid excessive loop resistance. At the junction of two line sections with different gauge, an impedence mismatch exists, again causing reflections.

Because of the large bandwidth (e.g., up to 1.1 MHz for ADSL), the channel frequency response typically has a large dynamic range. Moreover, the attenuation also heavily depends on the loop length. **Figure 1.3** illustrates the amplitude of the channel frequency response for a set of loop lengths. To mitigate the channel distortion and attenuation, a *channel equalizer* is employed at the receiver.

Contrary to a wireless environment, a wireline channel is typically slowly time-varying as channel variations are caused by changing weather conditions and temperature [60]. This allows for a training-based equalizer design during the

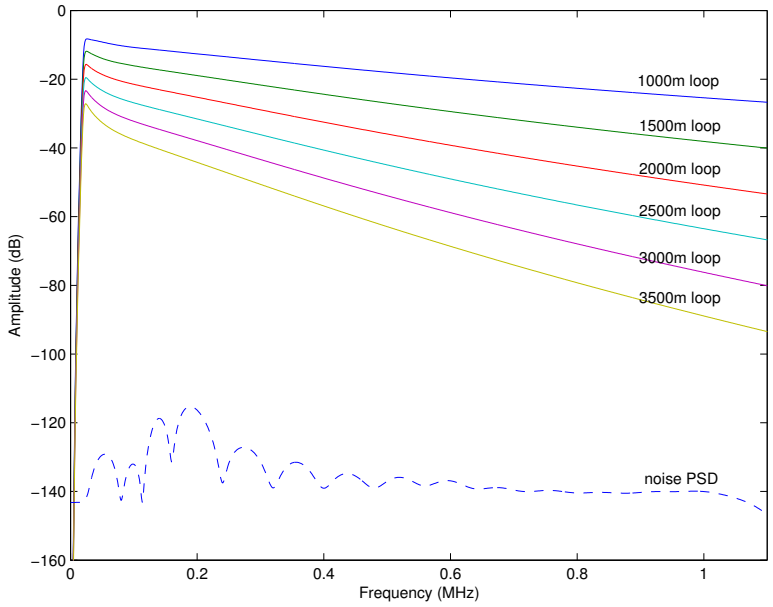


Figure 1.3: Typical channel frequency responses and noise PSD for ADSL.

connection set-up phase and an adaptive equalizer that can track changes during data transmission in a decision-directed mode [75]. *Adaptive training-based equalizer design* for DSL systems is the main topic of this thesis.

Echo

The twisted pair line carries bidirectional communication (i.e., upstream and downstream), hence a so-called hybrid is required to couple the transmitter and receiver to the single twisted pair line. Although this hybrid is designed to decouple the transmit and receive signals, it is impossible to design a hybrid that perfectly matches all loops. The part of the transmit signal that is reflected to the receiver because of an imperfect hybrid is called *echo*. The ADSL standard allows for two transmission modes to separate upstream and downstream: either two separate frequency bands are used, or the upstream and downstream frequency band (partially) overlap. In the former case, the echo signal and the desired signal occupy different frequency bands, which makes it easier to separate them using adequate front-end filtering. In the latter case, a larger bandwidth is available, hence a higher bit rate can be obtained, provided that an *echo canceller* is used. In this thesis, we adopt the former mode, referred to as the frequency-division duplexing (FDD) mode. Advanced echo cancellation schemes for DSL systems have been presented in [156].

Crosstalk

A twisted pair line consists of two copper wires that are individually insulated and twisted around each other to reduce crosstalk, i.e., electromagnetic coupling with other pairs. However, as up to 50 twisted pairs are grouped into one binder, crosstalk can not be completely avoided and can even become a dominant impairment.

So-called *near-end crosstalk* (NEXT) is caused by a neighbouring transmitter on a different twisted pair line. The NEXT power increases with frequency ($\sim f^{3/2}$). The impact of NEXT can be reduced by resorting to the FDD mode as the crosstalk and the desired signal then occupy different frequency bands. *Far-end crosstalk* (FEXT) originates from signals travelling in the same direction (e.g., both are upstream or downstream signals), hence they have overlapping frequency bands. The FEXT power also increases with frequeny ($\sim f^2$). FEXT is weak if the transmitters of the desired signal and the crosstalker are co-located, e.g., at the CO. However, if the crosstalk is caused by a transmitter in a cabinet in the field, a near-far problem can occur: if the crosstalker is much closer to the receiver of the desired signal, the crosstalk power can be large in comparison with the desired signal power. Currently, this problem attracts a lot of research interest, especially for the case of *self-crosstalk*, where systems using the same transmission technology (e.g., ADSL) are interfering [22, 23, 24, 49, 112, 162]. Figure 1.3 includes a typical noise power spectral density (PSD) in ADSL FDD mode. The residual echo and NEXT (from 24 ADSL crosstalkers), as experienced by the ADSL receiver after front-end filtering, are clearly visible.

A more difficult scenario occurs in the case of so-called *alien crosstalk*, where the crosstalker uses a different transmission technology (e.g., HDSL crosstalk in ADSL or VDSL) [71]. This causes a crosstalker that is non-stationary, but rather cyclostationary, with respect to the desired signal. Although not treated in this thesis, we have proposed a combined equalizer and alien crosstalk canceller that is capable of partially removing alien crosstalk in ADSL or VDSL by exploiting the cyclostationarity and excess bandwidth of the crosstalking signal. The result is a time-varying receiver based on so-called frequency-shift filtering [47, 145, 146].

Radio frequency interference (RFI)

The large transmission bandwidth of DSL systems results in spectral overlap with other communication systems, such as radio communications. Especially aerial twisted pair lines act as an antenna, hence they can suffer from narrowband RFI ingress. Some amateur radio bands (HAM, above 1.8 MHz) coincide with the VDSL transmission bandwidth. These amateur radios can be especially harmful as they frequently switch on and off and often change their carrier frequency. RFI ingress is nowadays also considered a problem in downstream ADSL and ADSL2+: amplitude modulation (AM) radio broadcasters

share their frequency bands with ADSL. Compared to amateur radios, AM radios are more stationary as they are broadcasting continuously. ADSL test scenarios including RFI ingress have been specified in [62]. In this thesis, we consider *combined equalizer and RFI mitigation strategies* for DSL systems.

Noise

There are several other noise sources in DSL. *Impulse noise* is highly non-stationary noise that is caused by switching of electronic devices such as a refrigerator, a computer, etc. This causes error bursts, which can be handled by applying an error correcting code, e.g., a Reed-Solomon code, in combination with an interleaver [115]. To account for other, stationary noise sources (e.g., thermal noise, quantization noise, ...), a *background noise* floor, modeled as additive white Gaussian noise (AWGN) at -140 dBm/Hz, is assumed.

1.3.2 Multicarrier modulation

At the time ADSL was conceived, it was clear that an appropriate and powerful transmission scheme would be needed to offer broadband data communication over the twisted pair telephone network. Especially the academic group, headed by J. M. Cioffi, argued that *multichannel (MCH) modulation* was a natural choice to deal with a harsh environment, as described in Section 1.3.1 [32, 163]. By partitioning the communication channel into a set of parallel and orthogonal subchannels, the development and implementation of a transmission scheme is reduced to a set of smaller and independent problems. The channel partitioning can be based on a set of theoretically optimal channel-dependent modulator and demodulator basis functions, the channel impairments can be tackled independently per subchannel and a specific energy and bit rate can be assigned separately for each subchannel, depending on the subchannel signal-to-noise ratio (SNR). The overall MCH system is then capable of achieving optimal performance, as will be explained in Chapter 2.

So-called *multicarrier (MC) modulation* forms a specific implementation of MCH modulation, where the channel is partitioned in the frequency-domain into a set of subchannels: ideally, the subchannels, referred to as *tones*, occupy disjoint frequency bands and parallel information streams are transferred independently on these tones (see **Figure 1.4**) [14, 67]. For ADSL, ADSL2, ADSL2+ and VDSL, an all-digital implementation of MC modulation, called *discrete multitone (DMT)* modulation, has been adopted and standardized [61, 121]. A more detailed description of the basic concepts of MCH modulation, MC modulation and DMT modulation is given in Chapter 2.

Example 1.1 **Figure 1.4** depicts the frequency content of an ADSL system and illustrates how each of the impairments in Section 1.3.1 can be handled with MC modulation. In DSL systems, specific sets of tones are assigned

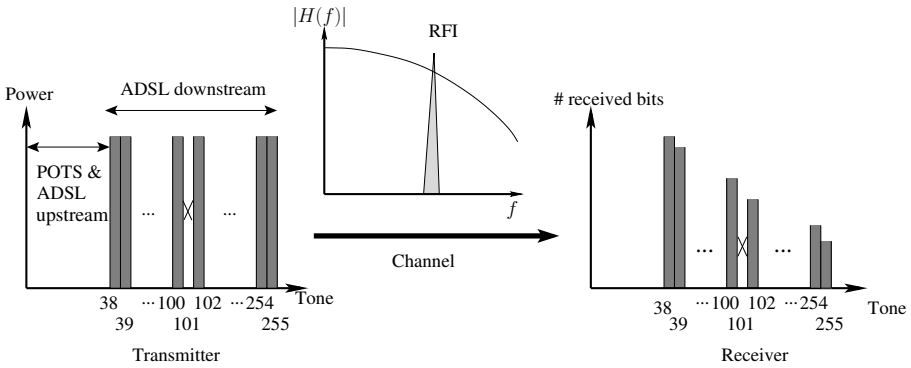


Figure 1.4: Example of ADSL downstream transmission over a frequency-selective channel, disturbed by an RFI.

to the POTS signal, the upstream data channel and the downstream data channel. E.g., in ADSL, there are 256 tones available (with index 0 to 255), each with a bandwidth of 4.1325 kHz. In the FDD mode, the lowest tones are assigned to the POTS signal (which is isolated from the ADSL signal by means of a POTS splitter), tone 6 to 32 (i.e., the lower frequencies) are reserved for upstream transmission and the largest portion of tones (38 to 255) are used for downstream transmission. This configuration, if supplemented with appropriate front-end filtering, avoids echo and NEXT problems.

In **Figure 1.4**, the impact of a channel with frequency response $H(f)$ and an RFI (coinciding with tone 101) are also depicted. The channel frequency response and noise sources, like RFI, determine the SNR at the receiver on each tone. As explained in Section 1.3.1, the transmission channel is frequency-selective with typically a much higher attenuation at the high frequencies than at the low frequencies. As is shown in the left plot, an ADSL system transmits a signal with equal power on all tones, except for the tones with an insufficient SNR (tone 101 in the example), which are turned off. The number of bits that is transferred on a particular tone depends on the SNR on that tone: in this example, it is clear that the highest tones (near tone 255) carry less bits than the lowest tones (near tone 38). The process of bit loading is further explained in Section 2.1.4. △

Remark 1.1 Due to its appealing properties, MC modulation has recently been adopted as the transmission format for several communication applications. Besides in ADSL and VDSL, it is also implemented in powerline communications [35] and wireless applications, such as digital audio/video broadcasting [43, 44] and WLANs, based on the IEEE 802.11a [92] and the Hiperlan/2 [42] standards. In wireless applications, MC modulation is referred to as orthogonal frequency-division multiplexing (OFDM), see also Remark 2.7. □

1.4 Thesis outline and contributions

In this section, an outline and an overview of the thesis can be found. The main contributions are summarized and references will be given to publications that were brought about in the frame of this thesis.

1.4.1 Research motivation

In the research work that is described in this thesis, we focus on how to tackle two of the impairments, mentioned in Section 1.3.1 and depicted in **Figure 1.4**, namely channel dispersion and RFI. In the previous section, it has been argued that an adequate transmission scheme is required to ensure reliable, high-speed communication over the twisted pair line. Because of its theoretically appealing properties, MC modulation was adopted as the transmission format for DSL communication. By using a sufficiently large number of tones, each separate tone becomes narrowband and the channel frequency response can be considered flat within the tone bandwidth and represented by a simple (complex-valued) scalar. The equalization is then straightforward and cheap. As the tones are disjoint, an RFI only destroys the tones that overlap with the RFI: as shown in **Figure 1.4**, turning off these tones (by not assigning any power and bits to these tones) then solves the RFI problem.

It will be shown in Chapter 2 that a *feasible* MC implementation, such as DMT modulation, results from several approximations of the *ideal* MC modulation scheme. Complexity constraints, especially on the required amount of memory and hardware, put a limit on the number of tones. Moreover, perfectly disjoint tones are unrealizable in practice: a certain frequency overlap between adjacent tones has to be tolerated. Whereas, ideally, MC modulation is capable of achieving optimal performance, DMT modulation — in its basic form — only achieves a fraction of this performance when applied in a true DSL environment. This limits the offered bit rate and excludes potential customers that are too far from the CO or that suffer from bad line conditions. In a DSL context, the channel frequency response can not be considered flat within the tone bandwidth and more advanced equalization strategies have to be adopted. Moreover, as there is frequency overlap between adjacent tones, an RFI can contaminate a large number of neighbouring tones, rather than only one or two tones. Again, advanced signal processing techniques are then required for RFI mitigation.

Despite the non-ideal behaviour of DMT transmission, its digital nature offers as an advantage that efficient and mathematically tractable digital signal processing (DSP) algorithms can be developed and applied. The ADSL modems that are currently on the market include a DSP or similar unit for channel equalization [153]; VDSL modems make use of basic DSP algorithms that mit-

igate RFI. Still, the currently implemented equalizer and RFI suppression solutions achieve a performance that remains far from optimal: the equalizer performance is often unpredictable and depends on the scenario, the design algorithm and certain parameter settings; the equalizer and the RFI suppression solution are typically obtained independently, while significant bit rate gains would be obtained with a joint design. Hence, current solutions cause a performance loss that can vary from only 100 kbps to several Mbps; this limits both the DSL coverage and the offered bit rate. Moreover, the even larger bandwidth as exploited in ADSL's successors, ADSL2+ and VDSL, adds to the need for enhanced DSP algorithms. Therefore, many new and improved equalizer design and RFI mitigation techniques have been and are still presented in the literature, despite the wide deployment of ADSL nowadays.

In our research, we have developed equalizer design and RFI suppression algorithms that improve upon existing techniques and that outperform them in terms of achievable bit rate. These new algorithms result in the following advantages.

- The bit rate benefit can be turned into a loop reach extension for a fixed bit rate, which results in a larger DSL coverage. Alternatively, it allows for a larger margin (see Section 2.1.4), which is a measure for the system robustness.
- The new design algorithms have a computational and memory cost that can be handled with today's state-of-the-art hardware.
- The new designs add adaptivity to the DMT receiver so that changing line conditions can be accommodated, an attractive feature that integrates well with the so-called seamless rate adaptation functionality (see Remark 2.3) in the newly standardized ADSL2 and ADSL2+ [60].
- The new designs can be used as a benchmark as they are capable of closely approaching the optimal performance within the considered DMT modulation framework.

An overview of the developed algorithms is given in the next section. Most algorithms (except for Chapter 7) envisage an enhanced DMT receiver that complies with the ADSL and VDSL standards. Nevertheless, they can give inspiration for other wireline and wireless DMT-based and MC-based systems.

1.4.2 Chapter-by-chapter overview

In **Chapter 2**, we will introduce the basic theoretical concepts behind MCH, MC and DMT modulation. We will show what makes MC modulation attractive for broadband DSL communication, how DMT modulation relates to MC

modulation, and why additional signal processing is required to make DMT modulation suited for DSL systems. We will also summarize the basic principles of channel equalization and RFI mitigation as applied in DSL communication and we will introduce the notation and the data model that will be used throughout the thesis.

A channel-shortening time-domain equalizer (TEQ) has been proposed as an appealing equalizer solution for DMT-based systems. However, optimal TEQ design has turned out to be difficult and costly. Therefore, TEQ design for ADSL has challenged many researchers. An overview of existing TEQ designs will be given in **Chapter 3**. Both suboptimal, cost-effective equalizer designs and equalizers that aim at bit rate maximization will be presented. This chapter also provides a unifying mathematical framework for the equalizer designs. This chapter is based on [82, 83], two papers that have been written in collaboration with the BARD research group of Cornell University, Ithaca, USA, headed by prof. C. R. Johnson, Jr. and the ESPL research group of Texas University, Austin, USA, headed by prof. B. L. Evans. These papers provide a unified mathematical framework and a unified notation for different equalizer designs, an extensive literature survey, and an objective evaluation in terms of performance and complexity.

In **Chapter 4**, we will first show that none of the TEQ designs presented so far achieve true bit rate maximization. We will indicate that the subchannel SNR model is crucial in this respect. Based on a new, compact and exact SNR model, we will then derive two, equivalent, bit rate maximizing TEQ (BM-TEQ) design criteria. Especially the second formulation, which is a least-squares (LS) based criterion, is attractive. It gives rise to an elegant and fast-converging iterative Gauss-Newton BM-TEQ design algorithm. Moreover, it allows to establish a common LS-based equalizer framework, which relates the new BM-TEQ design to the well-known and widely studied minimum mean-square-error (MMSE) TEQ design. The BM-TEQ turns out to outperform any other TEQ design and closely approach the performance of the so-called per-tone equalizer (PTEQ). The PTEQ is an alternative bit rate maximizing equalizer scheme, which was developed in our research group a few years ago as an alternative to suboptimal TEQ designs. The PTEQ outperforms any TEQ design with a comparable computational cost, but at the expense of a much larger memory cost. Publications that are related to the work in this chapter are [139, 140, 141, 143, 144].

In **Chapter 5**, the BM-TEQ design will first be extended to a so-called bit rate maximizing per-group equalizer (BM-PGEQ) design: the active tones are divided into a small number of groups; the solution to the (downscaled) BM-TEQ design criterion for each group results in a BM-PGEQ for the group. This BM-PGEQ design allows for a trade-off between memory cost and performance, keeping computational complexity during data transmission roughly at the same level. The BM-TEQ and the PTEQ are extreme cases of the

BM-PGEQ, with a single group of tones and single-tone groups, respectively. We will show that a BM-PGEQ with as few as 4 tone groups (hence with a moderate memory cost) achieves close-to-PTEQ performance in harsh, RFI dominated scenarios.

In current ADSL modems, the TEQ is typically designed during the connection set-up phase and then kept fixed during data transmission. The recent ADSL2 and ADSL2+ standards support so-called seamless rate adaptation: the DSL line conditions are observed continuously and the bit rate and bit allocation are adapted accordingly. This renders an adaptive bit rate maximizing equalizer, which tracks changing line conditions, highly desirable. Therefore, the second part of **Chapter 5** will discuss an adaptive BM-TEQ and BM-PGEQ design algorithm. A complete range of adaptive bit rate maximizing equalizers then opens up, offering full flexibility to trade off computational and memory cost. Publications related to this chapter are [137, 138, 142, 158].

In **Chapter 6**, we will consider the more general case where equalization is combined with receiver windowing to mitigate both channel dispersion and narrowband RFI ingress. Receiver windowing is a classical low-cost solution to RFI mitigation. The BM-TEQ design will be extended to incorporate an optimal window. Several important special cases will also be discussed, such as the bit rate maximizing windowing-only case, the per-group and per-tone combined equalizer and windowing case and the BM-TEQ design in combination with a fixed window. Guidelines for an iterative and adaptive bit rate maximizing combined equalizer and windowing design will be given. Publications related to this chapter are [158, 159, 160].

The techniques that we described so far comply with the DSL standards, which implies a fixed length for the so-called cyclic prefix (CP); the CP is a form of transmit redundancy that is introduced at the DMT transmitter to ease the equalization (see Section 2.2.1). In **Chapter 7**, we will reconsider equalization of a DMT-based system without a constrained cyclic prefix length and under the assumption of an infinite impulse response (IIR) model for the transmission channel. We will show that the standardized CP length is conservative. We will present low-cost linear and decision-feedback extensions of the PTEQ and the BM-TEQ that exploit so-called frequency-domain transmit redundancy from pilot and unused tones and allow to reduce the CP length. A shorter CP, in combination with these dedicated equalizers, results in a slightly smaller latency without performance loss and cost increase. The RFI suppression capability of the PTEQ extensions will also be discussed. Publications related to this chapter are [135, 136].

Chapter 4 to 7 include extensive simulations with a set of standardized test loops in an ADSL scenario. However, the presented techniques also apply to ADSL2+ and VDSL, which make use of an upscaled version of DMT modulation. **Chapter 8** presents the final conclusions and topics for further research.

Throughout the thesis, we present receiver structures, design criteria, design and adaptation algorithms for equalization-only and combined equalization and RFI mitigation. Figure 1.5 casts these structures, criteria and algorithms in a schematic overview of the thesis and indicates the chapters where they can be found. In Chapter 3 to 7, this scheme is repeated to show how the sections of each chapter fit in.

1.5 Conclusions

In this chapter, we have presented the DSL technology as a means to offer broadband communication over the twisted pair telephone network. We have discussed its current position as one of the most widely deployed broadband access media and we have indicated which challenges the DSL world will face in the future. We have enumerated a number of impairments that cause a harsh DSL environment. In order to further increase the DSL coverage and to offer new broadband services to as many customers as possible, a persistent search for new and enhanced signal processing algorithms that increase the bit rate or the loop reach is required. The advanced equalizer design and RFI mitigation algorithms, as introduced in this chapter, will be elaborated throughout the thesis.

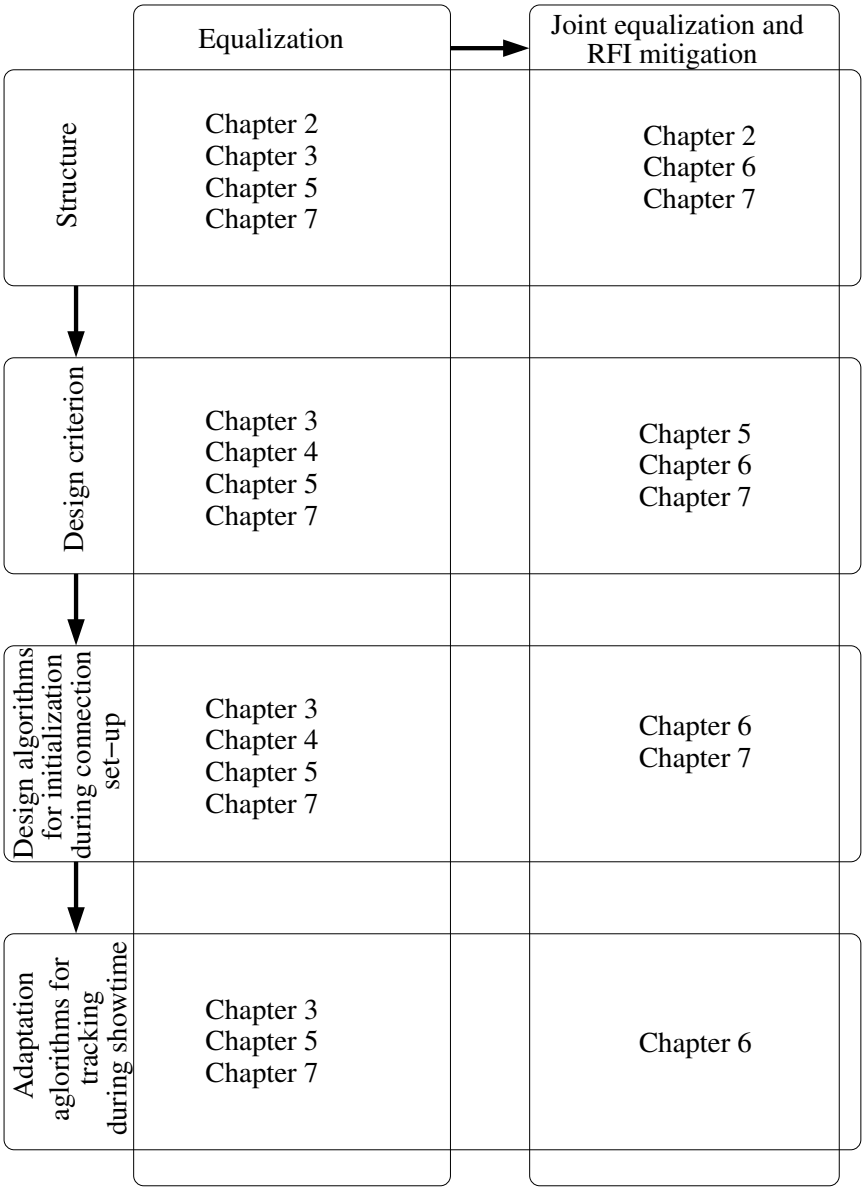


Figure 1.5: Schematic overview of the thesis.

Chapter 2

Basic concepts and data model

IN this chapter, we introduce the basic theoretical concepts behind multichannel (MCH), multicarrier (MC) and discrete multitone (DMT) modulation, as well as the basic principles of channel equalization and RFI mitigation as applied in DSL communication.

In Section 2.1, MCH and MC modulation, as well as vector coding are introduced. The MCH partitioning based on MC modulation is presented in Section 2.1.2. Based on the definition in Section 2.1.3 of the "channel capacity", which is a measure for the optimal performance, it is argued in Section 2.1.4 that MC modulation is capable of achieving the channel capacity. We will already point out in this section that several practical limitations (e.g., on the number of carriers and the bit loading) result in an actual performance that is below the channel capacity. Further practical concerns are addressed in Section 2.1.5: the restriction to finite-length MCH modulators leads to the principle of vector coding (VC), a digital version of MCH communication.

In Section 2.2, DMT modulation is treated in detail. In Section 2.2.1, a last modification is introduced by adding a cyclic prefix (CP) to the VC scheme. This leads to the efficient and attractive, all-digital DMT modulation scheme. In Section 2.2.2 and Section 2.2.3, the DMT transmitter and receiver are discussed, with emphasis on DSL specific issues. The discussion in Section 2.1 then allows the reader to assess why DMT modulation — in its basic form — is not suited for DSL communication, despite the theoretical optimality of "ideal" MC modulation. Section 2.2.4 gives first guidelines on the equalization techniques that are required to recover the performance loss with DMT modulation. Section 2.2.5 deals with the digital signal processing (DSP) tools for

RFI cancellation.

Section 2.3 describes the data models that will be used throughout the thesis. The data model in Section 2.3.1 is based on a finite impulse response (FIR) model of the transmission channel and will be used for equalizer and RFI canceller design (Chapters 3 to 6). The data model in Section 2.3.2 is based on an infinite impulse response (IIR) model of the transmission channel, which offers a parsimonious representation of the DSL transmission channel. It will be used in Chapter 7 for equalizer design. Section 2.4 concludes this chapter.

Inspiration for several parts of this chapter has been found in Chapter 4 of the course notes on "Advanced Digital Communication", taught at Stanford University by J. M. Cioffi [32].

2.1 Multicarrier modulation and vector coding

2.1.1 Multichannel modulation concept

Mulitchannel (MCH) modulation forms a general concept to conceive a reliable communication system by partitioning the transmission channel into N parallel and independent (or orthogonal) subchannels [32]. MCH modulation is a natural choice to deal with a harsh environment, as described in Section 1.3.1: by partitioning the communication channel into a set of parallel and orthogonal subchannels, the development and implementation of a transmission scheme is reduced to a set of smaller and independent problems. The channel partitioning is based on a set of theoretically optimal channel-dependent modulator and demodulator basis functions, the channel impairments can be tackled independently per subchannel and a specific energy and bit rate can be assigned separately for each subchannel, depending on the subchannel SNR.

2.1.2 Multicarrier modulation concept

Multicarrier (MC) modulation forms a specific class of multichannel (MCH) modulation. In MC transmission, the subchannel orthogonality is guaranteed by dividing the transmission bandwidth into N disjoint frequency bands, referred to as carriers or *tones*, as was depicted in **Figure 1.4**. In fact, an MC system implements a frequency-division multiplexing scheme, with all carriers assigned to the same user. The transceiver structure of an MC system, which realizes this bandwidth partitioning, is depicted in **Figure 2.1** [75].

The incoming bit stream is fed to a channel encoder for error-correction purposes, followed by an interleaver. The interleaver reorders the transmitted bytes to distribute a burst of errors, e.g., caused by impulse noise, over a longer interval in time, avoiding in this way that data segments contain more errors than

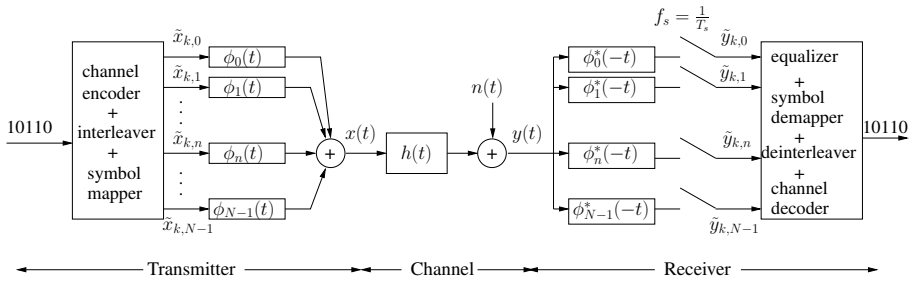


Figure 2.1: Concept of MC transmission.

can be corrected [115]. Then, the bit stream is split into N parallel bit streams that are assigned to the N tones, indexed from $n = 0$ to $n = N - 1$. After splitting each parallel bit stream n into a stream of bit words, a symbol mapper translates each bit word to a complex-valued transmit (TX) symbol $\tilde{x}_{k,n}$ (denoted by a symbol time index k and a tone index n); the tilde indicates that $\tilde{x}_{k,n}$ is a frequency-domain (or in general: a transform-domain) symbol. Each TX symbol $\tilde{x}_{k,n}$ corresponds to a point in a so-called quadrature-amplitude-modulation (QAM) constellation [75]: the constellation size (i.e., the number of constellation points M_n) is related to the number of bits b_n that is represented by the constellation, i.e., $M_n = 2^{b_n}$; each complex-valued constellation point then represents a certain bit word of length b_n. It will be explained in Section 2.1.4 how the number of bits b_n for each tone n is determined .

The transmitter generates a signal

$$x(t) = \sum_{n=0}^{N-1} \tilde{x}_{k,n} \phi_n(t - kT_s) \tag{2.1}$$

that is a superposition of N QAM signals. Each term in (2.1) corresponds to a particular output of a bank of orthogonal modulator functions $\phi_n(t) = \phi(t)e^{j2\pi f_n t}$. The bank is fed with a sequence of $N \times 1$ TX symbol vectors

$$\tilde{\mathbf{x}}_{k,N} = \left[\begin{array}{ccc} \tilde{x}_{k,0} & \cdots & \tilde{x}_{k,N-1} \end{array} \right]^T \tag{2.2}$$

at a symbol rate $f_s = \frac{1}{T_s}$ Hz. It is assumed that all modulator functions use the same pulse shaping filter $\phi(t)$; the modulators $e^{j2\pi f_n t}$ result in a frequency shift over $f_n = nf_s$ Hz. In order to realize brick-wall bandpass filters with bandwidth f_s as depicted in **Figure 1.4**, the pulse shaping filter should be equal to:

$$\phi(t) = \mathrm{sinc}\left(\frac{\pi t}{T_s}\right) \tag{2.3}$$

Example 2.1 In ADSL and ADSL2, the number of tones N is equal to 512. In ADSL2+, N is doubled to 1024. VDSL systems use up to 8192 tones. As DSL systems use baseband transmission, complex conjugate symmetry is imposed to $\tilde{\mathbf{x}}_{k,N}$ as explained in Section 2.2.2. △

The TX signal $x(t)$ is sent over the channel with impulse response $h(t)$ and corrupted by additive noise $n(t)$ so that the receive (RX) signal is given by:

$$y(t) = h(t) \star x(t) + n(t) \tag{2.4}$$

The demodulation of $y(t)$ is done by means of a bank of demodulator functions $\phi_n^*(-t)$, which is matched to the TX modulator bank. The N outputs of the demodulators are sampled at the symbol rate f_s and decoded per tone. The orthogonality of the brick-wall bandpass filters $\phi_n(t)$ guarantees that the channel does not introduce intercarrier interference (ICI) between the tones. However, the channel delay spread T_h (in seconds) causes intersymbol interference (ISI), hence frequency selectivity, within each tone. If the symbol time T_s (in seconds) is large with respect to T_h, i.e., for a large number of tones N, the tones can be considered narrowband. The ISI can then be ignored and the channel frequency response can be assumed flat within the tone bandwidth. In this case, the following discrete-time data model can be adopted for the RX symbol at symbol time k and tone n:

$$\tilde{y}_{k,n} = \tilde{h}_n \tilde{x}_{k,n} + \tilde{n}_{k,n} \tag{2.5}$$

where $\tilde{h}_n = \tilde{h}(f_n)$ is the channel frequency response, evaluated at $f = f_n$. An appropriate equalizer consists of a bank of simple complex-valued scalars $\tilde{h}_n^{-1}$, $n \in [0, N-1]$, to which we refer as *frequency-domain equalizers (FEQ)*. After introducing the definition of the "channel capacity" as a measure for the optimal performance in Section 2.1.3, we explain in Section 2.1.4, how this MC system is capable of achieving the channel capacity for a given TX power budget.

2.1.3 Channel capacity

The *capacity* C of a single communication channel forms the upper bound on the number of bits that can be transferred reliably, i.e., with zero error probability. Shannon derived an expression for the capacity of a flat channel in the presence of AWGN, which forms the basis of the field of information theory [108]:

$$C = Bb \text{ with } b = \log_2(1 + \text{SNR}) \tag{2.6}$$

where C is the channel capacity in bits per second (bps), b is the maximum number of bits (per TX symbol) that can be transferred reliably, B is the channel bandwidth (and equals the maximum symbol rate f_s) and SNR is the

signal-to-noise ratio at the receiver. Shannon also suggested in [108] to partition the channel into a large number of narrowband AWGN subchannels, in order to deal with frequency selectivity. The MC system described in Section 2.1.2 forms a possible implementation of this idea. The capacity of an MC system over N parallel and independent tones n, with a symbol rate f_s (which equals the tone bandwidth) and with SNR_n being the SNR at the receiver on tone n, is then obtained by summing the capacities of all individual tones:

$$C = \sum_{n=0}^{N-1} f_s b_n \text{ with } b_n = \log_2\left(1 + \mathrm{SNR}_n\right) \tag{2.7}$$

Under the assumption of a large N so that the discrete-time model (2.5) holds true, SNR_n is given by:

$$\mathrm{SNR}_n = \frac{\sigma^2_{n,\tilde{x}} \left|\tilde{h}_n\right|^2}{\sigma^2_{n,\tilde{n}}} \tag{2.8}$$

where $\sigma^2_{n,\tilde{x}} = \mathcal{E}\left\{\left|\tilde{x}_{k,n}\right|^2\right\}$ is the TX power on tone n and $\sigma^2_{n,\tilde{n}} = \mathcal{E}\left\{\left|\tilde{n}_{k,n}\right|^2\right\}$ is the power spectral density (PSD) of the noise on tone n.

2.1.4 Water-filling principle and bit loading

Only an infinitely complex coding scheme is capable of achieving the channel capacity. Practical modulation schemes are not capable of realizing error-free data transmission, even if the actual bit rate R is lower than the channel capacity C. A certain bit-error rate (BER) and gap between C and R have to be tolerated. A measure for the actual bit rate of an MC system is then typically obtained by introducing an *SNR gap* Γ_n in (2.7) for each tone:

$$R = \sum_{n=0}^{N-1} f_s b_n \text{ with } b_n = \log_2\left(1 + \frac{\mathrm{SNR}_n}{\Gamma_n}\right) \tag{2.9}$$

where b_n is now the actual number of bits per TX symbol that is transferred on tone n. The SNR gap Γ_n (which is often quantified in decibel (dB)) is determined by the target BER, the used finite-alphabet symbol mapping (e.g., QAM symbol mapping, see Section 2.1.2), the channel coding and a noise margin [14, 115]. The noise margin is a safety factor that accounts for unmodeled noise sources, such as nonlinearities and impulse noise [29].

Example 2.2 In ADSL, the same SNR gap Γ_n is chosen for all tones. For uncoded QAM symbol mapping and a target BER of 10^{-7}, a gap of 9.8 dB is obtained [67]. Channel coding reduces this gap. In ADSL, Reed-Solomon coding is applied, resulting in a coding gain of 3 dB. The gap could be further reduced by boosting the coding gain with a turbo receiver [149]. The noise

margin is typically set to 6 dB [29], resulting in an overall SNR gap $\Gamma_n = 9.8 - 3 + 6 = 12.8$ dB. △

It is clear from (2.8) and (2.9) that the bit rate increases with the TX power $\sigma^2_{n,\tilde{x}}$ that is allocated to each tone. The total TX power budget

$$\sigma^2_{\tilde{\mathbf{x}}} = \mathcal{E}\left\{\tilde{\mathbf{x}}^H_{k,N}\tilde{\mathbf{x}}_{k,N}\right\} = \sum_{n=0}^{N-1} \sigma^2_{n,\tilde{x}} \tag{2.10}$$

with $\tilde{\mathbf{x}}_{k,N}$ defined in (2.2), is however limited in a practical system. The question then arises how to allocate the given TX power budget to the tones in an MC system, so that the bit rate R is maximized. The answer to this question has been given in [67]. The TX power on tone n is determined from:

$$\sigma^2_{n,\tilde{x}} + \frac{\Gamma_n \sigma^2_{n,\tilde{n}}}{\left|\tilde{h}_n\right|^2} = K \tag{2.11}$$

where K is a constant. The constant K is not known a priori, but it can be determined from the TX power budget $\sigma^2_{\tilde{\mathbf{x}}}$ and the constraint of non-negative TX powers $\sigma^2_{n,\tilde{x}}$; tones that would require a negative power $\sigma^2_{n,\tilde{x}}$ to fulfill (2.11) are turned off, as they have a too low SNR. This solution is referred to as the *water-filling principle*, as explained in the example below. For $N \to \infty$, the MC system with TX power allocation based on the water-filling principle is capable of achieving the channel capacity for a given TX power budget, as predicted by (2.7) [67].

Example 2.3 Visualizing (2.11) for the case of Example 1.1 and **Figure 1.4** results in **Figure 2.2**: the assigned TX power $\sigma^2_{n,\tilde{x}}$ corresponds to the height of the water column that one obtains by water-filling a two-dimensional bowl with a shape that is determined by the second term in (2.11). In **Figure 2.2**, there is no power allocated to tone 101; it is turned off because of the RFI noise. The lowest tones (with high SNR) get more power than the highest tones (with low SNR). △

Once the TX power allocation has been determined, the number of bits b_n, and hence the constellation size M_n per tone, can be computed based on (2.7). Obviously, the largest number of bits is allocated to the tones with the highest SNR. In general, (2.7) results in non-integer numbers of bits b_n, which can only be realized with complex channel encoders and decoders. Therefore, many loading algorithms have been developed that jointly optimize the TX power allocation and an *integer bit loading* (see e.g., [19, 20, 30, 58, 73]).

Example 2.4 In ADSL, a suboptimal TX power allocation algorithm is adopted, which is referred to as *on/off power allocation* [30]. The same tones as

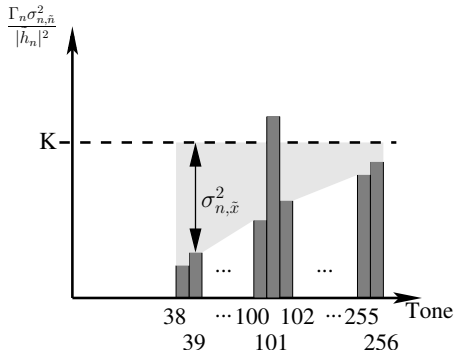


Figure 2.2: The water-filling principle.

with water-filling (i.e., tones with a large channel attenuation or a high noise level) are turned off. The other tones get an approximately *equal power*, rather than an optimized TX power per tone. In order to reach integer bit loading without wasting energy, small tuning gains are applied to all tones, so that a saw-tooth shaped ripple over the tones exists. This bit loading algorithm complies with the DSL standards, which impose a maximum TX PSD mask in order to limit the egress to other communication systems. The performance degradation, if compared to the water-filling scheme, is found to be small. Note also that the DSL standards limit the maximum number of bits per tone to 15, due to hardware constraints. △

Remark 2.1 The water-filling and bit loading algorithm, presented above, is called "rate-adaptive", since the bit rate is maximized for a constraint TX power budget and a fixed BER. In other applications than DSL communication, the target bit rate and TX power budget are fixed [123]; the goal is then to minimize the BER (or, equivalently, to maximize the so-called margin, which is the amount of extra noise a system can tolerate without violating the target BER) [30, 73]. This "margin-adaptive" criterion can be shown to be equivalent to the minimization of the TX power for a given bit rate and BER. The optimal margin-adaptive performance also obeys the water-filling principle and solutions for integer bit loading also exist for this case. □

Remark 2.2 The water-filling principle has recently been investigated for application in crosstalk-dominated DSL environments (see Section 1.3.1) [24, 112]. Rather than applying single-user water-filling to each DSL system separately while considering crosstalk as noise, competing DSL systems can jointly optimize their TX power allocation to maximize the aggregate bit rates while, at the same time, minimizing the harm they are causing to one another. □

Remark 2.3 The newly presented ADSL2 and ADSL2+ standards [63, 64] support so-called "seamless rate adaptation" or "bit-swapping": the line conditions are observed continuously and the bit rate and bit allocation are adapted accordingly, e.g., when temperature variations cause changing channel conditions or when an RFI is switched off [60]. Some loading algorithms, e.g., [19, 20], allow for efficient bit-swapping by incrementally changing the bit allocation to adapt to the new situation. □

2.1.5 Vector coding

In this section, further restrictions are imposed to render MC transmission possible in practice. The orthogonal modulator functions $\phi_n(t)$ in **Figure 2.1** are based on an infinite-length sinc-shaped filter $\phi(t)$ (2.3), which is not physically realizable. Therefore, the modulator functions have to be confined to a finite time-interval, e.g., the symbol time T_s. This can be done in several ways.

One way is to closely approximate the brick-wall spectrum of $\phi(t)$ with well-designed analog filters. In this way, ICI remains mostly avoided. The early MC implementations of the '60 and '70 followed this approach with varying success using analog signal processing tools [25, 102]. Alternatively, multimodal modulation, rather than multicarrier modulation, can be used: optimum finite-length orthogonal modulator functions $\phi_n(t)$ are channel-dependent, as they are the N dominating eigenfunctions (modes) of the autocorrelation of the channel impulse response (CIR) $h(t)$ [32, 75]. In both approaches, the analog implementation of the continuous-time modulator functions $\phi_n(t)$ poses a burden.

The introduction and development of discrete-time or digital signal processing (DSP) techniques alleviated many of the encountered problems. Both above-mentioned analog alternatives have a discrete-time counterpart.

In [27], so-called filtered multitone (FMT) transmission has been presented: the brick-wall spectrum of the modulator functions is approximated by means of digital filters that have small sidelobes. Several implementations, with different digital filter designs (e.g., using wavelets [103]) and equalization techniques have been presented in the literature. The major drawback of these methods stems from complexity constraints that limit the number of subchannels, hence the symbol time T_s: the ISI and possibly also the ICI can not be neglected any longer, so that complex equalization is often required.

The need for complex equalization can be overcome by resorting to the discrete-time version of multimodal modulation, called *vector coding* (VC), in combination with the use of a guard period [69]. The detection of the k-th TX symbol vector $\tilde{\mathbf{x}}_{k,N}$ (2.2) requires the demodulation of the RX signal $y(t)$ on the continuous-time interval $t \in ((k-1)T_s, kT_s)$. However, due to the channel delay spread, the first T_h seconds of this interval are corrupted by ISI from

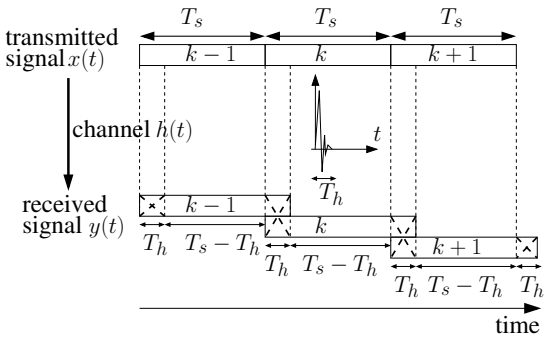


Figure 2.3: A guard period is inserted between consecutive TX symbols to easily eliminate ISI at the receiver.

the $k-1$-th TX symbol vector $\tilde{\mathbf{x}}_{k-1,N}$, as is depicted in **Figure 2.3**. When $T_h \ll T_s$, a so-called *guard period* $T_g \geq T_h$ can be introduced at the receiver to simply ignore the first T_g seconds, and demodulate the RX signal $y(t)$ during the ISI-free time slot $((k-1)T_s + T_g, kT_s)$.

By sampling the RX signal $y(t)$, the TX signal $x(t)$, the noise signal $n(t)$ and the CIR $h(t)$ at a sufficiently high rate $f_s' = \frac{1}{T_s'}$ and denoting the corresponding samples as $y_l = y(lT_s')$, $x_l = x(lT_s')$, $n_l = n(lT_s')$ and $h_l = h(lT_s')$, respectively, the following discrete-time equivalent model of the RX signal $y(t)$ (2.4) is obtained:

$$y_l = \sum_{m=0}^{L} h_m x_{l-m} + n_l \tag{2.12}$$

where the discrete-time CIR $\mathbf{h} = \left[\begin{array}{ccc} h_0 & \dots & h_L \end{array}\right]^T$ has a length of $L+1 = \left\lfloor \frac{T_h}{T_s'} \right\rfloor + 1$ samples. To recover the $N \times 1$ TX symbol vector $\tilde{\mathbf{x}}_{k,N}$ (2.2), at least N RX samples y_l from the ISI-free interval $((k-1)T_s + T_g, kT_s)$ are required. Hence, the sampling time T_s' should not be larger than $\frac{T_s - T_g}{N}$ seconds. Assuming that the guard period corresponds to $\nu = \left\lfloor \frac{T_g}{T_s'} \right\rfloor$ samples, the sampling rate f_s' should then obey $f_s' \geq f_s\,(N+\nu)$. Assuming that the strict equality $f_s' = f_s\,(N+\nu)$ holds, we stack the $N+\nu$ samples y_l and x_l from the k-th time-interval $((k-1)T_s, kT_s)$ in an RX vector $\mathbf{y}_{k,-\nu:N-1}$ and a TX vector $\mathbf{x}_{k,-\nu:N-1}$, respectively, where the following notation is adopted:

$$\mathbf{y}_{k,i:j} = \left[\begin{array}{ccc} y_{k,i} & \cdots & y_{k,j} \end{array}\right]^T \tag{2.13}$$

$$\mathbf{x}_{k,i:j} = \left[\begin{array}{ccc} x_{k,i} & \cdots & x_{k,j} \end{array}\right]^T \tag{2.14}$$

with $y_{k,m} = y_{(k-1)(N+\nu)+\nu+m}$ and $x_{k,m} = x_{(k-1)(N+\nu)+\nu+m}$. The first L RX samples $\mathbf{y}_{k,-\nu:-\nu+L-1}$ are corrupted by ISI from $\mathbf{x}_{k-1,N-L:N-1}$, hence a guard

period of ν samples, with $\nu \geq L$, must be adopted at the receiver by ignoring $\mathbf{y}_{k,-\nu:-1}$. Obviously, this reduces the bandwidth efficiency, and hence the bit rate, by a factor $\frac{N}{N+\nu}$.

Remark 2.4 Whereas we suggest here to fix the symbol rate $1/T_s$, to drop a guard period of T_g seconds or ν samples at the receiver and to sample at a sufficiently high rate $f_s^{'}$, an alternative and more common approach and view are obtained by fixing the sample rate $f_s^{'}$ and adding a guard period of ν samples at the transmitter, which is then dropped at the receiver. □

Assuming a minimum guard period of $\nu = L$ samples and stacking the remaining N ISI-free RX samples y_l in a vector $\mathbf{y}_{k,0:N-1}$, the following matrix-based VC data model is obtained from (2.12):

$$\underbrace{\begin{bmatrix} y_{k,0} \\ \vdots \\ y_{k,N-1} \end{bmatrix}}_{\mathbf{y}_{k,0:N-1}} = \underbrace{\begin{bmatrix} h_L & \cdots & h_0 & 0 & \cdots & 0 \\ 0 & h_L & \cdots & h_0 & \ddots & \\ \vdots & \ddots & \ddots & \ddots & \ddots & \vdots \\ 0 & \cdots & 0 & h_L & \cdots & h_0 \end{bmatrix}}_{\mathbf{H}_{\mathrm{T}}} \underbrace{\begin{bmatrix} x_{k,-\nu} \\ \vdots \\ x_{k,N-1} \end{bmatrix}}_{\mathbf{x}_{k,-\nu:N-1}} + \underbrace{\begin{bmatrix} n_{k,0} \\ \vdots \\ n_{k,N-1} \end{bmatrix}}_{\mathbf{n}_{k,0:N-1}} \tag{2.15}$$

The k-th sample vector $\mathbf{x}_{k,-\nu:N-1}$ is the discrete-time equivalent of the continuous-time TX signal $x(t)$ (2.1) on the time-interval $((k-1)T_s, kT_s)$ and can be written as:

$$\mathbf{x}_{k,-\nu:N-1} = \sum_{n=0}^{N-1} \mathbf{g}_n \tilde{x}_{k,n} = \mathbf{G}\tilde{\mathbf{x}}_{k,N} \tag{2.16}$$

Comparing (2.16) with (2.1), the $(N+\nu) \times 1$ column vector $\mathbf{g}_n$ is clearly the discrete-time version of the modulator function $\phi_n(t)$. The $(N+\nu) \times N$ modulation matrix $\mathbf{G} = \begin{bmatrix} \mathbf{g}_0 & \cdots & \mathbf{g}_{N-1} \end{bmatrix}$ maps the TX symbol vector $\tilde{\mathbf{x}}_{k,N}$ onto the TX sample vector $\mathbf{x}_{k,-L:N-1}$. At the receiver, the demodulation of the RX sample vector $\mathbf{y}_{k,0:N-1}$ can also be represented with a matrix operation:

$$\tilde{\mathbf{y}}_{k,N} = \mathbf{F}\mathbf{y}_{k,0:N-1} \tag{2.17}$$

where the rows of $\mathbf{F}$ replace the demodulator functions $\phi_n^*(-t)$ of the MC system in **Figure 2.1**. The question is then how to design the modulator $\mathbf{G}$ and the demodulator $\mathbf{F}$ so that N parallel and independent subchannels are created, which do not suffer from ICI at the receiver. A possible solution [69] is based on the singular value decomposition (SVD) [52] of the channel matrix $\mathbf{H}_{\mathrm{T}}$ in (2.15) :

$$\mathbf{H}_{\mathrm{T}} = \mathbf{U} \begin{bmatrix} \mathbf{S}_{\mathrm{D},N} & \mathbf{0}_{N \times L} \end{bmatrix} \mathbf{V}^H \tag{2.18}$$

where $\mathbf{U}$ and $\mathbf{V}$ are unitary matrices of size $N \times N$ and $(N+L) \times (N+L)$, respectively, and where $\mathbf{S}_{\mathrm{D},N}$ is a diagonal matrix with N singular values

s_n, $n \in [0, N-1]$ along the diagonal. Choosing $\mathbf{F} = \mathbf{U}^H$ and $\mathbf{G} = \mathbf{V}_{1:N}$ with $\mathbf{V}_{1:N}$ containing the first N columns of $\mathbf{V}$ and combining (2.15), (2.16) and (2.17) results in a multichannel system with N parallel, independent subchannels (rather than a multicarrier system with N independent tones):

$$\tilde{\mathbf{y}}_{k,N} = \mathbf{S}_{\mathrm{D},N}\tilde{\mathbf{x}}_{k,N} + \tilde{\mathbf{n}}_{k,N} \text{ and } \tilde{y}_{k,n} = s_n\tilde{x}_{k,n} + \tilde{n}_{k,n} \tag{2.19}$$

with $\tilde{\mathbf{n}}_{k,N} = \mathbf{F}\mathbf{n}_{k,0:N-1}$, $\tilde{y}_{k,n} = \tilde{\mathbf{y}}_{k,N}[n]$ and $\tilde{n}_{k,n} = \tilde{\mathbf{n}}_{k,N}[n]$. As (2.19) looks similar to (2.5), the equalization can also be done with a bank of (complex-valued) scalars s_n^{-1}, $n \in [0, N-1]$, the SNR per subchannel follows from (2.8) by replacing $\tilde{h}_n$ with s_n and the TX power allocation, based on the water-filling principle as discussed in Section 2.1.4, can again be used to approach channel capacity. Alternative VC techniques have been presented in the literature: e.g., the so-called filterbank transceivers in [105] optimize the information rate (which is a measure for the bit rate), given the finite block length N, the channel matrix $\mathbf{H}_{\mathrm{T}}$ and the covariance matrices of $\tilde{\mathbf{x}}_{k,N}$ and $\mathbf{n}_{k,0:N-1}$. The drawback of all of these VC techniques is their complexity, as one or more SVDs need to be computed to obtain the channel-dependent matrices $\mathbf{F}$ and $\mathbf{G}$ and the modulation and demodulation complexity is $\mathcal{O}(N^2)$. Both drawbacks can be overcome by imposing an additional constraint on the modulation matrix $\mathbf{G}$ in (2.16) and the demodulation matrix $\mathbf{F}$ in (2.17), as explained in the next section.

2.2 Discrete multitone transmission

In the previous section, we have introduced the concept of MC modulation and we have shown that it is theoretically capable of reaching Shannon's channel capacity. However, several issues have been raised that need to be addressed in order to implement an MC system in practice:

- the number of tones N is finite, hence, depending on its delay spread L, the channel can not always be considered flat within the tone bandwidth;
- the bank of (de)modulators functions has finite length;
- the introduction of a small guard time of ν samples (with $\nu \geq L$) allows to eliminate ISI without expensive equalization processing, but reduces the bit rate with a factor $\frac{N}{N+\nu}$;
- the QAM symbol mapper, which has finite granularity, introduces a non-zero BER and an SNR gap that can only be partially overcome by means of channel coding;
- in ADSL, a quasi-flat TX power spectrum, rather than a water-filling spectrum is assigned to the tones with a sufficient SNR;
- integer bit loading is used.

In this section, a last modification is introduced: a VC scheme that employs a cyclic prefix, as described in Section 2.2.1, allows for a channel-independent and efficient (de)modulation, and is referred to as DMT modulation; it is applied in DSL modems. The DMT transmitter and receiver are presented in detail in Section 2.2.2 and Section 2.2.3. It has already been argued in Section 1.4.1 that, despite the theoretically optimum properties of MC transmission, advanced equalization and RFI mitigation techniques are required to apply DMT modulation in DSL systems. An introduction to equalization for DMT-based systems is given in Section 2.2.4; RFI mitigation is the subject of Section 2.2.5.

2.2.1 Cyclic prefix

As already pointed out in Section 2.1.5, the VC technique, based on the SVD in (2.18), is not the only way to turn the transmission channel into N parallel and independent subchannels. A particularly efficient VC technique is obtained by constraining the first and the last ν elements of $\mathbf{x}_{k,-\nu:N-1}$ in (2.15) to be equal, i.e., $\mathbf{x}_{k,-\nu:-1} = \mathbf{x}_{k,N-\nu:N-1}$. This is accomplished by imposing that:

$$\mathbf{x}_{k,-\nu:N-1} = \underbrace{\left[\begin{array}{c|c} \mathbf{0}_{\nu\times(N-\nu)} & \mathbf{I}_\nu \\ \hline \multicolumn{2}{c}{\mathbf{I}_N} \end{array}\right]}_{\mathbf{P}_\nu} \mathbf{x}_{k,0:N-1} \tag{2.20}$$

The sample vector $\mathbf{x}_{k,-\nu:-1}$ is called a *cyclic prefix* (CP), as it forces the RX sample vector $\mathbf{y}_{k,0:N-1}$ to be the outcome of the *cyclic convolution* of $\mathbf{h}$ and $\mathbf{x}_{k,0:N-1}$. The VC data model (2.15) can then be rewritten as:

$$\mathbf{y}_{k,0:N-1} = \mathbf{H}_{\mathrm{C}}\mathbf{x}_{k,0:N-1} + \mathbf{n}_{k,0:N-1} \tag{2.21}$$

where the channel matrix $\mathbf{H}_{\mathrm{C}} = \mathbf{H}_{\mathrm{T}}\mathbf{P}_\nu$ is a square and *circulant* $N \times N$ matrix:

$$\mathbf{H}_{\mathrm{C}} = \begin{bmatrix} h_0 & 0 & \cdots & 0 & h_L & \cdots & h_1 \\ \vdots & \ddots & \ddots & & \ddots & \ddots & \vdots \\ h_{L-1} & \cdots & h_0 & 0 & \cdots & 0 & h_L \\ h_L & \cdots & h_1 & h_0 & 0 & \cdots & 0 \\ 0 & h_L & \cdots & h_1 & h_0 & \cdots & 0 \\ \vdots & \ddots & \ddots & & \ddots & \ddots & \vdots \\ 0 & \cdots & 0 & h_L & \cdots & h_1 & h_0 \end{bmatrix} \tag{2.22}$$

This CP idea has been first exploited in [96]. A circulant matrix has a very interesting discrete Fourier transform (DFT) based eigenvalue decomposition (EVD) [52]:

$$\mathbf{H}_{\mathrm{C}} = \mathcal{F}_N^H \mathbf{H}_{\mathrm{D},N} \mathcal{F}_N \tag{2.23}$$

where $\mathcal{F}_N$ is the unitary $N \times N$ DFT matrix, where its Hermitian $\mathcal{F}_N^H$ corresponds to the unitary IDFT matrix and where $\mathbf{H}_{\mathrm{D},N}$ is a diagonal matrix with

the discrete channel frequency response:

$$\tilde{\mathbf{h}}_N = \left[\begin{array}{ccc} \tilde{h}_0 & \cdots & \tilde{h}_{N-1} \end{array} \right]^T = \mathcal{F}_N \left[\begin{array}{c} \mathbf{h} \\ \mathbf{0}_{(N-L-1)\times 1} \end{array} \right] \tag{2.24}$$

along the diagonal. Based on this EVD, the modulation matrix $\mathbf{G}$ in (2.16) and the demodulation matrix $\mathbf{F}$ in (2.17) are chosen as the IDFT and DFT matrix, respectively, i.e.,

$$\mathbf{x}_{k,0:N-1} = \mathcal{F}_N^H \tilde{\mathbf{x}}_{k,N} \tag{2.25}$$

$$\tilde{\mathbf{y}}_{k,N} = \mathcal{F}_N \mathbf{y}_{k,0:N-1} \tag{2.26}$$

This choice of modulation and demodulation effectively decouples the channel into N parallel and independent *tones*, hence avoiding ICI:

$$\tilde{\mathbf{y}}_{k,N} = \mathbf{H}_{\mathrm{D},N} \tilde{\mathbf{x}}_{k,N} + \tilde{\mathbf{n}}_{k,N} \text{ and } \tilde{y}_{k,n} = \tilde{h}_n \tilde{x}_{k,n} + \tilde{n}_{k,n} \tag{2.27}$$

where $\tilde{\mathbf{n}}_{k,N} = \mathcal{F}_N \mathbf{n}_{k,0:N-1}$.

Indeed, the VC scheme with CP is a digital version of the original MC scheme of Section 2.1: the n-th row of the modulating IDFT matrix, $\mathcal{F}_n^*$, $n = 0, \ldots, N-1$, with

$$\mathcal{F}_n = \left[\begin{array}{cccc} 1 & e^{\frac{j2\pi n}{N}} & \cdots & e^{\frac{j2\pi n(N-1)}{N}} \end{array} \right] \tag{2.28}$$

is a discretized version of the modulator function $\phi_n(t)$ in (2.1); the pulse-shaping filter is now a rectangular time-window of N samples, rather than the sinc-shaped filter $\phi(t)$ (2.3). The channel partitioning then again corresponds to a set of N parallel tones. However, the tones are now overlapping in frequency: because of the rectangular time-window, the tones have sinc-shaped spectra with overlapping main lobes and sidelobes and a tone spacing of $\frac{f_s'}{N}$ Hz. Note that it was first suggested to implement an MC system based on the discrete Fourier transform (DFT) in [151].

The obvious advantage of the presented VC scheme with CP is that the modulation and demodulation matrices are now channel-independent, so the computation of the EVD (2.23) reduces to the computation of the discrete channel frequency response $\tilde{\mathbf{h}}$. Moreover, $\mathbf{x}_{k,0:N-1}$ in (2.25) and $\tilde{\mathbf{y}}_{k,N}$ in (2.26) can be computed using the efficient fast Fourier transform (FFT) [93], which requires $2N \log_2(N)$, rather than N^2 multiplications. The drawback of the use of a CP is a slight increase in transmit power, when compared to the VC techniques of Section 2.1.5: whereas the guard band consists of zeros in the case of VC transmission, some power is used for the transmission of the non-zero CP samples.

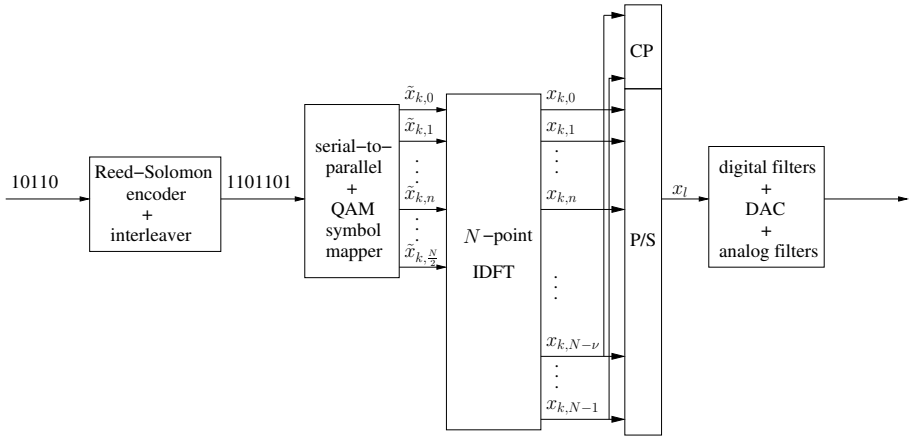


Figure 2.4: The DMT transmitter.

2.2.2 DMT transmitter

The principles and equations, presented in Section 2.2.1, form the basis of DMT modulation, as adopted in DSL systems. We are now ready to describe in detail the DMT transmitter and receiver structure.

Figure 2.4 depicts the DMT transmitter, which has a basic structure that is very similar to the original MC transmitter of **Figure 2.1**. As explained in Section 2.1.2, the incoming bit stream is first encoded (e.g., using a Reed-Solomon channel encoder [115]), interleaved and split into parallel bit streams. Each bit stream n is divided into bit words. These bit words are mapped to QAM symbols $\tilde{x}_{k,n}$. At each DMT symbol time instant k, a block of QAM symbols, denoted as an $N \times 1$ TX symbol vector $\tilde{\mathbf{x}}_{k,N}$ (2.2), is fed to the modulating IDFT at a DMT symbol rate $f_s = \frac{1}{T_s}$. The IDFT output at DMT symbol time k is given by the sample vector $\mathbf{x}_{k,0:N-1}$ in (2.25). As DSL systems use baseband transmission, the TX samples $x_{k,m}$ should be real. This is accomplished by imposing complex conjugate symmetry to $\tilde{\mathbf{x}}_{k,N}$: $\tilde{x}_{k,0}$ and $\tilde{x}_{k,\frac{N}{2}}$ are real pulse-amplitude-modulation symbols and the other (QAM) symbols $\tilde{x}_{k,n}$ obey $\begin{bmatrix} \tilde{x}_{k,1} & \cdots & \tilde{x}_{k,\frac{N}{2}-1} \end{bmatrix}^T = \begin{bmatrix} \tilde{x}^*_{k,N-1} & \cdots & \tilde{x}^*_{k,\frac{N}{2}+1} \end{bmatrix}^T$, hence only $\frac{N}{2}+1$ parallel bit streams can be used. Finally, a CP is added to obtain $\mathbf{x}_{k,-\nu:N-1}$; see (2.20). The $N+\nu$ samples of $\mathbf{x}_{k,-\nu:N-1}$ are then fed serially to the TX filter front-end at a sample rate equal to $f'_s = (N+\nu)f_s$.

The stream of discrete-time samples x_l is transformed into an analog signal, via digital front-end filters, a digital-to-analog converter (DAC) and analog front-end filters. The TX filter front-end, together with the RX filter front-end (see

also **Figure 2.5**), includes low-pass and high-pass analog and digital filters to separate the POTS, the DSL upstream and downstream transmission, as well as to avoid aliasing. The discrete-time CIR $\mathbf{h}$ then not only accounts for the channel dispersion that is caused by the twisted pair, but it also includes the impulse responses of the TX and RX filter front-ends. Similarly, the RX noise term in (2.21) corresponds to the channel noise (including background noise, crosstalk, RFI, etc.), filtered by the RX filter front-end.

Remark 2.5 The TX and RX filter front-ends increase the length of the channel impulse response. The cyclic prefix should then be long enough to also include these filter front-ends. □

Remark 2.6 The superposition of a large number of modulated exponentials makes that the samples x_l have approximately a Gaussian distribution. As a consequence, the signal x_l occasionally has a large amplitude, which poses a burden on the design of the analog circuitry and power amplifiers. Non-linear amplification and clipping can hardly be avoided and creates an additional noise source. Various methods, based on pilot tones and the exploitation of unused tones and coding, have been presented to deal with this so-called peak-to-average power ratio problem (e.g., [87, 118]). □

2.2.3 DMT receiver

Figure 2.5 depicts the DMT receiver. In essence, it performs the reverse operations of the DMT transmitter: the incoming RX signal $y(t)$ is sampled by an analog-to-digital converter (ADC) and processed by the RX filter front-end. Ignoring the TEQ block and the subscripts $\mathbf{w}$ in **Figure 2.5** until Section 2.2.4, the incoming samples y_l are stacked in an $(N+\nu)\times 1$ RX sample vector $\mathbf{y}_{k,-\nu:N-1}$, which forms the k-th RX DMT symbol. As explained in Section 2.1.5, the first ν samples $\mathbf{y}_{k,-\nu:-1}$ are used as a guard time and ignored to eliminate ISI. The remaining $N\times 1$ sample vector $\mathbf{y}_{k,0:N-1}$ is demodulated by means of a DFT (see (2.26)) to deliver $\tilde{\mathbf{y}}_{k,N}$. Again, because of the baseband nature of DSL transmission, only $\frac{N}{2}+1$ of the DFT outputs need to be determined; the remaining DFT outputs follow from the complex conjugate symmetry property. The rows $\mathcal{F}_n$ of the DFT matrix (2.28) are the discrete-time alternative for the bank of demodulators $\phi_n^*(-t)$ in **Figure 2.1**. These demodulators are matched to the modulating IDFT, hence they also have overlapping, sinc-shaped spectra.

In addition to reversing the TX operations, the DMT receiver equalizes the RX signal. The DMT modulation has turned the transmission channel into N parallel tones, described by (2.27). Hence, equalization is simple and easy: as in the original MC system (2.5), each tone just needs to be scaled by the

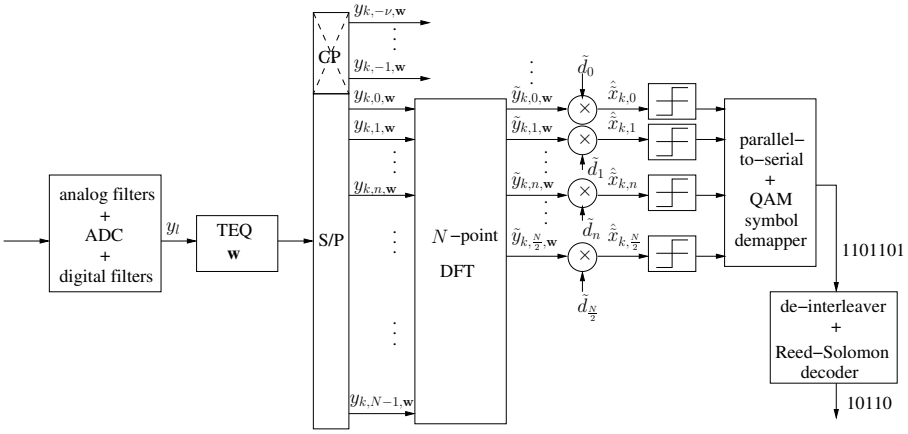


Figure 2.5: The DMT receiver.

inverse of the discrete channel frequency response $\tilde{d}_n = \tilde{h}_n^{-1}$. The estimate of the TX symbol $\tilde{x}_{k,n}$ is then given by:

$$\hat{\tilde{x}}_{k,n} = \tilde{d}_n \tilde{y}_{k,n} = \tilde{h}_n^{-1}(\tilde{h}_n \tilde{x}_{k,n} + \tilde{n}_{k,n}) = \tilde{x}_{k,n} + \tilde{h}_n^{-1}\tilde{n}_{k,n} \tag{2.29}$$

The 1-tap equalizer per tone is called a *frequency-domain equalizer (FEQ)*. It could seem remarkable that this simple equalization scheme suffices despite the overlap between the sinc-shaped tone spectra. This is exactly the strength of DMT modulation and the result of the introduction of the CP in combination with the use of DFT-based (de)modulation.

Finally, the noisy FEQ outputs (2.29) are de-interleaved and decoded to recover the original information bit stream. Either hard-decoding is applied, i.e., the decoder is fed with hard decisions on the TX QAM symbols, or the FEQ outputs are used to perform soft-decoding (based on, e.g., a convolutional coding or turbo coding).

In order to optimize the performance, TX power allocation and bit loading are applied. As explained in Example 2.4, ADSL systems use on/off power allocation in combination with integer bit loading. The bit loading is based on the SNR per tone: SNR_n (2.8), as obtained for MC modulation, also applies for DMT modulation.

Remark 2.7 The TX power allocation and bit loading on a particular ADSL connection are determined during a connection set-up phase [61]. Based on a training signal, the receiver determines the so-called *channel-state information* (CSI), i.e., the channel frequency response and noise PSD, as well as the TX

power allocation and bit loading. This information is fed back to the transmitter. ADSL2 and ADSL2+ allow for bit-swapping during the data transmission phase to adapt to changing channel conditions (see Remark 2.3). As stated in Remark 1.1, MC modulation, then referred to as orthogonal frequency-division multiplexing (OFDM), has been adopted as transmission format for several wireless applications [150]. The basic difference between OFDM and DMT modulation is the absence of bit loading in the former modulation scheme: whereas DSL channels are slowly time-varying, wireless channels typically vary much faster in time, especially in a mobile environment, rendering bit loading a difficult issue. Moreover, bit loading can not be applied in a broadcasting environment. A fixed constellation is used for all tones and coding is added to avoid that a channel notch causes detrimental data loss. OFDM then still offers the advantage over classical single-carrier systems of a very simple equalization structure that can be fast adapted. Recent research has focused on OFDM in combination with adaptive power and bit loading in scenarios where (partial) CSI can be fed back to the transmitter [123, 154]. □

Example 2.5 ADSL and ADSL2 transmission are specified and standardized in [61, 63]. The tone spacing $\frac{f'_s}{N}$ is fixed to 4.3125 kHz. As explained in Section 1.3.1, two operation modes are considered, which affect the allocation of tones to upstream and downstream. In this thesis, we assume the *FDD mode*, where upstream and downstream transmission use disjoint sets of tones. The standard allows to use tones 6 to 32 for upstream (the frequency band between 25.875 and 138 kHz); downstream transmission in FDD mode uses the tones 33 to 255, i.e., the frequency band from 138 kHz up to 1.104 MHz. Oftentimes, the TX and RX filter front-end, together with a guard band of a few tones, separate upstream and downstream; e.g., in the simulations, we mostly assume downstream transmission over the tones 38 to 255. In the *echo-cancelling mode*, the downstream transmission overlaps with the upstream transmission so that an echo-canceller is needed [128, 156]. ADSL upstream uses a DFT size $N = 64$, a CP length $\nu = 4$, hence a DMT symbol length of $N + \nu = 68$ samples, and a sample rate $f'_s = 276$ kHz. ADSL dowstream uses a DFT size $N = 512$, a CP length $\nu = 32$, hence a DMT symbol length of $N + \nu = 544$ samples, a sample rate $f'_s = 2.208$ MHz and a transmission bandwidth $\frac{f'_s}{2} = 1.104$ MHz. Both ADSL upstream and downstream have a DMT symbol rate $f_s = \frac{f'_s}{N+\nu} = 4.059$ kHz. Upstream transmission uses a power mask with a maximum of -38 dBm/Hz on the upstream tones; similarly, the downstream power mask allows for -40 dBm/Hz over the downstream tones. △

Example 2.6 The standards for ADSL2+ and VDSL guarantee interoperability with ADSL, by using DMT modulation with the same tone spacing $\frac{f'_s}{N} = 4.3125$ kHz [64, 121]. Compared to ADSL and ADSL2 systems, ADSL2+

[64] doubles the transmission bandwidth to 2.208 MHz, resulting in a DFT size N, CP length ν and sample rate f_s' that are also twice as large. VDSL [121] uses a transmission bandwidth up to 17.664 MHz, or 16 times the ADSL bandwidth. The DFT size N then becomes 8192, the sample rate f_s' is 35.328 MHz and the CP is 640 samples long. △

2.2.4 Time-domain equalization

In Section 2.2.1, it has been argued that the CP length ν should be larger than or equal to L (for a CIR $\mathbf{h}$ of $L+1$ samples) in order to avoid ISI and ICI. The introduction of a CP leads to a bit rate reduction by a factor $\frac{N}{N+\nu}$. Hence, the larger ν, the larger N should be chosen in order not to sacrifice too much efficiency. A large N on the other hand leads to a large latency, as well as high complexity and hardware requirements.

In Example 2.5, ADSL specifications have been given: the standard specifies that $N = 512$ and $\nu = 32$ so that the efficiency loss as well as the latency are limited. A typical ADSL CIR turns out to be several hundreds of samples long, hence $L \gg \nu$. As a consequence, the received tones at the receiver are not orthogonal and there is a significant amount of ISI/ICI at the input of the decision devices (see **Figure 2.5**). In [98], a mathematical model of the ISI/ICI is given. It turns out that the ISI/ICI especially occurs on tones near the transition band of the front-end filters, e.g., near tone 33 in the case of ADSL downstream.

Remark 2.8 The term "ICI" could be replaced with "*intra*-symbol interference". When detecting $\tilde{x}_{k,n}$, it refers to interference from symbols $\tilde{x}_{k,m}$, $m \neq n$ that are transmitted at the same DMT symbol time instant k; on the other hand, ISI (*inter*-symbol interference) refers to interference from DMT symbols, transmitted at a different DMT symbol time instant, e.g, $\tilde{\mathbf{x}}_{k-1,N}$. □

Additional equalization is required in order to render DMT modulation suited for ADSL communication. In [29], it was suggested to insert a digital filter $\mathbf{w}$ before DFT demodulation, as depicted in **Figure 2.5**. This so-called *time-domain equalizer (TEQ)* should act as a channel shortener: if the convolution of the T-tap TEQ filter $\mathbf{w}$ and the CIR $\mathbf{h}$ of $L+1$ samples (e.g., $L = 300$) is sufficiently short so that the overall impulse response, referred to as shortened impulse response (SIR), $\mathbf{c} = \mathbf{h} \star \mathbf{w}$ has length $\nu + 1$, then the orthogonality between the tones is restored and the ISI/ICI vanishes. However, the convolution $\mathbf{c} = \mathbf{h} \star \mathbf{w}$ has length $L + T$, which is typically much larger than $\nu + 1$. While the TEQ $\mathbf{w}$ is typically designed in such a way that the SIR $\mathbf{c}$ has most of its energy concentrated in a window of $\nu + 1$ samples, the tails of $\mathbf{c}$ outside this window cause ISI/ICI, which can not be completely avoided. We denote the

output of the TEQ $\mathbf{w}$ (see **Figure 2.5**) as the $N \times 1$ equalized sample vector:

$$\mathbf{y}_{k,-\nu:N-1,\mathbf{w}} = \left[\begin{array}{ccc} y_{k,-\nu,\mathbf{w}} & \cdots & y_{k,N-1,\mathbf{w}} \end{array} \right]^T \tag{2.30}$$

where the definition of the equalized samples $y_{k,m,\mathbf{w}}$ and equalized sample vector $\mathbf{y}_{k,i:j,\mathbf{w}}$ follows from the definition for the unequalized samples $y_{k,m}$ and sample vector $\mathbf{y}_{k,i:j}$ in (2.13). After discarding the CP $\mathbf{y}_{k,-\nu:-1,\mathbf{w}}$, the n-th equalized DFT output is now given by

$$\tilde{y}_{k,n,\mathbf{w}} = \check{c}_n \tilde{x}_{k,n} + \tilde{n}_{k,n,\mathbf{w}} + \text{ISI}_{k,n,\mathbf{w}} + \text{ICI}_{k,n,\mathbf{w}} \tag{2.31}$$

where $\tilde{y}_{k,n,\mathbf{w}} = \mathcal{F}_n \mathbf{y}_{k,0:N-1,\mathbf{w}}$ (a similar definition applies for $\tilde{n}_{k,n,\mathbf{w}}$), where the subscripts $\mathbf{w}$ denote signals that have been filtered by the TEQ $\mathbf{w}$ (see **Figure 2.5**), and where the residual terms $\text{ISI}_{k,n,\mathbf{w}}$ and $\text{ICI}_{k,n,\mathbf{w}}$ depend on the TEQ design $\mathbf{w}$.

The first term in (2.31) is the desired signal portion. Based on (2.27), one would intuitively expect this desired signal portion to be equal to the TX symbol $\tilde{x}_{k,n}$ scaled by the discrete frequency response of the SIR $\mathbf{c}$ on tone n, i.e., $\tilde{c}_n = \mathcal{F}_n \left[\begin{array}{cc} \mathbf{c}^T & \mathbf{0}_{1\times(N-L-T)} \end{array} \right]^T = \mathcal{F}_{n,0:L+T-1}\mathbf{c}$. However, the DMT block transmission nature causes a scalar $\check{c}_n$, which is close to, but not exactly equal to $\tilde{c}_n$. A matrix-based derivation of $\check{c}_n$ as well as the residual ISI/ICI will be given in Section 4.1. It follows from (2.31) that a possible choice for the FEQ $\tilde{d}_n$ in **Figure 2.5** is given by $\tilde{d}_n = \frac{1}{\check{c}_n}$. The optimal choice of FEQs will be further discussed in Section 4.2.2.

In order to serve a maximum number of customers (see Chapter 1), DSL system design aims at maximizing the bit rate R, which is still given by (2.9), be it with a modified SNR_n, $n \in [0, N-1]$ based on (2.31) to take the TEQ and the residual ISI/ICI into account:

$$\text{SNR}_n = \frac{\sigma^2_{n,\tilde{x}} \left|\check{c}_n\right|^2}{\sigma^2_{n,\tilde{n},\mathbf{w}} + \mathcal{E}\left\{\left|\text{ISI}_{k,n,\mathbf{w}}\right|^2\right\} + \mathcal{E}\left\{\left|\text{ICI}_{k,n,\mathbf{w}}\right|^2\right\}} \tag{2.32}$$

with $\sigma^2_{n,\tilde{n},\mathbf{w}} = \mathcal{E}\left\{\left|\tilde{n}_{k,n,\mathbf{w}}\right|^2\right\}$. TEQ design then appears both crucial and non-trivial. The TEQ design has an impact on all terms in (2.32). Moreover, the TEQ $\mathbf{w}$ is in front of the demodulating DFT, while SNR_n (2.32) is determined behind the DFT. Hence, the TEQ should act in such a way that it reduces jointly and adequately the ISI/ICI as well as the noise on all tones. The bad spectral containment of the sinc-shaped tone spectra, as described in Section 2.2.1, complicate the TEQ task, as it causes leakage of the desired signal, the residual ISI/ICI and the noise to neighbouring tones. The TEQ design problem has challenged researchers for over a decade, now, and many TEQ design methods have been presented so far in the literature. An overview of the most important, existing TEQ designs is given in Chapter 3 and we

argue why each of these TEQ design methods is suboptimal in terms of bit rate. Chapter 3 also describes the *per-tone equalizer (PTEQ)* [132], which has been developed as an attractive, alternative equalizer scheme for DMT-based systems. The PTEQ was the first DMT equalizer to guarantee bit rate maximization. Then, in Chapter 4, we present a TEQ design that truly maximizes the bit rate and hence outperforms the existing TEQ designs. We refer to it as a *bit rate maximizing TEQ (BM-TEQ) design.* In Chapter 5, the BM-TEQ design and the PTEQ design are shown to be extreme cases of so-called *bit rate maximizing per-group equalizers (BM-PGEQ).* This opens a complete range of bit rate maximizing DMT equalizers, which offers the flexibility to trade off computational and memory cost versus performance.

Remark 2.9 In fact, the TEQ filter can never reach the optimal bit rate of a DMT-based system. DMT modulation is in essence a block transmission scheme, as data blocks $\tilde{\mathbf{x}}_{k,N}$ are transmitted. This results in a TX signal x_l and RX signal y_l that are *cyclostationary* with period $N+\nu$, rather than stationary. The TEQ is a *time-invariant*, hence *stationary* equalizer, whereas the optimal receiver should be time-varying, hence cyclostationary [1, 4, 38]. Nevertheless, a TEQ is capable of recovering a large portion of the performance that is lost because of a too short CP. □

Remark 2.10 The TEQ is designed during the connection set-up phase. Optimal TEQ design should take into account the TX power allocation and the bit loading. However, this gives rise to a complex, iterative process, as the bit loading depends on SNR_n (2.32), and hence also on the TEQ design. A few algorithms have been presented in the literature that (partially) take into account the TX power allocation, e.g., [7].

After the initial TEQ design, the TEQ is oftentimes kept fixed during data transmission. However, the DSL environment is slowly time-varying, hence the TEQ becomes less adequate as time evolves. Therefore, we present an *adaptive version of the BM-TEQ* in Chapter 5, which can also be used in combination with the seamless rate adaptation functionality of ADSL2 and ADSL2+ (see Remark 2.3). □

Remark 2.11 As in *VDSL* the loops are shorter and as less front-end filters are needed, the VDSL CIRs are shorter. In combination with a slightly larger CP length (if expressed in seconds), VDSL then does not require a TEQ [153]. For *wireless* communications, there is an increased interest for TEQ design, despite the fact that wireless channel dispersion is in general much smaller than wireline channel dispersion. Several channel-shortening equalizer designs have been presented for so-called multiple-input multiple-output (MIMO) OFDM communication [2, 76, 100, 124]. The use of a CP, in combination with a channel shortening equalizer, has also been investigated for non-MC communication, such as CDMA-based communication [10]. □

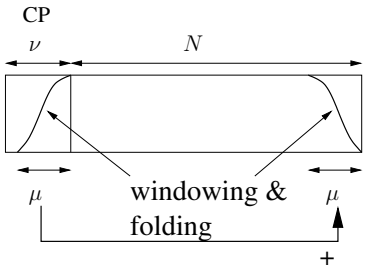


Figure 2.6: Windowing and folding of a DMT symbol.

2.2.5 Windowing

The large transmission bandwidth of ADSL, ADSL2, ADSL2+ and VDSL results in spectral overlap with other communication systems, such as radio communications. This results in narrowband RFI ingress, as described in Section 1.3.1. Ideal MC modulation is particularly robust against RFI: the tone orthogonality ensures that only the tone, with which the RFI coincides, is destroyed. The overlapping sinc-shaped tones render DMT modulation less robust against RFI ingress: due to the high sidelobes of the sinc-shaped spectrum, an RFI will not only disturb the tones, with which it overlaps, but there will be spectral leakage to many other tones. An RFI can even cause a complete breakdown of the DMT-based system.

RFI mitigation has been taken into account in the standardized specifications of a VDSL receiver, as it is considered to be an important issue [39, 121]. Some amateur radio bands coincide with the VDSL transmission bandwidth. These amateur radios can be especially harmful as they frequently switch on and off. RFI ingress is nowadays also considered a problem in downstream ADSL: AM radio broadcasters share their frequency bands with ADSL. Compared to amateur radios, AM radios are more stationary as they are broadcasting continuously. ADSL test scenarios including RFI ingress have been specified in [62].

A low-cost solution to RFI ingress has been presented in [113]. By applying a time-domain window (e.g., a raised cosine window) in front of the DFT, the spectral containment of the demodulating DFT is improved, as the window reduces the sidelobes of the sinc-shaped tones. The windowing operation is followed by a folding of the edges to preserve the DMT tone orthogonality.

The windowing and folding operation on an equalized sample vector $\mathbf{y}_{k,-\nu:N-1,\mathbf{w}}$ is illustrated in **Figure 2.6**. The window extends μ samples beyond the $N \times 1$ equalized sample vector $\mathbf{y}_{k,0:N-1,\mathbf{w}}$ into the cyclic prefix, so it is applied to the $(N+\mu) \times 1$ equalized sample vector $\mathbf{y}_{k,-\mu:N-1,\mathbf{w}}$. The window taper of length

μ, denoted as

$$\mathbf{u} = \begin{bmatrix} u_0 & \cdots & u_{\mu-1} \end{bmatrix}^T \tag{2.33}$$

multiplies the first μ samples $\mathbf{y}_{k,-\mu:-1,\mathbf{w}}$; the last μ samples $\mathbf{y}_{k,N-\mu:N-1,\mathbf{w}}$ are multiplied with a taper $\check{\mathbf{u}}$ that is symmetric with $\mathbf{u}$, i.e.,

$$\check{\mathbf{u}} = \mathbf{1}_\mu - \mathbf{u} \tag{2.34}$$

with $\mathbf{1}_\mu$ an $\mu \times 1$ all-one vector. The remaining $(N-\mu) \times 1$ sample vector $\mathbf{y}_{k,0:N-\mu-1,\mathbf{w}}$ is kept unchanged. The folding operation, which follows the windowing, consists of the addition of the first μ windowed samples $\mathbf{u} \odot \mathbf{y}_{k,-\mu:-1,\mathbf{w}}$ (where $\odot$ denotes the element-wise multiplication of two vectors) and the last μ windowed samples $\check{\mathbf{u}} \odot \mathbf{y}_{k,N-\mu:N-1,\mathbf{w}}$ in order to obtain an $N \times 1$ RX sample vector that is fed to the DFT.

The efficiency of the window increases with its taper length μ. It follows from the above discussion that the window should not extend beyond the CP to preserve the tone orthogonality, hence $\mu \leq \nu$. Moreover, the order of the SIR $\mathbf{c}$, L, should be of length $\nu - \mu$, rather than ν for the same orthogonality reason. In VDSL, a long CP has been foreseen, so that windowing can introduce a significant increase in spectral containment. Windowing is also useful in ADSL, be it that the CP length $\nu = 32$ limits the window length. Therefore, alternative RFI cancellation techniques may be devised. In Chapter 5, the performance of the BM-TEQ and BM-PGEQ design in the presence of RFI is investigated; it will be shown that the BM-TEQ design with a sufficient number of taps is capable of reducing RFI. In Chapter 6, bit rate maximizing joint window and TEQ (BM-WinTEQ) design is considered. In Chapter 7, RFI cancellation based on the exploitation of unused tones is discussed.

2.3 Data model

In this section, the basic data model and notation that will be used throughout the thesis is presented. The data model in Section 2.3.1 is based on an FIR model of the transmission channel. It will be used for equalizer and RFI canceller design in Chapters 3 to 6. The data model in Section 2.3.2 is based on an IIR channel model, which offers a parsimonious representation of the long DSL transmission channel impulse response. It will be used in Chapter 7 for equalizer design.

2.3.1 Data model based on an FIR channel model

This section describes the basic data model assuming that the transmission channel (including the TX and RX filter front-end) can be represented with an

FIR model $\mathbf{h}$. The k-th RX sample vector, which is used for the detection of the k-th TX symbol vector $\tilde{\mathbf{x}}_{k,N}$, is given by:

$$\underbrace{\begin{bmatrix} y_{k,l+\Delta} \\ \vdots \\ y_{k,N-1+\Delta} \end{bmatrix}}_{\mathbf{y}_{k,l+\Delta:N-1+\Delta}} = \underbrace{\begin{bmatrix} & \overbrace{\begin{array}{|ccc|} [& \bar{\mathbf{h}}^T &] \\ & \ddots & \\ \cdots & 0 & [\quad \bar{\mathbf{h}}^T \quad] \end{array}}^{\mathbf{H}_\mathrm{T}} & \\ \mathbf{0}_{(1)} & & \mathbf{0}_{(2)} \end{bmatrix} \cdot (\mathbf{I}_3 \otimes \mathbf{P}_\nu \mathcal{F}_N^H) \cdot}_{\mathbf{H}}$$

$$\underbrace{\begin{bmatrix} \tilde{\mathbf{x}}_{k-1,N} \\ \tilde{\mathbf{x}}_{k,N} \\ \tilde{\mathbf{x}}_{k+1,N} \end{bmatrix}}_{\tilde{\mathbf{x}}_{k-1:k+1,N}} + \underbrace{\begin{bmatrix} n_{k,l+\Delta} \\ \vdots \\ n_{k,N-1+\Delta} \end{bmatrix}}_{\mathbf{n}_{k,l+\Delta:N-1+\Delta}} \tag{2.35}$$

where:

- the notation for the RX sample vectors $\mathbf{y}_{k,i:j}$ and the RX samples $y_{k,m}$ has been introduced in (2.13); the subscripts $i:j$ will be omitted for reasons of conciseness, whenever this range is obvious;
- l determines the first considered sample of the k-th RX DMT symbol and depends on the number of equalizer taps T and/or the window taper length μ; Δ is a synchronization delay as explained below;
- $\bar{\mathbf{h}}$ is the CIR vector $\mathbf{h}$ with coefficients in reverse order;
- $\mathbf{I}_n$ is an $n \times n$ identity matrix; $\otimes$ denotes the Kronecker product; the $(N+\nu) \times N$ matrix $\mathbf{P}_\nu$, which adds the cyclic prefix of length ν, has been defined in (2.20); $\mathcal{F}_N^H = \mathcal{F}_N^*$ is the $N \times N$ IDFT matrix;
- the $N \times 1$ TX symbol vector $\tilde{\mathbf{x}}_{k,N}$ has been introduced in (2.2); its complex conjugate symmetry property has been clarified in Section 2.2.2;
- $\mathbf{n}_{k,l+\Delta:N-1+\Delta}$ is a sample vector with additive channel noise, including crosstalk, RFI, etc.; its autocorrelation matrix is denoted as $\mathbf{\Sigma}_\mathbf{n}^2 = \mathcal{E}\left\{\mathbf{n}_k \mathbf{n}_k^T\right\}$.

The transmission channel has a propagation delay δ_0. Moreover, a receiver typically includes a decision delay δ, a design parameter that allows for a (slightly) acausal receiver to optimize performance. This explains the appearance of the future $\tilde{\mathbf{x}}_{k+1,N}$ in (2.35). Often, δ_0 and δ are combined into a single synchronization design parameter $\Delta = \delta_0 + \delta$. The matrices $\mathbf{O}_{(1)}$ and $\mathbf{O}_{(2)}$ in (2.35) are then zero matrices of size $(N-l) \times (N-L+2\nu+\Delta+l)$ and $(N-l) \times (N+\nu-\Delta)$, respectively.

To model the ISI and ICI correctly, three consecutive TX symbol vectors, denoted as $\tilde{\mathbf{x}}_{k-1:k+1,N}$, are taken into account, where $\tilde{\mathbf{x}}_{k,N}$ is the symbol vector of interest and where $\tilde{\mathbf{x}}_{k-1,N}$ and $\tilde{\mathbf{x}}_{k+1,N}$ introduce ISI. Note that a large L and/or T and/or μ could even necessitate the introduction of an extra TX symbol vector $\tilde{\mathbf{x}}_{k-2,N}$.

The equalization and windowing operation of Section 2.2.4 and Section 2.2.5 can be described mathematically as follows. Define an $(N+\mu) \times T$ Toeplitz matrix $\mathbf{Y}_k$ of RX samples $y_{k,m}$ as:

$$\mathbf{Y}_k = \begin{bmatrix} y_{k,-\mu} & \cdots & y_{k,-\mu-T+1} \\ \vdots & \ddots & \vdots \\ y_{k,N-1} & \cdots & y_{k,N-T} \end{bmatrix} \tag{2.36}$$

where we assume for reasons of conciseness that the synchronization delay Δ is zero. Then, the $(N+\mu) \times 1$ sample vector at the TEQ output, which is windowed before being fed to the DFT, is the result of the matrix-vector product

$$\mathbf{y}_{k,\mathbf{w}} = \mathbf{y}_{k,-\mu:N-1,\mathbf{w}} = \mathbf{Y}_k \mathbf{w} \tag{2.37}$$

Hence, the equalized sample vector $\mathbf{y}_{k,\mathbf{w}}$ is the convolution of the k-th RX sample vector $\mathbf{y}_{k,-\mu-T+1:N-1}$ in (2.35) and the TEQ $\mathbf{w} = \begin{bmatrix} w_0 & \cdots & w_{T-1} \end{bmatrix}^T$. The windowing and folding operations result in the k-th $N \times 1$ equalized and windowed sample vector:

$$\mathbf{y}_{k,\mathbf{w},\mathbf{u}} = \mathbf{y}_{k,0:N-1,\mathbf{w},\mathbf{u}} = \begin{bmatrix} \mathbf{y}_{k,0:N-\mu-1,\mathbf{w}} \\ \mathbf{u} \odot \mathbf{y}_{k,-\mu:-1,\mathbf{w}} + \check{\mathbf{u}} \odot \mathbf{y}_{k,N-\mu:N-1,\mathbf{w}} \end{bmatrix} \tag{2.38}$$

Alternatively, the windowing operation can be written as the multiplication of $\mathbf{y}_{k,-\mu:N-1,\mathbf{w}}$ with the $N \times (N+\mu)$-matrix $\mathbf{\Omega}$:

$$\mathbf{\Omega} = \begin{bmatrix} \mathbf{0}_{(N-\mu)\times\mu} & \mathbf{I}_{N-\mu} & \mathbf{0}_{(N-\mu)\times\mu} \\ \mathrm{diag}(\mathbf{u}) & \mathbf{0}_{\mu\times(N-\mu)} & \mathrm{diag}(\check{\mathbf{u}}) \end{bmatrix} \tag{2.39}$$

The vector $\mathbf{y}_{k,\mathbf{w},\mathbf{u}}$ is then fed to the DFT. The $N \times 1$ DFT output vector and the DFT output on tone n are given by:

$$\tilde{\mathbf{y}}_{k,N,\mathbf{w},\mathbf{u}} = \mathcal{F}_N \mathbf{\Omega} \mathbf{Y}_k \mathbf{w} \text{ and } \tilde{y}_{k,n,\mathbf{w},\mathbf{u}} = \tilde{\mathbf{y}}_{k,N,\mathbf{w},\mathbf{u}}[n] = \mathcal{F}_n \mathbf{\Omega} \mathbf{Y}_k \mathbf{w} \tag{2.40}$$

respectively, where $\mathcal{F}_N$ is the unitary DFT matrix and $\mathcal{F}_n$ is the n-th row of $\mathcal{F}_N$ (see (2.28)).

In the case of a TEQ-only, i.e., $\mu = 0$, (2.40) reduces to

$$\tilde{\mathbf{y}}_{k,N,\mathbf{w}} = \mathcal{F}_N \mathbf{Y}_k \mathbf{w} \tag{2.41}$$

while, in the case of windowing-only, i.e., $T = 1$, (2.40) reduces to

$$\tilde{\mathbf{y}}_{k,N,\mathbf{u}} = \mathcal{F}_N \mathbf{\Omega} \mathbf{y}_{k,-\mu:N-1} \tag{2.42}$$

As explained in Example 2.5, not all tones are active: e.g., in downstream ADSL, only the tones 38 to 255 carry data. Hence, only the TX symbols on the N_a active tones, denoted as the tone set $\mathcal{S}_a$, should be demodulated. The $N_a \times 1$ vector with the TX symbols on the active tones is denoted as $\tilde{\mathbf{x}}_k$ (i.e., without subscript N) and the corresponding $N_a \times N$ submatrix of $\mathcal{F}_N$ is denoted as $\mathcal{F}_a$. The estimate for the TX symbol vector $\tilde{\mathbf{x}}_k$ and the TX symbol $\tilde{x}_{k,n}$ at the FEQ outputs (see **Figure 2.5**) is given by:

$$\hat{\tilde{\mathbf{x}}}_k = \text{diag}(\tilde{\mathbf{d}})\tilde{\mathbf{y}}_{k,\mathbf{w},\mathbf{u}} = \text{diag}(\tilde{\mathbf{d}})\mathcal{F}_a\mathbf{\Omega}\mathbf{Y}_k\mathbf{w} \text{ and } \hat{\tilde{x}}_{k,n} = \tilde{d}_n\tilde{y}_{k,n,\mathbf{w},\mathbf{u}} = \tilde{d}_n\mathcal{F}_n\mathbf{\Omega}\mathbf{Y}_k\mathbf{w} \tag{2.43}$$

respectively, where $\tilde{\mathbf{d}}$ is the $N_a \times 1$ vector of FEQs $\tilde{d}_n$ and where $\tilde{\mathbf{y}}_{k,\mathbf{w},\mathbf{u}}$ is obtained from the DFT output vector $\tilde{\mathbf{y}}_{k,N,\mathbf{w},\mathbf{u}}$ in (2.40) by only considering the tones $\mathcal{S}_a$.

Note again that a tilde is added over a frequency-domain symbol to distinguish it from time-domain symbols, e.g., the $N_a \times 1$ TX symbol vector at time k, $\tilde{\mathbf{x}}_k$; the subscript N is used to denote frequency-domain vectors or matrices that take the N DFT bins or tones (rather than only the N_a active tones in $\mathcal{S}_a$) into account (e.g., the $N \times 1$ TX symbol vector $\tilde{\mathbf{x}}_{k,N}$ versus the $N_a \times 1$ TX symbol vector $\tilde{\mathbf{x}}_k$).

2.3.2 Data model based on an IIR channel model

As already pointed out in Section 2.2.4, the CIR in a wired communication system, such as ADSL, is typically a few hundreds of samples long. An IIR channel model or pole-zero model then offers a parsimonious representation of the channel as observed in [29], [105]. In Chapter 7, we will reconsider DMT equalization under the assumption of an IIR channel model, in combination with an arbitrary CP length ν.

Assume that the CIR $\mathbf{h}$ can be represented with an IIR channel model $H(z)$, determined by a numerator $B(z)$ of order L_b, a denominator $A(z)$ of order L_a and a propagation delay δ_0:

$$H(z) = \frac{B(z)}{A(z)} = \frac{z^{-\delta_0}\sum_{m=0}^{L_b} b_m z^{-m}}{\sum_{m=0}^{L_a} a_m z^{-m}} \tag{2.44}$$

with $a_0 = 1$. The channel model (2.44) leads to the following relation between TX samples x_l, RX samples y_l and additive noise samples n_l:

$$\sum_{m=0}^{L_a} a_m(y_{\delta_0+l-m} - n_{\delta_0+l-m}) = \sum_{m=0}^{L_b} b_m x_{l-m} \tag{2.45}$$

This input-output relation gives rise to the following block-based description of N equations:

$$\underbrace{\begin{bmatrix} [& \bar{\mathbf{a}} &] & 0 & \cdots \\ & \ddots & & \ddots & \\ \cdots & 0 & [& \bar{\mathbf{a}} &] \end{bmatrix}}_{\mathbf{A}_{\mathrm{T}}} \left(\mathbf{y}_{k,-L_a+\Delta:N-1+\Delta} - \mathbf{n}_{k,-L_a+\Delta:N-1+\Delta}\right)$$

$$= \begin{bmatrix} \mathbf{0}_{(1)} & \underbrace{\begin{bmatrix} [& \bar{\mathbf{b}} &] & 0 & \cdots \\ & \ddots & & \ddots & \\ \cdots & 0 & [& \bar{\mathbf{b}} &] \end{bmatrix}}_{\mathbf{B}_{\mathrm{T}}} & \mathbf{0}_{(2)} \end{bmatrix} (\mathbf{I}_3 \otimes \mathbf{P}_\nu \mathcal{F}_N^H) \cdot \underbrace{\begin{bmatrix} \tilde{\mathbf{x}}_{k-1,N} \\ \tilde{\mathbf{x}}_{k,N} \\ \tilde{\mathbf{x}}_{k+1,N} \end{bmatrix}}_{\tilde{\mathbf{x}}_{k-1:k+1,N}} \quad (2.46)$$

where the right-hand term, determined by the channel numerator $B(z)$, is similar to the first right-hand term of the FIR data model (2.35) and where the left-hand term comes from the channel denominator $A(z)$. The matrices $\mathbf{A}_{\mathrm{T}}$ (of size $N \times (N + L_a)$) and $\mathbf{B}_{\mathrm{T}}$ (of size $N \times (N + L_b)$) are Toeplitz convolution matrices, which are built with vectors of denominator and numerator coefficients $\mathbf{a} = \begin{bmatrix} a_0 & \cdots & a_{L_a} \end{bmatrix}^T$ and $\mathbf{b} = \begin{bmatrix} b_0 & \cdots & b_{L_b} \end{bmatrix}^T$, respectively, in reverse order (hence denoted as $\bar{\mathbf{a}}$ and $\bar{\mathbf{b}}$). The matrices $\mathbf{O}_{(1)}$ and $\mathbf{O}_{(2)}$ in (2.46) are zero matrices of size $N \times (N + 2\nu + \delta - L_b)$ and $N \times (N + \nu - \delta)$, respectively, where δ is the earlier defined decision delay and $\Delta = \delta_0 + \delta$.

2.4 Conclusions

In this chapter, we have introduced the basic concepts of MCH, MC and DMT modulation, as well as the basic principles of channel equalization and RFI mitigation as applied in DSL communication. First, we have shown how MC modulation is theoretically capable of achieving the channel capacity. Then, restrictions and approximations were introduced in order to obtain an MC modulation scheme that can be implemented in practice, namely DMT modulation. We have shown that DMT modulation is a VC scheme, which introduces a CP at the transmitter and ignores this CP at the receiver. This results in an efficient, channel-independent modulation and demodulation, based on the DFT and IDFT, and a simple equalizer, based on a bank of 1-tap FEQs.

DMT modulation as such is not suited for DSL communication. The use of an insufficiently long CP, in combination with the overlapping sinc-shaped tone spectra, results in a bit rate that is far below the channel capacity. Therefore, additional equalization and RFI cancellation are needed to recover the bit rate loss. For equalization purposes, the basic concept of a TEQ has been introduced. The application of a time-window has been suggested to improve the DFT spectral containment.

Finally, data models for DMT modulation, based on an FIR and IIR channel model, have been presented. They will be used throughout the thesis.

Chapter 3

Equalization for discrete multitone-based systems

EQUALIZER design is a crucial issue when developing a communication receiver. In Chapter 2, we have explained that DMT modulation should be supplemented with appropriate equalization to obtain a well-performing ADSL receiver. A channel-shortening TEQ has been proposed as a possible solution. So far, TEQ design indeed has been mostly considered in the DSL context.

Recently, there has been an increased interest for TEQ design in OFDM-based wireless applications. In a wireless scenario, design objectives oftentimes include bit-error rate minimization and fast adaptation to nonstationary environments. For a system with multiple TX and RX antennas, the TEQ design should be extended to a multiple-input multiple-output (MIMO) version [2, 76, 100, 124].

In this thesis, we focus on the DSL context. In DMT-based DSL systems, bit rate maximization in a slowly time-varying, single-input single-output (SISO) environment is targeted. TEQ design for ADSL has challenged many researchers since bit rate optimization of a DMT *block transmission* scheme with a TEQ *filter* leads to a highly non-linear optimization problem. Since the TEQ is in front of the demodulating DFT, all tones are treated jointly. Moreover, the poor spectral containment of the DFT imposes a difficult interference structure and may lead to noise enhancement combined with "noise pick-up" caused by out-of-band noise.

Often, simplified procedures are resorted to, mainly based on the concept of time-domain channel shortening. Two of the most popular and early channel-

shortening TEQ designs are the minimum mean-square-error (MMSE) TEQ and the maximum shortening-SNR (MSSNR) TEQ. They are discussed in Section 3.2, together with some later extensions and enhancements. Several TEQ designs, claiming but actually not achieving true bit rate maximization, have also been presented throughout the years. Their suboptimality stems form an incorrect modelling of one or more terms in the SNR model (2.32). An overview is given in Section 3.3. The suboptimality of the above mentioned TEQ designs makes them suffer from an unpredictable performance as a function of the synchronization delay parameter Δ (see (2.35)). In Chapter 4, we will present a new TEQ design, referred to as the BM-TEQ design, as it truly maximizes the bit rate.

An attractive, alternative equalizer design that also guarantees bit rate maximization is the so-called *per-tone equalizer* (PTEQ), where an equalizer is designed for each tone separately. The PTEQ design is described in Section 3.4. It is based on *two key observations*, which are of special interest as they will be frequently exploited throughout the thesis.

This chapter also provides a unifying mathematical framework and a unified notation for the equalizer designs in Section 3.1. Each of the equalizer designs in Section 3.2 to 3.4 will be cast within this framework. Simulations with most of the methods presented in this chapter will be given in Chapter 4 and compared with the performance of the BM-TEQ design developed there.

Figure 3.1 clarifies the place of each section in this chapter in the schematic thesis overview of Figure 1.5.

3.1 Common framework

Many DMT equalizers have been presented in the literature over the last decade. Remarkably, almost all of the designs fit into the same framework, as will be shown in this chapter: the maximization of a single generalized Rayleigh quotient or a product of generalized Rayleigh quotients

$$\boxed{\max_{\mathbf{w}} \prod_{n=0}^{M-1} \frac{\mathbf{w}^T \mathbf{B}_n \mathbf{w}}{\mathbf{w}^T \mathbf{A}_n \mathbf{w}}} \tag{3.1}$$

where $\mathbf{w}$ is typically (but not always) the T-tap TEQ and where M is typically equal to 1 or the number of active tones N_a; the matrices $\mathbf{A}_n$ and $\mathbf{B}_n$ will be defined for the specific TEQ designs, described throughout this chapter. Note that the solution $\mathbf{w}$ that maximizes the product $\prod_{n=0}^{M-1}(\cdot)$ also maximizes the sum of logarithms $\sum_{n=0}^{M-1} \log(\cdot)$. In general, the solution to (3.1) is not well-understood when $M > 1$. The criterion (3.1) is mostly non-convex, so there

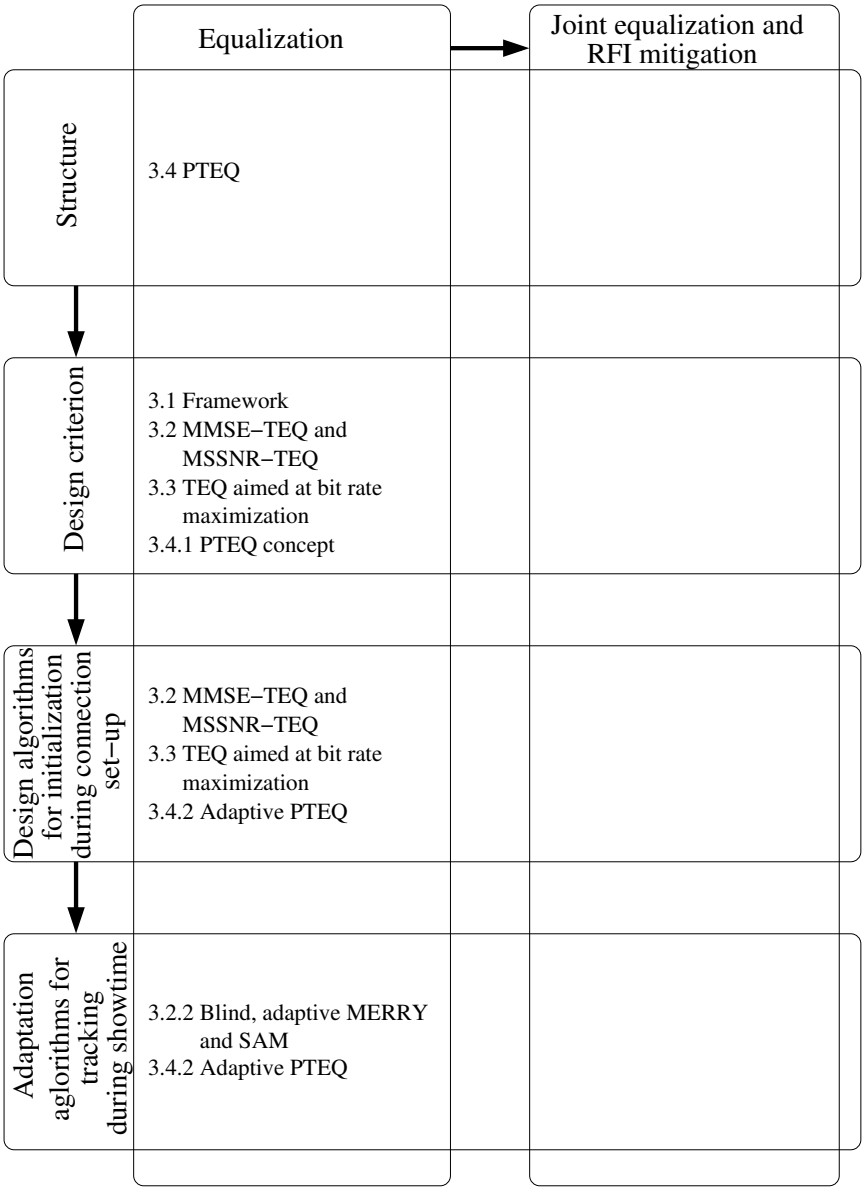


Figure 3.1: Schematic overview of this chapter.

may be many solutions that are locally optimal but not necessarily globally optimal.

Example 3.1 The TEQ designs, claiming bit rate maximization, by Al-Dhahir et al. [6], Arslan et al. [8] and Milosevic et al. [88] (see Section 3.3), as well as the new BM-TEQ design (see Chapter 4) [140, 144] obey (3.1). △

For $M = 1$, i.e.,

$$\boxed{\max_{\mathbf{w}} \frac{\mathbf{w}^T\mathbf{B}\mathbf{w}}{\mathbf{w}^T\mathbf{A}\mathbf{w}}} \tag{3.2}$$

the solution is the dominant generalized eigenvector of the generalized eigenvalue (GEV) problem

$$\mathbf{B}\mathbf{w} = \lambda\mathbf{A}\mathbf{w} \tag{3.3}$$

where the matrix pair $(\mathbf{B}, \mathbf{A})$ depends on the particular TEQ design procedure [52]. Equivalently, the inverse of the ratio in (3.2) is minimized by the generalized eigenvector of $(\mathbf{A}, \mathbf{B})$ corresponding to the smallest GEV.

Example 3.2 TEQ designs of the form (3.2) include, among others, all versions of the MMSE-TEQ design [5, 45] as well as the MSSNR-TEQ design [85], as presented in Section 3.2. In some cases, $\mathbf{A}$ or $\mathbf{B}$ is an identity matrix and (3.3) becomes a traditional eigenvalue (EV) problem. As for the PTEQ of Section 3.4, an equalizer is designed for each tone separately, which corresponds to solving (3.2) for each tone with a particular and tone-dependent matrix pair $(\mathbf{B}_n, \mathbf{A}_n)$. △

The motivation for introducing the common framework of (3.1) is to show how almost all TEQ designs require similar solution techniques, how the designs differ in terms of the number of generalized Rayleigh quotients M and the choices of the matrices $\mathbf{A}_n$ and $\mathbf{B}_n$, and how $\mathbf{A}_n$ and $\mathbf{B}_n$ arise. This allows for increased understanding of the performance of the different designs [83].

Remark 3.1 Some TEQ designs can be cast in several ways in this general framework. E.g., it will be shown in Section 4.3.4 that the BM-TEQ design, which was originally posted in a form that reduces to (3.1) (see Section 4.2), can also be formulated as the solution of an iteratively solved sequence of GEV problems (3.3), where the matrix pair $(\mathbf{B}, \mathbf{A})$ changes in each iteration. □

3.2 MMSE-TEQ and MSSNR-TEQ design

In Section 2.2.4, a channel-shortening TEQ has been suggested for equalization in DMT-based systems, such as ADSL, ADSL2 and ADSL2+. Two of the most

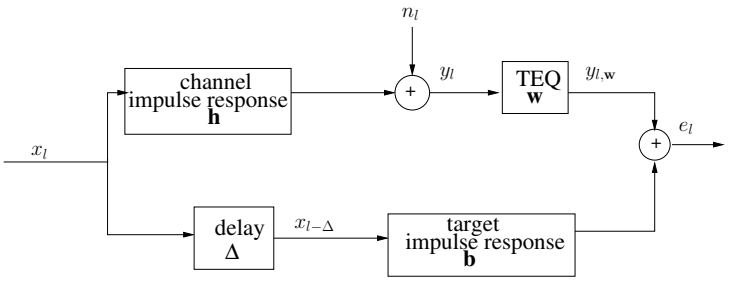


Figure 3.2: Block diagram used for MMSE channel shortening.

popular and early TEQ designs are the minimum mean-square-error (MMSE) TEQ and the maximum shortening-SNR (MSSNR) TEQ. Since their introduction, enhanced versions of the original TEQ designs have been described. Both TEQ designs and the proposed enhancements are discussed in this section. Moreover, they are cast in the common framework of Section 3.1.

3.2.1 MMSE-TEQ design

In the '70s, an MMSE method has been introduced to shorten the impulse response of a communication channel for maximum likelihood (ML) receivers [45]. The objective was to design a filter prior to the Viterbi algorithm, which is frequently used for ML data sequence estimation. This pre-filtering attempts to reduce the memory of the overall channel, resulting in an exponential decrease in computational complexity of the Viterbi algorithm.

In the early 90's, the MMSE channel shortening idea was applied to time-domain equalization in DMT-based systems [28]: a finite-length and an infinite-length TEQ have been presented to shorten the channel impulse response (CIR) to a $(\nu+1)$-tap *target impulse response* (TIR). Here, we will focus on the finite-length case. The *MMSE-TEQ design* is based on the block diagram in **Figure 3.2**. Define the $(\nu+1)\times 1$ TX sample vector $\mathbf{x}_l = \begin{bmatrix} x_l & \dots & x_{l-\nu} \end{bmatrix}^T$ and the $T\times 1$ RX sample vector $\mathbf{y}_l = \begin{bmatrix} y_l & \cdots & y_{l-T+1} \end{bmatrix}^T$. The TX signal x_l passes through the CIR $\mathbf{h}$, is corrupted by additive noise n_l and is equalized by the T-tap TEQ $\mathbf{w} = \begin{bmatrix} w_0 & \cdots & w_{T-1} \end{bmatrix}^T$. The equalizer output is compared with the TX signal, which is delayed with a synchronization delay Δ (see also the FIR data model (2.35)) and filtered by the TIR $\mathbf{b} = \begin{bmatrix} b_0 & \cdots & b_\nu \end{bmatrix}^T$. The resulting time-domain error e_l between the TEQ output, $y_{l,\mathbf{w}} = \mathbf{y}_l^T\mathbf{w}$ and the delayed TIR output $\mathbf{x}_{l-\Delta}^T\mathbf{b}$ is then minimized in the mean-square sense:

$$\min_{\mathbf{w},\mathbf{b}} \mathcal{E}\left\{|e_l|^2\right\} \;=\; \min_{\mathbf{w},\mathbf{b}} \mathcal{E}\left\{\left|\mathbf{y}_l^T\mathbf{w} - \mathbf{x}_{l-\Delta}^T\mathbf{b}\right|^2\right\} \tag{3.4}$$

$$= \min_{\mathbf{w},\mathbf{b}} \mathbf{w}^T \boldsymbol{\Sigma}_{\mathbf{y}}^2 \mathbf{w} + \mathbf{b}^T \boldsymbol{\Sigma}_{\mathbf{x}}^2 \mathbf{b} - 2\mathbf{b}^T \boldsymbol{\Sigma}_{\mathbf{xy}}(\Delta)\mathbf{w} \qquad (3.5)$$

where $\boldsymbol{\Sigma}_{\mathbf{y}}^2 = \mathcal{E}\left\{\mathbf{y}_l \mathbf{y}_l^T\right\}$ and $\boldsymbol{\Sigma}_{\mathbf{x}}^2 = \mathcal{E}\left\{\mathbf{x}_l \mathbf{x}_l^T\right\}$ are autocorrelation matrices, and where $\boldsymbol{\Sigma}_{\mathbf{xy}}(\Delta) = \mathcal{E}\left\{\mathbf{x}_{l-\Delta} \mathbf{y}_l^T\right\}$ is a crosscorrelation matrix. In the sequel, we will omit the parameter Δ for the sake of conciseness. The trivial all-zero solution $\mathbf{w} = \mathbf{0}$, $\mathbf{b} = \mathbf{0}$ is avoided by adding a constraint on the TEQ or TIR. Several proposed constraints are discussed below and the corresponding TEQ design criterion is cast in the common framework of Section 3.1. The MMSE-TEQ is computed during the connection set-up phase. The autocorrelation and crosscorrelation matrices can be computed, based on the FIR data model (2.35). A preceding channel and noise identification step is executed, based on a training signal [115].

Remark 3.2 Criterion (3.4) also applies for the design of an MMSE decision-feedback equalizer (DFE) for classical single carrier communication, as was shown in [3]. The filter $\mathbf{w}$ then corresponds to the feedforward-filter, while the filter $\mathbf{b}$ corresponds to the feedback-filter, with a straightforward unit-tap constraint (UTC), namely $b_0 = 1$. The TEQ can be viewed as a DFE, where the feedback path $\mathbf{b}$ has been omitted and replaced by a TIR $\mathbf{b}$. This introduces extra freedom as the TIR $\mathbf{b}$ is not constrained to be causal and monic, and other constraints (on $\mathbf{w}$ or $\mathbf{b}$) than a UTC can be considered [5]. □

Remark 3.3 We have argued before that DMT modulation is in essence a block transmission scheme, as data blocks, represented with symbol vectors $\tilde{\mathbf{x}}_{k,N}$, are transmitted. This results in a *cyclostationary* TX signal x_l and RX signal y_l with period $N + \nu$. The MMSE-TEQ design ignores the DMT block transmission nature. It is sample-based, hence the use of a sample index l in (3.4) rather than the DMT symbol index k (see the FIR data model (2.35)). Oftentimes, the signals x_l and y_l are assumed *stationary*, i.e., $\boldsymbol{\Sigma}_{\mathbf{x}}^2$ is approximated by an identity matrix (even when not all tones are active) and $\boldsymbol{\Sigma}_{\mathbf{y}}^2$ is assumed Toeplitz [5]. Also, the TEQ is a time-invariant filter, hence its behaviour is stationary, whereas the optimal receiver for any block transmission scheme is cyclostationary [1, 4, 32, 38]. As a consequence, a TEQ in general, and an MMSE-TEQ in particular, can never reach the optimal bit rate of a DMT-based system. Nevertheless, the simulations, presented throughout this thesis, indicate that a well-designed TEQ is capable of closely approaching the optimal bit rate. □

Unit-norm constraint (UNC) on the TEQ

Solving (3.5) subject to

$$\mathbf{w}^T \mathbf{w} = 1 \qquad (3.6)$$

using the method with Lagrange multipliers leads to a generalized Rayleigh quotient (3.2) and a GEV problem (3.3) with matrix pair

$$\mathbf{A} = \boldsymbol{\Sigma}_{\mathbf{y}}^2 - \boldsymbol{\Sigma}_{\mathbf{xy}}^T \left(\boldsymbol{\Sigma}_{\mathbf{x}}^2\right)^{-1} \boldsymbol{\Sigma}_{\mathbf{xy}} \quad (3.7)$$

$$\mathbf{B} = \mathbf{I}_T \quad (3.8)$$

As $\mathbf{B}$ is an identity matrix, the optimal TEQ is the eigenvector corresponding to the smallest EV of $\mathbf{A}$. In [134], the unsatisfactory performance of this constrained design has been reported. Under this constraint, the TEQ typically boosts "out-of-band" noise, which leaks into the band of interest due to the poor spectral containment of the demodulating DFT. In order to concentrate the TEQ energy into the desired passband region, virtual (i.e., mathematical) noise can be injected into the stopband, using a modified $\mathbf{A}$ matrix:

$$\mathbf{A} = \left(\boldsymbol{\Sigma}_{\mathbf{y}}^2 + \mu \boldsymbol{\Sigma}_{\mathbf{n},\text{virtual}}^2\right) - \boldsymbol{\Sigma}_{\mathbf{xy}}^T \left(\boldsymbol{\Sigma}_{\mathbf{x}}^2\right)^{-1} \boldsymbol{\Sigma}_{\mathbf{xy}} \quad (3.9)$$

Here, μ controls the level of the virtual noise with autocorrelation matrix $\boldsymbol{\Sigma}_{\mathbf{n},\text{virtual}}^2$. The TEQ tries to suppress the virtual noise, in this way lowering the undesired noise enhancement.

Unit-norm constraint (UNC) on the TIR

Similarly, the solution of (3.5) subject to

$$\mathbf{b}^T \mathbf{b} = 1 \quad (3.10)$$

gives rise to a classical EV problem in $\mathbf{b}$. After replacing $\mathbf{w}$ in (3.2) and (3.3) with $\mathbf{b}$, the matrix pair $(\mathbf{B}, \mathbf{A})$ is given by:

$$\mathbf{A} = \boldsymbol{\Sigma}_{\mathbf{x}}^2 - \boldsymbol{\Sigma}_{\mathbf{xy}} \left(\boldsymbol{\Sigma}_{\mathbf{y}}^2\right)^{-1} \boldsymbol{\Sigma}_{\mathbf{xy}}^T \quad (3.11)$$

$$\mathbf{B} = \mathbf{I}_{\nu+1} \quad (3.12)$$

The solution for $\mathbf{b}$ is the eigenvector corresponding to the smallest EV of $\mathbf{A}$. Based on the so-called orthogonality principle [5, 28], $\mathbf{w}$ can then be obtained as:

$$\mathbf{w} = \left(\boldsymbol{\Sigma}_{\mathbf{y}}^2\right)^{-1} \boldsymbol{\Sigma}_{\mathbf{xy}}^T \mathbf{b} \quad (3.13)$$

Note that, in [5], the term "unit-energy constraint" has been used instead of "unit-norm constraint".

Unit-tap constraint (UTC) on the TEQ

A UTC on $\mathbf{w}$ can be written compactly using the linear equation

$$\mathbf{e}_j^T \mathbf{w} = \pm 1 \quad (3.14)$$

for a specific choice of $\mathbf{e}_j$ where $\mathbf{e}_j$ is the canonical vector with element one in the j-th position. The GEV problem (3.3) is determined by:

$$\mathbf{A} = \boldsymbol{\Sigma}_{\mathbf{y}}^2 - \boldsymbol{\Sigma}_{\mathbf{xy}}^T \left(\boldsymbol{\Sigma}_{\mathbf{x}}^2\right)^{-1} \boldsymbol{\Sigma}_{\mathbf{xy}} \quad (3.15)$$

$$\mathbf{B} = \mathbf{e}_j \mathbf{e}_j^T \tag{3.16}$$

where $\mathbf{B}$ is a singular, rank-one matrix. Rather than determining the dominant generalized eigenvector, $\mathbf{w}$ can be obtained as the closed-form solution:

$$\mathbf{w} = \frac{\mathbf{A}^{-1}\mathbf{e}_j}{\mathbf{e}_j^T \mathbf{A}^{-1}\mathbf{e}_j} \tag{3.17}$$

Unit-tap constraint (UTC) on the TIR

Similarly, a UTC on $\mathbf{b}$ can be written as

$$\mathbf{e}_j^T \mathbf{b} = \pm 1 \tag{3.18}$$

The optimal TIR maximizes (3.2) with $\mathbf{w}$ replaced by $\mathbf{b}$ and

$$\mathbf{A} = \mathbf{\Sigma}_{\mathbf{x}}^2 - \mathbf{\Sigma}_{\mathbf{xy}} \left(\mathbf{\Sigma}_{\mathbf{y}}^2\right)^{-1} \mathbf{\Sigma}_{\mathbf{xy}}^T \tag{3.19}$$

$$\mathbf{B} = \mathbf{e}_j \mathbf{e}_j^T \tag{3.20}$$

After computing the solution for $\mathbf{b}$ as

$$\mathbf{b} = \frac{\mathbf{A}^{-1}\mathbf{e}_j}{\mathbf{e}_j^T \mathbf{A}^{-1}\mathbf{e}_j} \tag{3.21}$$

the TEQ coefficients can be obtained using (3.13). In [5], it has been shown that a UNC on $\mathbf{b}$ results in a lower MMSE (3.4) than a UTC on $\mathbf{b}$.

Unit-energy constraint (UEC) on TEQ and TIR

Three UECs can be considered:

$$\mathbf{w}^T \mathbf{\Sigma}_{\mathbf{y}}^2 \mathbf{w} = 1 \text{ or } \mathbf{b}^T \mathbf{\Sigma}^2{}_{\mathbf{x}} \mathbf{b} = 1 \text{ or } \mathbf{w}^T \mathbf{\Sigma}_{\mathbf{y}}^2 \mathbf{w} = 1 \,\&\, \mathbf{b}^T \mathbf{\Sigma}_{\mathbf{x}}^2 \mathbf{b} = 1 \tag{3.22}$$

It has been shown in [157] that each of these three constraints results in the same TEQ solution, up to a scaling, which can be incorporated into the one-tap FEQs. The corresponding bit rate is then the same for all UECs (3.22). Several GEV formulations are possible here:

$$\mathbf{A} = \mathbf{\Sigma}_{\mathbf{y}}^2 - \mathbf{\Sigma}_{\mathbf{xy}}^T \left(\mathbf{\Sigma}_{\mathbf{x}}^2\right)^{-1} \mathbf{\Sigma}_{\mathbf{xy}} \tag{3.23}$$

$$\mathbf{B} = \mathbf{\Sigma}_{\mathbf{y}}^2 \tag{3.24}$$

see [83], or

$$\mathbf{A} = \mathbf{I}_T \tag{3.25}$$

$$\mathbf{B} = \left(\mathbf{\Sigma}_{\mathbf{y}}^2\right)^{-1} \mathbf{\Sigma}_{\mathbf{xy}}^T \left(\mathbf{\Sigma}_{\mathbf{x}}^2\right)^{-1} \mathbf{\Sigma}_{\mathbf{xy}} \tag{3.26}$$

see [157], or, as will be shown in Section 4.3.1,

$$\mathbf{A} = \mathbf{\Sigma}_{\mathbf{y}}^2 \tag{3.27}$$

$$\mathbf{B} \quad = \quad \mathbf{\Sigma}_{\mathbf{xy}}^T \left(\mathbf{\Sigma}_{\mathbf{x}}^2\right)^{-1} \mathbf{\Sigma}_{\mathbf{xy}} \tag{3.28}$$

Iterative procedures for computing $\mathbf{w}$, based on iterative eigensolvers, have been presented in [157]. If x_l is white, then $\mathbf{\Sigma}_{\mathbf{x}}^2$ is an identity matrix and the UEC on $\mathbf{b}$ reduces to a UNC on $\mathbf{b}$, i.e., $\mathbf{b}^T\mathbf{\Sigma}_{\mathbf{x}}^2\mathbf{b} = \mathbf{b}^T\mathbf{b}$.

Discussion

The MMSE-TEQ design criterion (3.4) is very popular: as it is quadratic, it has a unique solution that can be obtained using well-known matrix computations, such as a matrix inverse or an EVD [52]. Recent advances in MMSE-TEQ design include the results of [81], which further reduce the complexity of the MMSE-TEQ design by imposing a symmetric TIR.

All of the presented MMSE-TEQ designs are time-domain (TD) criteria: they are based on a TD error e_l in front of the demodulating DFT, hence they do not account for the poor spectral containment of the DFT. As a consequence, it is hardly predictable which of the constrained designs gives the best performance. The lower MMSE of TEQ designs with a UNC, compared to a UTC, does not guarantee a better bit rate. Similarly, despite achieving a different MMSE, the TEQ designs based on any of the above mentioned UECs all attain the same bit rate, as all TEQ solutions appear to be scaled versions of one another. Moreover, as illustrated in the simulations of Section 4.4, the performance obtained with any of the MMSE-TEQ designs heavily depends on the synchronization delay Δ in (3.4), as the achievable bit rate is a non-smooth function of Δ. Hence, a search over a sufficiently large range of Δ is required to optimize the performance.

In [129], the TD-MMSE-TEQ design criterion (3.4) is supplemented with frequency weighting to disregard unused tones. This approach is further elaborated in Section 4.3. Starting from the *time-domain* (TD) MMSE-TEQ design criterion (3.4), we derive two so-called *frequency-domain* (FD) MMSE-TEQ design criteria that appear to be useful intermediate solutions between the TD-MMSE-TEQ and the bitrate maximizing TEQ (BM-TEQ) design, as they closely approach the bit rate performance of the BM-TEQ design.

3.2.2 MSSNR-TEQ design

Original MSSNR-TEQ design

The *maximum-shortening SNR (MSSNR) TEQ design* is solely based on shortening the CIR [85]. We define the following submatrices of the $T \times (L+T)$ Toeplitz channel convolution matrix $\mathbf{H}_{\mathrm{T}}$ (see also (2.35)):

$$\mathbf{H}_{\mathrm{wall},1} \quad = \quad \begin{bmatrix} h_{\Delta-T} & \cdots & h_0 & \cdots & 0 \\ \vdots & \ddots & & \ddots & \vdots \\ h_{\Delta-1} & \ldots & h_{\Delta-T} & \cdots & h_0 \end{bmatrix} \tag{3.29}$$

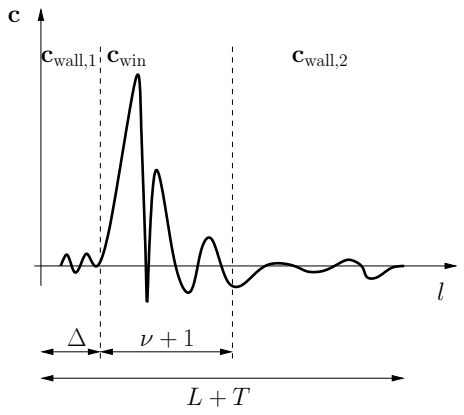


Figure 3.3: The "window" and "wall" parts of the SIR $\mathbf{c} = \mathbf{h} \star \mathbf{w}$.

$$\mathbf{H}_{\text{win}} = \begin{bmatrix} h_{\Delta+\nu-T+1} & \cdots & h_{\Delta-T+1} \\ \vdots & \ddots & \vdots \\ h_{\Delta+\nu} & \cdots & h_{\Delta} \end{bmatrix} \tag{3.30}$$

$$\mathbf{H}_{\text{wall},2} = \begin{bmatrix} h_L & \cdots & h_{\Delta+\nu+1} & \cdots & h_{\Delta+\nu-T+2} \\ \vdots & \ddots & & \ddots & \vdots \\ 0 & \cdots & h_L & \cdots & h_{\Delta+\nu+1} \end{bmatrix} \tag{3.31}$$

$$\mathbf{H}_{\text{wall}} = \begin{bmatrix} \mathbf{H}_{\text{wall},2} & \mathbf{H}_{\text{wall},1} \end{bmatrix} \tag{3.32}$$

$$\mathbf{H}_{\text{T}} = \begin{bmatrix} \mathbf{H}_{\text{wall},2} & \mathbf{H}_{\text{win}} & \mathbf{H}_{\text{wall},1} \end{bmatrix} \tag{3.33}$$

and recall that the *shortened impulse response* (SIR) was defined in Section 2.2.4 as $\mathbf{c} = \mathbf{h} \star \mathbf{w}$. Then, the MSSNR-TEQ design attempts to minimize the energy outside a window of $\nu + 1$ consecutive samples of the SIR $\mathbf{c}$, i.e., $\mathbf{c}_{\text{wall}} = \bar{\bar{\mathbf{H}}}_{\text{wall}}^T \mathbf{w} = \begin{bmatrix} \mathbf{c}_{\text{wall},1}^T & \mathbf{c}_{\text{wall},2}^T \end{bmatrix}^T$ with $\bar{\bar{\mathbf{H}}}_{\text{wall}} = \mathbf{J}_T \mathbf{H}_{\text{wall}} \mathbf{J}_{L+T-\nu-1}$ and $\mathbf{J}_m$ the $m \times m$ exchange matrix (i.e., with ones on the antidiagonal), while constraining the energy within the desired window of the SIR $\mathbf{c}$, i.e., $\mathbf{c}_{\text{win}} = \bar{\bar{\mathbf{H}}}_{\text{win}} \mathbf{w}$ with $\bar{\bar{\mathbf{H}}}_{\text{win}} = \mathbf{J}_T \mathbf{H}_{\text{win}} \mathbf{J}_{\nu+1}$, to one. The wall and the desired window of $\mathbf{c}$ are illustrated in **Figure 3.3**. The expressions for the energy outside and inside the window can be written as

$$\mathbf{c}_{\text{wall}}^T \mathbf{c}_{\text{wall}} = \mathbf{w}^T \bar{\bar{\mathbf{H}}}_{\text{wall}} \bar{\bar{\mathbf{H}}}_{\text{wall}}^T \mathbf{w} = \mathbf{c}_{\text{wall},1}^T \mathbf{c}_{\text{wall},1} + \mathbf{c}_{\text{wall},2}^T \mathbf{c}_{\text{wall},2} \tag{3.34}$$

$$\mathbf{c}_{\text{win}}^T \mathbf{c}_{\text{win}} = \mathbf{w}^T \bar{\bar{\mathbf{H}}}_{\text{win}} \bar{\bar{\mathbf{H}}}_{\text{win}}^T \mathbf{w} \tag{3.35}$$

respectively. The final TEQ coefficients are then found as

$$\min_{\mathbf{w}} \mathbf{w}^T \bar{\bar{\mathbf{H}}}_{\text{wall}} \bar{\bar{\mathbf{H}}}_{\text{wall}}^T \mathbf{w} \quad \text{subject to} \quad \mathbf{w}^T \bar{\bar{\mathbf{H}}}_{\text{win}} \bar{\bar{\mathbf{H}}}_{\text{win}}^T \mathbf{w} = 1 \tag{3.36}$$

When $\bar{\bar{\mathbf{H}}}_{\text{win}}\bar{\bar{\mathbf{H}}}_{\text{win}}^T$ has a non-trivial null space, i.e., when $\bar{\bar{\mathbf{H}}}_{\text{win}}$ has more rows than columns ($T > \nu + 1$), solving (3.36) becomes rather complicated [85].

Equivalent and enhanced MSSNR-TEQ designs

Alternatively, one can maximize the windowed energy (3.35), while constraining the wall energy (3.34) to one, as suggested in [155] and later in [107]. Since $\bar{\bar{\mathbf{H}}}_{\text{wall}}\bar{\bar{\mathbf{H}}}_{\text{wall}}^T$ is typically strictly positive definite ($L \geq \nu + 1$), this approach is preferred. It reduces to solving (3.2) with

$$\mathbf{A} = \bar{\bar{\mathbf{H}}}_{\text{wall}}\bar{\bar{\mathbf{H}}}_{\text{wall}}^T \tag{3.37}$$

$$\mathbf{B} = \bar{\bar{\mathbf{H}}}_{\text{win}}\bar{\bar{\mathbf{H}}}_{\text{win}}^T \tag{3.38}$$

One can prove that maximizing the window to wall energy $\frac{\mathbf{c}_{\text{win}}^T\mathbf{c}_{\text{win}}}{\mathbf{c}_{\text{wall}}^T\mathbf{c}_{\text{wall}}}$ provides the same TEQ solution as maximizing the overall channel to wall energy $\frac{\mathbf{c}^T\mathbf{c}}{\mathbf{c}_{\text{wall}}^T\mathbf{c}_{\text{wall}}}$ [32, 59]. The MSSNR approach tacitly assumes that the input signal is white, i.e., that all tones are active and equipowered. Furthermore, noise is ignored, so that the MSSNR-TEQ may be referred to as a zero-forcing (ZF) design [32]. In the absence of noise, the MSSNR-TEQ design is in fact equivalent to the MMSE-TEQ design of Section 3.2.1 given that the input signal is white [37].

The infinite-length MSSNR-TEQ turns out to be always symmetric or skew-symmetric [80, 81]. Therefore, it was proposed in [80, 81] to enforce a perfectly symmetric finite-length TEQ, as this allows for a drastically reduced design complexity at a negligible performance loss.

A generalization of the MSSNR-TEQ design, referred to as the *minimum ISI* (min-ISI) TEQ design, was presented in [8]. The min-ISI-TEQ design is a low-complexity approximation for Arslan's TEQ design, see Section 3.3.3. Under the assumption that $\mathbf{c}_{\text{wall}}^T\mathbf{c}_{\text{wall}}$ is a measure for the residual ISI, the min-ISI-TEQ attempts to spectrally shape the residual ISI, so that the ISI is placed on tones with a low SNR.

Blind, adaptive MSSNR-TEQ designs

All above presented TEQ designs are computed off-line during the connection set-up phase using training (to identify the channel and the noise PSD). In [79], a *blind, adaptive* channel-shortening algorithm has been presented. An adaptive algorithm is capable of tracking changing line conditions. A blind algorithm does not require training or prior channel knowledge. This method, called the MERRY ("multicarrier equalization by restoration of redundancy") TEQ design, exploits the CP redundancy to force the last sample in the equalized CP to be equal to the last sample in the equalized symbol. It adaptively solves the cost function that reflects this principle, namely

$$\min_{\mathbf{w}} \mathcal{E}\left\{\left|y_{k,\Delta-1,\mathbf{w}} - y_{k,\Delta+N-1,\mathbf{w}}\right|^2\right\} \tag{3.39}$$

where $y_{k,\Delta+N-1,\mathbf{w}}$ is the last sample of the k-th equalized sample vector $\mathbf{y}_{k,\mathbf{w}}$ (2.37) and $y_{k,\Delta-1,\mathbf{w}}$ is the last (discarded) sample of the corresponding equalized CP. A constraint, e.g., a UNC on $\mathbf{w}$ (3.6), avoids the trivial all-zero solution. From (3.39), it follows that the MERRY-TEQ design attempts to produce an SIR $\mathbf{c}$ of ν samples instead of $\nu+1$ samples, hence the wall portion of the SIR, $\mathbf{c}_{\text{wall}}$ is minimized (like in the MSSNR design) under a unit norm constraint $\mathbf{w}^T\mathbf{w} = 1$ and with an implicit noise gain limitation [79].

Another blind, adaptive TEQ design has been presented in [9]. It is referred to as the SAM ("sum-squared autocorrelation minimization") TEQ design, as it minimizes the sum-squared autocorrelation in terms of the SIR $\mathbf{c}$ outside a window of desired length $\nu + 1$:

$$\min_{\mathbf{w}} \sum_{l=\nu+1}^{L+T} |\sigma^2_{l,\mathbf{c}}|^2 \tag{3.40}$$

where $\sigma^2_{l,\mathbf{c}} = \sum_{m=0}^{L+T} \mathbf{c}[m]\mathbf{c}[m-l]$, $l = 0, \ldots, L+T$ is the autocorrelation sequence of $\mathbf{c}$ and where a constraint $\mathbf{w}^T\mathbf{w} = 1$ prevents the all-zero solution (other constraints are also possible). The rationale behind (3.40) is the fact that this cost function can be well approximated by a criterion in terms of the TEQ output $y_{k,m,\mathbf{w}}$, under the assumption that the transmit sequence x_l is white and wide-sense stationary:

$$\min_{\mathbf{w}} \sum_{l=\nu+1}^{L+T} \left|\mathcal{E}\left\{y_{k,m,\mathbf{w}} y_{k,m-l,\mathbf{w}}\right\}\right|^2 \tag{3.41}$$

This design criterion can be solved using a blind, stochastic gradient descent algorithm. As it is fourth-order in $\mathbf{w}$ (and hence multimodal), proper initialization is required.

Remark 3.4 Several other suboptimal TEQ designs have been presented in the literature. They include, among others, the minimum-delay-spread TEQ design [106], the carrier-nulling TEQ design [40] and an eigenfilter TEQ design [124]. □

3.3 TEQ design aimed at bit rate maximization

The DMT bit rate corresponds to the MC bit rate (2.9) and is given by:

$$R = \sum_{n \in \mathcal{S}_a} f_s \log_2\left(1 + \frac{\text{SNR}_n}{\Gamma_n}\right) \tag{3.42}$$

where $\mathcal{S}_a$ is the set of N_a active tones. The correct modelling of the dependence of SNR_n on the TEQ $\mathbf{w}$ poses a crucial burden. The general form of SNR_n has been given in (2.32) and is repeated here for convenience:

$$\mathrm{SNR}_n = \frac{\sigma^2_{n,\tilde{x}} \left|\check{c}_n\right|^2}{\sigma^2_{n,\tilde{n},\mathbf{w}} + \mathcal{E}\left\{\left|\mathrm{ISI}_{k,n,\mathbf{w}}\right|^2\right\} + \mathcal{E}\left\{\left|\mathrm{ICI}_{k,n,\mathbf{w}}\right|^2\right\}} \tag{3.43}$$

Since the TEQ is in front of the demodulating DFT, all tones are treated jointly. Moreover, the poor spectral containment of the DFT imposes a difficult interference (ISI/ICI) structure and may lead to noise enhancement combined with "noise pick-up" from out-of-band noise. As a consequence, the desired signal power term in the numerator of (3.43), as well as the ISI/ICI power and the noise power terms in the denominator of (3.43) are not obtained straightforwardly. Several approximations and (incorrect) assumptions have then lead to a number of TEQ designs, each based on a different SNR model.

This section discusses in chronological order several TEQ designs, which claim but actually do not achieve true bit rate optimization. We explain the approximations that are made and the progressively more rigorous SNR models that have been adopted. The development of the SNR models in the subsequent sections should be compared with the exact SNR model that is derived in Section 4.1. We will also show that most of these designs are equivalent to maximizing a product of $M = N_a$ generalized Rayleigh quotients, as in (3.1). For all of these TEQ designs, classical, computationally complex, non-linear optimization routines, such as the Broyden-Fletcher-Goldfarb-Shanno quasi-Newton algorithm, have been suggested to solve the resulting design criterion during the connection set-up phase. As the design cost criteria are non-convex, a locally optimal solution, which is not necesarrily the global optimum, is obtained.

3.3.1 Al-Dhahir's TEQ design

In [6, 7], Al-Dhahir et al. presented the first TEQ design that attempts to achieve bit rate maximization. The following bit rate expression can be shown to be equivalent to (3.42):

$$R = N_a f_s \log_2\left(1 + \frac{\mathrm{SNR}_{\mathrm{geom}}}{\Gamma}\right) \tag{3.44}$$

where the SNR gap Γ_n (see Section 2.1.3) is assumed equal for all tones and where $\mathrm{SNR}_{\mathrm{geom}}$ is a geometric SNR, given by:

$$\mathrm{SNR}_{\mathrm{geom}} \triangleq \Gamma\left\{\left[\prod_{n\in\mathcal{S}_a}\left(1 + \frac{\mathrm{SNR}_n}{\Gamma}\right)\right]^{\frac{1}{N_a}} - 1\right\} \tag{3.45}$$

Maximizing the bit rate (3.42) is then equivalent to maximizing SNR_{geom}. A first approximation in [6] assumes that $\text{SNR}_n \gg \Gamma$, so that SNR_{geom} becomes a true geometric mean of SNRs:

$$\text{SNR}_{\text{geom}} \approx \prod_{n \in \mathcal{S}_a} (\text{SNR}_n)^{\frac{1}{N_a}} \tag{3.46}$$

After defining the discrete frequency responses of the TIR $\mathbf{b}$, the TEQ $\mathbf{w}$ and the CIR $\mathbf{h}$ on tone n, $\tilde{b}_n = \mathcal{F}_{n,0:\nu}\mathbf{b}$, $\tilde{w}_n = \mathcal{F}_{n,0:T-1}\mathbf{w}$ and $\tilde{h}_n = \mathcal{F}_{n,0:L}\mathbf{h}$, respectively, and assuming that $\tilde{b}_n = \tilde{h}_n\tilde{w}_n$ (which only holds true in the case of perfect channel-shortening), an SNR model that neglects the ISI, ICI and DFT spectral leakage is adopted (compare with (3.43)):

$$\begin{aligned} \text{SNR}_n &= \frac{\sigma_{\tilde{x}}^2|\tilde{h}_n|^2}{\tilde{\sigma}_{n,\tilde{n}}^2} = \frac{\sigma_{\tilde{x}}^2|\tilde{h}_n|^2|\tilde{w}_n|^2}{\tilde{\sigma}_{n,\tilde{n}}^2|\tilde{w}_n|^2} && (3.47) \\ &= \frac{\sigma_{\tilde{x}}^2|\tilde{b}_n|^2}{\tilde{\sigma}_{n,\tilde{n}}^2|\tilde{w}_n|^2} && (3.48) \end{aligned}$$

where equal TX power $\sigma_{n,\tilde{x}}^2 = \sigma_{\tilde{x}}^2$ is assumed and where $\sigma_{n,\tilde{n}}^2$ is the noise PSD (prior to the TEQ filtering) on tone n. Maximizing (3.46) using (3.48), i.e.,

$$\max_{\mathbf{w},\mathbf{b}} \prod_{n \in \mathcal{S}_a} \left(\frac{|\tilde{b}_n|^2}{\tilde{\sigma}_{n,\tilde{n}}^2|\tilde{w}_n|^2} \right)^{\frac{1}{N_a}} \tag{3.49}$$

where $|\tilde{b}_n|^2 = \mathbf{b}^T\mathbf{G}_n\mathbf{b}$ with $\mathbf{G}_n = \mathcal{F}_{n,0:\nu}^H\mathcal{F}_{n,0:\nu}$, and under the extra assumption of independence of $\mathbf{w}$ on $\mathbf{b}$, then leads to Al-Dhahir's TEQ design criterion:

$$\max_{\mathbf{b}} \frac{1}{N_a} \sum_{n \in \mathcal{S}_a} \log\left(\mathbf{b}^T\mathbf{G}_n\mathbf{b}\right) \tag{3.50}$$

The trivial all-zero solution is avoided by imposing, e.g., a UNC on $\mathbf{b}$ (3.10). This corresponds to an optimization criterion of the form (3.1), where $\mathbf{w}$ is replaced by $\mathbf{b}$, where $M = N_a$ and where the matrix pairs $(\mathbf{B}_n, \mathbf{A}_n)$ are given by:

$$\begin{aligned} \mathbf{A}_n &= \mathbf{I}_{\nu+1} && (3.51) \\ \mathbf{B}_n &= \mathbf{G}_n && (3.52) \end{aligned}$$

An extra constraint could be added to avoid that $\mathbf{b}$ reduces to a single spike, e.g., by imposing an upper bound on the MSE (3.4). Once $\mathbf{b}$ is obtained, $\mathbf{w}$ is computed based on (3.13).

Remark 3.5 In [7], a slightly enhanced SNR model is adopted, which partially accounts for ISI. An improved, iterative solution strategy for Al-Dhahir's TEQ design is presented in [74]. □

3.3.2 Henkel's TEQ design

It is clear from the previous section that Al-Dhahir's TEQ design contains a large number of approximations and assumptions to model SNR_n (3.43). Acknowledging this fact, several improvements have been suggested by Henkel et al. in [56]. Their SNR model includes the DFT leakage effect on the noise as well as on the ISI, be it that it is assumed for the latter that all tones are active and equipowered; in fact, only the ICI term in SNR_n (3.43) is not accounted for. The leakage effect is incorporated in an original, but computationally expensive way, as the technique requires several $2N$-point DFT and IDFT operations (where N is the size of the DFT (de)modulator). The demodulating DFT performs an implicit rectangular windowing of the noise and the ISI, which can be modelled as a (twice as wide) triangular windowing of the autocorrelation function of the noise and the ISI. This autocorrelation function is obtained as the $2N$-point IDFT of the discrete noise PSD and ISI PSD, which are oversampled in the frequency domain by a factor of 2.

Later on, an approximate ICI model has been proposed [57], which allows for a further improvement of the SNR model. The simulations in Chapter 4 show that this enhanced SNR model results in a good bit rate performance, as long as almost all tones are active and equipowered. The above presented way of computing SNR_n renders the method outside of the general framework (3.1).

3.3.3 Arslan's TEQ design

The SNR model adopted by Arslan et al. in [8] improves Al-Dhahir's SNR model (3.48), based on the idea behind MSSNR-TEQ design of Section 3.2.2 to split the SIR $\mathbf{c}$ in a windowed part $\mathbf{c}_{\mathrm{win}}$ and walled parts $\mathbf{c}_{\mathrm{wall},1}$ and $\mathbf{c}_{\mathrm{wall},2}$. The windowed part $\mathbf{c}_{\mathrm{win}}$ is believed to contribute to the desired signal, hence to the numerator of SNR_n, while the walled parts $\mathbf{c}_{\mathrm{wall},1}$ and $\mathbf{c}_{\mathrm{wall},2}$ cause ISI. The new SNR model can then be seen as an enhanced version of (3.48):

$$\mathrm{SNR}_n = \frac{\sigma_{n,\tilde{x}}^2 \left|\tilde{c}_{n,\mathrm{win}}\right|^2}{\sigma_{n,\tilde{n}}^2 \left|\tilde{w}_n\right|^2 + \sigma_{n,\tilde{x}}^2 \left|\tilde{c}_{n,\mathrm{wall}}\right|^2} \tag{3.53}$$

The first term of the denominator accounts for the noise and is the same as in (3.48). The second term models the ISI. The following definitions apply:

$$\begin{aligned}
\tilde{c}_{n,\mathrm{win}} &= \mathcal{F}_n \left[\begin{array}{ccc} \mathbf{0}_{1\times\Delta} & \mathbf{c}_{\mathrm{win}}^T & \mathbf{0}_{1\times(N-\Delta-\nu-1)} \end{array} \right]^T \\
&= \mathcal{F}_{n,0:L+T-1} \mathrm{diag}(\mathbf{g}) \bar{\bar{\mathbf{H}}}_T^T \mathbf{w} \qquad (3.54) \\
\tilde{c}_{n,\mathrm{wall}} &= \mathcal{F}_n \left[\begin{array}{cccc} \mathbf{c}_{\mathrm{wall},1}^T & \mathbf{0}_{1\times(\nu+1)} & \mathbf{c}_{\mathrm{wall},2}^T & \mathbf{0}_{1\times(N-L-T)} \end{array} \right]^T \\
&= \mathcal{F}_{n,0:L+T-1} \underbrace{\left(\mathbf{I}_{L+T} - \mathrm{diag}(\mathbf{g})\right)}_{\mathrm{diag}(\check{\mathbf{g}})} \bar{\bar{\mathbf{H}}}_T^T \mathbf{w} \qquad (3.55)
\end{aligned}$$

$$\tilde{w}_n = \mathcal{F}_{n,0:T-1}\mathbf{w} \tag{3.56}$$

with $\bar{\bar{\mathbf{H}}}_T = \mathbf{J}_T\mathbf{H}_T\mathbf{J}_{L+T}$, $\mathbf{g} = \left[\begin{array}{ccc} \mathbf{0}_{1\times\Delta} & \mathbf{1}_{1\times(\nu+1)} & \mathbf{0}_{1\times(L+T-\Delta-\nu-1)} \end{array}\right]^T$ and $\mathbf{1}_{1\times m}$ an all-one vector of length m. Combining (3.53-3.56) results in the following SNR model:

$$\mathrm{SNR}_n = \frac{\mathbf{w}^T\tilde{\mathbf{B}}_n\mathbf{w}}{\mathbf{w}^T\tilde{\mathbf{A}}_n\mathbf{w}} \tag{3.57}$$

with

$$\tilde{\mathbf{A}}_n = \sigma^2_{n,\tilde{n}}\mathcal{F}^H_{n,0:T-1}\mathcal{F}_{n,0:T-1} + \sigma^2_{n,\tilde{x}}\bar{\bar{\mathbf{H}}}_T\mathrm{diag}(\check{\mathbf{g}})\mathcal{F}^H_n\mathcal{F}_n\mathrm{diag}(\check{\mathbf{g}})\bar{\bar{\mathbf{H}}}^T_T \tag{3.58}$$

$$\tilde{\mathbf{B}}_n = \sigma^2_{n,\tilde{x}}\bar{\bar{\mathbf{H}}}_T\mathrm{diag}(\mathbf{g})\mathcal{F}^H_n\mathcal{F}_n\mathrm{diag}(\mathbf{g})\bar{\bar{\mathbf{H}}}^T_T \tag{3.59}$$

Based on (3.57), the bit rate (3.42) can be modelled as a sum of logs of $M = N_a$ generalized Rayleigh quotients to obtain $\mathbf{A}_n = \Gamma_n\tilde{\mathbf{A}}_n$ and $\mathbf{B}_n = \Gamma_n\tilde{\mathbf{A}}_n + \tilde{\mathbf{B}}_n$.

Although Arslan's TEQ design improves upon Al-Dhahir's TEQ design, the partitioning of the SIR $\mathbf{c}$ as described in (3.54) and (3.55) does not tell the complete story about the desired signal part and the ISI/ICI part. Moreover, the impact of the DFT leakage on the ISI and the noise is ignored. All of this renders the SNR model inaccurate and suboptimal. Therefore, we prefer not to adopt the term "Maximum bit rate" TEQ design, which was suggested by Arslan et al. in [8].

3.3.4 Milosevic's TEQ design

A more rigorous SNR model, which again improves upon Arslan's SNR model (3.57), has been presented in [88]. The matrices $\tilde{\mathbf{A}}_n$ and $\tilde{\mathbf{B}}_n$ in the SNR model (3.57) are replaced by:

$$\tilde{\mathbf{A}}_n = 2\sigma^2_{\tilde{x}}\left(\bar{\bar{\mathbf{H}}}_{\mathrm{wall}}\left[\begin{array}{cc} \mathbf{Q}^H_{n,1}\mathbf{Q}_{n,1} & \mathbf{0} \\ \mathbf{0} & \mathbf{Q}^H_{n,2}\mathbf{Q}_{n,2} \end{array}\right]\bar{\bar{\mathbf{H}}}^T_{\mathrm{wall}}\right) + \mathbf{Q}^H_{n,n}\boldsymbol{\Sigma}^2_{\mathbf{n}}\mathbf{Q}_{n,n} + \sigma^2_{\mathrm{DNF}}\mathbf{I}_T \tag{3.60}$$

$$\tilde{\mathbf{B}}_n = \sigma^2_{\tilde{x}}\mathbf{H}_{\mathrm{T}}\mathbf{Q}^H_{x,n}\mathbf{Q}_{x,n}\mathbf{H}^T_{\mathrm{T}} \tag{3.61}$$

$\bar{\bar{\mathbf{H}}}_{\mathrm{wall}}$ and $\bar{\bar{\mathbf{H}}}_{\mathrm{T}}$ have been defined before; $\mathbf{Q}_{n,1}$, $\mathbf{Q}_{n,2}$ and $\mathbf{Q}_{n,n}$ are Hankel matrices, constructed from $\mathcal{F}_n$ (2.28) and $\mathbf{Q}_{x,n}$ is a circular Hankel matrix, also constructed from $\mathcal{F}_n$; $\boldsymbol{\Sigma}^2_{\mathbf{n}}$ is a noise autocorrelation matrix as defined below (2.35); σ^2_{DNF} allows to account for a digital noise floor from the rounding effect of the TEQ coefficients; we refer to [88] for the details on the data model. The matrices $\mathbf{A}_n$ and $\mathbf{B}_n$ in (3.1) can then be obtained from $\tilde{\mathbf{A}}_n$ and $\tilde{\mathbf{B}}_n$ in the same way as described in the previous section.

The desired signal power (i.e., the SNR numerator) is based on the assumption that the TEQ output is the result of a cyclic convolution of the SIR $\mathbf{c}$ and the TX signal x_l. However, this only holds true in the case of perfect channel shortening: as was argued in Section 2.2.4, a TEQ can not perfectly shorten an FIR channel $\mathbf{h}$ if $L > \nu$, hence the SNR numerator is only approximately correct. As a consequence, the ISI/ICI power in the SNR denominator, which is determined as the difference between the total RX signal power and the desired signal power, is also approximate. Moreover, (3.60-3.61) assumes that all tones are active and have equal TX power. Hence, (3.60) and (3.61) give rise to a suboptimal SNR model, be it that the approximations are small compared to Al-Dhahir's TEQ design of Section 3.3.1 and Arslan's TEQ design of Section 3.3.3.

3.4 Per-tone equalizer design

Whereas all previously presented TEQ designs do not maximize the bit rate, the attractive alternative *per-tone equalizer* (PTEQ) design for DMT-based systems [132] is the first equalizer scheme to achieve this goal. The PTEQ always performs at least as well as — and usually much better than — a TEQ while keeping the computational complexity during data transmission at the same level. The PTEQ consists of a set of complex-valued equalizers that are designed for each tone separately, hence the name. The PTEQ is explained in detail below. It is based on *two key observations*, which will be exploited throughout the rest of the thesis, e.g., in the derivation of the BM-TEQ design criterion in Chapter 4. Section 3.4.1 introduces the PTEQ and its underlying key observations. Section 3.4.2 describes efficient, *adaptive, training-based PTEQ design algorithms*. They will appear to be closely related to the adaptive BM-TEQ design, as developed in Chapter 5.

3.4.1 PTEQ concept

A **first key observation**, which underlies the PTEQ [132], is that the DFT output, $\tilde{\mathbf{y}}_{k,N,\mathbf{w}}$ in (2.41), can also be obtained as a linear combination $\mathbf{w}$ of the T outputs of a sliding DFT, applied to the unequalized RX sample vector $\mathbf{y}_{k,-T+1:N-1}$ in (2.35). This can be summarized mathematically by applying the associativity property to (2.41) [132]:

$$\boxed{\tilde{\mathbf{y}}_{k,N,\mathbf{w}} = \mathcal{F}_N \underbrace{(\mathbf{Y}_k \mathbf{w})}_{\mathbf{y}_{k,\mathbf{w}}} = \underbrace{(\mathcal{F}_N \mathbf{Y}_k)}_{\tilde{\mathbf{Y}}_{k,N}} \mathbf{w} \text{ and } \tilde{y}_{k,n,\mathbf{w}} = \mathcal{F}_n \underbrace{(\mathbf{Y}_k \mathbf{w})}_{\mathbf{y}_{k,\mathbf{w}}} = \underbrace{(\mathcal{F}_n \mathbf{Y}_k)}_{\tilde{\mathbf{y}}_{k,n}} \mathbf{w}} \tag{3.62}$$

The lef-hand side equations give the $N \times 1$ DFT output vector and the right-hand side equations correspond to a particular tone n. The $N \times T$ RX sample

Toeplitz matrix $\mathbf{Y}_k$ is obtained from (2.36) by setting $\mu = 0$. The sliding DFT $\mathcal{F}_N\mathbf{Y}_k$ (i.e., the DFT of the T columns of $\mathbf{Y}_k$) is denoted as $\tilde{\mathbf{Y}}_{k,N}$ ($N \times T$ matrix) and the n-th sliding DFT output is a $1 \times T$ row vector $\tilde{\mathbf{y}}_{k,n} = \mathcal{F}_n\mathbf{Y}_k$. It follows from (2.43) that the symbol estimate $\hat{\tilde{x}}_{k,n}$ at the n-th FEQ output can then be written as:

$$\hat{\tilde{x}}_{k,n} = \tilde{d}_n \tilde{y}_{k,n,\mathbf{w}} = \tilde{\mathbf{y}}_{k,n} \underbrace{(\tilde{d}_n \mathbf{w})}_{\mathbf{w}_n} \tag{3.63}$$

so that the TEQ $\mathbf{w}$ and FEQ $\tilde{d}_n$ can be combined in a single tone-dependent complex-valued $T \times 1$ *PTEQ coefficient vector* $\mathbf{w}_n$.

The n-th sliding DFT output $\tilde{\mathbf{y}}_{k,n}$ in (3.63) can be computed efficiently, without requiring the calculation of T consecutive DFTs of the columns of the Toeplitz matrix $\mathbf{Y}_k$. The outcomes $\tilde{\mathbf{y}}_{k,n}[t]$, $t \in [0, T-1]$ of the sliding DFT on tone n are related by the following recursion, which exploits the Toeplitz structure of $\mathbf{Y}_k$:

$$\tilde{\mathbf{y}}_{k,n}[t] = \alpha_n \tilde{\mathbf{y}}_{k,n}[t-1] + \underbrace{(y_{k,-t} - y_{k,N-t})}_{\Delta y_{k,-t}},\ t = 1, \ldots, T-1 \tag{3.64}$$

where $\alpha_n = \exp(-j2\pi(n-1)/N)/\sqrt{N}$. This is the **second key observation** [132]. In other words, the DFT of a column of $\mathbf{Y}_k$ can be derived from the DFT of its previous column plus some correction term. From (3.64), it follows that

$$\tilde{\mathbf{y}}_{k,n} = \underbrace{\begin{bmatrix} \Delta\mathbf{y}_k^T & \tilde{y}_{k,n} \end{bmatrix}}_{\mathbf{z}_{k,n}} \underbrace{\begin{bmatrix} 0 & \cdots & 0 & 1 \\ \vdots & \iddots & \iddots & \alpha_n \\ 0 & 1 & \iddots & \vdots \\ 1 & \alpha_n & \cdots & \alpha_n^{T-1} \end{bmatrix}}_{\mathbf{T}_n} \tag{3.65}$$

i.e., $\tilde{\mathbf{y}}_{k,n}$ is a linear combination of $T-1$ tone-independent differences of RX samples, referred to as *difference terms*, which are real-valued because of the baseband transmission nature of DSL communication:

$$\begin{aligned} \Delta\mathbf{y}_k &= \begin{bmatrix} (y_{k,-T+1} - y_{k,-T+N+1}) & \cdots & (y_{k,-1} - y_{k,N-1}) \end{bmatrix}^T \\ &= \begin{bmatrix} \Delta y_{k,-T+1} & \cdots & \Delta y_{k,-1} \end{bmatrix}^T \end{aligned} \tag{3.66}$$

and the complex-valued n-th output of the DFT of the RX sample vector $\mathbf{y}_{k,0:N-1}$:

$$\tilde{\mathbf{y}}_{k,N} = \mathcal{F}_N \mathbf{y}_{k,0:N-1},\ \tilde{\mathbf{y}}_k = \mathcal{F}_a \mathbf{y}_{k,0:N-1} \text{ and } \tilde{y}_{k,n} = \mathcal{F}_n \mathbf{y}_{k,0:N-1} = \tilde{\mathbf{y}}_{k,n}[0] \tag{3.67}$$

An efficient computation of the sliding DFT $\tilde{\mathbf{y}}_{k,n}$ for *all* N_a active tones in $\mathcal{S}_a$ then requires 1 DFT (3.67), $T-1$ differences (3.66) and $N_a(T-1)$ recursions

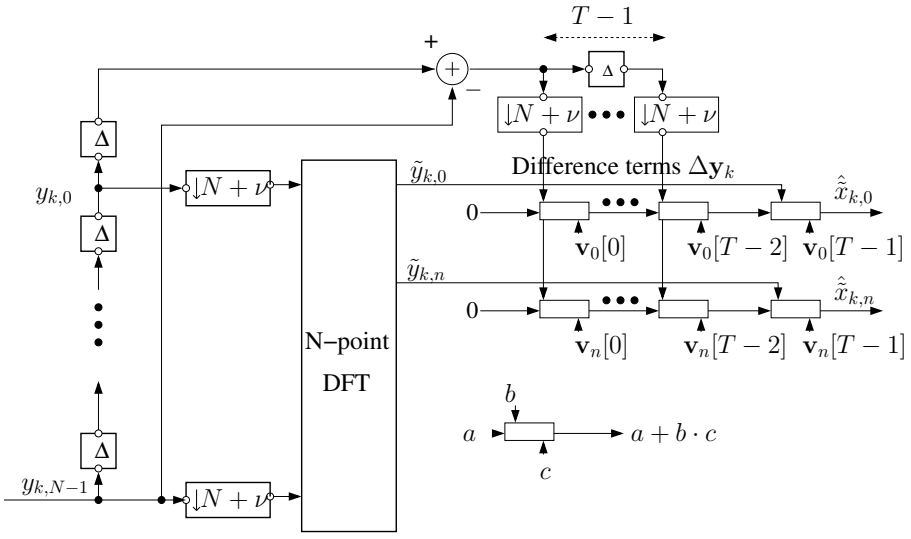


Figure 3.4: The per-tone equalizer.

(3.64). Alternatively, by combining (3.63) and (3.65), the symbol estimate $\hat{\tilde{x}}_{k,n}$ is obtained as a linear combination $\mathbf{v}_n$ of the difference terms $\Delta\mathbf{y}_k$ and the n-th DFT output $\tilde{y}_{k,n}$:

$$\hat{\tilde{x}}_{k,n} = \underbrace{\left[\begin{array}{cc} \Delta\mathbf{y}_k^T & \tilde{y}_{k,n} \end{array}\right]}_{\mathbf{z}_{k,n}} \mathbf{v}_n \tag{3.68}$$

where $\mathbf{v}_n = \mathbf{T}_n\mathbf{w}_n$. **Figure 3.4** depicts the resulting PTEQ scheme.

The PTEQ allows to determine a bit rate maximizing complex-valued $T \times 1$ PTEQ coefficient vector $\mathbf{v}_n$ for each tone separately: maximizing the bit rate (3.42) is achieved by maximizing the number of bits b_n on each tone. Maximizing b_n requires maximizing SNR_n on tone n. It then suffices to minimize the MSE at the PTEQ output, i.e., to solve the following linear MMSE cost criterion for tone n:

$$\min_{\mathbf{v}_n} \mathcal{E}\left\{|\mathbf{z}_{k,n}\mathbf{v}_n - \tilde{x}_{k,n}|^2\right\} \tag{3.69}$$

to obtain a bit rate maximizing PTEQ. The solution to (3.69) is given by

$$\mathbf{v}_n \;=\; \mathcal{E}\left\{\mathbf{z}_{k,n}^H\mathbf{z}_{k,n}\right\}^{-1}\mathcal{E}\left\{\mathbf{z}_{k,n}^H\tilde{x}_{k,n}\right\} = \left(\mathbf{\Sigma}_{n,\mathbf{z}}^2\right)^{-1}\boldsymbol{\sigma}_{n,\tilde{x}\mathbf{z}}^H \tag{3.70}$$

The autocorrelation matrix $\mathbf{\Sigma}_{n,\mathbf{z}}^2 = \mathcal{E}\left\{\mathbf{z}_{k,n}^H\mathbf{z}_{k,n}\right\}$ and crosscorrelation vector $\boldsymbol{\sigma}_{n,\tilde{x}\mathbf{z}} = \mathcal{E}\left\{\tilde{x}_{k,n}^*\mathbf{z}_{k,n}\right\}$ can be obtained, based on the definition of $\mathbf{z}_{k,n}$ in (3.68)

and the FIR data model (2.35), which requires an estimate of the channel impulse response and noise autocorrelation function.

Computational complexity and memory cost

The computational complexity of a PTEQ-based and a TEQ-based DMT receiver during data transmission is similar:

- a TEQ-based receiver requires, per DMT symbol, the convolution of the RX sample vector $\mathbf{y}_{k,-T+1:N-1}$ with the T-tap TEQ $\mathbf{w}$, i.e., NT real multiplications, plus one N-point DFT of the TEQ output;
- a PTEQ-based receiver requires, per DMT symbol, one DFT of the unequalized RX sample vector $\mathbf{y}_{k,0:N-1}$, as well as N_a linear combinations $\mathbf{v}_n$ (which is complex-valued) of 1 complex-valued DFT output $\tilde{y}_{k,n}$ and $T-1$ real-valued difference terms $\Delta\mathbf{y}_k$ (see (3.68)), i.e., $2N_a(T+1)$ real multiplications. Here, a multiplication of two complex-valued numbers has been counted as four real multiplications; similarly, the multiplication of a complex-valued an a real-valued number counts as two real multiplications.

Because of the baseband transmission nature of DSL communication, it holds true that at most $N_a = \frac{N}{2} + 1$ tones must be demodulated (see **Figure 2.5**) or $2N_a \leq N + 2$. Hence, a TEQ and a PTEQ have similar computational complexity during data transmission.

The drawback of the PTEQ structure is its memory cost: N_aT complex-valued equalizer taps $\mathbf{v}_n$ (e.g., N_a is around 220 in downstream ADSL) need to be stored, instead of T real-valued TEQ taps plus N_a complex-valued FEQ taps in the standard TEQ approach.

Remark 3.6 Equivalently to (3.69), a PTEQ $\mathbf{w}_n$ (instead of $\mathbf{v}_n$) can be computed, based on (3.63), as the solution to

$$\min_{\mathbf{w}_n} \mathcal{E}\left\{|\tilde{\mathbf{y}}_{k,n}\mathbf{w}_n - \tilde{x}_{k,n}|^2\right\} \tag{3.71}$$

The solution $\mathbf{w}_n$ is given by

$$\mathbf{w}_n \;=\; \mathcal{E}\left\{\tilde{\mathbf{y}}_{k,n}^H\tilde{\mathbf{y}}_{k,n}\right\}^{-1}\mathcal{E}\left\{\tilde{\mathbf{y}}_{k,n}^H\tilde{x}_{k,n}\right\} = \left(\mathbf{\Sigma}_{n,\tilde{\mathbf{y}}}^2\right)^{-1}\boldsymbol{\sigma}_{n,\tilde{x}\tilde{\mathbf{y}}}^H \tag{3.72}$$

so $\mathbf{\Sigma}_{n,\tilde{\mathbf{y}}}^2 = \mathcal{E}\left\{\tilde{\mathbf{y}}_{k,n}^H\tilde{\mathbf{y}}_{k,n}\right\}$ and $\boldsymbol{\sigma}_{n,\tilde{x}\tilde{\mathbf{y}}} = \mathcal{E}\left\{\tilde{x}_{k,n}^*\tilde{\mathbf{y}}_{k,n}\right\}$, and $\mathbf{w}_n$ is related to $\mathbf{v}_n$ in (3.70) by $\mathbf{v}_n = \mathbf{T}_n\mathbf{w}_n$. It will be shown in Section 4.3.6 that $\mathbf{w}_n$ is the dominant generalized eigenvector of the GEV problem (3.3) with $(\mathbf{B}_n, \mathbf{A}_n)$ given by:

$$\mathbf{A}_n \;=\; \mathbf{\Sigma}_{n,\tilde{\mathbf{y}}}^2 \tag{3.73}$$

$$\mathbf{B}_n = \boldsymbol{\sigma}^H_{n,\tilde{x}\tilde{\mathbf{y}}}\boldsymbol{\sigma}_{n,\tilde{x}\tilde{\mathbf{y}}} \tag{3.74}$$

hence the PTEQ design corresponds to maximizing a generalized Rayleigh quotient (3.2) for each tone. □

Remark 3.7 In contrast with a TEQ, the PTEQ is a linear combiner, rather than a filter: the N_a linear combinations $\mathbf{z}_{k,n}\mathbf{v}_n$ are computed once per DMT symbol. As a consequence, the PTEQ is a cyclostationary equalizer and can not be represented as a single time-invariant (stationary) filter. We have argued in Remark 2.9 that the optimal receiver in the case of a block transmission scheme such as DMT transmission is cyclostationary. An even more general cyclostationary equalizer exists where the cascade of the DFT and the PTEQs is replaced by a new set of parallel linear combiners [97, 147, 148]. Here, the linear combiners act directly on the RX samples y_l without performing a DFT to produce an estimate $\hat{\tilde{\mathbf{x}}}_k$. Simulations in [128] have shown that the PTEQ performance comes close to this more general and certainly more complex equalizer structure. □

3.4.2 Efficient, adaptive PTEQ design algorithm

Computing the MMSE solution (3.70) for all tones, based on a channel and noise model estimate, is often computationally too demanding. Therefore, an efficient, direct PTEQ design algorithm has been presented in [131], based on an *adaptive* square-root (SR) recursive least-squares (RLS) algorithm [54]. An adaptive least-mean-square (LMS) algorithm has also been considered, but turns out to converge too slowly. Using the so-called ADSL medley signal, i.e., a stream of DMT training symbols $\tilde{\mathbf{x}}_{k,N}$ that is transmitted during the DSL connection set-up phase, an RLS-update of the PTEQ for tone n at DMT symbol time k, $\mathbf{v}_{k,n}$, is given by:

$$\mathbf{v}_{k,n} \leftarrow \mathbf{v}_{k-1,n} + (1-\lambda)\left(\boldsymbol{\Sigma}^2_{k,n,\mathbf{z}}\right)^{-1}\mathbf{z}^H_{k,n}\left(\tilde{x}_{k,n} - \mathbf{z}_{k,n}\mathbf{v}_{k-1,n}\right) \tag{3.75}$$

$$\boldsymbol{\Sigma}^2_{k,n,\mathbf{z}} \leftarrow \lambda\boldsymbol{\Sigma}^2_{k-1,n,\mathbf{z}} + (1-\lambda)\mathbf{z}^H_{k,n}\mathbf{z}_{k,n} \tag{3.76}$$

The matrix $\boldsymbol{\Sigma}^2_{k,n,\mathbf{z}}$ is a recursive estimate of the PTEQ input autocorrelation matrix, encountered in (3.70), for which we define the following block-based description:

$$\boldsymbol{\Sigma}^2_{n,\mathbf{z}} = \mathcal{E}\left\{\begin{bmatrix}\Delta\mathbf{y}_k \\ \tilde{y}^*_{k,n}\end{bmatrix}\begin{bmatrix}\Delta\mathbf{y}^T_k & \tilde{y}_{k,n}\end{bmatrix}\right\} = \begin{bmatrix}\boldsymbol{\Sigma}^2_{\Delta\mathbf{y}} & \boldsymbol{\sigma}^H_{n,\tilde{y}\Delta\mathbf{y}} \\ \boldsymbol{\sigma}_{n,\tilde{y}\Delta\mathbf{y}} & \sigma^2_{n,\tilde{y}}\end{bmatrix} = \mathbf{U}^H_n\mathbf{U}_n \tag{3.77}$$

By including an exponential weighting λ, one allows for tracking of a changing environment [54].

The fact that the PTEQ has only one tone-dependent input $\tilde{y}_{k,n}$ per tone, together with $T-1$ inputs $\Delta\mathbf{y}_k$ that are common for all tones, has a beneficial

impact on the computational and memory cost of the updating algorithm (3.75-3.76). Instead of storing and updating $\mathbf{\Sigma}^2_{k,n,\mathbf{z}}$ for all active tones $\mathcal{S}_a$, it is preferable to store and update the inverse transpose of the Cholesky factor (square-root) $\mathbf{U}_{k,n}$ of $\mathbf{\Sigma}^2_{k,n,\mathbf{z}}$, i.e., an estimate $\mathbf{S}_{k,n}$ of the lower triangular matrix $\mathbf{S}_n$ with $\left(\mathbf{\Sigma}^2_{n,\mathbf{z}}\right)^{-1} = \mathbf{S}_n^H \mathbf{S}_n$. By construction, the $T-1$ first rows of $\mathbf{S}_n$ constitute a triangular matrix, denoted as $\mathbf{S}_\Delta$ (such that $\left(\mathbf{\Sigma}^2_{\Delta\mathbf{y}}\right)^{-1} = \mathbf{S}_\Delta^T \mathbf{S}_\Delta$), which is real-valued and common for all tones, and hence tone-independent; one update of the estimate $\mathbf{S}_{k,\Delta}$ requires $\mathcal{O}(T^2)$ computations; the memory cost to store $\mathbf{S}_{k,\Delta}$ is also $\mathcal{O}(T^2)$. Only the last, complex-valued row of $\mathbf{S}_n$, denoted as $\mathbf{s}_n$, is tone-dependent; the estimate $\mathbf{s}_{k,n}$ requires $\mathcal{O}(T)$ computations per update and T complex-valued coefficients per active tone. The partitioning $\mathbf{S}_{k,n} = \left[\begin{array}{cc} \mathbf{S}^T_{k,\Delta} & \mathbf{s}^H_{k,n} \end{array}\right]^H$ then leads to an efficient computation of the so-called Kalman gain vector in (3.75) [54]:

$$\left(\mathbf{\Sigma}^2_{k,n,\mathbf{z}}\right)^{-1} \mathbf{z}^H_{k,n} = \mathbf{S}^T_{k,\Delta} \mathbf{S}_{k,\Delta} \Delta\mathbf{y}_k + \mathbf{s}^H_{k,n} \left(\mathbf{s}_{k,n} \mathbf{z}^H_{k,n}\right) \tag{3.78}$$

The first term is tone-independent and requires $\mathcal{O}(T^2)$ computations, while the second, tone-dependent term requires $\mathcal{O}(T)$ computations per active tone. In ADSL downstream where $N_a \gg T$, the overall memory and computational cost is dominated by the tone-dependent (i.e., second) term in (3.78). One update (3.75-3.76) then requires $\mathcal{O}(18 N_a T)$ real multiplications per update. We refer to [131] for further details.

In [161], it has been shown that a further complexity reduction is possible with a so-called hybrid RLS/LMS-based adaptive PTEQ design algorithm. The idea is to ignore the two off-diagonal tone-dependent blocks of $\mathbf{\Sigma}^2_{n,\mathbf{z}}$ in (3.77) and use instead:

$$\check{\mathbf{\Sigma}}^2_{n,\mathbf{z}} = \left[\begin{array}{cc} \mathbf{\Sigma}^2_{\Delta\mathbf{y}} & \mathbf{0} \\ \mathbf{0} & \sigma^2_{n,\tilde{y}} \end{array}\right] = \check{\mathbf{U}}^H_n \check{\mathbf{U}}_n \tag{3.79}$$

The inverse transpose of the Cholesky factor $\check{\mathbf{U}}_n$ of $\check{\mathbf{\Sigma}}^2_{n,\mathbf{z}}$, denoted as $\check{\mathbf{S}}_n$, has the same $T-1$ first rows as $\mathbf{S}_n$, which are equal to $\mathbf{S}_\Delta$. In the last tone-dependent row $\check{\mathbf{s}}_n$, only the last element is non-zero and equal to $\check{\mathbf{s}}_n[T-1] = \sqrt{\sigma^{-2}_{n,\tilde{y}}}$. The Kalman gain vector (3.78) then reduces to:

$$\left(\check{\mathbf{\Sigma}}^2_{k,n,\mathbf{z}}\right)^{-1} \mathbf{z}^H_{k,n} = \left[\begin{array}{c} \mathbf{S}^T_{k,\Delta} \mathbf{S}_{k,\Delta} \Delta\mathbf{y}_k \\ \sigma^{-2}_{k,n,\tilde{y}} \tilde{y}^*_{k,n} \end{array}\right] \tag{3.80}$$

In the full RLS PTEQ algorithm (3.75-3.76), the complete PTEQ input vector $\mathbf{z}_{k,n}$ is whitened by $\mathbf{S}_{k,n}$. In the hybrid RLS/LMS PTEQ algorithm, the tone-independent part $\mathbf{S}_{k,\Delta}$ whitens the difference terms $\Delta\mathbf{y}_k$, while the non-zero element $\sqrt{\sigma^{-2}_{k,n,\tilde{y}}}$ normalizes the tone-dependent DFT output $\tilde{y}_{k,n}$ in a similar way as the normalized-LMS algorithm. The hybrid RLS/LMS PTEQ algorithm has a memory cost of $N_a + \frac{T(T-1)}{2}$ real coefficients and a computational complexity that is dominated by $\mathcal{O}(3T^2)$ real multiplications for the

tone-independent part [161]. Simulations with both adaptive PTEQ design algorithms, illustrating their convergence behaviour, are included in Chapter 5.

3.5 Conclusions

In this chapter, we have discussed existing equalizer designs for DMT-based systems and we have cast them in a general framework. TEQ design has inspired many researchers since bit rate optimization of a DMT-based system with a TEQ indeed leads to a complex non-linear optimization problem. Often, simplified procedures are resorted to, mainly based on the concept of time-domain channel shortening. Two of the most popular and early channel-shortening TEQ designs are the MMSE-TEQ design and the MSSNR-TEQ design. Several TEQ designs, claiming but actually not achieving true bit rate maximization, have also been presented throughout the years. We have given an overview of these designs and we have indicated that approximations and assumptions in the adopted SNR model render them suboptimal. The only bit rate maximizing DMT equalizer that has been presented so far is the PTEQ. The PTEQ is an alternative for the TEQ, where an equalizer is designed for each tone separately. The PTEQ is preferably designed adaptively. The presented RLS-based adaptive algorithm can then also be used for tracking purposes. It has been argued that the PTEQ and the TEQ have a similar computational complexity; the drawback of the PTEQ is the large memory requirement, as T equalizer tap values need to be stored per tone.

In Chapter 4, we therefore propose the *bit rate maximizing TEQ (BM-TEQ) design* that closely approaches the PTEQ performance. In Chapter 5, it will be shown that the BM-TEQ and the PTEQ are extreme cases of a so-called *bit rate maximizing per-group equalizer scheme*, where the active tones are divided into groups of tones and an equalizer is designed per tone group. An *adaptive* BM-TEQ design, which has the same memory cost as the adaptive PTEQ of Section 3.4.2, is also presented in Chapter 5. In Chapter 7, equalization for DMT-based transmission over *an IIR channel* is considered. It will be shown that the PTEQ is particularly suited for the equalization of an IIR channel and several *PTEQ extensions* will be proposed.

Chapter 4

Bit rate maximizing time-domain equalizer design

TEQ design that truly maximizes the bit rate of DMT-based DSL communication is a long standing problem. In the previous chapter, an overview has been given of the most important TEQ designs that have been developed over the last decade. MMSE-TEQ and MSSNR-TEQ designs are based on time-domain cost criteria that aim at low computational complexity, and, as such, do not provide bit rate maximization. A number of authors have presented TEQ design attempts to maximize bit rate, but several assumptions and approximations render these methods suboptimal. The adopted SNR model is crucial and should accurately account for the dependence of the residual ISI/ICI and DFT leakage of the noise on the TEQ coefficients. However, the TEQ design methods presented so far only partially do so.

In Section 4.1, an *exact SNR model* is derived, based on the FIR data model (2.35) presented in Section 2.3.1. For simplicity and clarity, a toy example is used with a short channel and a small DFT size and CP length. Comparing this exact SNR model with the earlier adopted SNR models of Section 3.3 allows to assess their accuracy. The exact SNR model depends in a non-trivial way on the TEQ, the FIR channel and the TX signal and noise statistics.

In Section 4.2, a *bit rate maximizing TEQ* (BM-TEQ) design is presented. Therefore, an alternative, exact SNR model is derived, which is equivalent to the SNR model of Section 4.1. Whereas the latter SNR model depends in a rather cumbersome way on the FIR channel and the TX signal and noise

second-order statistics (SOS), the new SNR model is described in a compact and elegant way in terms of the TX and RX signal SOS. The key element in the derivation of this new SNR model is the observation that the dependence of the SNR on the TEQ taps is easily accounted for when considering an SNR model at the *FEQ output*. For the TEQ designs described in Section 3.3, the SNR is considered at the *FEQ input*, i.e., the DFT output. This new SNR model then leads to the BM-TEQ design criterion, which fits in the general framework of Section 3.1.

The BM-TEQ design criterion of Section 4.2 is a non-linear cost criterion in $\mathbf{w}$, which asks for classical non-linear optimization routines and which hides the specific TEQ-FEQ receiver structure. In Section 4.3, an alternative, so-called *iteratively reweighted separable nonlinear least-squares (IR-SNLLS) based BM-TEQ design criterion* is presented. This least-squares (LS) based formulation has several advantages. The cost criterion can be optimized with an elegant, iterative, fast-converging *Gauss-Newton-based algorithm* or, alternatively, with an recursive Levenberg-Marquardt algorithm, as is explained in Chapter 5. Moreover, a common LS-based equalizer framework is elaborated, which allows to establish a close relationship between the LS-based BM-TEQ design and LS-based formulations of the (time-domain) MMSE-TEQ and PTEQ design criteria by means of two so-called frequency-domain (FD) MMSE-TEQ designs.

The simulations in Section 4.4 show that a T-tap BM-TEQ outperforms all earlier presented TEQ designs and approaches very closely the performance of the PTEQ with T taps per tone. Both the BM-TEQ and the PTEQ solve the often encountered problem with suboptimal TEQ designs, namely that they exhibit a performance that strongly depends on the synchronization delay Δ and hence require a delay optimization step to avoid poor performance. The performance of the two FD-MMSE-TEQ designs of Section 4.3 is also illustrated and the fast convergence of the iterative Gauss-Newton-based algorithm for optimizing the SNLLS-based FD-MMSE-TEQ and BM-TEQ designs is depicted.

Figure 4.1 clarifies the place of each section in this chapter in the schematic thesis overview of Figure 1.5.

4.1 Channel-based SNR model

In this section, an exact SNR model is derived, based on the FIR data model (2.35) presented in Section 2.3.1. For simplicity and clarity, a toy example is used with a DFT size $N = 4$, a CP length $\nu = 1$, a synchronization delay $\Delta = 1$, and an SIR $\mathbf{c} = \begin{bmatrix} c_0 & c_1 & c_2 & c_3 \end{bmatrix} = \mathbf{h} \star \mathbf{w}$ of length $L + T = 4$. This toy example then readily extends to the general case, for which we include guidelines. Comparing this exact SNR model with the earlier adopted SNR models of Section 3.3 allows to assess their accuracy. The derivation in this

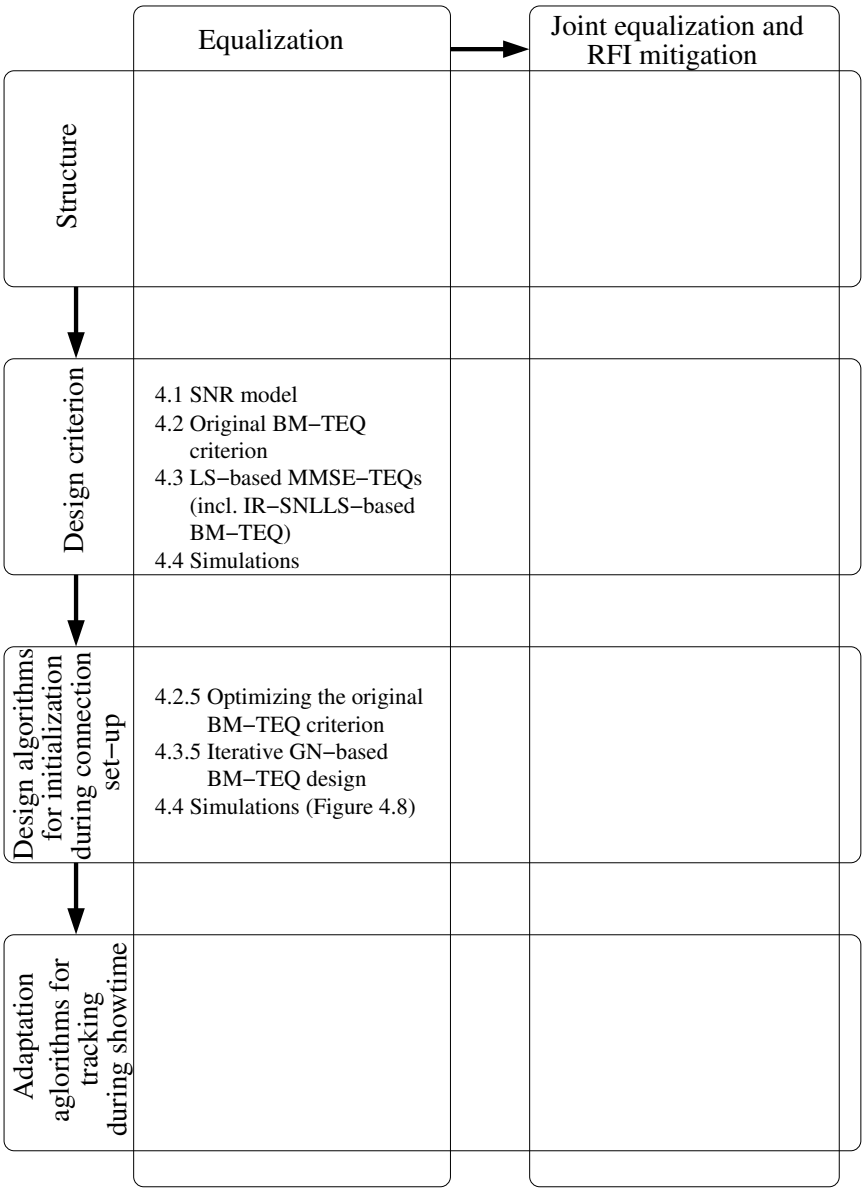


Figure 4.1: Schematic overview of this chapter.

section shows that all terms (the desired RX signal power, the residual ISI/ICI power and the noise power) in the exact SNR model (2.32) depend in a non-trivial way on the TEQ $\mathbf{w}$, the FIR channel and the noise and signal statistics.

The SNR model (2.32) is repeated here for convenience:

$$\mathrm{SNR}_n = \frac{\sigma^2_{n,\tilde{x}} \left|\check{c}_n\right|^2}{\sigma^2_{n,\tilde{n},\mathbf{w}} + \mathcal{E}\left\{\left|\mathrm{ISI}_{k,n,\mathbf{w}}\right|^2\right\} + \mathcal{E}\left\{\left|\mathrm{ICI}_{k,n,\mathbf{w}}\right|^2\right\}} \tag{4.1}$$

Data model

The k-th $N \times 1$ equalized sample vector $\mathbf{y}_{k,\mathbf{w}}$ follows from the FIR data model (2.35) by replacing $\mathbf{h}$ with $\mathbf{c}$. For the considered toy example, this results in:

$$\underbrace{\begin{bmatrix} y_{k,1,\mathbf{w}} \\ y_{k,2,\mathbf{w}} \\ y_{k,3,\mathbf{w}} \\ y_{k,4,\mathbf{w}} \end{bmatrix}}_{\mathbf{y}_{k,\mathbf{w}}} = \underbrace{\left[\begin{array}{cc|cccc|c} c_3 & c_2 & c_1 & c_0 & 0 & 0 & 0 \\ 0 & c_3 & c_2 & c_1 & c_0 & 0 & 0 \\ 0 & 0 & c_3 & c_2 & c_1 & c_0 & 0 \\ 0 & 0 & 0 & c_3 & c_2 & c_1 & c_0 \end{array}\right]}_{\mathbf{C}_{\mathrm{T}}} \begin{bmatrix} x_{k-1,3} \\ x_{k,3,(\mathrm{CP})} \\ x_{k,0} \\ x_{k,1} \\ x_{k,2} \\ x_{k,3} \\ x_{k+1,3,(\mathrm{CP})} \end{bmatrix} + \underbrace{\begin{bmatrix} n_{k,0,\mathbf{w}} \\ n_{k,1,\mathbf{w}} \\ n_{k,2,\mathbf{w}} \\ n_{k,3,\mathbf{w}} \end{bmatrix}}_{\mathbf{n}_{k,\mathbf{w}}} \tag{4.2}$$

where $\mathbf{n}_{k,\mathbf{w}}$ is the noise sample vector after TEQ filtering, where the CP has been denoted explicitly, where the delay $\Delta = 1$ causes a contribution from the future $(k+1)$-th DMT symbol and where the k-th TX sample vector (without CP) is the IDFT of the TX symbol vector $\tilde{\mathbf{x}}_{k,N}$:

$$\underbrace{\begin{bmatrix} x_{k,0} \\ x_{k,1} \\ x_{k,2} \\ x_{k,3} \end{bmatrix}}_{\mathbf{x}_k} = \mathcal{F}_N^H \underbrace{\begin{bmatrix} \tilde{x}_{k,0} \\ \tilde{x}_{k,1} \\ \tilde{x}_{k,2} \\ \tilde{x}_{k,3} \end{bmatrix}}_{\tilde{\mathbf{x}}_{k,N}} \tag{4.3}$$

A convenient way to obtain expressions for the ISI and ICI power is by enforcing a circulant channel matrix $\mathbf{C}_{\mathrm{C}}$ and rewriting (4.2) as follows:

$$\begin{aligned} \mathbf{y}_{k,\mathbf{w}} = & \underbrace{\begin{bmatrix} c_1 & c_0 & c_3 & c_2 \\ c_2 & c_1 & c_0 & c_3 \\ c_3 & c_2 & c_1 & c_0 \\ c_0 & c_3 & c_2 & c_1 \end{bmatrix}}_{\mathbf{C}_{\mathrm{C}}} \mathbf{x}_k + \underbrace{\begin{bmatrix} c_3 & c_2 \\ 0 & c_3 \\ 0 & 0 \\ 0 & 0 \end{bmatrix} \begin{bmatrix} x_{k-1,3} - x_{k,2} \\ \underbrace{x_{k,3} - x_{k,3}}_{0} \end{bmatrix}}_{\{1\}} \\ & + \underbrace{\begin{bmatrix} 0 \\ 0 \\ 0 \\ c_0 \end{bmatrix} \begin{bmatrix} x_{k+1,3} - x_{k,0} \end{bmatrix}}_{\{2\}} + \mathbf{n}_{k,\mathbf{w}} \end{aligned} \tag{4.4}$$

Note that the CP renders one of the differences in the term $\{1\}$ zero; in general, there are at most ν entries equal to zero. As in (2.23), we will exploit a

DFT-based decomposition of the circulant matrix $\mathbf{C}_{\mathrm{C}} = \mathcal{F}_N^H \mathbf{C}_{N,\mathrm{D}} \mathcal{F}_N$ where $\mathbf{C}_{N,\mathrm{D}} = \mathrm{diag}(\tilde{\mathbf{c}}_N)$ is a diagonal matrix with the discrete frequency response of the SIR, i.e., $\tilde{\mathbf{c}}_N = \mathcal{F}_{N,0:L+T-1}\mathbf{c} = \left[\begin{array}{cccc} \tilde{c}_0 & \tilde{c}_1 & \tilde{c}_2 & \tilde{c}_3 \end{array}\right]^T$, along the diagonal. By making use of (4.3) and by taking the DFT of (4.4), we then obtain:

$$\tilde{\mathbf{y}}_{k,N,\mathbf{w}} = \underbrace{\mathbf{C}_{N,\mathrm{D}}\tilde{\mathbf{x}}_{k,N}}_{\{1\}} + \underbrace{\mathcal{F}_N \left[\begin{array}{c|c} c_3 & 0 \\ 0 & 0 \\ \hline 0 & 0 \\ 0 & c_0 \end{array}\right] \left[\begin{array}{c} x_{k-1,3} - x_{k,2} \\ x_{k+1,3} - x_{k,0} \end{array}\right]}_{\{2\}} + \tilde{\mathbf{n}}_{k,N,\mathbf{w}} \tag{4.5}$$

where $\tilde{\mathbf{y}}_{k,N,\mathbf{w}} = \mathcal{F}_N \mathbf{y}_{k,\mathbf{w}}$ and $\tilde{\mathbf{n}}_{k,N,\mathbf{w}} = \mathcal{F}_N \mathbf{n}_{k,\mathbf{w}}$. Based on (4.5), we can derive expressions for the ISI, ICI, noise and desired RX signal power terms in (4.1). Below, we will concentrate on the demodulation of tone $n = 3$, i.e., the estimation of the TX symbol $\tilde{x}_{k,3}$, as an example.

ISI power

ISI is caused by neighbouring DMT symbols, transmitted at time instants $k-1$ and $k+1$. In our toy example (4.5), $x_{k-1,3}$ and $x_{k+1,3}$ in the term denoted by $\{2\}$ are causing ISI with power $\mathcal{E}\left\{\left|\mathrm{ISI}_{k,n,\mathbf{w}}\right|^2\right\}$ equal to:

$$\mathcal{F}_3 \left[\begin{array}{c|c} c_3 & 0 \\ 0 & 0 \\ 0 & 0 \\ \hline 0 & c_0 \end{array}\right] \underbrace{\mathcal{E}\left\{\left[\begin{array}{c} x_{k-1,3} \\ x_{k+1,3} \end{array}\right] \left[\begin{array}{cc} x_{k-1,3} & x_{k+1,3} \end{array}\right]\right\}}_{\{3\}} \left[\begin{array}{c|c} c_3 & 0 \\ 0 & 0 \\ 0 & 0 \\ \hline 0 & c_0 \end{array}\right]^T \mathcal{F}_3^H \tag{4.6}$$

In general, for an SIR $\mathbf{c}$ of arbitrary length $L+T$, a CP length ν and a delay Δ, c_3 and $x_{k-1,3}$ should be replaced with the upper triangular Toeplitz matrix

$$c_3 \leftarrow \left[\begin{array}{cccc} c_{L+T-1} & c_{L+T-2} & \cdots & c_{\Delta+\nu+1} \\ 0 & c_{L+T-1} & \ddots & c_{\Delta+\nu+2} \\ \vdots & \ddots & \ddots & \vdots \\ 0 & 0 & 0 & c_{L+T-1} \end{array}\right] \tag{4.7}$$

and vector

$$x_{k-1,3} \leftarrow \left[\begin{array}{c} x_{k-1,N-(L+T-\Delta-\nu-1)} \\ \vdots \\ x_{k-1,N-1} \end{array}\right] \tag{4.8}$$

respectively, and c_0 and $x_{k+1,3}$ should be replaced with the lower triangular Toeplitz matrix

$$c_0 \leftarrow \begin{bmatrix} c_0 & 0 & \cdots & 0 \\ \vdots & \ddots & \ddots & \vdots \\ c_{\Delta-2} & \ddots & c_0 & 0 \\ c_{\Delta-1} & \cdots & c_1 & c_0 \end{bmatrix} \tag{4.9}$$

and vector

$$x_{k+1,3} \leftarrow \begin{bmatrix} x_{k+1,N-\nu} \\ \vdots \\ x_{k+1,N-\nu+\Delta-1} \end{bmatrix} \text{ if } \Delta \leq \nu \text{ or } x_{k+1,3} \leftarrow \begin{bmatrix} x_{k+1,N-\nu} \\ \vdots \\ x_{k+1,N-1} \\ x_{k+1,0} \\ \vdots \\ x_{k+1,\Delta-1-\nu} \end{bmatrix} \text{ if } \Delta > \nu \tag{4.10}$$

respectively. The correlation matrix $\{3\}$ in (4.6) is a scaled identity matrix if the TX signal x_l is white, i.e., if all tones are active and have equal TX power $\sigma^2_{n,\tilde{x}}$. This is typically not the case. The correlation matrix $\{3\}$ in (4.6) is then a non-diagonal 2×2 matrix (in general: an $(L+T-1-\nu) \times (L+T-1-\nu)$ block diagonal matrix) that takes the TX power allocation into account.

ICI power

ICI is caused by interference from TX symbols $\tilde{x}_{k,m}$ within the k-th DMT symbol, with $m \neq 3$. As noted in Section 2.2.4, ICI could also be termed "*intra*-symbol" interference. The first term in (4.5), denoted by $\{1\}$, is decoupled per tone (because of the diagonal matrix $\mathbf{C}_{N,\mathrm{D}}$), so no ICI is caused by that term. All ICI stems from the second term $\{2\}$, more specifically, from the samples $x_{k,2}$ and $x_{k,0}$. Note that for a general SIR of length $L+T$, these samples should be replaced by the following vectors:

$$x_{k,2} \leftarrow \begin{bmatrix} x_{k,N-L-T+1+\Delta} \\ \vdots \\ x_{k,N-\nu-1} \end{bmatrix} \text{ and } x_{k,0} \leftarrow \begin{bmatrix} x_{k,\Delta-1} \\ \vdots \\ x_{k,0} \end{bmatrix} \tag{4.11}$$

However, the samples $x_{k,2}$ and $x_{k,0}$ also contain a contribution from the desired TX symbol $\tilde{x}_{k,3}$ which should not be considered as ICI:

$$\begin{aligned} x_{k,2} &= \mathcal{F}_2^* \tilde{\mathbf{x}}_{k,N} = \underbrace{\mathcal{F}^*_{2,0:2} \tilde{\mathbf{x}}_{k,0:2}}_{\{1\}} + \underbrace{\mathcal{F}^*_{2,3} \tilde{x}_{k,3}}_{\{2\}} \\ x_{k,0} &= \mathcal{F}_0^* \tilde{\mathbf{x}}_{k,N} = \underbrace{\mathcal{F}^*_{0,0:2} \tilde{\mathbf{x}}_{k,0:2}}_{\{1\}} + \underbrace{\mathcal{F}^*_{0,3} \tilde{x}_{k,3}}_{\{2\}} \end{aligned} \tag{4.12}$$

where $\mathcal{F}^*_{n,i:j}$ ($\mathcal{F}^*_{n,i}$) denotes the elements i to j (the i-th element) of the n-th row of the IDFT matrix and where $\tilde{\mathbf{x}}_{k,0:2}$ contains the first three elements of $\tilde{\mathbf{x}}_{k,N}$. Only the terms $\{1\}$ in (4.12) cause ICI, while the terms $\{2\}$ contribute to the desired RX signal. Hence the ICI power $\mathcal{E}\left\{\left|\mathrm{ICI}_{k,n,\mathbf{w}}\right|^2\right\}$ is given by:

$$\mathcal{F}_3 \left[\begin{array}{c|c} c_3 & 0 \\ 0 & 0 \\ 0 & 0 \\ 0 & c_0 \end{array}\right] \left[\begin{array}{c} \mathcal{F}^*_{2,0:2} \\ \mathcal{F}^*_{0,0:2} \end{array}\right] \mathcal{E}\left\{\tilde{\mathbf{x}}_{k,0:2}\tilde{\mathbf{x}}^H_{k,0:2}\right\} \left[\begin{array}{c} \mathcal{F}^*_{2,0:2} \\ \mathcal{F}^*_{0,0:2} \end{array}\right]^H \left[\begin{array}{c|c} c_3 & 0 \\ 0 & 0 \\ 0 & 0 \\ 0 & c_0 \end{array}\right]^T \mathcal{F}_3^H \tag{4.13}$$

Desired RX signal power

Based on the term $\{1\}$ in (4.5), we could conclude that the desired RX signal power on tone n is given by $\left|\tilde{c}_n\right|^2 \sigma^2_{n,\tilde{x}}$. However, the terms $\{2\}$ in (4.12) should also be taken into account. The desired RX signal power for tone 3 is then given by $\left|\check{c}_3\right|^2 \sigma^2_{3,\tilde{x}}$ with

$$\left|\check{c}_3\right|^2 = \left|\tilde{c}_3 - \mathcal{F}_3 \left[\begin{array}{c} c_3 \\ 0 \\ 0 \\ 0 \end{array}\right] \mathcal{F}^*_{2,3} - \mathcal{F}_2 \left[\begin{array}{c} 0 \\ 0 \\ 0 \\ c_0 \end{array}\right] \mathcal{F}^*_{0,3}\right|^2 \tag{4.14}$$

Noise power

It follows from (4.5) that the noise power on tone 3 is given by

$$\sigma^2_{3,\tilde{n},\mathbf{w}} = \mathcal{F}_3 \mathcal{E}\left\{\mathbf{n}_{k,\mathbf{w}}\mathbf{n}^T_{k,\mathbf{w}}\right\}\mathcal{F}_3^H \tag{4.15}$$

SNR model

Based on the power terms derived above, an exact SNR model of the form $\frac{\mathbf{w}^T\tilde{\mathbf{B}}_n\mathbf{w}}{\mathbf{w}^T\tilde{\mathbf{A}}_n\mathbf{w}}$ as in (3.57) can be given. However, it is clear that correct expressions for $\tilde{\mathbf{B}}_n$ and $\tilde{\mathbf{A}}_n$ are tedious. Therefore, we will derive an alternative, compact SNR model in the next section, that is equivalent to the SNR model derived here. Rather than describing SNR_n in terms of the SIR and the signal and noise statistics, the SNR model of Section 4.2 is given in terms of TX and RX signal SOS.

Remark 4.1 A derivation of the ISI and ICI power in a DMT-based system has first been given in [98]. The matrix-based derivation presented above coincides with these early results. As already suggested in Section 3.3.2 on Henkel's TEQ design, a derivation, similar to [98], was given later in [57]. This derivation of the ISI and ICI power expressions contains some simplifying assumptions (i.e.,

all tones are active and $\Delta = 0$). It is concluded that the ISI and ICI power are equal on all tones, but this conclusion ignores that the term $\{2\}$ in (4.12) contributes to the desired RX signal power instead of the ICI power. □

Accuracy of the SNR models of Section 3.3

Based on the above toy example, we now briefly assess the accuracy of the earlier adopted SNR models in Section 3.3. The approximations in each of the SNR models are summarized below.

- Al-Dhahir's SNR model (3.48) ignores the ISI and ICI power (4.6) and (4.13). The desired signal power is related to the DFT of the TIR ($\tilde{b}_n = \mathcal{F}_{n,0:\nu}\mathbf{b}$), which only roughly approximates $\check{c}_n$ in (4.14). By modelling the noise power as $\tilde{\sigma}^2_{n,\tilde{n}}|\tilde{w}_n|^2$ instead of (4.15), the possible noise enhancement by the TEQ in combination with the DFT spectral leakage is not accounted for.
- Henkel's SNR model (Section 3.3.2) computes the ISI power (assuming that all tones are active and equipowered) and the noise power in an alternative but accurate way, based on a discrete PSD estimate on an oversampled frequency grid. The ICI power is not accounted for. For the desired signal power, $\check{c}_n$ is approximated by the DFT of the SIR, $\tilde{c}_n$.
- Arslan's SNR model (3.53) ignores the ICI power and approximates the noise power in the same way as Al-Dhahir does. Under the assumption that all tones are active and equipowered, the ISI power approximation in (3.53) is obtained from (4.6) by replacing c_3 with the last column of (4.7), c_0 with the first column of (4.9) and the correlation matrix, denoted as $\{3\}$, with an all-one matrix, scaled with the signal power $\sigma^2_{n,\tilde{x}}$.
- Milosevic's SNR model takes the noise power correctly into account. For the desired signal power, it is assumed that c_3 and c_0 are zero, which would only hold true in the (infeasible) case of perfect channel shortening. The aggregate ISI/ICI power is then derived from the desired signal power, hence they are also approximate.

4.2 Bit rate maximizing TEQ design

In this section, we present a TEQ design criterion that has as its optimal solution the *bit rate maximizing TEQ* (BM-TEQ) for a given number of taps T. As explained in Section 4.2.1, the key element in the derivation is the observation that the dependence of SNR_n (4.1) on the TEQ taps $\mathbf{w}$ is easily accounted for when considering an alternative SNR model at the *FEQ output* (see **Figure 2.5**). As described in Section 3.3 and in Section 4.1, the SNR

model in [6, 8, 56, 88] applies to the *FEQ input*, i.e., the DFT output. Both options should give rise to completely equivalent SNR models. The optimal choice of FEQs and how to introduce them in the new SNR model is explained in Section 4.2.2. The new, compact and exact SNR model of Section 4.2.3 then leads to the BM-TEQ design criterion of Section 4.2.4. Some guidelines on how to optimize the non-linear and non-convex BM-TEQ criterion are given in Section 4.2.5.

Remark 4.2 The BM-TEQ design criterion presented here assumes a bit rate (3.42) that is a sum of non-integer numbers of bits per tone, as was also the case for the earlier TEQ designs of Section 3.3. TEQ design under the constraint of integer bit loading is far more difficult and not considered here. □

4.2.1 SNR model at the FEQ output

It has already been argued that the derivation of a TEQ design criterion that truly maximizes the bit rate requires that the dependence of SNR_n (4.1) on the TEQ $\mathbf{w}$ is accurately taken into account. The SNR model can be written formally as

$$\mathrm{SNR}_n = \frac{\sigma_{n,\mathrm{s}}^2}{\sigma_{n,\mathrm{e}}^2} \tag{4.16}$$

where $\sigma_{n,\mathrm{s}}^2$ is the desired RX signal power on tone n and $\sigma_{n,\mathrm{e}}^2$ is the power of the overall error signal on tone n, i.e., the RX signal minus the desired part of the RX signal, both on tone n. All SNR models, presented until now (see Section 3.3 and Section 4.1), assume that $\sigma_{n,\mathrm{s}}^2$ and $\sigma_{n,\mathrm{e}}^2$ are determined *at the DFT output*, i.e., the FEQ input. The equalized DFT output on tone n is given by (2.31), which is repeated here for convenience:

$$\tilde{y}_{k,n,\mathbf{w}} = \check{c}_n \tilde{x}_{k,n} + \tilde{n}_{k,n,\mathbf{w}} + \mathrm{ISI}_{k,n,\mathbf{w}} + \mathrm{ICI}_{k,n,\mathbf{w}} \tag{4.17}$$

and the corresponding SNR model was given in (4.1). We prefer to consider the energies $\sigma_{n,\mathrm{s}}^2$ and $\sigma_{n,\mathrm{e}}^2$ in (4.16) *at the FEQ output*, as this will provide us with a convenient way of modelling $\sigma_{n,\mathrm{s}}^2$ and $\sigma_{n,\mathrm{e}}^2$ *without any approximations*. Considering the SNR at the FEQ output is indeed equally valid, as the 1-tap FEQs do not alter SNR_n in the sense that they equally scale both the desired signal and residual error signal, hence both the numerator $\sigma_{n,\mathrm{s}}^2$ and denominator $\sigma_{n,\mathrm{e}}^2$ in (4.16). This effectively makes the FEQs showing up in the SNR model (4.16). However, as will be shown, the FEQs depend in an elegant way on the TEQ, hence the FEQs can be written as a function of the TEQ. In the end, we obtain an SNR model (4.16) and a BM-TEQ design criterion in terms of the TEQ $\mathbf{w}$ and the TX and RX signal SOS.

4.2.2 Unbiased versus biased FEQs

When designing a linear equalizer such as an FEQ, typically a choice is made between an MMSE and a zero forcing (ZF) equalizer. In [33, 38], we explained that the traditional *unconstrained MMSE equalizer* is *biased*, hence it is preferable to turn it into an *unbiased MMSE equalizer.* An unbiased MMSE equalizer gives an unbiased desired signal part at the equalizer output, resulting in a minimum error probability. In general, a ZF equalizer — if existing — is also unbiased, but has a lower SNR because of noise enhancement. In the case of a one-tap equalizer, such as the FEQs in a DMT-based system, there is no noise enhancement, as the one-tap FEQs scale both the desired signal and the noise signal. Hence, the ZF FEQ and unbiased MMSE FEQ (uMMSE FEQ) are equal ([115], p. 320) and so will be our FEQ of choice.

The estimate of $\tilde{x}_{k,n}$ at the FEQ output (2.43) can be written as:

$$\hat{\tilde{x}}_{k,n} = \tilde{d}_n \tilde{y}_{k,n,\mathbf{w}} = \beta_n \tilde{x}_{k,n} + \underbrace{\tilde{d}_n(\tilde{n}_{k,n,\mathbf{w}} + \mathrm{ISI}_{k,n,\mathbf{w}} + \mathrm{ICI}_{k,n,\mathbf{w}})}_{\tilde{e}_{k,n}} \tag{4.18}$$

where $\tilde{d}_n$ is the FEQ for tone n, $\tilde{y}_{k,n,\mathbf{w}}$ is the n-th equalized DFT output, $\beta_n \tilde{x}_{k,n}$ is a scaled version of the desired TX symbol $\tilde{x}_{k,n}$ and the remaining right-hand side terms form the error $\tilde{e}_{k,n,\mathbf{w}}$, which is the sum of the residual ISI/ICI and noise (including crosstalk, RFI, background noise, etc.) at the n-th FEQ output. The traditional, biased MMSE FEQ (bMMSE FEQ) $\tilde{d}_n$ is the solution to:

$$\min_{\tilde{d}_n} \mathcal{E}\left\{\left|\tilde{d}_n \tilde{y}_{k,n,\mathbf{w}} - \tilde{x}_{k,n}\right|^2\right\} \tag{4.19}$$

which is given by:

$$\tilde{d}_n^{\mathrm{bMMSE}} = \frac{\mathcal{E}\left\{\tilde{x}_{k,n}\tilde{y}^*_{k,n,\mathbf{w}}\right\}}{\mathcal{E}\left\{|\tilde{y}_{k,n,\mathbf{w}}|^2\right\}} \tag{4.20}$$

It can easily be shown that (4.20) leads to $\beta_n \neq 1$ in (4.18), hence the estimate $\hat{\tilde{x}}_{k,n}$ is biased. The scalar β_n in (4.18) is 1, i.e., the desired signal component at the FEQ output is unbiased, if an uMMSE FEQ $\tilde{d}_n$ is used:

$$\tilde{d}_n^{\mathrm{uMMSE}} = \frac{\sigma^2_{n,\tilde{x}}}{\mathcal{E}\left\{\tilde{x}^*_{k,n}\tilde{y}_{k,n,\mathbf{w}}\right\}} \tag{4.21}$$

which is the solution to the constrained MMSE criterion:

$$\min_{\tilde{d}_n} \mathcal{E}\left\{\left|\tilde{d}_n \tilde{y}_{k,n,\mathbf{w}} - \tilde{x}_{k,n}\right|^2\right\} \text{ subject to } \tilde{d}_n \mathcal{E}\left\{\tilde{x}^*_{k,n}\tilde{y}_{k,n,\mathbf{w}}\right\} = \mathcal{E}\left\{|\tilde{x}_{k,n}|^2\right\} \tag{4.22}$$

Remark 4.3 It follows from (4.17) and (4.21) that the uMMSE FEQ is given by $\tilde{d}_n^{\text{uMMSE}} = \frac{1}{\tilde{c}_n}$. The uMMSE FEQ is independent of the *residual* noise and ISI/ICI; of course, the uMMSE FEQ depends on the SIR $\mathbf{c}$ and hence on the TEQ $\mathbf{w}$, which is determined by the *unequalized* ISI/ICI structure and noise. On the other hand, the bMMSE FEQ depends on the residual ISI/ICI and noise: a large amount of residual ISI/ICI and/or noise results in a large bias. For large SNR_n, i.e., for a low residual ISI/ICI and noise level, the bMMSE FEQ converges to the uMMSE FEQ. □

4.2.3 SNR model revisited

With uMMSE FEQs, it follows from (4.18) that the desired signal power $\sigma_{n,\text{s}}^2$ becomes independent of TEQ and FEQ and equals $\sigma_{n,\tilde{x}}^2$. The error energy $\sigma_{n,\text{e}}^2$ is equal to the MSE at the FEQ output, $\mathcal{E}\left\{\left|\tilde{e}_{k,n}^{\text{uMMSE}}\right|^2\right\} = \sigma_{n,\tilde{e}}^2$, and takes the residual ISI/ICI and *all* external noise sources into account. Moreover, (4.16) is suited for an arbitrary TX power allocation scheme. An *exact* SNR model (4.16) can thus be written as:

$$\text{SNR}_n = \frac{\sigma_{n,\text{s}}^2}{\sigma_{n,\text{e}}^2} = \frac{\sigma_{n,\tilde{x}}^2}{\sigma_{n,\tilde{e}}^2} = \frac{\sigma_{n,\tilde{x}}^2}{\mathcal{E}\left\{\left|\tilde{d}_n^{\text{uMMSE}}\tilde{y}_{k,n,\mathbf{w}} - \tilde{x}_{k,n}\right|^2\right\}} \tag{4.23}$$

The *first key observation* (3.62), which has led to the PTEQ scheme of Section 3.4, will now be used to obtain a compact expression for SNR_n that only depends on $\mathbf{w}$. The n-th DFT output can be obtained in two ways by applying the associativity property to:

$$\tilde{y}_{k,n,\mathbf{w}} = \underbrace{\mathcal{F}_n(\mathbf{Y}_k\mathbf{w})}_{\{1\}} = \underbrace{(\mathcal{F}_n\mathbf{Y}_k)\mathbf{w}}_{\{2\}} = \tilde{\mathbf{y}}_{k,n}\mathbf{w} \tag{4.24}$$

i.e., the n-th equalized DFT output, $\tilde{y}_{k,n,\mathbf{w}}$ (see $\{1\}$), can also be obtained as a linear combination $\mathbf{w}$ of the T outputs on tone n of a sliding DFT, applied to the unequalized RX sample vector $\mathbf{y}_{k,-T+1:N-1}$ in (2.35), see $\{2\}$. The n-th sliding DFT output is denoted as the $1 \times T$ row vector $\tilde{\mathbf{y}}_{k,n} = \mathcal{F}_n\mathbf{Y}_k$. By exploiting (4.24), the uMMSE FEQ (4.21) can be re-written as:

$$\tilde{d}_n^{\text{uMMSE}} = \frac{\sigma_{n,\tilde{x}}^2}{\mathcal{E}\left\{\tilde{x}_{k,n}^*\tilde{\mathbf{y}}_{k,n}\right\}\mathbf{w}} = \frac{\sigma_{n,\tilde{x}}^2}{\boldsymbol{\sigma}_{n,\tilde{x}\tilde{\mathbf{y}}}\mathbf{w}} \tag{4.25}$$

where $\boldsymbol{\sigma}_{n,\tilde{x}\tilde{\mathbf{y}}} = \mathcal{E}\left\{\tilde{x}_{k,n}^*\tilde{\mathbf{y}}_{k,n}\right\}$ is the $1 \times T$ crosscorrelation vector of the n-th TX symbol $\tilde{x}_{k,n}$ and the n-th sliding DFT output $\tilde{\mathbf{y}}_{k,n}$. Introducing compact notation for the $T \times T$ autocorrelation matrix of the n-th sliding DFT output,

$\mathbf{\Sigma}^2_{n,\tilde{\mathbf{y}}} = \mathcal{E}\left\{\tilde{\mathbf{y}}^H_{k,n}\tilde{\mathbf{y}}_{k,n}\right\}$ and expanding the denominator of (4.23) gives:

$$\sigma^2_{n,\tilde{e}} = \left|\tilde{d}_n\right|^2 \mathbf{w}^T\mathbf{\Sigma}^2_{n,\tilde{\mathbf{y}}}\mathbf{w} - \tilde{d}_n\boldsymbol{\sigma}_{n,\tilde{x}\tilde{\mathbf{y}}}\mathbf{w} - \left(\tilde{d}_n\right)^* \mathbf{w}^T\boldsymbol{\sigma}^H_{n,\tilde{x}\tilde{\mathbf{y}}} + \sigma^2_{n,\tilde{x}} \quad (4.26)$$

$$= \sigma^2_{n,\tilde{x}}\left(\frac{\sigma^2_{n,\tilde{x}}\left(\mathbf{w}^T\mathbf{\Sigma}^2_{n,\tilde{\mathbf{y}}}\mathbf{w}\right)}{\left|\boldsymbol{\sigma}_{n,\tilde{x}\tilde{\mathbf{y}}}\mathbf{w}\right|^2} - 1\right) \quad (4.27)$$

where the second equation follows from the substitution of the uMMSE FEQs (4.25). By combining (4.27) and (4.23), we obtain a very compact SNR model that only depends on the TEQ $\mathbf{w}$:

$$\boxed{\mathrm{SNR}_n = \frac{1}{\rho^{-2}_{n,\mathbf{w}} - 1} = \frac{\rho^2_{n,\mathbf{w}}}{1-\rho^2_{n,\mathbf{w}}}} \quad (4.28)$$

where

$$\boxed{\rho^2_{n,\mathbf{w}} = \frac{\left|\boldsymbol{\sigma}_{n,\tilde{x}\tilde{\mathbf{y}}}\mathbf{w}\right|^2}{\sigma^2_{n,\tilde{x}}\left(\mathbf{w}^T\mathbf{\Sigma}^2_{n,\tilde{\mathbf{y}}}\mathbf{w}\right)} = \frac{\left|\mathcal{E}\left\{\tilde{x}^*_{k,n}\tilde{y}_{k,n,\mathbf{w}}\right\}\right|^2}{\mathcal{E}\left\{\left|\tilde{x}_{k,n}\right|^2\right\}\mathcal{E}\left\{\left|\tilde{y}_{k,n,\mathbf{w}}\right|^2\right\}}} \quad (4.29)$$

is a squared normalized correlation function of the n-th equalized DFT output $\tilde{y}_{k,n,\mathbf{w}}$ and the n-th TX symbol $\tilde{x}_{k,n}$; $\rho^2_{n,\mathbf{w}}$ is always positive and between 0 and 1; the second equality in (4.29) follows from the key observation (4.24).

Remark 4.4 The squared normalized correlation function for tone n, $\rho^2_{n,\mathbf{w}}$, relates the bMMSE FEQ (4.20) and the uMMSE FEQ (4.21):

$$\rho^2_{n,\mathbf{w}} = \frac{\tilde{d}^{\mathrm{bMMSE}}_n}{\tilde{d}^{\mathrm{uMMSE}}_n} \quad (4.30)$$

It follows from (4.18) that the bias β_n in the case of a bMMSE FEQ is equal to $\rho^2_{n,\mathbf{w}}$. □

4.2.4 BM-TEQ design criterion

Plugging SNR_n (4.28) and $\rho^2_{n,\mathbf{w}}$ (4.29) in the DMT bit rate expression (3.42) leads to the BM-TEQ design criterion:

$$\max_{\mathbf{w}} \sum_{n\in\mathcal{S}_a} \log\left(1 + \frac{\rho^2_{n,\mathbf{w}}}{\Gamma_n(1-\rho^2_{n,\mathbf{w}})}\right) = \max_{\mathbf{w}} \sum_{n\in\mathcal{S}_a} \log\left(\frac{\Gamma_n + (1-\Gamma_n)\rho^2_{n,\mathbf{w}}}{\Gamma_n(1-\rho^2_{n,\mathbf{w}})}\right) \quad (4.31)$$

or

$$\boxed{\min_{\mathbf{w}} \sum_{n\in\mathcal{S}_a} \log\left(\frac{\mathbf{w}^T\mathbf{B}_n\mathbf{w}}{\mathbf{w}^T\mathbf{A}_n\mathbf{w}}\right)} \quad (4.32)$$

where $\mathbf{A}_n$ and $\mathbf{B}_n$ are independent of $\mathbf{w}$ and depend on the second-order signal statistics (SOS) $\sigma^2_{n,\tilde{x}}$, $\mathbf{\Sigma}^2_{n,\tilde{\mathbf{y}}}$ and $\boldsymbol{\sigma}_{n,\tilde{x}\tilde{\mathbf{y}}}$:

$$\mathbf{A}_n = \Gamma_n \sigma^2_{n,\tilde{x}} \mathbf{\Sigma}^2_{n,\tilde{\mathbf{y}}} + (1-\Gamma_n)\boldsymbol{\sigma}^H_{n,\tilde{x}\tilde{\mathbf{y}}}\boldsymbol{\sigma}_{n,\tilde{x}\tilde{\mathbf{y}}} \quad (4.33)$$

$$\mathbf{B}_n = \Gamma_n \left(\sigma^2_{n,\tilde{x}} \mathbf{\Sigma}^2_{n,\tilde{\mathbf{y}}} - \boldsymbol{\sigma}^H_{n,\tilde{x}\tilde{\mathbf{y}}}\boldsymbol{\sigma}_{n,\tilde{x}\tilde{\mathbf{y}}}\right) \quad (4.34)$$

Remark 4.5 It should not come as a surprise that correlations with the sliding DFT of the RX signal, $\tilde{\mathbf{y}}_{k,n}$, $n \in \mathcal{S}_a$ are involved in the BM-TEQ design criterion: these correlations allow to link the multicarrier *frequency-domain* aspect of DMT modulation with the *time-domain* filtering of a TEQ. □

The solution to the BM-TEQ design criterion (4.32) has a scalar ambiguity: for a solution $\mathbf{w}$, $\gamma\mathbf{w}$ (with γ a scalar) is also a solution, as the FEQs compensate for the scaling by γ. In contrast to the MMSE-TEQ design of Section 3.2.1, imposing a constraint on $\mathbf{w}$, e.g., $\mathbf{w}^T\mathbf{w} = 1$, then does not influence the optimum bit rate, as the bit rate is independent of the scalar γ.

The above choice to derive the BM-TEQ design criterion (4.32) using *uMMSE FEQs* (4.21) provides a convenient way of modelling the numerator $\sigma^2_{n,\mathrm{s}}$ and denominator $\sigma^2_{n,\mathrm{e}}$ of SNR_n in (4.16) without approximation. However, it is important to note that, as the FEQs equally scale both $\sigma^2_{n,\mathrm{s}}$ and $\sigma^2_{n,\mathrm{e}}$, and hence do not alter SNR_n, the BM-TEQ design criterion (4.32) remains valid, even if the actual FEQs are the bMMSE FEQs.

This BM-TEQ design criterion fits in the framework, presented in Section 3.1, as (4.32) is equivalent to a product of $M = N_a$ generalized Rayleigh quotients (3.1). In contrast with the TEQ designs of Chapter 3, the matrices $\mathbf{A}_n$ and $\mathbf{B}_n$ are now described in terms of TX and RX signal SOS, which turns out to be more convenient and compact than a design criterion that is specified in terms of the CIR and the signal and noise statistics. We have argued in Section 3.1 that, in general, non-linear design criteria of the form (3.1) are non-convex. This also holds for the BM-TEQ design criterion, as is illustrated in the example below. The impact of the non-convexity on the attained locally optimal TEQ solution is investigated in Section 4.4.

Example 4.1 **Figure 4.2** depicts a cost contour plot of the BM-TEQ design criterion for a TEQ of $T = 3$ taps with a UNC. The CSA #4 loop in downstream transmission is considered (see Section 4.4 for details). The plot spans the whole parameter space; the axes show the second and third tap, w_1 and w_2, which obey $\sqrt{w_1^2 + w_2^2} \leq 1$ because of the UNC; the first tap then follows from the UNC: $w_0 = \sqrt{1 - w_1^2 - w_2^2}$. There are a clear minimum (corresponding to the BM-TEQ) and maximum. Because of the co-existence of minima and maxima, the design criterion must be non-convex. No local maxima appear in this case. However, simulations have indicated that local optima indeed exist

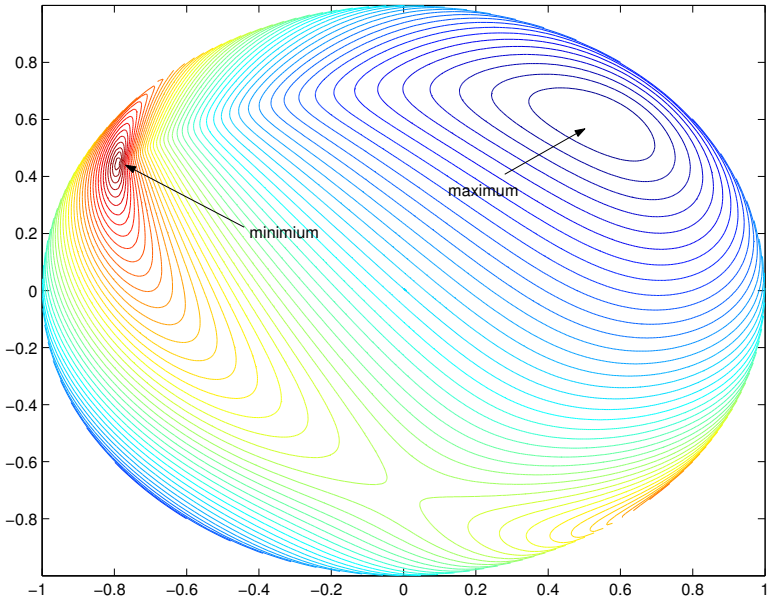


Figure 4.2: Cost contour plot of the BM-TEQ design criterion for the CSA #4 loop in downstream transmission.

for other scenarios; the corresponding bit rate loss depends on the scenario (see Section 4.4 and Section 5.4). △

Remark 4.6 As the BM-TEQ criterion (4.32) does not explicitly impose channel shortening any more, we could give up the conjugate symmetry at the DFT output by using a complex-valued TEQ. The extra degrees of freedom (namely the imaginary parts of the T TEQ taps) result in a slightly better performance than a real-valued TEQ (see Section 4.4) but cause extra computational complexity (e.g., a more complex DFT). □

Remark 4.7 As mentioned in Remark 2.10, optimal TEQ design should take into account the TX power allocation and the bit loading. This gives rise to a complex, iterative process, as the bit loading depends on SNR_n (4.1), and hence also on the TEQ design. Only a few TEQ design algorithms have been presented in the literature that (partially) take into account the TX power allocation. E.g., in [7], a TEQ is designed first, based on the assumption that all tones are active; this is followed by on/off power loading, which switches off tones with a too low SNR, as described in Example 2.4; then, the TEQ is redesigned, based on the reduced active tone set $\mathcal{S}_a$. This idea can also be combined with the BM-TEQ design presented here. Moreover, the BM-TEQ design criterion allows for an optimized TX power per tone, i.e., a water-filling TX power loading, rather than on/off loading can be used. □

4.2.5 Optimizing the BM-TEQ design criterion

Minimizing a non-linear, non-convex design criterion only assures convergence to a local optimum [77]. Non-linear *batch optimization methods* such as advanced, *iterative* (quasi-)Newton and simplex algorithms are implemented in commercial software packages such as the MATLAB optimization toolbox [122]. Estimates of the autocorrelation matrices $\mathbf{\Sigma}^2_{n,\tilde{\mathbf{y}}}$ and crosscorrelation vectors $\boldsymbol{\sigma}_{n,\tilde{x}\tilde{\mathbf{y}}}$ for all tones in $\mathcal{S}_a$ can be obtained accurately with the FIR data model (2.35) based on an estimate of the CIR $\mathbf{h}$ and the noise statistics $\mathbf{\Sigma}^2_{\mathbf{n}}$. Let us partition the RX sample vector of the FIR data model (2.35) in a desired signal term corresponding to the TX symbol of interest $\tilde{x}_{k,n}$ and a residual term:

$$\begin{aligned} \mathbf{y}_{k,-T+1:N-1} &= \mathbf{H}\tilde{\mathbf{x}}_{k-1:k+1,N} + \mathbf{n}_{k,-T+1:N-1} \\ &= \underbrace{\check{\mathbf{h}}\tilde{x}_{k,n}}_{\text{desired}} + \underbrace{\check{\mathbf{H}}\check{\tilde{\mathbf{x}}}_{k-1:k+1,N} + \mathbf{n}_{k,-T+1:N-1}}_{\text{residual}} \end{aligned} \tag{4.35}$$

where it has been assumed for simplicity that $\Delta = 0$, where the $(N-T+1) \times (3N)$ matrix $\mathbf{H}$ incorporates the modulating IDFT, the CP insertion and the CIR, where $\check{\mathbf{h}}$ is the $(N+n)$-th column of $\mathbf{H}$ which multiplies $\tilde{x}_{k,n}$, where the $(N-T+1) \times (3N-1)$ submatrix $\check{\mathbf{H}}$ is equal to $\mathbf{H}$ without the $(N+n)$-th column $\check{\mathbf{h}}$ and where the $(3N-1) \times 1$ TX symbol vector $\check{\tilde{\mathbf{x}}}_{k-1:k+1,N}$ is obtained from $\tilde{\mathbf{x}}_{k-1:k+1,N}$ by omitting $\tilde{x}_{k,n}$. Noting that the n-th sliding DFT output $\tilde{\mathbf{y}}_{k,n} = \mathcal{F}_n \mathbf{Y}_k$, see (4.24), can also be obtained from $\mathbf{y}_{k,-T+1:N-1}$ as

$$\tilde{\mathbf{y}}^T_{k,n} = \underbrace{\begin{bmatrix} 0 & \cdots & 0 & [& \mathcal{F}_n &] \\ \vdots & \iddots & [& \mathcal{F}_n &] & 0 \\ 0 & \iddots & \iddots & \iddots & \iddots & \vdots \\ [& \mathcal{F}_n &] & 0 & \cdots & 0 \end{bmatrix}}_{\mathbf{F}_n} \mathbf{y}_{k,-T+1:N-1} \tag{4.36}$$

with $\mathbf{F}_n$ a Hankel matrix, constructed with $\mathcal{F}_n$, it then follows from (4.35) and (4.36) that the required SOS are given by:

$$\mathbf{\Sigma}^2_{n,\tilde{\mathbf{y}}} = \mathbf{F}^*_n \left(\mathbf{H}^* \left(\mathbf{I}_3 \otimes \mathbf{\Sigma}^2_{\tilde{\mathbf{x}}} \right) \mathbf{H}^T + \mathbf{\Sigma}^2_{\mathbf{n}} \right) \mathbf{F}^T_n \tag{4.37}$$

$$\boldsymbol{\sigma}_{n,\tilde{x}\tilde{\mathbf{y}}} = \sigma^2_{n,\tilde{x}} \check{\mathbf{h}}^T \mathbf{F}^T_n \tag{4.38}$$

where $\mathbf{\Sigma}^2_{\tilde{\mathbf{x}}}$ is the autocorrelation matrix of $\tilde{\mathbf{x}}_{k,N}$. Alternatively, one can estimate these SOS (4.37) and (4.38) using the so-called medley training sequence (with cyclic prefix) that is typically transmitted during the connection set-up phase.

The BM-TEQ design criterion (4.32) hides the inherent TEQ-FEQ receiver structure. In the next section, an alternative LS-based formulation of the BM-TEQ design criterion is given, which is an iteratively reweighted sum of frequency-domain squared errors between the symbol estimates at the FEQ

outputs and the true TX symbols. This can then be optimized with an *iterative*, fast-converging Gauss-Newton-based algorithm that is driven by the FEQ output errors. In Chapter 5, a closely related *adaptive* BM-TEQ design algorithm, based on a recursive Levenberg-Marquardt algorithm, is derived.

4.3 Least-squares-based time-domain and frequency-domain MMSE-TEQ designs

It was shown in Section 3.2.1 that the MMSE-TEQ is obtained as the solution of a constrained, linear time-domain (TD) MMSE design criterion in the TEQ and (auxiliary) TIR coefficients. The PTEQ design (Section 3.4) is rather based on an unconstrained, linear MMSE design criterion that only depends on the PTEQ coefficients. The previous section described the BM-TEQ design criterion, which is a non-linear function of the TEQ coefficients and asks for a non-linear optimization routine. At first sight, these equalizer designs are very different in nature. In this section, we reconsider the TD-MMSE-TEQ, BM-TEQ and PTEQ design and develop an *LS-based design criterion* for each of them. In addition, we propose two intermediate LS-based frequency-domain (FD) MMSE-TEQ design criteria. This section then has two major contributions.

- An alternative LS-based BM-TEQ design criterion is presented, which is optimized with an iterative, fast-converging Gauss-Newton-based algorithm that is driven by the squared errors at the FEQ outputs and delivers the BM-TEQ and corresponding FEQs.
- A common LS-based equalizer framework is established, which allows to elaborate the correspondence between the LS-based BM-TEQ design criterion and LS-based formulations of the TD-MMSE-TEQ, FD-MMSE-TEQ and PTEQ design criteria.

The classical MMSE-TEQ design criterion can be formulated as a constrained linear least-squares (CLLS) based MMSE design criterion that minimizes a TD error energy, see Section 4.3.1. Starting from this CLLS-based TD-MMSE-TEQ design, we derive in Section 4.3.2 and 4.3.3 two new MMSE-TEQ designs that minimize a sum of *frequency-domain* (FD) error energies (i.e., after the DFT demodulation), rather than a TD error energy: the first FD-MMSE-TEQ design is based on a CLLS criterion, while the other is based on a — related — separable non-linear LS (SNLLS) criterion. Especially the SNLLS-based FD-MMSE-TEQ design appears a useful intermediate solution between the TD-MMSE-TEQ design and the BM-TEQ design: it consistently outperforms

the CLLS-based TD-MMSE-TEQ design and closely approaches the performance of, and is tightly related to, the BM-TEQ design. The BM-TEQ design criterion of Section 4.2 is then shown in Section 4.3.4 to be equivalent to a so-called *iteratively-reweighted (IR) version of the SNLLS-based FD-MMSE-TEQ design criterion*. Thanks to this LS-based formulation, both the SNLLS-based FD-MMSE-TEQ and the IR-SNLLS-based BM-TEQ design criteria can be optimized iteratively with an elegant, fast converging, Gauss-Newton-based algorithm that exploits the separability property of the design criterion, see Section 4.3.5. Section 4.3.6 shows that the PTEQ design is a special case of the presented FD-MMSE-TEQ designs, when considering a single tone. In each section, the close relationship between the LS-based formulations of the TD-MMSE-TEQ, FD-MMSE-TEQ, BM-TEQ and PTEQ design criteria is made explicit by turning the LS-based formulation into a GEV problem $\mathbf{B}\mathbf{w} = \lambda\mathbf{A}\mathbf{w}$, as in (3.3), where, loosely speaking, $\mathbf{A}$ is an autocorrelation metric of the RX signal y_l and $\mathbf{B}$ depends on a crosscorrelation metric between TX and RX signal x_l and y_l. In Section 4.3.7, the relation between all LS-based formulations is summarized and tabulated.

4.3.1 CLLS-based TD-MMSE-TEQ design

In Section 3.2.1, the MMSE-TEQ design has been presented. It minimizes the *time-domain* (TD) MSE between the output of the T-tap TEQ, $y_{l,\mathbf{w}} = \mathbf{y}_l^T\mathbf{w}$ and the output $\mathbf{x}_l^T\mathbf{b}$ of a virtual FIR channel, the so-called TIR $\mathbf{b}$ of length $\nu + 1$, which is fed with a vector of TX samples $\mathbf{x}_l$ (see also **Figure 3.2**). The corresponding design criterion (3.4) is repeated here for convenience, under the assumption that the synchronization delay $\Delta = 0$:

$$\min_{\mathbf{w},\mathbf{b}} \mathcal{E}\left\{|e_l|^2\right\} = \min_{\mathbf{w},\mathbf{b}} \mathcal{E}\left\{\left|\mathbf{y}_l^T\mathbf{w} - \mathbf{x}_l^T\mathbf{b}\right|^2\right\} \tag{4.39}$$

Several non-triviality constraints have been suggested in Section 3.2.1, namely a unit tap constraint $\mathbf{e}_j^T\mathbf{w} = 1$ or $\mathbf{e}_j^T\mathbf{b} = 1$ (with $\mathbf{e}_j$ the canonical vector with a 1 on position j), a unit norm constraint $\|\mathbf{w}\|^2 = \mathbf{w}^T\mathbf{w} = 1$ or $\|\mathbf{b}\|^2 = \mathbf{b}^T\mathbf{b} = 1$ and a weighted unit norm constraint $\mathbf{w}^T\mathbf{G}\mathbf{w} = 1$ or $\mathbf{b}^T\mathbf{G}\mathbf{b} = 1$ (with $\mathbf{G}$ a positive definite matrix). Particular choices of $\mathbf{G}$ lead to three so-called unit energy constraints (UEC) [157]:

$$\mathbf{w}^T\boldsymbol{\Sigma}_{\mathbf{y}}^2\mathbf{w} = 1 \text{ or } \mathbf{b}^T\boldsymbol{\Sigma}_{\mathbf{x}}^2\mathbf{b} = 1 \text{ or } \mathbf{w}^T\boldsymbol{\Sigma}_{\mathbf{y}}^2\mathbf{w} = 1 \,\&\, \mathbf{b}^T\boldsymbol{\Sigma}_{\mathbf{x}}^2\mathbf{b} = 1 \tag{4.40}$$

where $\boldsymbol{\Sigma}_{\mathbf{y}}^2 = \mathcal{E}\left\{\mathbf{y}_l\mathbf{y}_l^T\right\}$ and $\boldsymbol{\Sigma}_{\mathbf{x}}^2 = \mathcal{E}\left\{\mathbf{x}_l\mathbf{x}_l^T\right\}$ are autocorrelation matrices. Each of the three constraints (4.40) has been shown in [157] to lead to the same TEQ solution (up to a scaling). In the sequel, we will focus on the TD-MMSE-TEQ with a UEC as this will allow to derive new FD-MMSE-TEQ design criteria and to establish a relationship with the BM-TEQ and PTEQ.

Under the assumption of wide-sense stationarity of the involved signals and for $L \to \infty$, the stochastic linear MMSE design criterion (4.39) with UEC

constraint on $\mathbf{w}$ (4.40) is equivalent to the following deterministic **constrained linear least-squares (CLLS) based TD-MMSE-TEQ** criterion:

$$\boxed{\min_{\mathbf{w},\mathbf{b}} \frac{1}{L}\sum_{l=1}^{L}\left|\mathbf{y}_l^T\mathbf{w}-\mathbf{x}_l^T\mathbf{b}\right|^2 \text{ s.t. } \mathbf{w}^T\boldsymbol{\Sigma}_{L,\mathbf{y}}^2\mathbf{w}=1} \tag{4.41}$$

A subscript with the number of data samples, L, is used to distinguish between a (deterministic) correlation *estimate*, e.g., $\boldsymbol{\Sigma}_{L,\mathbf{y}}^2 = \frac{1}{L}\sum_{l=1}^{L}\mathbf{y}_l\mathbf{y}_l^T$, and the (stochastic) *true* correlation $\boldsymbol{\Sigma}_{\mathbf{y}}^2 = \mathcal{E}\left\{\mathbf{y}_l\mathbf{y}_l^T\right\}$. The UEC $\mathbf{b}^T\boldsymbol{\Sigma}_{L,\mathbf{x}}^2\mathbf{b}=1$ with $\boldsymbol{\Sigma}_{L,\mathbf{x}}^2 = \frac{1}{L}\sum_{l=1}^{L}\mathbf{x}_l\mathbf{x}_l^T$ gives again the same TEQ solution (up to a scaling) [157]. Due to the so-called orthogonality condition [5, 28], the solution for the unconstrained vector $\mathbf{b}$ depends on $\mathbf{w}$ through:

$$\mathbf{b} = \left(\boldsymbol{\Sigma}_{L,\mathbf{x}}^2\right)^{-1}\boldsymbol{\Sigma}_{L,\mathbf{xy}}\mathbf{w} \tag{4.42}$$

with $\boldsymbol{\Sigma}_{L,\mathbf{xy}} = \frac{1}{L}\sum_{l=1}^{L}\mathbf{x}_l\mathbf{y}_l^T$. Combining (4.42) with (4.41) gives:

$$\min_{\mathbf{w}} \mathbf{w}^T\left[\boldsymbol{\Sigma}_{L,\mathbf{y}}^2 - \boldsymbol{\Sigma}_{L,\mathbf{xy}}^T\left(\boldsymbol{\Sigma}_{L,\mathbf{x}}^2\right)^{-1}\boldsymbol{\Sigma}_{L,\mathbf{xy}}\right]\mathbf{w} \text{ s.t. } \mathbf{w}^T\boldsymbol{\Sigma}_{L,\mathbf{y}}^2\mathbf{w}=1 \tag{4.43}$$

This optimization criterion is equivalent to the following criteria:

$$\min_{\mathbf{w}} \frac{\mathbf{w}^T\left[\boldsymbol{\Sigma}_{L,\mathbf{y}}^2-\boldsymbol{\Sigma}_{L,\mathbf{xy}}^T\left(\boldsymbol{\Sigma}_{L,\mathbf{x}}^2\right)^{-1}\boldsymbol{\Sigma}_{L,\mathbf{xy}}\right]\mathbf{w}}{\mathbf{w}^T\boldsymbol{\Sigma}_{L,\mathbf{y}}^2\mathbf{w}} = 1 - \max_{\mathbf{w}} \frac{\mathbf{w}^T\overbrace{\left[\boldsymbol{\Sigma}_{L,\mathbf{xy}}^T\left(\boldsymbol{\Sigma}_{L,\mathbf{x}}^2\right)^{-1}\boldsymbol{\Sigma}_{L,\mathbf{xy}}\right]}^{\mathbf{B}}\mathbf{w}}{\mathbf{w}^T\underbrace{\boldsymbol{\Sigma}_{L,\mathbf{y}}^2}_{\mathbf{A}}\mathbf{w}} \tag{4.44}$$

Hence, solving the CLLS-based TD-MMSE-TEQ design criterion (4.41) reduces to the maximization of a generalized Rayleigh quotient $\frac{\mathbf{w}^T\mathbf{B}\mathbf{w}}{\mathbf{w}^T\mathbf{A}\mathbf{w}}$ (3.2). As we recall from Section 3.1, the solution is seen to be the dominant generalized eigenvector of the GEV problem (3.3) with the matrix pair

$$(\mathbf{B},\mathbf{A}) = \left(\boldsymbol{\Sigma}_{L,\mathbf{xy}}^T\left(\boldsymbol{\Sigma}_{L,\mathbf{x}}^2\right)^{-1}\boldsymbol{\Sigma}_{L,\mathbf{xy}}, \boldsymbol{\Sigma}_{L,\mathbf{y}}^2\right) \tag{4.45}$$

Alternative but equivalent matrix pairs $(\mathbf{B},\mathbf{A})$ for the MMSE-TEQ design with UEC have been suggested in Section 3.2.1.

4.3.2 CLLS-based FD-MMSE-TEQ design

As the TD-MMSE-TEQ design in (4.39) is *sample*-based and minimizes a *TD MSE*, the DMT *block* transmission structure (including the cyclic prefix and the *FD symbols of interest*) is not easily accounted for: as explained in Remark 3.3, the signals x_l and y_l are oftentimes assumed stationary, i.e., $\boldsymbol{\Sigma}_{\mathbf{x}}^2$ is approximated by an identity matrix (even when not all tones are active) and

$\mathbf{\Sigma}_{\mathbf{y}}^2$ is assumed Toeplitz. Also, there is no clear relation between minimizing the TD MSE $\mathcal{E}\left\{|e_l|^2\right\}$ in (4.39) and bit rate optimization. In this section and in the next section, we suggest two new, alternative MMSE-TEQ designs that do take into account the DMT block transmission structure and minimize a FD instead of TD MSE. The steps, explained below, that lead to these FD-MMSE-TEQ design criteria intuitively suggest that they are better related than the TD-MMSE-TEQ design criterion to the multicarrier, hence frequency-domain nature of DMT equalization. The simulations in Section 4.4 will show that especially the separable non-linear LS (SNLLS) based FD-MMSE-TEQ criterion, developed in Section 4.3.3, approaches the BM-TEQ performance.

We propose to first rewrite the TD-MMSE-TEQ design criterion (4.39) on a *per-DMT-symbol* basis:

$$\min_{\mathbf{w},\mathbf{b}} \mathcal{E}\left\{\left\|\underbrace{\mathbf{Y}_k\mathbf{w}-\mathbf{X}_k\mathbf{b}}_{\mathbf{e}_k}\right\|^2\right\} \text{ s.t. } \mathbf{w}^T\mathbf{\Sigma}_{\mathbf{Y}}^2\mathbf{w}=1 \tag{4.46}$$

where $\mathbf{\Sigma}_{\mathbf{Y}}^2 = \mathcal{E}\left\{\mathbf{Y}_k^T\mathbf{Y}_k\right\}$ is an autocorrelation matrix of the $N\times T$ RX sample Toeplitz matrix $\mathbf{Y}_k$, obtained from (2.36) by setting $\mu=0$, i.e.,

$$\mathbf{Y}_k = \begin{bmatrix} y_{k,0} & y_{k,-1} & \cdots & y_{k,-T+1} \\ y_{k,1} & y_{k,2} & \ddots & y_{k,-T+2} \\ \vdots & \ddots & \ddots & \vdots \\ y_{k,N-1} & y_{k,N-2} & \cdots & y_{k,N-T} \end{bmatrix} \tag{4.47}$$

and where the matrix $\mathbf{X}_k$ is of size $N\times(\nu+1)$ and columnwise circulant and incorporates the cyclic prefix in the upper right triangle with side ν:

$$\mathbf{X}_k = \begin{bmatrix} x_{k,0} & x_{k,N-1} & \cdots & x_{k,N-\nu} \\ \vdots & \ddots & \ddots & \vdots \\ x_{k,\nu} & \ddots & x_{k,0} & x_{k,N-1} \\ x_{k,\nu+1} & \ddots & x_{k,1} & x_{k,0} \\ \vdots & \ddots & \ddots & \vdots \\ x_{k,N-1} & \cdots & x_{k,N-\nu} & x_{k,N-\nu-1} \end{bmatrix} \tag{4.48}$$

We have argued before that the first term $\mathbf{Y}_k\mathbf{w}$ in (4.46) corresponds to the convolution of the k-th RX sample vector $\mathbf{y}_{k,-T+1:N-1}$ with the TEQ $\mathbf{w}$, see (2.37). Likewise, the second term $\mathbf{X}_k\mathbf{b}$ in (4.46) is the convolution of the k-th TX sample vector $\mathbf{x}_{k,-\nu:N-1}$ and the TIR $\mathbf{b}$.

In a second step, $\mathbf{X}_k$ is extended with $N-\nu-1$ columns to a circulant matrix

$\mathbf{X}_{k,\mathrm{C}}$ of size $N \times N$, so that

$$\mathbf{X}_k\mathbf{b} = \mathbf{X}_{k,\mathrm{C}} \begin{bmatrix} \mathbf{b} \\ \mathbf{0}_{(N-\nu-1)\times 1} \end{bmatrix} \tag{4.49}$$

with

$$\mathbf{X}_{k,\mathrm{C}} = \left[\begin{array}{cccc|ccc} x_{k,0} & x_{k,N-1} & \cdots & x_{k,N-\nu} & x_{k,N-\nu-1} & \cdots & x_{k,1} \\ x_{k,1} & x_{k,0} & \ddots & x_{k,N-\nu+1} & x_{k,N-\nu} & & x_{k,2} \\ \vdots & \ddots & \ddots & \vdots & \vdots & \ddots & \vdots \\ x_{k,N-1} & \cdots & & x_{k,N-\nu-1} & x_{k,N-\nu-2} & \cdots & x_{k,0} \end{array}\right] \tag{4.50}$$

A DFT-based decomposition of the circulant matrix $\mathbf{X}_{k,\mathrm{C}} = \mathcal{F}_N^H \tilde{\mathbf{X}}_{k,N,\mathrm{D}} \mathcal{F}_N$ with $\tilde{\mathbf{X}}_{k,N,\mathrm{D}} = \mathrm{diag}(\tilde{\mathbf{x}}_{k,N})$ is then plugged in:

$$\mathbf{X}_k\mathbf{b} = \mathbf{X}_{k,\mathrm{C}} \begin{bmatrix} \mathbf{b} \\ \mathbf{0} \end{bmatrix} = \mathcal{F}_N^H \tilde{\mathbf{X}}_{k,N,\mathrm{D}} \underbrace{\mathcal{F}_N \begin{bmatrix} \mathbf{b} \\ \mathbf{0} \end{bmatrix}}_{\tilde{\mathbf{b}}_N} = \mathcal{F}_N^H \tilde{\mathbf{X}}_{k,N,\mathrm{D}} \tilde{\mathbf{b}}_N \tag{4.51}$$

where $\tilde{\mathbf{b}}_N$ is the N-point DFT of the TIR $\mathbf{b}$ padded with zeros. Thirdly, the criterion and constraint (4.46) are transformed to the frequency-domain:

$$\min_{\mathbf{w},\mathbf{b}} \mathcal{E}\left\{\|\mathbf{e}_k\|^2\right\} = \min_{\mathbf{w},\mathbf{b}} \mathcal{E}\left\{\|\mathcal{F}_N\mathbf{e}_k\|^2\right\} = \min_{\mathbf{w},\mathbf{b}} \mathcal{E}\left\{\left\|\tilde{\mathbf{Y}}_{k,N}\mathbf{w} - \tilde{\mathbf{X}}_{k,N,\mathrm{D}}\tilde{\mathbf{b}}_N\right\|^2\right\} \tag{4.52}$$

$$\text{s.t. } \mathbf{w}^T\boldsymbol{\Sigma}^2_{N,\tilde{\mathbf{Y}}}\mathbf{w} = 1,\ \tilde{\mathbf{b}}_N = \mathcal{F}\begin{bmatrix} \mathbf{b} \\ \mathbf{0} \end{bmatrix} \text{ and real } \mathbf{w} \text{ and } \mathbf{b} \tag{4.53}$$

The first term of the error vector $\mathcal{F}_N\mathbf{e}_k$ in (4.52) corresponds to the equalized DFT output. It has already been argued in Section 3.4 (see (3.62)) and Section 4.2.2 (see (4.24)) that the equalized DFT output:

$$\tilde{\mathbf{y}}_{k,N,\mathbf{w}} = \underbrace{\mathcal{F}_N(\mathbf{Y}_k\mathbf{w})}_{\{1\}} = \underbrace{(\mathcal{F}_N\mathbf{Y}_k)\mathbf{w}}_{\{2\}} = \tilde{\mathbf{Y}}_{k,N}\mathbf{w} \tag{4.54}$$

can either be computed $\{1\}$ as the DFT of the TEQ output $\mathbf{Y}_k\mathbf{w}$ or $\{2\}$ as a linear combination $\mathbf{w}$ of the N-point sliding DFT of the k-th RX sample vector, $\tilde{\mathbf{Y}}_{k,N} = \mathcal{F}_N\mathbf{Y}_k$. This observation has led to the PTEQ design and is also a key observation in the derivation of the BM-TEQ design criterion (4.32). The autocorrelation matrix in (4.53) is then given by $\boldsymbol{\Sigma}^2_{N,\tilde{\mathbf{Y}}} = \mathcal{E}\left\{\tilde{\mathbf{Y}}^H_{k,N}\tilde{\mathbf{Y}}_{k,N}\right\} = \mathcal{E}\left\{\mathbf{Y}_k^T\mathbf{Y}_k\right\} = \boldsymbol{\Sigma}^2_{\mathbf{Y}}$. The additional, second constraint in (4.53) comes from the definition of $\tilde{\mathbf{b}}_N$ in (4.51) and stems from the original TD-MMSE-TEQ design that imposes channel shortening by means of a TIR $\mathbf{b}$ of length $\nu+1$. Criterion (4.46) and (4.52-4.53) are thus fully equivalent.

Finally, by selecting the appropriate elements of $\mathcal{F}_N\mathbf{e}_k$ in (4.52) and modifying the constraints (4.53) accordingly, one can restrict the criterion to the N_a active tones of $\mathcal{S}_a$:

$$\min_{\mathbf{w},\mathbf{b}} \mathcal{E}\left\{\|\mathcal{F}_a\mathbf{e}_k\|^2\right\} = \min_{\mathbf{w},\mathbf{b}} \mathcal{E}\left\{\left\|\tilde{\mathbf{Y}}_k\mathbf{w} - \tilde{\mathbf{X}}_{k,\mathrm{D}}\tilde{\mathbf{b}}\right\|^2\right\} \tag{4.55}$$

$$\text{s.t. } \mathbf{w}^T\boldsymbol{\Sigma}^2_{\tilde{\mathbf{Y}}}\mathbf{w} = 1,\ \tilde{\mathbf{b}} = \mathcal{F}_a\begin{bmatrix}\mathbf{b}\\ \mathbf{0}\end{bmatrix} \text{ and real } \mathbf{w} \text{ and } \mathbf{b} \tag{4.56}$$

where $\mathcal{F}_a$ is a submatrix of $\mathcal{F}_N$, containing only the N_a rows corresponding to the active tones $\mathcal{S}_a$ and where $\tilde{\mathbf{Y}}_k = \mathcal{F}_a\mathbf{Y}_k$, $\tilde{\mathbf{X}}_{k,\mathrm{D}} = \mathrm{diag}(\tilde{\mathbf{x}}_k)$ and $\boldsymbol{\Sigma}^2_{\tilde{\mathbf{Y}}} = \mathcal{E}\left\{\tilde{\mathbf{Y}}_k^H\tilde{\mathbf{Y}}_k\right\}$. Note that the subscripts N have been omitted, to indicate that only the active tones, rather than all N tones are considered now. The (modified) second constraint, $\tilde{\mathbf{b}} = \mathcal{F}_a\begin{bmatrix}\mathbf{b}\\ \mathbf{0}\end{bmatrix}$, still follows from imposing channel shortening by means of a TIR $\mathbf{b}$ of length $\nu+1$: from (4.51), it is seen that

$$\begin{aligned}\mathcal{F}_a\mathbf{X}_k\mathbf{b} &= \underbrace{\mathcal{F}_a\mathcal{F}_N^H}_{\mathbf{S}_a}\underbrace{\mathrm{diag}(\tilde{\mathbf{x}}_{k,N})}_{\tilde{\mathbf{X}}_{k,N,\mathrm{D}}}\underbrace{\mathcal{F}_N\begin{bmatrix}\mathbf{b}\\ \mathbf{0}\end{bmatrix}}_{\tilde{\mathbf{b}}_N}\\ &= \underbrace{\mathrm{diag}(\tilde{\mathbf{x}}_k)}_{\tilde{\mathbf{X}}_{k,\mathrm{D}}}\underbrace{\mathbf{S}_a\mathcal{F}_N\begin{bmatrix}\mathbf{b}\\ \mathbf{0}\end{bmatrix}}_{\tilde{\mathbf{b}}} = \tilde{\mathbf{X}}_{k,\mathrm{D}}\underbrace{\mathcal{F}_a\begin{bmatrix}\mathbf{b}\\ \mathbf{0}\end{bmatrix}}_{\tilde{\mathbf{b}}}\end{aligned} \tag{4.57}$$

where the $N_a \times N$ selection matrix $\mathbf{S}_a = \mathcal{F}_a\mathcal{F}_N^H$ is obtained from the $N \times N$ identity matrix $\mathbf{I}_N$ by selecting the N_a rows corresponding to the tones $\mathcal{S}_a$. This TEQ design criterion (4.55-4.56) has been previously presented in [129]. If we now drop the constraints on $\tilde{\mathbf{b}}$ in (4.56), i.e., the constraints of $\mathbf{b}$ being real and having length $\nu+1$, and solve instead

$$\min_{\mathbf{w},\tilde{\mathbf{b}}} \mathcal{E}\left\{\left\|\tilde{\mathbf{Y}}_k\mathbf{w} - \tilde{\mathbf{X}}_{k,\mathrm{D}}\tilde{\mathbf{b}}\right\|^2\right\} \text{ s.t. } \mathbf{w}^T\boldsymbol{\Sigma}^2_{\tilde{\mathbf{Y}}}\mathbf{w} = 1 \text{ and real } \mathbf{w} \tag{4.58}$$

we obtain an *FD-MMSE-TEQ design criterion* in the (typically) real-valued TEQ $\mathbf{w}$ and the complex-valued vector $\tilde{\mathbf{b}}$ instead of $\mathbf{b}$, that minimizes a sum of FD error energies at the DFT output of the active tones $\mathcal{S}_a$. By dropping the constraints on $\tilde{\mathbf{b}}$, the search space of $\tilde{\mathbf{b}}$ is enlarged, so that the FD error energy in (4.58) is smaller than in (4.55-4.56). The impact of removing the constraints on $\tilde{\mathbf{b}}$ is studied in the simulations of Section 4.4.

The optimum solution for the unconstrained $\tilde{\mathbf{b}}$, which follows from the so-called orthogonality principle applied to (4.58), is a vector with the inverses of the uMMSE FEQs $\tilde{\mathbf{d}}^{\mathrm{uMMSE}}$ (also referred to as zero-forcing FEQs, see (4.25)),

which are the optimal choice of FEQs for a given $\mathbf{w}$, as explained in Section 4.2.2:

$$\tilde{d}_n^{\text{uMMSE}} = \frac{\sigma_{n,\tilde{x}}^2}{\boldsymbol{\sigma}_{n,\tilde{x}\tilde{\mathbf{y}}}\mathbf{w}} = \frac{1}{\tilde{b}_n} \tag{4.59}$$

The numerator $\sigma_{n,\tilde{x}}^2 = \mathcal{E}\left\{|\tilde{x}_{k,n}|^2\right\}$ is the variance of $\tilde{x}_{k,n}$; the denominator is the crosscorrelation $\mathcal{E}\left\{\tilde{x}_{k,n}^* \tilde{y}_{k,n,\mathbf{w}}\right\}$ between the equalized DFT output $\tilde{y}_{k,n,\mathbf{w}}$ and the TX symbol $\tilde{x}_{k,n}$, both on tone n. We have explained in Section 4.2.2, that this crosscorrelation is equal to $\boldsymbol{\sigma}_{n,\tilde{x}\tilde{\mathbf{y}}}\mathbf{w}$, with $\boldsymbol{\sigma}_{n,\tilde{x}\tilde{\mathbf{y}}} = \mathcal{E}\left\{\tilde{x}_{k,n}^* \tilde{\mathbf{y}}_{k,n}\right\}$ the $1 \times T$ crosscorrelation vector of $\tilde{x}_{k,n}$ and the n-th sliding DFT output $\tilde{\mathbf{y}}_{k,n}$. Solving (4.58) then minimizes the sum of error energies between the DFT outputs and the scaled desired symbols $\frac{\tilde{x}_{k,n}}{\tilde{d}_n^{\text{uMMSE}}}$.

Remark 4.8 Following the derivation in [157], a design criterion that leads to the same TEQ as (4.58) (up to a scaling) is obtained with the alternative UEC $\tilde{\mathbf{b}}^H \boldsymbol{\Sigma}_{\tilde{\mathbf{x}},\text{D}}^2 \tilde{\mathbf{b}} = 1$ where $\boldsymbol{\Sigma}_{\tilde{\mathbf{x}},\text{D}}^2 = \mathcal{E}\left\{\tilde{\mathbf{X}}_{k,\text{D}}^* \tilde{\mathbf{X}}_{k,\text{D}}\right\}$ is a diagonal matrix with the variance of the TX symbols $\tilde{\mathbf{x}}_k$ on the diagonal. In the case of equipowered TX symbols $\tilde{x}_{k,n}$, this constraint reduces to a unit norm constraint $\tilde{\mathbf{b}}^H \tilde{\mathbf{b}} = 1$. □

Under the assumption of wide-sense stationary signals and for $K \to \infty$, a deterministic **CLLS-based FD-MMSE-TEQ design criterion**, equivalent with the stochastic criterion (4.58), is given by:

$$\boxed{\min_{\mathbf{w},\tilde{\mathbf{b}}} \frac{1}{K} \sum_{k=1}^{K} \left\| \tilde{\mathbf{Y}}_k \mathbf{w} - \tilde{\mathbf{X}}_{k,\text{D}} \tilde{\mathbf{b}} \right\|^2 \text{ s.t. } \mathbf{w}^T \boldsymbol{\Sigma}_{K,\tilde{\mathbf{Y}}}^2 \mathbf{w} = 1 \text{ and real } \mathbf{w}} \tag{4.60}$$

where a subscript with the number of DMT symbols, K, is used to distinguish between the (deterministic) correlation estimates, $\boldsymbol{\Sigma}_{K,\tilde{\mathbf{Y}}}^2 = \frac{1}{K}\sum_{k=1}^{K} \tilde{\mathbf{Y}}_k^H \tilde{\mathbf{Y}}_k$, and the (stochastic) true correlation $\boldsymbol{\Sigma}_{\tilde{\mathbf{Y}}}^2 = \mathcal{E}\left\{\tilde{\mathbf{Y}}_{k,n}^H \tilde{\mathbf{Y}}_{k,n}\right\}$. Note that $\boldsymbol{\Sigma}_{K,\tilde{\mathbf{Y}}}^2 = \sum_{n \in \mathcal{S}_a} \boldsymbol{\Sigma}_{K,n,\tilde{\mathbf{y}}}^2$ with $\boldsymbol{\Sigma}_{K,n,\tilde{\mathbf{y}}}^2 = \frac{1}{K}\sum_{k=1}^{K} \tilde{\mathbf{y}}_{k,n}^H \tilde{\mathbf{y}}_{k,n}$ the autocorrelation matrix of the n-th sliding DFT output $\tilde{\mathbf{y}}_{k,n}$. Solving (4.60) for the unconstrained $\tilde{\mathbf{b}}$ (again using the orthogonality principle) gives an LS estimate (for a given $\mathbf{w}$) of the inverses of the uMMSE FEQs (4.59):

$$\tilde{\mathbf{b}} = \left(\boldsymbol{\Sigma}_{K,\tilde{\mathbf{x}},\text{D}}^2\right)^{-1} \boldsymbol{\Sigma}_{K,\tilde{\mathbf{x}}\tilde{\mathbf{Y}}} \mathbf{w} \text{ with entries } \tilde{b}_n = \frac{\boldsymbol{\sigma}_{K,n,\tilde{x}\tilde{\mathbf{y}}}\mathbf{w}}{\sigma_{K,n,\tilde{x}}^2} \tag{4.61}$$

where $\boldsymbol{\Sigma}_{K,\tilde{\mathbf{x}},\text{D}}^2 = \frac{1}{K}\sum_{k=1}^{K} \tilde{\mathbf{X}}_{k,\text{D}}^* \tilde{\mathbf{X}}_{k,\text{D}}$ is diagonal with diagonal elements $\sigma_{K,n,\tilde{x}}^2 = \frac{1}{K}\sum_{k=1}^{K} |\tilde{x}_{k,n}|^2$, and where the rows of the $N_a \times T$ crosscorrelation matrix estimate $\boldsymbol{\Sigma}_{K,\tilde{\mathbf{x}}\tilde{\mathbf{Y}}} = \frac{1}{K}\sum_{k=1}^{K} \tilde{\mathbf{X}}_{k,\text{D}}^* \tilde{\mathbf{Y}}_k$ are the crosscorrelation vectors $\boldsymbol{\sigma}_{K,n,\tilde{x}\tilde{\mathbf{y}}} =$

$\frac{1}{K}\sum_{k=1}^{K}\tilde{x}_{k,n}^{*}\tilde{\mathbf{y}}_{k,n}$. The CLLS-based FD-MMSE-TEQ design criterion (4.60) is very similar to the original CLLS-based TD-MMSE-TEQ (4.41). Hence, combining (4.61) and (4.60) results in an optimization criterion that is very similar to (4.43), namely:

$$\min_{\mathbf{w}} \mathbf{w}^T \left[\boldsymbol{\Sigma}^2_{K,\tilde{\mathbf{Y}}} - \boldsymbol{\Sigma}^H_{K,\tilde{\mathbf{x}}\tilde{\mathbf{Y}}} \left(\boldsymbol{\Sigma}^2_{K,\tilde{\mathbf{x}},\mathrm{D}}\right)^{-1} \boldsymbol{\Sigma}_{K,\tilde{\mathbf{x}}\tilde{\mathbf{Y}}}\right] \mathbf{w} \text{ s.t. } \mathbf{w}^T \boldsymbol{\Sigma}^2_{K,\tilde{\mathbf{Y}}} \mathbf{w} = 1 \text{ s.t. real } \mathbf{w} \tag{4.62}$$

This optimization criterion (4.62) is equivalent to:

$$\begin{aligned}
&\min_{\mathbf{w}} \frac{\mathbf{w}^T \left[\boldsymbol{\Sigma}^2_{K,\tilde{\mathbf{Y}}} - \boldsymbol{\Sigma}^H_{K,\tilde{\mathbf{x}}\tilde{\mathbf{Y}}} \left(\boldsymbol{\Sigma}^2_{K,\tilde{\mathbf{x}},\mathrm{D}}\right)^{-1} \boldsymbol{\Sigma}_{K,\tilde{\mathbf{x}}\tilde{\mathbf{Y}}}\right] \mathbf{w}}{\mathbf{w}^T \boldsymbol{\Sigma}^2_{K,\tilde{\mathbf{Y}}} \mathbf{w}} \\
&\quad = 1 - \max_{\mathbf{w}} \frac{\mathbf{w}^T \left[\boldsymbol{\Sigma}^H_{K,\tilde{\mathbf{x}}\tilde{\mathbf{Y}}} \left(\boldsymbol{\Sigma}^2_{K,\tilde{\mathbf{x}},\mathrm{D}}\right)^{-1} \boldsymbol{\Sigma}_{K,\tilde{\mathbf{x}}\tilde{\mathbf{Y}}}\right] \mathbf{w}}{\mathbf{w}^T \boldsymbol{\Sigma}^2_{K,\tilde{\mathbf{Y}}} \mathbf{w}} \text{ s.t. real } \mathbf{w} \qquad (4.63) \\
&\quad = 1 - \max_{\mathbf{w}} \frac{\mathbf{w}^T \left[\Re\left\{\boldsymbol{\Sigma}^H_{K,\tilde{\mathbf{x}}\tilde{\mathbf{Y}}} \left(\boldsymbol{\Sigma}^2_{K,\tilde{\mathbf{x}},\mathrm{D}}\right)^{-1} \boldsymbol{\Sigma}_{K,\tilde{\mathbf{x}}\tilde{\mathbf{Y}}}\right\}\right] \mathbf{w}}{\mathbf{w}^T \Re\left\{\boldsymbol{\Sigma}^2_{K,\tilde{\mathbf{Y}}}\right\} \mathbf{w}} \qquad (4.64)
\end{aligned}$$

The constraint in (4.63) of a real-valued TEQ is imposed in (4.64) by inserting the real operators $\Re\{\cdot\}$. The equivalence of (4.63) and (4.64) then follows from the Hermitian property of the matrices $\boldsymbol{\Sigma}^2_{K,\tilde{\mathbf{Y}}}$ and $\boldsymbol{\Sigma}^H_{K,\tilde{\mathbf{x}}\tilde{\mathbf{Y}}} \left(\boldsymbol{\Sigma}^2_{K,\tilde{\mathbf{x}},\mathrm{D}}\right)^{-1} \boldsymbol{\Sigma}_{K,\tilde{\mathbf{x}}\tilde{\mathbf{Y}}}$, which ensures that the Rayleigh quotient in (4.63) is real. Criterion (4.64) reduces to a GEV problem (3.3), which is closely related to (4.45), namely with

$$\begin{aligned}
(\mathbf{B}, \mathbf{A}) &= \left(\Re\left\{\boldsymbol{\Sigma}^H_{K,\tilde{\mathbf{x}}\tilde{\mathbf{Y}}} \left(\boldsymbol{\Sigma}^2_{K,\tilde{\mathbf{x}},\mathrm{D}}\right)^{-1} \boldsymbol{\Sigma}_{K,\tilde{\mathbf{x}}\tilde{\mathbf{Y}}}\right\}, \Re\left\{\boldsymbol{\Sigma}^2_{K,\tilde{\mathbf{Y}}}\right\}\right) \\
&= \left(\Re\left\{\sum_{n\in\mathcal{S}_a} \sigma^{-2}_{K,n,\tilde{x}} \boldsymbol{\sigma}^H_{K,n,\tilde{x}\tilde{\mathbf{y}}} \boldsymbol{\sigma}_{K,n,\tilde{x}\tilde{\mathbf{y}}}\right\}, \Re\left\{\sum_{n\in\mathcal{S}_a} \boldsymbol{\Sigma}^2_{K,n,\tilde{\mathbf{y}}}\right\}\right) \qquad (4.65)
\end{aligned}$$

Simulation results with the CLLS-based TD-MMSE-TEQ (4.41) and CLLS-based FD-MMSE-TEQ (4.60) are included in Section 4.4 and compared with the CLLS-based FD-MMSE-TEQ design with constraints on $\tilde{\mathbf{b}}$ (4.55-4.56) of [129].

4.3.3 SNLLS-based FD-MMSE-TEQ design

Instead of minimizing the sum of *DFT output error* energies $\mathcal{E}\left\{\|\mathcal{F}_a \mathbf{e}_k\|^2\right\}$ (see (4.55)), an alternative FD criterion is obtained by minimizing the sum of *FEQ output error* energies:

$$\min_{\mathbf{w},\tilde{\mathbf{d}}} \mathcal{E}\left\{\|\tilde{\mathbf{e}}_k\|^2\right\} = \min_{\mathbf{w},\tilde{\mathbf{d}}} \mathcal{E}\left\{\left\|\mathrm{diag}(\tilde{\mathbf{d}})\tilde{\mathbf{Y}}_k \mathbf{w} - \tilde{\mathbf{x}}_k\right\|^2\right\} \text{ with real } \mathbf{w} \tag{4.66}$$

where $\tilde{\mathbf{e}}_k$ is the FEQ output error vector, which depends on both the real-valued TEQ $\mathbf{w}$ and complex-valued FEQ parameters $\tilde{\mathbf{d}}$, i.e., $\boldsymbol{\theta} = \begin{bmatrix} \mathbf{w}^H & \tilde{\mathbf{d}}^H \end{bmatrix}^H$; its first term $\text{diag}(\tilde{\mathbf{d}})\tilde{\mathbf{Y}}_k\mathbf{w}$ is a vector with the FEQ outputs, as defined in (2.43). The UEC constraint of (4.58) has been dropped as the criterion (4.66) does not have a trivial solution anymore. Under the assumption of wide-sense stationary signals and for $K \to \infty$, this criterion corresponds to a separable non-linear LS (SNLLS) criterion [16, 51]:

$$\boxed{\min_{\boldsymbol{\theta}} \frac{1}{K} \sum_{k=1}^{K} \left\| \underbrace{\text{diag}(\tilde{\mathbf{d}})\tilde{\mathbf{Y}}_k\mathbf{w} - \tilde{\mathbf{x}}_k}_{\tilde{\mathbf{e}}_k} \right\|^2 \quad \text{with real } \mathbf{w}} \tag{4.67}$$

which we refer to as an **SNLLS-based FD-MMSE-TEQ** design criterion: although the error $\tilde{\mathbf{e}}_k$ is non-linear in $\boldsymbol{\theta}$, the TEQ $\mathbf{w}$ and FEQs $\tilde{\mathbf{d}}$ appear linearly, hence the separability property. It follows from this separability property that solving (4.66) as a linear MMSE problem in $\tilde{\mathbf{d}}$, obtained by keeping $\mathbf{w}$ in (4.66) fixed, results in the biased MMSE (bMMSE) FEQs (4.20) for the given $\mathbf{w}$ [115]:

$$\tilde{d}_n^{\text{bMMSE}} = \frac{\mathbf{w}^T \boldsymbol{\sigma}_{n,\tilde{x}\tilde{\mathbf{y}}}^H}{\mathbf{w}^T \boldsymbol{\Sigma}_{n,\tilde{\mathbf{y}}}^2 \mathbf{w}} \tag{4.68}$$

where the numerator is equal to the complex conjugate of the denominator of the uMMSE FEQ (4.59) and where the denominator is the autocorrelation of the DFT output, i.e., $\mathcal{E}\left\{ |\tilde{y}_{k,n,\mathbf{w}}|^2 \right\} = \mathbf{w}^T \boldsymbol{\Sigma}_{n,\tilde{\mathbf{y}}}^2 \mathbf{w}$ with $\boldsymbol{\Sigma}_{n,\tilde{\mathbf{y}}}^2$ defined earlier.

It will be shown in Section 4.3.4 that the SNLLS-based FD-MMSE-TEQ design criterion (4.67) can be optimized iteratively with a sequence of GEV problems (3.3). An alternative, fast converging Gauss-Newton-based initialization algorithm that exploits the separability property of (4.67) is presented in Section 4.3.5. In Section 4.3.6, it will become clear that both the CLLS-based and the SNLLS-based FD-MMSE-TEQ designs are equivalent to the PTEQ design when considering only a single tone. The simulations of Section 4.4 show that the SNLLS-based FD-MMSE-TEQ design is a useful intermediate TEQ design as it consistently outperforms the CLLS-based TD-MMSE-TEQ design (4.41) and closely approaches the BM-TEQ performance.

4.3.4 IR-SNLLS-based BM-TEQ design

The bit rate maximizing TEQ (BM-TEQ) is the solution to the following constrained non-linear optimization problem in the joint TEQ-FEQ parameter vector $\boldsymbol{\theta} = \begin{bmatrix} \mathbf{w}^H & \tilde{\mathbf{d}}^H \end{bmatrix}^H$:

$$\max_{\boldsymbol{\theta}} \sum_{n \in \mathcal{S}_a} \log_2 \left(1 + \frac{\text{SNR}_n}{\Gamma_n} \right) \tag{4.69}$$

$$\text{with SNR}_n = \frac{\sigma^2_{n,\tilde{x}}}{\mathcal{E}\left\{\left|\tilde{e}^{\text{uMMSE}}_{k,n}\right|^2\right\}} = \frac{\sigma^2_{n,\tilde{x}}}{\mathcal{E}\left\{\left|\tilde{d}^{\text{uMMSE}}_n \tilde{\mathbf{y}}_{k,n}\mathbf{w} - \tilde{x}_{k,n}\right|^2\right\}} \tag{4.70}$$

$$\text{subject to a real } \mathbf{w} \text{ and } \tilde{d}^{\text{uMMSE}}_n = \frac{\sigma^2_{n,\tilde{x}}}{\boldsymbol{\sigma}_{n,\tilde{x}\tilde{\mathbf{y}}}\mathbf{w}},\ \forall n \in \mathcal{S}_a \tag{4.71}$$

i.e., maximizing the bit rate (3.42), hence the number of bits per DMT symbol (given a certain SNR gap Γ_n, see Section 2.1.3), over the joint TEQ-FEQ parameters $\boldsymbol{\theta}$, subject to the use of uMMSE FEQs (4.71) (see also (4.59)), which render the SNR model in (4.70) exact. This optimization problem (4.69-4.71) is equivalent to minimizing the original BM-TEQ design criterion (4.32). In the appendix of this chapter, we show, based on (4.69-4.71), that the original (stochastic) BM-TEQ criterion (4.32) is equivalent to the following (deterministic) **iteratively reweighted (IR) SNLLS-based bit rate maximizing FD-MMSE-TEQ** design criterion (explained below and to be compared to (4.67)) [18]:

$$\boxed{\min_{\boldsymbol{\theta}} \frac{1}{K}\sum_{k=1}^{K}\left\|\text{diag}\left(\sqrt{\boldsymbol{\gamma}_{K,\mathbf{w}_{\text{prev}}}}\right)\underbrace{\left(\text{diag}(\tilde{\mathbf{d}})\tilde{\mathbf{Y}}_k\mathbf{w} - \tilde{\mathbf{x}}_k\right)}_{\tilde{\mathbf{e}}_k}\right\|^2 \text{ with real } \mathbf{w}} \tag{4.72}$$

This is clearly a weighted LS criterion where the entry of the $N_a \times 1$ weight vector $\boldsymbol{\gamma}_{K,\mathbf{w}_{\text{prev}}}$ that corresponds to tone n is found to be:

$$\gamma_{K,n,\mathbf{w}} = \frac{(\text{SNR}_{K,n}+1)^2}{\sigma^2_{K,n,\tilde{x}}\,(\text{SNR}_{K,n}+\Gamma_n)} \tag{4.73}$$

$$\text{SNR}_{K,n} = \frac{1}{\rho^{-2}_{K,n,\mathbf{w}}-1} = \frac{\sigma^2_{K,n,\tilde{x}}}{\frac{1}{K}\sum_{k=1}^{K}|\tilde{e}_{k,n}|^2} \tag{4.74}$$

$$\rho^2_{K,n,\mathbf{w}} = \frac{\left|\boldsymbol{\sigma}_{K,n,\tilde{x}\tilde{\mathbf{y}}}\mathbf{w}\right|^2}{\sigma^2_{K,n,\tilde{x}}\left(\mathbf{w}^T\boldsymbol{\Sigma}^2_{K,n,\tilde{\mathbf{y}}}\mathbf{w}\right)} \tag{4.75}$$

The LS error vector $\tilde{\mathbf{e}}_k = \text{diag}(\tilde{\mathbf{d}})\tilde{\mathbf{Y}}_k\mathbf{w} - \tilde{\mathbf{x}}_k$ is the same FEQ output error vector as in the SNLLS-based FD-MMSE-TEQ design criterion (4.67), hence (4.72) is also an SNLLS-based criterion. The SNLLS-based FD-MMSE-TEQ design criterion (4.67) is indeed an unweighted version of, hence closely related to, the IR-SNLLS-based BM-TEQ design criterion (4.72). The algorithms for optimizing the IR-SNLLS-based BM-TEQ design criterion, which are given below, then also apply to the SNLLS-based FD-MMSE-TEQ design criterion by setting the weights $\boldsymbol{\gamma}_{K,\mathbf{w}_{\text{prev}}}$ equal to 1.

Remark 4.9 The subscripts K indicate that $\gamma_{K,n,\mathbf{w}}$, $\rho^2_{K,n,\mathbf{w}}$ and $\text{SNR}_{K,n}$ in (4.73-4.75) are based on the deterministic SOS estimates $\sigma^2_{K,n,\tilde{x}}$, $\boldsymbol{\sigma}_{K,n,\tilde{x}\tilde{\mathbf{y}}}$ and

$\boldsymbol{\Sigma}^2_{K,n,\tilde{\mathbf{y}}}$: $\rho^2_{K,n,\mathbf{w}}$ is a deterministic estimate of the squared normalized correlation $\rho^2_{n,\mathbf{w}}$ (4.29) of $\tilde{x}_{k,n}$ and $\tilde{y}_{k,n,\mathbf{w}}$; $\mathrm{SNR}_{K,n}$ is a deterministic estimate of SNR_n in (4.28). □

Remark 4.10 It holds true for (4.72), as for (4.67), that solving (4.72) as a linear LS problem in $\tilde{\mathbf{d}}$, obtained by keeping $\mathbf{w}$ in (4.72) fixed, results in an LS estimate of the biased MMSE (bMMSE) FEQs $\tilde{d}_n^{\mathrm{bMMSE}}$ (4.68) for the given $\mathbf{w}$. The solution for $\tilde{\mathbf{d}}$ appears indeed independent of the weights $\boldsymbol{\gamma}_{K,\mathbf{w}_{\mathrm{prev}}}$. The uMMSE FEQ $\tilde{d}_n^{\mathrm{uMMSE}}$ can then be obtained from $\tilde{d}_n^{\mathrm{bMMSE}}$ and $\mathbf{w}$ via the squared normalized correlation $\rho^2_{n,\mathbf{w}}$ (4.29) which relates $\tilde{d}_n^{\mathrm{uMMSE}}$ and $\tilde{d}_n^{\mathrm{bMMSE}}$, see (4.30). □

Note on the IR-SNLLS-based BM-TEQ design criterion (4.72)

We have mentioned before that DMT-based modulation is a *block transmission* scheme with *frequency-domain* symbols of interest. Hence it does not come as a surprise that the BM-TEQ is the solution of an LS criterion that sums over the N_a *frequency-domain errors* at the FEQ outputs. The importance or *weight* $\gamma_{K,n,\mathbf{w}}$ of each FD error depends on SNR_n, as the SNR determines the number of bits that can be transmitted on each tone. This SNR is determined by the residual ISI/ICI (see (4.1)), which is a function of the TEQ design, hence the *iteratively reweighting* property of (4.72).

It is clear that the PTEQ design criterion (3.71) is a special case of the BM-TEQ design criterion (4.72) for a single tone n (the weighting then does not play a role), which can then be solved as a classical linear LS problem: the PTEQ for a particular tone then combines the functionality of the TEQ and FEQ.

Iteratively reweighted least-squares criteria

The cost criterion (4.72) is a so-called *iteratively reweighted* (IR) LS criterion. An IR-LS criterion forms a representation of a non-linear cost criterion, which can be written as a weighted LS criterion where the weights $\boldsymbol{\gamma}_{K,\mathbf{w}_{\mathrm{prev}}}$ depend on the LS errors $\tilde{\mathbf{e}}_k$, $k = 1, \ldots, K$ (here: via the SNRs (4.74)), and hence on the optimization parameters $\boldsymbol{\theta}$ [18]. IR-LS criteria are typically optimized as an iterative sequence of weighted LS criteria with fixed weights in each iteration, computed with the parameter estimates from the previous iteration, $\boldsymbol{\theta}_{\mathrm{prev}}$. According to [18], convergence occurs provided that the weights are bounded and non-increasing in the (absolute value) of the LS errors. For a non-convex cost function, the IR-LS algorithm leads to a local optimum. For $K \to \infty$ and under the assumption of wide-sense stationarity, the iterative sequence of (deterministic) LS criteria (4.72) is equivalent to the original (stochastic) BM-TEQ criterion (4.32).

Naive three-step algorithm for optimizing the IR-SNLLS-based BM-TEQ criterion

According to [16, 51], SNLLS criteria such as the FD-MMSE-TEQ design criterion (4.67) and the BM-TEQ design criterion (4.72) are optimized iteratively, e.g., by alternately updating the parameters $\mathbf{w}$ and $\tilde{\mathbf{d}}$. An iteration step i for the IR-SNLLS-based BM-TEQ criterion then consists of the computation of

1. an estimate of the weights, $\boldsymbol{\gamma}_{K,\mathbf{w}_{\text{prev}}}$, based on (4.73-4.75), evaluated in the TEQ estimate $\mathbf{w}_{\text{prev}} = \mathbf{w}_{i-1}$ of the previous iteration;
2. an LS estimate of the bMMSE FEQs $\tilde{\mathbf{d}}_i^{\text{bMMSE}}$ (4.68), which are the solution of (4.72) for $\mathbf{w} = \mathbf{w}_{i-1}$:

$$\tilde{d}_{n,i}^{\text{bMMSE}} = \frac{\mathbf{w}_{i-1}^T \boldsymbol{\sigma}_{K,n,\tilde{x}\tilde{\mathbf{y}}}^H}{\mathbf{w}_{i-1}^T \boldsymbol{\Sigma}_{K,n,\tilde{\mathbf{y}}}^2 \mathbf{w}_{i-1}} \tag{4.76}$$

3. a BM-TEQ estimate $\mathbf{w}_i$, which is the LS solution of (4.72) for a fixed $\tilde{\mathbf{d}}_i = \tilde{\mathbf{d}}_i^{\text{bMMSE}}$:

$$\mathbf{w}_i = \Re\left\{\sum_{n\in\mathcal{S}_a} \gamma_{K,n,\mathbf{w}_{i-1}} \left|\tilde{d}_{n,i}\right|^2 \boldsymbol{\Sigma}_{K,n,\tilde{\mathbf{y}}}^2\right\}^{-1} \Re\left\{\sum_{n\in\mathcal{S}_a} \gamma_{K,n,\mathbf{w}_{i-1}} \tilde{d}_{n,i}^* \boldsymbol{\sigma}_{K,n,\tilde{x}\tilde{\mathbf{y}}}^H\right\} \tag{4.77}$$

For a complex-valued TEQ, the $\Re$-operators must be omitted. The iterations for optimizing the SNLLS-based FD-MMSE-TEQ design criterion (4.67) do not include the first step, i.e., the weights $\gamma_{K,n,\mathbf{w}_{\text{prev}}}$ are always equal to 1.

Remark 4.11 The TEQ estimate (4.77) is the solution (up to a scaling) of a GEV problem (3.3) with matrix pair:

$$(\mathbf{B},\mathbf{A}) = \left(\Re\left\{\sum_{n\in\mathcal{S}_a} \gamma_{K,n,\mathbf{w}_{i-1}} \tilde{d}_{n,i}^* \boldsymbol{\sigma}_{K,n,\tilde{x}\tilde{\mathbf{y}}}^H\right\} \Re\left\{\sum_{n\in\mathcal{S}_a} \gamma_{n,\mathbf{w}_{i-1}} \tilde{d}_{n,i} \boldsymbol{\sigma}_{K,n,\tilde{x}\tilde{\mathbf{y}}}\right\}, \right.$$
$$\left. \Re\left\{\sum_{n\in\mathcal{S}_a} \gamma_{K,n,\mathbf{w}_{i-1}} \left|\tilde{d}_{n,i}\right|^2 \boldsymbol{\Sigma}_{K,n,\tilde{\mathbf{y}}}^2\right\}\right) \tag{4.78}$$

As $\mathbf{A}$ is a positive-definite matrix and $\mathbf{B}$ has rank 1, the corresponding GEV problem has only 1 strictly positive GEV; the other GEVs are zero; the dominant generalized eigenvector has then indeed the closed form solution (4.77). The SNLLS-based FD-MMSE-TEQ and the IR-SNLLS-based BM-TEQ are thus the solution of an iteratively solved sequence of GEV problems where the matrix pair $(\mathbf{B},\mathbf{A})$ is adapted in each iteration to the new FEQ estimates $\tilde{\mathbf{d}}_i$, hence these TEQ design criteria also fit in the common optimization framework of Section 3.1. □

4.3.5 Iterative Gauss-Newton-based BM-TEQ design algorithm

The above presented three-step algorithm that alternately updates $\boldsymbol{\gamma}_{K,\mathbf{w}}$, $\mathbf{w}$ and $\tilde{\mathbf{d}}$ converges only linearly. It is argued in [16, 51] that the convergence speed of an iterative algorithm that optimizes an SNLLS problem can be increased dramatically and becomes quadratic by exploiting the separability property in an appropriate way. Therefore, an iterative Gauss-Newton (GN) based method (or Levenberg-Marquardt (LM) method, which includes regularization) must be applied. According to [51], it is advantageous for the convergence speed to eliminate a set of parameters, e.g., the FEQs $\tilde{\mathbf{d}}$, by writing them as a function of the remaining parameters, here the TEQ $\mathbf{w}$. The resulting expression for the FEQ on tone n, $\tilde{d}_n$, in the problem at hand corresponds to the LS estimate of the bMMSE FEQ in (4.76) and is a function of $\mathbf{w}$. After the elimination of $\tilde{\mathbf{d}}$, a non-linear design criterion in $\mathbf{w}$ is obtained, reminiscent of the original non-linear BM-TEQ design criterion (4.32), derived in Section 4.2. An algorithm for optimizing the IR-SNLLS-based BM-TEQ design criterion with quadratic convergence speed then consists of an iterative minimization, e.g., using a GN-based algorithm, of the (iteratively-reweighted) non-linear design criterion in $\mathbf{w}$ until convergence, followed by a computation of the parameters $\tilde{\mathbf{d}}$, by evaluating (4.76) in the obtained $\mathbf{w}$ [50]. A GN-based method makes use of a positive-definite Hessian approximation to guarantee that a downhill step is taken in each iteration.

According to [16, 70], a closely related alternative for this iterative GN-based algorithm exists, which makes use of an extra approximation of the Hessian with only a small impact on the convergence speed. This cheaper alternative is obtained from the iterative three-step algorithm (i.e., with alternate updating of $\boldsymbol{\gamma}_{K,\mathbf{w}}$, $\tilde{\mathbf{d}}$ and $\mathbf{w}$) where step (3) is replaced by a much faster converging update of $\mathbf{w}$. The update of $\mathbf{w}$ follows from the GN update to optimize the IR-SNLLS-based BM-TEQ design criterion in the joint parameter vector $\boldsymbol{\theta}$:

$$\boldsymbol{\theta}_i \leftarrow \boldsymbol{\theta}_{i-1} - \alpha_i \mathbf{R}_{\boldsymbol{\theta}_{i-1}}^{-1} \mathbf{g}_{\boldsymbol{\theta}_{i-1}} \tag{4.79}$$

where $\boldsymbol{\theta}_{i-1} = \begin{bmatrix} \mathbf{w}_{i-1}^H & \left(\tilde{\mathbf{d}}_i^{\text{bMMSE}}\right)^H \end{bmatrix}^H$, where $\mathbf{g}_{\boldsymbol{\theta}_{i-1}}$ and $\mathbf{R}_{\boldsymbol{\theta}_{i-1}}$ are the gradient and the positive-definite Hessian approximation of the IR-SNLLS-based BM-TEQ design criterion (4.72), evaluated in $\boldsymbol{\theta}_{i-1}$, and where α_i is a step size, obtained through a line search algorithm [16]. The gradient $\mathbf{g}_{\boldsymbol{\theta}}$ and approximate Hessian $\mathbf{R}_{\boldsymbol{\theta}}$ in (4.79) for a *complex-valued* TEQ are given by:

$$\mathbf{g}_{\boldsymbol{\theta}} = \begin{bmatrix} \mathbf{g}_{1,\boldsymbol{\theta}} \\ \mathbf{g}_{2,\boldsymbol{\theta}} \end{bmatrix} = \frac{1}{K} \sum_{k=1}^{K} \check{\mathbf{Y}}_{k,\boldsymbol{\theta}}^H \text{diag}\left(\boldsymbol{\gamma}_{K,\mathbf{w}_{\text{prev}}}\right) \tilde{\mathbf{e}}_k \tag{4.80}$$

$$\mathbf{R}_{\boldsymbol{\theta}} = \frac{1}{K} \sum_{k=1}^{K} \check{\mathbf{Y}}_{k,\boldsymbol{\theta}}^H \text{diag}\left(\boldsymbol{\gamma}_{K,\mathbf{w}_{\text{prev}}}\right) \check{\mathbf{Y}}_{k,\boldsymbol{\theta}} \tag{4.81}$$

where

$$\check{\mathbf{Y}}_{k,\boldsymbol{\theta}} = \left[\begin{array}{c|c} \mathrm{diag}\left(\tilde{\mathbf{d}}\right)\tilde{\mathbf{Y}}_k & \mathrm{diag}(\tilde{\mathbf{Y}}_k\mathbf{w}) \end{array} \right] \tag{4.82}$$

and where $\mathbf{g}_{1,\boldsymbol{\theta}}$ and $\mathbf{g}_{2,\boldsymbol{\theta}}$ are $T \times 1$ and $N_a \times 1$ subvectors of $\mathbf{g}_{\boldsymbol{\theta}}$, respectively. The expressions for a real-valued TEQ are similar, but more cumbersome, because $\boldsymbol{\theta}$ then contains real-valued TEQ coefficients and complex-valued FEQ coefficients. Based on (4.81), we define the following block-based description for the approximate Hessian:

$$\mathbf{R}_{\boldsymbol{\theta}} = \left[\begin{array}{cc} \mathbf{E} & \mathbf{F} \\ \mathbf{F}^H & \mathbf{G} \end{array} \right] \tag{4.83}$$

with

$$\begin{aligned} \mathbf{E} &= \frac{1}{K}\sum_{k=1}^{K} \tilde{\mathbf{Y}}_k^H \mathrm{diag}\left(\boldsymbol{\gamma}_{K,\mathbf{w}_{\mathrm{prev}}} \odot \left|\tilde{\mathbf{d}}\right|^2\right)\tilde{\mathbf{Y}}_k \\ &= \sum_{n\in\mathcal{S}_a} \gamma_{K,n,\mathbf{w}_{\mathrm{prev}}} \left|\tilde{d}_n\right|^2 \boldsymbol{\Sigma}^2_{K,n,\tilde{\mathbf{y}}} \end{aligned} \tag{4.84}$$

$$\begin{aligned} \mathbf{F}^H &= \frac{1}{K}\sum_{k=1}^{K} \mathrm{diag}\left(\tilde{\mathbf{Y}}_k\mathbf{w}\right)^* \mathrm{diag}\left(\boldsymbol{\gamma}_{K,\mathbf{w}_{\mathrm{prev}}} \odot \tilde{\mathbf{d}}\right)\tilde{\mathbf{Y}}_k \\ &= \left[\begin{array}{c} \vdots \\ \left[\gamma_{K,n,\mathbf{w}_{\mathrm{prev}}}\tilde{d}_n\left(\mathbf{w}^H\boldsymbol{\Sigma}^2_{K,n,\tilde{\mathbf{y}}}\right)\right] \\ \vdots \end{array} \right] \updownarrow N_a \text{ rows} \end{aligned} \tag{4.85}$$

$$\begin{aligned} \mathbf{G} &= \frac{1}{K}\sum_{k=1}^{K} \mathrm{diag}\left(\boldsymbol{\gamma}_{K,\mathbf{w}_{\mathrm{prev}}} \odot \left|\tilde{\mathbf{Y}}_k\mathbf{w}\right|^2\right) \\ &= \mathrm{diag}\left(\left[\begin{array}{ccc} \cdots & \gamma_{K,n,\mathbf{w}_{\mathrm{prev}}}\left(\mathbf{w}^H\boldsymbol{\Sigma}^2_{K,n,\tilde{\mathbf{y}}}\mathbf{w}\right) & \cdots \end{array} \right]\right) \end{aligned} \tag{4.86}$$

Each of the block matrices above has been written explicitly in terms of the $T \times T$ sliding DFT autocorrelation matrix estimates $\boldsymbol{\Sigma}^2_{K,n,\tilde{\mathbf{y}}}$, $n \in \mathcal{S}_a$. The SOS $\boldsymbol{\Sigma}^2_{K,n,\tilde{\mathbf{y}}}$ and the TEQ $\mathbf{w}$ are again decoupled, based on the first key observation (3.62). The inverse of $\mathbf{R}_{\boldsymbol{\theta}}$ is then given by [66]:

$$\mathbf{R}_{\boldsymbol{\theta}}^{-1} = \left[\begin{array}{cc} \mathbf{Q}^{-1} & -\mathbf{Q}^{-1}\mathbf{F}\mathbf{G}^{-1} \\ -\mathbf{G}^{-1}\mathbf{F}^H\mathbf{Q}^{-1} & \mathbf{G}^{-1}\left(\mathbf{I}_{N_a} + \mathbf{F}^H\mathbf{Q}^{-1}\mathbf{F}\mathbf{G}^{-1}\right) \end{array} \right] \tag{4.87}$$

with $\mathbf{Q}$ the Schur complement of $\mathbf{G}$ [52], i.e.,

$$\mathbf{Q} = \mathbf{E} - \mathbf{F}\mathbf{G}^{-1}\mathbf{F}^H \tag{4.88}$$

Although considering the GN update (4.79) to optimize the design criterion in $\boldsymbol{\theta}$, we in fact only use the update of $\mathbf{w}$ in the iterative 3-step algorithm; the update of $\tilde{\mathbf{d}}$ is ignored and replaced by the computation of the LS estimate of the bMMSE FEQs (4.76) in step (2). Moreover, it follows from (4.76) that $\mathbf{g}_{2,\boldsymbol{\theta}_{i-1}}$ is an all-zero vector in each iteration. For a complex-valued TEQ, the TEQ update in step (3) is then given by:

$$\boxed{\mathbf{w}_i \leftarrow \mathbf{w}_{i-1} - \alpha_i \mathbf{Q}_{\boldsymbol{\theta}_{i-1}}^{-1} \mathbf{g}_{1,\boldsymbol{\theta}_{i-1}}} \tag{4.89}$$

The subscript $\boldsymbol{\theta}_{i-1}$ indicates that $\mathbf{Q}$ does not only depend on the RX signal SOS, but also on the previous parameter estimate. One can show that the updating, in the case of a real-valued TEQ, becomes:

$$\mathbf{w}_i \leftarrow \mathbf{w}_{i-1} - \alpha_i \left(\Re \left\{ \mathbf{Q}_{\boldsymbol{\theta}_{i-1}} \right\} \right)^{-1} \Re \left\{ \mathbf{g}_{1,\boldsymbol{\theta}_{i-1}} \right\} \tag{4.90}$$

After each iteration, we normalize the TEQ to remove the scalar parameter ambiguity of (4.72), namely that if $\boldsymbol{\theta} = \begin{bmatrix} \mathbf{w}^H & \tilde{\mathbf{d}}^H \end{bmatrix}^H$ is a solution of (4.72), then $\boldsymbol{\theta} = \begin{bmatrix} \eta \mathbf{w}^H & \eta^{-1} \tilde{\mathbf{d}}^H \end{bmatrix}^H$ is also a solution.

The second-order statistics $\boldsymbol{\Sigma}^2_{K,n,\tilde{\mathbf{y}}}$ and $\boldsymbol{\sigma}_{K,n,\tilde{x}\tilde{\mathbf{y}}}$, required for the above outline iterative GN algorithm can be computed, based on a channel and noise estimate or recursively, based on (part of) the training signal with cyclic prefix that is transmitted during connection set-up. Below, an estimate of the dominant computational cost terms (in number of real multiplications per iteration) for the case of a real-valued TEQ is given. The following steps in the algorithm are the most expensive:

- the computation of the complex-valued vectors $\boldsymbol{\Sigma}^2_{K,n,\tilde{\mathbf{y}}} \mathbf{w}_{i-1}$, $n \in \mathcal{S}_a$, required for the weights $\boldsymbol{\gamma}_{K,\mathbf{w}_{\text{prev}}}$ as well as for $\mathbf{F}$, $\mathbf{G}$ and $\mathbf{g}_{1,\boldsymbol{\theta}_{i-1}}$, costs around $\mathcal{O}(2N_a T^2)$ real multiplications;
- the computation of the real part of $\mathbf{E}$ in (4.84), which is required for $\Re\{\mathbf{Q}_{\boldsymbol{\theta}_{i-1}}\}$ in (4.90) and which is a symmetric matrix (hence roughly half of the elements are to be computed), costs around $\mathcal{O}(N_a T^2/2)$ real multiplications;
- the computation of the real part of $\mathbf{F}\mathbf{G}^{-1}\mathbf{F}^H$, which is also a symmetric matrix required for $\Re\{\mathbf{Q}_{\boldsymbol{\theta}_{i-1}}\}$, costs around$\mathcal{O}(N_a T^2)$ real multiplications;
- the matrix inversion $\Re\{\mathbf{Q}_{\boldsymbol{\theta}_{i-1}}\}^{-1}$ costs $\mathcal{O}(T^3/6)$ real multiplications.

All other steps (e.g., the computation of the scalars $(\mathbf{w}_{i-1}^T \boldsymbol{\Sigma}^2_{K,n,\tilde{\mathbf{y}}})\mathbf{w}_{i-1}$ and $\mathbf{w}_{i-1}^T \boldsymbol{\sigma}^H_{K,n,\tilde{x}\tilde{\mathbf{y}}}$, $n \in \mathcal{S}_a$, the weights $\boldsymbol{\gamma}_{K,\mathbf{w}_{\text{prev}}}$ and the MMSE FEQs (4.76)) have a complexity of $\mathcal{O}(N_a T)$ or less, hence the overall computational cost per iteration is dominated by $\mathcal{O}(\frac{7}{2} N_a T^2) + \mathcal{O}(\frac{1}{6} T^3)$ real multiplications. From the

simulations in Section 4.4, we learn that roughly 30 iterations suffice for convergence. For typical values of N_a and T, e.g., $N_a = 219$ and $T = 32$, one iteration requires 8×10^5 multiplications, so roughly 24×10^6 multiplications are needed until convergence.

The connection set-up phase of an ADSL modem typically lasts for several seconds; e.g., the training signal with cyclic prefix is around 16000 DMT symbols or 4 seconds long [61]. Assuming that 1 second is used for the recursive estimation of the second-order statistics $\mathbf{\Sigma}^2_{K,n,\tilde{\mathbf{y}}}$ and $\boldsymbol{\sigma}_{K,n,\tilde{x}\tilde{\mathbf{y}}}$ (computational cost: $\mathcal{O}(N_a T)$ per DMT symbol, see also Section 3.4) and 3 seconds are used for the iterative GN algorithm, the latter requires a reasonable cost of around 5.2×10^6 real multiplications per second. Although in general the large computational cost and the presence of local optima may render a nonlinear optimization algorithm prohibitive for a real-time implementation, the above described iterative GN algorithm for IR-SNLLS-based BM-TEQ design turns out to be a worthwhile approach. Simulations illustrating the convergence speed of the iterative GN-based method that optimizes the SNLLS-based FD-MMSE-TEQ and the IR-SNLLS-based BM-TEQ design criteria are given in Section 4.4.

Remark 4.12 In an alternative approach, step 2 in the three-step algorithm, which determines an LS estimate of the FEQs in each iteration, could be omitted and replaced by the iterative FEQ estimate as part of the GN update of $\boldsymbol{\theta}$ (4.79). The resulting algorithm is then a two-step algorithm that alternates between an update of the weights $\boldsymbol{\gamma}_{K,\mathbf{w}_{\text{prev}}}$ and a GN update of the parameter vector $\boldsymbol{\theta}$. The asymptotic convergence speed of a GN-based method applied to the non-linear design criterion in $\mathbf{w}$ and the SNLLS-based design criterion in the joint parameter vector $\boldsymbol{\theta}$ has been shown to be the same [101]. However, the former has several advantages [51]. Thanks to the reduced parameter space for $\mathbf{w}$, the local minima of the non-linear criterion in $\mathbf{w}$ appear to be better defined. This results in faster initial convergence, and hence also faster overall convergence. Moreover, as the parameters $\tilde{\mathbf{d}}$ are determined by $\mathbf{w}$, the GN-based update of $\boldsymbol{\theta}$ in the IR-SNLLS-based BM-TEQ design criterion must become increasingly ill-conditioned as (and if) it converges to the optimal parameters [51]. Indeed, a GN-based method to optimize the IR-SNLLS-based BM-TEQ design criterion in $\boldsymbol{\theta}$ is more likely to run unstable, hence one should resort to a Levenberg-Marquardt type of algorithm, which includes a regularization [51].

A *recursive* or *adaptive* BM-TEQ equalizer design, derived from the above described iterative GN algorithm is pursued in Chapter 5. There, the LS estimation of $\tilde{\mathbf{d}}$ will be omitted to reduce the SOS memory cost and the full update of $\boldsymbol{\theta}$ (including the update of $\tilde{\mathbf{d}}$), based on (4.79), will be used instead. As discussed above, this goes at the expense of a lower (but sufficiently fast) convergence speed and a Levenberg-Marquardt type of algorithm, which includes a regularization, is then required. □

4.3.6 Relation between FD-MMSE-TEQ and PTEQ designs

The PTEQ has been presented in Section 3.4 as an alternative equalizer for DMT-based systems. An equalizer is designed for each tone separately by solving either the MMSE design criterion (3.69) in the PTEQ coefficients $\mathbf{v}_n$ or, equivalently, the MMSE design criterion (3.71) in the PTEQ coefficients $\mathbf{w}_n$. A deterministic **LS-based MMSE-PTEQ criterion**, equivalent with the stochastic criterion (3.71) is given by:

$$\boxed{\min_{\mathbf{w}_n} \frac{1}{K} \sum_{k=1}^{K} |\tilde{\mathbf{y}}_{k,n}\mathbf{w}_n - \tilde{x}_{k,n}|^2} \tag{4.91}$$

where the *complex-valued* PTEQ $\mathbf{w}_n$ implicitly combines the task of the FEQ and TEQ. The solution to (4.91) is given by

$$\mathbf{w}_n = \left(\boldsymbol{\Sigma}^2_{K,n,\tilde{\mathbf{y}}}\right)^{-1} \boldsymbol{\sigma}^H_{K,n,\tilde{x}\tilde{\mathbf{y}}} \tag{4.92}$$

where $\boldsymbol{\Sigma}^2_{K,n,\tilde{\mathbf{y}}}$ and $\boldsymbol{\sigma}_{K,n,\tilde{x}\tilde{\mathbf{y}}}$ have been defined in the previous section.

The PTEQ design criterion (4.91) is closely related to the CLLS-based and SNLLS-based FD-MMSE-TEQ design criteria of the previous section when only a single tone is considered. Criteria (4.60) and (4.67) then reduce to

$$\begin{aligned} \min_{\mathbf{w},\tilde{b}_n} \frac{1}{K} \sum_{k=1}^{K} |\mathcal{F}_n \mathbf{e}_k|^2 \quad &= \quad \min_{\mathbf{w},\tilde{b}_n} \frac{1}{K} \sum_{k=1}^{K} \left|\tilde{\mathbf{y}}_{k,n}\mathbf{w} - \tilde{x}_{k,n}\tilde{b}_n\right|^2 \\ &\qquad \text{s.t. } \mathbf{w}^T \boldsymbol{\Sigma}^2_{K,n,\tilde{\mathbf{y}}} \mathbf{w} = 1 \text{ and real } \mathbf{w} \end{aligned} \tag{4.93}$$

and

$$\min_{\mathbf{w},\tilde{d}_n} \frac{1}{K} \sum_{k=1}^{K} |\tilde{e}_{k,n}|^2 = \min_{\mathbf{w},\tilde{d}_n} \frac{1}{K} \sum_{k=1}^{K} \left|\tilde{d}_n \tilde{\mathbf{y}}_{k,n}\mathbf{w} - \tilde{x}_{k,n}\right|^2 \text{ with real } \mathbf{w} \tag{4.94}$$

By eliminating the linearly appearing LS-based bMMSE FEQ, which follows from (4.68):

$$\tilde{d}_n = \frac{\mathbf{w}^T \boldsymbol{\sigma}^H_{K,n,\tilde{x}\tilde{\mathbf{y}}}}{\mathbf{w}^T \boldsymbol{\Sigma}_{K,n,\tilde{\mathbf{y}}} \mathbf{w}} \tag{4.95}$$

the SNLLS-based criterion (4.94) is reduced to a non-linear criterion in $\mathbf{w}$:

$$\begin{aligned} &\min_{\mathbf{w}} \frac{1}{K} \sum_{k=1}^{K} \left| \frac{\mathbf{w}^T \boldsymbol{\sigma}^H_{K,n,\tilde{x}\tilde{\mathbf{y}}}}{\mathbf{w}^T \boldsymbol{\Sigma}^2_{K,n,\tilde{\mathbf{y}}} \mathbf{w}} \tilde{\mathbf{y}}_{k,n}\mathbf{w} - \tilde{x}_{k,n} \right|^2 \\ &\quad = \min_{\mathbf{w}} \sigma^2_{K,n,\tilde{\mathbf{x}}} - \frac{\mathbf{w}^T \boldsymbol{\sigma}^H_{K,n,\tilde{x}\tilde{\mathbf{y}}} \boldsymbol{\sigma}_{K,n,\tilde{x}\tilde{\mathbf{y}}} \mathbf{w}}{\mathbf{w}^T \boldsymbol{\Sigma}^2_{n,\tilde{\mathbf{y}}} \mathbf{w}} \text{ with real } \mathbf{w} \end{aligned} \tag{4.96}$$

$$= \sigma^2_{K,n,\tilde{x}} \left(1 - \max_{\mathbf{w}} \frac{\sigma^{-2}_{K,n,\tilde{\mathbf{x}}} \left(\mathbf{w}^T \Re \left\{ \boldsymbol{\sigma}^H_{K,n,\tilde{x}\tilde{\mathbf{y}}} \boldsymbol{\sigma}_{K,n,\tilde{x}\tilde{\mathbf{y}}} \right\} \mathbf{w} \right)}{\mathbf{w}^T \Re \left\{ \boldsymbol{\Sigma}^2_{K,n,\tilde{\mathbf{y}}} \right\} \mathbf{w}} \right) \quad (4.97)$$

The constraint in (4.96) of a real-valued TEQ is imposed in (4.97) by inserting the real operators $\Re\{\cdot\}$. The equivalence of (4.96) and (4.97) then follows from the Hermitian property of the matrices $\boldsymbol{\sigma}^H_{K,n,\tilde{x}\tilde{\mathbf{y}}} \boldsymbol{\sigma}_{K,n,\tilde{x}\tilde{\mathbf{y}}}$ and $\boldsymbol{\Sigma}^2_{K,n,\tilde{\mathbf{y}}}$, which ensures that the Rayleigh quotient in (4.96) is real. Criterion (4.97) is equivalent to a GEV problem (3.3) with

$$(\mathbf{B}, \mathbf{A}) = \left(\sigma^{-2}_{K,n,\tilde{\mathbf{x}}} \Re \left\{ \boldsymbol{\sigma}^H_{K,n,\tilde{x}\tilde{\mathbf{y}}} \boldsymbol{\sigma}_{K,n,\tilde{x}\tilde{\mathbf{y}}} \right\}, \Re \left\{ \boldsymbol{\Sigma}^2_{K,n,\tilde{\mathbf{y}}} \right\} \right) \quad (4.98)$$

where the $\Re$-operators ensure a real-valued TEQ $\mathbf{w}$. For a complex-valued $\mathbf{w}$, the $\Re$-operators should be dropped and the matrix $\mathbf{B}$ has rank 1 (for a real-valued TEQ, its rank is 2); in this case, (4.98) is the deterministic equivalent of the matrix pair $(\mathbf{B}, \mathbf{A})$, already suggested in (3.73-3.74). Then, there is only one strictly positive GEV (the other GEVs are zero), and the corresponding dominant generalized eigenvector $\mathbf{w}$ indeed has the closed form PTEQ solution (4.92) (up to a scaling), meaning that the complex-valued solution for (4.94) is the PTEQ (4.92) (up to a scaling). It also follows straightforwardly from (4.65) that the CLLS-based FD-MMSE-TEQ design criterion (4.60) for a single tone n is equivalent to the same GEV problem (4.98), hence the CLLS-based criterion (4.93) and the SNLLS-based criterion (4.94) have the same solution $\mathbf{w}$.

Remark 4.13 It follows from (4.94) that the real-valued or complex-valued PTEQ must be multiplied with an estimate of the uMMSE or bMMSE FEQ, (4.59) or (4.68). Combining (4.92) and (4.95), it turns out that the bMMSE FEQ estimate $\tilde{d}_n^{\text{bMMSE}}$ for a complex-valued PTEQ is equal to one, meaning that a (complex-valued) PTEQ effectively incorporates a bMMSE FEQ estimate. The uMMSE FEQ, which is preferred as it leads to an unbiased symbol estimate hence minimum bit-error rate (see Section 4.2.2), follows from (4.61) and (4.92) and is, in the case of a complex-valued PTEQ, given by:

$$\tilde{d}_n^{\text{uMMSE}} = \frac{\sigma^2_{K,n,\tilde{x}}}{\boldsymbol{\sigma}_{K,n,\tilde{x}\tilde{\mathbf{y}}} \mathbf{w}_n} = \frac{\sigma^2_{K,n,\tilde{x}}}{\boldsymbol{\sigma}_{K,n,\tilde{x}\tilde{\mathbf{y}}} \left(\boldsymbol{\Sigma}^2_{K,n,\tilde{\mathbf{y}}} \right)^{-1} \boldsymbol{\sigma}^H_{K,n,\tilde{x}\tilde{\mathbf{y}}}} \quad (4.99)$$

Finally, we re-iterate that the bMMSE FEQ and uMMSE FEQ converge to the same value for increasing SNR_n; in the case of a complex-valued PTEQ, the bMMSE FEQ is constant and always equals one, so the uMMSE FEQ converges to one, for increasing SNR_n. □

	B	**A**
CLLS-based TD-MMSE-TEQ	$\mathbf{\Sigma}_{L,\mathbf{xy}}^{T}\left(\mathbf{\Sigma}_{L,\mathbf{x}}^{2}\right)^{-1}\mathbf{\Sigma}_{L,\mathbf{xy}}$	$\mathbf{\Sigma}_{L,\mathbf{y}}^{2}$
CLLS-based FD-MMSE-TEQ	$\Re\left\{\mathbf{\Sigma}_{K,\tilde{\mathbf{x}}\tilde{\mathbf{Y}}}^{H}\left(\mathbf{\Sigma}_{K,\tilde{\mathbf{x}},\mathrm{D}}^{2}\right)^{-1}\mathbf{\Sigma}_{K,\tilde{\mathbf{x}}\tilde{\mathbf{Y}}}\right\}=\sum_{n\in\mathcal{S}_a}\sigma_{K,n,\tilde{\mathbf{x}}}^{-2}\Re\left\{\boldsymbol{\sigma}_{K,n,\tilde{x}\tilde{\mathbf{y}}}^{H}\boldsymbol{\sigma}_{K,n,\tilde{x}\tilde{\mathbf{y}}}\right\}$	$\Re\left\{\mathbf{\Sigma}_{K,\tilde{\mathbf{Y}}}^{2}\right\}=\sum_{n\in\mathcal{S}_a}\Re\left\{\mathbf{\Sigma}_{K,n,\tilde{\mathbf{y}}}^{2}\right\}$
SNLLS-based FD-MMSE-TEQ	$\Re\left\{\sum_{n\in\mathcal{S}_a}\tilde{d}_n^{*}\boldsymbol{\sigma}_{K,n,\tilde{x}\tilde{\mathbf{y}}}^{H}\right\}\times\Re\left\{\sum_{n\in\mathcal{S}_a}\tilde{d}_n\boldsymbol{\sigma}_{K,n,\tilde{x}\tilde{\mathbf{y}}}\right\}$	$\Re\left\{\sum_{n\in\mathcal{S}_a}\left\lvert\tilde{d}_n\right\rvert^{2}\mathbf{\Sigma}_{K,n,\tilde{\mathbf{y}}}^{2}\right\}$
IR-SNLLS-based BM-TEQ	$\Re\left\{\sum_{n\in\mathcal{S}_a}\gamma_{K,n,\mathbf{w}_{\mathrm{prev}}}\tilde{d}_n^{*}\boldsymbol{\sigma}_{K,n,\tilde{x}\tilde{\mathbf{y}}}^{H}\right\}\times\Re\left\{\sum_{n\in\mathcal{S}_a}\gamma_{K,n,\mathbf{w}_{\mathrm{prev}}}\tilde{d}_n\boldsymbol{\sigma}_{K,n,\tilde{x}\tilde{\mathbf{y}}}\right\}$	$\Re\left\{\sum_{n\in\mathcal{S}_a}\gamma_{K,n,\mathbf{w}_{\mathrm{prev}}}\left\lvert\tilde{d}_n\right\rvert^{2}\mathbf{\Sigma}_{K,n,\tilde{\mathbf{y}}}^{2}\right\}$
PTEQ	$\sigma_{K,n,\tilde{\mathbf{x}}}^{-2}\Re\left\{\boldsymbol{\sigma}_{K,n,\tilde{x}\tilde{\mathbf{y}}}^{H}\boldsymbol{\sigma}_{K,n,\tilde{x}\tilde{\mathbf{y}}}\right\}$	$\Re\left\{\mathbf{\Sigma}_{K,n,\tilde{\mathbf{y}}}^{2}\right\}$

Table 4.1: Real-valued TEQ and PTEQ designs formulated as a GEV problem $\mathbf{Bw}=\lambda\mathbf{Aw}$. Complex TEQs or PTEQs are obtained by omitting the $\Re$-operators.

4.3.7 Relation between the GEV problem formulations

Throughout Section 4.3, each LS-based design criterion has been shown to be equivalent to a GEV problem (3.3), with the SNLLS-based criteria giving rise to an iterative sequence of GEV problems. **Table 4.1** summarizes the encountered matrix pairs $(\mathbf{B},\mathbf{A})$ (for real-valued TEQ and PTEQ designs) and shows that the $\mathbf{A}$ matrices are closely related autocorrelation matrices of the RX signal y_l, while the $\mathbf{B}$ matrices are closely related, possibly low-rank, matrices determined by a crosscorrelation metric between the RX and TX signal y_l and x_l. Complex-valued TEQs or PTEQs are obtained by omitting the $\Re$-operators in Table 4.1.

4.4 Simulations

For the simulations throughout the thesis, we consider ADSL communication over the eight carrier serving area (CSA) reference loops, which are standardized test loops [62]. A detailed description of the CSA loops can be found in [5, 8, 62]. Some loops contain bridged taps and multiple wire gauges, which render the equalization more difficult (see Section 1.3.1). The loops include the analog and digital front-end filters of the DMT transmitter and the DMT receiver as described in Section 2.2.2 and Section 2.2.3. Some vendors make

use of steep front-end filters and a guard band to separate upstream and downstream; e.g., they use tones 38 to 255 for downstream transmission and tones 8 to 32 for upstream transmission. Other vendors allow for moderate front-end filters and use tones 33 to 255 for downstream transmission and tones 8 to 32 for upstream transmission, in combination with an echo canceller that removes the leakage from one transmission path into the other. The equalization is harder in the former case because the front-end filters introduce a larger amount of ISI/ICI. The noise is a superposition of AWGN with a power of -140 dBm/Hz, residual echo and NEXT from 24 ADSL disturbers. The other parameters of the ADSL configuration are adopted from Example 2.5.

Comparison of existing equalizer designs (Chapter 3) and the BM-TEQ design

Three ADSL scenarios are presented in detail: an upstream and 2 downstream simulations, all with the CSA #4 loop. They are representative of simulations with all 8 CSA loops, for which there is also a plot included.

Although the BM-TEQ design criterion (4.32) is non-linear and non-convex, simulations with the CSA test loops, employing the iterative GN-based design algorithm of Section 4.3.5 with random initialization, converge to locally optimal TEQs with corresponding bit rates that differ by less than 6 kbps. In harsh scenarios that include RFI, local optima with a larger but still moderate difference of a few 100 kbps is obtained, as will be shown in Chapter 5. In both scenarios (without and with RFI), the BM-TEQ outperforms other TEQ designs. We compare the BM-TEQ design with the PTEQ design (Section 3.4) and with other TEQ designs such as the MMSE-TEQ design with UNC and UTC on the TIR $\mathbf{b}$ (Section 3.2.1), the MSNNR-TEQ design and the min-ISI-TEQ design (Section 3.2.2) and the earlier TEQ design attempts by Al-Dhahir et al., Henkel et al., Arslan et al. and Milosevic et al. (see Section 3.3). The optimization algorithm for Arslan's TEQ design criterion is initialized with the min-ISI-TEQ design for each Δ, as suggested in [8]; for Al-Dhahir's TEQ design, an initialization with a target impulse response $[1\,1\,\ldots\,1]$ is used, as suggested in [6]; Henkel's TEQ design optimization is initialized with an MMSE-TEQ, as suggested in [56].

Figure 4.3 shows the bit rate as a function of the number of TEQ/PTEQ taps for the downstream CSA #4 loop *without* front-end filters (analog or digital) other than the POTS splitter. As there are no front-end filters included, we use all available tones, i.e., tone 8 to 255, in this simulation; we assume that the echo from upstream signaling is perfectly cancelled. The maximum energy window, which contains the $\nu + 1$ consecutive channel impulse response samples with maximum energy, starts at sample 28. The synchronization delay Δ has been optimized around sample 28 over the delay values $2, 6, \ldots, 58$. The plot shows that there is only a 4 % difference in bit rate between a "poorly" performing TEQ with 2 taps and a PTEQ with 32 taps. The reason for this small difference

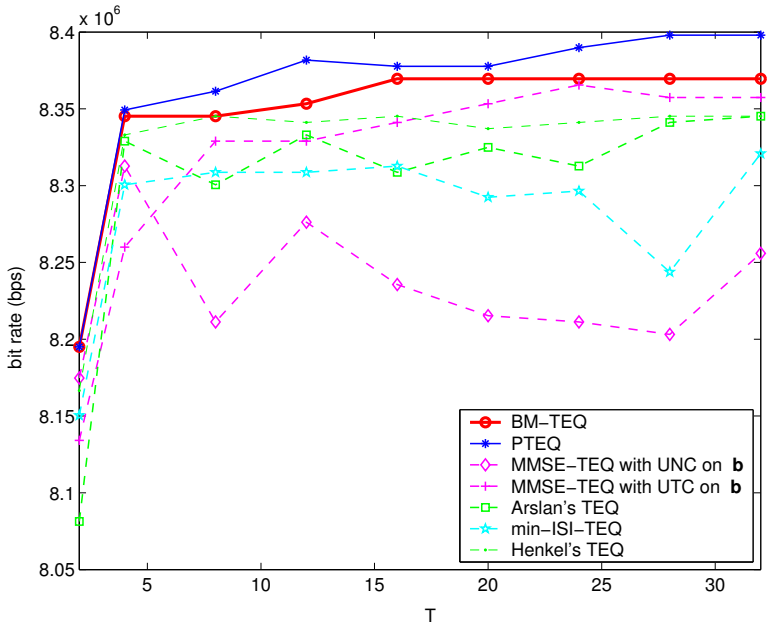


Figure 4.3: Bit rate as a function of the number of equalizer taps for the *downstream* CSA #4 loop *without* analog and digital front-end filters (except POTS splitter). The synchronization delay Δ has been optimized over the values $2, 6, \ldots, 58$.

between the studied equalizer designs is the absence of most of the front-end filters, which renders equalization much easier. As explained in Section 2.2.4, these filters introduce a considerable amount of ISI/ICI near the band edges [98] so that a larger number of taps is then needed.

Figure 4.4 shows the bit rate as a function of the number of TEQ/PTEQ taps for the downstream CSA #4 loop *with* front-end filters. The tones 38 to 255 are active. The synchronization delay Δ has been optimized over the delay values $16, 20, \ldots, 96$. Only the BM-TEQ and PTEQ perform consistently better for an increasing number of taps; Henkel's and Milosevic's TEQ designs almost do. The other designs do not, because they do not optimize the true bit rate. In this case, which closer matches reality, the performance difference between the equalizer designs is much clearer.

Figure 4.5 shows the bit rate for the same downstream scenario as a function of the synchronization delay Δ for equalizers with $T = 32$ taps. The maximum energy window starts at sample $\Delta = 46$. Again, the BM-TEQ outperforms the other TEQ designs, has a smooth behaviour as a function of Δ and has almost the same performance as the PTEQ. Among the other TEQ designs, the MMSE-TEQ design and Al-Dhahir's TEQ design perform well and Henkel's and Milosevic's TEQ designs approach very closely the BM-TEQ performance.

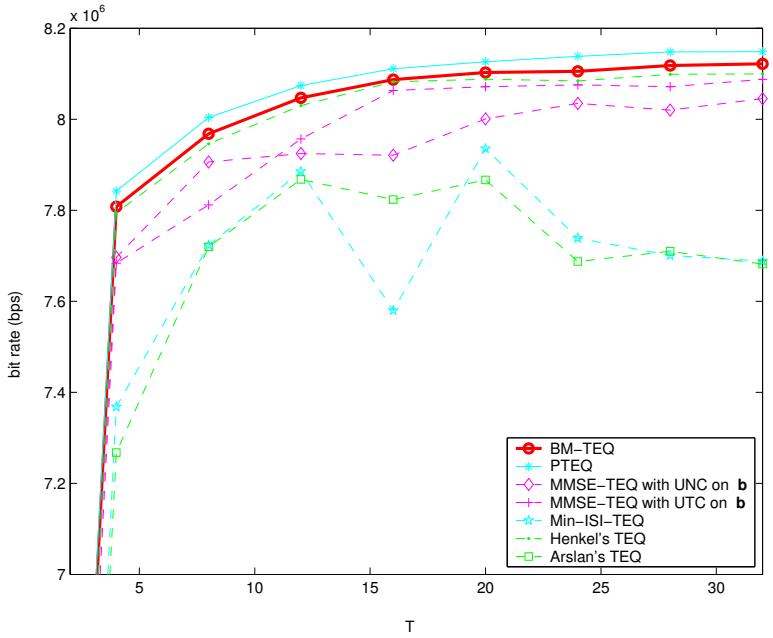


Figure 4.4: Bit rate as a function of the number of equalizer taps for the *downstream* CSA #4 loop *with* analog and digital front-end filters. The synchronization delay Δ has been optimized over the delay values $16, 20, \ldots, 96$.

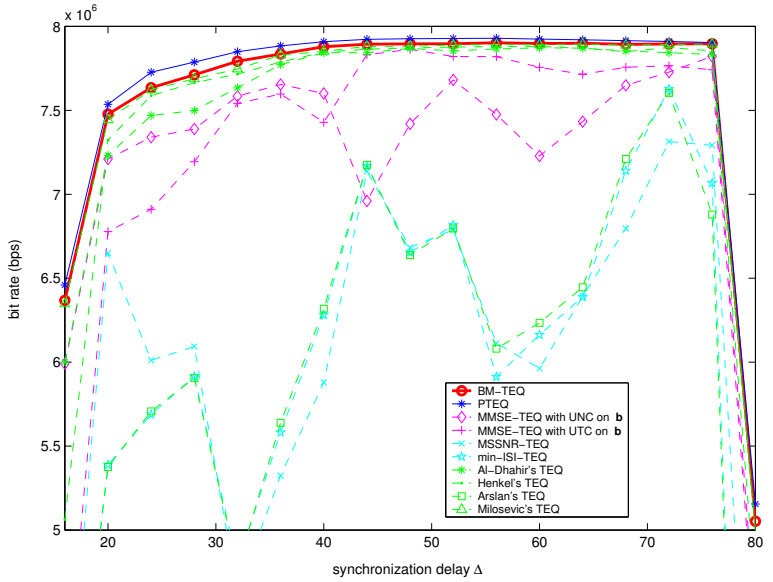


Figure 4.5: Bit rate as a function of the synchronization delay Δ for the *downstream* CSA4 loop *with* analog and digital front-end filters. $T = 32$.

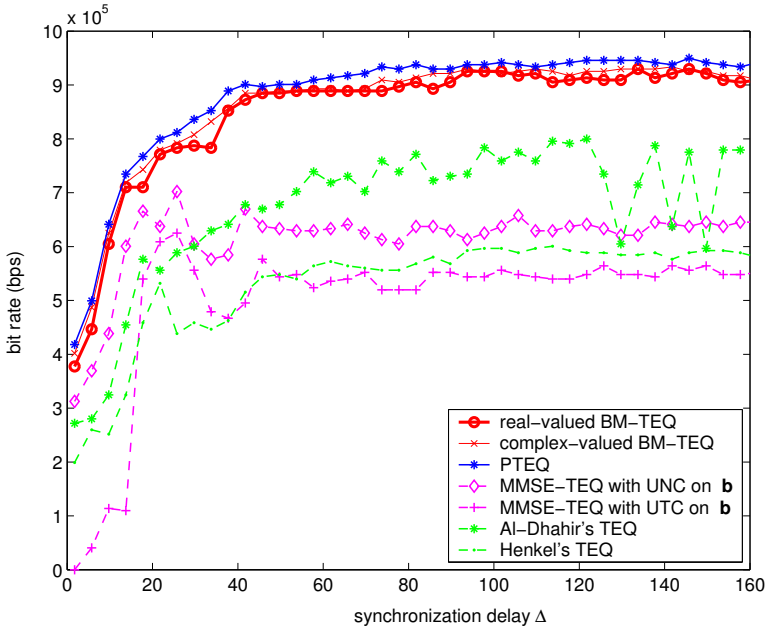


Figure 4.6: Bit rate as a function of the synchronization delay Δ for the *upstream* CSA #4 loop *with* analog and digital front-end filters. $T = 44$.

Note that the performance for all designs drops significantly for $\Delta \leq 16$ and $\Delta \geq 80$, which delimits a symmetric range around $\Delta = 46$ of around $2T$ samples with good BM-TEQ and PTEQ performance. Outside this range, an insufficient amount of useful RX energy is captured.

Figure 4.6 shows the bit rate as a function of the synchronization delay Δ for a TEQ of 44 taps applied to the *upstream* CSA #4 loop. Analog and digital front-end filters have been included. Tones 8 to 32 are active. The transmit IDFT size is 512 and the receiver DFT size is 128. The maximum energy window starts at sample 38. The real and complex BM-TEQs outperform all other TEQ designs. Its bit rate is smooth as a function of Δ and approaches the PTEQ performance. The other TEQ designs suffer from a non-smooth, hence unpredictable bit rate as a function of Δ. Al-Dhahir's TEQ design outperforms the MMSE-TEQ designs for most delays but, due to its suboptimal SNR model, it is outperformed by the BM-TEQ.

Figure 4.7 shows the performance for the 8 downstream CSA loops of the equalizer designs with $T = 32$ taps. The performance is obtained by optimizing the synchronization delay Δ over a range of $[-30 : 50]$ samples w.r.t. the maximum energy window. The results confirm the conclusion that the BM-TEQ design outperforms all earlier presented TEQ designs and closely approaches the PTEQ design.

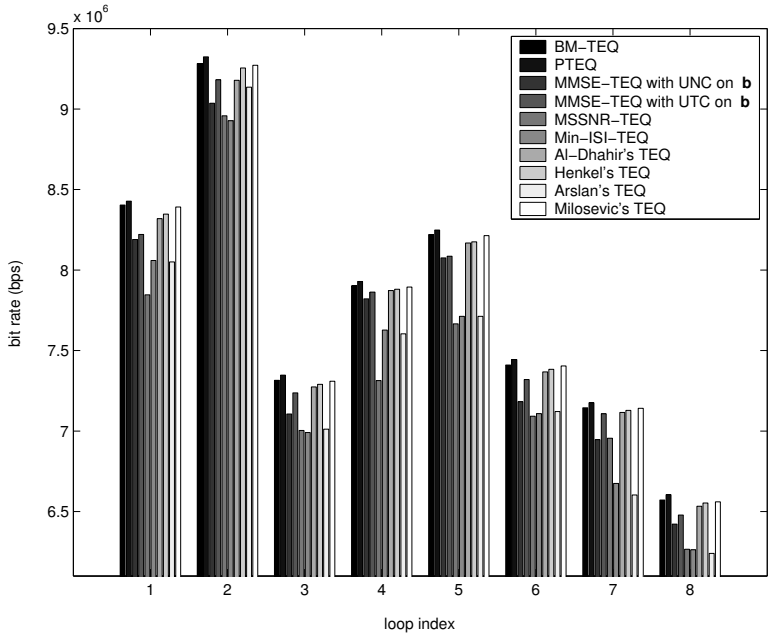


Figure 4.7: Bit rate performance for the 8 dowstream CSA loops of an equalizer with $T = 32$ taps.

Comparison of LS-based TD-MMSE-TEQ and FD-MMSE-TEQ designs

Figure 4.8 shows bit rate performance plots for the TD-MMSE-TEQ and FD-MMSE-TEQ designs of Section 4.3 with $T = 32$ taps (both real-valued and complex-valued TEQs and PTEQs are considered). The SNLLS-based FD-MMSE-TEQ design and IR-SNLLS-based BM-TEQ design have been computed using the iterative GN method suggested in Section 4.3.5. The bit rate is depicted for the 8 downstream CSA loops (active tones 38 to 255) with strong front-end filtering. For each loop, all TEQ designs are evaluated using the same synchronization delay Δ, which is determined by the first sample of the maximum energy window of the channel impulse response. The BM-TEQ and PTEQ (last 4 bars) outperform the suboptimal TEQ designs. The latter do not guarantee that a complex-valued equalizer performs better than a real-valued equalizer. The SNLLS-based FD-MMSE-TEQ (bars 5 and 6) consistently outperforms the CLLS-based FD-MMSE-TEQ design (bars 3 and 4) and closely approaches the BM-TEQ performance; apparently, it makes more sense to minimize the sum of FEQ output error energies than the sum of DFT output error energies. The impact of dropping the constraints on $\tilde{\mathbf{b}}$ in (4.56) on the performance of the CLLS-based FD-MMSE-TEQ design (4.60) appears significant: with these constraints on $\tilde{\mathbf{b}}$, the CLLS-based TD-MMSE-TEQ (4.41) (first bar) and FD-MMSE-TEQ (4.55-4.56) (second bar) achieve similar performance on

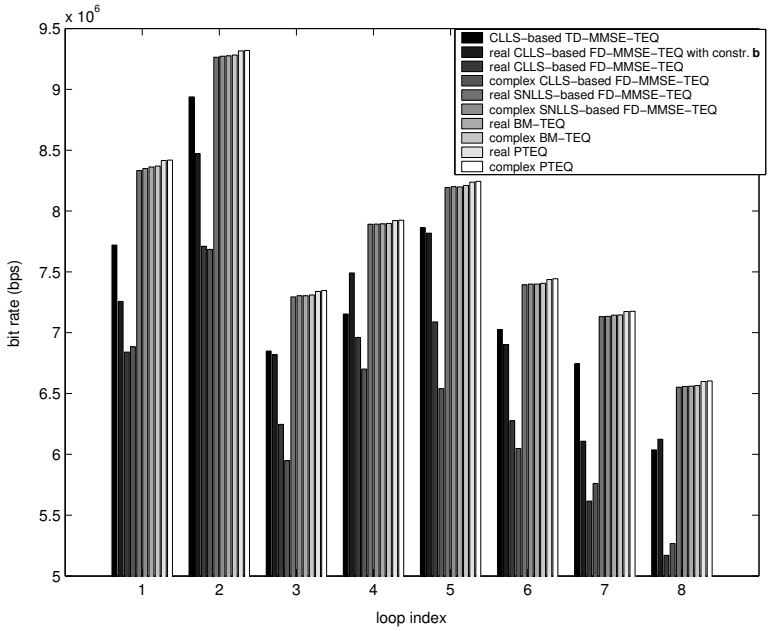


Figure 4.8: Bit rate performance of the TD-MMSE-TEQ and FD-MMSE-TEQ designs for the 8 downstream CSA loops and $T = 32$.

most loops; without these constraints, the CLLS-based FD-MMSE-TEQ (4.60) design fails.

Figure 4.9 illustrates the fast convergence of the iterative GN-based method to optimize the SNLLS-based FD-MMSE-TEQ and the IR-SNLLS-based BM-TEQ design criteria. The CSA #7 loop (with RFI) and a complex-valued TEQ are given as an example. Two different initializations are depicted: initialization from scratch with $\mathbf{w}_0 = \begin{bmatrix} 1 & 0 & \cdots & 0 \end{bmatrix}^T$ and initialization with the CLLS-based TD-MMSE-TEQ design. Initialization from scratch requires only 30 iterations, while convergence with a CLLS-based TD-MMSE-TEQ requires less than 10 iterations for both TEQ designs.

4.5 Conclusions

In this chapter, TEQ design criteria that truly maximize the bit rate have been derived. The first and original BM-TEQ design criterion follows from a compact and elegant SNR model, described in terms of the TX and RX signal SOS, rather than the FIR channel and TX signal and noise statistics. The key element in the derivation of this SNR model is the observation that the dependence of the SNR on the TEQ taps is easily accounted for when

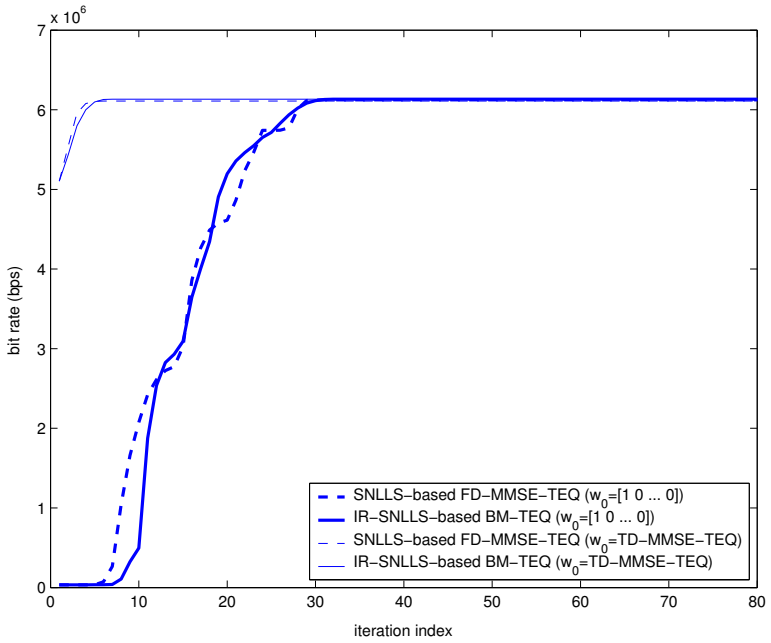


Figure 4.9: Convergence of the iterative GN-based method for solving the SNLLS-based FD-MMSE-TEQ and the IR-SNLLS-based BM-TEQ design criteria with 2 different initializations (from scratch, i.e., $\mathbf{w}_0 = \begin{bmatrix} 1 & 0 & \cdots & 0 \end{bmatrix}^T$ and from a CLLS-based TD-MMSE-TEQ design).

considering an SNR model at the FEQ output. This BM-TEQ design criterion fits in the common optimization framework as presented in Section 3.1.

Subsequently, a second and equivalent BM-TEQ design criterion has been derived, referred to as an iteratively-reweighted separable non-linear least-squares (IR-SNLLS) design criterion. This second formulation has several advantages over the original BM-TEQ design criterion. It has been indicated to closely match the frequency-domain, block transmission characteristic of DMT transmission. It has been casted in a common LS-based equalizer framework, which relates it to the channel-shortening TD-MMSE-TEQ design criterion by two suboptimal, but appealing FD-MMSE-TEQ design criteria. Moreover, it can be optimized using an iterative, fast converging Gauss-Newton-based algorithm that exploits the separability property of the SNLLS-based design criterion and delivers the BM-TEQ and corresponding FEQs. Finally, we have indicated that the TD-MMSE-TEQ design, the FD-MMSE-TEQ designs, the BM-TEQ design and the PTEQ design — although at first sight very different in nature — exhibit remarkable correspondence when turned into equivalent GEV problems (3.3).

Through simulation we have shown that the BM-TEQ succeeds in closely ap-

proaching the PTEQ performance. Both the BM-TEQ and the PTEQ exhibit a smooth bit rate curve as a function of the synchronization delay Δ, which renders the DMT receiver performance robust to the synchronization delay estimation.

In the next chapter, we show how the BM-TEQ design can be used in a bit rate maximizing "per group" equalization scheme where the active tones are divided into groups and each group is provided with a bit rate maximizing equalizer. This results in full flexibility when trading off performance versus cost of a DMT equalizer. In addition, we show that the iterative Gauss-Newton-based design algorithm for the IR-SNLLS-based design criterion can be turned into an adaptive Levenberg-Marquardt-based design.

4.A Appendix

In this appendix, we derive the **IR-SNLLS-based bit rate maximizing FD-MMSE-TEQ design criterion** for a complex-valued TEQ, based on the constrained BM-TEQ optimization problem (4.69-4.71), which is repeated here for convenience:

$$\max_{\boldsymbol{\theta}} \sum_{n\in\mathcal{S}_a} \log_2\left(1+\frac{\mathrm{SNR}_n}{\Gamma_n}\right) \tag{4.A.1}$$

$$\text{with } \mathrm{SNR}_n = \frac{\sigma^2_{n,\tilde{x}}}{\mathcal{E}\left\{\left|\tilde{e}^{\mathrm{uMMSE}}_{k,n}\right|^2\right\}} = \frac{\sigma^2_{n,\tilde{x}}}{\mathcal{E}\left\{\left|\tilde{d}^{\mathrm{uMMSE}}_n\tilde{\mathbf{y}}_{k,n}\mathbf{w}-\tilde{x}_{k,n}\right|^2\right\}} \tag{4.A.2}$$

$$\text{subject to a real } \mathbf{w} \text{ and } \tilde{d}^{\mathrm{uMMSE}}_n = \frac{\sigma^2_{n,\tilde{x}}}{\boldsymbol{\sigma}_{n,\tilde{x}\tilde{\mathbf{y}}}\mathbf{w}},\ \forall n\in\mathcal{S}_a \tag{4.A.3}$$

A constrained optimization problem is typically restated as the minimization of a Lagrangian criterion:

$$J_{\mathrm{L}}(\boldsymbol{\theta},\boldsymbol{\lambda}) = \sum_{n\in\mathcal{S}_a}\left[\log\left(1+\frac{\mathrm{SNR}_n}{\Gamma_n}\right)^{-1} - \Re\left\{\lambda^*_n\left(\tilde{d}_n\mathcal{E}\left\{\tilde{x}^*_{k,n}\tilde{y}_{k,n,\mathbf{w}}\right\}-\sigma^2_{n,\tilde{x}}\right)\right\}\right] \tag{4.A.4}$$

where λ is a vector with N_a Lagrange parameters λ_n and where the real operator $\Re\{\cdot\}$ ensures a real constraint term. Setting the gradient of J_{L} w.r.t. $\tilde{d}_n = \tilde{d}^{\mathrm{uMMSE}}_n$, denoted as $\nabla_{\tilde{d}_n} J_{\mathrm{L}} = \left(\frac{\partial}{\partial \tilde{d}^*_n} J_{\mathrm{L}}\right)$[1], equal to zero, i.e.,

$$\nabla_{\tilde{d}_n} J_{\mathrm{L}} = \check{\gamma}_{n,\mathbf{w}}\mathcal{E}\left\{\tilde{y}^*_{k,n,\mathbf{w}}\tilde{e}_{k,n}\right\} - \lambda_n\mathcal{E}\left\{\tilde{y}^*_{k,n,\mathbf{w}}\tilde{x}_{k,n}\right\} = 0 \tag{4.A.5}$$

where

$$\check{\gamma}_{n,\mathbf{w}} = \frac{\mathrm{SNR}^2_n}{\sigma^2_{n,\tilde{x}}(\mathrm{SNR}_n+\Gamma_n)} \tag{4.A.6}$$

and using the uMMSE FEQ constraint (4.A.3), equation (4.A.5) results in an expression for λ_n:

$$\begin{aligned}\lambda_n &= \check{\gamma}_{n,\mathbf{w}}\frac{\mathcal{E}\left\{\tilde{y}^*_{k,n,\mathbf{w}}\tilde{e}_{k,n}\right\}}{\mathcal{E}\left\{\tilde{y}^*_{k,n,\mathbf{w}}\tilde{x}_{k,n}\right\}} = \check{\gamma}_{n,\mathbf{w}}\frac{\tilde{d}_n\mathcal{E}\left\{|\tilde{y}_{k,n,\mathbf{w}}|^2\right\}-\mathcal{E}\left\{\tilde{y}^*_{k,n,\mathbf{w}}\tilde{x}_{k,n}\right\}}{\mathcal{E}\left\{\tilde{y}^*_{k,n,\mathbf{w}}\tilde{x}_{k,n}\right\}} \\ &= \check{\gamma}_{n,\mathbf{w}}\left(\frac{\sigma^2_{n,\tilde{x}}\mathcal{E}\left\{|\tilde{y}_{k,n,\mathbf{w}}|^2\right\}}{\left|\mathcal{E}\left\{\tilde{y}^*_{k,n,\mathbf{w}}\tilde{x}_{k,n}\right\}\right|^2}-1\right) = \check{\gamma}_{n,\mathbf{w}}\left(\rho^{-2}_{n,\mathbf{w}}-1\right) = \frac{\check{\gamma}_{n,\mathbf{w}}}{\mathrm{SNR}_n}\end{aligned} \tag{4.A.7}$$

[1] The partial derivative of $\tilde{d}_n$ and its complex conjugate w.r.t. itself are defined as $\frac{\partial}{\partial \tilde{d}_n}\tilde{d}_n = 1$ and $\frac{\partial}{\partial \tilde{d}_n}\tilde{d}^*_n = 0$, respectively.

The last two equations follow from the definition of the square normalized crosscorrelation between the n-th DFT equalized output $\tilde{y}_{k,n,\mathbf{w}}$ and the n-th TX symbol $\tilde{x}_{k,n}$, which was already given in (4.29):

$$\rho^2_{n,\mathbf{w}} = \frac{\left|\mathcal{E}\left\{\tilde{y}^*_{k,n,\mathbf{w}}\tilde{x}_{k,n}\right\}\right|^2}{\sigma^2_{n,\tilde{x}}\mathcal{E}\left\{|\tilde{y}_{k,n,\mathbf{w}}|^2\right\}} = \frac{\tilde{d}^{\text{bMMSE}}_n}{\tilde{d}^{\text{uMMSE}}_n} \tag{4.A.8}$$

and SNR_n, which was shown in (4.28) to be a function of $\rho^2_{n,\mathbf{w}}$:

$$\text{SNR}_n = \frac{1}{\rho^{-2}_{n,\mathbf{w}} - 1} \tag{4.A.9}$$

The gradient of J_{L} w.r.t. a complex-valued TEQ $\mathbf{w}$ is given by:

$$\nabla_{\mathbf{w}} J_{\text{L}} = \sum_{n\in\mathcal{S}_a} \gamma_{n,\boldsymbol{\theta}_n}\left(\tilde{d}^{\text{uMMSE}}_n\right)^* \mathcal{E}\left\{\tilde{\mathbf{y}}^H_{k,n}\tilde{e}_{k,n}\right\} - \lambda_n\left(\tilde{d}^{\text{uMMSE}}_n\right)^* \mathcal{E}\left\{\tilde{\mathbf{y}}^H_{k,n}\tilde{x}_{k,n}\right\} \tag{4.A.10}$$

In the case of a real-valued TEQ, $2\Re\{\nabla_{\mathbf{w}} J_{\text{L}}\}$ should be used. Combining the gradient w.r.t. $\mathbf{w}$ (4.A.10) and $\tilde{\mathbf{d}}$ (4.A.5) and filling in the Lagrange parameter λ_n (4.A.7), we obtain in matrix notation that $\nabla_{\boldsymbol{\theta}} J_L$ is given by:

$$\mathcal{E}\left\{\begin{bmatrix}\tilde{\mathbf{Y}}^H_k \text{diag}\left(\tilde{\mathbf{d}}^{\text{uMMSE}}\right)^* \\ \text{diag}(\tilde{\mathbf{Y}}_k\mathbf{w})^*\end{bmatrix} \text{diag}\left(\check{\boldsymbol{\gamma}}_{\mathbf{w}}\right)\left[\text{diag}\left(\tilde{\mathbf{d}}^{\text{uMMSE}}\right)\tilde{\mathbf{Y}}_k\mathbf{w} - \text{diag}(\boldsymbol{\rho}^{-2}_{\mathbf{w}})\tilde{\mathbf{x}}_k\right]\right\} \tag{4.A.11}$$

The entries of the $N_a \times 1$ vector $\check{\boldsymbol{\gamma}}_{\mathbf{w}}$ are $\check{\gamma}_{n,\mathbf{w}}$, defined in (4.A.5); they are a function of SNR_n (4.A.9). The vector $\boldsymbol{\rho}^{-2}_{\mathbf{w}}$ is short-hand notation for a vector whose entries are the inverses of $\rho^2_{n,\mathbf{w}}$. By making use of (4.A.8) and (4.A.9), the gradient $\nabla_{\boldsymbol{\theta}} J_L$ in (4.A.11) can be expressed in terms of the bMMSE FEQs instead of the uMMSE FEQs:

$$\mathcal{E}\left\{\underbrace{\begin{bmatrix}\tilde{\mathbf{Y}}^H_k \text{diag}\left(\tilde{\mathbf{d}}^{\text{bMMSE}}\right)^* \\ \text{diag}(\tilde{\mathbf{Y}}_k\mathbf{w})^*\end{bmatrix}}_{\check{\mathbf{Y}}^H_{k,\boldsymbol{\theta}}} \text{diag}\left(\boldsymbol{\gamma}_{\mathbf{w}}\right) \underbrace{\left[\text{diag}\left(\tilde{\mathbf{d}}^{\text{bMMSE}}\right)\tilde{\mathbf{Y}}_k\mathbf{w} - \tilde{\mathbf{x}}_k\right]}_{\tilde{\mathbf{e}}_k}\right\} \tag{4.A.12}$$

with

$$\gamma_{n,\mathbf{w}} = \frac{\left(\text{SNR}_n + 1\right)^2}{\sigma^2_{n,\tilde{x}}\left(\text{SNR}_n + \Gamma_n\right)} \tag{4.A.13}$$

Replacing the expectation operator in (4.A.12) and (4.A.8) with a time-average over K DMT symbols results in a generalized version (with weighting $\boldsymbol{\gamma}_{K,\mathbf{w}}$ and multiple-error vector $\tilde{\mathbf{e}}_k$) of the orthogonality condition that is typically

encountered when solving LS criteria:

$$\frac{1}{K}\sum_{k=1}^{K}\check{\mathbf{Y}}_{k,\boldsymbol{\theta}}^{H}\mathrm{diag}\left(\boldsymbol{\gamma}_{K,\mathbf{w}}\right)\tilde{\mathbf{e}}_k=\mathbf{0} \tag{4.A.14}$$

More specifically, it corresponds to the orthogonality condition, encountered in so-called iteratively-reweighted (IR) LS criteria. After replacing the weights $\boldsymbol{\gamma}_{K,\mathbf{w}}$ with $\boldsymbol{\gamma}_{K,\mathbf{w}_{\mathrm{prev}}}$, i.e., with weights $\boldsymbol{\gamma}_{K,\mathbf{w}_{\mathrm{prev}}}$ based on estimates $\mathrm{SNR}_{K,n}$ and $\rho^2_{K,n,\mathbf{w}_{\mathrm{prev}}}$ (over K symbols) that are evaluated in the parameter estimate $\mathbf{w}_{\mathrm{prev}}$ of the previous iteration, this orthogonality condition gives rise to the following so-called iteratively-reweighted (IR) LS-based BM-TEQ design criterion criterion:

$$\min_{\boldsymbol{\theta}}\frac{1}{K}\sum_{k=1}^{K}\left\|\mathrm{diag}\left(\sqrt{\boldsymbol{\gamma}_{K,\mathbf{w}_{\mathrm{prev}}}}\right)\tilde{\mathbf{e}}_k\right\|^2 \tag{4.A.15}$$

This criterion can be shown to be also valid in the case of real-valued TEQs.

Chapter 5

Adaptive bit rate maximizing time-domain and per-group equalizer design

CHANNEL and noise characteristics of a communication environment typically vary with time. E.g., in a DSL environment, changing weather conditions, temperature, crosstalk and/or RFI cause slow time-variations [60]. An *adaptive equalizer* that is capable of *tracking* a changing environment is thus preferable in order to keep the performance as high as possible [55]. Tracking can be achieved by means of a data-driven adaptive equalizer. An adaptive algorithm can also be used for *equalizer design* by means of a training signal transmitted during the connection set-up phase. The equalizer coefficients are then updated based on the previous equalizer coefficients (and possibly some SOS estimates) as new training data come in, in this way avoiding the need to store all available data.

In current ADSL modems, TEQ design is typically done offline: the TEQ is computed during the connection set-up phase and is then kept fixed during data transmission. The newest ADSL2 and ADSL2+ standards support "seamless rate adaptation" [60]: the ADSL line conditions are observed continuously and the bit rate and bit allocation are adapted accordingly. This renders *adaptive bit rate maximizing equalizer design*, which is the topic of this chapter, highly desirable.

We first show, in Section 5.1, how the BM-TEQ design of Chapter 4 can be

used in a *bit rate maximizing per-group equalizer (BM-PGEQ) scheme* : the active tones are divided into a small number of groups; the solution of the (downscaled) BM-TEQ design criterion for each group results in a BM-PGEQ for the group. This BM-PGEQ design allows for a trade-off between memory cost and performance, keeping computational complexity during data transmission roughly at the same level. It encompasses the BM-TEQ and PTEQ design as extreme cases. The BM-PGEQ outperforms an earlier presented tone grouping scheme where the whole tone group was assigned the PTEQ of the group center tone [130].

In Section 5.2, we show that the BM-TEQ and BM-PGEQ, despite their non-linear cost criterion, can be designed adaptively, based on a recursive Levenberg-Marquardt (RLM) algorithm, which is derived from the iterative GN-based BM-TEQ design method of Section 4.3.5. These *adaptive BM-TEQ and BM-PGEQ algorithms* make use of exactly the same SOS as the RLS-based adaptive PTEQ of Section 3.4.2. A *complete range of adaptive bit rate maximizing (BM) equalizers* then opens up, *offering full flexibility* to trade off computational and memory cost: the RLS-based adaptive PTEQ design is computationally efficient but involves a large number of equalizer taps; the adaptive BM-TEQ has a minimum number of equalizer taps at the expense of a larger design complexity; the adaptive BM-PGEQ has a similar design complexity as the BM-TEQ and an intermediate number of equalizer taps between the BM-TEQ and the PTEQ. A detailed memory and computational cost analysis of the adaptive BM-TEQ and BM-PGEQ is given in Section 5.3.

In the simulations of Section 5.4, the BM-PGEQ appears a useful intermediate between the BM-TEQ and the PTEQ and closely approaches the PTEQ performance for as few as 4 tone groups, especially in harsh ADSL environments with narrowband interference and crosstalk where the BM-TEQ design attains local optima that vary a few 100 kbps in bit rate. Similarly to the PTEQ, the BM-TEQ and BM-PGEQ appear to implicitly include receiver windowing, as their performance improves significantly by including extra taps. Through extensive simulations with several ADSL scenarios and parameter settings, we also show that the adaptive BM-TEQ and BM-PGEQ exhibit fast convergence, comparable to the adaptive PTEQ convergence. Besides providing an equalizer design algorithm, we illustrate that adaptive BM equalizers allow to track variations of the transmission channel and noise characteristics. This makes them a good candidate for integration with the seamless rate adaptation functionality of ADSL2 and ADSL2+ modems.

Figure 5.1 clarifies the place of each section in this chapter in the schematic thesis overview of Figure 1.5.

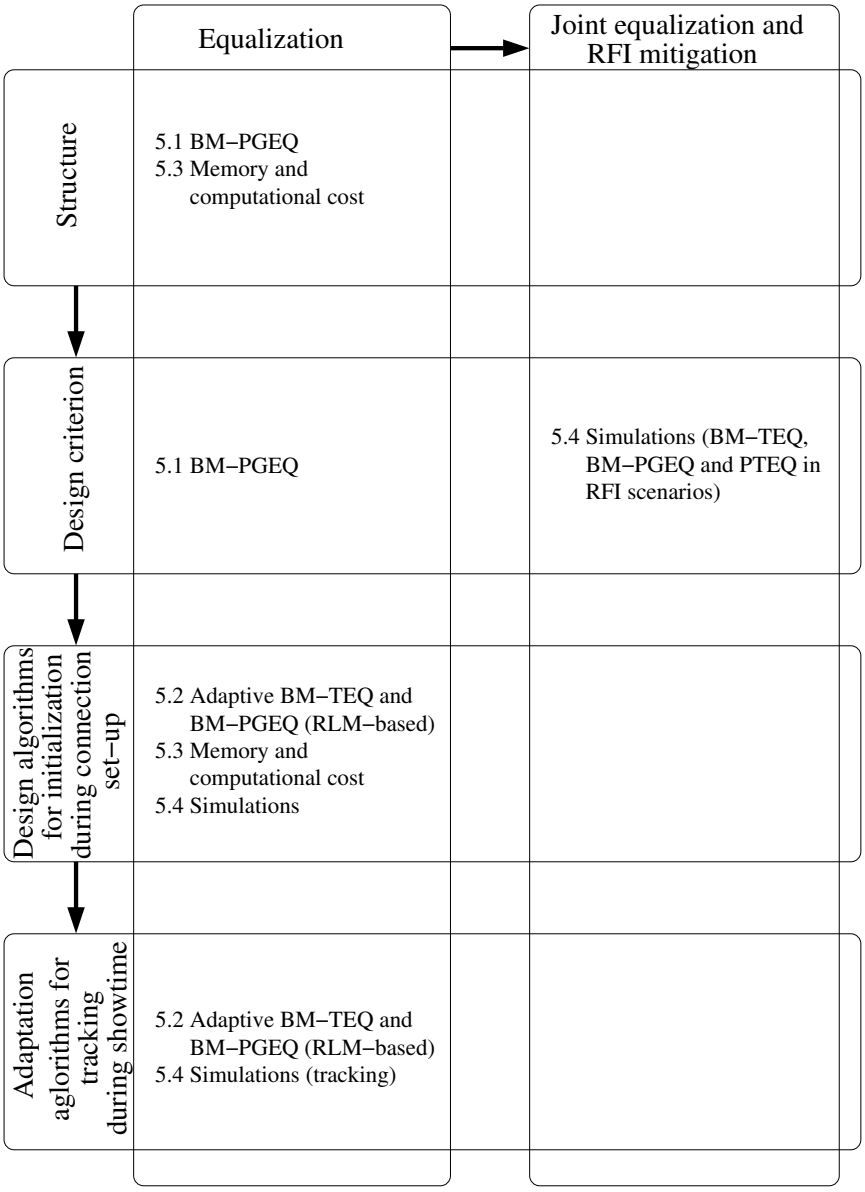


Figure 5.1: Schematic overview of this chapter.

5.1 Bit rate maximizing per-group equalizer design

In [130], a reduced complexity *tone grouping (TG) scheme* for the PTEQ of Section 3.4 has been introduced. The active tones are divided into N_g groups and only the PTEQ of the center tone of each group is optimized; the other tones in the group are operated with a PTEQ, corresponding to the equivalent TEQ of the center tone. This scheme allows for a considerable reduction in equalizer design complexity and memory cost as only N_g T-tap equalizers need to be designed and stored. However, by applying this TG scheme, the PTEQ loses its property to guarantee a better performance than a TEQ. Therefore, the PTEQ-with-TG typically uses a large number of small tone groups to minimize the performance loss.

The BM-TEQ criterion can be used in a new bit rate maximizing "per-group" (BM-PGEQ) equalizer scheme, which is intermediate (in terms of memory cost and performance) between the BM-TEQ and the PTEQ: the active tones are divided into N_g groups and each group is provided with a (possibly complex-valued) T-tap BM-PGEQ $\mathbf{w}_g$ by optimizing the downscaled non-linear BM-TEQ criterion (4.32) or IR-SNLLS-based BM-TEQ criterion (4.72) for the group:

$$\boxed{\min_{\mathbf{w}_g} \sum_{n \in \mathcal{S}_g} \log\left(\frac{\mathbf{w}_g^T \mathbf{B}_n \mathbf{w}_g}{\mathbf{w}_g^T \mathbf{A}_n \mathbf{w}_g}\right) \text{ for } g = 1, \ldots, N_g} \tag{5.1}$$

or

$$\boxed{\min_{\boldsymbol{\theta}_g} \frac{1}{K} \sum_{k=1}^{K} \left\| \text{diag}\left(\sqrt{\gamma_{K,\mathbf{w}_{g,\text{prev}}}}\right) \left(\text{diag}(\tilde{\mathbf{d}}_g)\tilde{\mathbf{Y}}_{k,g}\mathbf{w}_g - \tilde{\mathbf{x}}_{k,g}\right)\right\|^2, \; g = 1, \ldots, N_g} \tag{5.2}$$

where $\boldsymbol{\theta}_g = \begin{bmatrix} \mathbf{w}_g^H & \tilde{\mathbf{d}}_g^H \end{bmatrix}^H$ and where the subscripts g in $\tilde{\mathbf{d}}_g$, $\tilde{\mathbf{Y}}_{k,g}$, $\tilde{\mathbf{x}}_{k,g}$ and $\tilde{\mathbf{e}}_{k,g}$ denote that only the tones in the group are considered. As the PGEQ for each tone group optimizes the bit rate for this group, the BM-PGEQ scheme will perform better than the original PTEQ-with-TG and obviously better than a single BM-TEQ. Hence, the BM-PGEQ design encompasses the BM-TEQ and PTEQ design procedure as extreme cases. As will be shown in Section 5.4, the BM-PGEQ is less susceptible than a BM-TEQ to poorly performing local optima of the non-linear cost criterion, especially in harsh environments with narrowband interference. The number of required tone groups for the BM-PGEQ is considerably smaller than the number of tone groups for the PTEQ-with-TG: the BM-PGEQ with as few as 3 to 4 tone groups closely approaches the performance of the full PTEQ.

The BM-PGEQ is designed by optimizing the criterion (5.2) for each tone group with the iterative GN-based method of Section 4.3.5 or the adaptive algorithm

developed in Section 5.2. Based on the designed BM-PGEQ coefficients, the actual equalizer can then be implemented in one of two ways, depending on whether minimum memory or minimum computational complexity is preferred.

BM-PGEQ implementation with minimum memory cost

Assume we use N_g tone groups and a BM-PGEQ $\mathbf{w}_g$ ($g = 1, \cdots, N_g$) of T taps per group, then N_gT PGEQ taps plus N_a FEQs $\tilde{d}_n$ need to be stored. One could naively compute the $N \times 1$ TEQ output $\mathbf{y}_{k,\mathbf{w}_g} = \mathbf{Y}_k\mathbf{w}_g$ for each group and then apply a (partial) DFT $\mathcal{F}_g\mathbf{Y}_k\mathbf{w}_g$ for each group, where $\mathcal{F}_g$ is a submatrix of $\mathcal{F}_N$, which contains the rows corresponding to the tones in the group. However, it is often computationally cheaper to exploit the two key observations (3.62) and (3.65) and efficiently compute the BM-PGEQ as follows.

1. Compute the $T-1$ real-valued difference terms, $\Delta\mathbf{y}_k$ (3.66), and the DFT of the k-th RX sample vector, $\tilde{\mathbf{y}}_{k,N}$ (3.67).

2. Compute the sliding DFT outputs $\tilde{\mathbf{y}}_{k,n}$ for all N_a tones of $\mathcal{S}_a$ using the recursion (3.64):

$$\begin{aligned} \tilde{\mathbf{y}}_{k,n}[t] &= \alpha_n\tilde{\mathbf{y}}_{k,n}[t-1] + \Delta\mathbf{y}_{k,-t},\ t = 1, \ldots, T-1 \\ &= \tilde{y}_{k,n} = \tilde{\mathbf{y}}_{k,N}[n],\ t = 0 \end{aligned} \tag{5.3}$$

   with $\alpha_n = \exp(-j2\pi(n-1)/N)/\sqrt{N}$.

3. Compute for all N_a tones of $\mathcal{S}_a$ the inner product of $\tilde{\mathbf{y}}_{k,n}$ with the appropriate PGEQ $\mathbf{w}_g$ and multiply the result with the FEQ $\tilde{d}_n$ to obtain the TX symbol estimate for $\tilde{x}_{k,n}$:

$$\hat{\tilde{x}}_{k,n} = \tilde{d}_n\tilde{y}_{k,n,\mathbf{w}_g} = \tilde{d}_n(\tilde{\mathbf{y}}_{k,n}\mathbf{w}_g) \tag{5.4}$$

The computational cost per DMT symbol is then (in case of real PGEQs) $6N_aT$ real multiplications and 1 DFT operation.

BM-PGEQ implementation with minimum computational complexity

Alternatively, one can resort to a BM-PGEQ implementation with the same computational and memory cost as the PTEQ, see Section 3.4.1. Exploiting the key observations (3.62) and (3.65), the per-group equalizer output for tone n can be written as

$$\hat{\tilde{x}}_{k,n} = \tilde{d}_n\mathcal{F}_n\mathbf{Y}_k\mathbf{w}_g = \begin{bmatrix} \Delta\mathbf{y}_k^T & \tilde{y}_{k,n} \end{bmatrix}\mathbf{v}_n \tag{5.5}$$

where $\mathbf{v}_n$ can be computed from $\tilde{d}_n \mathbf{w}_g$ based on (3.65):

$$\mathbf{v}_n = \underbrace{\begin{bmatrix} 0 & \cdots & 0 & 1 \\ \vdots & \iddots & \iddots & \alpha_n \\ 0 & 1 & \iddots & \vdots \\ 1 & \alpha_n & \cdots & \alpha_n^{T-1} \end{bmatrix}}_{\mathbf{T}_n} (\tilde{d}_n \mathbf{w}_g) \tag{5.6}$$

The tone-dependent equalizers $\mathbf{v}_n$ can be obtained efficiently by exploiting the recursion in (5.6), which is very similar to the recursion (5.3):

$$\begin{aligned} \mathbf{v}_n[t] &= \alpha_n \mathbf{v}_n[t-1] + \tilde{d}_n \mathbf{w}_g[T-t-1],\ t = 1, \ldots, T-1 \\ &= \tilde{d}_n \mathbf{w}_g[T-1],\ t = 0 \end{aligned} \tag{5.7}$$

Instead of the N_g per-group equalizers $\mathbf{w}_g$, the N_a transformed, tone-dependent equalizers $\mathbf{v}_n$ are to be stored. The BM-PGEQ outputs are then obtained efficiently by means of the right-hand expression in (5.5). As with the PTEQ, $\mathbf{v}_n$ is a $T \times 1$ vector with complex-valued equalizer taps, hence this implementation requires memory for $N_a T$ complex-valued taps and has a computational cost of 1 DFT and $(2T+2)N_a$ real multiplications per DMT symbol.

A comparison of the memory and computational cost of a TEQ, a PGEQ and a PTEQ is given in Section 5.3.

5.2 Recursive Levenberg-Marquardt-based BM-TEQ and BM-PGEQ

As already mentioned, in current ADSL modems, a TEQ is typically designed *offline*, computed during the connection set-up phase and then kept fixed during data transmission. E.g., an MMSE-TEQ with UNC, see Section 3.2.1, is obtained as the solution of an eigenvalue problem. The non-linear TEQ designs of Section 3.3, which attempt bit rate minimization, on the other hand, ask for complex offline batch optimization routines.

A typical ADSL environment, however, varies with time (e.g., due to changing weather conditions, temperature, crosstalk and/or RFI) [60]. Moreover, the newest ADSL2 and ADSL2+ standards support "seamless rate adaptation" [63, 64]: the ADSL line conditions are observed continuously and the bit rate and bit allocation are adapted accordingly, e.g. when an RFI is switched off [60]. As a consequence, it is desirable that the TEQ tracks the changing conditions to keep the bit rate as high as possible. *Tracking* can be achieved with a data-driven *adaptive equalizer*. An adaptive equalizer can also be used for

TEQ *design*: during the ADSL connection set-up phase, a training signal, the so-called medley signal, is transmitted [61, 63, 64], consisting of 16384 DMT symbols for ADSL and up to 32256 DMT symbols for ADSL2+. The equalizer coefficients are then updated based on the previous equalizer coefficients (and possibly some SOS estimates) as new training data come in, in this way avoiding the need to store all available data. So far, only few adaptive equalizer designs have been presented in the literature;

- The *MMSE-TEQ* [5] can be designed adaptively, but LMS adaptation is cited as converging slowly [115]. Alternatively, Chow's algorithm is faster but is not guaranteed to reach the optimal MMSE-TEQ [115].
- Two recent, cheap, *blind*, adaptive TEQ algorithms have been presented in Section 3.2.2: the SAM algorithm [9] minimizes an estimate of the sum-squared autocorrelation of the SIR outside a window of length $\nu+1$; the MERRY algorithm [79] minimizes a design criterion related to the MSSNR TEQ design [85].
- Fast and reasonably cheap adaptive *PTEQs*, based on the RLS algorithm or a hybrid RLS/LMS algorithm (both with so-called inverse updating), have been presented in [131] and [161], respectively (see Section 3.4.2). An RLS-based algorithm requires second-order information; for the PTEQ, autocorrelation matrices of the sliding DFT of the RX signal are needed. As discussed in Section 3.4.2, most of the RLS processing for storing and updating these SOS can be shared over all active tones. The required number of coefficients to store the SOS is $\mathcal{O}(N_a T)$; the equalizer design requires $\mathcal{O}(N_a T)$ operations per update (including the SOS update). A further cost reduction, both in terms of SOS memory and equalizer design, is obtained by resorting to a hybrid RLS/LMS scheme [161].

In this section, it will be shown that the BM-TEQ can be designed *recursively* or *adaptively*, despite the non-linear and non-convex cost criterion. This may not seem obvious from the original BM-TEQ design criterion (4.32). However, the alternative IR-SNLLS-based BM-TEQ design criterion (4.72) is an iteratively reweighted sum of frequency-domain square errors between the symbol estimates at the FEQ output and the true TX symbols. The adaptive BM-TEQ design method, developed here, is then driven by the FEQ output errors. It is based on the *iterative* Gauss-Newton based algorithm of Section 4.3.5.

In Section 5.2.1, we introduce approximations and modifications to the iterative GN-based algorithm to turn it into a stable and efficient *adaptive* algorithm. In essence, the result is a *recursive Levenberg-Marquardt* (RLM) algorithm [77] that updates the joint TEQ-FEQ parameter vector $\boldsymbol{\theta}$ at each time instant k. In Section 5.2.2, we show that the RLM algorithm makes use of exactly the same SOS as the RLS-based adaptive PTEQ, based on the autocorrelation matrices

of the sliding DFT of the RX signal. Similar to the RLS and RLS/LMS-based adaptive PTEQ, the SOS memory cost can then be further reduced by exploiting the sliding DFT structure. In Section 5.2.3, the RLM algorithm is further refined. The regularization parameter, which ensures stability, is adapted in an efficient way, based on the method presented in [90] that takes the changing condition of the Hessian over time into account. The adaptive BM-TEQ algorithm is summarized in Section 5.2.4 and we explain how an adaptive BM-PGEQ merely solves several downscaled adaptive BM-TEQ problems in parallel.

A complete range of *adaptive BM equalizers* then opens up: from a single T-tap adaptive TEQ over an intermediate N_gT-tap PGEQ to a (complex-valued) N_aT-tap PTEQ. All designs have the same SOS memory cost, but a varying equalizer design cost. The adaptive BM-TEQ and BM-PGEQ require $\mathcal{O}(N_aT^2)$ computations per update, i.e., roughly T times more than a PTEQ update.

5.2.1 Basic RLM algorithm

In this section, several approximations and modifications are applied to the iterative GN-based method of Section 4.3.5, which then lead to an RLM-based adaptive BM-TEQ design method. *Iterative* GN and Levenberg-Marquardt (LM) methods are classical and well-studied strategies for solving non-linear batch optimization problems. The *recursive* LM (RLM) algorithm developed here is inspired by earlier presented algorithms for adaptively solving non-linear problems in, e.g., recursive system identification [36, 77] and neural-network-based adaptive filter training [55, 90]. The RLM algorithm is a modification of the recursive GN algorithm, e.g., it regularizes the Hessian to remedy its ill-conditioning, which is often encountered when solving non-linear problems. We refer to [77] for a detailed derivation and analysis of the RLM algorithm.

The RLM-based adaptive algorithm, developed below, optimizes a slightly modified version of the IR-SNLLS-based BM-TEQ criterion (4.72), which immediately provides an LS estimate of the uMMSE FEQs (4.21), rather than the bMMSE FEQs (4.20), as the solution for the parameters $\tilde{\mathbf{d}}$:

$$\min_{\boldsymbol{\theta}} \frac{1}{K}\sum_{k=1}^{K}\left\| \operatorname{diag}\left(\sqrt{\check{\boldsymbol{\gamma}}_{K,\mathbf{w}_{\text{prev}}}}\right) \underbrace{\left(\operatorname{diag}(\tilde{\mathbf{d}})\tilde{\mathbf{Y}}_k\mathbf{w} - \boldsymbol{\rho}^{-2}_{K,\mathbf{w}_{\text{prev}}} \odot \tilde{\mathbf{x}}_k\right)}_{\check{\mathbf{e}}_k} \right\|^2 \quad \text{with real } \mathbf{w} \tag{5.8}$$

This is also an **IR-SNLLS-based BM-TEQ design criterion** where $\check{\boldsymbol{\gamma}}_{K,\mathbf{w}_{\text{prev}}}$ and $\check{\mathbf{e}}_k$ are related to $\boldsymbol{\gamma}_{K,\mathbf{w}_{\text{prev}}}$ and $\tilde{\mathbf{e}}_k$ in (4.72), respectively, by:

$$\check{\gamma}_{K,n,\mathbf{w}_{\text{prev}}} = \left(\rho^2_{K,n,\mathbf{w}_{\text{prev}}}\right)^2 \gamma_{K,n,\mathbf{w}_{\text{prev}}} = \frac{\text{SNR}^2_{K,n}}{\sigma^2_{K,n,\tilde{x}}\left(\text{SNR}_{K,n}+\Gamma_n\right)} \tag{5.9}$$

$$\check{\mathbf{e}}_k = \boldsymbol{\rho}^{-2}_{K,\mathbf{w}_{\text{prev}}} \odot \tilde{\mathbf{e}}_k \tag{5.10}$$

The vector $\boldsymbol{\rho}^{-2}_{K,\mathbf{w}_{\text{prev}}}$ is short-hand notation for an $N_a \times 1$ vector with as entries the inverses of $\rho^2_{K,n,\mathbf{w}_{\text{prev}}}$ (4.75). The vector $\check{\mathbf{e}}_k$ (5.10) contains the errors between the uMMSE FEQ outputs and the virtual symbols $\rho^{-2}_{K,n,\mathbf{w}_{\text{prev}}}\tilde{x}_{k,n}$. Each error $\check{e}_{k,n}$ is a scaled version of the *biased* MMSE FEQ output error, i.e., $\tilde{e}_{k,n} = \rho^2_{K,n,\mathbf{w}_{\text{prev}}}\check{e}_{k,n}$. Note that for tones with a high SNR, $\rho^2_{K,n,\mathbf{w}_{\text{prev}}}$ is very close to 1. The iterative GN-based algorithm developed in Section 4.3.5 remains valid for optimizing (5.8) if $\boldsymbol{\gamma}_{K,\mathbf{w}_{\text{prev}}}$ and $\tilde{\mathbf{e}}_k$ are replaced by $\check{\boldsymbol{\gamma}}_{K,\mathbf{w}_{\text{prev}}}$ and $\check{\mathbf{e}}_k$, respectively.

Under the assumption of a complex-valued TEQ, the **RLM-based adaptive algorithm** to adapt the joint TEQ-FEQ parameter vector $\boldsymbol{\theta}$ at each time instant k is given by:

$$\boldsymbol{\theta}_k \leftarrow \boldsymbol{\theta}_{k-1} \underbrace{-\mathbf{R}^{-1}_{k,\boldsymbol{\theta}_{k-1},\delta_k}\mathbf{g}_{k,\boldsymbol{\theta}_{k-1}}}_{\Delta\boldsymbol{\theta}_k} \tag{5.11}$$

$$\tilde{\mathbf{d}}_k \leftarrow \tilde{\mathbf{d}}_k \cdot \|\mathbf{w}_k\| \tag{5.12}$$

$$\mathbf{w}_k \leftarrow \mathbf{w}_k / \|\mathbf{w}_k\| \tag{5.13}$$

with

$$\mathbf{g}_{k,\boldsymbol{\theta}} = \begin{bmatrix} \mathbf{g}_{k,1,\boldsymbol{\theta}} \\ \mathbf{g}_{k,2,\boldsymbol{\theta}} \end{bmatrix} = \check{\mathbf{Y}}^H_{k,\boldsymbol{\theta}}\text{diag}\left(\hat{\boldsymbol{\gamma}}_{k,\mathbf{w}_{k-1}}\right) \underbrace{\left(\text{diag}(\tilde{\mathbf{d}})\tilde{\mathbf{Y}}_k\mathbf{w} - \boldsymbol{\rho}^{-2}_{k,\mathbf{w}_{k-1}} \odot \tilde{\mathbf{x}}_k\right)}_{\check{\mathbf{e}}_k} \tag{5.14}$$

$$\mathbf{R}_{k,\boldsymbol{\theta},\delta_k} = \underbrace{\sum_{\kappa=1}^{k} \lambda^{k-\kappa}\check{\mathbf{Y}}^H_{\kappa,\boldsymbol{\theta}}\text{diag}\left(\hat{\boldsymbol{\gamma}}_{k,\mathbf{w}_{k-1}}\right)\check{\mathbf{Y}}_{\kappa,\boldsymbol{\theta}}}_{\mathbf{R}_{k,\boldsymbol{\theta}}} + \delta_k\mathbf{I}_{T+N_a} \tag{5.15}$$

Compared to the iterative GN update (4.79), several *approximations and modifications* are introduced. It will be illustrated in Section 5.4 that, nevertheless, the RLM-based adaptive algorithm converges sufficiently fast to a BM-TEQ with corresponding FEQs. The convergence speed of the adaptive BM-TEQ and PTEQ are comparable.

- In Section 4.3.4, we have argued that one could iteratively optimize the IR-SNLLS-based BM-TEQ criterion in two ways. Either a three-step algorithm is applied that alternates between an update of the weights $\boldsymbol{\gamma}_{K,\mathbf{w}_{\text{prev}}}$, an LS estimate of the FEQs $\tilde{\mathbf{d}}$ and a GN update of $\mathbf{w}$, or a two-step algorithm is used that omits the LS estimation of the FEQs $\tilde{\mathbf{d}}$ and alternates instead between an update of the weights $\boldsymbol{\gamma}_{K,\mathbf{w}_{\text{prev}}}$ and a GN-based update of the joint parameter vector $\boldsymbol{\theta}$. Here, we adopt the second approach and omit the computation of the LS estimate of the uMMSE

FEQs (4.21) to reduce complexity. In this way, the need to store and update the $1 \times T$ crosscorrelation vector estimates $\boldsymbol{\sigma}_{K,n,\tilde{x}\tilde{\mathbf{y}}}$, $n \in \mathcal{S}_a$, is avoided. Instead, the FEQ update as part of the RLM update (5.11) is used.

- We have mentioned in Remark 4.12 that the two above-mentioned alternatives have the same asymptotic convergence, but the three-step algorithm has the fastest initial convergence, hence also the fastest overall convergence, and is cited to be better conditioned [16, 51]. For stability reasons, the approximate Hessian estimate $\mathbf{R}_{k,\boldsymbol{\theta}}$ is then regularized by the second term $\delta_k \mathbf{I}_{T+N_a}$ in (4.81). An adaptation rule for the regularization parameter δ_k is given in Section 5.2.3 taking into account the varying condition of $\mathbf{R}_{k,\boldsymbol{\theta}}$. The regularization also solves the inherent singularity of $\mathbf{R}_{k,\boldsymbol{\theta}}$: it can easily be shown that the vector $\begin{bmatrix} \mathbf{w}^H & -\tilde{\mathbf{d}}^H \end{bmatrix}^H$ lies in the right null space of $\check{\mathbf{Y}}_{k,\boldsymbol{\theta}}$ and, hence, of $\mathbf{R}_{k,\boldsymbol{\theta}}$. The inverse of the regularized $\mathbf{R}_{k,\boldsymbol{\theta},\delta_k}$ can be computed in a similar way as the inverse of $\mathbf{R}_{\boldsymbol{\theta}}$ in (4.87).

- The weights $\check{\gamma}_{K,n,\mathbf{w}_{\text{prev}}}$ (5.9) assume knowledge of and depend on $\rho^2_{K,n,\mathbf{w}_{\text{prev}}}$ (4.75) via $\text{SNR}_{K,n}$ (4.74). This requires knowledge of $\boldsymbol{\Sigma}^2_{K,n,\tilde{\mathbf{y}}}$ and $\boldsymbol{\sigma}_{K,n,\tilde{x}\tilde{\mathbf{y}}}$, $n \in \mathcal{S}_a$, i.e., based on all data up to time K. Adopting the ideas from [36, 48], the optimal weights $\check{\gamma}_{K,n,\mathbf{w}}$ and $\text{SNR}_{K,n}$ are replaced by *instantaneous a priori* estimates at time k, i.e., based on $\mathbf{w}_{k-1}$ and $\tilde{d}_{k-1,n}$:

$$\begin{aligned} \hat{\gamma}_{k,n,\mathbf{w}_{k-1}} &= \frac{\widehat{\text{SNR}}^2_{k,n}}{\sigma^2_{k,n,\tilde{x}} \left(\widehat{\text{SNR}}_{k,n} + \Gamma_n \right)} \\ \text{with } \widehat{\text{SNR}}_{k,n} &= \frac{\sigma^2_{k,n,\tilde{x}}}{\left| \tilde{d}_{k-1,n} \tilde{\mathbf{y}}_{k,n} \mathbf{w}_{k-1} - \tilde{x}_{k,n} \right|^2} \end{aligned} \tag{5.16}$$

  The instantaneous estimate $\widehat{\text{SNR}}_{k,n}$ is also used in (5.14) to approximate the virtual symbols in $\check{e}_{k,n}$: $\rho^{-2}_{K,n,\mathbf{w}_{\text{prev}}} \tilde{x}_{k,n} \approx \hat{\rho}^{-2}_{k,n,\mathbf{w}_{k-1}} \tilde{x}_{k,n} = \left(1 + \frac{1}{\widehat{\text{SNR}}_{k,n}}\right) \tilde{x}_{k,n}$. Note that, in order to avoid an overly pessimistic (i.e., large) a priori error $\check{e}_{k,n}$, we impose that $\hat{\rho}^2_{k,n,\mathbf{w}_{k-1}}$ is bounded between 0.5 and 1. This corresponds to a realistic lower bound on $\widehat{\text{SNR}}_{k,n}$ of 1 (or 0 dB), as tones with a lower SNR can not reliably carry a single bit.

- The gradient (4.80) is replaced by an *instantaneous* gradient estimate $\mathbf{g}_{k,\boldsymbol{\theta}}$ (5.14). This is common practice when developing adaptive algorithms and is mainly done for complexity reasons.

- The approximate Hessian $\mathbf{R}_{\boldsymbol{\theta}}$ (4.81) is replaced by an exponentially weighted estimate $\mathbf{R}_{k,\boldsymbol{\theta}}$. As $\mathbf{R}_{\boldsymbol{\theta}}$ depends on the SOS $\boldsymbol{\Sigma}^2_{n,\tilde{\mathbf{y}}}$, it suffices to update

the SOS estimates $\mathbf{\Sigma}^2_{k,n,\tilde{\mathbf{y}}}$ using:

$$\mathbf{\Sigma}^2_{k,n,\tilde{\mathbf{y}}} = \lambda \mathbf{\Sigma}^2_{k-1,n,\tilde{\mathbf{y}}} + \tilde{\mathbf{y}}^H_{k,n} \tilde{\mathbf{y}}_{k,n} \tag{5.17}$$

An exponential weighting factor $\lambda < 1$ allows to track the SOS in a non-stationary environment.

It is clear from (4.87) that the inversion of the regularized approximate Hessian $\mathbf{R}_{k,\boldsymbol{\theta},\delta_k}$ does not require $\mathcal{O}((T+N_a)^3)$ operations, thanks to its block structure $\mathbf{R}_{k,\boldsymbol{\theta},\delta_k} = \begin{bmatrix} \mathbf{E}_k & \mathbf{F}_k \\ \mathbf{F}_k^H & \mathbf{G}_k \end{bmatrix}$. The diagonal submatrix $\mathbf{G}_k$ is easily inverted; only the inverse of the full $T \times T$ matrix $\mathbf{Q}_k$ ($\mathcal{O}(T^3)$ operations, see (4.88)) needs to be computed. Exploiting the block structure as in (4.87), the updating equation of $\boldsymbol{\theta}$ (5.11) can be split into an update of $\mathbf{w}$ and an update of $\tilde{\mathbf{d}}$. With the definitions of $\mathbf{Q}$ (4.88) and $\check{\mathbf{Y}}_{k,\boldsymbol{\theta}}$ (4.82), we obtain a GN-like update of $\mathbf{w}$:

$$\boxed{\mathbf{w}_k \leftarrow \mathbf{w}_{k-1} \underbrace{-\mathbf{Q}_k^{-1} \acute{\mathbf{g}}_k}_{\Delta \mathbf{w}_k}} \tag{5.18}$$

with

$$\acute{\mathbf{g}}_k = \sum_{n \in \mathcal{S}_a} \hat{\gamma}_{k,n,\mathbf{w}_{k-1}} \underbrace{\left(\tilde{\mathbf{y}}^H_{k,n} \tilde{d}^*_n - \frac{\left(\mathbf{\Sigma}^2_{k,n,\tilde{\mathbf{y}}} \mathbf{w} \right) \tilde{d}^*_n \tilde{y}^*_{k,n,\mathbf{w}_{k-1}}}{\mathbf{w}^H \mathbf{\Sigma}^2_{k,n,\tilde{\mathbf{y}}} \mathbf{w} + \delta_k} \right)}_{\acute{\mathbf{y}}^H_{k,n}} \check{e}_{k,n} \tag{5.19}$$

$$\mathbf{Q}_k = \sum_{n \in \mathcal{S}_a} \hat{\gamma}_{k,n,\mathbf{w}_{k-1}} \left(\left| \tilde{d}_n \right|^2 \mathbf{\Sigma}^2_{k,n,\tilde{\mathbf{y}}} - \frac{\left| \tilde{d}_n \right|^2 \mathbf{\Sigma}^2_{k,n,\tilde{\mathbf{y}}} \mathbf{w} \mathbf{w}^H \mathbf{\Sigma}^2_{k,n,\tilde{\mathbf{y}}}}{\mathbf{w}^H \mathbf{\Sigma}^2_{k,n,\tilde{\mathbf{y}}} \mathbf{w} + \delta_k} \right) + \delta_k \mathbf{I}_T \tag{5.20}$$

where $\tilde{d}_n = \tilde{d}_{k-1,n}$ and $\mathbf{w} = \mathbf{w}_{k-1}$. The n-th FEQ $\tilde{d}_n$ is updated as follows:

$$\boxed{\tilde{d}_{k,n} \leftarrow \tilde{d}_{k-1,n} + \Delta \tilde{d}_{k,n}} \tag{5.21}$$

with

$$\Delta \tilde{d}_{k,n} = -\left(\mathbf{w}^H \Sigma^2_{k,n,\tilde{\mathbf{y}}} \mathbf{w} + \delta_k \right)^{-1} \left(\tilde{y}^*_{k,n,\mathbf{w}_{k-1}} \check{e}_{k,n} + \tilde{d}_{k-1,n} \left(\mathbf{w}^H \mathbf{\Sigma}^2_{k,n,\tilde{\mathbf{y}}} \right) \Delta \mathbf{w}_k \right) \tag{5.22}$$

where $\mathbf{w} = \mathbf{w}_{k-1}$ and where $\Delta \mathbf{w}_k$ has already been computed in (5.18). It will be shown in Section 5.3 that the computational cost of the equalizer update is dominated by $\mathcal{O}(N_a T^2)$ computations to construct $\mathbf{Q}_k$. For a real-valued TEQ (of course maintaining complex-valued FEQs), $\Re\{\acute{\mathbf{g}}_k\}$ and $\Re\{\mathbf{Q}_k\}$ are used in (5.18).

Remark 5.1 The *iterative* and *recursive* update of $\mathbf{w}$, (4.89) and (5.18), respectively, are very similar; only the gradients differ slightly. The vector denoted as $\acute{\mathbf{y}}_{k,n}^H$ in (5.19), which determines the gradient direction, has an extra second term. This is a correction term, due to the GN-based updating of the FEQs $\tilde{\mathbf{d}}$ in (5.11). Remarkably, the matrix $\mathbf{Q}_k$ in (5.20) and the vectors $\acute{\mathbf{y}}_{k,n}^H$ in (5.19) are closely related as $\mathbf{Q}_k$ (ignoring the regularization parameter δ_k) turns out to be an estimate of $\mathbf{Q} = \sum_{n\in\mathcal{S}_a} \check{\gamma}_{k,n,\mathbf{w}_{k-1}} \mathcal{E}\left\{\acute{\mathbf{y}}_{k,n}^H \acute{\mathbf{y}}_{k,n}\right\}$ in (4.88), which is a weighted sum of the N_a autocorrelation matrices of $\acute{\mathbf{y}}_{k,n}$, $n \in \mathcal{S}_a$ with weights $\check{\gamma}_{k,n,\mathbf{w}_{k-1}}$. □

5.2.2 Reducing the SOS memory cost

Thanks to the block structure of the approximate Hessian $\mathbf{R}_{k,\boldsymbol{\theta}}$, which has size $(T + N_a) \times (T + N_a)$ (in the case of a complex-valued T-tap TEQ and N_a complex-valued 1-tap FEQs), the RLM algorithm only requires to store and update the N_a SOS estimates $\boldsymbol{\Sigma}_{k,n,\tilde{\mathbf{y}}}^2$ (size $T \times T$). Based on the sliding DFT shift structure, which is summarized by the second key observation (3.65), the memory cost can be further reduced from $N_a T^2$ complex-valued coefficients to $\mathcal{O}(N_a T)$ coefficients, as will be demonstrated.

It is instructive to mention that the same key observation has led to the efficient square-root RLS-based adaptive PTEQ, see Section 3.4.2. Based on the block description (3.77) of the $T\times T$ autocorrelation matrix of $\mathbf{z}_{k,n} = \left[\begin{array}{cc} \Delta\mathbf{y}_k^T & \tilde{y}_{k,n} \end{array}\right]$:

$$\boldsymbol{\Sigma}_{n,\mathbf{z}}^2 = \mathcal{E}\left\{\mathbf{z}_{k,n}^H \mathbf{z}_{k,n}\right\} = \left[\begin{array}{cc} \boldsymbol{\Sigma}_{\Delta\mathbf{y}}^2 & \boldsymbol{\sigma}_{n,\tilde{y}\Delta\mathbf{y}}^H \\ \boldsymbol{\sigma}_{n,\tilde{y}\Delta\mathbf{y}} & \sigma_{n,\tilde{y}}^2 \end{array}\right] = \mathbf{U}_n^H \mathbf{U}_n \qquad (5.23)$$

the square-root RLS PTEQ algorithm with inverse updating was shown in Section 3.4.2 to store and update in an efficient way the inverse transpose $\mathbf{S}_{k,n}$ of the (upper triangular) Cholesky factor $\mathbf{U}_{k,n}$ of the SOS estimate $\boldsymbol{\Sigma}_{k,n,\mathbf{z}}^2$.

A similar approach can be taken for the SOS estimates of the adaptive BM-TEQ algorithm. Now, the Cholesky factor itself $\mathbf{U}_{k,n}$ is updated, stored and then used to construct the autocorrelation matrices $\boldsymbol{\Sigma}_{k,n,\tilde{\mathbf{y}}}^2$, required for (5.18) and (5.21). The first $T-1$ columns $\mathbf{U}_{k,\Delta\mathbf{y}}$ of $\mathbf{U}_{k,n}$ are real-valued, tone-independent and determined by $\boldsymbol{\Sigma}_{k,\Delta\mathbf{y}}^2$. The SOS memory cost then amounts to $\frac{T(T-1)}{2}$ real-valued coefficients for storing the first $T-1$ columns $\mathbf{U}_{k,\Delta\mathbf{y}}$ of $\mathbf{U}_{k,n}$ plus $2T-1$ real-valued coefficients per tone for the $1\times T$ tone-dependent, complex-valued, last column $\mathbf{u}_{k,n}$ of $\mathbf{U}_{k,n}$, i.e., an overall number of $(2T-1)N_a + \frac{T(T-1)}{2}$ real-valued coefficients, which is the same SOS memory cost as for the RLS PTEQ algorithm. The SOS update cost is also similar and dominated by a term of $18N_aT$ real multiplications, mainly required for updating the tone-dependent last row $\mathbf{u}_{k,n}$.

Inspired by the hybrid RLS/LMS algorithm as described in Section 3.4.2 [161], the complexity can be further reduced by storing and updating the RLS/LMS-

based SOS, i.e., the Cholesky factor $\check{\mathbf{U}}_{k,n}$ of $\check{\mathbf{\Sigma}}^2_{k,n,\mathbf{z}}$ in (3.79), which consists of the tone-independent Cholesky factor $\mathbf{U}_{k,\Delta\mathbf{y}}$ and a single, non-zero, tone-dependent coefficient $\sqrt{\sigma^2_{k,n,\tilde{y}}}$. The SOS memory cost amounts to $N_a + \frac{T(T-1)}{2}$ real-valued coefficients and the SOS update cost is dominated by $3T^2$ multiplications for the tone-independent part. For the details on updating $\mathbf{U}_{k,n}$ and $\check{\mathbf{U}}_{k,n}$, e.g., based on a recursive QR update with Givens rotations, we refer to [52, 54].

As will be shown in Section 5.3 and in contrast to the adaptive PTEQ, the SOS updating is computationally not the most demanding part of the adaptive BM-TEQ. All PTEQ operations (the equalizer filtering as well as the SOS and equalizer updating) are based on the *transformed* inputs $\mathbf{z}_{k,n} = \tilde{\mathbf{y}}_{k,n}\mathbf{T}_n^{-1}$ and coefficients $\mathbf{v}_n = \mathbf{T}_n\mathbf{w}_n$ with $\mathbf{T}_n$ defined in (3.65). The adaptive BM-TEQ, on the other hand, requires that the SOS estimates $\mathbf{\Sigma}^2_{k,n,\mathbf{z}}$ or $\check{\mathbf{\Sigma}}^2_{k,n,\mathbf{z}}$ are *back-transformed* after each update, based on:

$$\mathbf{\Sigma}^2_{n,\tilde{\mathbf{y}}} = \mathbf{T}_n^H\mathbf{\Sigma}^2_{n,\mathbf{z}}\mathbf{T}_n \text{ and } \check{\mathbf{\Sigma}}^2_{n,\tilde{\mathbf{y}}} = \mathbf{T}_n^H\check{\mathbf{\Sigma}}^2_{n,\mathbf{z}}\mathbf{T}_n \tag{5.24}$$

which follow from (3.65). Based on the definition of $\mathbf{T}_n$, a recursive computation can be derived as follows:

$$\begin{aligned}
\mathbf{\Sigma}^2_{n,\tilde{\mathbf{y}}}[s,t] &= \mathbf{\Sigma}^2_{n,\tilde{\mathbf{y}}}[s-1,t-1] + \alpha_n^*\mathbf{\Sigma}^2_{n,\tilde{\mathbf{y}}}[s-1,t] + \alpha_n\mathbf{\Sigma}^2_{n,\tilde{\mathbf{y}}}[s,t-1] \\
&\quad +\mathbf{\Sigma}^2_{n,\mathbf{z}}[T-s-1,T-t-1], \text{ if } 1 \le s \le T-1,\ 1 \le t \le T-1 \\
\mathbf{\Sigma}^2_{n,\tilde{\mathbf{y}}}[0,t] &= \alpha_n\mathbf{\Sigma}^2_{n,\tilde{\mathbf{y}}}[0,t-1] + \mathbf{\Sigma}^2_{n,\mathbf{z}}[T-1,T-t-1] \text{ if } 1 \le t \le T-1 \\
\mathbf{\Sigma}^2_{n,\tilde{\mathbf{y}}}[s,0] &= \alpha_n^*\mathbf{\Sigma}^2_{n,\tilde{\mathbf{y}}}[s-1,0] + \mathbf{\Sigma}^2_{n,\mathbf{z}}[T-s-1,T-1] \text{ if } 1 \le s \le T-1 \\
\mathbf{\Sigma}^2_{n,\tilde{\mathbf{y}}}[0,0] &= \mathbf{\Sigma}^2_{n,\mathbf{z}}[T-1,T-1]
\end{aligned} \tag{5.25}$$

where $\alpha_n = \exp(-j2\pi(n-1)/N)/\sqrt{N}$. This requires $\mathcal{O}(N_aT^2)$ operations. The matrices $\mathbf{\Sigma}^2_{k,n,\tilde{\mathbf{y}}}$ or $\check{\mathbf{\Sigma}}^2_{k,n,\tilde{\mathbf{y}}}$ are needed for computing the $T \times 1$ vectors $\mathbf{\Sigma}^2_{k,n,\tilde{\mathbf{y}}}\mathbf{w}$ ($\mathcal{O}(N_aT^2)$ operations) and scalars $\mathbf{w}^H\mathbf{\Sigma}^2_{k,n,\tilde{\mathbf{y}}}\mathbf{w}$ ($\mathcal{O}(N_aT)$ operations) in (5.19), (5.20) and (5.22). Note that the back-transformation (5.25) being unnecessary is an exclusive advantage of the adaptive PTEQ with *complex-valued* taps $\mathbf{v}_n$ over the adaptive (real-valued or complex-valued) BM-TEQ and BM-PGEQ and even the adaptive PTEQ with *real-valued* taps, which is basically a real BM-PGEQ with single-tone-groups: an adaptive BM-TEQ update requires $\mathcal{O}(N_aT^2)$ operations, while $\mathcal{O}(N_aT)$ operations suffice for the RLS-based adaptive PTEQ update.

5.2.3 Further refinements to the RLM algorithm

5.2.3.1 Exponential weighting factor λ

As suggested by (5.17), SOS like $\mathbf{\Sigma}^2_{n,\mathbf{z}}$ can be estimated recursively using an exponential window:

$$\mathbf{\Sigma}^2_{k,n,\mathbf{z}} = \lambda\mathbf{\Sigma}^2_{k-1,n,\mathbf{z}} + \mathbf{z}^H_{k,n}\mathbf{z}_{k,n} \tag{5.26}$$

An exponential window with factor λ corresponds to an equivalent window length of $\frac{1}{1-\lambda}$. When adaptively solving a *linear* problem, as with the RLS-based adaptive PTEQ, λ trades off tracking of time-variations versus accuracy of the SOS estimates and hence the adapted parameters: when λ approaches 1, the equivalent window is large, hence the tracking performance is slower, but also the parameter estimates are more accurate, i.e., the excess MSE is smaller [54]. When adaptively solving a *non-linear* problem, an extra effect should be considered: when λ approaches 1, the adaptive algorithm converges slower [77]. During the first updates, the instantaneous gradient estimate (5.14) is inaccurate, due to poor initial parameter estimates. Hence, it is advised to depreciate these first estimates by using a smaller λ. In [77], λ is smoothly increased during convergence, e.g., from 0.95 to 0.99. In the simulations of Section 5.4, fast and accurate convergence is observed when starting with $\lambda = 0.9$ during the first 400 updates, switching to $\lambda = 0.95$ until update 800 and finishing with 200 updates with $\lambda = 0.99$.

5.2.3.2 Equalizer input power normalization

In contrast with the RLS algorithm, the stability of the RLM algorithm is not guaranteed by a nonsingular $\mathbf{R}_{k,\boldsymbol{\theta},\delta_k}$. The convergence speed and stability of the RLM method are to a large extent determined by the condition number or eigenvalue spread of the regularized approximate Hessian estimate (5.15). It is good practice to make sure that the eigenvalue spread only depends on the correlation among the equalizer inputs and not on the power spread of the equalizer inputs. In the case of a tapped delay-line equalizer/filter, the input autocorrelation matrix is Toeplitz, hence the diagonal elements are equal and so there is no input power spread. This does not necessarily hold true for the TEQ-FEQ-based receiver. We use the term "equalizer inputs" in a loose and general way here, as we are referring to the $N_a \times (N_a + T)$ matrix $\left[\text{diag}\left(\sqrt{\hat{\gamma}_{k,\mathbf{w}_{k-1}}}\right)\check{\mathbf{Y}}_{k,\boldsymbol{\theta}_{k-1}}\right]$, with $\check{\mathbf{Y}}_{k,\boldsymbol{\theta}}$ defined in (4.82), which appears in the gradient (5.14). Its autocorrelation matrix is estimated by the approximate Hessian $\mathbf{R}_{k,\boldsymbol{\theta}}$ in (5.15). The diagonal of $\mathbf{R}_{k,\boldsymbol{\theta}}$, denoted as $\boldsymbol{\epsilon}_k$, is a measure for the "equalizer input powers" . The first T entries, corresponding to the diagonal elements of $\mathbf{E}_k$, are almost equal to one another as they form the diagonal of a weighted sum of "almost-Toeplitz" matrices $\boldsymbol{\Sigma}^2_{k,n,\tilde{\mathbf{y}}}$. The last N_a entries, corresponding to the diagonal elements of $\mathbf{G}_k$ however can have a large dynamic range, depending on the frequency-dependent channel attenuation. Therefore, we normalize the input powers before each update by applying a diagonal transformation to the "equalizer input" and to the approximate Hessian in (5.15):

$$\left[\text{diag}\left(\sqrt{\hat{\gamma}_{k,\mathbf{w}_{k-1}}}\right)\check{\mathbf{Y}}_{k,\boldsymbol{\theta}_{k-1}}\right] \leftarrow \left[\text{diag}\left(\sqrt{\hat{\gamma}_{k,\mathbf{w}_{k-1}}}\right)\check{\mathbf{Y}}_{k,\boldsymbol{\theta}_{k-1}}\right]\text{diag}\left(\sqrt{\boldsymbol{\epsilon}_k}\right)^{-1} \quad (5.27)$$

$$\mathbf{R}_{k,\boldsymbol{\theta}} \leftarrow \text{diag}\left(\sqrt{\boldsymbol{\epsilon}_k}\right)^{-1}\mathbf{R}_{k,\boldsymbol{\theta}}\text{diag}\left(\sqrt{\boldsymbol{\epsilon}_k}\right)^{-1} \quad (5.28)$$

The joint TEQ-FEQ vector $\boldsymbol{\theta}$ should be transformed accordingly with diag $\left(\sqrt{\boldsymbol{\epsilon}_k}\right)$ before and diag $\left(\sqrt{\boldsymbol{\epsilon}_k}\right)^{-1}$ after the update (5.11). The diagonal of $\mathbf{R}_{k,\boldsymbol{\theta}}$ (5.28) is then reduced to an identity matrix $\mathbf{I}_{T+N_a}$. In the next section, we consider the regularization of this transformed $\mathbf{R}_{k,\boldsymbol{\theta}}$ (5.28).

5.2.3.3 Adaptive regularization

Both the convergence speed and stability are affected by a suitable choice of the regularization parameter δ_k in (5.15): a too small δ_k could cause the RLM algorithm to run unstable, while a too large δ_k could induce slow convergence in directions in the parameter space that correspond to small eigenvalues of $\mathbf{R}_{k,\boldsymbol{\theta}_{k-1}}$. The parameter δ_k should be adapted, as the condition of $\mathbf{R}_{k,\boldsymbol{\theta}_{k-1}}$ depends on the estimates $\boldsymbol{\theta}_{k-1}$ and hence changes during convergence. There exists a vast literature on regularization for *iterative,* batch optimization methods where the condition changes while iterating. An *adaptive* regularization algorithm, based on instantaneous estimates of the actual and predicted cost criterion reduction, is proposed in [90]. We adapt this algorithm for use with the adaptive BM-TEQ as follows.

For each update, the RLM algorithm (5.11) optimizes a local, instantaneous, quadratic approximation $J_{k,\text{approx}}(\boldsymbol{\theta})$ of the IR-SNLLS-based design criterion $J_k(\boldsymbol{\theta})$ in (5.8):

$$J_{k,\text{approx}}(\boldsymbol{\theta}) = J_k(\boldsymbol{\theta}_{k-1}) + \Delta\boldsymbol{\theta}^H \mathbf{g}_{k,\boldsymbol{\theta}_{k-1}} + \Delta\boldsymbol{\theta}^T \mathbf{g}^*_{k,\boldsymbol{\theta}_{k-1}} + \Delta\boldsymbol{\theta}^H \mathbf{R}_{k,\boldsymbol{\theta}_{k-1},\delta_k} \Delta\boldsymbol{\theta} \tag{5.29}$$

with $\Delta\boldsymbol{\theta} = \boldsymbol{\theta} - \boldsymbol{\theta}_{k-1}$, $\mathbf{g}_{k,\boldsymbol{\theta}_{k-1}}$ and $\mathbf{R}_{k,\boldsymbol{\theta}_{k-1},\delta_k}$ defined in (5.11-5.15). Minimizing $J_{k,\text{approx}}(\boldsymbol{\theta})$ w.r.t. $\boldsymbol{\theta}$ indeed gives the RLM update (5.11). The *predicted* instantaneous cost reduction estimate is obtained by substituting $\Delta\boldsymbol{\theta}_k$ (5.11) in (5.29):

$$\begin{aligned} \varepsilon_{k,\text{p}} &= J_k(\boldsymbol{\theta}_{k-1}) - J_{k,\text{approx}}(\boldsymbol{\theta}_k) \\ &= \mathbf{g}^H_{k,\boldsymbol{\theta}_{k-1}} \mathbf{R}^{-1}_{k,\boldsymbol{\theta}_{k-1},\delta_k} \mathbf{g}_{k,\boldsymbol{\theta}_{k-1}} \qquad (5.30) \\ &= -\mathbf{g}^H_{k,\boldsymbol{\theta}_{k-1}} \Delta\boldsymbol{\theta}_k \qquad (5.31) \end{aligned}$$

The predicted cost reduction estimate $\varepsilon_{k,\text{p}}$ is cheaply computed with (5.31). Note that in the case of a real-valued TEQ, the predicted instantaneous cost reduction estimate $\varepsilon_{k,\text{p}}$ is given by $\varepsilon_{k,\text{p}} = -\mathbf{g}^T_{k,1,\boldsymbol{\theta}_{k-1}} \Delta\mathbf{w}_k - 2\Re\{\mathbf{g}^H_{k,2,\boldsymbol{\theta}_{k-1}} \Delta\tilde{\mathbf{d}}_k\}$, with $\mathbf{g}_{k,1,\boldsymbol{\theta}}$ and $\mathbf{g}_{k,2,\boldsymbol{\theta}}$ defined in (5.14) and with $\Delta\mathbf{w}_k$ and $\Delta\tilde{\mathbf{d}}_k$ defined in (5.18) and (5.22), respectively.

The *actual* instantaneous cost reduction estimate follows from (5.8) and is determined by the vector of a priori errors $\check{\mathbf{e}}_{k,\boldsymbol{\theta}_{k-1}}$ and a posteriori errors $\check{\mathbf{e}}_{k,\boldsymbol{\theta}_k}$:

$$\varepsilon_{k,\text{a}} = \left\| \text{diag}\left(\sqrt{\hat{\gamma}_{k,\mathbf{w}_{k-1}}}\right) \check{\mathbf{e}}_{k,\boldsymbol{\theta}_{k-1}} \right\|^2 - \left\| \text{diag}\left(\sqrt{\hat{\gamma}_{k,\mathbf{w}_{k-1}}}\right) \check{\mathbf{e}}_{k,\boldsymbol{\theta}_k} \right\|^2 \tag{5.32}$$

The a posteriori error vector is efficiently computed from the a priori error vector as:

$$\begin{aligned}\check{\mathbf{e}}_{k,\boldsymbol{\theta}_k} &= \operatorname{diag}\left(\tilde{\mathbf{d}}_k\right)\tilde{\mathbf{Y}}_k\mathbf{w}_k - \boldsymbol{\rho}^{-2}_{k,\mathbf{w}_{k-1}} \odot \tilde{\mathbf{x}}_k \qquad (5.33)\\ &= \operatorname{diag}\left(\Delta\tilde{\mathbf{d}}_k\right)\left(\tilde{\mathbf{Y}}_k\mathbf{w}_{k-1} + \tilde{\mathbf{Y}}_k\Delta\mathbf{w}_k\right) + \operatorname{diag}\left(\tilde{\mathbf{d}}_{k-1}\right)\tilde{\mathbf{Y}}_k\Delta\mathbf{w}_k \\ &\quad + \underbrace{\operatorname{diag}\left(\tilde{\mathbf{d}}_{k-1}\right)\tilde{\mathbf{Y}}_k\mathbf{w}_{k-1} - \boldsymbol{\rho}^{-2}_{k,\mathbf{w}_{k-1}} \odot \tilde{\mathbf{x}}_k}_{\check{\mathbf{e}}_{k,\boldsymbol{\theta}_{k-1}}} \qquad (5.34)\end{aligned}$$

where $\tilde{\mathbf{Y}}_k\Delta\mathbf{w}_k$ in the first and second term of (5.34) dominates the computational cost ($4N_aT$ real multiplications).

Both the *actual* and *predicted* instantaneous cost reduction estimates are averaged using an exponential window with $\lambda_\varepsilon = 0.9$: $\bar{\varepsilon}_{k,\mathrm{a}} = \sum_{\kappa=1}^{k}\lambda_\varepsilon^{k-\kappa}\varepsilon_{\kappa,\mathrm{a}}$ and $\bar{\varepsilon}_{k,\mathrm{p}} = \sum_{\kappa=1}^{k}\lambda_\varepsilon^{k-\kappa}\varepsilon_{\kappa,\mathrm{p}}$. The following adaptation rule is then applied, once per 10 BM-TEQ updates, based on the ratio $r_k = \frac{\bar{\varepsilon}_{k,\mathrm{a}}}{\bar{\varepsilon}_{k,\mathrm{p}}}$, which is a measure for the match between the local quadratic approximation (5.29) and the actual design criterion (5.8) [90]:

$$\delta_{k+1} \leftarrow \begin{cases} 2\delta_k & \text{if } r_k < 0.25 \\ \max(\delta_k/2, \delta_{\min}) & \text{if } r_k > 0.75 \\ \delta_k & \text{otherwise} \end{cases} \qquad (5.35)$$

A lower bound of, e.g., $\delta_{\min} = 10^{-12}$, prevents a numerically singular $\mathbf{R}_{k,\boldsymbol{\theta}_{k-1},\delta_k}$. If $\bar{\varepsilon}_{k,\mathrm{a}}$ happens to drop below zero (due to the stochastic nature of the incoming data), the update (5.11) is ignored. In addition, if this occurs twice in a row, the regularization is increased: $\delta_{k+1} \leftarrow 2\delta_k$. The larger the confidence in the initial parameter estimate, the smaller the initial δ_0 should be chosen. This adaptive regularization algorithm introduces a minor extra computational cost and a memory cost of 2 real-valued coefficients $\bar{\varepsilon}_{k,\mathrm{a}}$ and $\bar{\varepsilon}_{k,\mathrm{p}}$.

5.2.4 Summary of the adaptive BM-TEQ and BM-PGEQ algorithm

The adaptive BM-TEQ algorithm (for the case of RLS-based SOS and a complex-valued TEQ) is summarized in **Table 5.1**. The presented algorithm is easily extended to an adaptive BM-PGEQ by solving several downscaled adaptive BM-TEQ problems in parallel. The steps 1 to 5 are then identical, as they are independent of the tone groups. Step 6 to 8 need to be executed for each tone group.

Table 5.1: Adaptive BM-TEQ algorithm.

Initialize $\mathbf{w}$, $\tilde{\mathbf{d}}$, $\bar{\varepsilon}_{k,\mathrm{a}}$ and $\bar{\varepsilon}_{k,\mathrm{p}}$ as well as $\mathbf{U}_{k,n}$ for each tone $n \in \mathcal{S}_a$.
For $k = 1, \ldots, \infty$

- *Filtering*:

  1. Compute the sliding DFT output, $\tilde{\mathbf{y}}_{k,n}$, for each tone $n \in \mathcal{S}_a$:

  $$\tilde{\mathbf{y}}_{k,n}[0] = \mathcal{F}_n \mathbf{y}_{k,0:N-1} \text{ and } \tilde{\mathbf{y}}_{k,n}[t] = \alpha_n \tilde{\mathbf{y}}_{k,n}[t-1] + (y_{k,-t} - y_{k,N-t}),\ t = 1, \cdots, T-1 \tag{5.36}$$

  2. Compute the FEQ output $\hat{\tilde{x}}_{k,n}$, for each tone $n \in \mathcal{S}_a$:

  $$\hat{\tilde{x}}_{k,n} = \tilde{d}_{k-1,n} \tilde{y}_{k,n,\mathbf{w}_{k-1}} \text{ with } \tilde{y}_{k,n,\mathbf{w}_{k-1}} = \tilde{\mathbf{y}}_{k,n} \mathbf{w}_{k-1} \tag{5.37}$$

- *Updating*:

  1. Compute the FEQ output error $\tilde{e}_{k,n}$, for each tone $n \in \mathcal{S}_a$:

  $$\tilde{e}_{k,n} = \hat{\tilde{x}}_{k,n} - \tilde{x}_{k,n} \tag{5.38}$$

  2. Compute $\widehat{\mathrm{SNR}}_{k,n}$ and $\hat{\gamma}_{k,n,\mathbf{w}_{k-1}}$, for each tone $n \in \mathcal{S}_a$:

  $$\hat{\gamma}_{k,n,\mathbf{w}_{k-1}} = \frac{\widehat{\mathrm{SNR}}_{k,n}^2}{\sigma_{k,n,\tilde{x}}^2 \left(\widehat{\mathrm{SNR}}_{k,n} + \Gamma_n \right)} \text{ with } \widehat{\mathrm{SNR}}_{k,n} = \frac{\sigma_{k,n,\tilde{x}}^2}{|\tilde{e}_{k,n}|^2} \tag{5.39}$$

  3. Compute the "virtual error" $\check{e}_{k,n}$, for each tone $n \in \mathcal{S}_a$:

  $$\check{e}_{k,n} = \tilde{e}_{k,n} - \frac{\tilde{x}_{k,n}}{\max\left(\widehat{\mathrm{SNR}}_{k,n}, 1 \right)} \tag{5.40}$$

  4. Update the SOS $\mathbf{\Sigma}_{k,n,\tilde{\mathbf{y}}}^2$, for each tone $n \in \mathcal{S}_a$:

  1. Use Givens rotations [54, 52] to update the Cholesky factor $\mathbf{U}_{k,n}$ (i.e., the common $\mathbf{U}_{k,\Delta\mathbf{y}}$ as well as the last columns $\mathbf{u}_{k,n}$ of $\mathbf{U}_{k,n}$ for each tone $n \in \mathcal{S}_a$) with $\mathbf{z}_{k,n} = \begin{bmatrix} \Delta\mathbf{y}_k^T & \tilde{y}_{k,n} \end{bmatrix}$:

  $$\mathbf{U}_{k,n} = \mathrm{givens}(\mathbf{U}_{k-1,n}, \lambda, \mathbf{z}_{k,n}) \tag{5.41}$$

  2. Compute $\mathbf{\Sigma}_{k,n,\mathbf{z}}^2$, i.e., $\mathbf{\Sigma}_{k,\Delta\mathbf{y}}^2$ as well as $\boldsymbol{\sigma}_{k,n,\tilde{y}\Delta\mathbf{y}}$ and $\sigma_{k,n,\tilde{y}}^2$ for each tone $n \in \mathcal{S}_a$:

  $$\mathbf{\Sigma}_{k,n,\Delta\mathbf{y}}^2 = \mathbf{U}_{k,\Delta\mathbf{y}}^H \mathbf{U}_{k,\Delta\mathbf{y}},\ \boldsymbol{\sigma}_{k,n,\tilde{y}\Delta\mathbf{y}} = \mathbf{u}_{k,n}^H \mathbf{U}_{k,\Delta\mathbf{y}} \text{ and } \sigma_{k,n,\tilde{y}}^2 = \mathbf{u}_{k,n}^H \mathbf{u}_{k,n} \tag{5.42}$$

  3. Compute $\mathbf{\Sigma}_{k,n,\tilde{\mathbf{y}}}^2$ recursively, for each tone $n \in \mathcal{S}_a$:

  $$\begin{aligned} \mathbf{\Sigma}_{k,n,\tilde{\mathbf{y}}}^2[s,t] \ = \ & \mathbf{\Sigma}_{k,n,\tilde{\mathbf{y}}}^2[s-1,t-1] + \alpha_n^* \mathbf{\Sigma}_{k,n,\tilde{\mathbf{y}}}^2[s-1,t] + \alpha_n \mathbf{\Sigma}_{k,n,\tilde{\mathbf{y}}}^2[s,t-1] \\ & + \mathbf{\Sigma}_{k,n,\mathbf{z}}^2[T-s-1, T-t-1],\ 0 \le s \le T-1,\ 0 \le t \le T-1 \end{aligned} \tag{5.43}$$

  5. Compute for each tone $n \in \mathcal{S}_a$:

  $$\mathbf{b}_{k,n} = \mathbf{w}_{k-1}^H \mathbf{\Sigma}_{k,n,\tilde{\mathbf{y}}}^2 \text{ and } b_{k,n} = \mathbf{w}_{k-1}^H \left(\mathbf{\Sigma}_{k,n,\tilde{\mathbf{y}}}^2 \mathbf{w}_{k-1} \right) \tag{5.44}$$

Table 5.1: Adaptive BM-TEQ algorithm *(continued)*

6. Compute the update $\Delta\mathbf{w}_k$ (the equalizer input power normalization has been omitted, see Section 5.2.3.2):

$$\mathbf{w}_k \leftarrow \mathbf{w}_{k-1} \underbrace{-\mathbf{Q}_k^{-1}\acute{\mathbf{g}}_k}_{\Delta\mathbf{w}_k} \tag{5.45}$$

with

$$\mathbf{g}_{k,1} = \sum_{n\in\mathcal{S}_a} \hat{\gamma}_{k,n,\mathbf{w}_{k-1}} \tilde{\mathbf{y}}_{k,n}^H \tilde{d}_{k-1,n}^* \check{e}_{k,n} \text{ and } g_{k,n,2} = \hat{\gamma}_{k,n,\mathbf{w}_{k-1}} \tilde{d}_{k-1,n}^* \tilde{y}_{k,n,\mathbf{w}_{k-1}}^* \check{e}_{k,n} \tag{5.46}$$

$$\acute{\mathbf{g}}_k = \mathbf{g}_{k,1} - \sum_{n\in\mathcal{S}_a} \frac{\mathbf{b}_{k,n}^H g_{k,n,2}}{b_{k,n}+\delta_k} \tag{5.47}$$

$$\mathbf{Q}_k = \sum_{n\in\mathcal{S}_a} \hat{\gamma}_{k,n,\mathbf{w}_{k-1}} \left(\left|\tilde{d}_{k-1,n}\right|^2 \boldsymbol{\Sigma}_{k,n,\tilde{\mathbf{y}}}^2 - \frac{\left|\tilde{d}_{k-1,n}\right|^2 \mathbf{b}_{k,n}^H \mathbf{b}_{k,n}}{b_{k,n}+\delta_k} \right) + \delta_k \mathbf{I}_T \tag{5.48}$$

7. Compute the update $\Delta\tilde{d}_{k,n}$, for each tone $n \in \mathcal{S}_a$:

$$\tilde{d}_{k,n} \leftarrow \tilde{d}_{k-1,n} \underbrace{-(b_{k,n}+\delta_k)^{-1}\left(\tilde{y}_{k,n,\mathbf{w}_{k-1}}^* \check{e}_{k,n} + \tilde{d}_{k-1,n}\mathbf{b}_{k,n}\Delta\mathbf{w}_k\right)}_{\Delta\tilde{d}_{k,n}} \tag{5.49}$$

8. Update the regularization parameter δ_{k+1}:

1. Compute the predicted cost reduction estimate $\varepsilon_{k,\mathrm{p}}$:

$$\varepsilon_{k,\mathrm{p}} = -\mathbf{g}_{k,1}^H \Delta\mathbf{w}_k - \sum_{n\in\mathcal{S}_a} g_{k,n,2}\Delta\tilde{d}_{k,n} \tag{5.50}$$

2. Compute the actual cost reduction estimate $\varepsilon_{k,\mathrm{a}}$:

$$\varepsilon_{k,\mathrm{a}} = \sum_{n\in\mathcal{S}_a} \hat{\gamma}_{k,n,\mathbf{w}_{k-1}} \left(|\check{e}_{k,n}|^2 - \left|\check{e}_{k,n,\boldsymbol{\theta}_k}\right|^2 \right) \tag{5.51}$$

with

$$\check{e}_{k,n,\boldsymbol{\theta}_k} = \Delta\tilde{d}_{k,n}\left(\tilde{y}_{k,n,\mathbf{w}_{k-1}} + \Delta\tilde{y}_{k,n,\mathbf{w}}\right) + \tilde{d}_{k-1,n}\Delta\tilde{y}_{k,n,\mathbf{w}} + \check{e}_{k,n} \tag{5.52}$$
$$\text{with } \Delta\tilde{y}_{k,n,\mathbf{w}} = \tilde{\mathbf{y}}_{k,n}\Delta\mathbf{w}_k$$

3. Update $\bar{\varepsilon}_{k,\mathrm{a}} = \lambda_\varepsilon \bar{\varepsilon}_{k-1,\mathrm{a}} + \varepsilon_{k,\mathrm{a}}$ and $\bar{\varepsilon}_{k,\mathrm{p}} = \lambda_\varepsilon \bar{\varepsilon}_{k-1,\mathrm{p}} + \varepsilon_{k,\mathrm{p}}$.

4. If $\bar{\varepsilon}_{k,\mathrm{a}} < 0$, then $\Delta\mathbf{w}_k \leftarrow \mathbf{0}$ and $\Delta\tilde{d}_{k,n} \leftarrow 0$. If $\bar{\varepsilon}_{k-1,\mathrm{a}} < 0$ and $\bar{\varepsilon}_{k,\mathrm{a}} < 0$, then $\delta_{k+1} \leftarrow 2\delta_k$.

5. If $k = 10, 20, 30, \ldots$, then compute $r_k = \frac{\bar{\varepsilon}_{k,\mathrm{a}}}{\bar{\varepsilon}_{k,\mathrm{p}}}$ and update δ_{k+1}:

$$\delta_{k+1} \leftarrow \begin{cases} 2\delta_k & \text{if } r_k < 0.25 \\ \max(\delta_k/2, \delta_{\min}) & \text{if } r_k > 0.75 \\ \delta_k & \text{otherwise} \end{cases} \tag{5.53}$$

End

Table 5.2: Memory cost (number of real coefficients) and computational complexity (number of real multiplications per DMT symbol) of *equalizer filtering* with a TEQ, a PGEQ and a PTEQ-based receiver. All receivers need 1 DFT per DMT symbol.

Equalizer		Computational cost per DMT symbol	Memory cost
real TEQ	TEQ	NT	T
	FEQ	$4N_a$	$2N_a$
	Total	$NT + 4N_a$	$T + 2N_a$
real PGEQ (min. memory)	PGEQ	$(6T - 4)N_a$	N_gT
	FEQ	$4N_a$	$2N_a$
	Total	$6N_aT$	$N_gT + 2N_a$
real PGEQ (min. computations)	Total	$(2T + 2)N_a$	$2N_aT$
real PTEQ (min. memory)	PTEQ	$(6T - 4)N_a$	N_aT
	FEQ	$4N_a$	$2N_a$
	Total	$6N_aT$	$(T + 2)N_a$
complex PTEQ	Total	$(2T + 2)N_a$	$2N_aT$

A complete range of *adaptive BM equalizers* then opens up: from a single (real-valued or complex-valued) T-tap adaptive TEQ over an intermediate N_gT-tap adaptive PGEQ to a complex-valued N_aT-tap adaptive PTEQ. All designs have the same SOS memory cost, but a varying equalizer design cost. As explained in Section 5.2.2, the adaptive BM-TEQ and BM-PGEQ require $\mathcal{O}(N_aT^2)$ computations per update, i.e., roughly T times more than an adaptive PTEQ update. The adaptive BM-TEQ and BM-PGEQ have roughly the same complexity, as is detailed in Section 5.3.

5.3 Memory and computational cost of the adaptive BM equalizers

In this section, the overall memory cost and computational complexity of the adaptive BM equalizers are summarized. A clear distinction is made between memory and computational cost related to *equalizer "filtering"*, i.e., computing the equalizer outputs, versus *equalizer updating*, i.e. adapting the equalizer coefficients. Note that the term "filtering" is used in a loose sense here: e.g., the PTEQ is a "linear combiner", rather than a "filter".

Table 5.2 summarizes the memory cost and overall computational complexity per DMT symbol related to *equalizer filtering* with a (real-valued) TEQ, a

Table 5.3: Computational cost in real multiplications of the adaptive BM-TEQ algorithm for a real-valued and a complex-valued TEQ as well as for RLS-based and RLS/LMS-based SOS. N_a is the number of active tones and T is the number of TEQ taps.

Step	Equations	Real-valued TEQ	Complex-valued TEQ
Filtering: (5.36)-(5.37)		$6N_aT + 1$ DFT	$8N_aT + 1$ DFT
Updating:			
1	(5.38)	0	0
2	(5.39)	$6N_a$	$6N_a$
3	(5.40)	$2N_a$	$2N_a$
4	1) (5.41) $\mathbf{U}_{k,\Delta\mathbf{y}}$	$\frac{5T^2}{2} + \frac{5T}{2} - 5$	$\frac{5T^2}{2} + \frac{5T}{2} - 5$
	1) (5.41) $\mathbf{u}_{k,n}$ (RLS)	$N_a(10T + 8)$	$N_a(10T + 8)$
	1) (5.41) $\sqrt{\sigma^{-2}_{k,n,\tilde{y}}}$ (RLS/LMS)	$3N_a$	$3N_a$
	2) (5.42) $\mathbf{\Sigma}^2_{k,\Delta\mathbf{y}}$	$\sum_{n=1}^{T-1} nT - n^2$	$\sum_{n=1}^{T-1} nT - n^2$
	2) (5.42) $\mathbf{\Sigma}^2_{k,n,\mathbf{z}}$ (RLS)	$N_a(T^2 + T - 1)$	$N_a(T^2 + T - 1)$
	2) (5.42) $\check{\mathbf{\Sigma}}^2_{k,n,\mathbf{z}}$ (RLS/LMS)	$2N_a$	$2N_a$
	3) (5.43)	$N_a(4T^2-12T+4)$	$N_a(4T^2-12T+4)$
5	(5.44)	$2N_aT^2$	$4N_aT^2$
6	(5.46)-(5.47)	$N_a(10T + 4) + T$	$N_a(12T + 4) + T$
	(5.48)	$N_a(\frac{3}{2}T^2+\frac{5}{2}T+3)$	$N_a(3T^2+5T+3)$
	(5.45)	$\frac{T}{6}^3 + \frac{T}{2}^2 + \frac{T}{2}$	$\frac{2T}{3}^3 + 2T^2$
7	(5.49)	$N_a(2T + 10)$	$N_a(4T + 10)$
8	(5.50)-(5.53)	$2N_aT+18N_a+T$	$4N_aT+18N_a+2T$

(real-valued) PGEQ (for the cases of minimum memory cost as well as mimimum computational cost, see Section 5.1) and a (real-valued and complex-valued) PTEQ-based receiver. The real-valued PTEQ has been discussed in Section 4.3.6. All receivers need 1 DFT per DMT symbol. Note that, in ADSL, the number of active tones N_a is at most equal to $N/2$, so $N \geq 2N_a$. A multiplication of 2 complex-valued numbers counts as 4 real multiplications.

Remark 5.2 A DSP unit typically incorporates a multiply-accumulate unit. In DSP algorithms, the number of additions and multiplications are typically of the same order and a multiplication is often accompanied by an addition, hence an estimate of the number of multiplications also provides an estimate of the number of multiply-accumulate operations. □

The computational complexity of the adaptive BM-TEQ algorithm of Table 5.1 is summarized in **Table 5.3**. We distinguish between RLS-based and

RLS/LMS-based SOS as well as between a real-valued and a complex-valued TEQ). As in [132], the number of real multiplications is given, where a division is counted as a multiplication. Some remarks are as follows:

- In step 1, we choose to compute $\hat{\tilde{\mathbf{x}}}_k$ based on a linear combination $\mathbf{w}$ of the T sliding DFT outputs $\tilde{\mathbf{Y}}_k$, rather than the classical convolution with the TEQ (see key observations (3.62) and (3.65)), as $\tilde{\mathbf{Y}}_k$ is also needed in the update of $\mathbf{w}$ (step 6) and the regularization update (step 8).
- Symmetric or Hermitian matrices are involved in steps 4 and 6, so roughly only half of the elements of these matrices must be computed.
- The inverse of the symmetric positive definite matrix $\mathbf{Q}_k$ in step 6 can be computed via its Cholesky decomposition [52].

The complexity is dominated by the cost of steps 4 and 5, more specifically the update of the SOS estimates $\mathbf{\Sigma}^2_{k,n,\tilde{\mathbf{y}}}$ or $\check{\mathbf{\Sigma}}^2_{k,n,\tilde{\mathbf{y}}}$ and the computation of $\mathbf{Q}_k$, namely $8.5N_aT^2$ multiplications for a real-valued TEQ and $12N_aT^2$ multiplications for a complex-valued TEQ. The computational advantage of using the RLS/LMS-based SOS of (3.79) is minor: only around N_aT^2 computations are saved. The cost of the matrix inversion $\mathbf{Q}_k^{-1}$ ($\mathcal{O}(T^3)$ multiplications) in step 5 is considerably smaller than the $\mathcal{O}(N_aT^2)$ terms in steps 4 and 5 and some $\mathcal{O}(N_aT)$ terms for typical values of N_a and T.

For the adaptive BM-PGEQ algorithm, all dominant cost terms still hold true, except for the inversion of $\mathbf{Q}_k$: the inversion is computed for each of the N_g tone groups, causing a dominant cost term $\frac{N_gT^3}{6}$. Still, the $\mathcal{O}(N_aT^2)$ terms dominate the overall cost for typical values of N_a, N_g and T: e.g., for $N_a = 224$, $T = 32$ and real-valued PGEQs, it always holds that $8.5N_aT^2 > \frac{N_gT^3}{6}$, independent of N_g.

Table 5.4 compares the dominant terms in the memory cost and computational complexity of equalizer filtering and updating for the adaptive BM-TEQ, BM-PGEQ and PTEQ. Memory and complexity figure estimates (excl. DFT) are included for $N_a = 224$, $T = 16 \rightarrow 32$ and $N_g = 4$.

- The computational cost of *filtering* is roughly the same for all presented adaptive BM equalizers: $\mathcal{O}(N_aT)$ + 1 DFT.
- The adaptive BM-TEQ and BM-PGEQ have roughly the same *updating* complexity. The PTEQ updating appears to be 8 to 16 times less complex than the BM-TEQ/BM-PGEQ updating. As already pointed out in Section 5.2.2, the PTEQ has the exclusive advantage that its SOS computations are based on the transformed inputs $\mathbf{z}_{k,n}$ and equalizer taps $\mathbf{v}_n$ and that it does not require the back-transformation (5.25).

Table 5.4: Dominant terms of the memory cost and computational complexity (excl. DFT) of *equalizer filtering and updating* for the adaptive BM-TEQ, BM-PGEQ and PTEQ. Memory and complexity figure estimates for $N_a = 224$, $T = 16 \rightarrow 32$ and $N_g = 4$.

	Memory cost		Computational cost per DMT symbol	
	EQ taps (K = 10^3)	SOS coeffs ($\times 10^3$)	Filtering ($\times 10^3$)	Updating ($\times 10^3$)
real BM-TEQ				
RLS-based SOS	$T + 2N_a$	$2N_aT$	$6N_aT$	$8.5N_aT^2$
	$464 \rightarrow 480$	$7 \rightarrow 15$	$22 \rightarrow 43$	$570 \rightarrow 2100$
RLS/LMS-based SOS	$T + 2N_a$	$N_a + \frac{T^2}{2}$	$6N_aT$	$7.5N_aT^2$
	$464 \rightarrow 480$	$0.35 \rightarrow 0.50$	$22 \rightarrow 43$	$470 \rightarrow 2070$
real BM-PGEQ	$N_gT + 2N_a$	$2N_aT$	$6N_aT$	$8.5N_aT^2$
(min. memory)	$512 \rightarrow 528$	$7 \rightarrow 15$	$22 \rightarrow 43$	$570 \rightarrow 2110$
complex PTEQ				
RLS	$2N_aT$	$2N_aT$	$2N_aT$	$18N_aT$
	$7\text{K} \rightarrow 14\text{K}$	$7 \rightarrow 15$	$8 \rightarrow 15$	$68 \rightarrow 134$
RLS/LMS	$2N_aT$	$N_a + \frac{T^2}{2}$	$2N_aT$	$2N_aT$
	$7\text{K} \rightarrow 14\text{K}$	$0.35 \rightarrow 0.50$	$8 \rightarrow 15$	$9 \rightarrow 18$

- However, there is a large difference in equalizer taps memory cost: from N_aT complex-valued taps for the PTEQ, over N_gT real-valued or complex-valued taps plus N_a complex-valued FEQ taps (with typically $N_g \ll N_a$) for the BM-PGEQ (with minimum memory cost), towards only T real-valued or complex-valued TEQ taps plus N_a complex-valued FEQ taps for a single BM-TEQ.
- All adaptive BM equalizers have the same SOS memory cost for equalizer *updating*, dominated by $\mathbf{U}_{k,n}$ or $\mathbf{S}_{k,n}$ (see Section 5.2.2). The adaptive BM-TEQ stores two extra coefficients $\bar{\varepsilon}_{k,\text{a}}$ and $\bar{\varepsilon}_{k,\text{p}}$ for the adaptive regularization (see Section 5.2.3.3). The adaptive BM-PGEQ stores these elements for each tone group. This extra memory cost is negligible.

Assuming a typical number of 4000 DMT symbols per second, the RLS-based adaptive PTEQ updating requires 272×10^6 to 536×10^6 real multiplications per second (rmps), while the BM-TEQ updating requires 2280×10^6 to 8400×10^6 rmps. However, in an application such as ADSL, equalizer design and tracking can typically be done at a rate that is much lower than the equalizer filtering rate of 4 kHz: assuming that 16000 DMT training symbols are available during connection set-up while convergence occurs within 200 to 300 symbols

(see the simulations in Section 5.4), then the updating rate can be decimated by a factor 50 to 80, resulting in a complexity of 3.4×10^6 to 10.7×10^6 rmps for the PTEQ and 28.5×10^6 to 168×10^6 rmps for the BM-TEQ.

Remark 5.3 The complexity and memory figures, as given above and as included throughout the thesis, give only a rough estimate of the computational and memory cost of an actual implementation: e.g., the computational cost also involves comparisons and data transfers (memory accesses); apart from the mentioned memory cost, registers or memory are needed to store intermediate results. The exact computational and memory cost (e.g., in terms of gate logic) then also depends on implementation aspects (e.g., word lengths, the degree of parallellism and operator sharing) and the chosen platform and technology: e.g., the implementation of the BM-TEQ design could be split in a part that computes and updates the BM-TEQ at a decimated rate and a real-time part that performs the actual filtering at a 4 kHz rate. Still, the given figures suggest that the BM-TEQ and BM-PGEQ designs can form a viable alternative for the PTEQ design. □

5.4 Simulations

BM-PGEQ performance

In Section 4.4, ADSL simulations showed that the BM-TEQ approaches the performance of the PTEQ very closely, even with crosstalk noise and strong front-end filters introducing a significant amount of ISI/ICI. Moreover, the attained local minima of the non-convex BM-TEQ cost criterion corresponded to bit rates with a negligible difference.

Here, we consider even harsher conditions, where the noise also contains narrowband radio frequency interference (RFI). RFI, especially ingress from AM radio stations, can be an important interferer in ADSL [62]. There exist specific solutions to deal with RFI as explained in Section 2.2.5, e.g., based on *receiver windowing* combined with a cyclic prefix extension [113]. It was shown in [133] that receiver windowing has an equivalent, implicit implementation by means of the PTEQ: by using a sufficient number of PTEQ taps, one obtains a receiver that optimizes the equalizer *and* the window in a per tone fashion, see Section 6.3.

In this section, we investigate by simulation whether the BM-TEQ and BM-PGEQ incorporate likewise implicit RFI mitigation when using a sufficiently large number of taps. We compare their performance with the PTEQ, the PTEQ-with-TG of [130] (see Section 5.1) and the MMSE-TEQ design (see Section 3.2.1). Bit rate maximizing combined receiver windowing and equalizer design is the topic of Chapter 6.

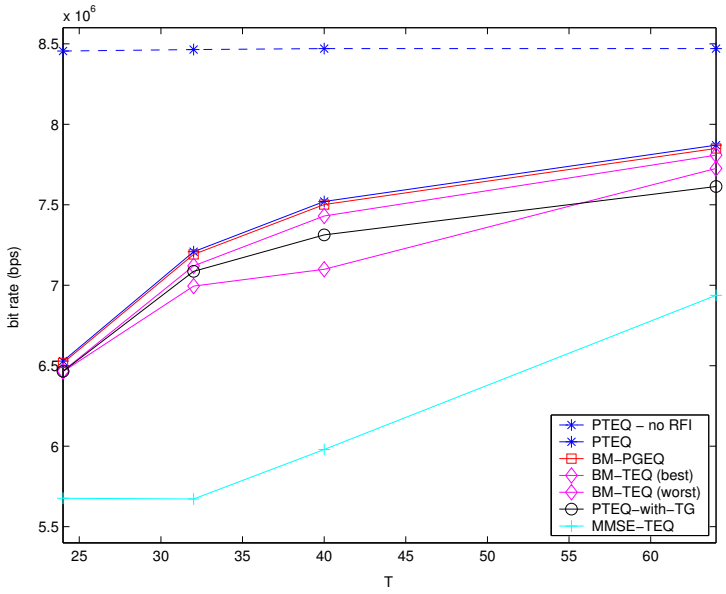


Figure 5.2: Bit rate as a function of the number of equalizer taps T for the downstream CSA #4 loop with RFI (the PTEQ performance without RFI is also depicted). The BM-PGEQ and the PTEQ-with-TG use 7 groups of 32 tones. Depicted number of taps T: 24, 32, 40 and 64.

The simulations below are done for the CSA #4 downstream loop (active tones 33 to 255) and are representative of simulations with all 8 CSA loops [5, 8]. The included front-end filters are moderate and introduce only a small amount of ISI/ICI. The synchronization delay Δ is fixed to 46 for all equalizer designs and lengths, and corresponds to the first sample index of a channel impulse response window of $\nu + 1$ samples with maximum energy. The noise includes AWGN with a power of -140 dBm/Hz, residual echo and near-end crosstalk (NEXT) coming from 24 ADSL disturbers [62]. We consider an RFI scenario with 7 RFIs, taken from [62] where we omitted the out-of-band RFIs, which fold back into the ADSL band through aliasing. The carrier frequencies are 540, 650, 680, 760, 790, 840 and 1080 kHz. The first two RFIs have a power of -30 dBm, the remaining five have -50 dBm. Because of its small bandwidth, an RFI can be considered a deterministic signal [115]; we model the narrowband RFI as a sinusoidal signal, for simplicity. We use the iterative GN-based method of Section 4.3.5 to optimize the BM-TEQ and BM-PGEQ design criteria. The BM-TEQ and BM-PGEQ design algorithms are run with 100 random starting points; the worst and best performance over these 100 runs are considered.

Figure 5.2 shows the bit rate as a function of the number of equalizer taps for the MMSE-TEQ, the BM-TEQ, the PTEQ-with-TG as well as the BM-PGEQ scheme, both with 7 groups (of 32 tones), and the PTEQ. We also include the

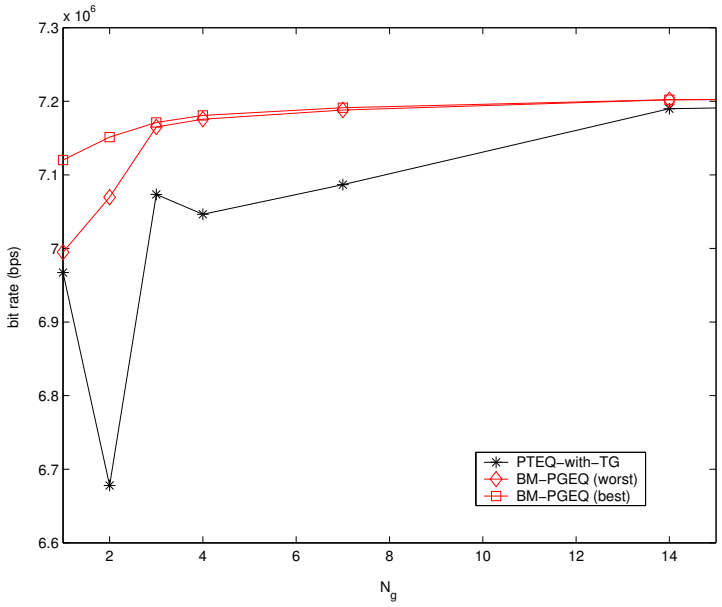


Figure 5.3: Bit rate as a function of the number of tone groups N_g for the downstream CSA #4 loop. Depicted number of groups N_g: 1, 2, 3, 4, 7 and 14.

PTEQ performance if there is no RFI present. The latter curve and simulations suggest that only a small number of taps (far less than 24) is needed to equalize the channel; the resulting bit rate without RFI is 8.47 Mbps. If RFI is present, the extra taps clearly help to mitigate the RFI: with 16 taps (not shown), the PTEQ only reaches 4.04 Mbps, whereas 64 taps per tone result in 7.87 Mbps, corresponding to a loss of less than 10 % w.r.t. the bit rate without RFI. Increasing the number of taps even more gives no significant further increase. The presence of AM RFI has indeed a dramatic impact on the achieved bit rate. It increases the performance gap between different equalization solutions, e.g., between the MMSE-TEQ, the BM-TEQ and the PTEQ. The MMSE-TEQ is clearly outperformed by the other schemes. The PTEQ-with-TG loses up to 257 kbps at 64 taps w.r.t. the PTEQ. Note that this performance would be even worse if an RFI (almost) would coincide with a group center tone, as this would destroy the equalization of a whole tone group. Due to the RFIs, the BM-TEQ is more susceptible to less performant local optima: there is a performance gap between the worst and best performing BM-TEQ of 125 kbps for 32 taps, 400 kbps for 40 taps and 85 kbps for 64 taps; without RFIs, this gap was found to be only around 6 kbps. The BM-PGEQ performance almost coincides with the PTEQ performance. It is concluded that, *similar to the PTEQ, the BM-TEQ and BM-PGEQ implicitly include receiver windowing, as their performance improves significantly by including extra taps.*

In scenarios with RFI, it is useful to use a BM-PGEQ, as this fills the performance gap between the BM-TEQ and the PTEQ. **Figure 5.3** shows the bit rate as a function of the number of tone groups N_g (with an equal number of tones and a typical 32 taps per group) for the PTEQ-with-TG and the BM-PGEQ. Note that "1 group" corresponds to the BM-TEQ whereas the (not depicted) PTEQ corresponds to the maximum number of groups (i.e., 223 groups for this downstream loop). This PTEQ performance is 7.203 Mbps, i.e., roughly equal to the depicted BM-PGEQ performance with 14 groups. The PTEQ-with-TG does not guarantee better performance for a larger number of groups: when going from 1 to 2 groups, the bit rate drops significantly with almost 300 kbps. The performance of the PTEQ-with-TG depends on the quality of the PTEQ of the center tone as an equalizer for the whole group, which is indeed unpredictable. In contrast, the bit rate of the BM-PGEQ does increase with the number of groups. Moreover, as can be seen in Figure 5.3, the susceptibility to poorly performing local optima, reduces with an increasing number of groups (i.e., with smaller groups). Apparently, different equalizers designed for smaller groups correspond to local optima that do not differ much in bit rate. Figure 5.3 suggests to use at least 3 groups. A BM-PGEQ with 3 groups performs only 50 kbps below the PTEQ; a BM-PGEQ with 7 groups further reduces the loss to only 20 kbps.

Adaptive BM equalizers

In this section, we provide extensive simulation results for the adaptive BM equalizers in various typical ADSL scenarios and parameter settings. They confirm that the adaptive BM-TEQ converges to a (locally optimal) TEQ with a similar bit rate as the iterative GN-based BM-TEQ. A similar conclusion is drawn for the adaptive BM-PGEQ, which is simulated with $N_g = 4$ equally sized tone groups. All simulations are done for $T = 32$ taps. The TEQ and PGEQ are initialized with $\mathbf{w}_0 = \begin{bmatrix} 1 & 0 & \cdots & 0 \end{bmatrix}^T$ unless stated otherwise. The regularization parameter δ_k is initialized with $\delta_0 = 10^{-5}$. The exponential weighting factor for the SOS of the BM-TEQ is increased from $\lambda = 0.9$ during the first 400 updates over $\lambda = 0.95$ during the next 400 updates to $\lambda = 0.99$ for the last 200 updates; the RLS-based and RLS/LMS-based adaptive PTEQ simulations use $\lambda = 0.998$ and $\lambda = 0.996$, respectively, which result in a sufficiently small excess MSE. When assessing the simulation results below, one should take into account that the choice of λ affects the convergence speed. We include plots for the downstream CSA #4 loop and summarize the performance for all downstream CSA #1-8 loops [5, 8] (with active tones 33 to 255) in tables. Again, moderate front-end filters to separate upstream and downstream transmission are included in the channel. The synchronization delay Δ is determined by the first sample index of a channel impulse response window of $\nu+1$ samples with maximum energy. The noise is a superposition of AWGN at -140 dBm/Hz, residual echo and near-end crosstalk from 24 ADSL disturbers. We also include simulations with the severe RFI scenario as described above.

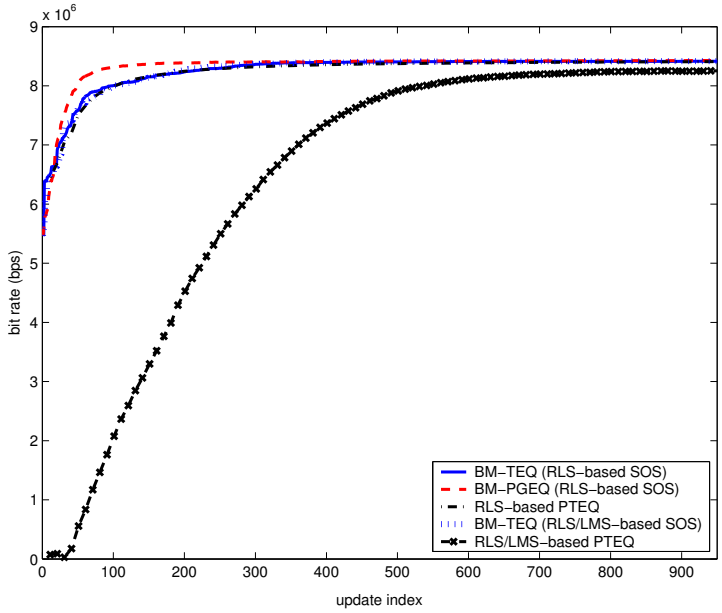


Figure 5.4: Bit rate convergence of the adaptive BM-TEQ, BM-PGEQ (4 tone groups) and PTEQ for the CSA #4 loop if no RFI is present. The BM-TEQ and PTEQ are depicted for RLS-based and RLS/LMS-based SOS. $T = 32$.

In Section 4.4, the BM-TEQ was found to approach the PTEQ performance very closely, despite possible local minima of the non-convex BM-TEQ design criterion. This result is confirmed here, when comparing the adaptive PTEQ with the adaptive BM-TEQ. **Figure 5.4** shows bit rate convergence curves as a function of the number of updates for the case *without RFI*. The RLS-based and RLS/LMS-based adaptive PTEQ are compared with the RLM-based adaptive BM-TEQ (with RLS-based and RLS/LMS-based SOS) and the BM-PGEQ (with RLS-based SOS). They all reach the same bit rate of 8.4 Mbps. The RLS-based PTEQ and BM-TEQ curves almost coincide, while the BM-PGEQ converges the fastest. The RLS/LMS-based adaptive PTEQ has the slowest convergence.

If *RFI is present*, the convergence of all methods is slower, see **Figure 5.5**. The adaptive BM-TEQ achieves 6.87 Mbps, which is only 300 kbps (or 4 %) below the adaptive PTEQ bit rate; the adaptive BM-PGEQ fills the gap in convergence speed and bit rate between the adaptive PTEQ and the BM-TEQ. Note that the RLS/LMS-based adaptive PTEQ is too slow in RFI scenarios and so is not shown here. As shown on the same Figure 5.5, the convergence time can be decreased by initializing the RLM algorithm with a cheaply computed suboptimal TEQ (e.g., an MMSE-TEQ, see the thick dotted line; $\delta_0 = 10^{-8}$).

We have shown in Figure 5.3 that the BM-PGEQ is less susceptible to poorly

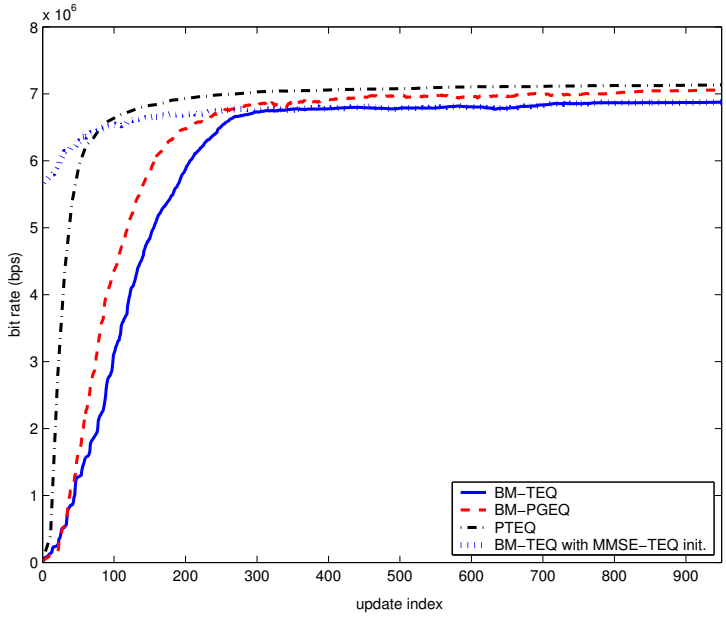


Figure 5.5: Bit rate convergence of the adaptive BM-TEQ, BM-PGEQ (4 tone groups) and PTEQ for the CSA #4 loop if RFI is present. $T = 32$. The thick dotted line shows the adaptive BM-TEQ, initialized with an MMSE-TEQ.

performing *local optima* than the BM-TEQ, especially if RFI is present. We have run 25 different initializations $\mathbf{w}_0$ to check this property for the adaptive algorithms. **Figure 5.6** shows convergence plots for the initializations with worst and best performance after 1000 updates. Also here, it is clear that the adaptive BM-PGEQ is less susceptible to poorly performing local optima than the adaptive BM-TEQ: while the two BM-PGEQ curves almost coincide (around 7.06 Mbps), the adaptive BM-TEQ reaches a local optimum between 6.52 and 7.00 Mbps.

As suggested in [60], the seamless rate adaptation functionality of ADSL2 and ADSL2+ allows to adapt the bit rate to new channel conditions, e.g., when one or more RFIs are switched off. **Figure 5.7** shows the tracking capability of the adaptive BM-TEQ and BM-PGEQ (with $\lambda = 0.9$), when the first two RFIs are switched off at time instant 1500. Both algorithms track the change, but the adaptive BM-PGEQ is faster than the adaptive BM-TEQ.

Table 5.5 and **Table 5.6** illustrate the performance for the other CSA loops. **Table 5.5** gives the number of updates, for the case *without RFI*, to reach 98.5 % of the optimal BM-TEQ, BM-PGEQ and PTEQ bit rate for the adaptive BM-TEQ, the adaptive BM-PGEQ and the adaptive PTEQ, respectively. The adaptive BM-TEQ performance appears independent of the choice of RLS-based or RLS/LMS-based SOS. The adaptive BM-PGEQ only requires around

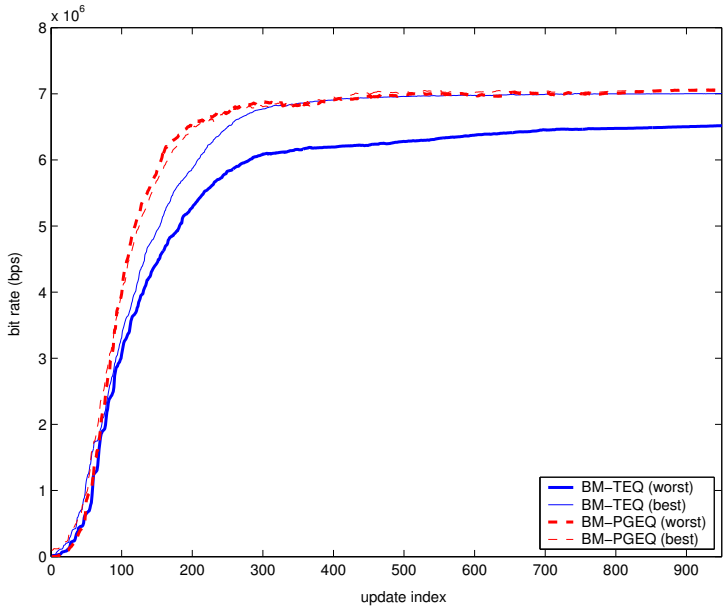


Figure 5.6: Bitrate convergence of the adaptive BM-TEQ and BM-PGEQ (4 tone groups) for different initializations if RFI is present. The best and worse performing initializations are depicted. CSA #4 loop. $T = 32$.

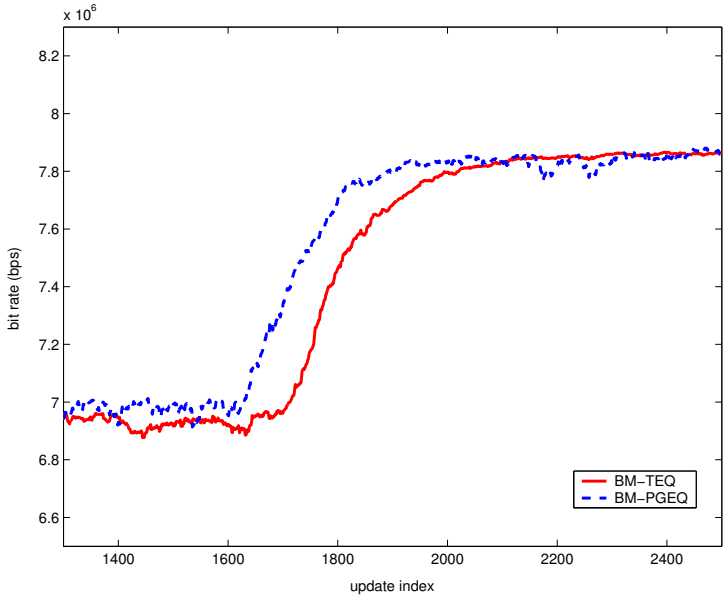


Figure 5.7: Tracking performance of the adaptive BM-TEQ and BM-PGEQ (4 tone groups). CSA #4 loop. $T = 32$. $\lambda = 0.9$. Tracking of the disappearance of 2 RFIs at time instant 1500.

Table 5.5: Convergence of the adaptive BM-TEQ (with RLS-based and RLS/LMS-based SOS), BM-PGEQ (4 tone groups, RLS-based SOS) and PTEQ (RLS and RLS/LMS) for the CSA #1-8 loops if *no RFI* is present. Number of updates to reach 98.5 % of the optimal BM-TEQ, BM-PGEQ and PTEQ rate.

	#updates to reach 98.5 % of bit rate					optimal bit rate (Mbps)		
loop	BM-TEQ		BM-PGEQ	PTEQ		BM-TEQ	BM-PGEQ	PTEQ
	RLS-based	RLS/LMS-based	RLS-based	RLS	RLS/LMS			
1	128	121	105	349	1025	9.039	9.079	9.133
2	228	306	94	333	1028	9.233	9.258	9.338
3	182	171	124	388	1054	8.292	8.303	8.364
4	235	210	89	382	908	8.414	8.419	8.475
5	99	113	85	339	1066	9.286	9.300	9.356
6	176	188	108	387	1009	8.043	8.039	8.101
7	93	104	100	406	1055	7.422	7.422	7.486
8	139	143	114	436	1158	7.332	7.337	7.394

100 updates. **Table 5.6** gives the number of updates, for the case *with RFI*, to reach 95 % and 98.5 % of the optimal BM-TEQ, BM-PGEQ and PTEQ bit rate for the adaptive BM-TEQ, the adaptive BM-PGEQ and the adaptive PTEQ, respectively. All adaptive algorithms use RLS-based SOS now. The adaptive BM-PGEQ performance is more uniform than the adaptive BM-TEQ performance: for all loops, the 95 % threshold is reached after 250-300 updates; the 98.5 % threshold requires 400-500 updates. Note that for loop 8, this particular run of the adaptive BM-TEQ reaches a rate of 6.64 Mbps, due to a local optimum, which is below the 98.5 % threshold. The convergence speed of the adaptive BM-PGEQ and PTEQ are comparable.

5.5 Conclusions

In this chapter, we have shown how the BM-TEQ design can be used in a BM-PGEQ scheme. The BM-PGEQ allows for a trade-off between memory cost and performance, while keeping computational complexity during data transmission roughly at the same level. Through simulation, we have illustrated that the BM-PGEQ outperforms an earlier presented tone grouping scheme where the whole tone group was assigned the PTEQ of the group center tone. The BM-PGEQ with as few as 4 tone groups is a useful intermediate between the BM-TEQ and the PTEQ: especially in harsh environments with RFI, the BM-

Table 5.6: Convergence of the adaptive BM-TEQ, BM-PGEQ (4 tone groups) and PTEQ for the CSA #1-8 loops if *RFI* is present. Number of updates to reach 95 % and 98.5 % of the optimal BM-TEQ, BM-PGEQ and PTEQ rate.

	#updates to reach 95 % and 98.5 % of bit rate						optimal bit rate (Mbps)		
loop	BM-TEQ		BM-PGEQ		PTEQ		BM-TEQ	BM-PGEQ	PTEQ
	95%	98.5%	95%	98.5%	95%	98.5%			
1	261	315	277	496	128	435	7.915	8.128	8.183
2	277	417	290	492	123	429	8.335	8.403	8.460
3	466	756	226	412	134	488	7.634	7.670	7.716
4	260	703	255	681	157	467	6.945	7.100	7.208
5	255	321	229	409	139	467	7.964	8.102	8.200
6	424	660	225	424	147	488	7.390	7.427	7.495
7	270	325	223	498	146	499	6.582	6.628	6.719
8	591	-	254	512	144	533	6.771	6.793	6.850

PGEQ is less susceptible than a BM-TEQ to poorly performing local optima.

Then, we have shown that the BM-TEQ and BM-PGEQ, despite their non-linear cost criterion, can be designed adaptively, based on a recursive Levenberg-Marquardt algorithm, which was derived from the IR-SNLLS-based BM-TEQ design criterion. This *adaptive BM-TEQ and BM-PGEQ* make use of exactly the same second-order statistics as the RLS-based adaptive PTEQ of Section 3.4.2. A *complete range of adaptive bit rate maximizing (BM) equalizers* then opens up, *offering full flexibility* to trade off computational and memory cost: from the computationally efficient RLS-based adaptive PTEQ with a large number of equalizer taps, over the adaptive BM-PGEQ, towards a single adaptive BM-TEQ with a larger equalizer update complexity.

Through extensive simulations with several ADSL scenarios and parameter settings, the adaptive BM-TEQ is shown to exhibit fast convergence, comparable to the adaptive PTEQ. Moreover, the adaptive BM-PGEQ closely approaches the performance of the adaptive PTEQ in harsh environments with RFI. In these environments, the adaptive BM-TEQ turns out to be more susceptible to local optima, which can result in a performance loss of a few 100 kbps. Similar to the PTEQ, the BM-TEQ and BM-PGEQ appear to implicitly incorporate RX windowing if a sufficient number of taps is used.

Besides providing an equalizer design algorithm, adaptive BM equalizers allow to track variations of the transmission channel and noise characteristics. This makes them a good candidate for integration with the seamless rate adaptation functionality of ADSL2 and ADSL2+ modems.

Chapter 6

Bit rate maximizing window and time-domain equalizer design

RADIO frequency interference (RFI) is an important issue in DMT transmission, as described in Section 1.3.1. The large transmission bandwidth of ADSL, ADSL2, ADSL2+ and VDSL results in spectral overlap with radio communications. Especially AM broadcasters and HAM radio cause RFI ingress [39].

Ideal MC modulation is particularly robust against RFI: the tone orthogonality ensures that the narrowband RFI only affects a single tone. However, the overlapping sinc-shaped tone spectra render DMT modulation less robust against RFI ingress: due to the high sidelobes of the sinc-shaped spectrum, there will be spectral leakage of the RFI to many other tones. An RFI can even cause a complete breakdown of the DMT-based system [39].

Until now, we have mainly focused on the problem of equalization in DMT-based systems. In this chapter, we consider the more general case where equalization is combined with receiver windowing to mitigate both channel dispersion and narrowband RFI ingress. In the literature, two approaches to RFI mitigation in DMT transmission can be distinguished.

1. *Window-only design.* In this case, equalization and receiver windowing are tackled separately. Provided that the length of the SIR $\mathbf{c}$ is limited to $\nu - \mu + 1$ samples, receiver windowing [113] can reduce the effect of external noise such as RFI by improving the spectral containment of

the DFT basis functions, while preserving the tone orthogonality of the DMT signal. Therefore, a windowing and folding operation is applied to the equalized RX sample vector, as was explained in Section 2.2.5. In [68, 99], enhanced *fixed* or *adaptive* window designs are discussed, but without considering the equalization problem. The presented algorithms are suboptimal in the sense that the resulting window does not necessarily optimize the bit rate.

2. *Window incorporated PTEQ design.* Here, an equalizer is designed and implemented for each tone separately in the presence of a *fixed* window [34, 89, 133] or an *adaptive* window [133] to optimize the bit rate. The PTEQ with adaptive window has already been discussed in the simulations of Section 5.4: by using a sufficiently large number of equalizer taps per tone, i.e., $T + \mu$, the PTEQ inherently combines an equalizer and window that is optimized for each tone. This comes at the expense of a large memory cost to store all the equalizer coefficients.

In this chapter, we consider *the design of a combined window and time-domain equalizer (WinTEQ).* The result is referred to as a bit rate maximizing combined window and TEQ (BM-WinTEQ). As the equalizer and window are designed jointly, the above mentioned restriction of a SIR $\mathbf{c}$ with length $\nu - \mu$ instead of ν vanishes. Compared to the above mentioned window incorporated PTEQ designs, the BM-WinTEQ has a significantly smaller memory cost.

After elaborating the data model in Section 6.1, the BM-WinTEQ design criterion is derived in Section 6.2. The BM-WinTEQ design criterion is formulated as an extension to the original BM-TEQ design criterion of Section 4.2, as well as to the IR-SNLLS-based BM-TEQ design criterion of Section 4.3.4. By considering special cases of the BM-WinTEQ design criterion, see Section 6.3, one obtains a BM-TEQ with fixed window (BM-FWinTEQ), a per-group combined window and equalizer scheme, a windowing-only design, a PTEQ design, etc. Section 6.4 gives complexity figures for several of these cases. The IR-SNLLS-based BM-WinTEQ design criterion then allows to give guidelines for an iterative and an adaptive design algorithm in Section 6.5, which are similar to the iterative GN algorithm of Section 4.3.5 and the RLM algorithm of Section 5.2. Section 6.6 illustrates the performance of the BM-WinTEQ and BM-FWinTEQ designs and compares them to classical window designs.

Figure 6.1 clarifies the place of each section in this chapter in the schematic thesis overview of Figure 1.5. Part of the work, presented in this chapter, has been done in collaboration with Geert Ysebaert and was also reported on in [156], be it that we add a number of results here.

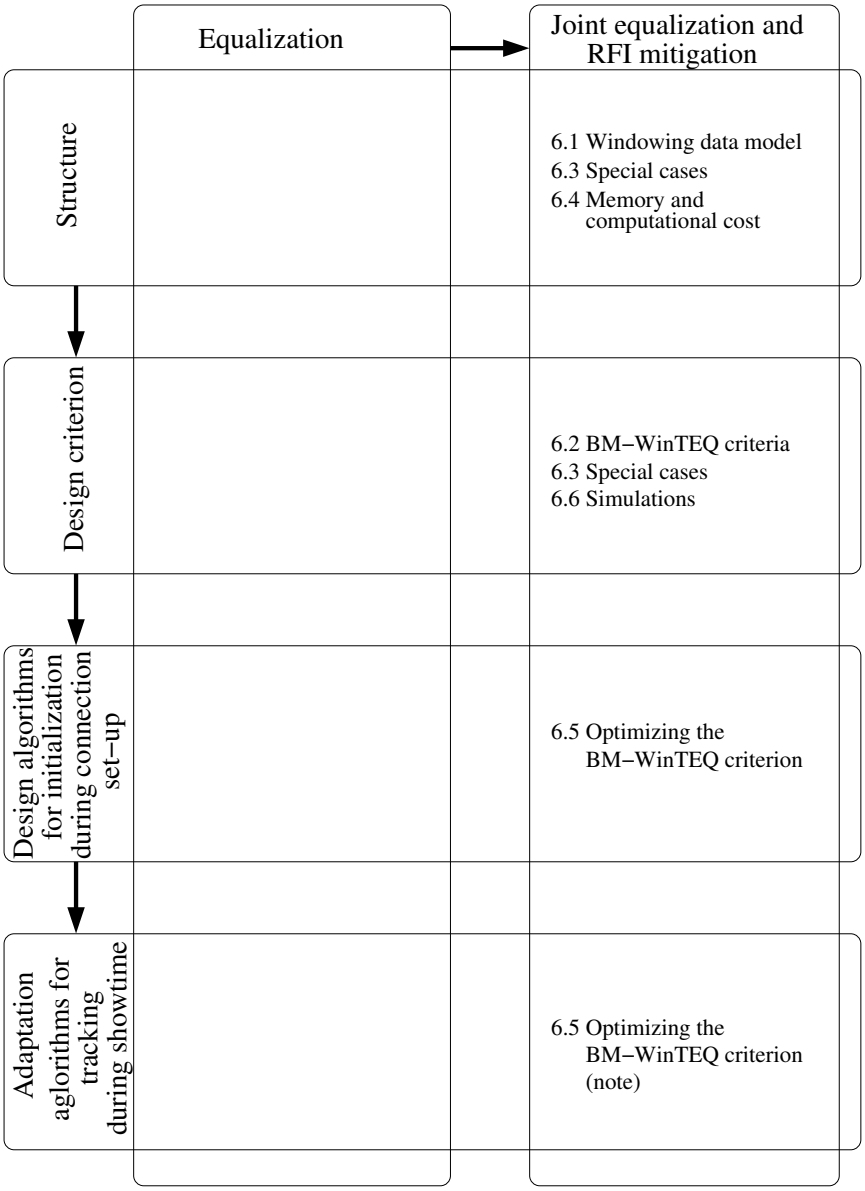


Figure 6.1: Schematic overview of this chapter.

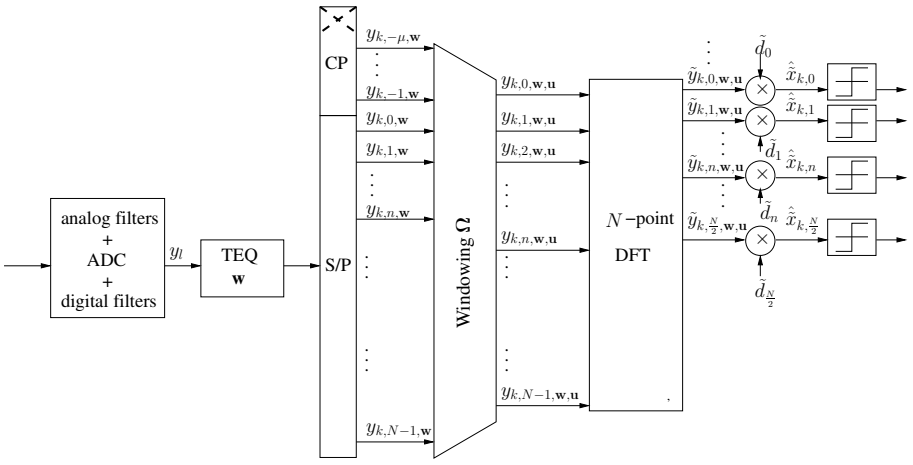


Figure 6.2: A DMT receiver with TEQ filtering followed by receiver windowing.

6.1 Data model

Figure 6.2 shows a DMT receiver, which includes TEQ filtering and receiver windowing. Note that the TEQ filtering operates at the sample rate, while the windowing operations are performed at the symbol rate, rendering windowing much cheaper than TEQ filtering.

The data model and notation for receiver windowing have been presented in Section 2.3.1 and are briefly repeated here for convenience. The windowing and folding operation results in the k-th $N \times 1$ equalized and windowed sample vector

$$\mathbf{y}_{k,\mathbf{w},\mathbf{u}} = \mathbf{y}_{k,0:N-1,\mathbf{w},\mathbf{u}} = \begin{bmatrix} \mathbf{y}_{k,0:N-\mu-1,\mathbf{w}} \\ \mathbf{u} \odot \mathbf{y}_{k,-\mu:-1,\mathbf{w}} + \check{\mathbf{u}} \odot \mathbf{y}_{k,N-\mu:N-1,\mathbf{w}} \end{bmatrix} \tag{6.1}$$

where $\mathbf{y}_{k,-\mu:N-1,\mathbf{w}} = \mathbf{Y}_k \mathbf{w}$ is the $(N+\mu)\times 1$ vector at the output of the TEQ, $\mathbf{u}$ is the window taper of length μ and $\check{\mathbf{u}}$ is symmetric with $\mathbf{u}$, i.e., $\check{\mathbf{u}} = \mathbf{1}_\mu - \mathbf{u}$ with $\mathbf{1}_\mu$ a $\mu \times 1$ all-one vector. Alternatively, the windowing and folding operation can be written as the multiplication of $\mathbf{y}_{k,-\mu:N-1,\mathbf{w}}$ with the $N\times(N+\mu)$-matrix $\mathbf{\Omega}$:

$$\mathbf{\Omega} = \begin{bmatrix} \mathbf{0}_{(N-\mu)\times\mu} & \mathbf{I}_{N-\mu} & \mathbf{0}_{(N-\mu)\times\mu} \\ \mathrm{diag}(\mathbf{u}) & \mathbf{0}_{\mu\times(N-\mu)} & \mathrm{diag}(\check{\mathbf{u}}) \end{bmatrix} \tag{6.2}$$

$$= \underbrace{\begin{bmatrix} \mathbf{0} & \mathbf{I}_{N-\mu} & \mathbf{0} \\ \mathbf{0} & \mathbf{0} & \mathbf{I}_\mu \end{bmatrix}}_{\mathbf{\Omega}_1} + \underbrace{\begin{bmatrix} \mathbf{0} & \mathbf{0} & \mathbf{0} \\ \mathrm{diag}(\mathbf{u}) & \mathbf{0} & -\mathrm{diag}(\mathbf{u}) \end{bmatrix}}_{\mathbf{\Omega}_2} \tag{6.3}$$

The vector $\mathbf{y}_{k,\mathbf{w},\mathbf{u}}$ is then fed to the DFT to obtain:

$$\tilde{\mathbf{y}}_{k,N,\mathbf{w},\mathbf{u}} = \mathcal{F}_N \mathbf{\Omega} \mathbf{Y}_k \mathbf{w} \text{ and } \tilde{y}_{k,n,\mathbf{w},\mathbf{u}} = \tilde{\mathbf{y}}_{k,N,\mathbf{w},\mathbf{u}}[n] = \mathcal{F}_n \mathbf{\Omega} \mathbf{Y}_k \mathbf{w} \tag{6.4}$$

The dependence of the DFT output (6.4) on the TEQ coefficients $\mathbf{w}$ and the window taper $\mathbf{u}$ can be expressed in several alternative ways, which will appear useful later. The n-th DFT output can be modified into:

$$\begin{aligned} \tilde{y}_{k,n,\mathbf{w},\mathbf{u}} &= \mathcal{F}_n(\mathbf{\Omega}_1 + \mathbf{\Omega}_2)\mathbf{Y}_k \mathbf{w} && (6.5) \\ &= \tilde{\mathbf{y}}_{k,n}\mathbf{w} + \tilde{\mathbf{u}}_n^T \Delta \mathbf{Y}_k \mathbf{w} && (6.6) \end{aligned}$$

where $\tilde{\mathbf{y}}_{k,n}$ is the n-th sliding DFT output (3.62) (size $1 \times T$) and where $\mathbf{u}_n$ denotes a vector of frequency modulated windowing coefficients, i.e.,

$$\tilde{\mathbf{u}}_n^T = \mathcal{F}_{n,N-\mu:N-1}\text{diag}(\mathbf{u}) = \mathbf{u}^T \text{diag}(\mathcal{F}_{n,N-\mu:N-1}) \tag{6.7}$$

Note that (6.6), together with (6.7), can be interpreted as an *extended version* of the first key observation (3.62). The $\mu \times T$ matrix $\Delta \mathbf{Y}_k$ is Toeplitz and given by

$$\begin{aligned} \Delta \mathbf{Y}_k &= \left[\begin{array}{c|c|c} \mathbf{I}_\mu & \mathbf{0}_{\mu \times (N-\mu)} & -\mathbf{I}_\mu \end{array} \right] \mathbf{Y}_k && (6.8) \\ &= \begin{bmatrix} \Delta y_{k,-\mu} & \cdots & \Delta y_{k,-\mu-T+1} \\ \vdots & \ddots & \vdots \\ \Delta y_{k,-1} & \cdots & \Delta y_{k,-T} \end{bmatrix} && (6.9) \end{aligned}$$

It can be constructed based on the following vector $\Delta \mathbf{y}_k$ of $\mu + T - 1$ difference terms (instead of $T-1$ in the previous chapters):

$$\Delta \mathbf{y}_k = \begin{bmatrix} \Delta y_{k,-\mu-T+1} & \cdots & \Delta y_{k,-1} \end{bmatrix}^T \tag{6.10}$$

Note that the vector of common inputs to the PTEQ in Section 3.4 is a sub-vector of (6.10) as it only contains the last $T-1$ difference terms. The second term in (6.6) can be written as

$$\tilde{\mathbf{u}}_n^T \Delta \mathbf{Y}_k \mathbf{w} = \Delta \mathbf{y}_k^T \mathbf{\Omega}_n \mathbf{w} = \underbrace{\Delta \mathbf{y}_k^T \mathbf{W}_n}_{\Delta \tilde{\mathbf{y}}_{k,n,\mathbf{w}}^T} \mathbf{u} \tag{6.11}$$

Here $\mathbf{\Omega}_n$ and $\mathbf{W}_n$ are tone-dependent matrices of size $(\mu + T - 1) \times T$ and $(\mu + T - 1) \times \mu$, respectively:

$$\mathbf{\Omega}_n = \begin{bmatrix} \mathbf{0} & & \begin{bmatrix} \tilde{\mathbf{u}}_n^T \end{bmatrix} \\ & \begin{bmatrix} \tilde{\mathbf{u}}_n^T \end{bmatrix} & \\ \iddots & \iddots & \\ \begin{bmatrix} \tilde{\mathbf{u}}_n^T \end{bmatrix} & & \mathbf{0} \end{bmatrix}^T \tag{6.12}$$

$$\mathbf{W}_n = \begin{bmatrix} [\ \bar{\mathbf{w}}\ ] & & \mathbf{0} \\ & \ddots & \\ \mathbf{0} & & [\ \bar{\mathbf{w}}\ ] \end{bmatrix}^T \operatorname{diag}(\mathcal{F}_{n,N-\mu:N-1}) \quad (6.13)$$

where $\bar{\mathbf{w}}$ contains the TEQ coefficients in reverse order.

6.2 Bit rate maximizing combined window and TEQ design

Based on the data model and notation of the previous section, we first develop a BM-WinTEQ design criterion in $\mathbf{w}$ and $\mathbf{u}$ along the lines of the original BM-TEQ design criterion (4.32) in Section 4.2. Then, we use this result to arrive at an IR-SNLLS-based BM-WinTEQ design criterion.

6.2.1 First BM-WinTEQ design criterion

Along the lines of the derivation of the original BM-TEQ design criterion (4.32), we show below how to obtain a similar BM-WinTEQ design criterion. Our starting point is again the exact SNR model at the FEQ output, SNR_n in (4.23), with the optimal choice of uMMSE FEQs $\tilde{d}_n^{\mathrm{uMMSE}}$ (4.21):

$$\mathrm{SNR}_n = \frac{\sigma_{n,\tilde{x}}^2}{\mathcal{E}\left\{\left|\tilde{d}_n^{\mathrm{uMMSE}}\tilde{y}_{k,n,\mathbf{w},\mathbf{u}} - \tilde{x}_{k,n}\right|^2\right\}} \quad (6.14)$$

$$\tilde{d}_n^{\mathrm{uMMSE}} = \frac{\sigma_{n,\tilde{x}}^2}{\mathcal{E}\left\{\tilde{x}_{k,n}^* \tilde{y}_{k,n,\mathbf{w},\mathbf{u}}\right\}} \quad (6.15)$$

Combining (6.14) and (6.15) gives the same compact expression (4.28) for SNR_n as obtained in Section 4.2.3:

$$\mathrm{SNR}_n = \frac{1}{\rho_{n,\mathbf{w},\mathbf{u}}^{-2} - 1} = \frac{\rho_{n,\mathbf{w},\mathbf{u}}^2}{1 - \rho_{n,\mathbf{w},\mathbf{u}}^2} \quad (6.16)$$

where the squared normalized correlation function $\rho_{n,\mathbf{w},\mathbf{u}}^2$ of the n-th DFT output $\tilde{y}_{k,n,\mathbf{w},\mathbf{u}}$ and the n-th TX symbol $\tilde{x}_{k,n}$ now also depends on the window taper $\mathbf{u}$, i.e.,

$$\rho_{n,\mathbf{w},\mathbf{u}}^2 = \frac{\left|\mathcal{E}\left\{\tilde{x}_{k,n}^* \tilde{y}_{k,n,\mathbf{w},\mathbf{u}}\right\}\right|^2}{\mathcal{E}\left\{|\tilde{x}_{k,n}|^2\right\}\mathcal{E}\left\{|\tilde{y}_{k,n,\mathbf{w},\mathbf{u}}|^2\right\}} \quad (6.17)$$

We then define the following SOS:

$$\begin{aligned} \sigma^2_{n,\tilde{x}} &= \mathcal{E}\left\{|\tilde{x}_{k,n}|^2\right\}, & \boldsymbol{\sigma}_{n,\tilde{x}\Delta\mathbf{y}} &= \mathcal{E}\left\{\tilde{x}^*_{k,n}\Delta\mathbf{y}^T_k\right\} \\ \boldsymbol{\sigma}_{n,\tilde{x}\tilde{\mathbf{y}}} &= \mathcal{E}\left\{\tilde{x}^*_{k,n}\tilde{\mathbf{y}}_{k,n}\right\}, & \boldsymbol{\Sigma}_{n,\tilde{\mathbf{y}}\Delta\mathbf{y}} &= \mathcal{E}\left\{\tilde{\mathbf{y}}^H_k\Delta\mathbf{y}^T_k\right\} \\ \boldsymbol{\Sigma}^2_{n,\tilde{\mathbf{y}}} &= \mathcal{E}\left\{\tilde{\mathbf{y}}^H_{k,n}\tilde{\mathbf{y}}_{k,n}\right\}, & \boldsymbol{\Sigma}^2_{\Delta\mathbf{y}} &= \mathcal{E}\left\{\Delta\mathbf{y}_k\Delta\mathbf{y}^T_k\right\} \end{aligned} \tag{6.18}$$

where only $\boldsymbol{\Sigma}^2_{\Delta\mathbf{y}}$ is tone-independent. Note that the three SOS in the left column correspond to those required for the BM-TEQ design criterion (4.32); the SOS in the right column are new**.** With these definitions, $\rho^2_{n,\mathbf{w},\mathbf{u}}$ in (6.17) and $\tilde{d}^{\text{uMMSE}}_n$ in (6.15) can be expressed as a function of SOS on the one hand and $\mathbf{w}$ and $\mathbf{u}$ on the other hand. When combining (6.6), (6.11), (6.15), (6.17) and (6.18), one obtains:

$$\tilde{d}^{\text{uMMSE}}_n = \frac{\sigma^2_{n,\tilde{x}}}{\left(\boldsymbol{\sigma}_{n,\tilde{x}\tilde{\mathbf{y}}} + \boldsymbol{\sigma}_{n,\tilde{x}\Delta\mathbf{y}}\boldsymbol{\Omega}_n\right)\mathbf{w}} \tag{6.19}$$

$$\rho^2_{n,\mathbf{w},\mathbf{u}} = \frac{\left|\overbrace{\left(\boldsymbol{\sigma}_{n,\tilde{x}\tilde{\mathbf{y}}} + \boldsymbol{\sigma}_{n,\tilde{x}\Delta\mathbf{y}}\boldsymbol{\Omega}_n\right)\mathbf{w}}^{\boldsymbol{\sigma}_{n,\tilde{x}\tilde{\mathbf{y}},\mathbf{u}}}\right|^2}{\sigma^2_{n,\tilde{x}}\left(\mathbf{w}^T\underbrace{\left(\boldsymbol{\Sigma}^2_{n,\tilde{\mathbf{y}}} + \boldsymbol{\Sigma}_{n,\tilde{\mathbf{y}}\Delta\mathbf{y}}\boldsymbol{\Omega}_n + \boldsymbol{\Omega}^H_n\boldsymbol{\Sigma}^H_{n,\tilde{\mathbf{y}}\Delta\mathbf{y}} + \boldsymbol{\Omega}^H_n\boldsymbol{\Sigma}^2_{\Delta\mathbf{y}}\boldsymbol{\Omega}_n\right)}_{\boldsymbol{\Sigma}^2_{n,\tilde{\mathbf{y}},\mathbf{u}}}\mathbf{w}\right)} \tag{6.20}$$

The correlation function $\rho^2_{n,\mathbf{w},\mathbf{u}}$ (6.20) looks very similar to $\rho^2_{n,\mathbf{w}}$ (4.29), be it with modified SOS, $\boldsymbol{\sigma}_{n,\tilde{x}\tilde{\mathbf{y}},\mathbf{u}}$ and $\boldsymbol{\Sigma}^2_{n,\tilde{\mathbf{y}},\mathbf{u}}$, which depend on the window taper $\mathbf{u}$ (via the matrix $\boldsymbol{\Omega}_n$). Combining (6.16) and (6.20) with the DMT bit rate expression (3.42), we obtain the following **BM-WinTEQ design criterion**:

$$\boxed{\min_{\mathbf{w},\mathbf{u}} \sum_{n\in\mathcal{S}_a} \log\left(\frac{\mathbf{w}^T\mathbf{B}_n(\mathbf{u})\mathbf{w}}{\mathbf{w}^T\mathbf{A}_n(\mathbf{u})\mathbf{w}}\right)} \tag{6.21}$$

i.e., where $\mathbf{B}_n$ and $\mathbf{A}_n$ now depend on the windowing taper $\mathbf{u}$ and are given by:

$$\mathbf{A}_n(\mathbf{u}) = \Gamma_n\sigma^2_{n,\tilde{x}}\boldsymbol{\Sigma}^2_{n,\tilde{\mathbf{y}},\mathbf{u}} + (1-\Gamma_n)\boldsymbol{\sigma}^H_{n,\tilde{x}\tilde{\mathbf{y}},\mathbf{u}}\boldsymbol{\sigma}_{n,\tilde{x}\tilde{\mathbf{y}},\mathbf{u}} \tag{6.22}$$

$$\mathbf{B}_n(\mathbf{u}) = \Gamma_n\left(\sigma^2_{n,\tilde{x}}\boldsymbol{\Sigma}^2_{n,\tilde{\mathbf{y}},\mathbf{u}} - \boldsymbol{\sigma}^H_{n,\tilde{x}\tilde{\mathbf{y}},\mathbf{u}}\boldsymbol{\sigma}_{n,\tilde{x}\tilde{\mathbf{y}},\mathbf{u}}\right) \tag{6.23}$$

The BM-WinTEQ design criterion (6.21) is an unconstrained, non-linear cost criterion, which calls for non-linear optimization techniques. The guidelines for optimizing the BM-TEQ design criterion (4.32) (see Section 4.2.5) then also apply for optimizing (6.21).

In the next section, an alternative IR-SNLLS-based formulation of the BM-WinTEQ design criterion is derived. Similar to the IR-SNLLS-based BM-TEQ design criterion, this alternative BM-WinTEQ design criterion allows for an *iterative*, fast-converging GN-based algorithm that is driven by the FEQ output errors and which requires the SOS (6.18), see Section 6.5.

6.2.2 IR-SNLLS-based BM-WinTEQ design criterion

The bit rate maximizing combined window and TEQ design is the solution to the following constrained non-linear optimization problem in the joint parameter vector $\boldsymbol{\theta} = \begin{bmatrix} \mathbf{w}^H & \mathbf{u}^H & \tilde{\mathbf{d}}^H \end{bmatrix}^H$:

$$\max_{\boldsymbol{\theta}} \sum_{n \in \mathcal{S}_a} \log_2 \left(1 + \frac{\mathrm{SNR}_n}{\Gamma_n} \right) \tag{6.24}$$

$$\text{with } \mathrm{SNR}_n = \frac{\sigma^2_{n,\tilde{x}}}{\mathcal{E}\left\{ \left| \tilde{e}^{\mathrm{uMMSE}}_{k,n} \right|^2 \right\}} = \frac{\sigma^2_{n,\tilde{x}}}{\mathcal{E}\left\{ \left| \tilde{d}^{\mathrm{uMMSE}}_n \left(\tilde{\mathbf{y}}_{k,n}\mathbf{w} + \tilde{\mathbf{u}}_n^T \Delta \mathbf{Y}_k \mathbf{w} \right) - \tilde{x}_{k,n} \right|^2 \right\}} \tag{6.25}$$

$$\text{subject to real } \mathbf{w} \text{ and } \mathbf{u} \text{ and } \tilde{d}^{\mathrm{uMMSE}}_n = \frac{\sigma^2_{n,\tilde{x}}}{\left(\boldsymbol{\sigma}_{n,\tilde{x}\tilde{\mathbf{y}}} + \boldsymbol{\sigma}_{n,\tilde{x}\Delta\mathbf{y}} \boldsymbol{\Omega}_n \right) \mathbf{w}}, \ \forall n \in \mathcal{S}_a \tag{6.26}$$

i.e., maximizing the bit rate (6.24), hence the number of bits per DMT symbol (given a certain SNR gap Γ_n, see Section 2.1.3), over the joint parameters $\boldsymbol{\theta}$, subject to the use of uMMSE FEQs (6.26) (see also (6.15)), which render the SNR model in (6.25) exact. This optimization problem (6.24-6.26) is equivalent to minimizing the original BM-WinTEQ design criterion (6.21). Along the lines of the derivation in Appendix 4.A, it can be shown that the original (stochastic) BM-WinTEQ criterion (6.21) is equivalent to the following (deterministic) **iteratively reweighted (IR) SNLLS-based bit rate maximizing BM-WinTEQ design criterion**:

$$\boxed{\min_{\boldsymbol{\theta}} \frac{1}{K} \sum_{k=1}^{K} \left\| \mathrm{diag}\left(\sqrt{\boldsymbol{\gamma}_{K,\{\mathbf{w},\mathbf{u}\}_{\mathrm{prev}}}} \right) \underbrace{\left(\mathrm{diag}(\tilde{\mathbf{d}}) \left(\tilde{\mathbf{Y}}_k \mathbf{w} + \tilde{\mathbf{U}}^T \Delta \mathbf{Y}_k \mathbf{w} \right) - \tilde{\mathbf{x}}_k \right)}_{\tilde{\mathbf{e}}_k} \right\|^2} \tag{6.27}$$

where $\tilde{\mathbf{U}}$ is a $\mu \times N_a$ matrix which collects the frequency modulated window tapers $\tilde{\mathbf{u}}_n$, $n \in \mathcal{S}_a$, see (6.7), as its columns. For $K \to \infty$ and under the assumption of wide-sense stationarity, the iterative sequence of (deterministic) LS criteria (6.27) is equivalent to the original (stochastic) BM-WinTEQ criterion (6.21). The criterion (6.27) is clearly an extended version of the IR-SNLLS-based BM-TEQ design criterion (4.72) where the FEQ output error vector $\tilde{\mathbf{e}}_k$

contains an extra (second) term and where the weights in the $N_a \times 1$ weight vector $\boldsymbol{\gamma}_{K,\{\mathbf{w},\mathbf{u}\}_{\text{prev}}}$ are still given by:

$$\gamma_{K,n,\mathbf{w},\mathbf{u}} = \frac{(\text{SNR}_{K,n}+1)^2}{\sigma^2_{K,n,\tilde{x}}\,(\text{SNR}_{K,n}+\Gamma_n)} \tag{6.28}$$

be it that $\text{SNR}_{K,n}$ is now obtained as a deterministic estimate of (6.16), hence $\text{SNR}_{K,n}$ depends on both $\mathbf{w}$ and $\mathbf{u}$ via $\rho^2_{K,n,\mathbf{w},\mathbf{u}}$, see (6.20).

Remark 6.1 The LS criterion (6.27) is non-linear in the joint parameter vector $\boldsymbol{\theta}$, but separable in the three parameter subsets $\mathbf{w}$, $\mathbf{u}$ and $\tilde{\mathbf{d}}$. The separability property in $\mathbf{u}$ follows from the following equality for the second term in $\tilde{\mathbf{e}}_k$:

$$\tilde{\mathbf{U}}^T \Delta\mathbf{Y}_k \mathbf{w} = \Delta\tilde{\mathbf{Y}}^T_{k,\mathbf{w}} \mathbf{u} \tag{6.29}$$

where the $\mu \times N_a$ matrix $\Delta\tilde{\mathbf{Y}}_{k,\mathbf{w}}$ collects in its columns the filtered and frequency modulated difference terms $\Delta\tilde{\mathbf{y}}_{k,n,\mathbf{w}} = \mathbf{W}_n^T \Delta\mathbf{y}_k$, $n \in \mathcal{S}_a$, defined in (6.11). It holds true for (6.27), as for (4.72), that optimizing (6.27) as a linear LS problem in $\tilde{\mathbf{d}}$, obtained by keeping $\mathbf{w}$ and $\mathbf{u}$ in (6.27) fixed, results again in an LS estimate of the bMMSE FEQs $\tilde{d}_n^{\text{bMMSE}}$ for the given $\mathbf{w}$ and $\mathbf{u}$, which are now given by:

$$\tilde{d}_n^{\text{bMMSE}} = \frac{\mathcal{E}\left\{\tilde{x}_{k,n}\tilde{y}^*_{k,n,\mathbf{w},\mathbf{u}}\right\}}{\mathcal{E}\left\{|\tilde{y}_{k,n,\mathbf{w},\mathbf{u}}|^2\right\}} = \frac{\mathbf{w}^T \boldsymbol{\sigma}^H_{n,\tilde{x}\tilde{\mathbf{y}},\mathbf{u}}}{\mathbf{w}^T \boldsymbol{\Sigma}^2_{n,\tilde{\mathbf{y}},\mathbf{u}} \mathbf{w}} \tag{6.30}$$

with $\boldsymbol{\sigma}_{n,\tilde{x}\tilde{\mathbf{y}},\mathbf{u}}$ and $\boldsymbol{\Sigma}^2_{n,\tilde{\mathbf{y}},\mathbf{u}}$ defined in (6.20). □

6.3 Special cases

The IR-SNLLS-based BM-WinTEQ design criterion provides a general framework that allows to derive several special cases of interest. In the following subsections, we consider the per-group combined window and equalizer design (PGWinEQ), the per-tone combined window and equalizer design, the windowing-only design and the equalizer design with fixed window (FWinTEQ).

6.3.1 Bit rate maximizing per-group combined window and equalizer design (BM-PGWinEQ)

In (6.27), all active tones are taken into account for the computation of a single TEQ and a single window. As already shown in Chapter 5 for the BM-PGEQ

case, bit rate improvements are possible by dividing the active tones into N_g groups. Each tone group is then assigned a separate equalizer $\mathbf{w}_g$ and window taper $\mathbf{u}_g$, hence the term *bit rate maximizing per-group combined window and equalizer (BM-PGWinEQ)*. The design criterion for tone group g is given by:

$$\min_{\boldsymbol{\theta}_g} \frac{1}{K} \sum_{k=1}^{K} \left\| \text{diag}\left(\sqrt{\gamma_{K,\{\mathbf{w}_g,\mathbf{u}_g\}_{\text{prev}}}}\right) \left(\text{diag}(\tilde{\mathbf{d}}_g) \left(\tilde{\mathbf{Y}}_{k,g}\mathbf{w}_g + \Delta\tilde{\mathbf{Y}}^T_{k,g,\mathbf{w}_g}\mathbf{u}_g \right) - \tilde{\mathbf{x}}_{k,g} \right) \right\|^2 \tag{6.31}$$

where $\boldsymbol{\theta}_g = \begin{bmatrix} \mathbf{w}_g^H & \mathbf{u}_g^H & \tilde{\mathbf{d}}_g^H \end{bmatrix}^H$ and where the subscripts g in $\tilde{\mathbf{d}}_g$, $\tilde{\mathbf{Y}}_{k,g}$, $\Delta\tilde{\mathbf{Y}}_{k,g,\mathbf{w}_g}$ and $\tilde{\mathbf{x}}_{k,g}$ denote that only the tones in the group are considered.

6.3.2 Per-tone combined window and equalizer design (PTEQ)

A special case of the per-group approach occurs when a complex-valued equalizer and window are designed for each individual tone. Optimizing (6.31) for a single tone n is equivalent to optimizing the following cost criterion over the complex-valued PTEQ $\mathbf{w}_n$, per-tone window taper $\mathbf{u}_n$ and FEQ $\tilde{d}_n$:

$$\min_{\mathbf{w}_n,\mathbf{u}_n,\tilde{d}_n} \frac{1}{K} \sum_{k=1}^{K} \left| \tilde{d}_n \underbrace{\left(\tilde{\mathbf{y}}_{k,n}\mathbf{w}_n + \Delta\tilde{\mathbf{y}}_k\mathbf{W}_n\mathbf{u}_n \right)}_{\tilde{y}_{k,n,\mathbf{w},\mathbf{u}}} - \tilde{x}_{k,n} \right|^2 \tag{6.32}$$

We will show that the solution for this problem effectively corresponds to a deterministic estimate of the MMSE-PTEQ $\mathbf{v}_n$ in (3.70), see Section 3.4, with $\mu + T$ rather than T taps. In other words, *the windowing operation can be incorporated in the PTEQ operation by increasing the number of PTEQ taps from T to $\mu + T$*. This result has been presented previously in [133] and it has been confirmed by the simulations presented in Section 5.4.

We have shown in Section 3.4.1, based on the second key observation (3.65), that the n-th sliding DFT output $\tilde{\mathbf{y}}_{k,n}$ (which has size $1 \times T$) can be computed efficiently from one DFT output $\tilde{y}_{k,n}$ and $T-1$ difference terms Δy_k, $k = -T+1, \ldots, -1$. These difference terms form a subset containing the last $T-1$ entries of $\Delta\mathbf{y}_k$ in (6.10). Hence, $\tilde{y}_{k,n,\mathbf{w},\mathbf{u}}$ in (6.32) can be re-written, based on (3.65), as:

$$\tilde{y}_{k,n,\mathbf{w},\mathbf{u}} = \begin{bmatrix} \Delta\mathbf{y}_k^T & \tilde{y}_{k,n} \end{bmatrix} \begin{bmatrix} \mathbf{0}_{\mu\times T} \\ \mathbf{T}_n \end{bmatrix} \mathbf{w}_n + \Delta\mathbf{y}_k^T\mathbf{W}_n\mathbf{u}_n \tag{6.33}$$

By replacing the joint windowing and TEQ operation $\mathbf{W}_n\mathbf{u}$ with one tone-dependent $(T+\mu-1)\times 1$ vector of unknowns, it is found that the second term in (6.33) comprises a linear combination per tone $\mathbf{v}_n$ of the $T+\mu-1$ difference terms $\Delta\mathbf{y}_k$. Hence, the overall DFT output (6.33) can be written in general as a linear combination of the DFT output on tone n, $\tilde{y}_{k,n}$, and the $\mu+T-1$

real-valued difference terms $\Delta\mathbf{y}_k$. Absorbing the FEQ $\tilde{d}_n$ into the set of $T+\mu$ PTEQ coefficients $\mathbf{v}_n$, (6.32) is then equivalent to the following PTEQ design criterion:

$$\boxed{\min_{\mathbf{v}_n} \mathcal{E}\left\{\left|\underbrace{\begin{bmatrix}\Delta\mathbf{y}_k^T & \tilde{y}_{k,n}\end{bmatrix}}_{\mathbf{z}_{k,n}}\mathbf{v}_n - \tilde{x}_{k,n}\right|^2\right\}} \tag{6.34}$$

This criterion looks like the original PTEQ criterion (3.69), be it that $\mathbf{v}_n$ now has $\mu+T$ taps instead of T taps and incorporates in this way a per-tone window. As already shown in the simulations of Section 5.4, the PTEQ consistently leads to improved performance. However, the associated memory cost amounts to $N_a(T+\mu)$ complex-valued taps, compared to $T+\mu$ coefficients for a single window and TEQ. Moreover, the computational cost of the PTEQ is $\mathcal{O}(N_a(T+\mu))$, while the receiver windowing cost is negligible in the case of a single TEQ and window (see also Section 6.4).

The RLS-based PTEQ algorithm of Section 3.4.2 is directly applicable for adaptively solving (6.34). The adaptive algorithm requires to store and update the $(T+\mu-1)\times(T+\mu-1)$ common tone-independent triangular part $\mathbf{S}_\Delta$ of the inverse transpose Cholesky factor $\mathbf{S}_n$ of $\mathbf{\Sigma}^2_{n,\mathbf{z}} = \mathcal{E}\{\mathbf{z}^H_{k,n}\mathbf{z}_{k,n}\}$, as well as the tone-dependent last rows $\mathbf{s}_n$ of $\mathbf{S}_n$ with length $T+\mu$.

Remark 6.2 As explained in Section 4.3.6, the solution $\mathbf{v}_n$ of (6.34) corresponds to a biased MMSE equalizer. By cascading the PTEQ $\mathbf{v}_n$ with a complex scalar, corresponding to an unbiased MMSE FEQ $\tilde{d}_n^{\text{uMMSE}}$ (6.15), an unbiased MMSE PTEQ is obtained. □

6.3.3 Bit rate maximizing window-only design (BM-Win)

It is obvious that the case $\mu = 0$ removes the receiver windowing and leads to the BM-TEQ design, which was studied extensively in Chapter 4 and 5. Likewise, the case $T = 1$ reduces the TEQ to a scalar (which can be set to 1), hence it gives rise to a DMT receiver that only incorporates receiver windowing. The question is then how to design a *bit rate maximizing window* (BM-Win).

To make the mathematical derivation as simple as possible, we assume in this section that the CIR $\mathbf{h}$ has a length of $\nu-\mu+1$ samples or less. This is, e.g., the case in an asynchronous Zipper VDSL system [86, 109, 110, 111]. Alternatively, a SIR $\mathbf{c}$ of the same length could be considered. The results are easily extended to the case where the channel is not perfectly shortened.

Referring to (6.5) with $T = 1$, the DFT output for tone n after windowing can be written as:

$$\tilde{y}_{k,n,\mathbf{u}} \quad = \quad \mathcal{F}_n(\mathbf{\Omega}_1 + \mathbf{\Omega}_2)\mathbf{y}_{k,-\mu:N-1} \tag{6.35}$$

$$= \tilde{y}_{k,n} + \underbrace{\mathbf{u}^T \mathrm{diag}(\mathcal{F}_{n,N-\mu:N-1})}_{\tilde{\mathbf{u}}_n^T} \Delta\mathbf{y}_k \tag{6.36}$$

where $\Delta\mathbf{y}_k = \begin{bmatrix} \Delta y_{k,-\mu} & \cdots & \Delta y_{k,-1} \end{bmatrix}^T$ has length μ now. Hence, the windowed DFT output for tone n, $\tilde{y}_{k,n,\mathbf{u}}$, is the sum of the corresponding unwindowed DFT output plus a correction based on a linear combination $\tilde{\mathbf{u}}_n$ of difference terms $\Delta\mathbf{y}_k$; $\tilde{\mathbf{u}}_n$ are the frequency modulated window coefficients (6.7). Because we assume a CIR $\mathbf{h}$ that is not longer than $\nu - \mu + 1$ samples (and assuming appropriate synchronization), $\Delta\mathbf{y}_k$ is only determined by external noise, hence the window only acts on the external noise without destroying the DMT signal orthogonality.

Remark 6.3 Since $\Delta\mathbf{y}_k$ only contains external noise information, which is uncorrelated with the TX symbols $\tilde{x}_{k,n}$, i.e., $\mathcal{E}\{\tilde{x}_{k,n}^* \Delta\mathbf{y}_k\} = 0$, it follows from (6.36) that the uMMSE FEQ (6.15) is independent of the window $\mathbf{u}$ and equals the uMMSE FEQ of the unwindowed case, i.e.,

$$\tilde{d}_n^{\mathrm{uMMSE}} = \frac{\mathcal{E}\left\{|\tilde{x}_{k,n}|^2\right\}}{\mathcal{E}\left\{\tilde{x}_{k,n}^* \tilde{y}_{k,n}\right\}} \tag{6.37}$$

□

Using (6.36) to modify (6.27), the following IR-SNLLS-based BM-Win design criterion is obtained:

$$\min_{\mathbf{u},\tilde{\mathbf{d}}} \frac{1}{K} \sum_{k=1}^{K} \left\| \mathrm{diag}\left(\sqrt{\boldsymbol{\gamma}_{K,\mathbf{u}_{\mathrm{prev}}}}\right) \left(\mathrm{diag}(\tilde{\mathbf{d}}) \left(\tilde{\mathbf{y}}_k + \Delta\tilde{\mathbf{Y}}_k^T \mathbf{u} \right) - \tilde{\mathbf{x}}_k \right) \right\|^2 \tag{6.38}$$

where the $\mu \times N_a$ matrix $\Delta\tilde{\mathbf{Y}}_k$ collects the vectors $\mathrm{diag}(\mathcal{F}_{n,N-\mu:N-1})\Delta\mathbf{y}_k$, $n \in \mathcal{S}_a$, in its columns. As noted before, (6.38) delivers an LS estimate of the *bMMSE* FEQs $\tilde{\mathbf{d}}^{\mathrm{bMMSE}}$. Using the same trick as in Section 5.2.1, (6.38) can be modified into:

$$\boxed{\min_{\mathbf{u}} \frac{1}{K} \sum_{k=1}^{K} \left\| \mathrm{diag}\left(\sqrt{\tilde{\boldsymbol{\gamma}}_{K,\mathbf{u}_{\mathrm{prev}}}}\right) \left(\mathrm{diag}(\tilde{\mathbf{d}}) \left(\tilde{\mathbf{y}}_k + \Delta\tilde{\mathbf{Y}}_k^T \mathbf{u} \right) - \boldsymbol{\rho}_{K,\mathbf{u}_{\mathrm{prev}}}^{-2} \odot \tilde{\mathbf{x}}_k \right) \right\|^2} \tag{6.39}$$

so that the solution for $\tilde{\mathbf{d}}$ immediately provides an LS estimate of the *uMMSE* FEQs (6.37). As these uMMSE FEQs are independent of the window taper $\mathbf{u}$, they can be computed beforehand. Hence, (6.39) is an **iteratively reweighted linear LS-based BM-Win design criterion** that only depends on $\mathbf{u}$. It can be optimized by alternately computing the window taper $\mathbf{u}$ as the LS

solution to (6.39) and updating the weights $\check{\boldsymbol{\gamma}}_{K,\mathbf{u}_{\text{prev}}}$. As the LS criterion in each iteration is linear, hence *convex*, and as the iterative weights are bounded and non-increasing in the (absolute value) of the LS errors [18], this algorithm converges to a globally optimum window.

The entries of the weight vector $\check{\boldsymbol{\gamma}}_{K,\mathbf{u}_{\text{prev}}}$ are given by:

$$\check{\gamma}_{K,n,\mathbf{u}_{\text{prev}}} = \frac{\text{SNR}_{K,n}^2}{\sigma_{K,n,\tilde{x}}^2 \left(\text{SNR}_{K,n} + \Gamma_n\right)} \tag{6.40}$$

$$\text{SNR}_{K,n} = \frac{1}{\rho_{K,n,\mathbf{u}}^{-2} - 1} \tag{6.41}$$

$$\rho_{K,n,\mathbf{u}}^2 = \frac{\left|\sigma_{K,n,\tilde{x}\tilde{y}}\right|^2}{\sigma_{K,n,\tilde{x}}^2 \sigma_{K,n,\tilde{y},\mathbf{u}}^2} \tag{6.42}$$

As $\mathcal{E}\{\tilde{x}_{k,n}^* \Delta\mathbf{y}_k\} = 0$, the numerator of $\rho_{K,n,\mathbf{u}}^2$ is determined by $\sigma_{K,n,\tilde{x}\tilde{y}} = \frac{1}{K}\sum_{k=1}^{K} \tilde{x}_{k,n}^* \tilde{y}_{k,n}$. In the denominator of $\rho_{K,n,\mathbf{u}}^2$, $\sigma_{K,n,\tilde{y},\mathbf{u}}^2$ is given by:

$$\begin{aligned}\sigma_{K,n,\tilde{y},\mathbf{u}}^2 &= \frac{1}{K}\sum_{k=1}^{K} \left|\tilde{y}_{k,n,\mathbf{u}}\right|^2 \\ &= \sigma_{K,n,\tilde{y}}^2 + 2\Re\{\boldsymbol{\sigma}_{K,n,\tilde{y}\Delta\mathbf{y}} \text{diag}(\mathcal{F}_{n,N-\mu:N-1})\mathbf{u}\} \\ &\quad + \mathbf{u}^T \text{diag}(\mathcal{F}_{n,N-\mu:N-1}^*) \boldsymbol{\Sigma}_{K,\Delta\mathbf{y}}^2 \text{diag}(\mathcal{F}_{n,N-\mu:N-1})\mathbf{u}\end{aligned} \tag{6.43}$$

with $\sigma_{K,n,\tilde{y}}^2 = \frac{1}{K}\sum_{k=1}^{K} \left|\tilde{y}_{k,n}\right|^2$, $\boldsymbol{\sigma}_{K,n,\tilde{y}\Delta\mathbf{y}} = \frac{1}{K}\sum_{k=1}^{K} \tilde{y}_{k,n}^* \Delta\mathbf{y}_k^T$ and $\boldsymbol{\Sigma}_{K,\Delta\mathbf{y}}^2 = \frac{1}{K}\sum_{k=1}^{K} \Delta\mathbf{y}_k \Delta\mathbf{y}_k^T$.

Remark 6.4 In [99], an alternative window design criterion has been formulated, based on a sum of squared DFT output errors, i.e.,

$$\min_{\mathbf{u}} \frac{1}{K}\sum_{k=1}^{K} \left\| \left(\left(\tilde{\mathbf{y}}_k + \Delta\tilde{\mathbf{Y}}_k^T \mathbf{u} \right) - \text{diag}(\tilde{\mathbf{d}})^{-1} \tilde{\mathbf{x}}_k \right) \right\|^2 \tag{6.44}$$

This design criterion has no direct relation with bit rate optimization and, as will be shown in the simulations of Section 6.6, results in suboptimal performance. □

Remark 6.5 Similar to the BM-PGWinEQ design, one can perform *bit rate maximizing per group windowing (BM-PGWin)*, where (6.39) is now used to design a μ-tap window taper for each tone group. When a window is designed for each tone separately, one again ends up with an MMSE PTEQ design:

$$\min_{\mathbf{v}_n} \frac{1}{K}\sum_{k=1}^{K} \left| \underbrace{\tilde{d}_n \begin{bmatrix} \tilde{\mathbf{u}}_n^T & 1 \end{bmatrix}}_{\mathbf{v}_n^T} \begin{bmatrix} \Delta\mathbf{y}_k \\ \tilde{y}_{k,n} \end{bmatrix} - \tilde{x}_{k,n} \right|^2 \tag{6.45}$$

The resulting cost criterion (6.45) looks the same as (6.34), be it that $\mathbf{v}_n$ in (6.45) has length $\mu + 1$ and linearly combines the DFT output $\tilde{y}_{k,n}$ and the μ difference terms Δy_k, $k = -\mu, \ldots, -1$. □

6.3.4 Bit rate maximizing TEQ design with fixed window (BM-FWinTEQ)

In the literature, special attention has been given to PTEQ design in the presence of a *fixed window* [34, 89], such as a raised-cosine (Hann) window with

$$\mathbf{u}[l] = \frac{1}{2}\left(1 - \cos\frac{\pi(l+1)}{\mu+1}\right), \, l = 0, \ldots, \mu - 1 \tag{6.46}$$

or a trapezoidal (Bartlett) window with

$$\mathbf{u}[l] = \frac{l+1}{\mu+1}, \, l = 0, \ldots, \mu - 1 \tag{6.47}$$

The BM-WinTEQ design criterion (6.27) can also be solved for the case of a fixed window, simply by optimizing (6.27) for $\mathbf{w}$ and $\tilde{\mathbf{d}}$ while keeping the window taper $\mathbf{u}$ fixed to a particular window design.

AM broadcasters and HAM amateur radios are the main cause of RFI in DSL. HAM radios can be especially harmful to VDSL, as they tend to regularly switch on and off [39]. AM broadcasters, on the other hand, which are the main cause of RFI in ADSL, are much more stationary. While a (non-fixed) window that is optimized for a specific RFI scenario typically outperforms a fixed window, a *fixed* window can be especially useful in frequency bands with HAM radios, as it adds robustness to the receiver. An optimized (non-fixed) window may suffer from a large performance loss if an RFI appears after the window design (see simulations in Section 6.6).

6.4 Memory and computational cost

In this section, figures of the computational and memory cost (during data transmission) for several of the above described combined window and equalizer design strategies are presented in **Table 6.1** and **Table 6.2**, respectively. Note that the PTEQ is assumed to be complex-valued, whereas the WinTEQ and the PGWinEQ are considered to be real-valued. As discussed in the previous chapters for the equalizer-only case, the computation of the equalizer output and the storage of the equalizer taps can be done in several ways. The figures presented here correspond to the lowest memory cost and (for typical values of N_a, μ and T) corresponding lowest computational cost.

Table 6.1: Computational cost (number of real multiplications per DMT symbol) of different combined window and equalizer designs.

Design	Step	Computational cost
WinTEQ	TEQ	$(N+\mu)T$
	windowing	2μ
	FEQ	$4N_a$
PGWinEQ with 1 (fixed) window	recursion (5.3)	$4N_a(T-1)$
	$\tilde{\mathbf{Y}}_k\mathbf{w}_g$	$2N_aT$
	$\tilde{\mathbf{u}}_n$	$2\mu N_a$
	$\Delta\mathbf{Y}_k\mathbf{w}_g$	μTN_g
	$\tilde{\mathbf{u}}_n^T\Delta\mathbf{Y}_k\mathbf{w}_g$	$2\mu N_a$
	FEQ	$4N_a$
PGWinEQ with window per group		idem
PTEQ (incl. per-tone window)	PTEQ	$2N_a(T+\mu+1)$

Table 6.2: Memory cost (number of real coefficients) of different combined window and equalizer designs.

Design	Memory cost
WinTEQ	$T+\mu+2N_a$
PGWinEQ (1 window)	$N_gT+\mu+2N_a$
PGWinEQ (window per group)	$N_g(T+\mu)+2N_a$
PTEQ (incl. per-tone window)	$2N_a(T+\mu)$

Table 6.3: Numerical example of the computational and memory cost of different combined window and equalizer designs with $N_a = 218$, $N_g = 4$, $T = 16$ and $\mu = 10$.

Design	Memory cost	Computational cost
WinTEQ	462	9244
PGWinEQ (1 window)	510	30288
PGWinEQ (window per group)	540	30288
PTEQ (incl. per-tone window)	11772	11336

For the WinTEQ, TEQ filtering is applied first, followed by a windowed DFT. The output of the PGWinEQ is obtained, based on (6.6). For the first term in (6.6), which corresponds to a PGEQ output, the sliding DFT output is computed, based on the recursion (5.3).

Example 6.1 As a numerical example of the computational and memory cost for the different combined window and equalizer designs, we consider a downstream scenario with $T = 16$ equalizer taps, $\mu = 10$ windowing coefficients and $N_a = 218$ active tones. For the BM-PGWinEQ design, $N_g = 4$ groups are considered. The resulting computational and memory cost are given in **Table 6.3**. △

Based on Table 6.3, the following conclusions can be drawn:

- Since μ is typically much smaller than N, the extra computational and memory cost of adding a single window on top of a single TEQ is almost negligible.
- The memory cost of the PTEQ is much higher than the memory required for a TEQ. The difference becomes even larger if the PTEQ implicitly incorporates per-tone windows: the complexity figures correspond to those of an ordinary PTEQ with an increased number of taps per tone, $T + \mu$.
- The computational cost for a PGWinEQ is larger than the cost for a PTEQ. A PGWinEQ can also be used with a single window for all tone groups. This reduces the memory cost, but it follows from (6.6) that it has the same computational cost as a PGWinEQ with a window per tone group.

6.5 Guidelines for optimizing the BM-WinTEQ design criterion

The BM-WinTEQ can be designed iteratively or adaptively with algorithms that are closely related to the iterative GN-based algorithm of Section 4.3.5 or

the RLM algorithm of Section 5.2, respectively, which optimize the IR-SNLLS-based BM-TEQ design criterion. In this section, we give guidelines on how to extend the iterative GN-based algorithm of Section 4.3.5 for optimizing the IR-SNLLS-based BM-WinTEQ design criterion (6.27). These guidelines can then also be used to develop an adaptive design algorithm.

An iterative algorithm to optimize the BM-WinTEQ design criterion consists of the following three steps per iteration:

1. Computation of the weights, $\boldsymbol{\gamma}_{K,\{\mathbf{w},\mathbf{u}\}_{\text{prev}}}$, based on (6.28), evaluated in the window and TEQ estimates $\mathbf{u}_{\text{prev}} = \mathbf{u}_{i-1}$ and $\mathbf{w}_{\text{prev}} = \mathbf{w}_{i-1}$ of the previous iteration.

2. Computation of an LS estimate of the bMMSE FEQs $\tilde{\mathbf{d}}_i^{\text{bMMSE}}$ (6.30), which are the solution of (6.27) for $\mathbf{u} = \mathbf{u}_{i-1}$ and $\mathbf{w} = \mathbf{w}_{i-1}$:

$$\tilde{d}_{n,i}^{\text{bMMSE}} = \frac{\mathbf{w}_{i-1}^T \boldsymbol{\sigma}_{K,n,\tilde{x}\tilde{\mathbf{y}},\mathbf{u}}^H}{\mathbf{w}_{i-1}^T \boldsymbol{\Sigma}_{K,n,\tilde{\mathbf{y}},\mathbf{u}}^2 \mathbf{w}_{i-1}} \tag{6.48}$$

3. Computation of new estimates $\mathbf{u}_i$ and $\mathbf{w}_i$. As suggested in Section 4.3.5, fast convergence is obtained based on a GN update:

$$\boldsymbol{\theta}_i \leftarrow \boldsymbol{\theta}_{i-1} - \alpha_i \mathbf{R}_{\boldsymbol{\theta}_{i-1}}^{-1} \mathbf{g}_{\boldsymbol{\theta}_{i-1}} \tag{6.49}$$

where $\boldsymbol{\theta}_{i-1} = \begin{bmatrix} \mathbf{w}_{i-1}^H & \mathbf{u}_{i-1}^H & \left(\tilde{\mathbf{d}}_i^{\text{bMMSE}}\right)^H \end{bmatrix}^H$, where $\mathbf{g}_{\boldsymbol{\theta}_{i-1}}$ and $\mathbf{R}_{\boldsymbol{\theta}_{i-1}}$ are the gradient and a positive-definite Hessian approximation of the IR-SNLLS-based BM-WinTEQ design criterion (6.27), evaluated in $\boldsymbol{\theta}_{i-1}$, and where α_i is a step size, obtained through a line search algorithm [16].

Further elaborating on the GN update, the gradient $\mathbf{g}_{\boldsymbol{\theta}}$ and Hessian $\mathbf{R}_{\boldsymbol{\theta}}$ in (6.49) for a *complex-valued* TEQ and window taper are given by:

$$\mathbf{g}_{\boldsymbol{\theta}} = \begin{bmatrix} \mathbf{g}_{1,\boldsymbol{\theta}} \\ \mathbf{g}_{2,\boldsymbol{\theta}} \\ \mathbf{g}_{3,\boldsymbol{\theta}} \end{bmatrix} = \frac{1}{K} \sum_{k=1}^{K} \check{\mathbf{Y}}_{k,\boldsymbol{\theta}}^H \text{diag}\left(\boldsymbol{\gamma}_{K,\{\mathbf{w},\mathbf{u}\}_{\text{prev}}}\right) \tilde{\mathbf{e}}_k \tag{6.50}$$

$$\mathbf{R}_{\boldsymbol{\theta}} = \frac{1}{K} \sum_{k=1}^{K} \check{\mathbf{Y}}_{k,\boldsymbol{\theta}}^H \text{diag}\left(\boldsymbol{\gamma}_{K,\{\mathbf{w},\mathbf{u}\}_{\text{prev}}}\right) \check{\mathbf{Y}}_{k,\boldsymbol{\theta}} \tag{6.51}$$

where

$$\check{\mathbf{Y}}_{k,\boldsymbol{\theta}} = \left[\begin{array}{c|c|c} \text{diag}\left(\tilde{\mathbf{d}}\right) \tilde{\mathbf{Y}}_k & \text{diag}\left(\tilde{\mathbf{d}}\right) \Delta\tilde{\mathbf{Y}}_{k,\mathbf{w}}^T & \text{diag}(\tilde{\mathbf{Y}}_k \mathbf{w}) \end{array} \right] \tag{6.52}$$

and where $\mathbf{g}_{1,\boldsymbol{\theta}}$, $\mathbf{g}_{2,\boldsymbol{\theta}}$ and $\mathbf{g}_{3,\boldsymbol{\theta}}$ are $T \times 1$, $\mu \times 1$ and $N_a \times 1$ subvectors of $\mathbf{g}_{\boldsymbol{\theta}}$, respectively. Based on (6.51), we define, as in Section 4.3.5, the following

block-based description for the approximate Hessian:

$$\mathbf{R}_{\boldsymbol{\theta}} = \begin{bmatrix} \mathbf{E} & \mathbf{F} \\ \mathbf{F}^H & \mathbf{G} \end{bmatrix} \tag{6.53}$$

The $N_a \times N_a$ submatrix $\mathbf{G}$ is again diagonal with elements

$$g_n = \frac{1}{K} \sum_{k=1}^{K} \gamma_{K,n,\{\mathbf{w},\mathbf{u}\}_{\text{prev}}} \left| \tilde{y}_{k,n,\mathbf{w},\mathbf{u}} \right|^2 = \gamma_{K,n,\{\mathbf{w},\mathbf{u}\}_{\text{prev}}} \left(\mathbf{w}^H \boldsymbol{\Sigma}^2_{K,n,\tilde{\mathbf{y}},\mathbf{u}} \mathbf{w} \right) \tag{6.54}$$

where $\boldsymbol{\Sigma}^2_{K,n,\tilde{\mathbf{y}},\mathbf{u}}$ is a deterministic estimate of $\boldsymbol{\Sigma}^2_{n,\tilde{\mathbf{y}},\tilde{\mathbf{u}}}$, defined in (6.20). The submatrix $\mathbf{E}$ has now size $(T+\mu) \times (T+\mu)$ instead of $T \times T$ and $\mathbf{F}$ has size $(T+\mu) \times N_a$ instead of $T \times N_a$. Based on the SOS defined in (6.18), $\mathbf{E}$ can be written as

$$\mathbf{E} = \begin{bmatrix} \mathbf{E}_{11} & \mathbf{E}_{12} \\ \mathbf{E}_{12}^H & \mathbf{E}_{22} \end{bmatrix} \tag{6.55}$$

with

$$\mathbf{E}_{11} = \sum_{n \in \mathcal{S}_a} \gamma_{K,n,\{\mathbf{w},\mathbf{u}\}_{\text{prev}}} \left| \tilde{d}_n \right|^2 \boldsymbol{\Sigma}^2_{K,n,\tilde{\mathbf{y}},\mathbf{u}} \tag{6.56}$$

$$\mathbf{E}_{12} = \sum_{n \in \mathcal{S}_a} \gamma_{K,n,\{\mathbf{w},\mathbf{u}\}_{\text{prev}}} \left| \tilde{d}_n \right|^2 \underbrace{\left(\boldsymbol{\Sigma}_{K,n,\tilde{\mathbf{y}}\Delta\mathbf{y}} \mathbf{W}_n + \boldsymbol{\Omega}_n^H \boldsymbol{\Sigma}^2_{K,\Delta\mathbf{y}} \mathbf{W}_n \right)}_{\mathbf{E}_{12,n}} \tag{6.57}$$

$$\mathbf{E}_{22} = \sum_{n \in \mathcal{S}_a} \gamma_{K,n,\{\mathbf{w},\mathbf{u}\}_{\text{prev}}} \left| \tilde{d}_n \right|^2 \mathbf{W}_n^H \boldsymbol{\Sigma}^2_{K,\Delta\mathbf{y}} \mathbf{W}_n \tag{6.58}$$

Defining the block description $\mathbf{F} = \begin{bmatrix} \mathbf{F}_1^H & \mathbf{F}_2^H \end{bmatrix}^H$ and based on the definitions of $\boldsymbol{\Sigma}^2_{K,n,\tilde{\mathbf{y}},\mathbf{u}}$ in (6.20) and $\mathbf{E}_{12,n}$ in (6.57), the N_a columns of $\mathbf{F}_1$ and $\mathbf{F}_2$ can be written as:

$$\mathbf{f}_{1,n} = \gamma_{K,n,\{\mathbf{w},\mathbf{u}\}_{\text{prev}}} \tilde{d}_n^* \boldsymbol{\Sigma}^2_{K,n,\tilde{\mathbf{y}},\mathbf{u}} \mathbf{w} \tag{6.59}$$

$$\mathbf{f}_{2,n} = \gamma_{K,n,\{\mathbf{w},\mathbf{u}\}_{\text{prev}}} \tilde{d}_n^* \mathbf{E}_{12,n}^H \mathbf{w} \tag{6.60}$$

The inverse of $\mathbf{R}_{\boldsymbol{\theta}}$ is then given by [66]:

$$\mathbf{R}_{\boldsymbol{\theta}}^{-1} = \begin{bmatrix} \mathbf{Q}^{-1} & -\mathbf{Q}^{-1}\mathbf{F}\mathbf{G}^{-1} \\ -\mathbf{G}^{-1}\mathbf{F}^H\mathbf{Q}^{-1} & \mathbf{G}^{-1}\left(\mathbf{I}_{N_a} + \mathbf{F}^H\mathbf{Q}^{-1}\mathbf{F}\mathbf{G}^{-1}\right) \end{bmatrix} \tag{6.61}$$

with $\mathbf{Q}$ the Schur complement of $\mathbf{G}$:

$$\mathbf{Q} = \mathbf{E} - \mathbf{F}\mathbf{G}^{-1}\mathbf{F}^H \tag{6.62}$$

which is a full matrix of size $(T+\mu)\times(T+\mu)$. Finally, as $\mathbf{g}_{3,\boldsymbol{\theta}}$ in (6.50) is an all-zero vector in each iteration, due to (6.48), the update of the complex-valued

vector $\left[\begin{array}{cc} \mathbf{w}^H & \mathbf{u}^H \end{array}\right]^H$ is given by:

$$\boxed{\left[\begin{array}{c} \mathbf{w}_i \\ \mathbf{u}_i \end{array}\right] \leftarrow \left[\begin{array}{c} \mathbf{w}_{i-1} \\ \mathbf{u}_{i-1} \end{array}\right] - \alpha_i \mathbf{Q}_{\boldsymbol{\theta}_{i-1}}^{-1} \left[\begin{array}{c} \mathbf{g}_{1,\boldsymbol{\theta}_{i-1}} \\ \mathbf{g}_{2,\boldsymbol{\theta}_{i-1}} \end{array}\right]} \tag{6.63}$$

The simulations in Section 6.6 make use of the iterative GN-based method presented here to optimize the IR-SNLLS-based BM-WinTEQ design criterion.

The iterative GN method requires estimates of the SOS in (6.18). However, a reduction of the SOS memory cost is possible, based on the second key observation (3.65). The SOS (6.18), where a $(1 \times T)$ sliding DFT output $\tilde{\mathbf{y}}_{k,n}$ is involved, can be computed recursively, based on:

$$\begin{aligned} \boldsymbol{\sigma}_{n,\tilde{x}\tilde{\mathbf{y}}} = \mathcal{E}\left\{\tilde{x}_{k,n}^* \tilde{\mathbf{y}}_{k,n}\right\} &= \mathcal{E}\left\{\tilde{x}_{k,n}^* \mathbf{z}_{k,n}\right\} \left[\begin{array}{c} \mathbf{0}_{\mu \times T} \\ \mathbf{T}_n \end{array}\right] \\ \boldsymbol{\Sigma}_{n,\tilde{\mathbf{y}}\Delta\mathbf{y}} = \mathcal{E}\left\{\tilde{\mathbf{y}}_k^H \Delta\mathbf{y}_k^T\right\} &= \left[\begin{array}{cc} \mathbf{0}_{T \times \mu} & \mathbf{T}_n^H \end{array}\right] \mathcal{E}\left\{\mathbf{z}_k^H \Delta\mathbf{y}_k^T\right\} \\ \boldsymbol{\Sigma}_{n,\tilde{\mathbf{y}}}^2 = \mathcal{E}\left\{\tilde{\mathbf{y}}_{k,n}^H \tilde{\mathbf{y}}_{k,n}\right\} &= \left[\begin{array}{cc} \mathbf{0}_{T \times \mu} & \mathbf{T}_n^H \end{array}\right] \mathcal{E}\left\{\mathbf{z}_k^H \mathbf{z}_k\right\} \left[\begin{array}{c} \mathbf{0}_{\mu \times T} \\ \mathbf{T}_n \end{array}\right] \end{aligned} \tag{6.64}$$

where the $1 \times (T + \mu)$ vector $\mathbf{z}_{k,n}$ and the $T \times T$ transformation matrix $\mathbf{T}_n$ have been defined in (6.34) and (3.65), respectively. Hence, by considering both (6.18) and (6.64), we conclude that only the following SOS estimates need to be stored:

- the tone-dependent scalars $\sigma_{n,\tilde{x}\tilde{y}} = \mathcal{E}\left\{\tilde{x}_{k,n}^* \tilde{y}_{k,n}\right\}$,
- the tone-dependent $1 \times (T + \mu - 1)$ vectors $\boldsymbol{\sigma}_{n,\tilde{x}\Delta\mathbf{y}} = \mathcal{E}\left\{\tilde{x}_{k,n}^* \Delta\mathbf{y}_k^T\right\}$ and $\boldsymbol{\sigma}_{n,\tilde{y}\Delta\mathbf{y}} = \mathcal{E}\left\{\tilde{y}_{k,n}^* \Delta\mathbf{y}_k^T\right\}$
- (the square-root of) the tone-independent $(T+\mu-1) \times (T+\mu-1)$ matrix $\boldsymbol{\Sigma}_{\Delta\mathbf{y}}^2 = \mathcal{E}\left\{\Delta\mathbf{y}_k \Delta\mathbf{y}_k^T\right\}$.

When deriving an *adaptive* BM-WinTEQ design algorithm along the lines of the adaptive BM-TEQ of Section 5.2, we end up with an algorithm that requires exactly the same SOS as the RLS-based algorithm to solve the PTEQ design criterion with implicit windowing (6.34), i.e., recursive estimates of $\boldsymbol{\Sigma}_{\Delta\mathbf{y}}^2$ and $\boldsymbol{\sigma}_{n,\tilde{y}\Delta\mathbf{y}}$ (or the related square-roots).

Remark 6.6 The *iterative design of a BM-FWinTEQ* follows from the above derivation by imposing a fixed window and omitting the window update. Update equation (6.63) then becomes:

$$\mathbf{w}_i \leftarrow \mathbf{w}_{i-1} - \alpha_i \mathbf{Q}_{\boldsymbol{\theta}_{i-1}}^{-1} \mathbf{g}_{1,\boldsymbol{\theta}_{i-1}} \tag{6.65}$$

where $\mathbf{Q} = \mathbf{E}_{11} - \mathbf{F}_1\mathbf{G}^{-1}\mathbf{F}_1^H$. When comparing (6.63) and (6.65), the same SOS are required, but the computational cost of (6.65) is lower. □

6.6 Simulations

To illustrate the performance of the bit rate maximizing window and/or equalizer designs, we consider the downstream scenario with the CSA reference loops (tones 38 to 255), as described in Section 4.4, including strong front-end filtering and external noise that is a superposition of AWGN with a power of -140 dBm/Hz, residual echo and near-end crosstalk from 24 ADSL disturbers. For each loop, all TEQ designs are evaluated using the same synchronization delay Δ, which is determined by the first sample of the maximum energy window of the channel impulse response. In the simulations with RFI, the scenario from Section 5.4 is adopted. It consists of 7 RFIs, taken from [62] where we omitted the out-of-band RFIs, which fold back into the ADSL band through aliasing. The carrier frequencies are 540, 650, 680, 760, 790, 840 and 1080 kHz. The first two RFIs have a power of -30 dBm, the remaining five have a power of -50 dBm. The BM-WinTEQ and BM-FWinTEQ design criteria are optimized with the iterative GN method of Section 6.5. To avoid local optima, the optimization routine is initialized with 5 random starting points.

Performance of BM-Win design to mitigate RFI

First, the sensitivity of a DMT-based system to RFI is investigated. **Figure 6.3** compares the SNR of the BM-Win design (6.39) with Redfern's window design (6.44) [99] and the classical *fixed* Hann (raised-cosine) window (6.46) and Bartlett (trapezoidal) window (6.47). An artificial channel was created based on a downstream CSA #4 loop, which was first forced to be of length $\nu - \mu + 1$ (with $\nu = 32$ and $\mu = 10$) by shortening it with an MMSE-based TEQ and by zeroing the resulting SIR outside the desired frame of 23 samples. Hence the simulation is representative of what could be obtained in a VDSL scenario where the CIR typically has a length of at most $\nu - \mu + 1$ samples. The figure also shows the SNR when no windowing is applied and the SNR when no RFIs are present. It is clear that a DMT receiver is indeed sensitive to RFI due to the poor spectral containment of the demodulating DFT and that a window can effectively prevent that all tones are affected by an RFI. Since Redfern's window design method [99] is not related to bit rate maximization, the BM-Win design leads to substantially better SNRs and a higher bit rate.

Further insight into the shape of the window taper $\mathbf{u}$ is gained from **Figure 6.4** by comparing the BM-Win design with Redfern's window design and the fixed Hann and Bartlett window. The BM-Win solution turns out to be smooth and lies in between the Bartlett and Hann window tapers.

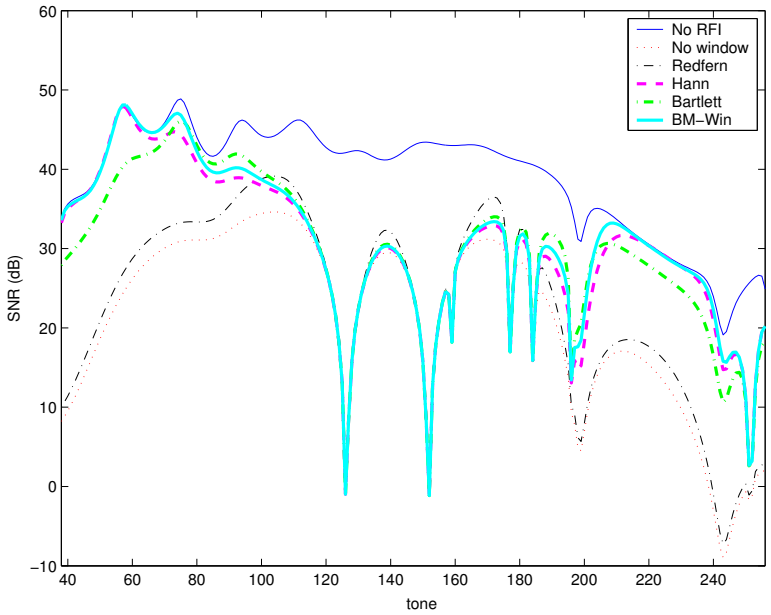


Figure 6.3: SNR for the downstream CSA #4 loop when windowing is applied ($\mu = 10$).

Figure 6.5 evaluates the BM-Win design method for 8 artificial channels, obtained from the 8 downstream CSA channels as described above. The BM-Win design is compared with the fixed Hann window, the fixed Bartlett window and Redfern's window design. The BM-Win design always outperforms the other designs. The difference between the BM-Win and a fixed window ranges from 150 to over 500 kbps.

Performance of the BM-WinTEQ and BM-FWinTEQ design in the absence of RFI

Whereas a TEQ primarily aims at channel equalization, a window is meant to improve the robustness to RFI. Nevertheless, the application of a window can also improve the equalization performance if no RFI is present. As explained in Section 2.2.4, the TEQ aims at reducing ICI (as well as ISI). As receiver windowing reduces the DFT sidelobes, hence improves the DFT spectral containment, increasing the length of the window taper can assist in reducing the ICI leakage to neighbouring tones. *It turns out that TEQ taps T can be traded for windowing coefficients μ.*

Figure 6.6 depicts the bit rate as a function of the number of TEQ taps T and windowing coefficients μ for 4 combined window and equalizer designs in the case of the CSA #4 loop. The MMSE-TEQ design with UEC on $\mathbf{b}$ (Section 3.2.1) and Arslan's TEQ design (Section 3.3.3), both supplemented

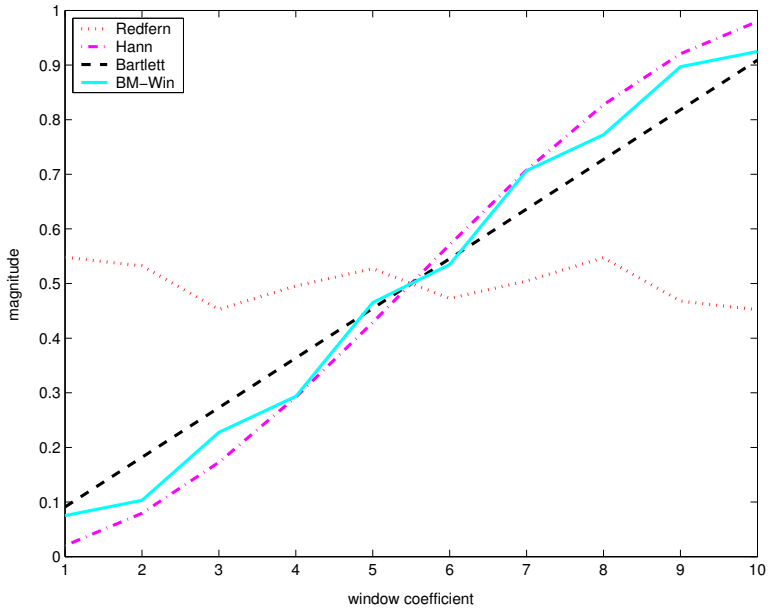


Figure 6.4: Window tapers for the downstream CSA #4 loop ($\mu = 10$).

with a windowed DFT using a fixed Hann window, are compared to the BM-FWinTEQ design (with Hann window) and the BM-WinTEQ design. The curves for $T = 1$ correspond to the windowing-only case; the curves for $\mu = 0$ show the TEQ performance without windowing. It is clear that, in all cases, TEQ taps can be traded for windowing coefficients to obtain the same performance, especially at a low number of taps: e.g., a BM-WinTEQ with $T = 3$ and $\mu = 8$ attains the same performance as a single BM-TEQ with $T = 6$, while the former has a much lower complexity. Even using a window *instead of* a TEQ results in a substantial bit rate improvement. The BM-FWinTEQ design has only a slightly reduced performance, compared to the BM-WinTEQ design. Although a window improves in general the performance of the suboptimal MMSE-TEQ and Al-Dhahir's TEQ design, it is not capable of completely removing the rather unpredictable behaviour as a function of T.

Performance of the BM-WinTEQ and BM-FWinTEQ design in the presence of RFI

In the following simulations, we investigate the combined effect of a TEQ and a receiver window on equalization and RFI mitigation. **Figure 6.7** shows the SNR on the active tones $\mathcal{S}_a$ using the BM-TEQ, the BM-FWinTEQ (with a Hann window) and the BM-WinTEQ design for the downstream CSA #3 loop with $T = 32$ and $\mu = 10$. The positions of the RFIs are easily deduced from the figure. As noted in Section 5.4, a BM-TEQ is capable of reducing the RFI

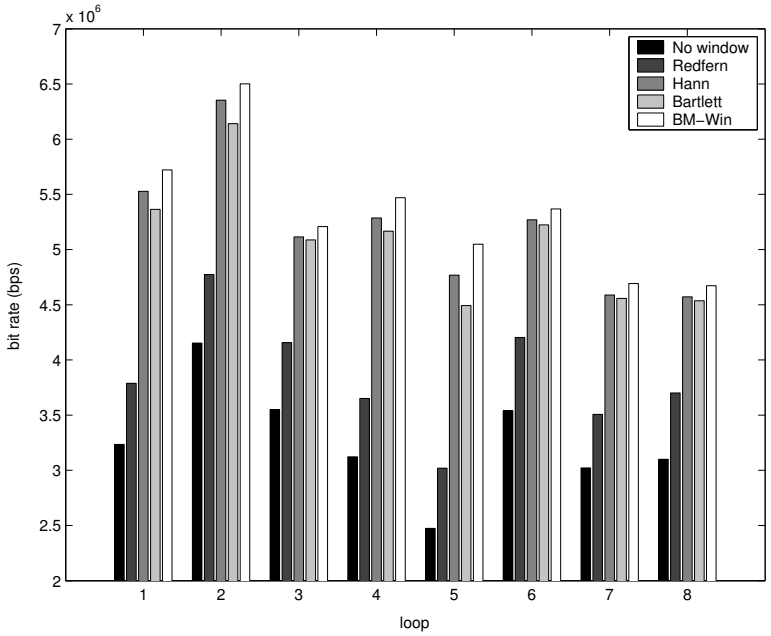


Figure 6.5: Bit rate performance of different window designs for the 8 downstream CSA loops with $\mu = 10$.

impact: there, we have shown that the BM-TEQ exhibits similar performance as a PTEQ, which implicitly incorporates a per-tone window. Adding a fixed window to a BM-TEQ gives only slightly better SNRs. A further SNR increase is caused by including an optimized window, hence using a BM-WinTEQ. To explain this behaviour, **Figure 6.8** shows the frequency response of the TEQ in the BM-TEQ design, the BM-FWinTEQ design and the BM-WinTEQ design. In all cases, the TEQ clearly places a notch on the RFI frequencies to reduce spreading of the RFI by the demodulating DFT.

Figure 6.9 depicts the bit rate performance as a function of the number of TEQ taps T (T =16, 20, 24, 28, 32) and windowing coefficients μ (μ =0, 2, 4, 6, 8, 10) of the MMSE-TEQ design (with UEC on **b**) with a fixed Hann window, the BM-FWinTEQ design (with a fixed Hann window) and the BM-WinTEQ design for the downstream CSA #4 loop. Only the BM-WinTEQ design guarantees a bit rate increase for both an increasing T and μ. The BM-FWinTEQ only guarantees a bit rate increase for an increasing T at a fixed μ. It does not guarantee an increasing bit rate for an increasing μ at a fixed T because of the fixed window. Especially the MMSE-TEQ design does not necessarily improve the bit rate as a function of T or μ. In fact, as the TEQ design minimizes a TD MSE, it does not account for the windowing operation.

As explained in Table 6.1, the TEQ is computationally much more expensive

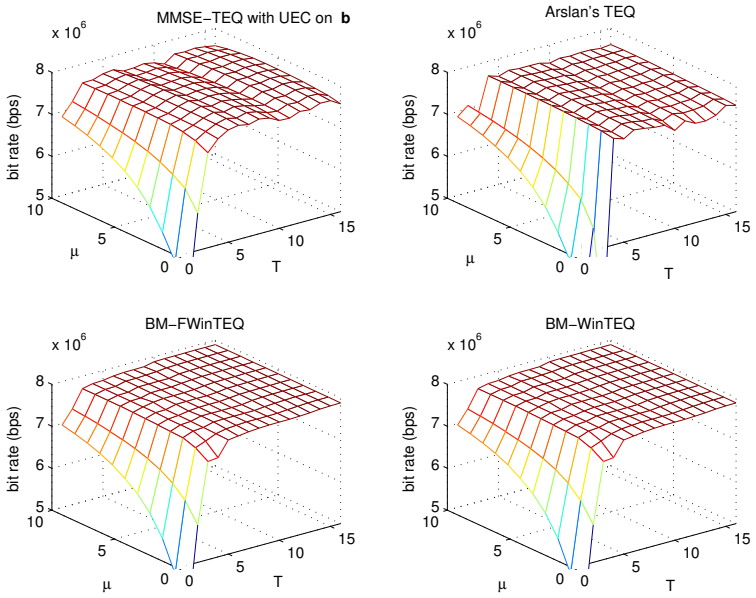


Figure 6.6: Bit rate as a function of the number of TEQ taps T and window coefficients μ for the downstream CSA #4 loop (without RFI) and 4 combined window and equalizer designs. The MMSE-TEQ design, Arslan's TEQ design and the BM-FWinTEQ design make use of a windowed DFT with a fixed Hann window.

than the receiver window. As for the BM-WinTEQ, it then follows from Figure 6.9 that it is preferred to use a TEQ with the largest affordable number of taps (with a maximum around $T = 64$) and combine it with a window for further performance enhancement.

Figure 6.10 depicts the bit rate performance of the MMSE-TEQ design (with and without fixed Hann window), the BM-TEQ design, the BM-FWinTEQ design (with fixed Hann window) and the BM-WinTEQ design for the 8 downstream CSA loops in two cases: (a) $T = 16$, $\mu = 10$ and (b) $T = 32$, $\mu = 10$. Note the large difference in bit rate (several Mbps) between both plots: if affordable, it is clearly preferred to use a large number of taps, e.g., $T = 32$. For $T = 32$ (see Figure b), the BM-TEQ design, the BM-FWinTEQ design and the BM-WinTEQ design achieve similar performance: sometimes, the BM-FWinTEQ design performs slightly worse than the BM-TEQ design, while the BM-WinTEQ design always outperforms the BM-TEQ and BM-FWinTEQ design. For $T = 16$ (see Figure a), adding a fixed or optimized window to a BM-TEQ results in a substantial benefit. Using a windowed DFT in combination with an MMSE-TEQ design can be interesting if $T = 16$, but this seems to be avoided if $T = 32$.

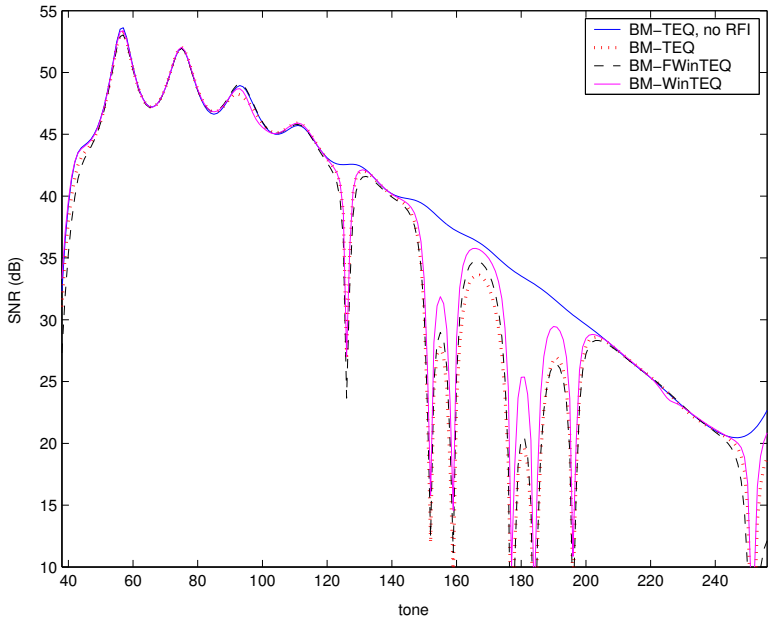


Figure 6.7: SNR in the presence of RFI for the downstream CSA #3 loop for the BM-WinTEQ design, the BM-FWinTEQ design (with a Hann window) and the BM-TEQ design with $\mu = 10$ and $T = 32$.

Figure 6.11 shows the bit rate performance for the same scenarios as Figure 6.10, be it that now the RFI at 680 kHz was not present during the window and equalizer design phase. The simulations then mimic a scenario where an RFI appears after TEQ and window design. For $T = 16$, there is a slight performance decrease of around 100 kbps for the BM-FWinTEQ and the BM-WinTEQ design; the performance of the other designs hardly changes. For $T = 32$, however, all designs have a large performance loss, up to several Mbps. Apparently, the performance gain, by using $T = 32$ instead of $T = 16$ taps, comes at the expense of robustness to an additional RFI. Especially the BM-TEQ and BM-WinTEQ suffer from a large performance loss. The BM-FWinTEQ appears the most robust in this case and maintains a bit rate that remains larger than the bit rate of all considered designs with $T = 16$. This suggests, as a rule thumb, that *a large number of equalizer taps T (e.g., $T = 32$) is preferably combined with a fixed window, if non-stationary RFI, e.g., from HAM radios, is expected; in case the number of equalizer taps T is limited to a smaller number, e.g., $T = 16$, an optimized window can be used as this results in increased performance without significant robustness issue.*

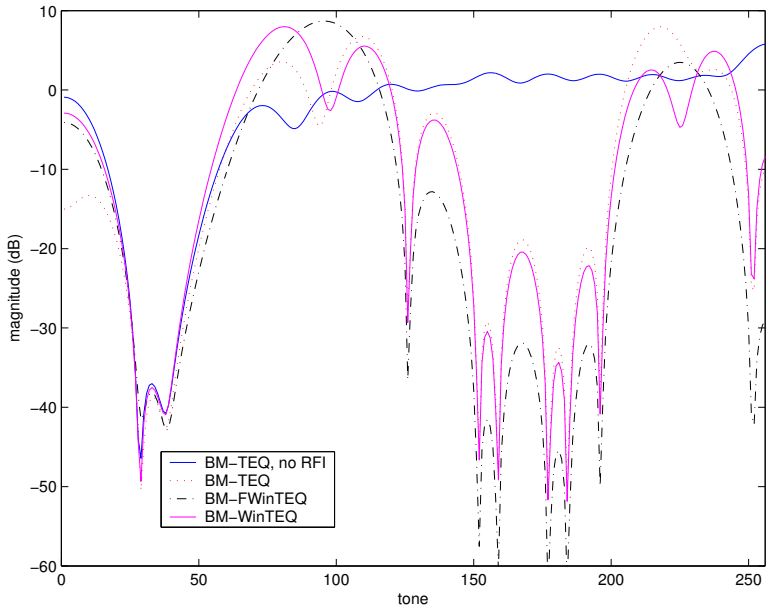


Figure 6.8: Frequency response of the TEQ in the BM-TEQ design, BM-FWinTEQ design and BM-WinTEQ design with $\mu = 10$ and $T = 32$ for the downstream CSA #3 loop in the presence of RFI.

6.7 Conclusions

In this chapter, we have presented a general framework for bit rate maximizing combined window and TEQ (BM-WinTEQ) design. We have derived two equivalent design criteria, which both are extensions of the BM-TEQ design criteria as derived in Chapter 4. An iterative GN-based algorithm was presented for optimizing the IR-SNLLS-based BM-WinTEQ design criterion. Furthermore, some special design cases were addressed: a per-group design (BM-PGWinEQ), a windowing-only design (BM-Win) and an equalizer design in the presence of a fixed window (BM-FWinTEQ).

Traditionally, equalization in ADSL is performed by means of a TEQ-FEQ combination. On the other hand, receiver windowing in combination with one-tap FEQs, but without a TEQ, is commonly applied in DMT-based VDSL to reduce the susceptibility of the receiver to RFI. However, simulations showed that the capability of receiver windowing to reduce the sidelobe level of the demodulating DFT can also help the ADSL equalizer in reducing the ICI. Alternatively, a VDSL receiver may benefit from an additional TEQ to notch out RFIs. Therefore, we suggested to always apply a TEQ using the largest affordable number of taps and combine it with a window, which indeed adds negligible complexity. Furthermore, the BM-WinTEQ design turned out to

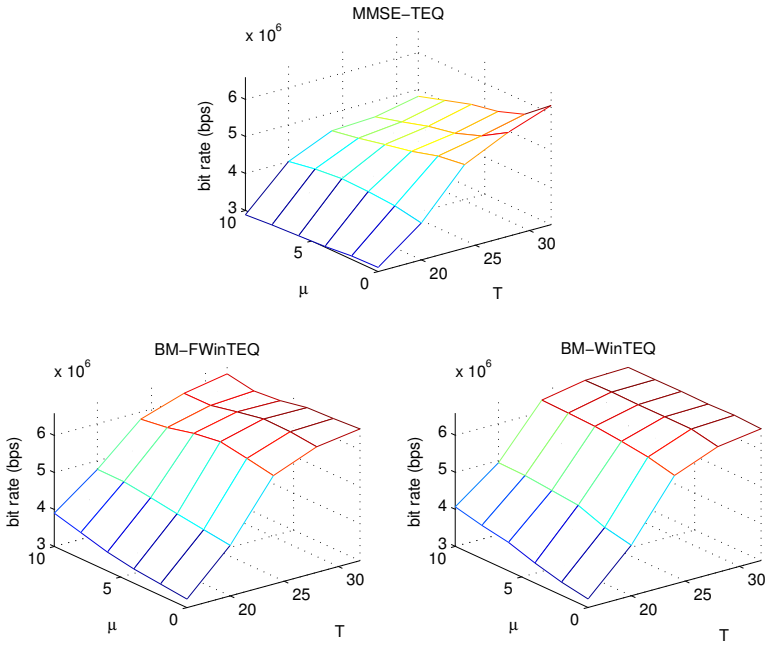
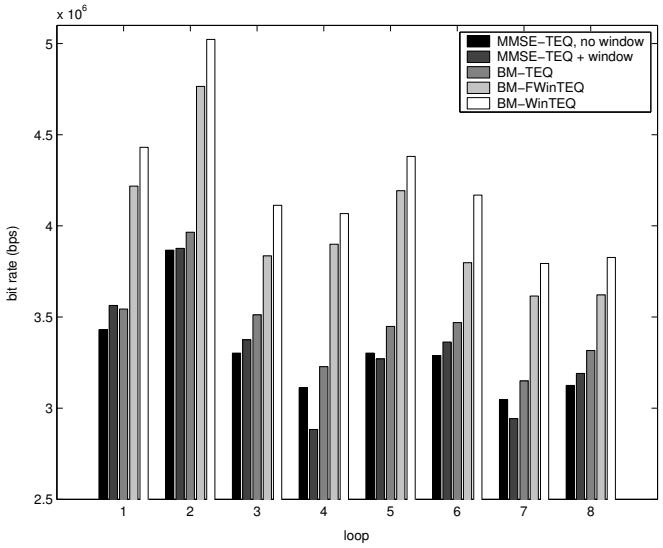


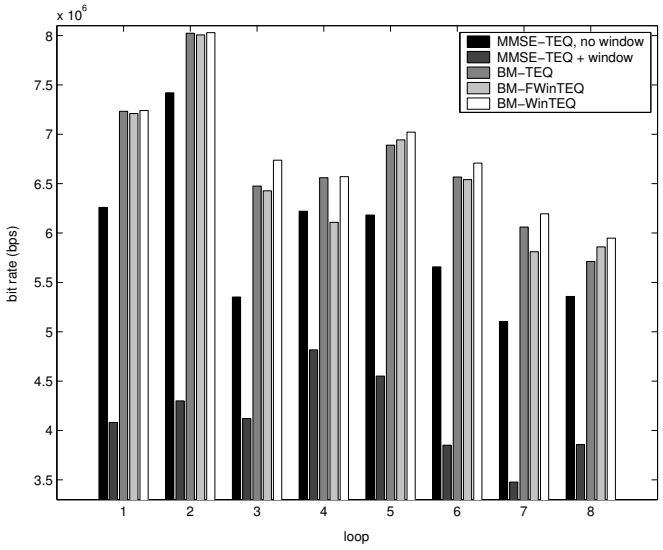
Figure 6.9: Bit rate performance as a function of the number of TEQ taps T (T =16, 20, 24, 28, 32) and windowing coefficients μ (μ =0, 2, 4, 6, 8, 10) of the MMSE-TEQ design (with UEC on $\mathbf{b}$) with a fixed Hann window, the BM-FWinTEQ design (with a fixed Hann window) and the BM-WinTEQ design for the downstream CSA #4 loop with RFI.

outperform any other design, be it at the expense of robustness to an RFI that appears *after* the window and equalizer were designed. Therefore, we suggested to make use of a BM-FWinTEQ design when using a large number of equalizer taps and in the presence of non-stationary RFI, e.g., from HAM radios.

Finally, we mention that in Chapter 7 it is shown that receiver windowing can be supplemented with the exploitation of unused tones around the RFI carrier frequency to further improve the RFI mitigation performance.

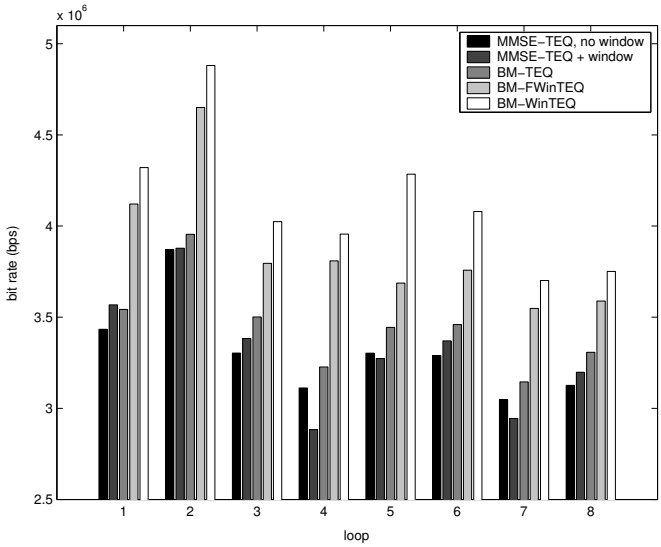


(a) $T = 16, \mu = 10$

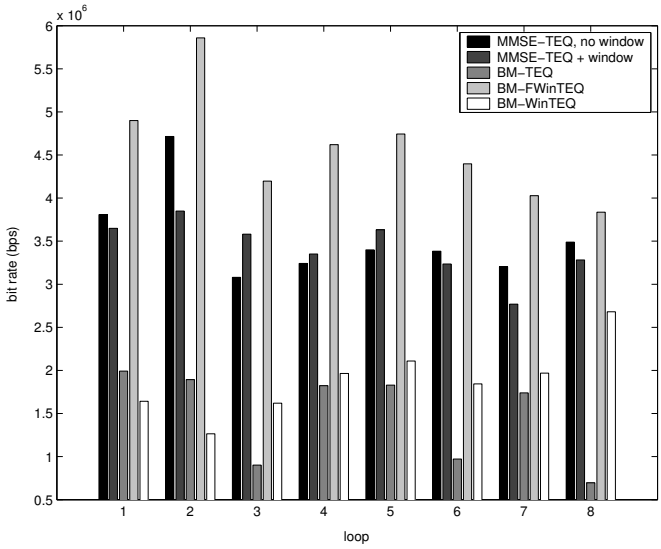


(b) $T = 32, \mu = 10$

Figure 6.10: Bit rate performance of the MMSE-TEQ design (with and without fixed Hann window), the BM-TEQ design, the BM-FWinTEQ design (with fixed Hann window) and the BM-WinTEQ design for the 8 downstream CSA loops with RFI.



(a) $T = 16, \mu = 10$



(b) $T = 32, \mu = 10$

Figure 6.11: Bit rate performance of the MMSE-TEQ design (with and without fixed Hann window), the BM-TEQ design, the BM-FWinTEQ design (with fixed Hann window) and the BM-WinTEQ design for the 8 downstream CSA loops, when the RFI at 680 kHz is not present during window/equalizer design and appears afterwards.

Chapter 7

Equalization of DMT-based systems over IIR channels

UNTIL now, we have considered DMT receiver solutions without modification of the DMT transmitter. Hence, the presented schemes comply with the ADSL standards. As explained in Section 2.2.4, the standardized choice of a CP length of 32 samples (together with an IDFT/DFT block (de)modulation of $N = 512$ samples) is the result of a trade-off between latency, efficiency loss and equalizer complexity. In this chapter, we allow for an arbitrary CP length. Then, the standardized CP length of 32 samples turns out to be a conservative choice: by employing an appropriate equalizer structure, the CP length can be reduced to 16 samples, which results in a smaller latency and efficiency loss, without increasing the computational cost of the equalizer design and filtering and the associated memory cost.

In order to develop an appropriate equalizer for an arbitrary CP length, we reconsider DMT equalization under the assumption of an infinite impulse response (IIR) channel model. As the ADSL transmission channel impulse response typically has a long tail, a parsimonious IIR or pole-zero model has been previously adopted in, e.g., [29], [105]. Section 7.1 elaborates the DMT block data model, based on the initial data model of Section 2.3.2. Two cases are considered. Section 7.2 deals with the case of a numerator order that is smaller than or equal to the CP length; Section 7.3 deals with the case of a numerator order that is larger than the CP length. For both cases, *necessary and sufficient linear zero-forcing (L-ZF) conditions* are derived, which include conditions on the IIR channel order (i.e., the numerator and denominator order) and the required amount of *TX redundancy* per DMT symbol block. Then, we derive *optimum L-ZF block equalizers*, which appear to allow in both cases for a computationally advantageous decoupling per tone, hence they lead to a

so-called *L-ZF PTEQ*, i.e., with only one tone-dependent input.

In Section 7.4, we propose *low-complexity extensions of the original linear MMSE (L-MMSE) PTEQ* to accommodate an arbitrary IIR channel order and CP length. The so-called *linear PTEQ (L-PTEQ) extension* makes use of the FD TX redundancy that is provided in DMT transmission by unused tones and pilot tones: by adding a few DFT outputs of unused and pilot tones (and the corresponding pilot symbols), containing ISI/ICI from the active data-carrying tones, as common inputs to the PTEQ, the equalization of these active tones is enhanced. The so-called *decision-feedback PTEQ (DF-PTEQ) extension* is based on the observation that each decision on an FD data symbol can be treated in the same way as the a priori knowledge of a pilot symbol: the ISI/ICI in the DFT output of the considered active tone can again be exploited to enhance the equalization of the remaining active tones. The DF-PTEQ extension then feeds back a few symbol decisions within the DMT symbol and uses them, together with the corresponding DFT outputs, as extra, common PTEQ inputs. The RLS-based and hybrid RLS/LMS-based adaptive PTEQ algorithms of Section 3.4.2 are then straightforwardly extended with shared RLS processing for these extra, common inputs. The RFI suppression capability of the PTEQ extensions is also discussed.

Although the derivations in this chapter focus on PTEQ extensions, the earlier established close relationship between the BM-TEQ and the PTEQ suggests that very similar *linear BM-TEQ and decision-feedback BM-TEQ extensions* are possible. These BM-TEQ extensions are briefly discussed in Section 7.5.

Section 7.6 includes simulation results for different scenarios (several loops with and without RFI), different amounts of exploited FD TX redundancy, CP lengths and numbers of equalizer taps. The simulations show that DMT systems, employing an appropriate L-PTEQ or DF-PTEQ extension, have extra flexibility: the CP overhead can be reduced so that the same bit rate is achieved at a lower computational and memory cost or, alternatively, a higher bit rate is reached without considerable cost increase.

Figure 7.1 clarifies the place of each section in this chapter in the schematic thesis overview of Figure 1.5.

Remark 7.1 In the context of DMT/OFDM transmission, the introduction of TX redundancy has been previously studied and exploited under different forms (e.g., at bit level: through channel coding; in the time-domain, i.e., after the DFT modulation: by means of a CP, zero padding or known-symbol padding; in the frequency-domain: by means of pilot symbols) and for several purposes (e.g., to improve symbol detection (and bit error rate), to simplify equalization, to guarantee perfect ZF equalization, for blind channel estimation or for blind direct equalizer design). The fact that FD TX redundancy from unused and pilot tones can enhance the equalization in the case of an insufficiently long

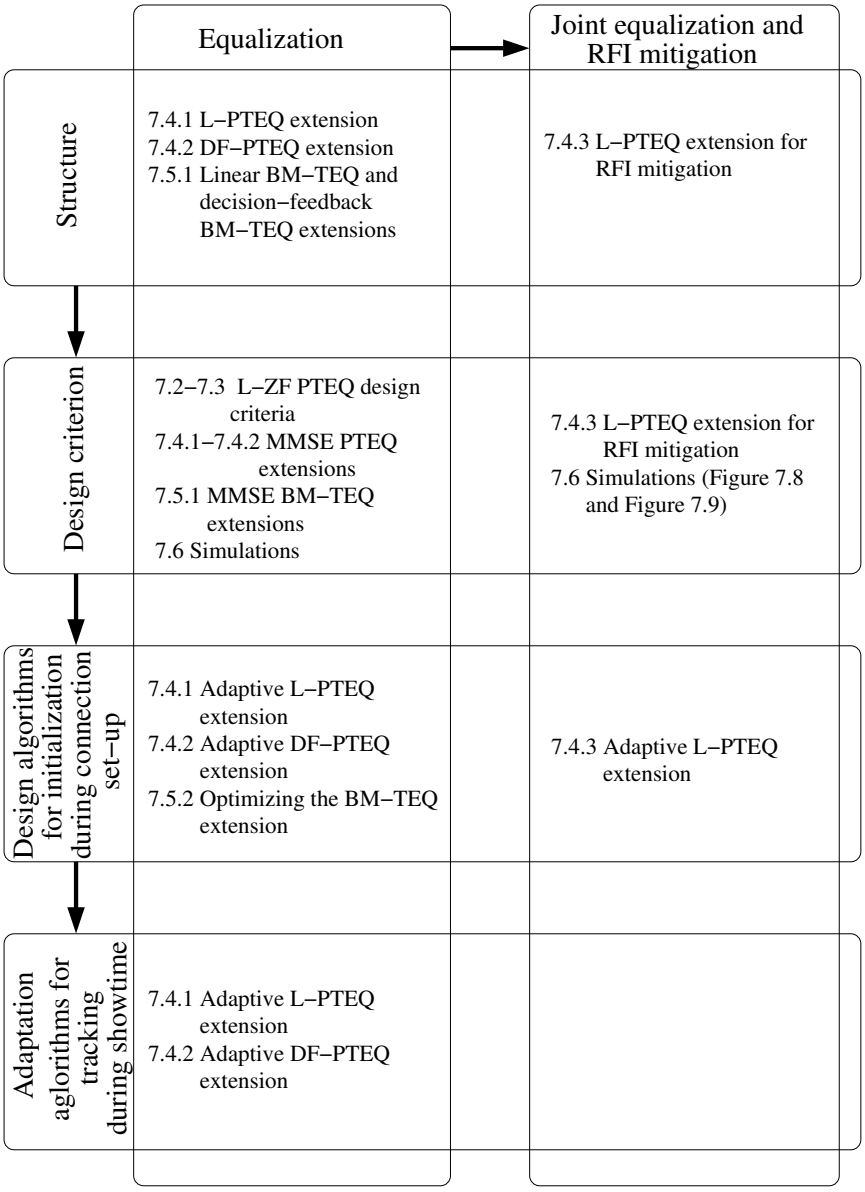


Figure 7.1: Schematic overview of this chapter.

or even absent CP has been reported independently and simultaneously in [125, 126, 127]. Throughout the chapter, we will indicate how our work relates to and is a generalization of the results obtained in [125, 126, 127]. □

7.1 Notation and DMT data model

7.1.1 Notation

Our notation in this chapter follows to a large extent the notation of the previous chapters. Some modifications and extensions are as follows.

In the derivations, we will assume for simplicity that the TX symbol vector $\tilde{\mathbf{x}}_{k,N}$ can be partitioned as $\tilde{\mathbf{x}}_{k,N} = \left[\begin{array}{ccc} \tilde{\mathbf{x}}_{k,a}^H & \tilde{\mathbf{x}}_{k,p}^H & \tilde{\mathbf{x}}_{k,u}^H \end{array} \right]^H$ where $\tilde{\mathbf{x}}_{k,a}$, $\tilde{\mathbf{x}}_{k,p}$ and $\tilde{\mathbf{x}}_{k,u} = \mathbf{0}$ are TX symbol vectors for the set of N_a active data-carrying tones $\mathcal{S}_a = \{0, 1, \ldots, N_a - 1\}$ (previously denoted as $\tilde{\mathbf{x}}_k$), the set of N_p pilot tones $\mathcal{S}_p = \{N_a, N_a + 1, \ldots, N_a + N_p - 1\}$ and the set of N_u unused tones $\mathcal{S}_u = \{N_a + N_p, \ldots, N_a + N_p + N_u - 1\}$, respectively (note that $N = N_a + N_p + N_u$). In practice, a different partitioning will be used, also because tones belonging to a certain set usually appear in complex conjugate pairs. In this chapter, the tone sets $\mathcal{S}_a$, $\mathcal{S}_p$ and $\mathcal{S}_u$ and the corresponding number of tones N_a, N_p and N_u include the complex conjugate tones for convenience. E.g., the active tones 38 to 255 in ADSL downstream transmission give rise to the set of $N_a = 2 \times 218 = 436$ tones, $\mathcal{S}_a = \{38, \ldots, 255, 257, \ldots, 474\}$. Such alternative partitionings can be accommodated by redefining the DFT matrix $\mathcal{F}_N$ (and hence also the DFT operation) as a row-permuted version of the original DFT matrix.

As the above notation suggests, the subscript N still denotes FD vectors and matrices that take all N DFT bins into account, while the subscripts a, p and u are used in connection with the tone sets $\mathcal{S}_a$, $\mathcal{S}_p$ and $\mathcal{S}_u$. E.g., the $N_a \times N$ submatrix of $\mathcal{F}_N$ with the N_a rows that correspond to the active tone set $\mathcal{S}_a$ is denoted as $\mathcal{F}_a$; likewise, $\mathcal{F}_p$ is an $N_p \times N$ submatrix of $\mathcal{F}_N$ with rows corresponding to the pilot tone set $\mathcal{S}_p$. For the sake of conciseness, we will only consider active data-carrying tones $\mathcal{S}_a$ and pilot tones $\mathcal{S}_p$ in the derivations; the unused tones $\mathcal{S}_u$ can then be seen as a special case of pilot tones where the pilot symbols are zero.

7.1.2 Data model

Based on the IIR channel model $H(z)$:

$$H(z) = \frac{B(z)}{A(z)} = \frac{z^{-\delta_0} \sum_{m=0}^{L_b} b_m z^{-m}}{\sum_{m=0}^{L_a} a_m z^{-m}} \tag{7.1}$$

where δ_0 is a propagation delay, $B(z)$ is the numerator of order L_b and $A(z)$ is the denominator of order L_a, the following initial IIR-channel-based data model (2.46) has been presented in Section 2.3.2:

$$\underbrace{\begin{bmatrix} [& \bar{\mathbf{a}} &] & 0 & \cdots \\ & \ddots & & \ddots & \\ \cdots & 0 & [& \bar{\mathbf{a}} &] \end{bmatrix}}_{\mathbf{A}_{\mathrm{T}}} (\mathbf{y}_{k,-L_a+\Delta:N-1+\Delta} - \mathbf{n}_{k,-L_a+\Delta:N-1+\Delta})$$

$$= \begin{bmatrix} \mathbf{0}_{(1)} & \underbrace{\left| \begin{matrix} [& \bar{\mathbf{b}} &] & 0 & \cdots \\ & \ddots & & \ddots & \\ \cdots & 0 & [& \bar{\mathbf{b}} &] \end{matrix} \right|}_{\mathbf{B}_{\mathrm{T}}} & \mathbf{0}_{(2)} \end{bmatrix} (\mathbf{I}_3 \otimes \mathbf{P}_\nu \mathcal{F}_N^H) \cdot \underbrace{\begin{bmatrix} \tilde{\mathbf{x}}_{k-1,N} \\ \tilde{\mathbf{x}}_{k,N} \\ \tilde{\mathbf{x}}_{k+1,N} \end{bmatrix}}_{\tilde{\mathbf{x}}_{k-1:k+1,N}} \quad (7.2)$$

The right-hand expression, determined by the channel numerator $B(z)$, is similar to the first right-hand term of the FIR data model (2.35); the left-hand term comes from the channel denominator $A(z)$. The matrices $\mathbf{A}_{\mathrm{T}}$ (of size $N \times (N + L_a)$) and $\mathbf{B}_{\mathrm{T}}$ (of size $N \times (N + L_b)$) are Toeplitz convolution matrices, which are built with vectors of denominator and numerator coefficients $\mathbf{a} = \begin{bmatrix} a_0 & \cdots & a_{L_a} \end{bmatrix}^T$ and $\mathbf{b} = \begin{bmatrix} b_0 & \cdots & b_{L_b} \end{bmatrix}^T$, respectively, in reverse order (hence denoted by a bar). The matrices $\mathbf{O}_{(1)}$ and $\mathbf{O}_{(2)}$ in (7.2) are zero matrices of size $N \times (N+2\nu+\delta-L_b)$ and $N \times (N+\nu-\delta)$, respectively, where δ is a decision delay (as explained in Section 2.3.1) and $\Delta = \delta_0 + \delta$.

Remark 7.2 The choice of N equations in (7.2) will give rise to an elegant data model as N corresponds to the DFT size. It relates the k-th TX and RX sample vectors, $\mathbf{x}_{k,-L_b:N-1}$ and $\mathbf{y}_{k,-L_a:N-1}$, respectively, which both include all or part of the CP samples, depending on L_b and L_a. □

Without loss of generality, we will assume from now on that the propagation delay δ_0 is equal to 0. Since a linear convolution over a time interval can be turned into a circular convolution with appropriate correction terms at the interval edges, (7.2) can be rewritten as:

$$\mathbf{A}_{\mathrm{C}}\mathbf{y}_{k,0:N-1} + \mathbf{A}_\Delta \Delta\mathbf{y}_k = \mathbf{B}_{\mathrm{C}}\mathbf{x}_{k,0:N-1} + \mathbf{B}_\Delta \Delta\mathbf{x}_k + \check{\mathbf{n}}_k \quad (7.3)$$

where $\check{\mathbf{n}}_k = \mathbf{A}_{\mathrm{T}}\mathbf{n}_{k,-L_a:N-1}$ denotes an $N \times 1$ sample vector of channel noise n_l, coloured by the denominator $\mathbf{a}$. The $N \times N$ matrices $\mathbf{A}_{\mathrm{C}}$ and $\mathbf{B}_{\mathrm{C}}$ are circulant with appropriately zero-padded vectors $\mathbf{a}$ and $\mathbf{b}$, respectively, as their first column vectors. The tall $N \times L_b$ Toeplitz matrix $\mathbf{B}_\Delta$ is given by:

$$\mathbf{B}_\Delta = \left[\begin{array}{ccc} b_{L_b} & \cdots & b_1 \\ \vdots & \ddots & \vdots \\ 0 & 0 & b_{L_b} \\ \hline \multicolumn{3}{c}{\mathbf{0}_{(N-L_b)\times L_b}} \end{array}\right] \tag{7.4}$$

The tall $N \times L_a$ Toeplitz matrix $\mathbf{A}_\Delta$ is similarly obtained. The TX and RX difference terms $\Delta\mathbf{x}_k$ and $\Delta\mathbf{y}_k$, which are real-valued in the case of baseband transmission, are defined as:

$$\begin{aligned} \Delta\mathbf{x}_k &= \left[\begin{array}{ccc} \Delta x_{k,-L_b} & \cdots & \Delta x_{k,-1} \end{array}\right]^T \\ &= \left[\begin{array}{ccc} (x_{k,-L_b} - x_{k,N-L_b}) & \cdots & (x_{k,-1} - x_{k,N-1}) \end{array}\right]^T \qquad (7.5) \\ \Delta\mathbf{y}_k &= \left[\begin{array}{ccc} \Delta y_{k,-L_a} & \cdots & \Delta y_{k,-1} \end{array}\right]^T \\ &= \left[\begin{array}{ccc} (y_{k,-L_a} - y_{k,N-L_a}) & \cdots & (y_{k,-1} - y_{k,N-1}) \end{array}\right]^T \qquad (7.6) \end{aligned}$$

The sample vector $\mathbf{x}_{k,0:N-1}$ in (7.3) is the TX IDFT output, i.e., $\mathbf{x}_{k,0:N-1} = \mathcal{F}_N^H \tilde{\mathbf{x}}_{k,N}$. Similarly, $\tilde{\mathbf{y}}_{k,N} = \mathcal{F}_N \mathbf{y}_{k,0:N-1}$ is the DFT of the k-th unequalized RX sample vector.

When deriving equalizers based on (7.3) in the next sections, we assume that the decision delay δ is zero to keep the derivations tractable. The extensions to $\delta > 0$ and $\delta < 0$ follow a similar reasoning, based on an appropriately modified data model (7.3).

The final data model and starting point for the equalizer derivations in the next sections is obtained by taking the N-point DFT of the set of equations (7.3) and exploiting a DFT-based decomposition of the circulant matrices $\mathbf{A}_\mathrm{C}$ and $\mathbf{B}_\mathrm{C}$, e.g., $\mathbf{B}_\mathrm{C} = \mathcal{F}_N^H \tilde{\mathbf{B}}_{N,\mathrm{D}} \mathcal{F}_N$, where $\tilde{\mathbf{B}}_{N,\mathrm{D}} = \mathrm{diag}(\tilde{\mathbf{b}}_N)$ with $\tilde{\mathbf{b}}_N = \left[\begin{array}{ccc} \tilde{b}_0 & \cdots & \tilde{b}_{N-1} \end{array}\right]^T = \mathcal{F}_N \left[\begin{array}{cc} \mathbf{b}^T & \mathbf{0}^T_{(N-L_b-1)\times 1} \end{array}\right]^T$, i.e., $\tilde{\mathbf{B}}_{N,\mathrm{D}}$ is a diagonal matrix with on the diagonal the DFT of the zero-padded vector $\mathbf{b}$ ($\mathbf{A}_\mathrm{C}$ can be decomposed in the same way):

$$\tilde{\mathbf{A}}_{N,\mathrm{D}} \tilde{\mathbf{y}}_{k,N} + \mathcal{F}_N \mathbf{A}_\Delta \Delta\mathbf{y}_k = \tilde{\mathbf{B}}_{N,\mathrm{D}} \tilde{\mathbf{x}}_{k,N} + \mathcal{F}_N \mathbf{B}_\Delta \Delta\mathbf{x}_k + \mathcal{F}_N \check{\mathbf{n}}_k \tag{7.7}$$

The first right-hand term of (7.7) can then be split into a contribution from the data symbols, $\tilde{\mathbf{x}}_{k,a}$, and the pilot symbols, $\tilde{\mathbf{x}}_{k,p}$:

$$\tilde{\mathbf{B}}_{N,\mathrm{D}} \tilde{\mathbf{x}}_{k,N} = \left[\begin{array}{c} \tilde{\mathbf{B}}_{a,\mathrm{D}} \\ \mathbf{0}_{N_p \times N_a} \end{array}\right] \tilde{\mathbf{x}}_{k,a} + \left[\begin{array}{c} \mathbf{0}_{N_a \times N_p} \\ \tilde{\mathbf{B}}_{p,\mathrm{D}} \end{array}\right] \tilde{\mathbf{x}}_{k,p} \tag{7.8}$$

where $\tilde{\mathbf{B}}_{a,\mathrm{D}} = \mathrm{diag}(\tilde{\mathbf{b}}_a)$ and $\tilde{\mathbf{B}}_{p,\mathrm{D}} = \mathrm{diag}(\tilde{\mathbf{b}}_p)$ and where $\tilde{\mathbf{b}}_a$ and $\tilde{\mathbf{b}}_p$ are obtained from $\tilde{\mathbf{b}}_N$ by selection of the entries corresponding to $\mathcal{S}_a$ and $\mathcal{S}_p$, respectively. Rearranging (7.7), so that all known data (i.e., the RX signal y_l and the pilot

symbols $\tilde{\mathbf{x}}_{k,p}$) are grouped on the left-hand side, results in:

$$\boxed{\tilde{\mathbf{z}}_{k,N} = \begin{bmatrix} \tilde{\mathbf{B}}_{a,\mathrm{D}} \\ \mathbf{0} \end{bmatrix} \tilde{\mathbf{x}}_{k,a} + \mathcal{F}_N \mathbf{B}_\Delta \Delta\mathbf{x}_k + \mathcal{F}_N \check{\mathbf{n}}_k} \tag{7.9}$$

with

$$\boxed{\tilde{\mathbf{z}}_{k,N} = \begin{bmatrix} \tilde{\mathbf{z}}_{k,a} \\ \tilde{\mathbf{z}}_{k,p} \end{bmatrix} = \tilde{\mathbf{A}}_{N,\mathrm{D}} \tilde{\mathbf{y}}_{k,N} + \mathcal{F}_N \mathbf{A}_\Delta \Delta\mathbf{y}_k - \begin{bmatrix} \mathbf{0} \\ \tilde{\mathbf{B}}_{p,\mathrm{D}} \end{bmatrix} \tilde{\mathbf{x}}_{k,p}} \tag{7.10}$$

This **IIR-channel-based DMT block data model** (7.9-7.10) relates the DFT output vector $\tilde{\mathbf{y}}_{k,N}$ with the TX symbol vectors $\tilde{\mathbf{x}}_{k,a}$ and $\tilde{\mathbf{x}}_{k,p}$ using some (correcting) TX and RX difference terms (7.5-7.6). The data model allows to isolate terms that cause ISI/ICI in each DFT output. After left multiplication of (7.9-7.10) with $\tilde{\mathbf{A}}_{N,\mathrm{D}}^{-1}$ and some rearranging, the DFT output $\tilde{\mathbf{y}}_{k,N}$ can be expressed as:

$$\begin{aligned} \tilde{\mathbf{y}}_{k,N} \;=\; & \tilde{\mathbf{A}}_{N,\mathrm{D}}^{-1} \left(\begin{bmatrix} \tilde{\mathbf{B}}_{a,\mathrm{D}} \\ \mathbf{0} \end{bmatrix} \tilde{\mathbf{x}}_{k,a} + \begin{bmatrix} \mathbf{0} \\ \tilde{\mathbf{B}}_{p,\mathrm{D}} \end{bmatrix} \tilde{\mathbf{x}}_{k,p} \right. \\ & \left. + \mathcal{F}_N \mathbf{B}_\Delta \Delta\mathbf{x}_k - \mathcal{F}_N \mathbf{A}_\Delta \Delta\mathbf{y}_k + \mathcal{F}_N \check{\mathbf{n}}_k \right) \end{aligned} \tag{7.11}$$

When considering the n-th DFT output, $\tilde{y}_{k,n} = \tilde{\mathbf{y}}_{k,N}[n]$, the diagonal nature of $\tilde{\mathbf{B}}_{a,\mathrm{D}}$, $\tilde{\mathbf{B}}_{p,\mathrm{D}}$ and $\tilde{\mathbf{A}}_{N,\mathrm{D}}$ makes that the first two right-hand terms do not cause ISI/ICI: they cause a contribution from a TX symbol $\tilde{x}_{k,n}$, scaled with $\frac{\tilde{b}_n}{\tilde{a}_n}$, which either corresponds to a data symbol ($n \in \mathcal{S}_a$) or a pilot symbol ($n \in \mathcal{S}_p$). The third and fourth term do cause ISI/ICI, as both $\Delta\mathbf{x}_k$ and $\Delta\mathbf{y}_k$ are built with TD samples, hence they are a superposition of a desired signal contribution from $\tilde{x}_{k,n}$ and ISI/ICI, caused by the channel $H(z)$, from all other TX symbols $\tilde{x}_{l,m}$ with $l \neq k$ or $m \neq n$. The fifth term is the additive noise.

Remark 7.3 The IIR-channel-based data model (7.9-7.10) is very similar to the FIR-channel-based data model (4.5) for the toy example, derived in Section 4.1. The FIR-channel-based data model (4.5) for a typical ADSL channel can be considered a special case of the IIR-channel-based data model (7.9-7.10) with a denominator $A(z) = 1$ and a high-order numerator $B(z)$. □

The data model (7.9-7.10) is of special interest for DMT equalization as it suggests a relation with the PTEQ. As explained in Section 3.4, the T-tap PTEQ $\mathbf{v}_n^{\mathrm{PTEQ}}$ for tone n is the solution of the following L-MMSE design criterion:

$$\boxed{\mathbf{v}_n^{\mathrm{PTEQ}} = \arg\min_{\mathbf{v}_n} \mathcal{E}\left\{ \left| \begin{bmatrix} \Delta\mathbf{y}_k^T & \tilde{y}_{k,n} \end{bmatrix} \mathbf{v}_n - \tilde{x}_{k,n} \right|^2 \right\}} \tag{7.12}$$

hence the **L-MMSE PTEQ for tone** n linearly combines one single tone-dependent DFT output, $\tilde{y}_{k,n}$, with $T-1$ RX difference terms $\Delta\mathbf{y}_k$. If $L_a =$

$T-1$, these difference terms are the same as those defined in (7.6). The fact that there is only one tone-dependent PTEQ input decouples the equalizer design per tone and, at the same time, has a beneficial impact on the computational and memory cost of the RLS-based adaptive PTEQ design (see Section 3.4.2).

7.1.3 Outline of this chapter

In Section 7.2 and 7.3, necessary and sufficient L-ZF conditions are derived and optimum L-ZF block equalizers are developed, based on the IIR-channel-based DMT block data model (7.9-7.10). In Section 7.2, we consider the case of a numerator order L_b that is smaller than or equal to the CP length ($L_b \leq \nu$); Section 7.3 deals with the case of a numerator order L_b that is larger than the CP length ($L_b > \nu$). In both cases, the L-ZF block equalizer turns out to reduce to an L-ZF PTEQ, i.e., with only one tone-dependent input. Based on the L-ZF PTEQ, low-complexity linear and decision-feedback extensions of the original L-MMSE PTEQ design (7.12) are then presented in Section 7.4.

7.2 DMT equalization of an IIR channel with $L_b \leq \nu$

In general, if all tones are active and data-carrying, i.e. $\mathcal{S}_a = \{0, \ldots, N-1\}$, $N = N_a$ and $\mathcal{S}_p = \emptyset$, the data model (7.9-7.10) does not have an L-ZF block equalizer. In the noiseless case, (7.9-7.10) then corresponds to an underdetermined set of N (real) equations in $N + L_b$ (real) unknown variables $\left[\begin{array}{cc} \tilde{\mathbf{x}}_{k,a}^H & \Delta\mathbf{x}_k^T \end{array} \right]^H$: the tones 0 and $\frac{N}{2}$ each result in one real equation and one real-valued variable $\tilde{x}_{k,n}$; the $\frac{N}{2}-1$ (complex-conjugate) tones each add two complex conjugate equations and two complex conjugate variables $\tilde{x}_{k,n}$ and $\tilde{x}_{k,n}^*$, which correspond to two real equations and two real-valued variables $\Re\{\tilde{x}_{k,n}\}$ and $\Im\{\tilde{x}_{k,n}\}$; finally, there are L_b unknown TX difference terms $\Delta\mathbf{x}_k$. However, the cyclic prefix renders ν difference terms $\Delta x_{k,l}$ equal to zero and there are oftentimes unused tones and/or pilot tones, so that the actual number of unknowns is typically smaller than $N + L_b$.

If $L_b \leq \nu$, all L_b TX difference terms $\Delta\mathbf{x}_k$ vanish, due to the cyclic prefix ($x_{k,N-l} = x_{k,-l}$ for $l = 1, \ldots, \nu$, see (7.5)), and so the data model (7.9-7.10) becomes:

$$\boxed{\tilde{\mathbf{z}}_{k,N} = \tilde{\mathbf{A}}_{N,\mathrm{D}}\tilde{\mathbf{y}}_{k,N} + \mathcal{F}_N\mathbf{A}_\Delta\Delta\mathbf{y}_k - \left[\begin{array}{c} \mathbf{0} \\ \tilde{\mathbf{B}}_{p,\mathrm{D}} \end{array} \right] \tilde{\mathbf{x}}_{k,p} = \left[\begin{array}{c} \tilde{\mathbf{B}}_{a,\mathrm{D}} \\ \mathbf{0} \end{array} \right] \tilde{\mathbf{x}}_{k,a} + \mathcal{F}_N\check{\mathbf{n}}_k} \tag{7.13}$$

Now, only the term with RX difference terms $\Delta\mathbf{y}_k$ causes ISI/ICI.

7.2.1 Optimum L-ZF block equalization

If $L_b \leq \nu$, the number of equations N in (7.13) is always larger than or equal to the number of unknowns N_a. Provided that a necessary and sufficient condition (see further) is met, there exist one (if $N = N_a$) or multiple (if $N > N_a$) L-ZF block equalizers. The MMSE L-ZF block equalizer, i.e., with the lowest MSE among all L-ZF block equalizers, leads to the following L-ZF block estimate [38, 72, 152]:

$$\hat{\tilde{\mathbf{x}}}_{k,a}^{\text{L-ZF}} = \left(\underbrace{\left[\tilde{\mathbf{B}}_{a,\text{D}}^H \;\; \mathbf{0} \right] \left(\mathcal{F}_N \boldsymbol{\Sigma}_{\check{\mathbf{n}}}^2 \mathcal{F}_N^H \right)^{-1} \begin{bmatrix} \tilde{\mathbf{B}}_{a,\text{D}} \\ \mathbf{0} \end{bmatrix}}_{\{1\}} \right)^{-1} \underbrace{\left[\tilde{\mathbf{B}}_{a,\text{D}}^H \;\; \mathbf{0} \right] \left(\mathcal{F}_N \boldsymbol{\Sigma}_{\check{\mathbf{n}}}^2 \mathcal{F}_N^H \right)^{-1}}_{\{2\}} \tilde{\mathbf{z}}_{k,N} \tag{7.14}$$

where $\mathcal{F}_N \boldsymbol{\Sigma}_{\check{\mathbf{n}}}^2 \mathcal{F}_N^H$ is the autocorrelation matrix of the FD noise vector $\mathcal{F}_N \check{\mathbf{n}}_k$ with $\boldsymbol{\Sigma}_{\check{\mathbf{n}}}^2 = \mathcal{E}\left\{ \check{\mathbf{n}}_k \check{\mathbf{n}}_k^T \right\} = \mathbf{A}_{\text{T}} \mathcal{E}\left\{ \mathbf{n}_{k,-L_a:N-1} \mathbf{n}_{k,-L_a:N-1}^T \right\} \mathbf{A}_{\text{T}}^T$. In the derivations below, we assume that $\boldsymbol{\Sigma}_{\check{\mathbf{n}}}^2$ is non-singular, which holds true for broadband noise; a solution to narrowband RFI, which results in $\boldsymbol{\Sigma}_{\check{\mathbf{n}}}^2$ being of low-rnak, is considered in Section 7.4.3. The factors {1} and {2} in (7.14) can be simplified to:

$$\begin{aligned} \{1\} \quad & \left[\tilde{\mathbf{B}}_{a,\text{D}}^H \;\; \mathbf{0} \right] \left(\mathcal{F}_N \boldsymbol{\Sigma}_{\check{\mathbf{n}}}^2 \mathcal{F}_N^H \right)^{-1} \begin{bmatrix} \tilde{\mathbf{B}}_{a,\text{D}} \\ \mathbf{0} \end{bmatrix} = \tilde{\mathbf{B}}_{a,\text{D}}^H \mathcal{F}_a \left(\boldsymbol{\Sigma}_{\check{\mathbf{n}}}^2 \right)^{-1} \mathcal{F}_a^H \tilde{\mathbf{B}}_{a,\text{D}} \\ \{2\} \quad & \left[\tilde{\mathbf{B}}_{a,\text{D}}^H \;\; \mathbf{0} \right] \left(\mathcal{F}_N \boldsymbol{\Sigma}_{\check{\mathbf{n}}}^2 \mathcal{F}_N^H \right)^{-1} = \tilde{\mathbf{B}}_{a,\text{D}}^H \mathcal{F}_a \left(\boldsymbol{\Sigma}_{\check{\mathbf{n}}}^2 \right)^{-1} \left[\mathcal{F}_a^H \mid \mathcal{F}_p^H \right] \end{aligned} \tag{7.15}$$

where the last equality makes use of the fact that $\mathcal{F}_N = \left[\mathcal{F}_a^H \mid \mathcal{F}_p^H \right]^H$. Combining (7.15) and (7.14) leads to the **optimum L-ZF block estimate**:

$$\boxed{\hat{\tilde{\mathbf{x}}}_{k,a}^{\text{L-ZF}} = \left[\tilde{\mathbf{B}}_{a,\text{D}}^{-1} \mid \mathbf{M}_1 \right] \tilde{\mathbf{z}}_{k,N} = \tilde{\mathbf{B}}_{a,\text{D}}^{-1} \tilde{\mathbf{z}}_{k,a} + \mathbf{M}_1 \tilde{\mathbf{z}}_{k,p}} \tag{7.16}$$

with $\mathbf{M}_1$ a non-sparse $N_a \times N_p$ matrix:

$$\boxed{\mathbf{M}_1 = \tilde{\mathbf{B}}_{a,\text{D}}^{-1} \left(\mathcal{F}_a \left(\boldsymbol{\Sigma}_{\check{\mathbf{n}}}^2 \right)^{-1} \mathcal{F}_a^H \right)^{-1} \underbrace{\mathcal{F}_a \left(\boldsymbol{\Sigma}_{\check{\mathbf{n}}}^2 \right)^{-1} \mathcal{F}_p^H}_{\{1\}}} \tag{7.17}$$

and $\tilde{\mathbf{B}}_{a,\text{D}}^{-1}$ a diagonal matrix. It follows from (7.16) that a **necessary and sufficient condition** for the existence of the L-ZF block equalizer if $L_b \leq \nu$ requires that $\tilde{\mathbf{b}}_a$ does not have zero entries, i.e., the channel $H(z)$, and hence the numerator $B(z)$, does not have zeros on the N-point DFT grid at frequencies that correspond to the tones $\mathcal{S}_a$.

Using the definition of $\tilde{\mathbf{z}}_{k,N}$ (7.10), the **optimum L-ZF symbol estimate**

for tone n, $\hat{\tilde{x}}_{k,n}^{\mathrm{L-ZF}}$, is given by:

$$\hat{\tilde{x}}_{k,n}^{\mathrm{L-ZF}} = \underbrace{\left[\begin{array}{c|c|c|c} \tilde{b}_n^{-1}\mathcal{F}_n\mathbf{A}_\Delta + \mathbf{m}_{n,1}\mathcal{F}_p\mathbf{A}_\Delta & \mathbf{m}_{n,1}\tilde{\mathbf{A}}_{p,\mathrm{D}} & -\mathbf{m}_{n,1}\tilde{\mathbf{B}}_{p,\mathrm{D}} & \tilde{b}_n^{-1}\tilde{a}_n \end{array}\right]}_{\left(\mathbf{v}_n^{\mathrm{L-ZF}}\right)^T} \left[\begin{array}{c} \Delta\mathbf{y}_k \\ \tilde{\mathbf{y}}_{k,p} \\ \tilde{\mathbf{x}}_{k,p} \\ \tilde{y}_{k,n} \end{array}\right] \tag{7.18}$$

where $\tilde{\mathbf{A}}_{p,\mathrm{D}} = \mathrm{diag}(\tilde{\mathbf{a}}_p)$ and $\tilde{\mathbf{a}}_p$ is obtained from $\tilde{\mathbf{a}}_N$ by selecting the entries that correspond to the pilot tone set $\mathcal{S}_p$, where $\mathbf{m}_{n,1}$ is the row of $\mathbf{M}_1$ that corresponds to tone $n \in \mathcal{S}_a$ and where $\mathbf{v}_n^{\mathrm{L-ZF}}$ is the optimum L-ZF equalizer for tone n.

7.2.2 Discussion and interpretation

One can effectively say that *the optimum L-ZF equalizer for tone n,* $\mathbf{v}_n^{\mathrm{L-ZF}}$ *in (7.18), is a PTEQ*, as it decouples the equalization per active tone n: the $(L_a + 1 + 2N_p)$-tap PTEQ $\mathbf{v}_n^{\mathrm{L-ZF}}$ linearly combines one single tone-dependent DFT output $\tilde{y}_{k,n}$ with tone-independent PTEQ inputs that are common for all tones, namely L_a real-valued RX difference terms $\Delta\mathbf{y}_k$, the N_p DFT outputs of the pilot tones $\tilde{\mathbf{y}}_{k,p}$ and the N_p pilot symbols $\tilde{\mathbf{x}}_{k,p}$. The overall computational and memory cost is then dominated by a term that depends linearly on N_a, L_a and N_p (see below).

If $N = N_a$ and $N_p = 0$, i.e., the number of equations and unknowns in (7.13) is equal, hence there are no pilot tones, $\mathbf{v}_n^{\mathrm{L-ZF}}$ in (7.18) reduces to an (L_a+1)-tap L-ZF PTEQ, which linearly combines the n-th DFT output with L_a RX difference terms $\Delta\mathbf{y}_k$:

$$\boxed{\hat{\tilde{x}}_{k,n}^{\mathrm{L-ZF}} = \tilde{b}_n^{-1}\tilde{z}_{k,n} = \underbrace{\left[\begin{array}{c|c} \tilde{b}_n^{-1}\mathcal{F}_n\mathbf{A}_\Delta & \tilde{b}_n^{-1}\tilde{a}_n \end{array}\right]}_{\left(\mathbf{v}_n^{\mathrm{L-ZF}}\right)^T} \left[\begin{array}{c} \Delta\mathbf{y}_k \\ \tilde{y}_{k,n} \end{array}\right]} \tag{7.19}$$

The first L_a coefficients of the PTEQ $\mathbf{v}_n^{\mathrm{L-ZF}}$ in (7.19) compensate for the ISI/ICI, caused by the denominator $A(z)$ of the IIR channel, while the last coefficient compensates for the amplitude and phase distortion $\frac{\tilde{b}_n}{\tilde{a}_n}$; the CP takes care of the time dispersion by the numerator $B(z)$, so that $B(z)$ does not cause ISI/ICI. In fact, (7.19) is nothing but an alternative implementation of the early TEQ design of [29], which is based on an IIR channel identification of $H(z)$ in (7.1): the TEQ is then an FIR filter with transfer function $A(z)$ and the FEQs compensate for the discrete frequency response $\tilde{b}_n$ of $B(z)$, provided that $L_b \leq \nu$. The importance of the alternative formulation (7.19) lies in its close relation with the original PTEQ (7.12): *in the noiseless case, the L-ZF PTEQ* $\mathbf{v}_n^{\mathrm{L-ZF}}$ *(7.19) is equivalent to the T-tap PTEQ* $\mathbf{v}_n^{\mathrm{PTEQ}}$ *in (7.12), provided that* $L_b \leq \nu$ *and* $L_a + 1 \leq T$.

If $N > N_a$, (7.19) is a valid L-ZF PTEQ, be it that it does not provide the *MMSE* L-ZF symbol estimate: (7.18) suggests that the MMSE L-ZF PTEQ should have the DFT outputs of the pilot tones and the pilot symbols as additional, common inputs. However, it can be shown that *the MMSE L-ZF PTEQ (7.18) only loosely depends on the pilot tones and reduces for $N \to \infty$ to the simplified L-ZF PTEQ (7.19).* The reasoning, which is developed below, is based on the asymptotic equivalence of Toeplitz and circulant matrices, as described in [53]. The $N \times N$ noise autocorrelation matrix $\mathbf{\Sigma}^2_{\check{\mathbf{n}}}$, which shows up in (7.17), is Toeplitz. If only a band of d diagonals around the main diagonal of $\mathbf{\Sigma}^2_{\check{\mathbf{n}}}$ is significantly different from zero, with $d \ll N$, $\mathbf{\Sigma}^2_{\check{\mathbf{n}}}$ can be well approximated by a circulant matrix $\mathbf{\Sigma}^2_{\check{\mathbf{n}},\mathrm{C}}$. It is said that $\mathbf{\Sigma}^2_{\check{\mathbf{n}}}$ and $\mathbf{\Sigma}^2_{\check{\mathbf{n}},\mathrm{C}}$ are asymptotically equivalent, i.e., for $N \to \infty$, $\mathbf{\Sigma}^2_{\check{\mathbf{n}}} = \mathbf{\Sigma}^2_{\check{\mathbf{n}},\mathrm{C}}$, which will be denoted as $\mathbf{\Sigma}^2_{\check{\mathbf{n}}} \sim \mathbf{\Sigma}^2_{\check{\mathbf{n}},\mathrm{C}}$ [53]. For larger N, smaller denominator order L_a and less coloured noise (i.e., with a shorter support of the noise autocorrelation function around lag zero), d/N is smaller and the approximation is better. Invoking a DFT-based decomposition, $\mathbf{\Sigma}^2_{\check{\mathbf{n}},\mathrm{C}} = \mathcal{F}_N^H \mathbf{\Sigma}^2_{N,\tilde{\check{\mathbf{n}}},\mathrm{D}} \mathcal{F}_N$, where $\mathbf{\Sigma}^2_{N,\tilde{\check{\mathbf{n}}},\mathrm{D}}$ is diagonal with the DFT of the first column of $\mathbf{\Sigma}^2_{\check{\mathbf{n}},\mathrm{C}}$ on the diagonal, $\mathbf{M}_1$ in (7.17) tends to zero for $N \to \infty$ because the following asymptotical equivalence holds true for the factor $\{1\}$ in (7.17):

$$\begin{aligned}
\mathcal{F}_a \left(\mathbf{\Sigma}^2_{\check{\mathbf{n}}}\right)^{-1} \mathcal{F}_p^H &\sim \mathcal{F}_a \left(\mathbf{\Sigma}^2_{\check{\mathbf{n}},\mathrm{C}}\right)^{-1} \mathcal{F}_p^H \\
&= \mathcal{F}_a \mathcal{F}_N^H \left(\mathbf{\Sigma}^2_{N,\tilde{\check{\mathbf{n}}},\mathrm{D}}\right)^{-1} \mathcal{F}_N \mathcal{F}_p^H \qquad (7.20) \\
&= \begin{bmatrix} \mathbf{I}_{N_a} & \mathbf{0}_{N_a \times N_p} \end{bmatrix} \left(\mathbf{\Sigma}^2_{N,\tilde{\check{\mathbf{n}}},\mathrm{D}}\right)^{-1} \begin{bmatrix} \mathbf{0}_{N_a \times N_p} \\ \mathbf{I}_{N_p} \end{bmatrix} = \mathbf{0}_{N_a \times N_p}
\end{aligned}$$

Hence, for $N \to \infty$, $\mathbf{M}_1$ becomes an all-zero matrix and the MMSE L-ZF PTEQ in (7.18) reduces to the simpler L-ZF PTEQ of (7.19).

The **optimum L-MMSE block estimate** is obtained from the L-ZF block estimate (7.16) as [72, 152]:

$$\begin{aligned}
\hat{\tilde{\mathbf{x}}}^{\mathrm{L-MMSE}}_{k,a} &= \left(\mathbf{I}_{N_a} + \left(\mathbf{\Sigma}^2_{a,\tilde{\mathbf{x}}} \begin{bmatrix} \tilde{\mathbf{B}}^H_{a,\mathrm{D}} & \mathbf{0} \end{bmatrix} \left(\mathcal{F}_N \mathbf{\Sigma}^2_{\check{\mathbf{n}}} \mathcal{F}_N^H\right)^{-1} \begin{bmatrix} \tilde{\mathbf{B}}_{a,\mathrm{D}} \\ \mathbf{0} \end{bmatrix}\right)^{-1}\right)^{-1} \hat{\tilde{\mathbf{x}}}^{\mathrm{L-ZF}}_{k,a} \\
&\overset{(7.15)}{=} \left(\mathbf{I}_{N_a} + \left(\underbrace{\mathbf{\Sigma}^2_{a,\tilde{\mathbf{x}}} \tilde{\mathbf{B}}^H_{a,\mathrm{D}} \overbrace{\mathcal{F}_a \left(\mathbf{\Sigma}^2_{\check{\mathbf{n}}}\right)^{-1} \mathcal{F}_a^H}^{\{1\}} \tilde{\mathbf{B}}_{a,\mathrm{D}}}_{\mathbf{M}_2}\right)^{-1}\right)^{-1} \hat{\tilde{\mathbf{x}}}^{\mathrm{L-ZF}}_{k,a} \qquad (7.21)
\end{aligned}$$

where, under the assumption of independent TX symbols $\tilde{\mathbf{x}}_{k,a}$, the autocorrelation matrix $\mathbf{\Sigma}^2_{a,\tilde{\mathbf{x}}} = \mathcal{E}\left\{\tilde{\mathbf{x}}_{k,a} \tilde{\mathbf{x}}^H_{k,a}\right\}$ is diagonal, with diagonal elements equal to the TX power $\sigma^2_{n,\tilde{x}}$ on the tones $\mathcal{S}_a$. The optimum L-MMSE block estimate (7.21) does in general not allow for a decoupling per tone n: the matrix $\mathbf{M}_2$

in (7.21) is not diagonal, due to the non-diagonal factor $\{1\}$ in (7.21). As a consequence, the estimate for tone n, $\hat{\tilde{x}}_{k,n}^{\mathrm{L-MMSE}}$, depends on all DFT outputs $\tilde{\mathbf{y}}_{k,N}$ via the L-ZF block estimate $\hat{\tilde{\mathbf{x}}}_{k,a}^{\mathrm{L-ZF}}$ and the computational and memory cost is $\mathcal{O}(N_a^2)$. However, invoking again the asymptotic equivalence $\mathbf{\Sigma}_{\check{\mathbf{n}}}^2 \sim \mathbf{\Sigma}_{\check{\mathbf{n}},\mathrm{C}}^2$ and the DFT-based decomposition $\mathbf{\Sigma}_{\check{\mathbf{n}},\mathrm{C}}^2 = \mathcal{F}_N^H \mathbf{\Sigma}_{N,\check{\tilde{\mathbf{n}}},\mathrm{D}}^2 \mathcal{F}_N$, $\mathbf{M}_2$ appears asymptotically equivalent with a diagonal matrix. Hence, *for $N \to \infty$, the optimum L-MMSE block equalizer is decoupled per tone and reduces to the T-tap PTEQ $\mathbf{v}_n^{\mathrm{PTEQ}}$ in (7.12), provided that $L_b \leq \nu$ and $L_a + 1 \leq T$*. For finite N, the optimality of the PTEQ (7.12) depends on $\frac{d}{N}$, hence on the noise colour and on L_a.

7.3 DMT equalization of an IIR channel with $L_b > \nu$

If $L_b > \nu$, not all L_b TX difference terms in (7.9) vanish. There are ν difference terms $\Delta\mathbf{x}_k$ equal to zero because of the cyclic prefix: $\Delta x_{k,-l} = x_{k,-l} - x_{k,N-l} = 0$ with $l = 1, \ldots, \nu$. The remaining $L_b - \nu$ non-zero TX difference terms cause ISI/ICI. We denote the vector of non-zero TX difference terms as $\Delta\underline{\mathbf{x}}_k = \left[\begin{array}{ccc} \Delta x_{k,-L_b} & \cdots & \Delta x_{k,-\nu-1} \end{array} \right]^T$. $\underline{\mathbf{B}}_\Delta$ denotes the corresponding $N \times (L_b - \nu)$ submatrix of $\mathbf{B}_\Delta$:

$$\underline{\mathbf{B}}_\Delta = \left[\begin{array}{ccc} b_{L_b} & \cdots & b_{\nu+1} \\ \vdots & \ddots & \vdots \\ 0 & 0 & b_{L_b} \\ \hline \multicolumn{3}{c}{\mathbf{0}_{(N-L_b+\nu)\times(L_b-\nu)}} \end{array} \right] \tag{7.22}$$

The data model (7.9) then reduces to:

$$\boxed{\tilde{\mathbf{z}}_{k,N} = \left[\begin{array}{c|c} \tilde{\mathbf{B}}_{a,\mathrm{D}} & \mathcal{F}_N \underline{\mathbf{B}}_\Delta \\ \hline \mathbf{0}_{N_p \times N_a} & \end{array} \right] \left[\begin{array}{c} \tilde{\mathbf{x}}_{k,a} \\ \Delta\underline{\mathbf{x}}_k \end{array} \right] + \mathcal{F}_N \check{\mathbf{n}}_k} \tag{7.23}$$

7.3.1 Optimum L-ZF block equalization

The data model (7.23) forms a set of N equations in $N_a + (L_b - \nu)$ unknowns $\left[\begin{array}{cc} \tilde{\mathbf{x}}_{k,a}^H & \Delta\underline{\mathbf{x}}_k^T \end{array} \right]^H$. A necessary condition for the existence of an L-ZF block equalizer for (7.23) is then given by $N \geq N_a + (L_b - \nu)$ or $N - N_a = \boxed{N_p \geq L_b - \nu}$. Hence, the insufficient *time-domain* TX redundancy in the form of a CP can be compensated for by *frequency-domain* TX redundancy in the form of pilot (and unused) tones. At this point, we should remind the reader that we assume baseband transmission, so each (pilot) tone goes together with

a complex conjugate (pilot) tone, hence $\frac{N_p}{2}$ pairs of (complex conjugate) pilot tones suffice for L-ZF equalization. In [125, 126, 127], a similar L-ZF condition has been derived: for an *FIR channel* of order L, the authors conclude that $L-\nu$ unused tones are required, without considering the particular case of baseband transmission; pilot tones are claimed to result in a slightly more stringent condition (namely $L-\nu+1$ pilot tones are required), while we have shown here that pilot tones and unused tones can be treated in the same way and give rise to the same L-ZF condition.

If $N_p \geq L_b-\nu$, there exist again one (if $N_p = L_b-\nu$) or multiple (if $N_p > L_b-\nu$) L-ZF block equalizers. The MMSE L-ZF block equalizer leads to the following block estimate [38, 72, 152]:

$$\begin{bmatrix} \hat{\tilde{\mathbf{x}}}_{k,a}^{\text{L-ZF}} \\ \widehat{\Delta \underline{\mathbf{x}}}_k^{\text{L-ZF}} \end{bmatrix} = \underbrace{\left(\left[\begin{array}{c|c} \tilde{\mathbf{B}}_{a,\text{D}}^H & \mathbf{0} \\ \hline \underline{\mathbf{B}}_{\Delta}^T \mathcal{F}_N^H & \end{array} \right] \left(\mathcal{F}_N \boldsymbol{\Sigma}_{\tilde{\mathbf{n}}}^2 \mathcal{F}_N^H \right)^{-1} \left[\begin{array}{c|c} \tilde{\mathbf{B}}_{a,\text{D}} & \\ \hline \mathbf{0} & \mathcal{F}_N \underline{\mathbf{B}}_{\Delta} \end{array} \right] \right)}_{\{1\}}^{-1} \times \underbrace{\left[\begin{array}{c|c} \tilde{\mathbf{B}}_{a,\text{D}}^H & \mathbf{0} \\ \hline \underline{\mathbf{B}}_{\Delta}^T \mathcal{F}_N^H & \end{array} \right] \left(\mathcal{F}_N \boldsymbol{\Sigma}_{\tilde{\mathbf{n}}}^2 \mathcal{F}_N^H \right)^{-1}}_{\{2\}} \tilde{\mathbf{z}}_{k,N} \tag{7.24}$$

The derivation in the appendix shows that (7.24) leads naturally to a two-step procedure, where $\Delta \underline{\mathbf{x}}_k$ is estimated in a first step and used in a second step to estimate $\tilde{\mathbf{x}}_{k,a}$.

1. The TX difference terms $\Delta \underline{\mathbf{x}}_k$ can be estimated first from:

$$\underline{\mathbf{B}}_{\Delta} \widehat{\Delta \underline{\mathbf{x}}}_k^{\text{L-ZF}} = \left[\begin{array}{c} \mathbf{M}_4 \\ \hline \mathbf{0}_{(N-L_b+\nu)\times N_p} \end{array} \right] \tilde{\mathbf{z}}_{k,p} \tag{7.25}$$

   where $\mathbf{M}_4$ is the following non-sparse $(L_b-\nu) \times N_p$ matrix:

$$\mathbf{M}_4 = \left[\begin{array}{c|c} \mathbf{I}_{L_b-\nu} & \mathbf{0} \end{array} \right] \mathbf{M}_3^{-1} \left[\begin{array}{c} \mathbf{I}_{L_b-\nu} \\ \hline \mathbf{0}^T \end{array} \right] \left[\begin{array}{c|c} \mathbf{I}_{L_b-\nu} & \mathbf{0} \end{array} \right] \mathbf{M}_3 \mathcal{F}_p^H \tag{7.26}$$

   with $\mathbf{M}_3 = \left(\boldsymbol{\Sigma}_{\tilde{\mathbf{n}}}^2\right)^{-1} - \left(\boldsymbol{\Sigma}_{\tilde{\mathbf{n}}}^2\right)^{-1} \mathcal{F}_a^H \left(\mathcal{F}_a \left(\boldsymbol{\Sigma}_{\tilde{\mathbf{n}}}^2\right)^{-1} \mathcal{F}_a^H \right)^{-1} \mathcal{F}_a \left(\boldsymbol{\Sigma}_{\tilde{\mathbf{n}}}^2\right)^{-1}$ an $N \times N$ matrix (which can be decomposed into a concatenation of a noise whitening with $\left(\boldsymbol{\Sigma}_{\tilde{\mathbf{n}}}^2\right)^{-1/2}$, a projection on the orthogonal complement of $\left(\boldsymbol{\Sigma}_{\tilde{\mathbf{n}}}^2\right)^{-1/2} \mathcal{F}_a^H$ and another noise whitening) and with the all-zero matrix $\mathbf{0}$ being of size $(L_b-\nu) \times (N-L_b+\nu)$. The L-ZF estimate $\widehat{\Delta \underline{\mathbf{x}}}_k^{\text{L-ZF}}$ is thus a linear combination of $\tilde{\mathbf{z}}_{k,p}$, which is in itself a linear combination of $\tilde{\mathbf{y}}_{k,p}$, $\tilde{\mathbf{x}}_{k,p}$ and $\Delta \mathbf{y}_k$ (see (7.10)). Information about the ISI/ICI, caused by the non-zero TX difference terms $\Delta \underline{\mathbf{x}}_k$, is extracted from the FD TX redundancy (pilot tones) and the RX difference terms.

2. The estimation of $\hat{\tilde{\mathbf{x}}}_{k,a}$ can now make use of $\widehat{\Delta\underline{\mathbf{x}}}_k^{\mathrm{L-ZF}}$ and is shown in the appendix to lead to the following **optimum L-ZF block estimate**:

$$\boxed{\hat{\tilde{\mathbf{x}}}_{k,a}^{\mathrm{L-ZF}} = \left[\begin{array}{c|c} \tilde{\mathbf{B}}_{a,\mathrm{D}}^{-1} & \mathbf{M}_1 \end{array}\right] \left(\tilde{\mathbf{z}}_{k,N} - \mathcal{F}_N \underline{\mathbf{B}}_\Delta \widehat{\Delta\underline{\mathbf{x}}}_k^{\mathrm{L-ZF}}\right)} \tag{7.27}$$

with $\mathbf{M}_1$ defined in (7.17), or:

$$\boxed{\hat{\tilde{\mathbf{x}}}_{k,a}^{\mathrm{L-ZF}} = \tilde{\mathbf{B}}_{a,\mathrm{D}}^{-1}\tilde{\mathbf{z}}_{k,a} + \mathbf{M}_5\tilde{\mathbf{z}}_{k,p}} \tag{7.28}$$

where $\mathbf{M}_5 = \mathbf{M}_1 + \left(\tilde{\mathbf{B}}_{a,\mathrm{D}}^{-1}\mathcal{F}_a + \mathbf{M}_1\mathcal{F}_p\right)\left[\begin{array}{c} \mathbf{M}_4 \\ \hline \mathbf{0} \end{array}\right]$ is a non-sparse $N_a \times N_p$ matrix. The **optimum L-ZF symbol estimate for tone** n, $\hat{\tilde{x}}_{k,n}^{\mathrm{L-ZF}}$, is then a linear combination of $\tilde{y}_{k,n}$, with the common inputs $\tilde{\mathbf{y}}_{k,p}$, $\tilde{\mathbf{x}}_{k,p}$ and $\Delta\mathbf{y}_k$:

$$\hat{\tilde{x}}_{k,n}^{\mathrm{L-ZF}} = \underbrace{\left[\begin{array}{c|c|c|c} \tilde{b}_n^{-1}\mathcal{F}_n\mathbf{A}_\Delta + \mathbf{m}_{n,5}\mathcal{F}_p\mathbf{A}_\Delta & \mathbf{m}_{n,5}\tilde{\mathbf{A}}_{p,\mathrm{D}} & -\mathbf{m}_{n,5}\tilde{\mathbf{B}}_{p,\mathrm{D}} & \tilde{b}_n^{-1}\tilde{a}_n \end{array}\right]}_{\left(\mathbf{v}_n^{\mathrm{L-ZF}}\right)^T} \left[\begin{array}{c} \Delta\mathbf{y}_k \\ \tilde{\mathbf{y}}_{k,p} \\ \tilde{\mathbf{x}}_{k,p} \\ \tilde{y}_{k,n} \end{array}\right] \tag{7.29}$$

where $\mathbf{m}_{n,5}$ is the row of $\mathbf{M}_5$ that corresponds to tone $n \in \mathcal{S}_a$.

It follows from the above derivation that the **necessary and sufficient conditions** for the existence of an L-ZF equalizer if $L_b > \nu$ are given by:

1. $N_p \geq L_b - \nu$;
2. $\tilde{\mathbf{b}}_a$ does not have zero entries, i.e., the channel $H(z)$, and hence the numerator $B(z)$, does not have zeros on the N-point DFT grid at frequencies that correspond to the tones $\mathcal{S}_a$.

7.3.2 Discussion and interpretation

The L-ZF block estimates $\hat{\tilde{\mathbf{x}}}_{k,a}^{\mathrm{L-ZF}}$ in (7.27-7.28) for $L_b > \nu$ and in (7.16-7.17) for $L_b \leq \nu$ look very similar, as they both reveal a linear combination of $\tilde{y}_{k,n}$, with the common inputs $\tilde{\mathbf{y}}_{k,p}$, $\tilde{\mathbf{x}}_{k,p}$ and $\Delta\mathbf{y}_k$. The difference is in the compensation for the ISI/ICI from $\mathcal{F}_N\underline{\mathbf{B}}_\Delta\Delta\underline{\mathbf{x}}_k$ (see (7.27)) using the L-ZF estimate $\widehat{\Delta\underline{\mathbf{x}}}_k^{\mathrm{L-ZF}}$ in (7.25). As a consequence, the matrices $\mathbf{M}_1$ in (7.17) and $\mathbf{M}_5$ in (7.28) are considerably different. We have shown in Section 7.2.2 that $\mathbf{M}_1$ tends to an all-zero matrix for $N \to \infty$, hence, for the case $L_b \leq \nu$, $\hat{\tilde{\mathbf{x}}}_{k,a}^{\mathrm{L-ZF}}$ only loosely depends on $\tilde{\mathbf{y}}_p$ and $\tilde{\mathbf{x}}_p$. For $N \to \infty$, $\mathbf{M}_5$ tends to $\tilde{\mathbf{B}}_{a,\mathrm{D}}^{-1}\mathcal{F}_a\left[\begin{array}{c} \mathbf{M}_4 \\ \hline \mathbf{0} \end{array}\right]$, which is non-zero

as $\mathbf{M}_4$ does not tend to zero for $N \to \infty$. Still, *the optimum L-ZF equalizer for tone n,* $\mathbf{v}_n^{\mathrm{L-ZF}}$ *in (7.29), is a PTEQ*, as it decouples the equalization per active tone n: the complex-valued $(L_a + 1 + 2N_p)$-tap PTEQ $\mathbf{v}_n^{\mathrm{L-ZF}}$ linearly combines one tone-dependent input $\tilde{y}_{k,n}$ and the L_a common, real-valued inputs $\Delta\mathbf{y}_k$ with additional, common inputs $\tilde{\mathbf{y}}_{k,p}$ and $\tilde{\mathbf{x}}_{k,p}$, exploiting the FD TX redundancy (pilot tones).

It is important to note that these additional inputs come in *pairs*: each DFT output of a pilot tone, $\tilde{y}_{k,m}$ with $m \in \mathcal{S}_p$, appears together with the corresponding pilot symbol, $\tilde{x}_{k,m}$. This allows the PTEQ to (implicitly) remove the contribution of $\tilde{x}_{k,m}$ from $\tilde{y}_{k,m}$, so that only the ISI/ICI, introduced by the $L_b - \nu$ non-zero TX difference terms $\Delta\mathbf{x}_k$, and noise are left. The ISI/ICI information then allows to enhance the equalization of the active tones $\mathcal{S}_a$. Of course, the DFT output of an *unused* tone only has ISI/ICI and noise, as then $\tilde{x}_{k,m} = 0$. This result is a generalization of the results obtained in [125, 126, 127]: there, it has been shown that an L-ZF equalizer for tone n in case of an FIR channel of order L is obtained by linearly combining the n-th DFT output with $L - \nu$ DFT outputs of unused tones, and is, as such, an alternative for a TEQ-based receiver. Here, we show that both pilot and unused tones can be incorporated, as unused tones are a special case of pilot tones; moreover, we present the exploitation of FD TX redundancy as an extension of the capability of the L-ZF PTEQ (7.19) to eliminate ISI/ICI, rather than an equalization solution on its own.

The optimum L-MMSE block estimate differs from the L-ZF block estimate (7.24) in that the factor denoted by $\{1\}$ now contains a second term, which depends on the autocorrelation matrix of $\left[\begin{array}{cc} \tilde{\mathbf{x}}_{k,a}^H & \Delta\underline{\mathbf{x}}_k^T \end{array}\right]^H$ (see (7.23)). Due to his extra term, the L-MMSE block equalizer does not lead to an equalizer that is decoupled per tone.

7.4 Low-complexity extensions of the L-MMSE PTEQ

Based on the optimum L-ZF block equalizers derived in Section 7.2 and 7.3, we present in this section low-complexity extensions of the original L-MMSE PTEQ (7.12). In Section 7.4.1, a linear PTEQ (L-PTEQ) extension is presented that exploits the FD TX redundancy as offered by pilot (and unused) tones. In Section 7.4.2, a decision-feedback PTEQ (DF-PTEQ) extension is presented, which is based on the observation that the decision on a FD data symbol can be treated in the same way as the a priori knowledge of a pilot symbol. *A particular MMSE PTEQ design, based on a CP length* ν, $T - 1$ *RX difference terms* $\Delta\mathbf{y}_k$, N_p *pilot tones and* N_f *feedback tones then implicitly assumes an IIR channel model with* $L_b = \nu + N_p + N_f$ *and* $L_a = T - 1$. *Moreover, both*

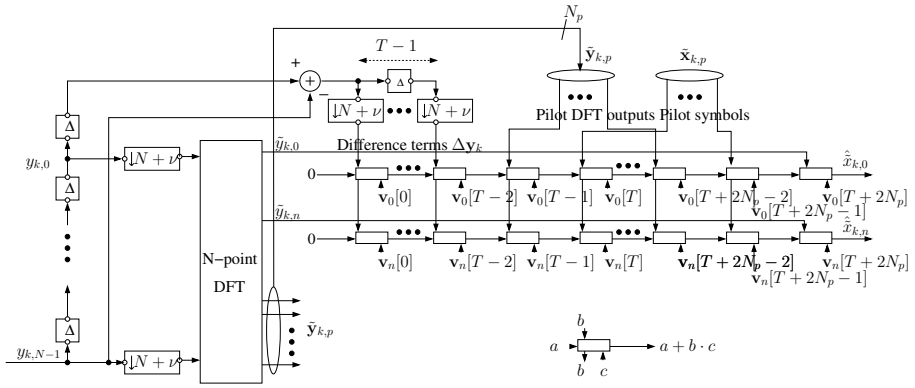


Figure 7.2: Principle scheme of the L-PTEQ extension.

the L-PTEQ and DF-PTEQ extension can be designed using a modified version of the RLS-based adaptive algorithm, presented in Section 3.4.2. Section 7.4.3 explains why the L-PTEQ and DF-PTEQ extensions increase the robustness of a DMT receiver to RFI.

7.4.1 The L-PTEQ extension

Based on the L-ZF PTEQs (7.18) and (7.29), we propose the following **L-PTEQ extension** for (7.12), which takes the DFT outputs on the pilot tones $\tilde{\mathbf{y}}_{k,p}$, as well as the pilot symbols $\tilde{\mathbf{x}}_{k,p}$, as additional inputs:

$$\boxed{\mathbf{v}_n^{\mathrm{L-PTEQ}} = \arg\min_{\mathbf{v}_n} \mathcal{E}\left\{\left|\begin{bmatrix} \Delta\mathbf{y}_k^T & \tilde{\mathbf{y}}_{k,p}^T & \tilde{\mathbf{x}}_{k,p}^T & \tilde{y}_{k,n} \end{bmatrix}\mathbf{v}_n - \tilde{x}_{k,n}\right|^2\right\}} \tag{7.30}$$

The principle scheme is depicted in **Figure 7.2**. The RLS-based PTEQ algorithm (3.75-3.76), described in Section 3.4.2, can be extended in a straightforward way to solve (7.30) with the additional, common inputs $\tilde{\mathbf{y}}_{k,p}$ and $\tilde{\mathbf{x}}_{k,p}$ in the same way as the RX difference terms $\Delta\mathbf{y}_k$. The common tone-independent part $\mathbf{S}_\Delta$ in the inverse transpose of the Cholesky factor, $\mathbf{S}_n$, of $\mathbf{\Sigma}_{n,\mathbf{z}}^2$ in (3.77) should be replaced with a tone-independent matrix $\mathbf{S}_{\Delta,p}$ such that:

$$\left(\mathcal{E}\left\{\begin{bmatrix} \Delta\mathbf{y}_k \\ \tilde{\mathbf{y}}_{k,p}^* \\ \tilde{\mathbf{x}}_{k,p}^* \end{bmatrix}\begin{bmatrix} \Delta\mathbf{y}_k^T & \tilde{\mathbf{y}}_{k,p}^T & \tilde{\mathbf{x}}_{k,p}^T \end{bmatrix}\right\}\right)^{-1} = \mathbf{S}_{\Delta,p}^H\mathbf{S}_{\Delta,p} \tag{7.31}$$

Whereas we have assumed until now that all available FD TX redundancy are exploited, it is in fact only useful to exploit pilot and unused tones that have a sufficiently high ISI/ICI-to-noise ratio (INR). As will be argued below, it then

typically holds in an ADSL scenario that the actual number of exploited pilot (and unused) tones obeys $N_p < N - N_a$. Some rules of thumb can be devised regarding which TD and FD TX redundancy to exploit.

- In ADSL, the CP length is standardized to be 32 samples, see Example 2.5. However, the number of non-zero TX difference terms $\Delta\underline{\mathbf{x}}_k$, $L_b - \nu$, hence the CP length, affects the ISI/ICI level and the INR: a shorter CP will result in a higher ISI/ICI level, hence a higher INR. It turns out (see Section 7.6) that it can be beneficial to increase the ISI/ICI level by reducing the CP length, e.g., to 16 samples, as this renders the exploitation of FD TX redundancy more effective. In fact, by reducing the CP length and using pilot and unused tones instead, *TD TX redundancy (CP overhead) is exchanged for FD TX redundancy (pilot and unused tones).*

- One could introduce FD TX redundancy by turning off one or more tones, be it that this results in capacity loss that is not necessarily recovered by the enhanced equalization. It is therefore often preferred to make use of already available pilot and unused tones. E.g., in FDD ADSL transmission, the available tones are assigned either to upstream or downstream with some unused guard tones (e.g., $n = 33, \ldots, 37$) in between. Hence, in downstream, the lower tones, up to tone 37, are unused. However, most of these tones are contaminated, e.g., by the echo of the upstream signal, and only a few of them are useful. Other candidates are tones that are unused because of an insufficient SNR caused by a channel zero.

- Through extensive simulations, we have observed (see Section 7.6) that there is no need to incorporate all available pilot and unused tones: only a few, well-chosen pilot and unused tones suffice to attain good performance at a low complexity. Also, performance improves with increasing interspacing between the pilot/unused tones: the ISI/ICI on tones that lie close together is correlated, hence it is better to choose tones that are farther apart and less coherent.

- It has been observed in [98] that, in an ADSL context, the front-end filtering (e.g., to separate upstream and downstream transmission), rather than the transmission channel itself, is oftentimes the main cause of ISI/ICI; ISI/ICI then primarily shows up near the transition band of the front-end filters, see Section 2.2.4. In the simulations of Section 7.6, we will take this into account when choosing $\mathcal{S}_p$ and $\mathcal{S}_u$.

Remark 7.4 As we deal with baseband transmission, both $\tilde{\mathbf{y}}_{k,p}$ and $\tilde{\mathbf{x}}_{k,p}$ have complex conjugate entries (e.g., $\tilde{y}_{k,m}$ and $\tilde{y}^*_{k,m}$ with $m \in \mathcal{S}_p$), which are linearly combined using complex-valued coefficients (e.g., $\mathbf{v}_n[i]\tilde{y}_{k,m} + \mathbf{v}_n[j]\tilde{y}^*_{k,m}$). One can save on computations (two multiplications per complex conjugate

pair of inputs) by linearly combining the real and imaginary part instead (i.e., $(\mathbf{v}_n[i] + \mathbf{v}_n[j])\,\Re\{\tilde{y}_{k,m}\} + j\,(\mathbf{v}_n[i] - \mathbf{v}_n[j])\,\Im\{\tilde{y}_{k,m}\}$). In the sequel, we keep the notation based on the complex-valued variables $\tilde{\mathbf{y}}_{k,p}$ and $\tilde{\mathbf{x}}_{k,p}$ for the sake of conciseness. □

In baseband transmission, only half of the N_a active tones need to be demodulated (the other tones are complex conjugate). The overall memory cost then amounts to $\frac{N_a}{2}(L_a + 1 + 2N_p)$ complex-valued equalizer coefficients $\mathbf{v}_n$, while the computational cost amounts to $N_a(L_a + 2 + 2N_p)$ real multiplications per DMT symbol. If N_u unused tones are incorporated, the overall memory cost amounts to $\frac{N_a}{2}(L_a + 1 + 2N_p + N_u)$ complex-valued coefficients and the computational cost amounts to $N_a(L_a + 2 + 2N_p + N_u)$ real multiplications per DMT symbol.

7.4.2 The DF-PTEQ extension

As argued in the previous section, the number of useful pilot and unused tones is often limited, e.g., because of a too low ISI/ICI level. On the other hand, there could be active data-carrying tones that have a high ISI/ICI level. A symbol decision on such an active tone can then be treated in the same way as the a priori knowledge of a pilot symbol: the ISI/ICI in the DFT output of the considered active tone can again be exploited to enhance the equalization of the remaining active tones. The idea is then to feed back the symbol decisions of a few well-chosen tones within the DMT symbol and include the corresponding DFT outputs of these tones to use them in the very same way as pilot tones and symbols. Similar rules of thumb as already given for pilot and unused tones apply for the choice of feedback tones. Of course, the L-PTEQ and DF-PTEQ extensions can be combined.

Denoting the DFT outputs and symbol decisions on the set of N_f (complex conjugate) feedback tones $\mathcal{S}_f$ by $\tilde{\mathbf{y}}_{k,f}$ and $\hat{\tilde{\mathbf{x}}}_{k,f}$, respectively, a **decision-feedback (DF) PTEQ extension** is then based on the following MMSE design criterion:

$$\boxed{\mathbf{v}_n^{\mathrm{DF-PTEQ}} = \arg\min_{\mathbf{v}_n} \mathcal{E}\left\{\left|\begin{bmatrix} \Delta\mathbf{y}_k^T & \tilde{\mathbf{y}}_{k,f}^T & \hat{\tilde{\mathbf{x}}}_{k,f}^T & \tilde{y}_{k,n} \end{bmatrix}\mathbf{v}_n - \tilde{x}_{k,n}\right|^2\right\}} \quad (7.32)$$

In order to avoid the need for an iterative solution method, (7.32) is only applied to the tones $n \in \mathcal{S}_a \setminus \mathcal{S}_f$. Ignoring for simplicity the complex conjugate tones, the equalization of the tones n in $\mathcal{S}_f$ is done serially, based on:

$$\min_{\mathbf{v}_n} \mathcal{E}\left\{\left|\begin{bmatrix} \Delta\mathbf{y}_k^T & \tilde{\mathbf{y}}_{k,0:n_f-1,f}^T & \hat{\tilde{\mathbf{x}}}_{k,0:n_f-1,f}^T & \tilde{y}_{k,n} \end{bmatrix}\mathbf{v}_n - \tilde{x}_{k,n}\right|^2\right\} \quad (7.33)$$

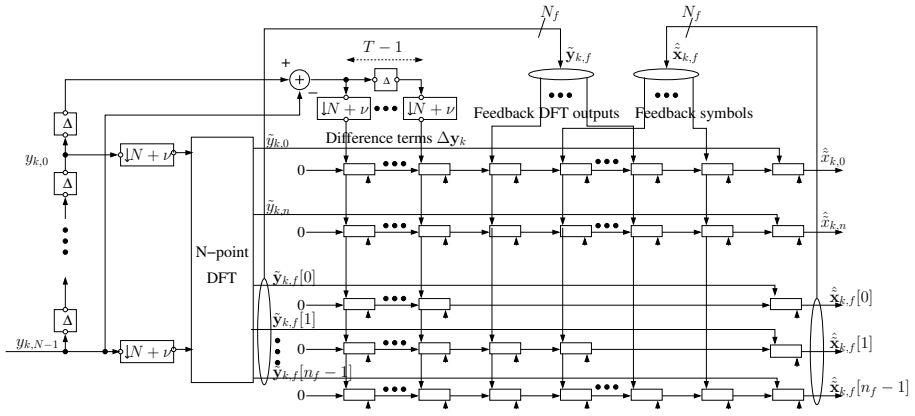


Figure 7.3: Principle scheme of the DF-PTEQ extension.

with $0 \leq n_f \leq \frac{N_f}{2} - 1$ and where

$$\tilde{\mathbf{y}}_{k,0:n_f-1,f} = \left[\begin{array}{ccc} \tilde{\mathbf{y}}_{k,f}[0] & \cdots & \tilde{\mathbf{y}}_{k,f}[n_f-1] \end{array} \right]^T \tag{7.34}$$

$$\hat{\tilde{\mathbf{x}}}_{k,0:n_f-1,f} = \left[\begin{array}{ccc} \hat{\tilde{\mathbf{x}}}_{k,f}[0] & \cdots & \hat{\tilde{\mathbf{x}}}_{k,f}[n_f-1] \end{array} \right]^T \tag{7.35}$$

hence the PTEQ of the n_f-th feedback tone in $\mathcal{S}_f$ only exploits the ISI/ICI on the feedback tones $0, \ldots, n_f - 1$ in $\mathcal{S}_f$. This means indeed that the equalization of the N_f feedback tones $\mathcal{S}_f$ does not fully benefit from the exploited ISI/ICI information. However, it is found in Section 7.6 that this has no detrimental effect on the performance, as only a small number of feedback tones, N_f, is required. Ignoring the fact that the equalizers for the feedback tones do not use all fed-back symbol decisions, the overall memory cost is equal to $\frac{N_a}{2}(L_a+1+2N_f)$ complex-valued equalizer coefficients, while the computational cost amounts to $N_a(L_a+2+2N_f)$ real multiplications per DMT symbol. A principle scheme of the DF-PTEQ extension is depicted in **Figure 7.3**. The lower n_f branches display to the equalization of the feedback tones $\mathcal{S}_f$. The corresponding decisions $\hat{\tilde{\mathbf{x}}}_{k,f}$ and DFT outputs $\tilde{\mathbf{y}}_{k,f}$ are fed back for the equalization of the remaining tones in $\mathcal{S}_a$. The equalizer taps are not denoted explicitly for reasons of conciseness (compare with Figure 7.2).

In [114, 117], DFE structures for OFDM transmission over FIR channels 'with an insufficiently long CP have already been presented. In [117], an OFDM system without cyclic prefix is considered; the ISI from the previous ODFM symbol is first removed in a DF fashion, followed by a linear equalization of the ISI-free OFDM symbol to remove ICI. In [114], a ZF-DFE and an MMSE-DFE are presented: in both DFEs, all decisions on the previous and current OFDM symbol are fed back; in addition, the MMSE-DFE uses three consecutive RX DMT symbols (the current, the previous and the next symbol) in the forward

path. All tones are equalized in a joint, block-wise fashion. While these DFE structures could be acceptable for implementation in OFDM systems, such as WLAN equipment based on the HIPERLAN/2 [119] standard, which employs a DFT/IDFT size of $N = 64$ and a CP length of $\nu = 16$, they are definitely too complex for implementation in DMT-based systems, such as ADSL, which employs a DFT/IDFT size of $N = 512$ and a CP length of $\nu = 32$. The low-complexity DF-PTEQ extension (7.32) developed here only feeds back a few ($N_f \ll N$) symbol decisions *within* the current DMT symbol and uses the original PTEQ in its forward path. Its complexity depends linearly, rather than quadratically on N. Hence, the DF-PTEQ extension is a drastically simplified and truncated version of the MMSE-DFE of [114].

Again, (7.32-7.33) can be solved adaptively with an extended version of the RLS-based PTEQ algorithm (3.75-3.76). By an appropriate choice of the ordering of the DF-PTEQ inputs, e.g.,

$$\left[\begin{array}{c|c|c} \Delta\mathbf{y}_k^T & \left(\left[\begin{array}{cc} 1 & 0 \end{array} \right] \otimes \tilde{\mathbf{y}}_{k,f}^T + \left[\begin{array}{cc} 0 & 1 \end{array} \right] \otimes \hat{\tilde{\mathbf{x}}}_{k,f}^T \right) & \tilde{y}_{k,n} \end{array} \right] \tag{7.36}$$

where $\otimes$ denotes a Kronecker product, which ensures that the DFT outputs $\tilde{\mathbf{y}}_{k,f}^T$ and the symbol decisions $\hat{\tilde{\mathbf{x}}}_{k,f}^T$ are interlaced, the inverse transpose $\mathbf{S}_{\Delta,f}$ of the Cholesky factor of the $(L_a + 2N_f) \times (L_a + 2N_f)$ autocorrelation matrix of $\left[\begin{array}{c|c} \Delta\mathbf{y}_k^T & \left(\left[\begin{array}{cc} 1 & 0 \end{array} \right] \otimes \tilde{\mathbf{y}}_{k,f}^T + \left[\begin{array}{cc} 0 & 1 \end{array} \right] \otimes \hat{\tilde{\mathbf{x}}}_{k,f}^T \right) \end{array} \right]$ is again common for all tones. For the feedback tone n_f, only the $(L_a + 2n_f)$ first rows of $\mathbf{S}_{\Delta,f}$, corresponding to $\left[\begin{array}{c|c} \Delta\mathbf{y}_k^T & \left(\left[\begin{array}{cc} 1 & 0 \end{array} \right] \otimes \tilde{\mathbf{y}}_{k,0:n_f-1,f}^T + \left[\begin{array}{cc} 0 & 1 \end{array} \right] \otimes \hat{\tilde{\mathbf{x}}}_{k,0:n_f-1,f}^T \right) \end{array} \right]$, are needed. Each tone has its own tone-dependent last row of the Cholesky factor $\mathbf{S}_n$ with length $L_a + 2n_f$ for the feedback tone n_f and length $L_a + 2N_f$ for the other tones.

It is clear from the above discussion that the L-PTEQ and DF-PTEQ extensions add flexibility when designing DMT-based systems. CP overhead and FD TX redundancy can be traded off against each other. *A particular PTEQ design, based on a CP length ν, $T-1$ RX difference terms $\Delta\mathbf{y}_k$ and $N_p + N_f$ pilot/feedback tones then implicitly assumes an IIR channel model with $L_b = \nu + N_p + N_f$ and $L_a = T - 1$.* It will be shown in Section 7.6 that a good choice of these design parameters allows to achieve the same performance as with the original PTEQ at a lower computational and memory cost or, alternatively, a better performance is achieved without considerable cost increase.

7.4.3 RFI suppression capability

In Section 5.4, we have shown that a PTEQ-based DMT receiver with a sufficient number of taps, i.e., incorporating a sufficient number of RX difference terms, has an increased robustness to RFI, when compared to a TEQ-based

receiver, even if the latter includes a receiver window [113]. As explained in Section 6.3, the PTEQ implicitly includes a receiver window that is optimized per-tone, so that, for a tone that is affected by ISI/ICI as well as RFI, equalization and RFI suppression are traded off against each other [133].

In [91], an L-MMSE based RFI canceller has been presented that estimates and eliminates the spectral leakage of an RFI on individual tones by measuring the RFI on a few unused (or used) measurement tones (and their complex conjugates) around the RFI center frequency. It turns out that a well performing L-MMSE RFI canceller is obtained, based on a rough a priori knowledge of the PSD of the RFI (i.e., an estimate of center frequency and bandwidth, and assuming a flat spectrum). Based on the time-bandwidth product of the RFI signal over one DMT symbol, a rule of thumb for the required number of measurement tones is equal to the RFI bandwidth (expressed as a multiple of the DFT tone spacing) plus one to three. The center frequency and bandwidth of the RFI can be estimated using the squared magnitude of the DFT outputs, as in a periodogram, searching for the tones with the strongest interference [91].

Here, we suggest to combine this RFI canceller with the PTEQ and design the equalizer and the RFI canceller in a joint and direct fashion. In fact, if the L-PTEQ extension (7.30) makes use of a sufficient number of DFT outputs of unused tones, $\tilde{\mathbf{y}}_{k,u}$, around the RFI center frequency, it already incorporates the proposed RFI canceller. Alternatively, one can make use of the DF-PTEQ extension (7.32) with feedback measurement tones that are centered around the RFI center frequency. If the RFI is present during the connection set-up phase, the equalizer and RFI canceller can be designed jointly by adaptively solving (7.30) or (7.32) using the ADSL medley training signal. It will be shown in Section 7.6 that both kinds of RFI suppresssion, namely based on adding RX difference terms [133] and exploiting unused tones around the RFI center frequency [91] can again be traded off against each other to optimize computational and memory cost versus performance.

7.5 Low-complexity extensions of the BM-TEQ

Although the derivations in this chapter focus on PTEQ extensions, the earlier established close relationship between the BM-TEQ and the PTEQ suggests that very similar *linear BM-TEQ and decision-feedback BM-TEQ extensions* are possible. The IR-SNLLS-based BM-TEQ design (4.72) minimizes an iteratively reweighted sum of FEQ output errors. The PTEQ forms then an extreme case of the BM-TEQ where the FEQ output error on each tone n is minimized independently by means of an equalizer that combines the functionality of a TEQ and FEQ for that tone, see (3.71).

7.5.1 Linear and decision-feedback BM-TEQ extensions

With the above relation in mind, we suggest the following *linear BM-TEQ extension*. Instead of using a 1-tap FEQ $\tilde{d}_n$ per tone, which scales the equalized DFT output $\tilde{y}_{k,n,\mathbf{w}}$, we propose to apply a complex-valued $(2N_p+1)$-tap FEQ $\tilde{\mathbf{d}}_n = \begin{bmatrix} \tilde{d}_{n,0}^* & \tilde{\mathbf{d}}_{n,p}^H \end{bmatrix}^H$ per tone, which scales the *equalized* DFT output $\tilde{y}_{k,n,\mathbf{w}}$ with the classical FEQ $\tilde{d}_{n,0}$ and linearly combines the result with $2N_p$ extra inputs, namely the N_p *unequalized* DFT outputs on the pilot tones $\tilde{\mathbf{y}}_{k,p}$ and the corresponding pilot symbols $\tilde{\mathbf{x}}_{k,p}$; the vector of additional coefficients for tone n equals $\tilde{\mathbf{d}}_{n,p}$. This gives rise to the following **IR-SNLLS-based linear BM-TEQ extension**:

$$\min_{\boldsymbol{\theta}} \frac{1}{K} \sum_{k=1}^{K} \left\| \operatorname{diag}\left(\sqrt{\boldsymbol{\gamma}_{K,\{\mathbf{w},\tilde{\mathbf{D}}_p\}_{\text{prev}}}} \right) \underbrace{\left(\operatorname{diag}(\tilde{\mathbf{d}}_0)\tilde{\mathbf{Y}}_k\mathbf{w} + \tilde{\mathbf{D}}_p^T \begin{bmatrix} \tilde{\mathbf{y}}_{k,p} \\ \tilde{\mathbf{x}}_{k,p} \end{bmatrix} - \tilde{\mathbf{x}}_{k,a} \right)}_{\tilde{\mathbf{e}}_k} \right\|^2 \tag{7.37}$$

where the TX symbol vector $\tilde{\mathbf{x}}_{k,a}$ is explicitly denoted by a subscript a to indicate that (as before) only the FEQ output errors $\tilde{\mathbf{e}}_k$ on the active data-carrying tones are accounted for, where the $N_a \times 1$ vector $\tilde{\mathbf{d}}_0$ has the original 1-tap FEQs $\tilde{d}_{n,0}$ as entries, where the columns of the $2N_p \times N_a$ matrix $\tilde{\mathbf{D}}_p$ are the additional $2N_p \times 1$ vectors $\tilde{\mathbf{d}}_{n,p}$, where $\boldsymbol{\theta} = \begin{bmatrix} \mathbf{w}^T & \tilde{\mathbf{d}}^H \end{bmatrix}^H$ is the joint parameter vector of TEQ and multitap FEQ coefficients and where the $(2N_p+1)N_a \times 1$ vector $\tilde{\mathbf{d}}$ is obtained by stacking the multitap FEQs $\tilde{\mathbf{d}}_n$ for all tones $\mathcal{S}_a$. The symbol estimate at the output of the n-th FEQ, which follows from the first two terms of $\tilde{\mathbf{e}}_k$ in (7.37), is then given by:

$$\hat{\tilde{x}}_{k,n} = \begin{bmatrix} \tilde{y}_{k,n,\mathbf{w}} & \tilde{\mathbf{y}}_{k,p}^T & \tilde{\mathbf{x}}_{k,p}^T \end{bmatrix} \tilde{\mathbf{d}}_n \tag{7.38}$$

The weights $\boldsymbol{\gamma}_{K,\{\mathbf{w},\tilde{\mathbf{D}}_p\}_{\text{prev}}}$ still obey (4.73), where $\text{SNR}_{K,n}$ and $\rho_{K,n}^2$ now depend on both the TEQ $\mathbf{w}$ and the additional FEQ coefficients $\tilde{\mathbf{D}}_p$ (we omit the exact expressions here).

A principle scheme for the linear BM-TEQ extension (7.37) can be obtained from the L-PTEQ extension in Figure 7.2 by introducing a TEQ that replaces the part of the L-PTEQ extension with difference terms $\Delta\mathbf{y}_k$ as inputs. This implies that a first part of the equalization is now done before the DFT with a classical TEQ $\mathbf{w}$, while the second part of the equalization is done with a multitap FEQ per tone. In the noiseless case, the TEQ then compensates for the denominator $A(z)$ of the IIR channel $H(z)$ while the multitap FEQs compensate for the numerator $B(z)$, which can have an order L_b, which satisfies $\nu < L_b \leq N_p + \nu$ (see Section 7.3). When the number of TEQ taps T equals 1, the TEQ becomes a scalar and (7.37) decouples per tone. The resulting cost criterion then corresponds to the L-PTEQ extension (7.30) where the number

of RX difference terms $\Delta\mathbf{y}_k$ is set to zero.

For the case where there are unused tones $\mathcal{S}_u$ instead of pilot tones $\mathcal{S}_p$, the multitap FEQ $\tilde{\mathbf{d}}_n$ reduces to an $(N_u+1)\times 1$ vector, as the inputs $\tilde{\mathbf{x}}_{k,u}$ are zero. The *equalizer memory cost* (in case of a real-valued TEQ) for N_p pilot tones and N_u unused tones amounts to $T+\frac{N_a}{2}(2N_p+N_u+1)$ real-valued coefficients. Typical values of T, N_p and N_u (see Section 7.6) are $T=16$, $N_p=2$ and $N_u=2$, hence $T>N_p+N_u$. For this example, the equalizer memory cost of the linear BM-TEQ extension is only one third of the memory cost of the L-PTEQ extension. The *equalizer computational cost* depends on the chosen approach to compute the symbol estimates (7.38). E.g., we preferred in Section 5.3 to compute the classical TEQ-FEQ output $\tilde{d}_{n,0}\tilde{y}_{k,n,\mathbf{w}}$ by exploiting the key observations (3.62) and (3.65), i.e., based on an efficient computation of the sliding DFT of the RX signal, as this reduces the overall complexity of the adaptive BM-TEQ algorithm. This approach is also preferred here. The DFT of the (unequalized) RX sample vector $\mathbf{y}_{k,0:N-1}$, which is required for the efficient computation of the sliding DFT, also gives the DFT outputs of the pilot tones $\tilde{\mathbf{y}}_p$, as is required in (7.38).

Similarly to the linear BM-TEQ extension, a *decision-feedback BM-TEQ* extension can be proposed, based on the following **IR-SNLLS-based design criterion**:

$$\min_{\boldsymbol{\theta}} \frac{1}{K}\sum_{k=1}^{K}\left\| \operatorname{diag}\left(\sqrt{\boldsymbol{\gamma}_{K,\{\mathbf{w},\tilde{\mathbf{D}}_f\}_{\text{prev}}}}\right) \underbrace{\left(\operatorname{diag}(\tilde{\mathbf{d}}_0)\tilde{\mathbf{Y}}_k\mathbf{w}+\tilde{\mathbf{D}}_f^T\begin{bmatrix}\tilde{\mathbf{y}}_{k,f}\\ \hat{\tilde{\mathbf{x}}}_{k,f}\end{bmatrix}-\tilde{\mathbf{x}}_{k,a}\right)}_{\tilde{\mathbf{e}}_k}\right\|^2 \tag{7.39}$$

Similar to the DF-PTEQ extension of Section 7.4.2, the decision-feedback BM-TEQ is made causal by only using the earlier equalized and demodulated feedback tones and decisions of $\mathcal{S}_f$ to equalize and demodulate the next feedback tone. As a consequence, the $2N_f\times N_a$ matrix $\tilde{\mathbf{D}}_f$ consists of two $N_f\times N_a$ submatrices that are strictly lower triangular. Note that we assume here for simplicity that the feedback tones $\mathcal{S}_f$ are the first n_f tones in $\mathcal{S}_a$, hence the first n_f entries of $\tilde{\mathbf{x}}_{k,a}$ correspond to $\tilde{\mathbf{x}}_{k,f}$.

Remark 7.5 We have explained in Remark 3.2 that the MMSE-TEQ design criterion is closely related to the MMSE-DFE design criterion for classical single-carrier communication. The TIR $\mathbf{b}$ in (3.4) then corresponds to the feedback path of the MMSE-DFE. However, as only the feedforward path is actually implemented in the case of a TEQ, while *the TIR is virtual*, the TIR should not be causal and other constraints than a UTC on $\mathbf{b}$ can be imposed. Remarkably enough, (7.39) results in a *true DFE structure*, which generalizes the TEQ-based DMT receiver with a multitap FEQ and with feedback of the

decisions on the FD TX symbols. Whereas the MMSE-TEQ design is suboptimal as it does not account for the DMT block transmission nature with its FD symbols of interest (see Chapter 3 and 4), the global optimum of (7.39) achieves the maximum bit rate for the considered receiver structure. □

7.5.2 Guidelines for optimizing the linear BM-TEQ extension

Both the linear and decision-feedback BM-TEQ extension can be designed iteratively or adaptively with algorithms that are closely related to the iterative GN-based algorithm of Section 4.3.5 or the RLM algorithm of Section 5.2, respectively, which optimize the IR-SNLLS-based BM-TEQ design criterion. Without the aim of expanding these design algorithms in detail here, we give some guidelines on how the iterative GN-based step for optimizing the linear BM-TEQ extension design criterion (7.37) comes about and how it relates to the iterative GN-based step (4.79) of Section 4.3.5. Similar guidelines can be given for the decision-feedback BM-TEQ extension (7.39). These guidelines can then also be used to develop an adaptive design algorithm.

The GN-based update in step i for a complex-valued TEQ can again be summarized with

$$\boldsymbol{\theta}_i \leftarrow \boldsymbol{\theta}_{i-1} - \alpha_i \mathbf{R}_{\boldsymbol{\theta}_{i-1}}^{-1} \mathbf{g}_{\boldsymbol{\theta}_{i-1}} \tag{7.40}$$

where $\boldsymbol{\theta} = \begin{bmatrix} \mathbf{w}^T & \tilde{\mathbf{d}}^H \end{bmatrix}^H$. The gradient can be split as $\mathbf{g}_{\boldsymbol{\theta}} = \begin{bmatrix} \mathbf{g}_{1,\boldsymbol{\theta}}^H & \mathbf{g}_{2,\boldsymbol{\theta}}^H \end{bmatrix}^H$ where the $T \times 1$ subvector $\mathbf{g}_{1,\boldsymbol{\theta}}$ is similar to $\mathbf{g}_{1,\boldsymbol{\theta}}$ in (4.80), i.e.,

$$\mathbf{g}_{1,\boldsymbol{\theta}} = \tilde{\mathbf{Y}}_k^H \mathrm{diag}(\tilde{\mathbf{d}}_0^* \odot \boldsymbol{\gamma}_{K,\{\mathbf{w},\tilde{\mathbf{D}}_p\}_{\mathrm{prev}}}) \tilde{\mathbf{e}}_k \tag{7.41}$$

and where the $(2N_p+1)N_a \times 1$ subvector $\mathbf{g}_{2,\boldsymbol{\theta}}$ stacks the $(2N_p+1) \times 1$ vectors $\mathbf{g}_{2,n}$ for all tones n, $n \in \mathcal{S}_a$:

$$\mathbf{g}_{2,n} = \begin{bmatrix} \tilde{y}_{k,n,\mathbf{w}}^* \\ \tilde{\mathbf{y}}_{k,p}^* \\ \tilde{\mathbf{x}}_{k,p}^* \end{bmatrix} \gamma_{K,n,\{\mathbf{w},\tilde{\mathbf{d}}_{n,p}\}_{\mathrm{prev}}} \tilde{e}_{k,n} \tag{7.42}$$

If no pilot tones are used, i.e., $N_p = 0$, the gradient (4.80) is obtained.

The approximate Hessian of (7.37) has a block structure, similar to $\mathbf{R}_{\boldsymbol{\theta}}$ in (4.81), i.e.,

$$\mathbf{R}_{\boldsymbol{\theta}} = \begin{bmatrix} \mathbf{E} & \mathbf{F} \\ \mathbf{F}^H & \mathbf{G} \end{bmatrix} \tag{7.43}$$

be it that $\mathbf{R}_{\boldsymbol{\theta}}$ now has size $(T+(2N_p+1)N_a) \times (T+(2N_p+1)N_a)$. The $T \times T$ matrix $\mathbf{E}$ is given by:

$$\mathbf{E} = \sum_{n \in \mathcal{S}_a} \gamma_{K,n,\{\mathbf{w},\tilde{\mathbf{d}}_{n,p}\}_{\mathrm{prev}}} \left| \tilde{d}_{n,0} \right|^2 \boldsymbol{\Sigma}_{K,n,\tilde{\mathbf{y}}}^2 \tag{7.44}$$

which is very similar to $\mathbf{E}$ in (4.84). $\mathbf{F}^H$ is the following $(2N_p+1)N_a \times T$ matrix:

$$\mathbf{F}^H = \left[\begin{array}{c} \vdots \\ \left[\begin{array}{c} \gamma_{K,n,\{\mathbf{w},\tilde{\mathbf{d}}_{n,p}\}_{\text{prev}}} \tilde{d}_{n,0} \left(\mathbf{w}^H \boldsymbol{\Sigma}^2_{K,n,\tilde{\mathbf{y}}} \right) \\ \gamma_{K,n,\{\mathbf{w},\tilde{\mathbf{d}}_{n,p}\}_{\text{prev}}} \tilde{d}_{n,0} \boldsymbol{\Sigma}_{K,n,p} \end{array} \right] \\ \vdots \end{array} \right] \updownarrow N_a \text{ block rows} \quad (7.45)$$

where $\boldsymbol{\Sigma}_{K,n,p} = \frac{1}{K} \sum_{k=1}^{K} \left[\begin{array}{c} \tilde{\mathbf{y}}^*_{k,p} \\ \tilde{\mathbf{x}}^*_{k,p} \end{array} \right] \tilde{\mathbf{y}}_{k,n}$. Whereas $\mathbf{G}$ was diagonal in (4.83), $\mathbf{G}$ in (7.43) is a block diagonal matrix with the following $(2N_p+1) \times (2N_p+1)$ matrix $\mathbf{G}_n$ as block diagonal element corresponding to tone n:

$$\mathbf{G}_n = \gamma_{K,n,\{\mathbf{w},\tilde{\mathbf{d}}_{n,p}\}_{\text{prev}}} \left[\begin{array}{cc} \mathbf{w}^H \boldsymbol{\Sigma}^2_{K,n,\tilde{\mathbf{y}}} \mathbf{w} & \mathbf{w}^H \boldsymbol{\Sigma}^H_{K,n,p} \\ \boldsymbol{\Sigma}_{K,n,p} \mathbf{w} & \boldsymbol{\Sigma}^2_{K,p} \end{array} \right] \quad (7.46)$$

where $\boldsymbol{\Sigma}^2_{K,p} = \frac{1}{K} \sum_{k=1}^{K} \left[\begin{array}{c} \tilde{\mathbf{y}}^*_{k,p} \\ \tilde{\mathbf{x}}^*_{k,p} \end{array} \right] \left[\begin{array}{cc} \tilde{\mathbf{y}}^T_{k,p} & \tilde{\mathbf{x}}^T_{k,p} \end{array} \right]$. In order to invert the approximate Hessian $\mathbf{R}_{\boldsymbol{\theta}}$ as in (4.87), the inverse of the Schur complement of $\mathbf{G}$, i.e., the $T \times T$ matrix $\mathbf{Q} = \mathbf{E} - \mathbf{F}\mathbf{G}^{-1}\mathbf{F}^H$, and hence the inverse of the block diagonal matrix $\mathbf{G}$ are needed. The inverse $\mathbf{G}^{-1}$ is also block diagonal with the inverse of the block diagonal elements $\mathbf{G}_n$ along its diagonal. As $\mathbf{G}_n$ is a matrix where the lower right $(2N_p) \times (2N_p)$ submatrix $\boldsymbol{\Sigma}^2_{K,p}$ is common and tone-independent, computing the inverses $\mathbf{G}_n^{-1}$ then requires a single inversion of this submatrix, together with $\mathcal{O}((2N_p)^2)$ computations for each separate tone n.

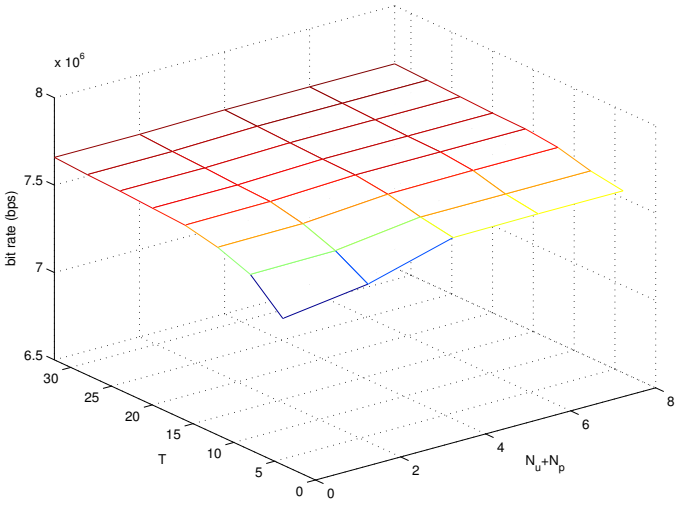
The cost to compute the matrices $\mathbf{F}$ and $\mathbf{Q}$ is $\mathcal{O}(N_a T^2)$. Hence, the overall computational complexity of the iterative GN-based algorithm (and also of a related RLM algorithm) is dominated by $\mathcal{O}(N_a T^2) + \mathcal{O}(N_a (2N_p)^2)$, which is in accordance with what can be expected from the computational cost of the RLM algorithm for the original BM-TEQ (see Section 5.3). The SOS that are required to construct $\mathbf{R}_{\boldsymbol{\theta}}$ in (7.43) are $\boldsymbol{\Sigma}^2_{k,n,\tilde{\mathbf{y}}}$, $\boldsymbol{\Sigma}_{k,n,p}$ and $\boldsymbol{\Sigma}^2_{k,p}$ (see (7.44), (7.45) and (7.46)). It is easy to see that these can be derived from exactly the same SOS as are required for the L-PTEQ extension (7.30), based on the Cholesky decomposition in (7.31). Hence, regarding the computational and memory cost of the equalizer design and updating, the same conclusions as were drawn for the original BM-TEQ can be given for the linear BM-TEQ extension: the linear BM-TEQ extension and the L-PTEQ extension make use of the same SOS, while the linear BM-TEQ extension design and updating cost depends quadratically on T and N_p, while the L-PTEQ extension design and updating cost depends linearly on T and N_p.

7.6 Simulations

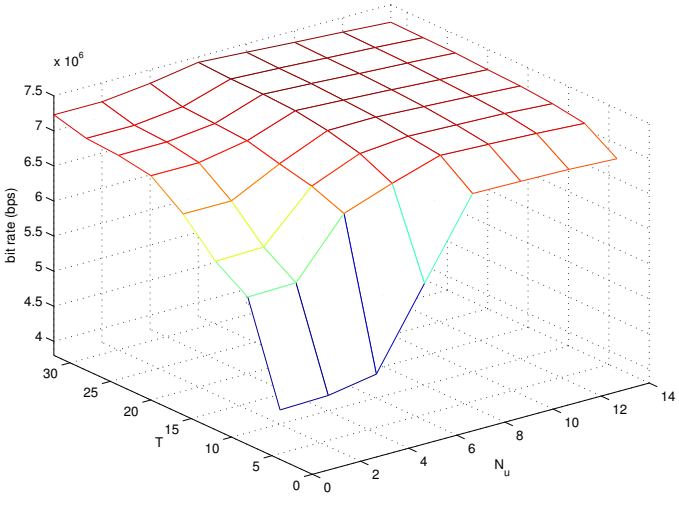
In this section, we provide extensive ADSL simulation results for the L-PTEQ and DF-PTEQ extension in different scenarios (with and without RFI) and with varying amounts of exploited FD TX redundancy (pilot tones $\mathcal{S}_p$, unused tones $\mathcal{S}_u$ and feedback tones $\mathcal{S}_f$), CP lengths ν and numbers of RX difference terms $T-1$. All L-PTEQ and DF-PTEQ designs have been obtained using the described *RLS-based adaptive PTEQ algorithm*. We include plots for the FDD ADSL downstream CSA #1-8 loops [5, 8] with active tones 38 to 255 (and their complex conjugates). The loops are described by an FIR channel impulse response of length N where $N = 512$ is the DFT size. The synchronization delay Δ is determined by the first sample index of the channel impulse response window of $\nu + 1$ samples with maximum energy. The noise is a superposition of AWGN at -140 dBm/Hz, residual echo of the upstream signal and near-end crosstalk from 24 ADSL disturbers. Strong front-end filters to separate up- and downstream transmission are included in the channel; as already pointed out, they are known to be the major source of ISI/ICI [98]. Therefore, the unused tones, pilot tones and feedback tones are chosen within a tone range around the transition band of the front-end filters, i.e., around tone 38. Tone 33 to 37 are used as guard tones between upstream and downstream. In ADSL, tone 64 is used as a pilot tone for synchronization and can also be exploited for equalization.

Figure 7.4 shows the bit rate performance of the L-PTEQ extension for the CSA #4 loop as a function of T and $N_u + N_p$ for $\nu = 16$ (Figure 7.4a) and standardized $\nu = 32$ (Figure 7.4b). The values $T = \{4, 8, 12, 16, 20, 24, 28, 32\}$ are considered. FD TX redundancy is added in complex conjugate pairs of tones, hence N_u and N_p are even. For conciseness, we exclude the complex conjugate tones in the sequel, when referring to the used FD TX redundancy. We order the FD TX redundancy as $\{64, 37, 36, 35\}$, where tone 64 is a pilot tone and the other tones are unused tones. The effect of using FD TX redundancy is larger for a shorter CP length ν: the ISI/ICI level is higher when $L_b - \nu$ is larger, hence the exploitation of ISI/ICI information on pilot and unused tones is more effective. The bit rate saturates when tones 64 and 37 ($N_u + N_p = 4$) are included; extra unused tones 36 and 35 do not result in further performance improvement, presumably because they are next to tone 37, with which they have strongly correlated ISI/ICI; the residual echo signal also contaminates the guard tones 33 to 37. Note that the equalizer scheme, proposed in [127], would correspond to a curve for $T = 0$ and varying N_u, which is not depicted here as it gives considerably worse performance than with $T \geq 4$: this is probably due to the more difficult simulation scenarios adopted here, which include non-white crosstalker noise, residual echo, front-end filters, etc.

Based on Figure 7.4, we choose the following four L-PTEQ configurations to compare the performance on the CSA #1-8 loops in **Figure 7.5**: (1) $\nu = 32$,



(a) $\nu = 16$



(b) $\nu = 32$

Figure 7.4: Bit rate performance of the L-PTEQ extension for the CSA #4 loop as a function of T and $N_u + N_p$ for $\nu = 16$ and standardized $\nu = 32$.

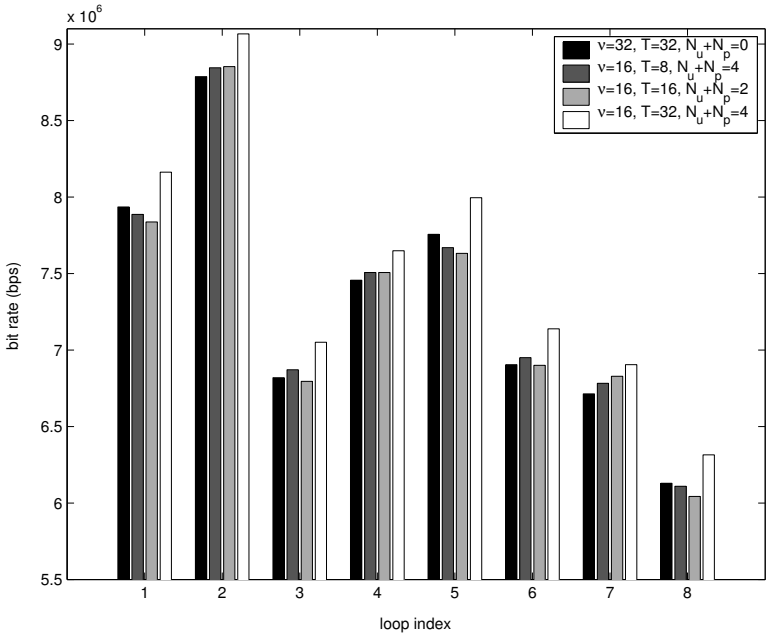
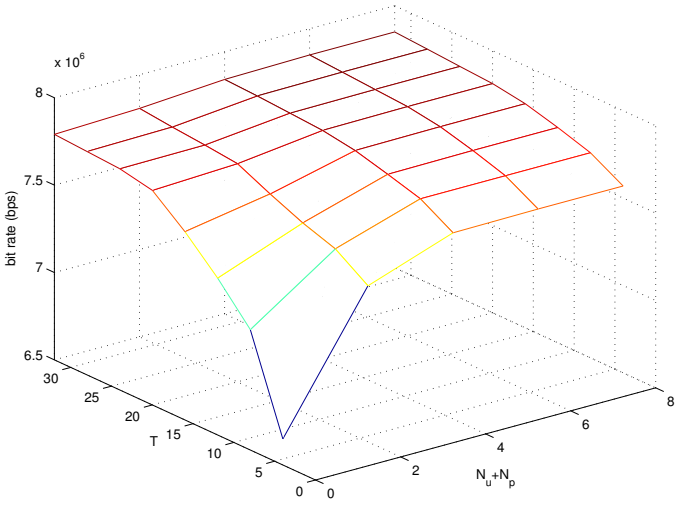


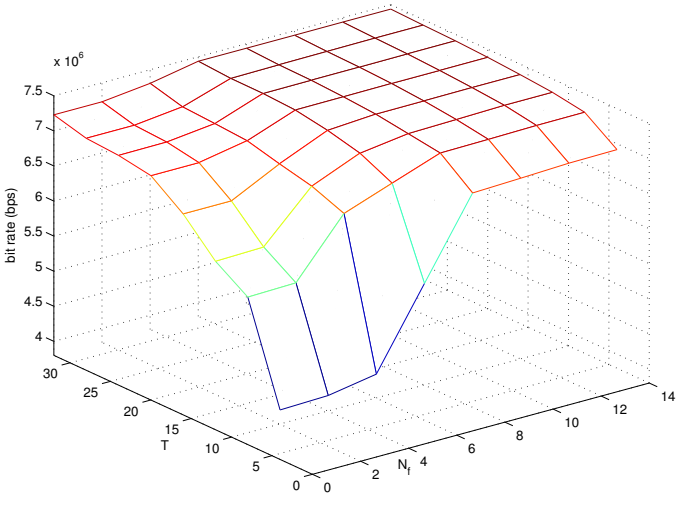
Figure 7.5: Bit rate performance of the L-PTEQ extension on the CSA #1-8 loops for 4 scenarios.

$T = 32$ and $N_u = N_p = 0$, (2) $\nu = 16$, $T = 8$, $N_p = 2$ and $N_u = 2$, (3) $\nu = 16$, $T = 16$, $N_p = 2$ and $N_u = 0$, (4) $\nu = 16$, $T = 32$, $N_p = 2$ and $N_u = 2$. The computational and memory cost of the 4 configurations (with $N_a = 218$ active tones) is summarized in **Table 7.1**. For all loops, the first three configurations give rise to similar performance, while configurations 2 and 3 (with $\nu = 16$) are 45 to 55 % less complex than configuration 1 (with $\nu = 32$): hence, by choosing an appropriate L-PTEQ extension, equalization complexity can be reduced, even if there is more ISI/ICI because of a shorter CP. The 4th configuration ($\nu = 16$) is slightly more complex (less than 20 %) than the 1st configuration, but reaches a bit rate that is consistently around 200 to 300 kbps higher, which is due to a better bandwidth efficiency because of the reduced CP.

Figure 7.6 shows the bit rate performance of the DF-PTEQ extension for the CSA #4 loop as a function of T and $N_u + N_p$ for $\nu = 16$ (Figure 7.6a) and standardized $\nu = 32$ (Figure 7.6b). The values $T = \{4, 8, 12, 16, 20, 24, 28, 32\}$ are considered. The N_f feedback tones are taken from $\{38, 44, 50, 56\}$, i.e., near the front-end filter transition band and sufficiently interspaced. As with pilot and unused tones, the impact of using feedback tones is larger for shorter CP length. For small T, including up to 4 feedback tones is beneficial, while for $T \geq 12$, 2 feedback tones suffice. Similar to Figure 7.5, **Figure 7.7** compares the performance on the CSA #1-8 loops for 4 DF-PTEQ configurations: (1)



(a) $\nu = 16$



(b) $\nu = 32$

Figure 7.6: Bit rate performance of the DF-PTEQ extension for the CSA #4 loop as a function of T and N_f for $\nu = 16$ and standardized $\nu = 32$.

Table 7.1: Computational cost (in # real multiplications per DMT symbol) and memory cost (in # complex coefficients) of the scenarios considered in Figure 7.5 (L-PTEQ extension) and Figure 7.7 (DF-PTEQ extension).

Configuration	L-PTEQ extension		DF-PTEQ extension	
	memory cost	comp. cost	memory cost	comp. cost
$\nu = 32$, $T = 32$, $N_u + N_p = N_f = 0$	6976	14388	6976	14388
$\nu = 16$, $T = 8$, $N_u + N_p = N_f = 4$	3052	6540	3476	7388
$\nu = 16$, $T = 16$, $N_u + N_p = N_f = 2$	4360	9156	4356	9148
$\nu = 16$, $T = 32$, $N_u + N_p = N_f = 4$	8284	17004	8708	17852

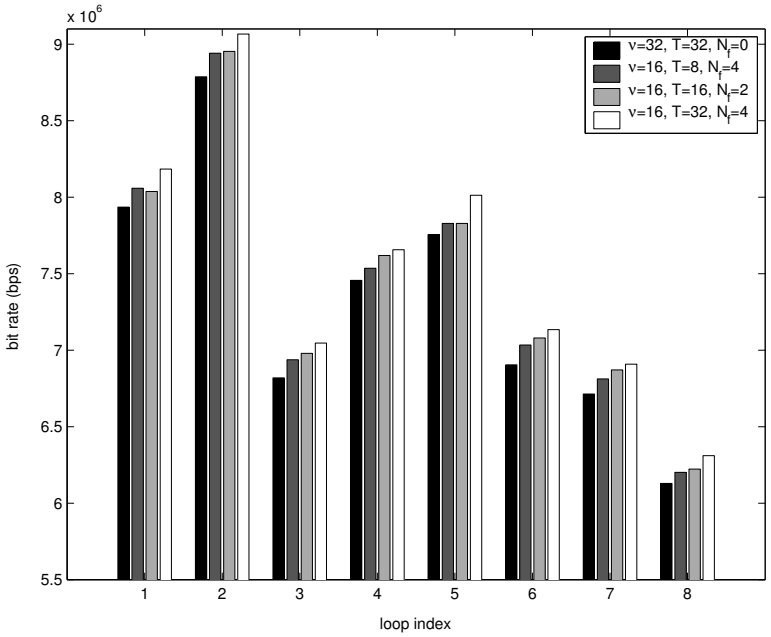


Figure 7.7: Bit rate performance of the DF-PTEQ extension for the CSA #1-8 loops for 4 scenarios.

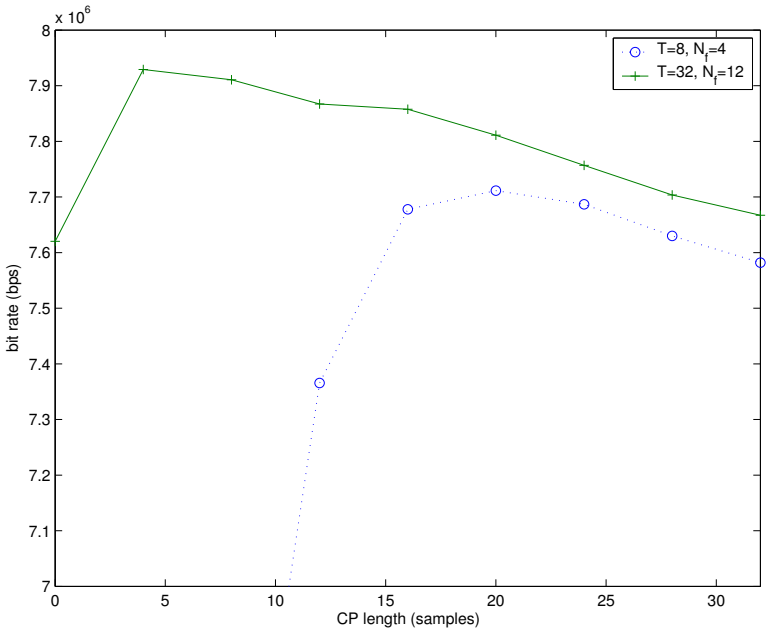
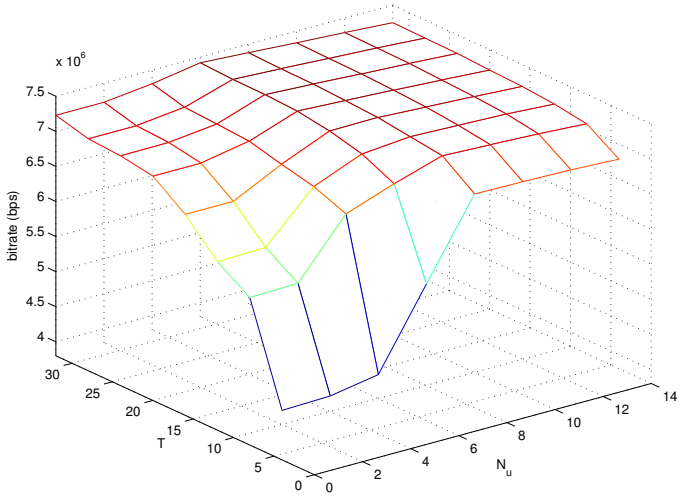


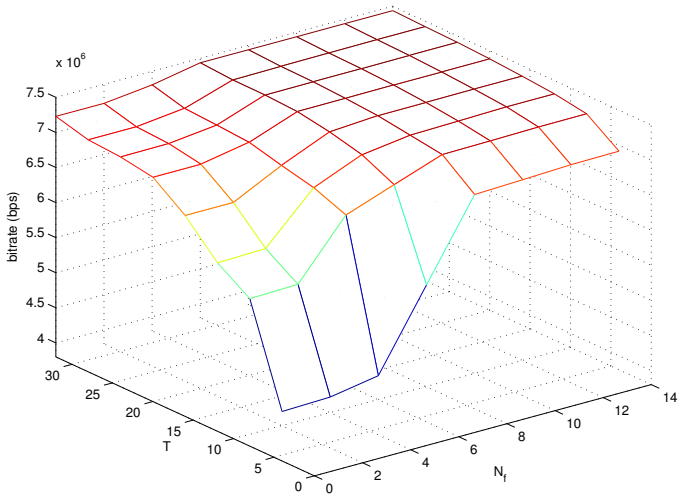
Figure 7.8: Bit rate as a function of the CP length ν for two DF-PTEQ configurations with the CSA #4 loop.

$\nu = 32$, $T = 32$ and $N_f = 0$, (2) $\nu = 16$, $T = 8$ and $N_f = 4$, (3) $\nu = 16$, $T = 16$ and $N_f = 2$, (4) $\nu = 16$, $T = 32$ and $N_f = 4$. The computational and memory cost is also given in **Table 7.1**. The less complex 2nd and 3rd configuration ($\nu = 16$) consistently outperform the 1st configuration ($\nu = 32$). The 4th configuration ($\nu = 32$) reaches again a bit rate that is up to 300 kbps higher than with the 1st configuration. **Figure 7.8** shows the achieved bit rate as a function of the CP length ν for two DF-PTEQ configurations: (1) a low complexity configuration with $T = 8$ and $N_f = 4$ and (2) a high-complexity configuration with $T = 32$ and $N_f = 12$, which is expected to perform close to the upper bound that is achievable with the DF-PTEQ extension. The curves suggest that a good performance versus complexity trade-off is obtained with a value for ν between 16 and 20.

To illustrate the RFI suppression capability of the L-PTEQ and the DF-PTEQ extension, we include **Figure 7.9**, which shows the bit rate as a function of T and N_u or N_f on the CSA #4 loop ($\nu = 32$) with an RFI with a flat PSD of -40 dBm/Hz, a center frequency at 430 kHz (i.e., between tone 100 and 101) and a bandwidth of 4.3 kHz (i.e., equal to the DFT tone spacing). The considered measurement tones are ordered as follows: $\{101, 99, 103, 97, 105, 95, 107\}$. The curve in **Figure 7.9a** for $N_u = 0$ illustrates that the robustness of the original PTEQ increases with T (see Section 5.4), as observed in [133]. In accordance with the proposed rule of thumb, 3 to 4 measurement tones (and their



(a) L-PTEQ extension



(b) DF-PTEQ extension

Figure 7.9: Bit rate performance of the L-PTEQ and DF-PTEQ extension on the CSA #4 loop ($\nu = 32$) with one RFI as a function of T and N_u or N_f.

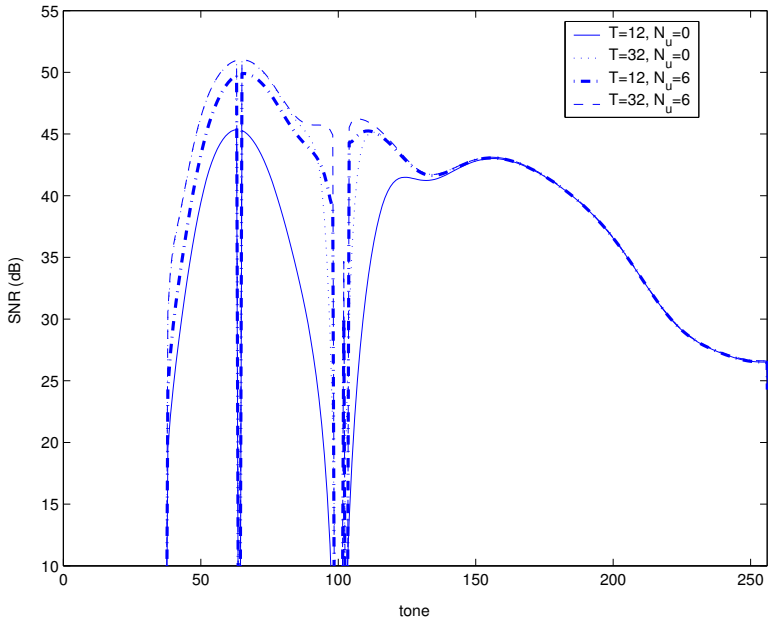


Figure 7.10: SNR per tone on the CSA #4 loop with one RFI for several L-PTEQ configurations.

complex conjugates) result in a further performance improvement. Adding 6 measurement tones increases the performance for $T = 32$ with 200 kbps; the configuration with $T = 12$ and $N_u = 8$ measurement tones gives about the same performance as the configuration with $T = 32$ without measurement tones, be it at a 40 % lower complexity. Adding 8 or more instead of 6 measurement tones reduces the performance as tones with a sufficient SNR to carry data are turned off. **Figure 7.9b** shows the performance when feedback tones are used as measurement tones. The curves in Figure 7.9a and Figure 7.9b coincide up to 6 measurement tones: the tones $\{101, 99, 103\}$ have a too low SNR after RFI suppression, so that they can not carry data, hence there is no need to use decision-feedback. For 8 or more measurement tones and $T = 32$, the bit rate does not decrease, as the extra measurement tones do carry data now. However, using 8 or more measurement tones appears not to lead to better performance. **Figure 7.10** shows the impact of different L-PTEQ extensions on the RFI suppression capability: the effect of a larger number of RX difference terms and the impact of including measurement tones are depicted. Both RFI suppression techniques ((1) increasing T from 12 to 32 with $N_u = 0$ and (2) including $N_u = 6$ unused measurement tones with $T = 12$) have a beneficial impact on all affected tones. In addition, the measurement tones appear to locally increase robustness in the neighbourhood of the RFI (compare $T = 32$, $N_u = 0$

with $T = 32$, $N_u = 6$), while a larger T results in a better ISI/ICI suppression at the lower tones (compare $T = 12$, $N_u = 6$ with $T = 32$, $N_u = 6$).

7.7 Conclusions

The PTEQ-based receiver was originally presented as an alternative for TEQ-based receivers over FIR channels, such as ADSL channels. In this chapter, we have reconsidered DMT equalization under the realistic assumption that the wireline channel impulse response is well approximated by an IIR model. Based on the corresponding block data model and the optimum L-ZF block equalizers, we have shown that a PTEQ-based receiver is also suited for the equalization of an IIR channel. A low-complexity *L-PTEQ extension* has been developed to accommodate arbitrary IIR model orders and CP lengths: FD transmit redundancy as introduced by pilot and unused tones can be used to enhance the original PTEQ; alternatively, by treating symbol decisions in the same way as pilot symbols, a *DF-PTEQ extension* is obtained. These PTEQ extensions also improve the RFI suppression capability of the PTEQ.

In the simulations, we have shown that the PTEQ extensions add flexibility when designing DMT-based systems: they allow to *trade off CP overhead and FD transmit redundancy* against each other. With a CP length of 16 samples instead of the standardized CP length of 32 samples, a similar bit rate as with the original PTEQ can be achieved at a lower memory and computational cost or, alternatively, a higher bit rate is achieved without a considerable cost increase. Moreover, by trading off the number of RX difference terms and FD transmit redundancy the RFI robustness can be enhanced.

Although the derivations in this chapter focused on PTEQ extensions, similar *BM-TEQ extensions* have been briefly discussed. They are expected to closely approach the performance of the PTEQ extensions while offering the advantage of a *lower equalizer memory cost*.

7.A Appendix

In this appendix, we show that the optimum L-ZF block equalizer for the case where $N_p \geq L_b - \nu$ gives rise to a two-step procedure: in a first step, an estimate of the $L_b - \nu$ TX difference terms are obtained; these are used in a second step to provide the L-ZF estimate of the TX symbol vector $\tilde{\mathbf{x}}_{k,a}$.

The MMSE L-ZF block equalizer leads to the following block estimate (see also (7.24)):

$$\begin{bmatrix} \hat{\tilde{\mathbf{x}}}_{k,a}^{\mathrm{L-ZF}} \\ \widehat{\Delta \underline{\mathbf{x}}_k}^{\mathrm{L-ZF}} \end{bmatrix} = \underbrace{\left(\left[\begin{array}{c|c} \tilde{\mathbf{B}}_{a,\mathrm{D}}^H & \mathbf{0} \\ \hline \underline{\mathbf{B}}_\Delta^T \mathcal{F}_N^H & \end{array} \right] \left(\mathcal{F}_N \boldsymbol{\Sigma}_{\check{\mathbf{n}}}^2 \mathcal{F}_N^H \right)^{-1} \left[\begin{array}{c|c} \tilde{\mathbf{B}}_{a,\mathrm{D}} & \\ \hline \mathbf{0} & \mathcal{F}_N \underline{\mathbf{B}}_\Delta \end{array} \right] \right)}_{\{1\}}^{-1} \times \underbrace{\left[\begin{array}{c|c} \tilde{\mathbf{B}}_{a,\mathrm{D}}^H & \mathbf{0} \\ \hline \underline{\mathbf{B}}_\Delta^T \mathcal{F}_N^H & \end{array} \right] \left(\mathcal{F}_N \boldsymbol{\Sigma}_{\check{\mathbf{n}}}^2 \mathcal{F}_N^H \right)^{-1}}_{\{2\}} \tilde{\mathbf{z}}_{k,N} \tag{7.A.1}$$

The derivation below leads naturally to a two-step procedure, where $\Delta \underline{\mathbf{x}}_k$ is estimated in a first step and used in a second step to estimate $\tilde{\mathbf{x}}_{k,a}$. We introduce the following block-based description for the factors $\{1\}$ and $\{2\}$ in (7.A.1):

$$\{1\} = \begin{bmatrix} \mathbf{E} & \mathbf{F} \\ \mathbf{F}^H & \mathbf{G} \end{bmatrix} = \left[\begin{array}{c|c} \tilde{\mathbf{B}}_{a,\mathrm{D}}^H \mathcal{F}_a \left(\boldsymbol{\Sigma}_{\check{\mathbf{n}}}^2 \right)^{-1} \mathcal{F}_a^H \tilde{\mathbf{B}}_{a,\mathrm{D}} & \tilde{\mathbf{B}}_{a,\mathrm{D}}^H \mathcal{F}_a \left(\boldsymbol{\Sigma}_{\check{\mathbf{n}}}^2 \right)^{-1} \underline{\mathbf{B}}_\Delta \\ \hline \underline{\mathbf{B}}_\Delta^T \left(\boldsymbol{\Sigma}_{\check{\mathbf{n}}}^2 \right)^{-1} \mathcal{F}_a^H \tilde{\mathbf{B}}_{a,\mathrm{D}} & \underline{\mathbf{B}}_\Delta^T \left(\boldsymbol{\Sigma}_{\check{\mathbf{n}}}^2 \right)^{-1} \underline{\mathbf{B}}_\Delta \end{array} \right] \tag{7.A.2}$$

$$\{2\} = \begin{bmatrix} \mathbf{K} \\ \mathbf{L} \end{bmatrix} = \begin{bmatrix} \tilde{\mathbf{B}}_{a,\mathrm{D}}^H \mathcal{F}_a \left(\boldsymbol{\Sigma}_{\check{\mathbf{n}}}^2 \right)^{-1} \mathcal{F}_N^H \\ \underline{\mathbf{B}}_\Delta^T \left(\boldsymbol{\Sigma}_{\check{\mathbf{n}}}^2 \right)^{-1} \mathcal{F}_N^H \end{bmatrix} \tag{7.A.3}$$

The inverse of the factor $\{1\}$ in (7.A.1) and (7.A.2) is given by:

$$\begin{bmatrix} \mathbf{E} & \mathbf{F} \\ \mathbf{F}^H & \mathbf{G} \end{bmatrix}^{-1} = \begin{bmatrix} \mathbf{E}^{-1} + \mathbf{E}^{-1}\mathbf{F}\mathbf{Q}^{-1}\mathbf{F}^H\mathbf{E}^{-1} & -\mathbf{E}^{-1}\mathbf{F}\mathbf{Q}^{-1} \\ -\mathbf{Q}^{-1}\mathbf{F}^H\mathbf{E}^{-1} & \mathbf{Q}^{-1} \end{bmatrix} \tag{7.A.4}$$

with

$$\mathbf{Q} = \mathbf{G} - \mathbf{F}^H \mathbf{E}^{-1} \mathbf{F} \tag{7.A.5}$$

$$= \underline{\mathbf{B}}_\Delta^T \underbrace{\left(\left(\boldsymbol{\Sigma}_{\check{\mathbf{n}}}^2 \right)^{-1} - \left(\boldsymbol{\Sigma}_{\check{\mathbf{n}}}^2 \right)^{-1} \mathcal{F}_a^H \left(\mathcal{F}_a \left(\boldsymbol{\Sigma}_{\check{\mathbf{n}}}^2 \right)^{-1} \mathcal{F}_a^H \right)^{-1} \mathcal{F}_a \left(\boldsymbol{\Sigma}_{\check{\mathbf{n}}}^2 \right)^{-1} \right)}_{\mathbf{M}_3} \underline{\mathbf{B}}_\Delta \tag{7.A.6}$$

Using (7.A.1-7.A.6) and (7.10), $\Delta \underline{\mathbf{x}}_k$ can be estimated first. It follows from (7.A.1-7.A.4) that:

$$\widehat{\Delta \underline{\mathbf{x}}_k}^{\mathrm{L-ZF}} = -\mathbf{Q}^{-1} \left(\mathbf{F}^H \mathbf{E}^{-1} \mathbf{K} - \mathbf{L} \right) \tilde{\mathbf{z}}_{k,N} \tag{7.A.7}$$

Using the definitions of the matrices $\mathbf{E}$, $\mathbf{F}$, $\mathbf{K}$ and $\mathbf{L}$ in (7.A.2-7.A.3) results in:

$$\widehat{\Delta\underline{\mathbf{x}}}_k^{\mathrm{L-ZF}} = -\mathbf{Q}^{-1}\underline{\mathbf{B}}_\Delta^T \left(\mathbf{\Sigma}_{\check{\mathbf{n}}}^2\right)^{-1} \Bigg(\underbrace{\mathcal{F}_a^H \left(\mathcal{F}_a \left(\mathbf{\Sigma}_{\check{\mathbf{n}}}^2\right)^{-1} \mathcal{F}_a^H\right)^{-1} \mathcal{F}_a \left(\mathbf{\Sigma}_{\check{\mathbf{n}}}^2\right)^{-1} \mathcal{F}_N^H - \mathcal{F}_N^H}_{\{1\}} \Bigg) \tilde{\mathbf{z}}_{k,N} \tag{7.A.8}$$

As $\mathcal{F}_N = \left[\begin{array}{cc} \mathcal{F}_a^H & \mathcal{F}_p^H \end{array}\right]^H$, the factor $\{1\}$ in (7.A.8) can be split into two parts, where the first part appears to be an all-zero matrix:

$$\{1\} = \left[\begin{array}{c|c} \mathbf{0}_{N\times N_a} & \mathcal{F}_a^H \left(\mathcal{F}_a \left(\mathbf{\Sigma}_{\check{\mathbf{n}}}^2\right)^{-1} \mathcal{F}_a^H\right)^{-1} \mathcal{F}_a \left(\mathbf{\Sigma}_{\check{\mathbf{n}}}^2\right)^{-1} \mathcal{F}_p^H - \mathcal{F}_p^H \end{array}\right] \tag{7.A.9}$$

From the definition of $\tilde{\mathbf{z}}_{k,N}$ (7.10), it follows that the L-ZF estimate $\widehat{\Delta\underline{\mathbf{x}}}_k^{\mathrm{L-ZF}}$ is a linear combination of $\tilde{\mathbf{z}}_{k,p}$:

$$\widehat{\Delta\underline{\mathbf{x}}}_k^{\mathrm{L-ZF}} = -\mathbf{Q}^{-1}\underline{\mathbf{B}}_\Delta^T \left(\mathbf{\Sigma}_{\check{\mathbf{n}}}^2\right)^{-1} \Bigg(\mathcal{F}_a^H \left(\mathcal{F}_a \left(\mathbf{\Sigma}_{\check{\mathbf{n}}}^2\right)^{-1} \mathcal{F}_a^H\right)^{-1} \mathcal{F}_a \left(\mathbf{\Sigma}_{\check{\mathbf{n}}}^2\right)^{-1} \mathcal{F}_p^H - \mathcal{F}_p^H \Bigg) \tilde{\mathbf{z}}_{k,p} \tag{7.A.10}$$

The definitions of $\mathbf{Q}$ and $\mathbf{M}_3$ in (7.A.5) and (7.A.6) then lead to:

$$\widehat{\Delta\underline{\mathbf{x}}}_k^{\mathrm{L-ZF}} = \left(\underline{\mathbf{B}}_\Delta^T \mathbf{M}_3 \underline{\mathbf{B}}_\Delta\right)^{-1} \underline{\mathbf{B}}_\Delta^T \mathbf{M}_3 \mathcal{F}_p^H \tilde{\mathbf{z}}_{k,p} \tag{7.A.11}$$

or

$$\underline{\mathbf{B}}_\Delta \widehat{\Delta\underline{\mathbf{x}}}_k^{\mathrm{L-ZF}} = \left[\begin{array}{c} \mathbf{M}_4 \\ \hline \mathbf{0} \end{array}\right] \tilde{\mathbf{z}}_{k,p} \tag{7.A.12}$$

with $\mathbf{0} = \mathbf{0}_{(N-L_b+\nu)\times(L_b-\nu)}$ and

$$\mathbf{M}_4 = \left[\begin{array}{c|c} \mathbf{I}_{L_b-\nu} & \mathbf{0}^T \end{array}\right] \mathbf{M}_3^{-1} \left[\begin{array}{c} \mathbf{I}_{L_b-\nu} \\ \hline \mathbf{0} \end{array}\right] \left[\begin{array}{c|c} \mathbf{I}_{L_b-\nu} & \mathbf{0}^T \end{array}\right] \mathbf{M}_3 \mathcal{F}_p^H \tag{7.A.13}$$

The estimation of $\hat{\tilde{\mathbf{x}}}_{k,a}$ can now make use of $\widehat{\Delta\underline{\mathbf{x}}}_k^{\mathrm{L-ZF}}$, as it follows from (7.A.1-7.A.4) that:

$$\begin{aligned} \hat{\tilde{\mathbf{x}}}_{k,a}^{\mathrm{L-ZF}} &= \mathbf{E}^{-1}\left(\mathbf{K}\tilde{\mathbf{z}}_{k,N} - \mathbf{F}\widehat{\Delta\underline{\mathbf{x}}}_k^{\mathrm{L-ZF}}\right) && (7.A.14)\\ &= \mathbf{E}^{-1}\tilde{\mathbf{B}}_{a,\mathrm{D}}^H \mathcal{F}_a \left(\mathbf{\Sigma}_{\check{\mathbf{n}}}^2\right)^{-1} \mathcal{F}_N^H \left(\tilde{\mathbf{z}}_{k,N} - \mathcal{F}_N \underline{\mathbf{B}}_\Delta \widehat{\Delta\underline{\mathbf{x}}}_k^{\mathrm{L-ZF}}\right) && (7.A.15) \end{aligned}$$

Using (7.A.12), the definition of $\mathbf{E}$ in (7.A.2) and $\mathcal{F}_N = \left[\begin{array}{c|c} \mathcal{F}_a^H & \mathcal{F}_p^H \end{array}\right]^H$, (7.A.15) reduces to the following **optimum L-ZF block estimate**:

$$\begin{aligned} \hat{\tilde{\mathbf{x}}}_{k,a}^{\mathrm{L-ZF}} &= \left[\begin{array}{c|c} \tilde{\mathbf{B}}_{a,\mathrm{D}}^{-1} & \mathbf{M}_1 \end{array}\right] \left(\tilde{\mathbf{z}}_{k,N} - \mathcal{F}_N \underline{\mathbf{B}}_\Delta \widehat{\Delta\underline{\mathbf{x}}}_k^{\mathrm{L-ZF}}\right) && (7.A.16)\\ &= \tilde{\mathbf{B}}_{a,\mathrm{D}}^{-1}\tilde{\mathbf{z}}_{k,a} + \mathbf{M}_5\tilde{\mathbf{z}}_{k,p} && (7.A.17) \end{aligned}$$

where

$$\mathbf{M}_1 = \tilde{\mathbf{B}}_{a,\mathrm{D}}^{-1}\left(\mathcal{F}_a\left(\boldsymbol{\Sigma}_{\check{\mathbf{n}}}^2\right)^{-1}\mathcal{F}_a^H\right)^{-1}\mathcal{F}_a\left(\boldsymbol{\Sigma}_{\check{\mathbf{n}}}^2\right)^{-1}\mathcal{F}_p^H \tag{7.A.18}$$

$$\mathbf{M}_5 = \mathbf{M}_1 + \left(\tilde{\mathbf{B}}_{a,\mathrm{D}}^{-1}\mathcal{F}_a + \mathbf{M}_1\mathcal{F}_p\right)\left[\frac{\mathbf{M}_4}{\mathbf{0}}\right] \tag{7.A.19}$$

Chapter 8

Conclusions and further research

IN this last chapter, we draw general conclusions in Section 8.1 and formulate suggestions for further research in Section 8.2.

8.1 Conclusions

DSL systems offer broadband data communication over the twisted pair telephone network. In Chapter 1, we have discussed the current position of DSL as one of the most widely deployed broadband access media. We have also indicated which challenges the DSL world will face in the future. We have enumerated a number of impairments that render the DSL environment harsh. In this thesis, we have developed advanced algorithms for equalizer design and RFI mitigation that allow to increase the DSL coverage and to offer new broadband services to as many customers as possible.

In Chapter 2, we have introduced the basic concepts of MCH, MC and DMT modulation. We showed that MCH and MC modulation are capable of achieving the channel capacity and that DMT modulation is a feasible, all-digital, complexity-constrained transmission scheme to approximate ideal MC modulation. DMT modulation makes use of a very efficient, channel-independent modulation and demodulation, based on a DFT, and a simple equalizer, based on a bank of 1-tap FEQs. DMT modulation as such is not suited for DSL communication. The use of an insufficiently long CP, in combination with the bad spectral DFT containment, results in a bit rate that is far below the channel capacity. Therefore, additional equalization and RFI mitigation are needed to

recover the bit rate loss.

In Chapter 3, we have discussed existing equalizer designs for DMT-based systems and we have cast them in a general framework. TEQ design has inspired many researchers since bit rate optimization of a DMT-based system with a TEQ leads to a non-linear optimization problem. Often, simplified procedures (e.g., the MMSE-TEQ and the MSSNR-TEQ) are resorted to, mainly based on the concept of time-domain channel shortening. Several TEQ designs, claiming but actually not achieving true bit rate maximization, have also been discussed. We have given an overview of these designs and we have indicated that approximations and assumptions in the adopted SNR model render them suboptimal. The only bit rate maximizing DMT equalizer that has been presented so far is the PTEQ, an alternative equalizer structure that outperforms any TEQ design for a given number of taps. The PTEQ and the TEQ have a similar computational complexity; the drawback of the PTEQ is its large memory requirement. The PTEQ is typically designed with an RLS-based adaptive algorithm, which can also be used for tracking purposes.

In Chapter 4, we have proposed two BM-TEQ design methods that closely approach the PTEQ performance. The first BM-TEQ design criterion follows from a compact and elegant SNR model, described in terms of the TX and RX signal SOS, rather than based on the FIR channel and TX signal and noise statistics. The key element in the derivation of this SNR model is the observation that the dependence of the SNR on the TEQ taps is easily accounted for when considering an SNR model at the FEQ output.

Subsequently, a second and equivalent BM-TEQ design criterion has been derived, referred to as an IR-SNLLS-based design criterion. This second formulation has several advantages over the original BM-TEQ design criterion. It clearly shows the frequency-domain, block transmission characteristic of DMT transmission. It has been casted in a common LS-based equalizer framework, which relates it to the channel-shortening TD-MMSE-TEQ design criterion by two suboptimal, but appealing FD-MMSE-TEQ design criteria. Moreover, it can be optimized using an iterative, fast converging GN-based algorithm that exploits the separability property of the SNLLS-based design criterion. Finally, we indicated that the TD-MMSE-TEQ design, the FD-MMSE-TEQ designs, the BM-TEQ design and the PTEQ design — although at first sight very different in nature — exhibit remarkable correspondence when turned into equivalent GEV problems. Through simulation we have shown that the BM-TEQ succeeds in closely approaching the PTEQ performance. Both the BM-TEQ and the PTEQ exhibit a smooth bit rate curve as a function of the synchronization delay, which renders the DMT receiver performance robust to the synchronization delay estimation.

In Chapter 5, we have shown how the BM-TEQ design can be used in a BM-PGEQ scheme. The BM-PGEQ allows for a trade-off between memory cost

and performance, while keeping computational complexity during data transmission roughly at the same level. Through simulation, we have illustrated that the BM-PGEQ outperforms an earlier presented tone grouping scheme where the whole tone group was assigned the PTEQ of the group center tone. Then, we have shown that the BM-TEQ and BM-PGEQ, despite their non-linear cost criterion, can be designed adaptively, based on a recursive Levenberg-Marquardt algorithm, which was derived from the IR-SNLLS-based BM-TEQ design criterion. The adaptive BM-TEQ turns out to exhibit fast convergence, which is comparable to the adaptive PTEQ. Moreover, the adaptive BM-PGEQ closely approaches the performance of the adaptive PTEQ in harsh environments with RFI where the local optima, attained by the adaptive BM-TEQ, can differ a few 100 kbps in bit rate. Besides providing an equalizer design algorithm, the adaptive BM-TEQ and BM-PGEQ allow to track variations of the transmission channel and noise characteristics. This makes them a good candidate for integration with the seamless rate adaptation functionality of ADSL2 and ADSL2+ modems.

In Chapter 6, we have presented a general framework for bit rate maximizing combined window and TEQ (BM-WinTEQ) design. We have derived two equivalent design criteria, which both are extensions of the BM-TEQ design criteria as derived in Chapter 4. An iterative GN-based algorithm was presented for optimizing the IR-SNLLS-based BM-WinTEQ design criterion. Furthermore, some interesting special design cases were addressed: a per-group design, a windowing-only design and an equalizer design in the presence of a fixed window. Simulations showed that the capability of receiver windowing to reduce the sidelobe level of the demodulating DFT can help the ADSL equalizer in reducing the ICI. Alternatively, a VDSL receiver may benefit from an additional TEQ to notch out RFIs. Furthermore, the BM-WinTEQ design turned out to outperform any other design, be it at the expense of robustness to an RFI that appears after the window and equalizer were designed. Therefore, we suggested to make use of a BM-FWinTEQ design when using a large number of equalizer taps and in the presence of non-stationary RFI, e.g., from HAM radios.

In Chapter 7, we have reconsidered DMT equalization under the realistic assumption that the wireline channel impulse response is well approximated by an IIR model. Based on the corresponding block data model and the optimum L-ZF block equalizers, we have shown that a PTEQ-based receiver is also suited for the equalization of an IIR channel. A low-complexity linear PTEQ extension has been developed to accommodate arbitrary IIR model orders and CP lengths: FD transmit redundancy as introduced by pilot and unused tones can be used to enhance the original PTEQ; alternatively, by treating symbol decisions in the same way as pilot symbols, a decision-feedback PTEQ extension is obtained. These PTEQ extensions also improve the RFI suppression capability of the PTEQ. Although the derivations in this chapter focused on

PTEQ extensions, similar BM-TEQ extensions have been briefly discussed.

To conclude, we give an overview of the *trade-offs* for bit rate maximizing equalizer and window design that have been suggested throughout the thesis.

- In Chapter 5, the computational and memory cost of the adaptive BM-TEQ, BM-PGEQ and PTEQ have been compared. Concerning the filtering, all algorithms have roughly the same computational cost but the PTEQ needs a much larger memory for storing the equalizer taps ($N_a T$ PTEQ taps instead of T TEQ taps). As for the equalizer design, all algorithms require the same SOS memory cost, but the BM-TEQ and the BM-PGEQ have a computational cost that is about $T/2$ times larger. We concluded that we now have a complete range of adaptive BM equalizers at our disposal, offering full flexibility to trade off computational and memory cost: from the computationally efficient RLS-based adaptive PTEQ with a large number of equalizer taps, over the adaptive BM-PGEQ, towards a single adaptive BM-TEQ with a larger equalizer update complexity.

- In Chapter 5, a BM-PGEQ has been presented as an intermediate solution between a BM-TEQ and a PTEQ. Especially in RFI scenarios, a BM-PGEQ with a few tone groups turns out to be less susceptible to poorly performing local optima than a BM-TEQ. A BM-PGEQ with 4 tone groups achieves the same performance as a PTEQ in a harsh RFI scenario.

- In Chapter 6, we have shown that, in the absence of RFI, equalizer taps can be exchanged for window coefficients: a longer window taper results in better ICI suppression, hence similar performance at a lower computational cost can be achieved by reducing the number of equalizer taps and increasing the window taper length.

- Throughout the thesis, three methods for RFI mitigation have been presented. In Chapter 5, we have suggested that an increase of the number of BM-TEQ taps results in a significant amount of RFI suppression. This behaviour is similar to what is observed with the PTEQ, which implicitly combines an equalizer and a window. In Chapter 6, the impact of receiver windowing has been investigated. As the cost of a TEQ is much higher than the windowing cost, we have suggested to always apply a TEQ with the largest affordable number of taps (with a maximum around 64 taps) and combine it with a window. In Chapter 7, we have shown that the exploitation of the information on a number of unused measurement tones around an RFI improves the RFI suppression, especially on the tones near the RFI. Therefore, by trading off the number of RX difference terms and FD transmit redundancy the RFI robustness can be enhanced. As this RFI suppression method requires a number of extra PTEQ taps (or FEQ taps in case of a BM-TEQ extension) for each RFI, it is complexer than

receiver windowing, hence it is especially useful in the case of a small number of RFIs.

- In Chapter 7, we have shown that the PTEQ extensions, which exploit FD transmit redundancy, add flexibility when designing DMT-based systems. TD and FD transmit redundancy can be traded off against each other. With a CP length of 16 samples, instead of the standardized CP length of 32 samples, and an adequately chosen PTEQ extension, a similar bit rate as with the original PTEQ can be achieved at a lower memory and computational cost or, alternatively, a higher bit rate is achieved without a considerable cost increase.

8.2 Further research

Adaptive BM-TEQ and BM-WinTEQ

As explained in Chapter 5 and 6, the adaptive BM-TEQ and BM-WinTEQ design require the same SOS as the adaptive PTEQ, be it that they have a larger computational cost. There are adaptive algorithms for non-linear optimization available in the literature, e.g., for neural network learning, that have a computational complexity and convergence speed in-between the (fast but complex) recursive Gauss-Newton or Levenberg-Marquardt algorithms and the (slow but cheap) stochastic gradient algorithms (e.g., conjugate gradient algorithms). Further research is required to explore their applicability to the non-linear BM-TEQ and BM-WinTEQ design criteria.

As has been shown in Section 6.6, an RFI that appears after the BM-WinTEQ design causes a significant performance loss. Especially in VDSL where HAM radios cause non-stationary RFI, this is an important issue that needs to be addressed.

Equalization for MIMO-DSL

In this thesis, we have focused on DSL communication in a single-input single-output (SISO) context: one DMT transmitter communicates with one DMT receiver over a single twisted pair (see Figure 1.2); crosstalk, which is the electromagnetic coupling between twisted pairs in a binder, is treated as an impairment (see Section 1.3.1) that causes additive noise. Recently, there has been an increased research interest for so-called multiple-input multiple-output DSL (MIMO-DSL) [22, 23, 24, 49, 112, 162]: additional performance gains can be obtained by considering the binder of twisted pairs as a MIMO system and exploiting the so-called far-end crosstalk (FEXT), i.e., the crosstalk that originates from signals traveling in the same direction (upstream or downstream). The FEXT level increases with frequency, hence it is of particular interest for ADSL2+ and VDSL.

Several levels of MIMO-DSL are investigated, depending on the assumed amount

of coordination and cooperation. In the case of *dynamic spectrum management* (DSM), all transmitters dynamically adapt their TX power spectrum in a centralized or decentralized fashion to the crosstalk environment; however, the signaling remains uncoordinated. If co-located modems are able to cooperate at one end of the binder (which is typically at the central office), so-called *vectoring* can be used: downstream crosstalk can be pre-compensated at the CO before transmission, while upstream crosstalk can be cancelled upon signal reception. The highest level of cooperation is achieved when the transmitters and receivers at both ends of the binder are cooperating. This kind of vectoring is referred to as *bonding*.

Until now, it has been assumed in the literature that all channels in MIMO-DSL are synchronized and perfectly shortened so that coordination and cooperation can be done for each tone separately. These assumptions do not necessarily hold true: e.g., in ADSL2+, the transmission and crosstalk channel impulse responses are longer than the CP. Hence, the MIMO-DSL techniques should be combined with appropriate equalization. Further research is then required to investigate the impact of imperfect channel shortening on DSM (and how to combine DSM and equalization), as well as to integrate vectoring or bonding with MIMO equalization.

Equalization for wireless communications

In this thesis, we have focused on wireline DSL communication. However, MC modulation has also been adopted for several wireless applications, e.g., for WLANs in the IEEE 802.11a [92] and the Hiperlan/2 [42] standards. Instead of DMT modulation, it is then referred to as OFDM modulation (see Section 2.2.3). Several tendencies and specific aspects in wireless communications lead to interesting topics of further research.

Initially, it was mostly assumed that a TEQ is not needed for OFDM as the wireless channel is typically shorter than the CP length [150]. However, the radio-frequency front-end in each wireless system includes shaping filters that increase the overall channel impulse response length. Therefore, there has recently emerged an increased interest for equalizer design in a wireless context [2, 76, 84, 124]. It would be interesting to investigate the applicability and possible extension to a wireless context of the TEQ design methods that are presented in the thesis.

Time-varying channels

One of the crucial differences between wireline and wireless systems is that the wireless channel typically varies much faster in time. Therefore, the equalizer should be *time-varying and adaptive* in order to track the time-variations of the channel. Two approaches can be envisaged here:

- to avoid a large efficiency loss due to training sequences, one could resort

to *(semi)blind* channel-shortening algorithms [9, 65, 79, 84, 100];

- a so-called *basis-expansion model* allows to model a fast time-varying frequency-selective channel as a weighted sum of basis functions, e.g., complex exponentials, where the weights are slowly time-varying. A dedicated adaptive equalizer, which matches the basis-expansion channel model, is then capable of tracking channel variations [11, 12].

Design objective

The BM-TEQ design criterion that we presented in this thesis corresponds to the actual design objective of a DSL system, namely providing the highest possible bit rate for a fixed bit error rate (BER). The equalizer design criteria that are currently proposed for wireless OFDM systems, on the other hand, are not related to the actual design objective: e.g., in [2], an MMSE-TEQ criterion (see Section 3.2.1) is considered; in [84], the design criterion is related to the MSSNR-TEQ design of Section 3.2.2. If there is no channel state information (CSI) available at the OFDM transmitter, a fixed constellation over all tones in combination with channel coding is typically used [150]; a suitable design objective would then be to *minimize the coded BER*. Recently, OFDM systems have been presented with full or partial CSI at the transmitter [154]. This allows to introduce adaptive modulation (similar to bit and power loading in DSL) in order to *maximize the data rate* at a fixed BER (for a rate-adaptive system) [154], which is related to the BM-TEQ design, or to *minimize the BER* for a fixed data rate (for a margin-adaptive system) [123], see Remark 2.1.

MIMO context

Whereas we considered in this thesis DSL communication over a single line, i.e., a SISO system, MIMO wireless systems are a hot research topic as the use of *multiple TX and/or RX antennas* in combination with space-time coding, adaptive modulation and/or smart antenna technology can give tremendous gains in capacity and/or quality [21, 95]. These gains must allow next-generation wireless systems to achieve similar performance as current wireline systems. In addition to the above mentioned wireless-specific issues, the extension from SISO to MIMO (and intermediate) systems should be made, in a similar way as for the above outlined MIMO-DSL context.

Other transmission schemes

Apart from OFDM, other transmission schemes are considered in wireless systems. So-called *single-carrier modulation with CP* has some interesting advantages (concerning carrier synchronization and nonlinear distortion) over OFDM modulation [78, 104]. *Code-division multiple access* (CDMA) allows to multiplex several users by spreading the TX signals with a particular orthogonal code for each user; a CDMA scheme with CP has been considered in, e.g., [10]. For both modulation schemes, particular channel shortening design algorithms are required for the case of a too long CIR.

Bibliography

[1] N. Al-Dhahir. Time-varying versus time-invariant finite-length MMSE-DFE on stationary dispersive channels. *IEEE Trans. Communications*, 46(1):11–15, January 1998.

[2] N. Al-Dhahir. FIR channel-shortening equalizers for MIMO ISI channels. *IEEE Trans. Communications*, 49(2):213–218, February 2001.

[3] N. Al-Dhahir and J. M. Cioffi. MMSE decision feedback equalizers: finite-length results. *IEEE Trans. Information Theory*, 41(4):961–976, July 1995.

[4] N. Al-Dhahir and J. M. Cioffi. Block transmission over dispersive channels: transmit filter optimization and realization, and MMSE-DFE receiver performance. *IEEE Trans. Information Theory*, 42(1):137–160, January 1996.

[5] N. Al-Dhahir and J. M. Cioffi. Efficiently computed reduced-parameter input-aided MMSE equalizers for ML detection: A unified approach. *IEEE Trans. Information Theory*, 42(3):903–915, May 1996.

[6] N. Al-Dhahir and J. M. Cioffi. Optimum finite-length equalization for multicarrier transceivers. *IEEE Trans. Communications*, 44(1):56–64, January 1996.

[7] N. Al-Dhahir and J. M. Cioffi. A bandwidth-optimized reduced-complexity equalized multicarrier transceiver. *IEEE Trans. Communications*, 45(8):948–956, August 1997.

[8] G. Arslan, B. L. Evans, and S. Kiaei. Equalization for discrete multitone transceivers to maximize bit rate. *IEEE Trans. Signal Processing*, 49(12):3123–3135, December 2001.

[9] J. Balakrishnan, R. K. Martin, and C. R. Johnson, Jr. Blind, adaptive channel shortening by sum-squared auto-correlation minimization (SAM). *IEEE Trans. Signal Processing*, 51(12):3086–3093, December 2003.

[10] S. Barbarossa, G. Scutari, and A. Swami. MUI-free CDMA systems incorporating space-time coding and channel shortening. In *Proc. IEEE Int. Conf. Acoustics, Speech, and Signal Processing (ICASSP)*, pages 2213–2216, Orlando, Florida, May 2002.

[11] I. Barhumi, G. Leus, and M. Moonen. Time-domain and frequency-domain per-tone equalization for OFDM over doubly-selective channels. *Accepted for publication in Signal Processing*, 2004.

[12] I. Barhumi, G. Leus, and M. Moonen. Time varying FIR equalization of doubly-selective channels. *Accepted for publication in IEEE Trans. Wireless Comm.*, 2004.

[13] Internet Service Providers Association Belgium. `http://www.ispa.be`.

[14] J. A. C. Bingham. Multicarrier modulation for data transmission: An idea whose time has come. *IEEE Commun. Mag.*, 28(5):5–14, May 1990.

[15] J. A. C. Bingham. *ADSL, VDSL, and Multicarrier Modulation*. Wiley-Interscience, 2000.

[16] A. Bjorck. *Least-Squares Methods*. Elsevier, 1987.

[17] C. Bouchat, S. van den Bosch, and T. Pollet. QoS in DSL access. *IEEE Commun. Mag.*, 41(9):108–114, September 2003.

[18] R. H. Byrd and D. A. Payne. Convergence of the iteratively reweighted least squares algorithm for robust regression. Technical Report 313, The Johns Hopkins University, Baltimore, MD, June 1979.

[19] J. Campello. Optimal discrete bit loading for multicarrier modulation systems. In *Proc. IEEE Int. Symp. on Information Theory*, page 193, Cambridge, MA, USA, August 1998.

[20] J. Campello. Practical bit loading for DMT. In *Proc. IEEE Int. Conf. Communications (ICC)*, volume 2, pages 801–805, Vancouver, Canada, June 1999.

[21] S. Catreux, V. Erceg, D. Gesbert, and Jr. Heath, R. W. Adaptive modulation and MIMO coding for broadband wireless data networks. *IEEE Commun. Mag.*, 40(6):108–115, June 2002.

[22] R. Cendrillon, M. Moonen, G. Ginis, K. Van Acker, T. Bostoen, and P. Vandaele. Partial crosstalk cancellation for upstream VDSL. *EURASIP J. Applied Signal Processing*, (10):1520–1535, October 2004.

[23] R. Cendrillon, M. Moonen, D. Gore, and P. Paulraj. Low complexity crosstalk cancellation with line selection in upstream VDSL. In *Proc. IEEE Int. Conf. Acoustics, Speech, and Signal Processing (ICASSP)*, volume 4, pages 692–695, Hong Kong SAR, China, April 2003.

[24] R. Cendrillon, W. Yu, M. Moonen, J. Verlinden, and J. Bostoen. Optimal multi-user spectrum management for digital subscriber lines. In *Proc. IEEE Int. Conf. Communications (ICC)*, pages 1–5, Paris, France, June 2004.

[25] R. W. Chang. Synthesis of band-limited orthogonal signals for multichannel data transmission. *Bell System Tech. Journal*, 45:1775–1796, December 1966.

[26] S. M. Cherry. The wireless last mile. *IEEE Spectrum*, 40(9):18–22, September 2003.

[27] G. Cherubini, E. Eleftheriou, and S. Olcer. Filtered multitone modulation for very high-speed digital subscriber lines. *IEEE J. Select. Areas Commun.*, 20(5):1016–1028, June 2002.

[28] J. S. Chow and J. M. Cioffi. A cost-effective maximum likelihood receiver for multicarrier systems. In *Proc. IEEE Int. Conf. Communications (ICC)*, volume 2, pages 948–952, June 1992.

[29] J. S. Chow, J. C. Tu, and J. M. Cioffi. A discrete multitone transceiver system for HDSL applications. *IEEE J. Select. Areas Commun.*, 9(6):895–907, August 1991.

[30] P. S. Chow, J. M. Cioffi, and J. A. C. Bingham. A practical discrete multitone transceiver loading algorithm for data transmission over spectrally shaped channels. *IEEE Trans. Communications*, 43(2/3/4):773–775, February/March/April 1995.

[31] D. Chrissan. Uni-DSL: One DSL for universal service. Technical report, Texas Instruments, June 2004. White paper.

[32] J. M. Cioffi. Advanced digital communication: course notes EE379C. Technical Report Available via http://www.stanford.edu/class/ee379c/readerfiles/chap4.pdf, Stanford University, 2002.

[33] J. M. Cioffi, G. P. Dudevoir, M. V. Eyuboglu, and G. D. Forney Jr. MMSE decision-feedback equalizers and coding - Part I: Equalization results. *IEEE Trans. Communications*, 43(10):2582–2594, October 1995.

[34] G. Cuypers, M. Ysebaert, G. Moonen, and P. Vandaele. Combining per tone equalization and windowing in DMT receivers. In *Proc. IEEE Int. Conf. Acoustics, Speech, and Signal Processing (ICASSP)*, volume 3, pages 2341–2344, 2002.

[35] H. Dai and H. V. Poor. Advanced signal processing for power line communications. *IEEE Commun. Mag.*, 41(5):100–107, May 2003.

[36] H. Dai and N. K. Sinha. Robust recursive least-squares method with modified weights for bilinear system identification. *Proc. IEEE*, 136(3):122–126, May 1989.

[37] D. Daly, C. Heneghan, and A. D. Fagan. A minimum mean-squared error interpretation of residual ISI channel shortening for discrete multitone transceivers. In *Proc. IEEE Int. Conf. Acoustics, Speech, and Signal Processing (ICASSP)*, volume 4, pages 2065–2068, May 2001.

[38] E. de Carvalho and D. T. M. Slock. Burst mode equalization: Optimal approach and suboptimal continuous-processing approximation. *Signal Processing*, 80(10):1999–2015, October 2000.

[39] L. de Clercq, M. Peeters, S. Schelstraete, and T. Pollet. Mitigation of radio interference in xDSL transmission. *IEEE Commun. Mag.*, 38(3):168–173, March 2000.

[40] M. de Courville, P. Duhamel, P. Madec, and J. Palicot. Blind equalization of OFDM systems based on the minimization of a quadratic criterion. In *Proc. IEEE Int. Conf. Communications (ICC)*, pages 1318–1321, Dallas, TX, June 1996.

[41] C. Drewes, W. Aicher, and J. Hausner. The wireless art and the wired force of subscriber access. *IEEE Commun. Mag.*, 39(5):118–124, May 2001.

[42] The European Telecomm. Standards Inst. (ETSI). Broadband radio access networks (BRAN); high performance radio local area networks (HIPERLAN) type 2; system overview, 101 683 v1.1.1, 2000.

[43] The European Telecomm. Standards Inst. (ETSI). Digital video broadcasting (DVB); framing structure, channel coding and modulation for digital terrestrial television, EN 300 744 v1.4.1, 2001.

[44] The European Telecomm. Standards Inst. (ETSI). Radio broadcasting systems; digital audio broadcasting (DAB) to mobile, portable and fixed receivers, EN 300 401 v1.3.3, 2001-2005.

[45] D. D. Falconer and F. R. Magee. Adaptive channel memory truncation for maximum likelihood sequence estimation. *Bell Sys. Tech. Journal*, pages 1541–1562, November 1973.

[46] DSL Forum. `http://www.dslforum.org`.

[47] W. A. Gardner. Cyclic wiener filtering: Theory and method. *IEEE Trans. Communications*, 41(1):151–163, January 1993.

[48] A. T. Georgiadis and B. Mulgrew. Adaptive Bayesian decision feedback equalizer for alpha-stable noise environments. *Signal Processing*, 81(8):1603–1623, August 2001.

[49] G. Ginis and J. M. Cioffi. Vectored transmission for digital subscriber line systems. *IEEE J. Select. Areas Commun.*, 20(5):1085–1104, June 2002.

[50] G. H. Golub and V. Pereyra. The differentiation of pseudo-inverses and nonlinear least squares problems whose variables separate. *SIAM J. Numer. Anal.*, 10:413–432, 1973.

[51] G. H. Golub and V. Pereyra. Separable nonlinear least squares: the variable projection method and its applications. *Institute of Physics, Inverse Problems*, 19(2):R1–R26, April 2003.

[52] G. H. Golub and C. F. Van Loan. *Matrix Computations - Third Edition*. The John Hopkins University Press, 1996.

[53] R. M. Gray. Toeplitz and circulant matrices: A review. Technical Report Available via http://www-ee.stanford.edu/g̃ray/toeplitz.pdf, Stanford University, August 2002.

[54] S. Haykin. *Adaptive Filter Theory*. Englewood Cliffs, NJ: Prentice-Hall, 3rd edition, 1996.

[55] S. Haykin. Adaptive digital communication receivers. *IEEE Commun. Mag.*, 38(12):106–114, December 2000.

[56] W. Henkel and T. Kessler. Maximizing the channel capacity of multicarrier transmission by suitable adaptation of the time-domain equalizer. *IEEE Trans. Communications*, 48(12):2000–2004, December 2000.

[57] W. Henkel, G. Tauböck, P. Ödling, P. O. Börjesson, and N. Petersson. The cyclic prefix of OFDM/DMT - an analysis. In *International Zurich Seminar on Broadband Communications*, pages 22–1 – 22–3, February 2002.

[58] D. Hughes-Hartogs. Ensemble modem structure for imperfect transmission media. U.S. Patents Nos. 4,679,227 (July 1987), 4,731,816 (March 1988) and 4,833,706 (May 1989).

[59] I. Ilani. Time domain equalizer for DMT transceivers – a geometric approach. US patent no. 6341298.

[60] Aware Inc. ADSL2 and ADSL2+ - the new ADSL standards. Technical report, March 2003. White paper.

[61] International Telecommunications Union (ITU). Recommendation G.992.1. Asymmetric digital subscriber line (ADSL) transceivers, July 1999.

[62] International Telecommunications Union (ITU). Recommendation G.996.1. Test procedures for digital subscriber line (DSL) transceivers, February 2001.

[63] International Telecommunications Union (ITU). Recommendation G.992.3. Asymmetric digital subscriber line (ADSL) transceivers - 2 (ADSL2), July 2002.

[64] International Telecommunications Union (ITU). Recommendation G.992.5. Asymmetrical digital subscriber line (ADSL) transceivers - extended bandwidth ADSL2 (ADSL2+), May 2003.

[65] C. R. Johnson, Jr., P. Schniter, T. J. Endres, J. D. Behm, D. R. Brown, and R. A. Casas. Blind equalization using the constant modulus criterion: a review. *Proc. IEEE*, 86(10):1927–1950, October 1998.

[66] T. Kailath, A. H. Sayed, and B. Hassibi. *Linear Estimation*. Prentice Hall, 2000.

[67] I. Kalet. The multitone channel. *IEEE Trans. Communications*, 37(2):119–124, February 1989.

[68] S. Kapoor and S. Nedic. Interference suppression in DMT receiver. In *Proc. IEEE Int. Conf. Communications (ICC)*, volume 2, pages 778–782, New Orleans, USA, June 2000.

[69] S. Kasturia, J. T. Aslanis, and J. M. Cioffi. Vector coding for partial response channels. *IEEE Trans. Information Theory*, 36(7):741–761, July 1990.

[70] L. Kaufman. A variable projection method for solving separable nonlinear least squares problems. *BIT*, 15:49–57, 1975.

[71] K. J. Kerpez. DSL spectrum management standard. *IEEE Commun. Mag.*, 40(11):116–123, November 2002.

[72] A. Klein, G. K. Kaleh, and B. W. Baier. Zero forcing and minimum mean-square-error equalization for multiuser detection in code-division multiple-access channels. *IEEE Trans. Vehicular Technology*, 45(2):276–287, May 1996.

[73] B. S. Krongold, K. Ramchandran, and D. L. Jones. Computationally efficient optimal power allocation algorithms for multicarrier communication systems. *IEEE Trans. Communications*, 48(1):23–27, January 2000.

[74] N. Lashkarian and S. Kiaei. Optimum equalization of multicarrier systems: A unified geometric approach. *IEEE Trans. Communications*, 49:1762–1769, October 2001.

[75] E. A. Lee and D. G. Messerschmitt. *Digital Communication*. Kluwer Academic Publishers, second edition, 1994.

[76] G. Leus and M. Moonen. Per-tone equalization for MIMO OFDM systems. *IEEE Trans. Signal Processing*, 51(11):2965–2975, November 2003.

[77] L. Ljung and T. Söderström. *Theory and Practice of Recursive Identification*. Cambridge, MA: MIT Press, 1983.

[78] J. Louveaux, L. Vandendorpe, and T. Sartenaer. Cyclic prefixed single carrier and multicarrier transmission: bit rate comparison. *IEEE Commun. Lett.*, 7(4):180–182, April 2003.

[79] R. K. Martin, J. Balakrishnan, W. A. Sethares, and C. R. Johnson, Jr. A blind, adaptive TEQ for multicarrier systems. *IEEE Signal Processing Lett.*, 9(11):341–343, November 2002.

[80] R. K. Martin, C. R. Johnson, Jr., M. Ding, and B. L. Evans. Exploiting symmetry in channel shortening equalizers. In *Proc. IEEE Int. Conf. Acoustics, Speech, and Signal Processing (ICASSP)*, volume 5, pages 97–100, Hong Kong SAR, China, April 2003.

[81] R. K. Martin, D. Ming, B. L. Evans, and C. R. Johnson, Jr. Efficient channel shortening equalizer design. *EURASIP J. Applied Signal Processing*, (13):1279–1290, December 2003.

[82] R. K. Martin, K. Vanbleu, M. Ding, G. Ysebaert, M. Milosevic, B. L. Evans, M. Moonen, and C. R. Johnson, Jr. Implementation complexity and communication performance tradeoffs in discrete multitone modulation equalizers. *In preparation for submission to IEEE Trans. Signal Processing* .

[83] R. K. Martin, K. Vanbleu, M. Ding, G. Ysebaert, M. Milosevic, B. L. Evans, M. Moonen, and C. R. Johnson, Jr. Unification and evaluation of equalization structures and design algorithms for discrete multitone modulation systems. *Submitted to IEEE Trans. Signal Processing*, December 2003.

[84] R. K. Martin, J. M. Walsh, and C. R. Johnson, Jr. Low complexity MIMO blind, adaptive channel shortening. *Accepted for publication in IEEE Trans. Signal Processing*, 2004.

[85] P. J. W. Melsa, R. C. Younce, and C. E. Rohrs. Impulse response shortening for discrete multitone transceivers. *IEEE Trans. Communications*, 44(12):1662–1672, December 1996.

[86] D. G. Mestdagh, M. R. Isaksson, and P. Ödling. Zipper VDSL: a solution for robust duplex communication over telephone lines. *IEEE Commun. Mag.*, 38(5):90–96, May 2000.

[87] D. J. Mestdagh and P. M. Spruyt. A method to reduce the probability of clipping in DMT-based transceivers. *IEEE Trans. Communications*, 44(10):1234–1238, October 1996.

[88] M. Milosevic, L. F. C. Pessoa, B. L. Evans, and R. Baldick. Optimal time domain equalization design for maximizing data rate of discrete multitone systems. *Submitted to IEEE Trans. Signal Processing*, 2002.

[89] S. Nedic and N. Popovic. Per tone adaptive equalization in DMT receivers with selective windowing. In *Proc. IEEE Int. Conf. Communications (ICC)*, volume 1, pages 179–183, Helsinki, Finland, June 2001.

[90] L. S. H. Ngia and J. Sjöberg. Efficient training of neural nets for nonlinear adaptive filtering using a recursive Levenberg-Marquardt algorithm. *IEEE Trans. Signal Processing*, 48(7):1915–1927, July 2000.

[91] R. Nilsson, F. Sjöberg, and J. P. LeBlanc. A rank-reduced LMMSE canceller for narrowband interference suppression in OFDM-based systems. *IEEE Trans. Communications*, 51(12):2126–2140, December 2003.

[92] The Institute of Electrical and Electronics Engineers. Wireless LAN medium access control (MAC) and physical layer (PHY) specifications. IEEE std. 802.11a. 1999.

[93] A. Oppenheim and R. Schafer. *Discrete-Time Signal Processing*. Englewood Cliffs, NJ: Prentice Hall, New Jersey, 1989.

[94] K. Pahlavan and J. L. Holsinger. Voice-band data communication modems – a historical review: 1919-1988. *IEEE Commun. Mag.*, 26(1):16–27, January 1988.

[95] A. J. Paulraj and C. B. Papadias. Space-time processing for wireless communications. *IEEE Signal Processing Mag.*, 14(6):49–83, June 1997.

[96] A. Peled and A. Ruiz. Frequency domain data transmission using reduced computational complexity algorithms. In *Proc. IEEE Int. Conf. Acoustics, Speech, and Signal Processing (ICASSP)*, pages 964–967, Denver, Colorado, April 1980.

[97] T. Pollet, M. Peeters, M. Moonen, and L. Vandendorpe. Equalization for DMT-based broadband modems. *IEEE Commun. Mag.*, 38(5):106–113, May 2000.

[98] T. Pollet, H. Steendam, and M. Moeneclaey. Performance degradation of multi-carrier systems caused by an insufficient guard interval duration. In *Proc. Intern. Workshop on Copper Wire Access Systems "Bridging the Last Copper Drop" (CWAS)*, pages 265–270, Budapest, Hungary, October 1997.

[99] A. J. Redfern. Receiver window design for multicarrier communication systems. *IEEE J. Select. Areas Commun.*, 20(5):1029–1036, June 2002.

[100] F. Romano and S. Barbarossa. Non-data aided adaptive channel shortening for efficient multi-carrier systems. In *Proc. IEEE Int. Conf. Acoustics, Speech, and Signal Processing (ICASSP)*, pages 233–236, Hong Kong SAR, China, April 2003.

[101] A. Ruhe and P.-A. Wedin. Algorithms for separable nonlinear least squares. *SIAM Rev.*, 22:318–337, 1980.

[102] B. R. Saltzberg. Performance of an efficient parallel data transmission system. *IEEE Trans. on Comm. Technology*, 15(6):805–811, December 1967.

[103] S. D. Sandberg and M. A. Tzannes. Overlapped discrete multitone modulation for high speed copper wire communications. *IEEE J. Select. Areas Commun.*, 13(9):1571–1585, December 1995.

[104] H. Sari, G. Karam, and I. Jeanclaude. Transmission techniques for digital terrestrial TV broadcasting. *IEEE Commun. Mag.*, 33(2):100–109, February 1995.

[105] A. Scaglione, S. Barbarossa, and G. B. Giannakis. Filterbank transceivers optimizing information rate in block transmissions over dispersive channels. *IEEE Trans. Information Theory*, 45(3):1019–1032, April 1999.

[106] R. Schur and J. Speidel. An efficient equalization method to minimize delay spread in OFDM/DMT systems. In *Proc. IEEE Int. Conf. Communications (ICC)*, volume 5, pages 1481–1485, Helsinki, Finland, June 2001.

[107] R. Schur, J. Speidel, and R. Angerbauer. Reduction of guard interval by impulse compression for DMT modulation on twisted pair cables. In *Proc. IEEE Global Comm. Conf. (GLOBECOM)*, pages 1632–1636, November 2000.

[108] C. Shannon. A mathematical theory of communication. *Bell System Technical Journal*, 27(5):379–423 and 623–656, July and October 1948.

[109] F. Sjöberg. *The Zipper Duplex Method in Very High-Speed Digital Subscriber Lines*. PhD thesis, Luleå University of Technology, 2000.

[110] F. Sjöberg, M. Isaksson, R. Nilsson, P. Ödling, S. K. Wilson, and P. A. Börjesson. Zipper: A duplex method for VDSL based on DMT. *IEEE Trans. Communications*, 47(8):1245–1252, August 1999.

[111] F. Sjöberg, R. Nilsson, M. Isaksson, P. Ödling, and P. O. Börjesson. Asynchronous zipper. In *Proc. IEEE Int. Conf. Communications (ICC)*, volume 1, pages 231–235, Vancouver, Canada, June 1999.

[112] K. B. Song, S. T. Chung, G. Ginis, and J. M. Cioffi. Dynamic spectrum management for next-generation DSL systems. *IEEE Trans. Communications*, 40(10):101–109, October 2002.

[113] P. Spruyt, P. Reusens, and S. Braet. Performance of improved DMT transceiver for VDSL. ANSI T1E1.4 Committee contribution 96-104, Colorado Springs, April 1996.

[114] A. Stamoulis, G. B. Giannakis, and A. Scaglione. Block FIR decision-feedback equalizers for filterbank precoded transmissions with blind channel estimation capabilities. *IEEE Trans. Communications*, 49(1):69–83, January 2001.

[115] T. Starr, J. M. Cioffi, and P. J. Silvermann. *Understanding Digital Subscriber Line Technology*. Englewood Cliffs, NJ: Prentice Hall, 1999.

[116] Internet Usage World Stats. `http://www.internetworldstats.com`.

[117] Y. Sun. Bandwidth-efficient wireless OFDM. *IEEE J. Select. Areas Commun.*, 19(11):2267–2278, November 2001.

[118] J. Tellado and J. M. Cioffi. Efficient algorithms for reducing PAR in multicarrier systems. In *Proc. IEEE Int. Symp. on Information Theory (ISIT)*, page 191, Boston, August 1998.

[119] The European Telecomm. Standards Inst. (ETSI). Broadband radio access networks (BRAN); HIPERLAN type 2; Physical (PHY) layer. TS 101 475 v1.3.1., December 2001.

[120] The European Telecomm. Standards Inst. (ETSI). Transmission and multiplexing (TM); Access transmission systems on metallic access cables; Asymmetric digital subscriber line (ADSL) - European specific requirements. TS 101 388 v1.3.1., May 2002.

[121] The European Telecomm. Standards Inst. (ETSI). Transmission and multiplexing (TM); Access transmission systems on metallic access cables; Very high speed digital subscriber line (VDSL). TS 101 270 v1.3.1., July 2003.

[122] The MathWorks, Inc. *Matlab Optimization Toolbox User's Guide*. 2002.

[123] S. Thoen, L. Van der Perre, M. Engels, and H. De Man. Adaptive loading for OFDM/SDMA-based wireless networks. *IEEE Trans. Communications*, 50(11):1798–1810, November 2002.

[124] A. Tkacenko and P. P. Vaidyanathan. Eigenfilter design of MIMO equalizers for channel shortening. In *Proc. IEEE Int. Conf. Acoustics, Speech, and Signal Processing (ICASSP)*, pages 2361–2364, Orlando, Florida, May 2002.

[125] S. Trautmann and N. J. Fliege. A new equalizer for multitone sysems without guard time. *IEEE Commun. Lett.*, 6(1):34–36, January 2002.

[126] S. Trautmann and N. J. Fliege. Perfect equalization for DMT systems without guard interval. *IEEE J. Select. Areas Commun.*, 20(5):987–996, June 2002.

[127] S. Trautmann, T. Karp, and N. J. Fliege. Frequency domain equalization of DMT/OFDM systems with insufficient guard interval. In *Proc. IEEE Int. Conf. Communications (ICC)*, pages 1646–1650, April 2002.

[128] K. Van Acker. *Equalization and Echo Cancellation for DMT-Based DSL Modems*. PhD thesis, K.U.Leuven, Belgium, January 2001.

[129] K. Van Acker, G. Leus, M. Moonen, S. Claes, and O. van de Wiel. An improved optimization algorithm for time domain equalizer design in ADSL modems. In *Proc. Intern. Workshop on Copper Wire Access Systems "Bridging the Last Copper Drop"(CWAS)*, Budapest, Hungary, 1997.

[130] K. Van Acker, G. Leus, M. Moonen, and T. Pollet. Frequency domain equalization with tone grouping in DMT/ADSL-receivers. In *Proc. Asilomar Conf. on Signals, Systems and Computers*, Pacific Grove, California, October 1999.

[131] K. Van Acker, G. Leus, M. Moonen, and T. Pollet. RLS-based initialization for per-tone equalizers in DMT receivers. *IEEE Trans. Communications*, 51(6):885–889, June 2003.

[132] K. Van Acker, G. Leus, M. Moonen, O. van de Wiel, and T. Pollet. Per-tone equalization for DMT-based systems. *IEEE Trans. Communications*, 49(1):109–119, January 2001.

[133] K. Van Acker, T. Pollet, G. Leus, and M. Moonen. Combination of per tone equalization and windowing in DMT-receivers. *Signal Processing*, 81(8):1571–1579, August 2001.

[134] J.-F. Van Kerckhove and P. Spruyt. Adapted optimization criterion for FDM-based DMT-ADSL equalization. In *Proc. IEEE Int. Conf. Communications (ICC)*, volume 3, pages 1328–1334, June 1996.

[135] K. Vanbleu, G. Leus, and M. Moonen. Per-tone equalization for DMT-based transmission over IIR channels. In *Proc. IEEE Global Comm. Conf. (GLOBECOM)*, pages 405–409, November 2001.

[136] K. Vanbleu, M. Moonen, and G. Leus. Linear and decision-feedback per tone equalization for DMT-based transmission over IIR channels. Technical Report ESAT-SISTA/TR 2003-49. *Accepted for publication in IEEE Trans. Signal Processing*. Available at ftp://ftp.esat.kuleuven.ac.be/pub/sista/vanbleu/reports/04-49.pdf, ESAT, K.U.Leuven, Belgium, April 2004.

[137] K. Vanbleu, G. Ysebaert, G. Cuypers, and M. Moonen. Bitrate maximizing per group equalization for DMT-based systems. Technical Report ESAT-SISTA/TR 2003-48. *Submitted to Signal Processing*. Available at ftp://ftp.esat.kuleuven.ac.be/pub/sista/vanbleu/reports/03-48.pdf, ESAT, K.U.Leuven, Belgium, August 2003.

[138] K. Vanbleu, G. Ysebaert, G. Cuypers, and M. Moonen. Adaptive bitrate maximizing time-domain equalization design for DMT-based systems. Technical Report ESAT-SISTA/TR 2003-168. *Submitted to IEEE Trans. Signal Processing*. Available at ftp://ftp.esat.kuleuven.ac.be/pub/sista/vanbleu/reports/03-168.pdf, ESAT, K.U.Leuven, Belgium, May 2004.

[139] K. Vanbleu, G. Ysebaert, G. Cuypers, and M. Moonen. On the relation between time-domain equalizers and per-tone equalizers for DMT-based systems. In *Proc. IEEE Benelux Sign. Proc. Symposium (SPS)*, Hilvarenbeek, the Netherlands, April 2004.

[140] K. Vanbleu, G. Ysebaert, G. Cuypers, and M. Moonen. On time-domain and frequency-domain MMSE-based TEQ design for DMT transmission. Technical Report ESAT-SISTA/TR 2004-02. *Accepted for publication in IEEE Trans. Signal Processing*. Available at ftp://ftp.esat.kuleuven.ac.be/pub/sista/vanbleu/reports/04-02.pdf, ESAT, K.U.Leuven, Belgium, January 2004.

[141] K. Vanbleu, G. Ysebaert, G. Cuypers, and M. Moonen. On time-domain and frequency-domain MMSE-based TEQ designs for DMT transmission. In *Proc. European Signal Processing Conf. (EUSIPCO)*, Vienna, Austria, September 2004.

[142] K. Vanbleu, G. Ysebaert, G. Cuypers, M. Moonen, and G. Leus. Adaptive bitrate maximizing TEQ design for DMT-based systems. In *Proc. IEEE Int. Conf. Acoustics, Speech, and Signal Processing (ICASSP)*, pages 1057–1060, Montreal, Canada, May 2004.

[143] K. Vanbleu, G. Ysebaert, G. Cuypers, M. Moonen, and K. Van Acker. Bitrate maximizing time-domain equalizer design for DMT-based systems. In *Proc. IEEE Int. Conf. Communications (ICC)*, pages 2360–2364, Anchorage, Alaska, May 2003.

[144] K. Vanbleu, G. Ysebaert, G. Cuypers, M. Moonen, and K. Van Acker. Bitrate maximizing time-domain equalizer design for DMT-based systems. *IEEE Trans. Communications*, 52(6):871–876, June 2004.

[145] K. Vanbleu, G. Ysebaert, M. Moonen, and P. Vandaele. Combined equalization and alien crosstalk cancellation in ADSL receivers. In *Proc. European Signal Processing Conf. (EUSIPCO)*, pages 281–284, Toulouse, France, September 2002.

[146] K. Vanbleu, G. Ysebaert, M. Moonen, and P. Vandaele. Combined equalization and alien crosstalk cancellation in ADSL receivers. In *Proc. IEEE Benelux Sign. Proc. Symposium (SPS)*, pages 49–52, Leuven, Belgium, March 2002.

[147] L. Vandendorpe. Fractionally spaced linear and DF MIMO equalizers for multitone systems without guard time. *Annals of Telecommunications*, 52(1-2):21–30, January/February 1997.

[148] L. Vandendorpe, J. Louveaux, B. Maison, and A. Chevreuil. About the asymptotic performance of MMSE MIMO DFE for filter-bank based multicarrier transmission. *IEEE Trans. Communications*, 47(10):1472–1475, October 1999.

[149] H. Vanhaute and M. Moonen. Turbo per tone equalization for ADSL systems. In *Proc. IEEE Int. Conf. Communications (ICC)*, Paris, France, June 2004.

[150] Z. Wang and G. B. Giannakis. Wireless multicarrier communications. *IEEE Signal Processing Mag.*, 17:29–48, May 2000.

[151] S. B. Weinstein and P. M. Ebert. Data transmission by frequency-division multiplexing using the discrete Fourier transform. *IEEE Trans. on Commun. Technology*, 19(5):628–634, October 1971.

[152] A. D. Whalen. *Detection of signals in noise*. New York: Academic, 1971.

[153] B. R. Wiese and J. S. Chow. Programmable implementations of xDSL transceiver systems. *IEEE Commun. Mag.*, 38(5):114–119, May 2000.

[154] P. Xia, S. Zhou, and G. B. Giannakis. Adaptive MIMO-OFDM based on partial state information. *IEEE Trans. Signal Processing*, 52(1):202–213, January 2004.

[155] C. Yin and G. Yue. Optimal impulse response shortening for discrete multitone transceivers. *Electronics Letters*, 34:35–36, January 1998.

[156] G. Ysebaert. *Equalization and Echo Cancellation in DMT-based Systems*. PhD thesis, K.U.Leuven, Belgium, April 2004.

[157] G. Ysebaert, K. Van Acker, M. Moonen, and B. De Moor. Constraints in channel shortening equalizer design for DMT-based systems. *Signal Processing*, 83(3):641–648, March 2003.

[158] G. Ysebaert, K. Vanbleu, G. Cuypers, and M. Moonen. ADSL per-tone/per-group optimal equalizer and windowing design. In *Proc. Asilomar Conf. on Signals, Systems and Computers*, Pacific Grove, California, November 2002.

[159] G. Ysebaert, K. Vanbleu, G. Cuypers, and M. Moonen. Bit rate maximizing window and equalizer design for DMT-systems. In *Proc. European Signal Processing Conf. (EUSIPCO)*, Vienna, Austria, September 2004.

[160] G. Ysebaert, K. Vanbleu, G. Cuypers, and M. Moonen. Joint window and time domain equalizer design for bit rate maximization in DMT-receivers. *Accepted for publication in IEEE Trans. Signal Processing*, 2004.

[161] G. Ysebaert, K. Vanbleu, G. Cuypers, M. Moonen, and T. Pollet. Combined RLS-LMS initialization for per tone equalizers in DMT-receivers. *IEEE Trans. Signal Processing*, 51(7):1916–1927, July 2003.

[162] W. Yu, G. Ginis, and J. M. Cioffi. Distributed multiuser power control for digital subscriber lines. *IEEE J. Select. Areas Commun.*, 20(5):1105–1115, June 2002.

[163] N. A. Zervos and I. Kalet. Optimized decision feedback equalization versus optimized orthogonal frequency division multiplexing for high-speed data transmission over the local cable network. In *Proc. IEEE Int. Conf. Communications (ICC)*, pages 1080–1085, Boston, MA, September 1989.

List of publications

International journal papers

- K. Vanbleu, G. Ysebaert, G. Cuypers, M. Moonen, K. Van Acker. Bitrate maximizing time-domain equalizer design for DMT-based systems. In *IEEE Transactions on Communications*, vol. 52, no. 6, pp. 871-876, Jun. 2004.

- K. Vanbleu, G. Ysebaert, G. Cuypers, M. Moonen. On time-domain and frequency-domain MMSE-based TEQ design for DMT transmission. To appear in *IEEE Transactions on Signal Processing*, 2004.

- K. Vanbleu, G. Leus, M. Moonen. Linear and decision-feedback per-tone equalization and narrow-band interference suppression for DMT transmission over IIR channels. Accepted for publication (with minor revision) in *IEEE Transactions on Signal Processing*, 2004.

- G. Ysebaert, K. Vanbleu, G. Cuypers, M. Moonen, T. Pollet. Combined RLS-LMS initialization for per tone equalizers in DMT-receivers. In *IEEE Transactions on Signal Processing*, vol. 51, no. 7, pp. 1916-1927, Jul. 2003.

- G. Ysebaert, K. Vanbleu, G. Cuypers, M. Moonen. Split SR-RLS for the joint initialization of the per-tone equalizers and per-tone echo cancelers in DMT-based receivers. In *EURASIP Journal on Applied Signal Processing*, vol. 2004, no. 10, pp. 1433-1445.

- G. Ysebaert, K. Vanbleu, G. Cuypers, M. Moonen. Joint window and time domain equalizer design for bit rate maximization in DMT-receivers. To appear in *IEEE Transactions on Signal Processing*, 2004.

International conference papers

- K. Vanbleu, G. Leus, M. Moonen. Per tone equalization for DMT-based transmission over IIR channels. In *Proc. of IEEE Global Communications Conference (GLOBECOM)*, pp. 405-409, San Antonio, Texas, Nov. 2001.

- K. Vanbleu, G. Ysebaert, M. Moonen, P. Vandaele. Combined Equalization and Alien Crosstalk Cancellation in ADSL. In *Proc. of IEEE Benelux Signal Processing Symposium (SPS)*, pp. 49-52, Leuven, Belgium, Mar. 2002.

- K. Vanbleu, G. Ysebaert, M. Moonen, P. Vandaele. Combined equalization and alien crosstalk cancellation in ADSL receivers. In *Proc. of European Signal Processing Conference (EUSIPCO)*, pp. 281-284, Toulouse, France, Sep. 2002.

- K. Vanbleu, G. Ysebaert, G. Cuypers, M. Moonen, K. Van Acker. Bitrate maximizing time-domain equalizer design for DMT-based systems. In *Proc. of IEEE International Conference on Communications (ICC)*, pp. 2360-2364, Anchorage, Alaska, May 2003.

- K. Vanbleu, G. Ysebaert, G. Cuypers, M. Moonen. On the relation between time-domain equalizers and per-tone equalizers for DMT-based systems. In *Proc. of IEEE Benelux Signal Processing Symposium (SPS)*, Hilvarenbeek, the Netherlands, Apr. 2004.

- K. Vanbleu, G. Ysebaert, G. Cuypers, M. Moonen. Adaptive bitrate maximizing TEQ design for DMT-based systems. In *Proc. of IEEE International Conference on Acoustics, Speech and Signal Processing (ICASSP)*, pp. 1057-1060, Montreal, Canada, May 2004.

- K. Vanbleu, G. Ysebaert, G. Cuypers, M. Moonen. On time-domain and frequency-domain MMSE-based TEQ designs for DMT transmission. In *Proc. of the European Conference on Signal Processing (EUSIPCO)*, Vienna, Austria, Sep. 2004.

- G. Ysebaert, K. Vanbleu, G. Cuypers, M. Moonen, K. Van Acker. Double talk cancellation in echo cancelled DMT-systems. In *Proc. of IEEE Benelux Signal Processing Symposium (SPS)*, pp. 169-172, Leuven, Belgium, Mar. 2002.

- G. Ysebaert, K. Vanbleu, G. Cuypers, M. Moonen, K. Van Acker. Double talk cancellation in echo cancelled DMT-systems. In *Proc. of the European Signal Processing Conference (EUSIPCO)*, pp. 381-384, Toulouse, France, Sep. 2002.

- G. Ysebaert, K. Vanbleu, G. Cuypers, M. Moonen. ADSL Per-Group/Per-Tone Equalizer and Window Design. In *Proc. of Asilomar Conference on Signals, Systems and Computers*, pp. 383-387, Pacific Grove, California, Nov. 2002.

- G. Cuypers, K. Vanbleu, G. Ysebaert, M. Moonen. Reduction by intra-symbol windowing in DMT-based transmitters. In *Proc. of IEEE International Conference on Acoustics, Speech and Signal Processing (ICASSP)*, pp. 532-535, , Hong Kong, China, Apr. 2003.

- G. Ysebaert, K. Vanbleu, G. Cuypers, M. Moonen, J. Verlinden. Echo cancellation for discrete multitone frame-asynchronous ADSL transceivers. In *Proc. of IEEE International Conference on Communications (ICC)*, pp. 2421-2425, Anchorage, Alaska, May 2003.

- G. Cuypers, K. Vanbleu, G. Ysebaert, M. Moonen, P. Vandaele. Combining raised Cosine windowing and per tone equalization for RFI mitigation in DMT receivers. In *Proc. of IEEE International Conference on Communications (ICC)*, pp. 2852-2856, Anchorage, Alaska, May 2003.

- G. Ysebaert, K. Vanbleu, G. Cuypers, M. Moonen. Bit rate maximizing window and equalizer design for DMT-systems. In *Proc. of the European Conference on Signal Processing (EUSIPCO)*, Vienna, Austria, Sep. 2004.

Abstracts

- K. Vanbleu, M. Moonen. On the relationship between frequency domain system identification and the equalization of a DMT/OFDM system. IUAP study day, Leuven, Belgium, Dec. 2000.

- K. Vanbleu, M. Moonen. On the relationship between frequency domain system identification and the equalization of a DMT/OFDM system. 20th Benelux Meeting on Systems and Control, Houffalize, Belgium, Mar. 2001.

Submitted papers

- K. Vanbleu, G. Ysebaert, G. Cuypers, M. Moonen. Bitrate maximizing per-group equalization for DMT-based systems. Internal report ESAT-SISTA/TR2003-48, K.U.Leuven, Belgium, submitted to *Signal Processing*, Aug. 2003.

- K. Vanbleu, G. Ysebaert, G. Cuypers, M. Moonen. Adaptive bitrate maximizing time-domain equalizer design for DMT-based systems. Internal report ESAT-SISTA/TR2003-168, K.U.Leuven, Belgium, submitted to *IEEE Transactions on Signal Processing*, May 2004.

- G. Cuypers, K. Vanbleu, G. Ysebaert, M. Moonen, P. Vandaele. Combined per tone equalization and receiver windowing in DSL receivers : WiPTEQ. Internal report ESAT-SISTA/TR2002-125, K.U.Leuven, Belgium, submitted to *Signal Processing*, Aug. 2002.

- R. K. Martin, K. Vanbleu, M. Ding, G. Ysebaert, M. Milosevic, B. Evans, M. Moonen, C. Johnson Jr. Unification and evaluation of equalization structures and design algorithms for discrete multitone modulation systems. Internal report ESAT-SISTA/TR2003-51, K.U.Leuven, Belgium, submitted to *IEEE Transactions on Signal Processing*, Dec. 2003.

- R. K. Martin, K. Vanbleu, M. Ding, G. Ysebaert, M. Milosevic, B. Evans, M. Moonen, C. Johnson Jr.. Implementation complexity and communication performance tradeoffs in discrete multitone modulation equalizers. Internal report ESAT-SISTA/TR2003-52, K.U.Leuven, Belgium, in preparation for submission to *IEEE Transactions on Signal Processing*.

- G. Ysebaert, K. Vanbleu, G. Cuypers, M. Moonen, J. Verlinden. Echo cancellation for discrete multitone frame-asynchronous ADSL transceivers. Internal report ESAT-SISTA/TR2002-186, K.U.Leuven, Belgium, submitted to *IEEE Transactions on Communications*, Dec. 2002.

Curriculum vitae

Koen vanbleu was born in Bonheiden, Belgium, in 1976. In 1999, he received the electrical engineering degree in applied sciences (summa cum laude) from the Katholieke Universiteit Leuven, Belgium. For his Master's thesis, entitled 'Speech enhancement using iterative Wiener filtering techniques', he visited Aalborg University, Aalborg, Denmark (Prof. Søren Holdt Jensen). In October 1999, he started his Ph.D. at the SCD-SISTA laboratories of the Department of Electrical Engineering (Faculty of Applied Sciences) under the supervision of Prof. Marc Moonen. His research interests are in the area of digital signal processing techniques for telecommunication systems.

From 1999 until 2003, he was funded by the Fonds voor Wetenschappelijk Onderzoek - Vlaanderen. He has been involved in several research projects in cooperation with Alcatel, Antwerp. During the fall of 2002, he visited the BARD research group, headed by Prof. C.R. Johnson, Jr., at Cornell University, NY, USA.